OFFICIAL FILE COPY

AMMRC MS 82-4

AD A119 510

PROCEEDINGS OF THE ARMY SYMPOSIUM ON SOLID MECHANICS, 1982 - CRITICAL MECHANICS PROBLEMS IN SYSTEMS DESIGN

September 1982

Approved for public release; distribution unlimited.

ARMY MATERIALS AND MECHANICS RESEARCH CENTER
Watertown, Massachusetts 02172

OFFICIAL FILE COPY

The findings in this report are not to be construed as an official Department of the Army position, unless so designated by other authorized documents.

Mention of any trade names or manufacturers in this report shall not be construed as advertising nor as an official indorsement or approval of such products or companies by the United States Government.

DISPOSITION INSTRUCTIONS

Destroy this report when it is no longer needed.
Do not return it to the originator.

UNCLASSIFIED

SECURITY CLASSIFICATION OF THIS PAGE (When Data Entered)

REPORT DOCUMENTATION PAGE		READ INSTRUCTIONS BEFORE COMPLETING FORM
1. REPORT NUMBER AMMRC MS 82-4	2. GOVT ACCESSION NO.	3. RECIPIENT'S CATALOG NUMBER
4. TITLE (and Subtitle) Proceedings of the Army Symposium on Solid Mechanics, 1982 - Critical Mechanics Problems in Systems Design		5. TYPE OF REPORT & PERIOD COVERED Final Report 6. PERFORMING ORG. REPORT NUMBER
7. AUTHOR(s)		8. CONTRACT OR GRANT NUMBER(s)
9. PERFORMING ORGANIZATION NAME AND ADDRESS Army Materials and Mechanics Research Center Watertown, MA 02172 DRXMR-S		10. PROGRAM ELEMENT, PROJECT, TASK AREA & WORK UNIT NUMBERS
11. CONTROLLING OFFICE NAME AND ADDRESS US Army Materiel Development and Readiness Command Alexandria, VA 22333		12. REPORT DATE September 1982 13. NUMBER OF PAGES 484
14. MONITORING AGENCY NAME & ADDRESS(if different from Controlling Office)		15. SECURITY CLASS. (of this report) Unclassified 15a. DECLASSIFICATION/DOWNGRADING SCHEDULE

16. DISTRIBUTION STATEMENT (of this Report)

Approved for public release; distribution unlimited.

17. DISTRIBUTION STATEMENT (of the abstract entered in Block 20, if different from Report)

18. SUPPLEMENTARY NOTES

19. KEY WORDS (Continue on reverse side if necessary and identify by block number)

Ballistics	Fatigue	Mechanical Properties
Engineering	Impact	Mechanics
Failure (Mechanics)	Ordnance	Shock

20. ABSTRACT (Continue on reverse side if necessary and identify by block number)

Proceedings of the Army Symposium on Solid Mechanics, 1982-4 Critical Mechanics Problems in Systems Design, held at Bass River, Cape Cod, Massachusetts September 21-23, 1982

DD FORM 1 JAN 73 1473 EDITION OF 1 NOV 65 IS OBSOLETE

UNCLASSIFIED

SECURITY CLASSIFICATION OF THIS PAGE (When Data Entered)

PREFACE

The Army Symposium on Solid Mechanics, 1982 was the eighth in a series of biennial meetings sponsored by the Army Materials and Mechanics Research Center (AMMRC) in Watertown, Massachusetts. A Work-In-Progress Session(s) has been incorporated into these conferences since 1974 (called Ongoing Case Studies Session at the 1978 meeting). These sessions are comprised of a series of brief presentations and discussions of current, but not necessarily complete, research relating to the theme of the meeting. Abstracts of these presentations are published in a companion document to the regular proceedings; those presented at this 1982 symposium are published in AMMRC MS 82-5, dated September 1982. The transactions of earlier symposia are listed on page iv of this document.

Participation in these symposia has broadened with time. Starting with the 1972 meeting, papers have been solicited from in-house and contract researchers and designers for the Navy, Air Force, and other government agencies, in addition to those for the Army. The symposium committee has been expanded several times; its current membership is as shown on page v. These expansions were made in recognition of the fact that many mechanics research and/or design problems are not unique to a single service or government agency.

Essentially, these symposia are a vehicle for enhancing the responsiveness of mechanics research efforts for the design of advanced military systems. They also facilitate communications and coordination between and among researchers and designers having common military theme interests, whether they work for a government service or agency, industry, or at some university or research institute.

No endeavor of the magnitude of this 1982 symposium could have been successfully conducted without the enthusiastic cooperation and support of many individuals and organizations. We greatfully acknowledge:

The many authors, participants and session chairmen who made this conference such a success.

The manuscript reviewers from universities, industry and government organizations, for their diligence in carrying out a thankless task.

Brigadier General Church M. Matthews, Jr., Deputy Commanding General for Research and Development, of the U.S. Army Tank-Automotive Command in Warren, Michigan, who delivered a very interesting and relevant Keynote Address.

Finally, the staff of the Technical Reports Office of AMMRC for their unflagging efforts in the preparation and printing of numerous sympsoium materials.

DOCUMENTS IN THIS SYMPOSIA SERIES*

1968 Theme: (General - Solid Mechanics)
Proceedings: AMMRC MS 68-09, September 1968, AD 675463

1970 Theme: Lightweight Structures
Proceedings: AMMRC MS 70-05, December 1970, AD 883455L

1972 Theme: The Role of Mechanics in Design - Ballistic Problems
Proceedings: AMMRC MS 73-2, September 1973, AD 772827

1974 Theme: The Role of Mechanics in Design - Structural Joints
Proceedings: AMMRC MS 74-8, September 1974, AD 786543
Work-In-Progress: AMMRC MS 74-9, September 1974, AD 786524
Bibliography: AMMRC MS 74-10, September 1974, AD 786520

1976 Theme: Composite Materials: The Influence of Mechanics of Failure on Design
Proceedings: AMMRC MS 76-2, September 1976, AD AO29735
Work-In-Progress: AMMRC MS 76-3, September 1976, AD AO29736

1978 Theme: Case Studies on Structural Integrity and Reliability
Proceedings: AMMRC MS 78-3, September 1978, AD AO59834/2G1
Ongoing Case Studies: AMMRC MS 78-4, September 1978, AD AO59605/6G1

1980 Theme: Designing for Extremes: Environment, Loading, and Structural Behavior
Proceedings: AMMRC MS 80-4, September 1980, AD AO90684
Work-In-Progress: AMMRC MS 80-5, September 1980, AD AO90685
Opening Session Addresses: AMMRC MS 80-6, September 1980, AD AO90686

1982 Theme: Critical Mechanics Problems in Systems Design
Proceedings: AMMRC MS 82-4, September 1982
Work-In-Progress: AMMRC MS 82-5, September 1982

---

* These documents may be ordered from the National Technical Information Service, U.S. Department of Commerce, Springfield, VA 22161

SYMPOSIUM COMMITTEE

E. M. LENOE, Chairman, AMMRC
J. F. MESCALL, Vice Chairman, AMMRC
R. J. MORRISSEY, Secretary, AMMRC
J. M. AYOUB, Coordinator, AMMRC

TECHNICAL PAPERS AND PROGRAM

J. ADACHI, Chairman, AMMRC
A. A. ANCTIL, AMMRC
R. BARSOUM, AMMRC
L. BERKE, NASA-Lewis Research Center
C. I. CHANG, Naval Research Laboratory
H. D. CURCHACK, Harry Diamond Laboratories
C. M. ELDRIDGE, Army Missile command
J. FEROLI, Army Test and Evaluation Command
G. L. FILBEY, Jr., Ballistic Research Laboratories
R. FOYE, Army Aviation R&D Command
J. T. GARVIN, AMMRC
A. J. GUSTAFSON, Army Aviation R&D Command
H. HATCH, AMMRC
G. E. MADDUX, Air Force Wright Aeronautical Labs
J. F. MESCALL, AMMRC
D. R. MULVILLE, Naval Research Laboratory
D. M. NEAL, AMMRC
D. W. OPLINGER, AMMRC
R. P. PAPIRNO, AMMRC
R. QUATTRONE, Army Construction R&E Lab
E. W. ROSS, Jr., Army Natick R&D Command
M. E. ROYLANCE, AMMRC
E. SAIBEL, Army Resarch Office
T. SIMKINS, Army Armament R&D Command
J. H. SMITH, National Bureau of Standards
D. M. TRACEY, AMMRC

WORK-IN-PROGRESS SESSIONS

G. E. MADDUX, Co-Chairman, Air Force Wright Aeronautical Labs
R. P. PAPIRNO, Co-Chairman, AMMRC

SIMULATIONS OF BALLISTIC IMPACT SITUATIONS INVOLVING DEEP PENETRATION AND PERFORMATION OF TARGETS WITH A LAGRANGIAN IMPACT CODE 96

B. E. Ringers, Army Ballistic Research Laboratory

LABORATORY TESTING OF LONG ROD PENETRATOR AND SABOT COMPONENTS . . 110

M. A. Scavullo and J. H. Underwood, Army
Armament R&D Command

SESSION II: FATIGUE AND FRACTURE

ENERGY DENSITY THRESHOLDS ASSOCIATED WITH A MOVING HEAT SOURCE . . 129

G. C. Sih, Lehigh University, and
C. I. Chang, Naval Research Laboratory

ANALYSIS OF MIXED MODE CRACK GROWTH IN SHIP HULL MATERIAL UNDER DYNAMIC LOADING 143

C. R. Barnes, J. Ahmad, and
M. F. Kanninen, Battelle Columbus Laboratories

FATIGUE AND FRACTURE EVALUATION OF THE A-7E ARRESTING GEAR DRAG LINK 159

D. L. Merkord, C. E. Dumesnil, and T. D. Gray
Vought Corporation

A NONLINEAR FRACTURE MECHANICS PREDICTIVE PROCEDURE FOR THE SHORT CRACK EFFECT IN FATIGUE 177

J. Ahmad, A. T. Hopper, M. F. Kanninen,
B. N. Leis, and V. Papaspyropoulos
Battelle Columbus Laboratories

ELASTIC-PLASTIC FRACTURE MECHANICS ANALYSIS OF SMALL CRACKS 203

G. G. Trantina and H. G. deLorenzi
General Electric Company

APPLICATION OF AN ELASTIC-PLASTIC METHODOLOGY TO STRUCTURAL INTEGRITY EVALUATION 215

H. A. Ernst and J. D. Landes
Westinghouse R&D Center

CONTENTS

OPENING SESSION

WELCOME 3

Col. G. W. Sibert, Deputy Director/Commander,
Army Materials and Mechanics Research Center

INTRODUCTORY REMARKS 7

E. M. Lenoe, Chief, Mechanics of Materials Division,
Army Materials and Mechanics Research Center

KEYNOTE ADDRESS 9

BG C. M. Matthews, Jr., Deputy Commanding General
for Research and Development, Army Tank-Automotive
Command

SESSION I: SHOCK-IMPACT

VULNERABILITY OF ARMORED PANELS TO AIR BLAST 13

N. J. Huffington, Jr., Army Ballistics Research Laboratory

MAGNESIUM PROJECTILE IMPACT BEHAVIOR 28

J. C. Schulz, O. E. R. Heimdahl and S. Finnegan
Naval Weapons Center

BLAST RESPONSE OF A HARDENED ARMY ISO SHELTER 43

R. W. Milligan and A. Lush, Kaman AviDyne, and
W. L. Crenshaw, Army Natick Laboratories

SHOCKS IN SATURATED SAND 66

B. M. Lempriere, The Boeing Aerospace Company

THEORETICAL AND EXPERIMENTAL STUDY OF THE RESPONSE OF CLAMPED ROLLED
HOMOGENEOUS STEEL ARMOR PLATES TO CLOSE-IN BLAST LOADING 80

A. R. Kiwan, Army Ballistic Research Laboratory

FLAW DETECTION RELIABILITY ASSESSMENT AND ANALYSIS 238

W. D. Rummel and R. A. Rathke
Martin Marietta Corporation

SESSION III: COMPOSITE STRUCTURES

COMPOSITE MATERIAL STRUCTURES FOR TACTICAL SHELTERS:
A COST/WEIGHT STUDY 257

J. P. Fanucci, Kaman AviDyne

FAILURE ANALYSIS OF COMPOSITE LAMINATES USING A TENSOR
POLYNOMIAL STRENGTH CRITERION 271

R. C. Tennyson, G. Elliott, and J. S. Hansen, University of
Toronto

STATIC INDENTATION TESTS ON COMPOSITE PLATES FOR IMPACT
SUSCEPTABILITY EVALUATION 288

G. M. Bostaph, Army Aviation R&D Command, and W. Elber,
NASA-Langley Research Center

MECHANICS PROBLEMS IN COMPOSITE MAIN ROTOR BLADE DESIGN 318

R. L. Foye and D. J. Baker, Army Aviation R&D Command, and
S. P. Petrie and A. O. King, Army Materials and Mechanics
Research Center

AN EFFICIENT METHOD FOR DETERMINING THE "A" AND "B" DESIGN
ALLOWABLES 343

D. M. Neal and L. Spiridigliozzi, Army Materials and Mechanics
Research Center

DESIGN AND FABRICATION OF LOW COST COMPOSITE COMPRESSOR
BLADES 380

C. D. Houghton, W. W. Houghton, and M. E. Roylance, Army
Materials and Mechanics Research Center, and J. A. McElman,
University of Lowell

EFFECTS OF SIMULATED LIGHTNING ON COMPOSITE AND METAL JOINTS 400

W. E. Howell, NASA-Langley Research Center, and J. A. Plumer,
Lightning Technologies, Inc.

SESSION IV: STRUCTURAL DESIGN

CYCLIC TORSION OF A CIRCULAR CYLINDER 405

P. C. T. Chen, Army Armament R&D Command, and M. R. Aboutorabi and H. C. Wu, The University of Iowa

DETERMINATION OF PROOF LOAD CRITERIA FOR THE F-14 ARRESTING GEAR HOOK SHANK 416

K. D. Jordan, C. E. Dumesnil, and T. D. Gray, Vought Corporation

EVALUATION OF THE RELATIVE HYDROGEN EMBRITTLEMENT SUSCEPTABILITY OF ESR 4340 STEEL 439

L. Raymond, METTEK Laboratories, and C. Beneker, Parker Hannifin Corporation

A PHOTOELASTIC INVESTIGATION OF STRESSES AND LOAD DISTRIBUTIONS IN LUG-GROOVE JOINTS 454

Y. F. Cheng, Army Armament R&D Command

IMPROVED M-11 COPPER CRUSHER GAGE 471

J. M. Bender, Army Ballistic Research Laboratory

NONLINEAR ANALYSIS OF IN-BORE PROJECTILES 481

S. C. Chu, Army Armament R&D Command

OPENING SESSION

Chairman: R. Shea
Chief, Mechanics and Engineering Laboratory
Army Materials and Mechanics Research Center

WELCOME 3

Col. G. W. Sibert, Deputy Director/Commander,
Army Materials and Mechanics Research Center

INTRODUCTORY REMARKS 7

E. M. Lenoe, Chief, Mechanics of Materials Division,
Army Materials and Mechanics Research Center

KEYNOTE ADDRESS 9

BG C. M. Matthews, Jr., Deputy Commanding General
for Research and Development, Army Tank-Automotive
Command

WELCOME

GEORGE W. SIBERT
Colonel, Infantry
Deputy Director/Commander
Army Materials and Mechanics Research Center
Watertown, Massachusetts 02172

It is my pleasure to initiate this year's Army Symposium on Solid Mechanics and to welcome you here today. In addition to greeting you, the Symposium Committee has asked that I make a few introductory remarks. Since some of you are newcomers to this Symposium series, as am I, it seems appropriate to describe briefly some of the Army Materials and Mechanics Research Center (AMMRC) activities and capabilities. I will also highlight recent areas of emphasis at the Center. While AMMRC may be new to some of you, it is interesting to reflect that AMMRC is not new to the United States defense activities. AMMRC is proud, not only of its present achievements, but also of its history, traceable to the era of Andrew Jackson's Presidency. For over 164 years, AMMRC and it predecessor agencies at the Watertown Arsenal have made important contributions to the U.S. Army.

THE AMMRC MISSION

MATERIAL/MATERIEL - a one-letter difference which results in a change in meaning that summarizes the relationship between AMMRC and its parent command, the US Army Materiel Development and Readiness Command (DARCOM). The transition of raw materials into Army equipment has been the concern of AMMRC and its forerunner, the Watertown Arsenal, since 1816; from cast iron, leather and wood to the high strength metals, ceramics and composites required for the high technology battlefield.

Today's AMMRC is the modern materials research and development activity responsible for managing and conducting the DARCOM research and exploratory development program in materials and solid mechanics. Its charters as lead laboratory for materials, solid mechanics, and materials testing technologies (MTT) require the Center to possess the in-house technical expertise and facilities to perform research and development (R&D) projects ranging from the synthesis of new and improved materials and designs to the prototype manufacturing of components for Army weapons systems.

OTHER FUNCTIONS

In addition to its management of the materials and mechanics research program, AMMRC serves the Army in several other capacities. The Center develops both destructive and nondestructive methods of materials testing and manages the MTT program for DARCOM. As an integral part of this mission AMMRC conducts the DARCOM Nondestructive Testing (NDT) Training Certification Program and provides NDT field support throughout the Department of Defense (DOD). The Center is also responsible for managing and directing a major portion of the Defense Standards and Specifications Program for materials.

The Ballistic Missile Defense Materials Program Office (BMDMPO) at AMMRC is a special project organization executing high priority research and development programs concerned with the development of materials for advanced strategic and tactical missiles.

RESEARCH PROGRAM

Through its efforts, AMMRC addresses the major materials issues facing the Army today. Worldwide operational capability for the Army requires an increase in performance, durability and survivability of Army materiel and the capability to produce that material in sufficient quantities at reasonable cost. Logistical burdens in a fuel-short environment dictate the development of new lightweight materials concepts, and the integrated battlefield of the future will expose Army materials to the threat of chemical, nuclear and laser attack, as well as improved conventional weapons.

In addressing these problems AMMRC has expanded its scope over the years to include a wide range of new materials. Early emphasis on metals development continues today with projects in the armor and armor penetrating materials areas, research into materials processing and net-shape forming techniques, corrosion susceptibility, and surface hardening processes for gear and bearing applications. Research in ceramics has led to many new applications for these materials: silicon nitride components for heat engines, fused silica radomes, laser rods for rangefinders, and photochromic glass for laser protection. Ceramics are also finding increased use in combination with other materials for lightweight armor applications.

The continued development of metal and organic matrix composites will assure the availability of lightweight high performance materiel for utilization by rapid deployment forces where light weight and high mobility will be key factors in the logistics of future combat. Organic materials such as adhesives, elastomers and polymers are also receiving increased attention with research directed toward such applications as fuel-handling equipment, materials and coatings for protection against chemical agents, fire-resistant materials and wear-resistant track pads for combat vehicles.

Future plans call for increased emphasis in the areas of materials processing technology to insure quantity production of materials at reasonable cost, an advanced development effort in support of specifications and standards and the establishment of an expanded elastomer/rubber capability.

PROGRAM PLANNING

The Center's research program is planned within seven major thrust areas: Aircraft, Armament, Combat and Tactical Vehicles, Missiles, Mobility Equipment, Logistics, and Personnel Support. Among the primary guidance sources in formulating and prioritizing the program are the DARCOM Long Range Research, Development and Acquisition Plan, Training and Doctrine Command priorities and mission area analyses, and the materials need of the DARCOM major subordinate commands and program managers.

In-house research projects are carried out by three Laboratories organized along technology lines, as well as the BMDMPO. The accompanying chart illustrates many of the technology areas in which each in-house Laboratory is currently active.

AMMRC STATISTICS

Vital statistics for the Center include a budget of over 37 million dollars, a manpower strength of 598 civilians and 17 military, half of which are scientific and technical personnel, and a total of 382,000 square feet of laboratory space. These assets are combined to conduct priority technical programs at the leading edge of materials technology, and through close coordination within the entire DARCOM community AMMRC is able to fulfill its mission of assisting the Army in developing and maintaining the finest in modern weapons systems.

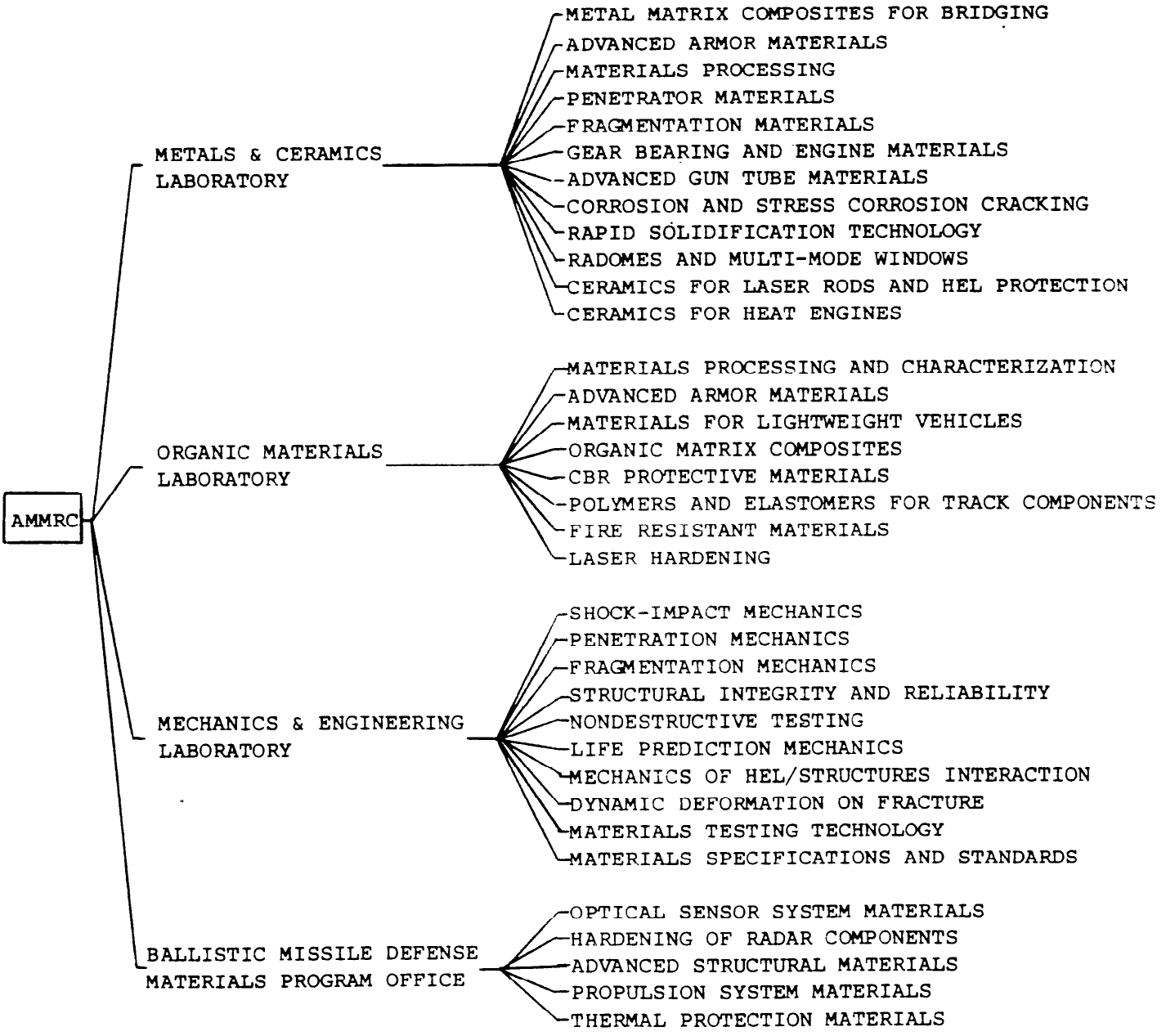
AMMRC
METALS & CERAMICS LABORATORY
METAL MATRIX COMPOSITES FOR BRIDGING
ADVANCED ARMOR MATERIALS
MATERIALS PROCESSING
PENETRATOR MATERIALS
FRAGMENTATION MATERIALS
GEAR BEARING AND ENGINE MATERIALS
ADVANCED GUN TUBE MATERIALS
CORROSION AND STRESS CORROSION CRACKING
RAPID SOLIDIFICATION TECHNOLOGY
RADOMES AND MULTI-MODE WINDOWS
CERAMICS FOR LASER RODS AND HEL PROTECTION
CERAMICS FOR HEAT ENGINES
ORGANIC MATERIALS LABORATORY
MATERIALS PROCESSING AND CHARACTERIZATION
ADVANCED ARMOR MATERIALS
MATERIALS FOR LIGHTWEIGHT VEHICLES
ORGANIC MATRIX COMPOSITES
CBR PROTECTIVE MATERIALS
POLYMERS AND ELASTOMERS FOR TRACK COMPONENTS
FIRE RESISTANT MATERIALS
LASER HARDENING
MECHANICS & ENGINEERING LABORATORY
SHOCK-IMPACT MECHANICS
PENETRATION MECHANICS
FRAGMENTATION MECHANICS
STRUCTURAL INTEGRITY AND RELIABILITY
NONDESTRUCTIVE TESTING
LIFE PREDICTION MECHANICS
MECHANICS OF HEL/STRUCTURES INTERACTION
DYNAMIC DEFORMATION ON FRACTURE
MATERIALS TESTING TECHNOLOGY
MATERIALS SPECIFICATIONS AND STANDARDS
BALLISTIC MISSILE DEFENSE MATERIALS PROGRAM OFFICE
OPTICAL SENSOR SYSTEM MATERIALS
HARDENING OF RADAR COMPONENTS
ADVANCED STRUCTURAL MATERIALS
PROPULSION SYSTEM MATERIALS
THERMAL PROTECTION MATERIALS

INTRODUCTORY REMARKS*

DR. EDWARD M. LENOE
Symposium Chairman
Chief, Mechanics of Materials Division
Army Materials and Mechanics Research Center
Watertown, Massachusetts

* The text of this presentation was not available in time to be included in these proceedings.

SYNOPSIS OF KEYNOTE ADDRESS

C. M. MATTHEWS, JR.
Brigadier General, USA
Deputy Commanding General
for Research and Development
US Army Tank-Automotive Command
Warren, Michigan

The United States Army is beginning a major modernization of its forces. This effort will bring us from the technology of the early fifties and sixties to that of the eighties and nineties. During the next decade we will witness an influx of some 400 new systems, many of them characterized by a remarkable level of technological sophistication.

We are now in the process of developing and fielding these new systems. To be successful will require the combined effort of the Government and industrial technological base. Government labs are a key ingredient in that effort. Our labs must recognize therefore the need to maintain competence in their assigned mission areas and to respond quickly to real-world problems.

SESSION I: SHOCK-IMPACT

Chairman: J. T. Frasier
Deputy Director, Large Caliber Weapon
Systems Laboratory
Army Armament Research and Development Command

VULNERABILITY OF ARMORED PANELS TO AIR BLAST 13

N. J. Huffington, Jr., Army Ballistics Research Laboratory

MAGNESIUM PROJECTILE IMPACT BEHAVIOR 28

J. C. Schulz, O. E. R. Heimdahl and S. Finnegan
Naval Weapons Center

BLAST RESPONSE OF A HARDENED ARMY ISO SHELTER 43

R. W. Milligan and A. Lush, Kaman AviDyne, and
W. L. Crenshaw, Army Natick Laboratories

SHOCKS IN SATURATED SAND 66

B. M. Lempriere, The Boeing Aerospace Company

THEORETICAL AND EXPERIMENTAL STUDY OF THE RESPONSE OF CLAMPED ROLLED HOMOGENEOUS STEEL ARMOR PLATES TO CLOSE-IN BLAST LOADING 80

A. R. Kiwan, Army Ballistic Research Laboratory

SIMULATIONS OF BALLISTIC IMPACT SITUATIONS INVOLVING DEEP PENETRATION AND PERFORMATION OF TARGETS WITH A LAGRANGIAN IMPACT CODE 96

B. E. Ringers, Army Ballistic Research Laboratory

LABORATORY TESTING OF LONG ROD PENETRATOR AND SABOT COMPONENTS . . 110

M. A. Scavullo and J. H. Underwood, Army
Armament R&D Command

VULNERABILITY OF ARMOR PANELS TO AIR BLAST

NORRIS J. HUFFINGTON, JR.
Mechanical Engineer
US Army Ballistic Research Laboratory
US Army Armament Research and Development Command
Aberdeen Proving Ground, MD 21005

ABSTRACT

A methodology suitable for predicting the damage inflicted upon armor panels by blast from nearby high explosive detonations has been developed by extensive modifications of an existing finite-difference structural response code. A new constitutive formulation involving prescribed through-thickness stresses was introduced to account for the effects of intense surface pressures. A triaxial stress criterion for material failure has been incorporated into the analysis to permit prediction of panel rupture and of post-failure response. This methodology was then applied to a case for which comparable experimental results are available.

INTRODUCTION

In the design of lightly armored vehicles it is of critical importance to be able to predict the vulnerability of these systems to effects of high explosive warheads. An especially difficult aspect of this problem is the assessment of the enhanced damage from shaped charge warheads caused by the detonation of the high explosive in close proximity to the target. This paper reports the results of an analysis of the response of structural panels to intense air blast loading with particular concern for the conditions under which a perforation of the panel occurs. However, the peak reflected pressure will be assumed insufficient to produce spallation from the back side of the target panel, thus excluding consideration of explosives in contact with the target. This is not a serious restriction since stand-off explosions can produce catastrophic damage to structural panels.

In selecting an analytical model for structural response calculations the following considerations were taken into account. The model should be capable of treating finite amplitude elastoplastic response of shell structures having a variety of physical edge conditions when subjected to transient distributions of surface pressures. It should have flexibility regarding material constitutive representation, including strain hardening and strain-rate dependence. Further, since the blast loading will initially appear at some interior point on the panel

and then spread rapidly to cover the entire panel, the analysis should properly account for the propagation of shear waves as well as flexural and membrane waves. Also, for the sake of computational economy it was desired to avoid a general three-dimensional analysis. On the basis of these considerations it was concluded that the PETROS 4 code [1,2] provided the most favorable point of departure for developing a satisfactory panel response prediction capability.

RESPONSE METHODOLOGY MODIFICATIONS

The original PETROS 4 computer program offered the user a variety of options and sub-options. For the projected application only the SHEAR option, which includes the effect of transverse shear deformation in a moderately thick shell, would be appropriate. Within this option the user has a choice of elastoplastic constitutive models and of the manner in which the vector $\overline{D}$ is evaluated. $\overline{D}$ represents the three additional degrees-of-freedom associated with the SHEAR model in addition to those possessed by a Kirchhoff shell model. All combinations of these sub-options were exercised and none were found satisfactory for the contemplated application. The difficulties experienced have been discussed by Huffington and Wisniewski [3]. To circumvent these difficulties two major and several minor modifications were performed on the PETROS 4 code.

THROUGH-THICKNESS NORMAL STRESSES

Blast loading from nearby explosive charges produces large values of normal stresses τ_3^3 in the through-thickness direction which should be taken into account in the ensuing elastoplastic response. A study of the multiple reflections of τ_3^3 stress waves has convinced the author that, short of a general three-dimensional treatment, the best representation consistent with the SHEAR model is to prescribe a linear variation of τ_3^3 from the negative of the pressure at the loaded surface to zero at the unloaded surface.

The implementation of this change required an extensive reformulation of the elastoplastic stress calculation procedure. Now only eight strain increment components $\Delta\gamma_j^i$ plus $\Delta\tau_3^3$ are prescribed at each Gauss point* and eight stress increments $\Delta\tau_j^i$ are determined using the von Mises yield function and the associated flow rule. If desired, the value of the strain increment $\Delta\gamma_3^3$ consistent with the constitutive model can also be calculated. Details of this revised elastoplastic stress formulation are given in reference [3].

---

* The geometrically determined $\Delta\gamma_3^3$ is ignored.

CONSTRAINED VARIATION OF THE $\bar{D}$ VARIABLE

The displacement function employed in the PETROS 4 code may be expressed as

$$\bar{u}(\xi^\alpha, \zeta, t) = \bar{u}_K(\xi^\alpha, \zeta, t) + \zeta \bar{D}(\xi^\alpha, t) \qquad \alpha = 1,2 \tag{1}$$

where

$\bar{u}_K$ = displacement variation of the Kirchhoff theory

$\bar{D}$ = additional displacement associated with the SHEAR model

ξ^α = curvilinear coordinates embedded in the shell reference surface (midsurface)

ζ = coordinate normal the shell reference surface

t = time

There are two inconsistencies associated with this displacement function. When the strain-displacement relations are applied to this function it is found that the through-thickness normal strain γ_{33} is independent of ζ. Of course, this is contradicted by the constitutive model cited above which provides generally different values of through-thickness strain at each Gaussian integration point. Further, the three equations of motion for $\bar{D}$ derived by a variational procedure (in rectangular Cartesian coordinates) in the PETROS 4 formulation report [1] appear to contain no restoring force to inhibit the growth or diminution of the normal component of $\bar{D}$.

While it would certainly be appropriate to modify the equations of motion for $\bar{D}$ to remedy this defect, this does not appear feasible without extensive generalization and complication of the PETROS 4 formulation. Alternatively, a procedure has been developed in which

(a) the results from applying the $\bar{D}$ equations of motion are used to calculate strains and stresses (as usual),

(b) the constitutive relations are used to calculate $\Delta\gamma_3^3$ at each Gauss point and these values are averaged through the thickness,

(c) the computational algorithm then branches back to (a) where the components of $\overline{D}$ are modified so as to be (approximately) compatible with the averaged value of $\Delta\gamma_3^3$ and then proceeds forward in the algorithm, recalculating strains and stresses.

This procedure could be repeated iteratively until some convergence criterion is satisfied; however, it has been found that a single recycling step per time step is satisfactory for control of $\overline{D}$ and γ_3^3. The formulation employed for this procedure is also presented in reference [3].

OTHER CHANGES

It was discovered that terms pertaining to surface tractions were absent in the PETROS 4 equations of motion. These terms were introduced symbolically early in the PETROS 4 formulation report [1], then discarded with the argument that they are negligible for thin shells. This may be true but it is definitely not the case for moderately thick shells. Specific relations for calculating these quantities were derived and added to the equations of motion (see [3]).

From equilibrium considerations the contravariant stress tensor τ^{ij} must be symmetric (in the absence of couple stresses). However, the calculations in the STRESS subroutine which provide values of τ^{ij} do not satisfy this requirement exactly. In the original version of PETROS 4 this was handled by selecting τ^{12}, τ^{13}, and τ^{23} as the correct off-diagonal terms and equating τ^{21}, τ^{31}, and τ^{32} to these quantities, respectively. It was felt that this procedure could bias the problem solution so the program was modified to calculate all nine components τ^{ij} and then average the respective symmetrically off-diagonal components; i.e.,

$$\overline{\tau}^{ij} = \overline{\tau}^{ji} = (\tau^{ij} + \tau^{ji})/2 \qquad \text{for } i \neq j \tag{2}$$

This modification was found to have a small but not entirely negligible effect upon lengthy solutions.

The PETROS 4 time marching algorithm requires use of the mixed tensor stresses τ_j^i from the previous time step. However, these quantities were not saved. Rather, they were reconstituted by calculation from the contravariant components which require less memory for storage. But, at an intervening step in the algorithm the metric tensor employed in the reconstitution is updated so

that the reconstituted values of τ_j^i are not identical with those of the previous time step. To avoid error accumulation, the code was revised to store the τ_j^i at some cost in memory but with a corresponding reduction in running time.

MATERIAL FAILURE MODELING

It was decided that initial efforts to model panel rupture would begin with a relatively simple stress-criterion for material failure, eschewing more elaborate progressive failure representations. Although several possible models have been considered, only the two-parameter stress-criterion due to Torre [4] will be discussed. This criterion postulates that the critical factor is a linear combination of the first invariant of the stress tensor and the second invariant of the deviatoric stress tensor. Analytically the Torre criterion may be expressed as

$$\begin{aligned}\Psi(\tau_j^i) \equiv\ & (\tau_1^1)^2 + (\tau_2^2)^2 + (\tau_3^3)^2 - \tau_1^1\tau_2^2 - \tau_2^2\tau_3^3 - \tau_3^3\tau_1^1 \\ & + 3\left[\tau_3^2\tau_2^3 + \tau_1^3\tau_3^1 + \tau_2^1\tau_1^2\right] \\ & + (\beta-1)\sigma_T(\tau_1^1 + \tau_2^2 + \tau_3^3) - \beta\sigma_T{}^2 = 0\end{aligned} \tag{3}$$

where

σ_T = uniaxial tension failure stress

σ_C = uniaxial compression failure stress

$\beta = \sigma_C / \sigma_T$

Failure is assumed to occur when the predicted stresses at the material point under consideration result in $\Psi \geqslant 0$. Alternatively, the Torre failure function may be formulated in terms of principal stresses as

$$\begin{aligned}\Psi(\sigma_i) \equiv\ & \sigma_1{}^2 + \sigma_2{}^2 + \sigma_3{}^2 - \sigma_1\sigma_2 - \sigma_2\sigma_3 - \sigma_3\sigma_1 \\ & + (\beta-1)\sigma_T(\sigma_1 + \sigma_2 + \sigma_3) - \beta\sigma_T{}^2 = 0\end{aligned} \tag{4}$$

As shown in Figure 1 this function corresponds to a paraboloid of revolution in a space whose axes are the principal stresses, which is coaxial with the space diagonal $\sigma_1 = \sigma_2 = \sigma_3$. For $\beta = 1$ the Ψ surface becomes a von Mises

cylinder [5] with intercepts on the axes at $\pm \sigma_T$ while for $\beta \rightarrow \infty$ it becomes the plane $\sigma_1 + \sigma_2 + \sigma_3 = \sigma_T$. When $\beta = 1.5$ the vertex of the Torre paraboloid is located at (σ_T, σ_T, σ_T).

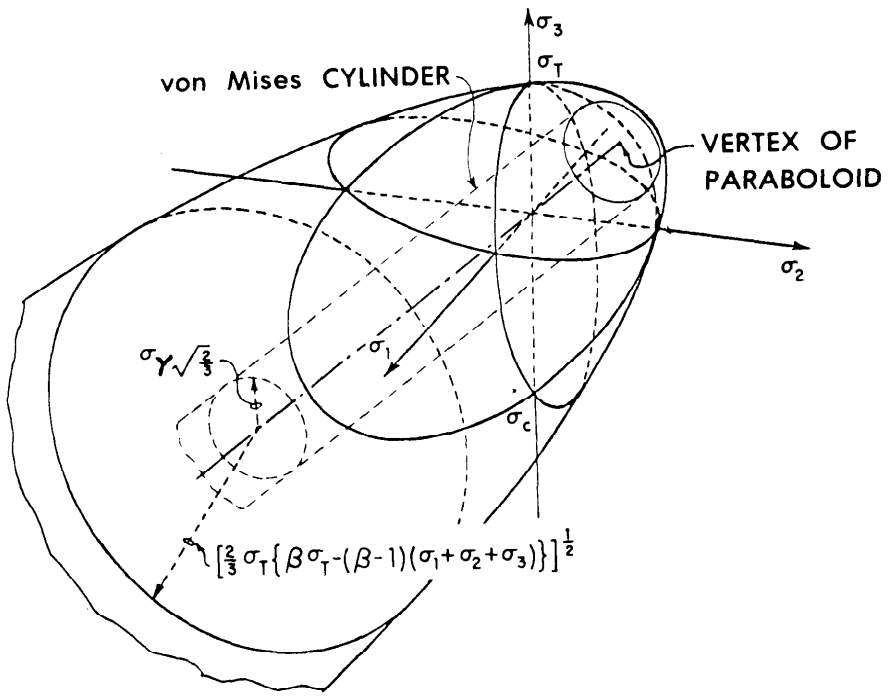

Figure 1. Representation of Failure and Yield Surfaces in Principal Stress Space

Figure 1 also shows the von Mises cylinder in its usual role as a yield function, where it has axis intercepts at $\pm\sigma_Y$. This geometrical representation permits an interesting interpretation. If the material stress state, represented by a point in principal stress space, moves so as to stay within the von Mises cylinder until it reaches the Torre "cap" then the material is elastic to the point of rupture; i.e., the failure is brittle. On the other hand, if the state point moves through the von Mises cylinder before encountering the failure surface plastic deformation occurs before rupture and the failure would be classed as ductile. Since the radius of the von Mises cylinder is non-zero it may be seen that ductile failure cannot occur for stress paths along or close to the space diagonal. Of course, if one is willing to reject the premise of classical plasticity that yielding does not depend upon the mean normal stress, then a yield

function which "closes over" within the failure surface in the triaxial tension octant of stress space may be used and ductile failure will always be possible.

In sequel the Torre criterion is used in conjunction with the von Mises yield criterion. When the Torre criterion is satisfied this material location is flagged by the modified PETROS 4 code and all components of the stress tensor τ_j^i at this location are set to zero. Conceptually the failed material is treated as having been pulverized, i.e., as being incapable of sustaining tension or shear. At each future time step the code calculates stresses at the flagged locations based on incremental strains and then tests on the hydrostatic component of stress $\tau_s = (\tau_1^1 + \tau_2^2 + \tau_3^3) /3$. If this quantity is ≥ 0 all components of stress are again set to zero. For hydrostatic compression at flagged points the normal stress components are each set equal to τ_s but the shear components are set to zero. While other post-failure models are under investigation, results are available at this writing only for the procedure just described.

MATERIAL CHARACTERIZATION

Data on strength properties of rolled homogeneous armor are apparently not as complete as would be desired. The sources identified by the author are (a) dynamic compression data from split Hopkinson bar tests [6] provided by Dr. S. C. Chou of the Army Materials and Mechanics Research Center and (b) quasi-static tensile test curves reported by Benck [7]. These data have been replotted as Cauchy stress versus Almansi strain (the appropriate input for the PETROS 4 code) as the dashed curves in Figure 2. These quantities are related to engineering stress σ and engineering strain ϵ by

$$\text{Almansi strain} = \epsilon (1 + \tfrac{1}{2} \epsilon) \tag{5}$$

$$\text{Cauchy stress} = \sigma (1 + \epsilon) \tag{6}$$

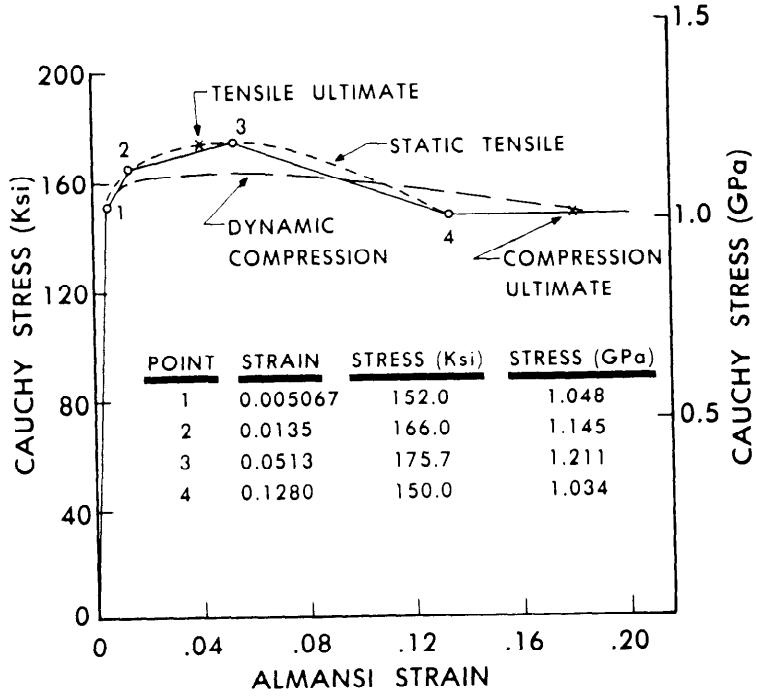

Figure 2. Uniaxial Stress-Strain Data for Rolled Homogeneous Armor

The static tensile specimens failed in the range of 0.127 to 0.150 Almansi strain while the compression specimens did not fail, the maximum strain simply being the largest value obtained in the dynamic tests. Since the present version of the PETROS 4 code has no provision for treating a difference between tensile and compressive stress-strain data the linear segment representation shown by solid lines in Figure 2 was chosen as input to the mechanical sublayer strain hardening constitutive model. The material is assumed to fail in uniaxial tension at point 4 but for compression the stress is taken to be constant beyond this point with no failure occurring. The author does not believe that there are sufficient dynamic data available to justify any formulation for explicit strain-rate dependence of these material properties.

APPLICATION OF ANALYSIS

Calculations have been performed using the PETROS 4 code modified to incorporate the corrections and additions discussed above. The calculations pertain to a 42 inch (1.07 m) square panel of 3/8 inch (9.53 mm) thick rolled homogeneous steel armor having fixed boundaries (see Figure 3).

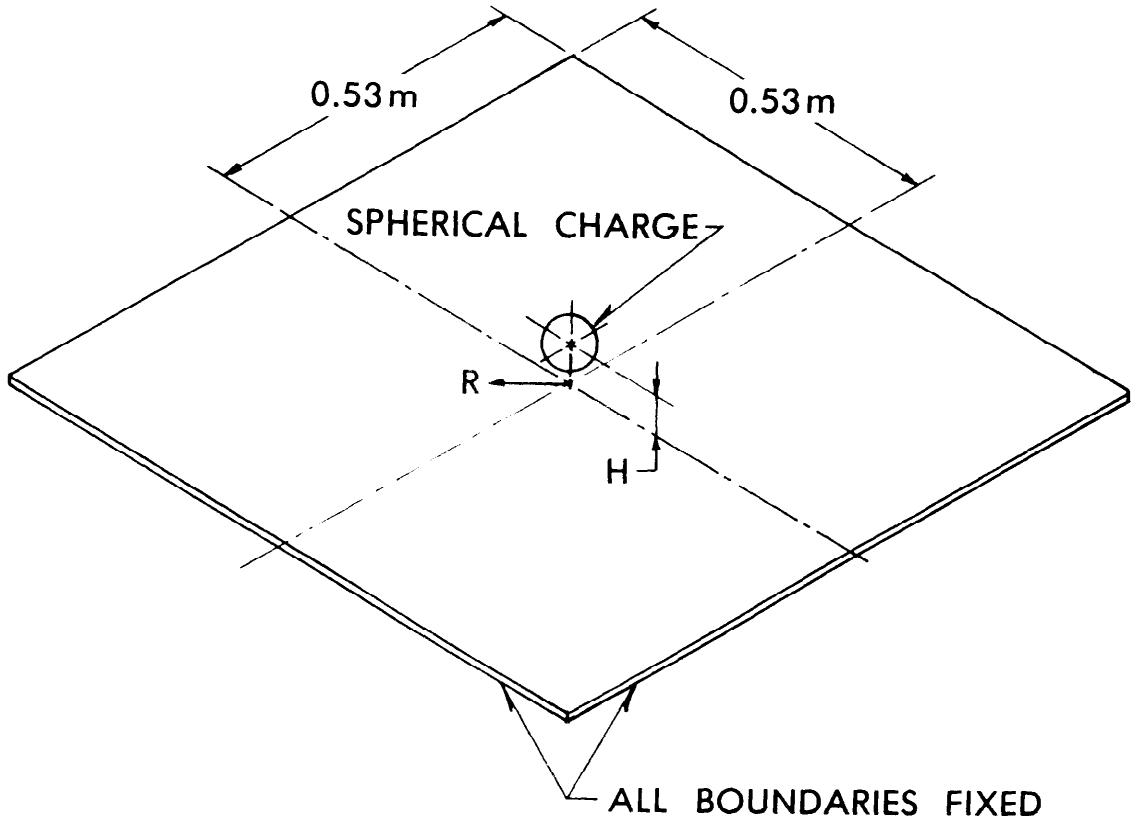

Figure 3. Structural Panel Configuration

BLAST LOADING

The loading selected for this example is that produced by the detonation of a 2 pound (0.907 kg) spherical charge of 50/50 Pentolite at a height-of-burst H = 2.5 inches (63.5 mm) from the center of the sphere to the panel surface (see Figure 3). While there is considerable uncertainty regarding the magnitudes of peak reflected pressure and reflected impulse from charges detonated in such close proximity to targets, the most complete and consistent blast loading definition for this case has been obtained by use of the HULL hydrocode [8] to treat this axisymmetric loading problem (the target panel is regarded as being flush in an infinite plane baffle). The transient surface pressures at selected horizontal radii R from the panel midpoint obtained in this manner are illustrated in Figure 4. The results of the HULL code calculations were interpolated as required in order to obtain pressure-time input for each mesh point of the finite difference grid employed by the PETROS 4 code. No attempt was made to take account of the effect of plate deformation upon the blast loading since it was anticipated that the majority of the plate motion would occur after the blast loading had decayed to negligible values.

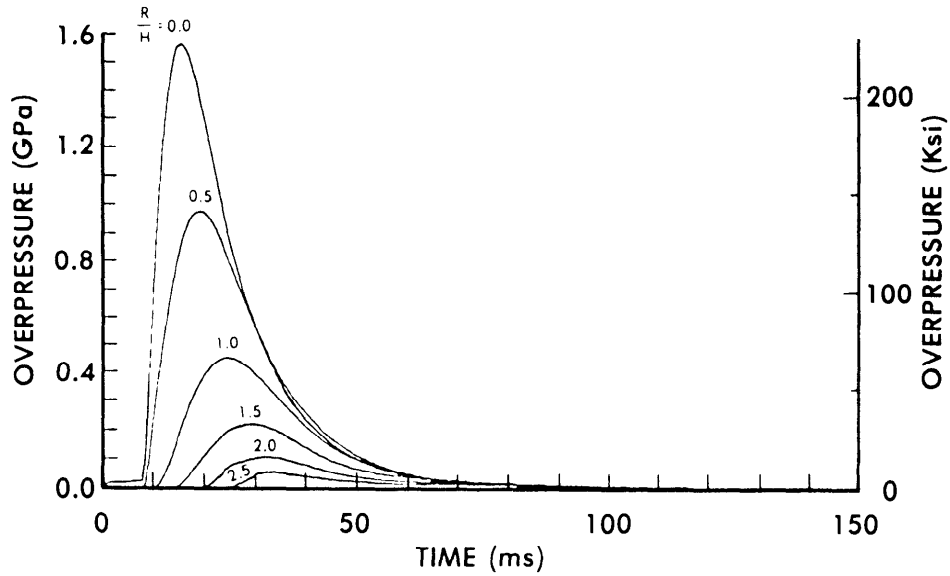

Figure 4. Hydrocode Pressure Plots for Selected Radii

PANEL RESPONSE

For the preceding target material and loading parameters the modified PETROS 4 code predicts that the armor panel will be ruptured. This is consistent with experimental data reported by Kiwan [9]; in fact, the height-of-burst is just slightly below Kiwan's threshold for perforation. Figure 5 shows the predicted deformation pattern (of one-quarter of the panel) and the extent of the region over which the material is predicted to have failed at all Gauss points through the thickness. An estimate of hole size and shape can be made on the basis of this failed region, where the material may be regarded as "flying free."

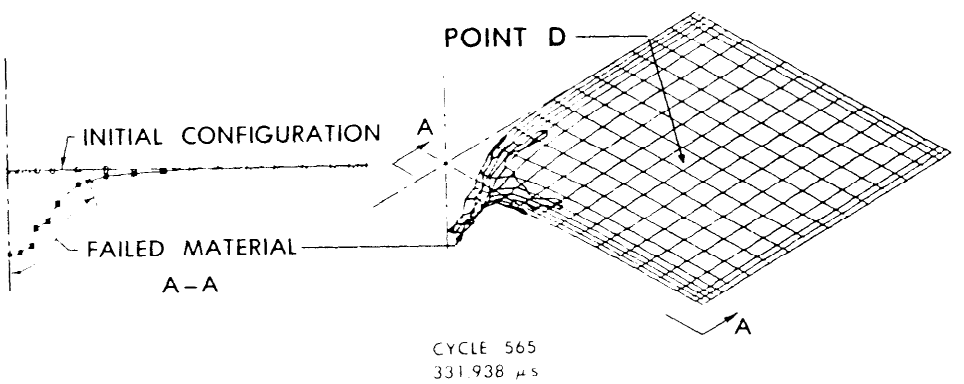

Figure 5. Predicted Panel Deformation

The PETROS 4 code provides a variety of other information of interest to systems designers or vulnerability analysts. The deflection history of a point outside the failed region, point D of Figure 5, is depicted in Figure 6. It may be seen that this location has reached a maximum deflection and started to oscillate before damping was initiated at 528.75 μs. Transient components of strain at the same location are displayed in Figure 7. Stress components at another representative location are illustrated in Figure 8. The stress τ_3^3 is the prescribed through-thickness normal stress component. At this location the Torre failure criterion was triggered at 109.3 μs, after which all stress components were set equal to zero.

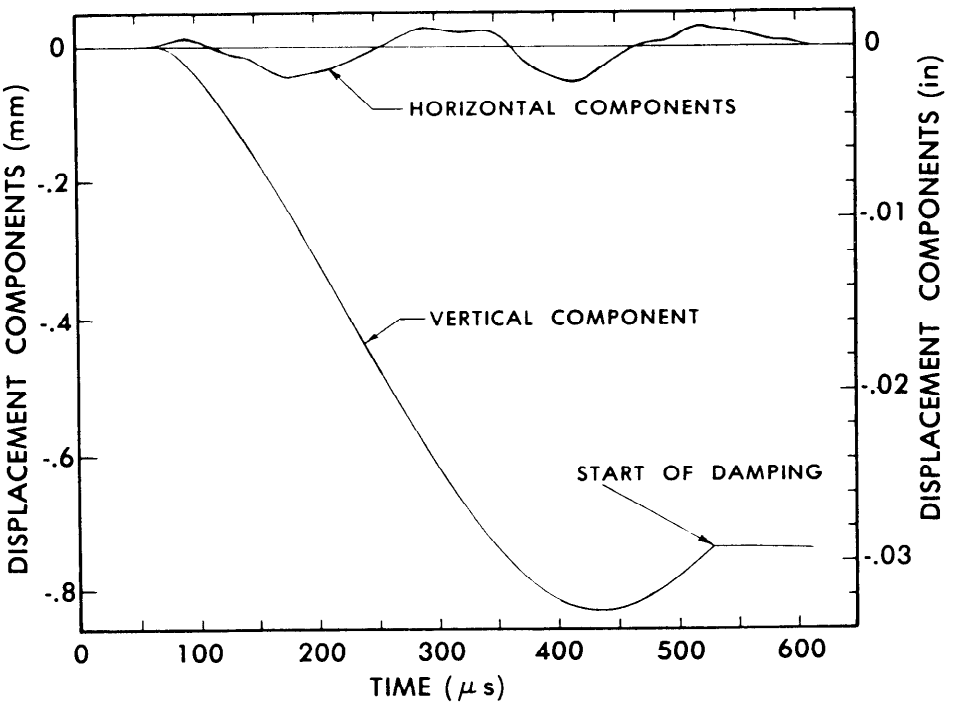

Figure 6. Transient Displacement Components at Point D

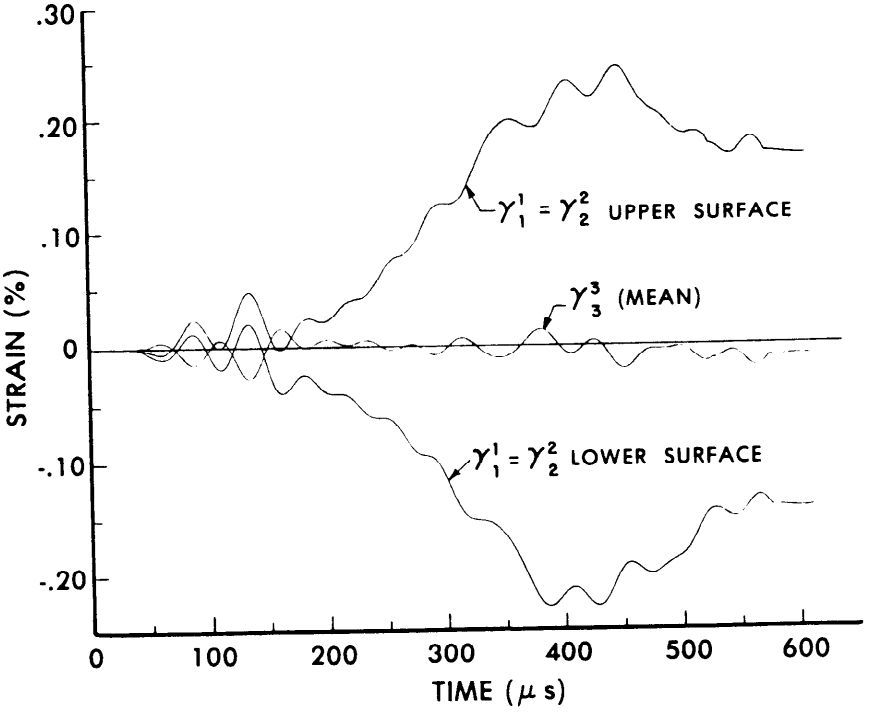

Figure 7. Transient Strain Components at Point D

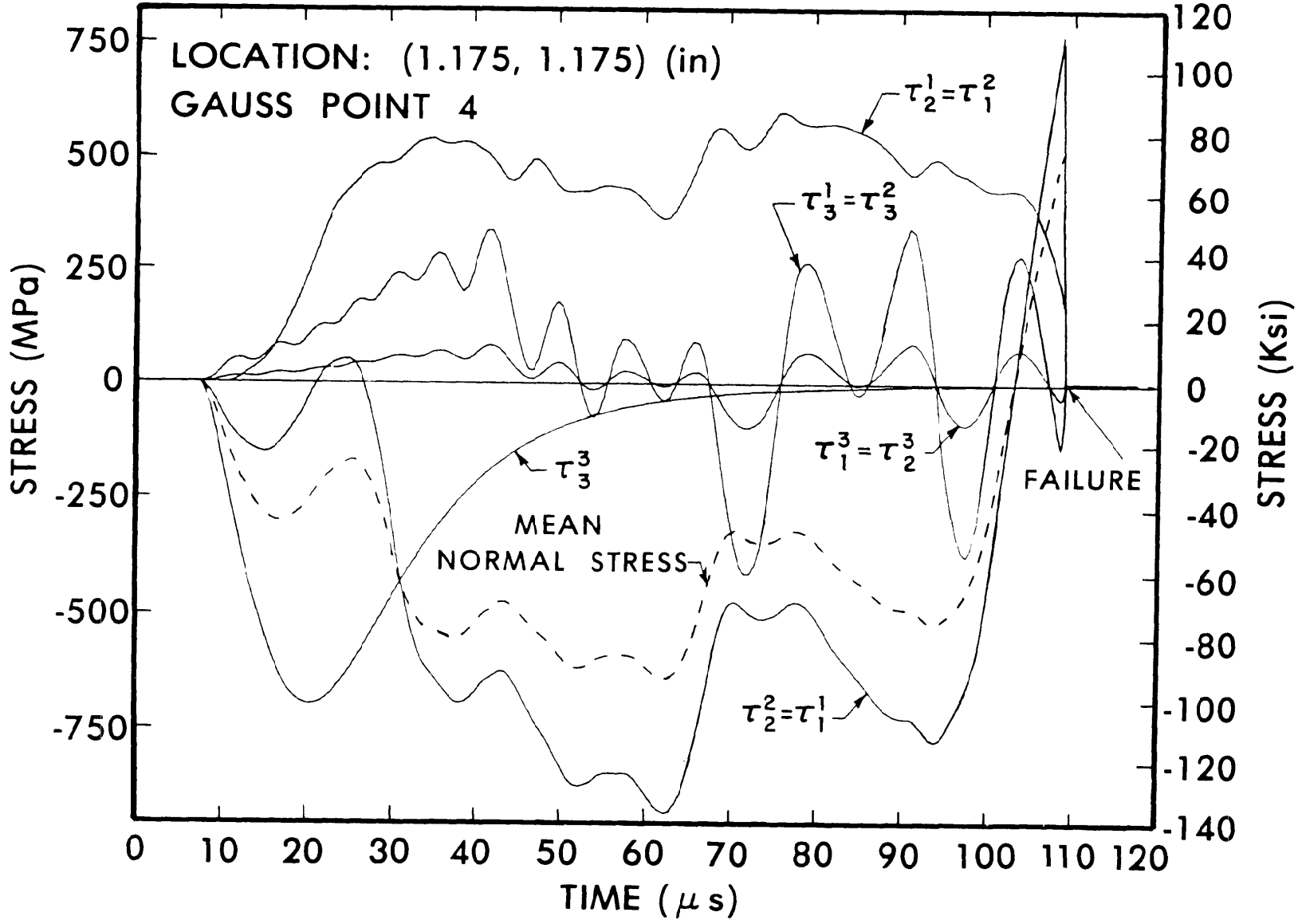

Figure 8. Transient Stress Components

CONCLUDING REMARKS

By extensive modification of the PETROS 4 code a version suitable for treating the response of armor panels to nearby explosive detonations has been developed. A stress-based material failure criterion was incorporated into the response model in order to predict conditions under which panel rupture may be expected. Preliminary comparisons with experimental evidence indicate that this criterion may adequately represent the failure characteristics of blast loaded panels. However, additional study of this and other failure representations is necessary before a conclusive determination can be made. When uncertainties regarding blast loading intensities are resolved it should be possible to conduct parametric evaluations of the vulnerability of armor panels to air blast loading.

ACKNOWLEDGMENT

The author is greatly indebted to Mr. Henry Wisniewski for his assistance with the PETROS 4 code calculations and to Mr. Richard E. Lottero for providing the HULL code blast loading distribution.

REFERENCES

1. Pirotin, S. D., Morino, L., Witmer, E. A., and Leech, J. W., "Finite-Difference Analysis for Predicting Large Elastic-Plastic Transient Deformations of Variable-Thickness Kirchhoff, Soft-Bonded Thin, and Transverse-Shear-Deformable Thicker Shells," US Army Ballistic Research Laboratory Contract Report No. 315, September 1976.

2. Pirotin, S. D., Berg, B. A., and Witmer, E. A., "PETROS 4: New Developments and Program Manual for the Finite-Difference Calculation of Large Elastic-Plastic, and/or Viscoelastic Transient Deformations of Multilayer Variable-Thickness (1) Thin Hard-Bonded, (2) Moderately-Thick Hard-Bonded, or (3) Thin Soft-Bonded Shells," US Army Ballistic Research Laboratory Contract Report No. 316, September 1976.

3. Huffington, N. J., Jr. and Wisniewski, H., "Revisions to the PETROS 4 Shell Response Code," US Army Ballistic Research Laboratory Technical Report (in publication).

4. Torre, C., "Die Grenzzustande Statisch Beanspruchter Stoffe," Schweiz. Arch. Angew. Wiss. U. Tech., Vol. 15, No. 4, 1940.

5. Hill, R., "The Mathematical Theory of Plasticity," Oxford, London, 1950, p.17.

6. Private communication from Dr. S. C. Chou (AMMRC) to Dr. T. W. Wright (BRL), April 1980.

7. Benck, R. F., "Quasi-Static Tensile Stress Strain Curves--II, Rolled Homogeneous Armor," US Army Ballistic Research Laboratory Memorandum Report No. 2703, November 1976.

8. Fry, M. A., Durret, R. E., Ganong, G. P., Matuska, D. A., Stucker, M. D., Chambers, B. S., Needham, C. E., and Westmoreland, C. D., "The HULL Hydrodynamics Computer Code," US Air Force Weapons Laboratory Technical Report 76-183, September 1977.

9. Kiwan, A. R. and Goodman, H. J., "The Response of Rolled Homogeneous Steel Armor Plates to Explosive Blast Loading," US Army Ballistic Research Laboratory Technical Report ARBRL-TR-02393, February 1982.

MAGNESIUM PROJECTILE IMPACT BEHAVIOR

J. C. SCHULZ
Mechanical Engineer

O. E. R. HEIMDAHL
Mathematician

S. FINNEGAN
Research Physicist

Naval Weapons Center
China Lake, California 93555

ABSTRACT

Firings of small, hollow magnesium cylinders at normal incidence against simulated concrete targets were conducted. The purpose of these tests was to gather basic data regarding the impact behavior of magnesium which can be used as a starting point in magnesium-case warhead design. Significantly different deformation and failure modes were found for the magnesium projectiles as compared to similar geometry steel projectiles tested previously.

INTRODUCTION

The use of magnesium in proposed warhead designs has prompted renewed interest in the impact behavior of this metal. Previous work has dealt primarily with the use of magnesium as an armor material [1,2]. The present study is concerned with its suitability as a penetrator. The lesser density and strength of magnesium mean lower penetration depths and survival velocities for magnesium projectiles as compared to steel projectiles with similar geometry. Information is needed regarding suitable design parameters for magnesium-case warheads possessing satisfactory penetration and survival characteristics.

Experimental firings of small, hollow, cylindrical steel projectiles at normal incidence against simulated concrete targets have been reported by Stronge and Schulz [3]. These firings have provided useful information regarding the failure modes and survival velocities of steel projectiles. The data obtained has been used in the development and verification of finite element analysis procedures for impacting warheads.

The present investigation involves similar firings of magnesium projectiles against simulated concrete targets. Solid cylindrical projectiles, as well as projectiles with three different diameter internal cavities were fired. As would be expected, the magnesium projectiles failed at lower impact velocities than did comparable steel projectiles. In addition, there were significant differences in the deformation and fracture behavior of magnesium under impact conditions. In particular, "spiral" fractures in the cavity wall occurred in the magnesium projectiles, which have not been observed in steel projectiles.

Finite element structural analyses of some of the magnesium projectiles were performed. It was found that a plastic modulus of about one-tenth the elastic modulus was required to match the bulging of the cavity observed experimentally. Selected projectiles were examined metallurgically to shed light on the nature of the fracture processes.

MAGNESIUM PROJECTILE FIRINGS

PROJECTILES

The magnesium projectiles were all flat-fronted cylinders, 2.5 inches long and 0.5 inch in diameter. In addition to solid cylinders, projectiles having a 1/4-, 5/16- or 3/8-inch inside diameter internal cavity were tested. The internal cavity was hemispherically fronted with the front end of the cavity 0.25 inch from the front end of the projectile. The hollow projectiles were filled with an explosive simulant (plasticine). All of the projectiles were machined from ZK60A magnesium bar stock. Cross-sectional views of the magnesium projectiles are shown in Figure 1.

TARGETS

The simulated concrete targets were made of Thorite (® Standard Dry Wall Products), a fast-setting, high-strength (3950 psi compressive strength) concrete patching compound consisting of sand, cement and additives to promote rapid curing. The largest sand grains are about 0.4 inch in diameter. The Thorite was poured into 1 gallon metal cans and cured for 7 days prior to the firings.

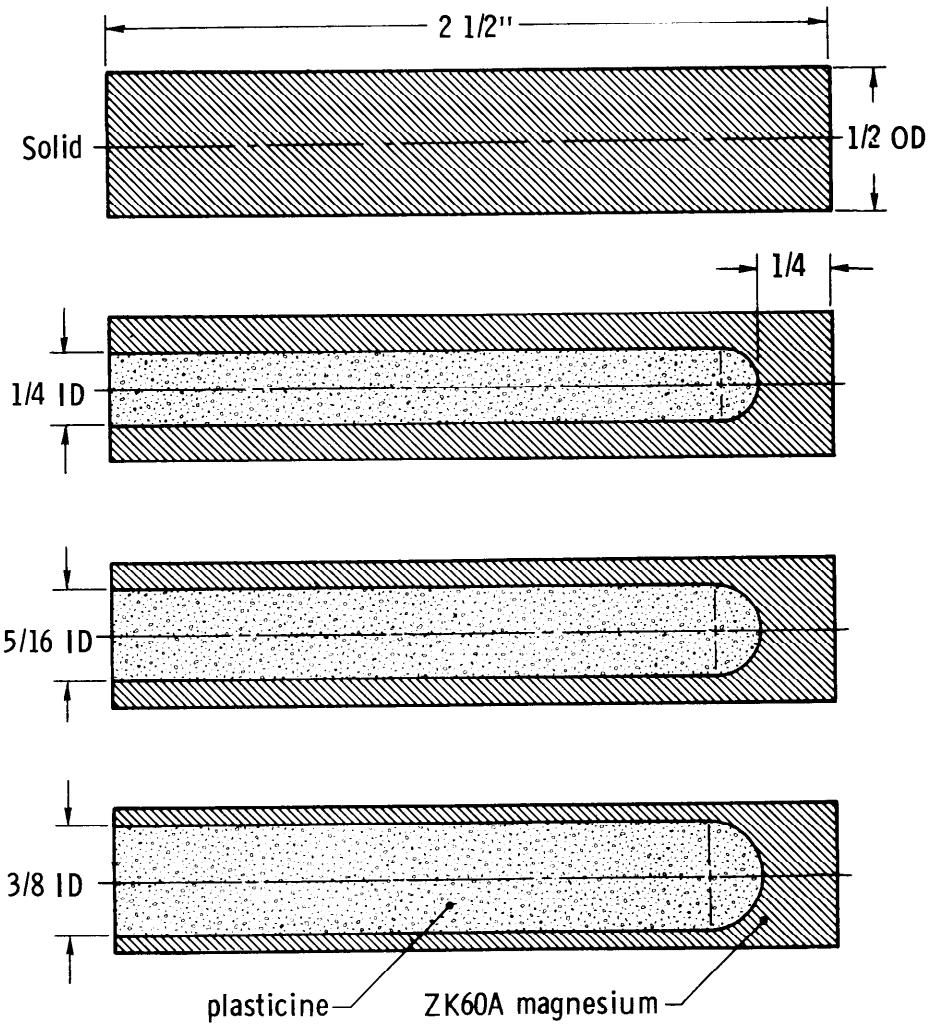

FIGURE 1. Cross-Sectional Views of Magnesium Projectiles.

EXPERIMENTAL PROCEDURE

The projectiles were fired from a smooth-bore, 50-caliber compressed-gas gun. (Some of the higher velocity rounds were fired from a 50-caliber powder gun.) Exit velocities of the projectiles from the gun were measured with a photo diode system coupled to an interval counter. The Thorite targets were placed about 18 inches from the end of the barrel. The apparatus is described more fully by Goldsmith and Finnegan [4].

EXPERIMENTAL RESULTS

Altogether 22 firings of magnesium projectiles were made at impact velocities ranging from 423 to 1675 fps. The test results are summarized in Table I. Photographs of selected projectiles after test are shown in Figure 2.

At lower velocities bulging occurred in the cavity region of the hollow projectiles (Figure 2c and g). Damage to these projectiles consisted primarily of longitudinal scratches in the side near the front end. At higher velocities fracturing occurred (Figure 2b. d, e, f, and ..). For the hollow projectiles, cracking characteristically followed a spiral path inclined at an angle of ±60 degrees to the longitudinal axis (Figure 2e, f, and h). In some instances, the front portion of the cavity shattered into a number of small fragments (Figure 2d). For the solid projectiles fracturing was confined to the front end and bending also occurred such that the axis was no longer linear (Figure 2b).

The behavior of the magnesium projectiles was different from that of steel projectiles tested previously in two important respects. First, bulging in the cavity region extended for a considerable distance in the axial direction rather than being confined to the front of the cavity. Second, the spiral fractures present in the magnesium projectiles were not observed in steel projectiles. It is tempting to associate the spirals with the fact that magnesium is a hexagonal-close-packed material, which might somehow tend to slip along 60-degree planes. However, no such tendency was found in the literature, and it is hard to see how such an effect could dominate in the polycrystalline bar stock material tested.

PENETRATION DEPTH

Penetration depth versus impact velocity is plotted in Figure 3. The solid line is the penetration curve for a 0.5-inch-diameter projectile calculated from the theory of Bernard and Creighton [5]. The test results are also shown. (Since plasticine and magnesium have about the same density, all four projectile types have roughly the same mass, 14 grams, and can be compared on one plot.) It can be seen that the experimental points lie somewhat below the theoretical curve. An explanation for this discrepancy between theory and experiment is that Bernard and Creighton assume an undeforming projectile, while the test projectiles bulged (and in some cases shattered) during penetration. If the points for projectiles that shattered (shown shaded in the figure) are excluded, better agreement with theory is obtained. The dashed line is the penetration curve for a projectile with a fictitious diameter of 0.53 inch (an average of the bulged diameters in Table I). It results in still better agreement between theory and experiment.

TABLE I. Tabulated Results of Magnesium Projectile Firings.

Inside diam., in.	Impact velocity, fps	Pen. depth, in.	Bulge diam., in.	Description of projectile after test
Solid	810	0.36	0.518	Longitudinal scratches in side near front end
Solid	1139	0.91	0.528	Longitudinal scratches extending further down side
Solid	1232	0.92	---	Wedge-shaped piece chipped from front end
Solid	1310	0.91	0.528	Longitudinal scratches
Solid	1352	0.83	---	Chips broken off front end, projectile bent
Solid	1410	0.84	---	Projectile not recovered
Solid	1675	1.27	---	Front end eroded away, projectile bent
1/4	1410	1.08	0.528	Small wedge-shaped chip out of front end
1/4	1450	1.11	0.534	Incipient chip in front end
1/4	1471	0.56	---	Middle portion shattered into several fragments
1/4	1491	1.17	---	Chip out of front end, incipient chip, slightly bent
1/4	1520	0.59	---	Middle portion shattered
5/16	922	0.45	0.529	Longitudinal scratches
5/16	967	0.59	---	Spiral crack in cavity wall
5/16	980	0.56	0.536	Longitudinal scratches
5/16	1056	0.73	0.534	Longitudinal scratches
5/16	1165	0.66	---	Spiral cracks in cavity wall, middle portion shattered
3/8	423	0.11	0.534	Slight longitudinal scratches
3/8	626	0.17	---	Longitudinal and circumferential cracks in cavity wall
3/8	704	0.25	---	Spiral and longitudinal cracks
3/8	792	0.20	---	Middle portion shattered
3/8	895	0.22	---	Middle portion shattered

a. Solid, 1310 fps

b. Solid, 1352 fps

c. 1/4" ID, 1450 fps

d. 1/4" ID, 1520 fps

FIGURE 2. Photographs of Magnesium Projectiles After Test.

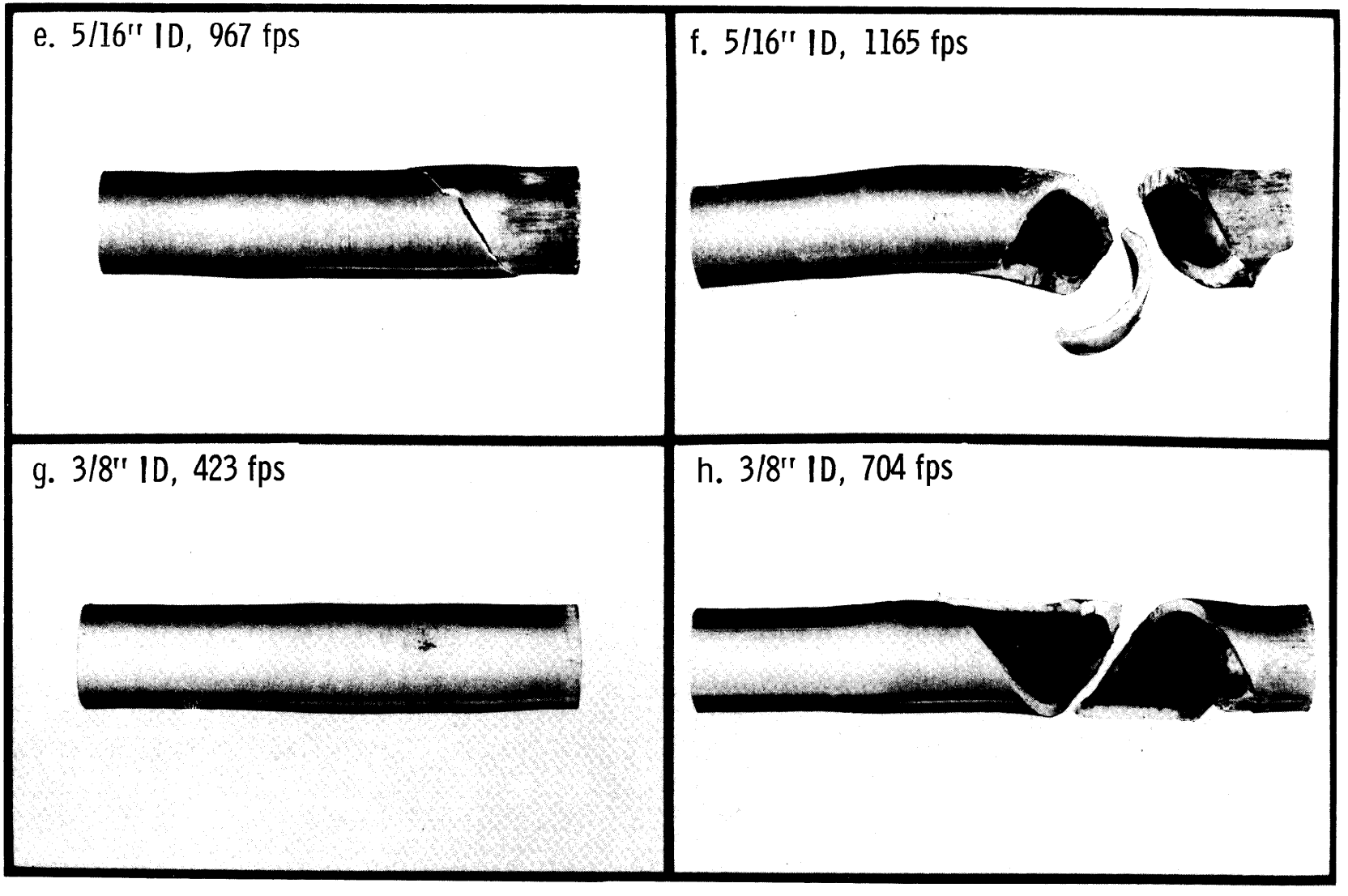

FIGURE 2. Photographs of Magnesium Projectiles After Test (Cont'd).

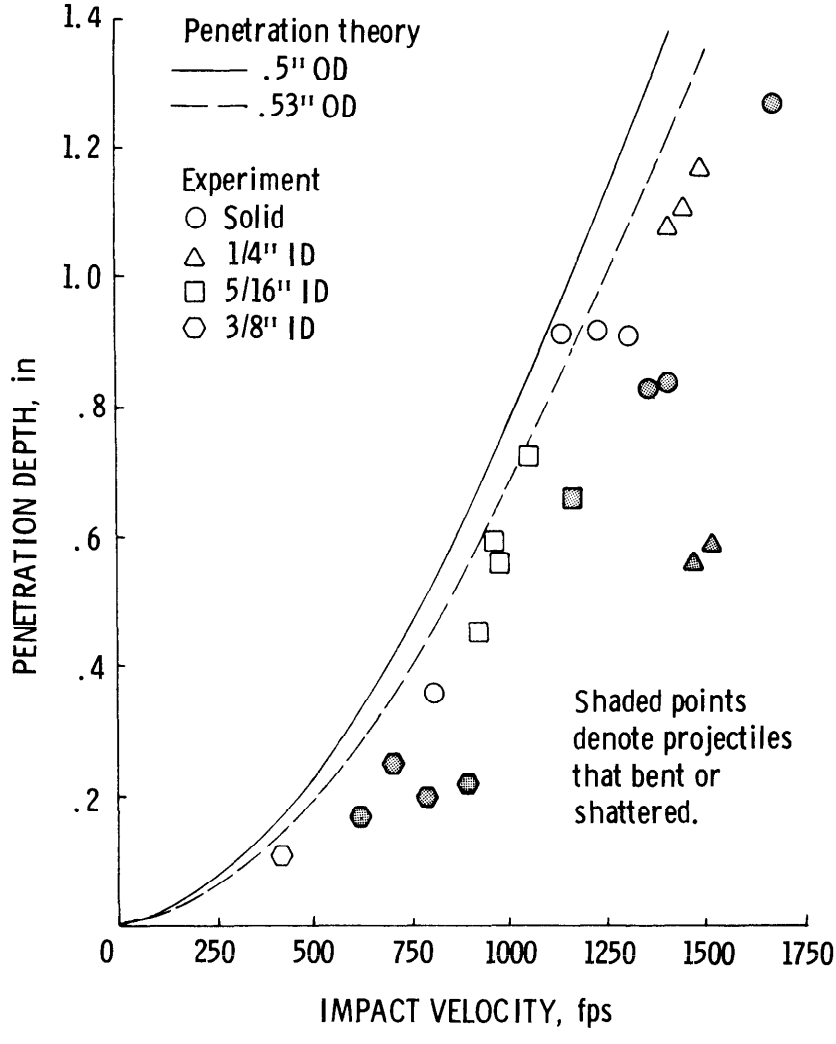

FIGURE 3. Penetration Depth Versus Impact Velocity for Magnesium Projectiles.

SURVIVAL VELOCITY

The survival velocity can be taken as that velocity below which the projectiles bulged and above which they either fractured in the cylindrical section or, in the case of the solid projectiles, bent severely. Survival velocity versus cavity wall thickness is plotted in Figure 4. Due to the limited amount of data collected these values are rather approximate. As would be expected, survival velocity increased with increasing cavity wall thickness (except for the solid projectiles where the lack of an internal cavity leads to a different mode of failure).

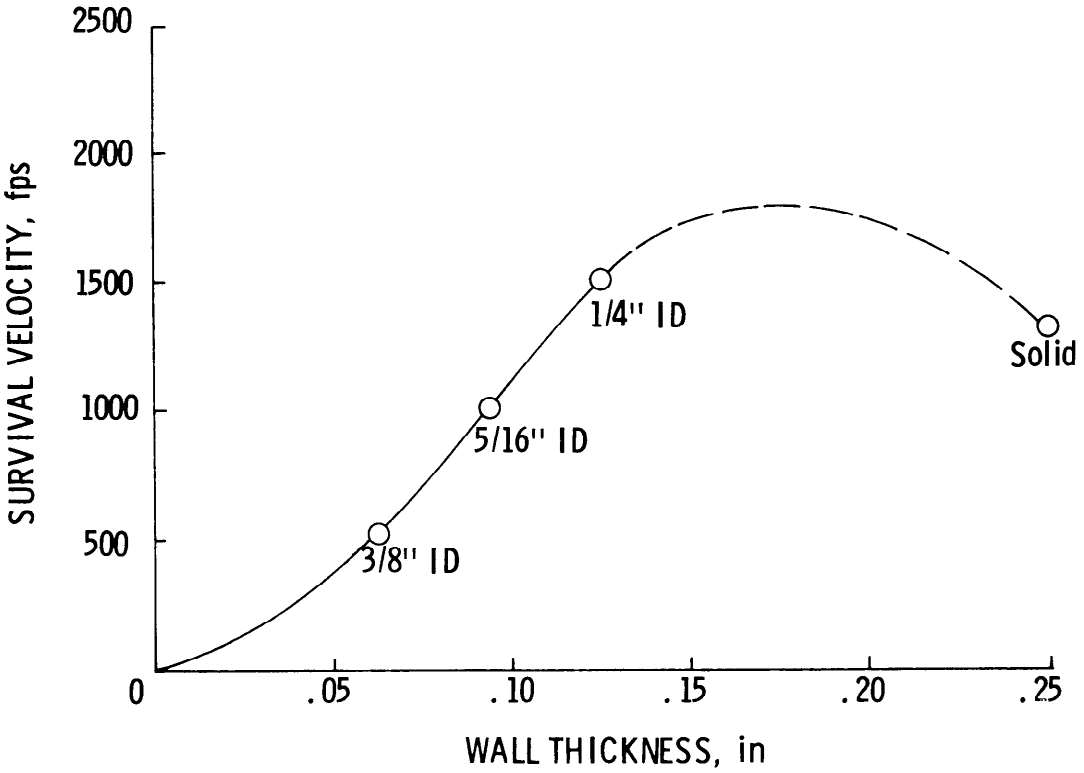

FIGURE 4. Survival Velocity Versus Wall Thickness for Magnesium Projectiles.

FINITE ELEMENT ANALYSIS

Finite element structural analyses of selected projectiles were performed using the HONDO II computer code [6]. Pressure loads to represent the effect of the target material on the projectile were calculated from the penetration theory of Bernard and Creighton [5], with the addition of an initial transient pressure spike. This computational technique, described in [3], has been used successfully in predicting the deformations of steel projectiles from pervious firings.

Initial runs were made assuming elastic, perfectly plastic material behavior (zero plastic modulus). The deformed shape of a 3/8-inch-ID projectile impacting at 423 feet per second is shown in Figure 5. This theoretical shape obviously differs from that of the actual projectile as shown in Figure 2g. The model projectile developed a severe bulge at the front of the internal cavity. Bulging in the test projectile was more moderate and extended over a considerable distance in the longitudinal direction.

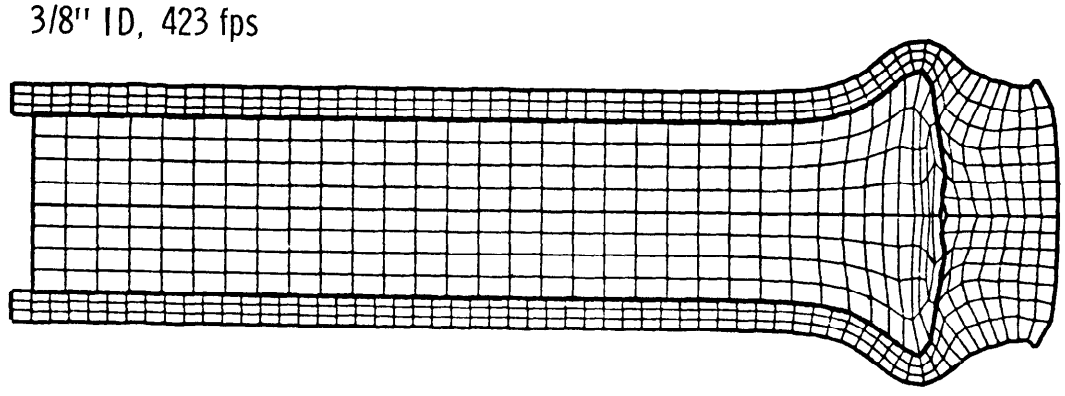

FIGURE 5. Deformed Shape of Magnesium Projectile Model Without Work Hardening ($E_p/E = 0$).

It was found that bulging in the model is strongly influenced by the plastic modulus assumed for magnesium. A plastic modulus of one-tenth the elastic modulus spread out the bulging in the model to produce agreement with test results. Data on the dynamic properties of magnesium [7] indicate that this is a reasonable value for the plastic modulus. Material properties for magnesium and plasticine used in the improved computer runs are given in Table II.

TABLE II. Material Properties Used in Improved Computer Runs.

Material	Property	Value
ZK60A	Density, ρ_m	1.85×10^{-4} lb-sec^2/in^4
Magnesium	Elastic modulus, E	6.5×10^6 psi
	Poisson's ratio, ν	0.35
	Yield stress, σ_y	3.1×10^4 psi
	Plastic modulus, E_p	0.65×10^6 psi
Plasticine	Density, ρ_p	1.75×10^{-4} lb-sec^2/in^4
	Bulk modulus, B	1.0×10^6 psi

Final deformed shapes computed for the 3/8- and 1/4-inch-ID projectiles fired at 423 and 1450 feet per second, respectively are shown in Figure 6. Plots of bulge height (increase in radius) versus distance along the projectile side are shown in Figure 7. Excellent agreement between analytical and measured bulge heights are obtained at 423 feet per second. Quantitative agreement at 1450 feet per second is not as good, although the shapes of the bulges are qualitatively similar. It is likely that still better agreement between theory and experiment could be obtained through further modification of the material properties.

3/8" ID, 423 fps

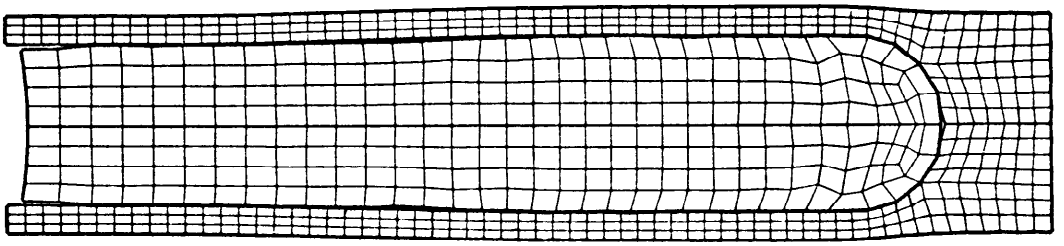

1/4" ID, 1450 fps

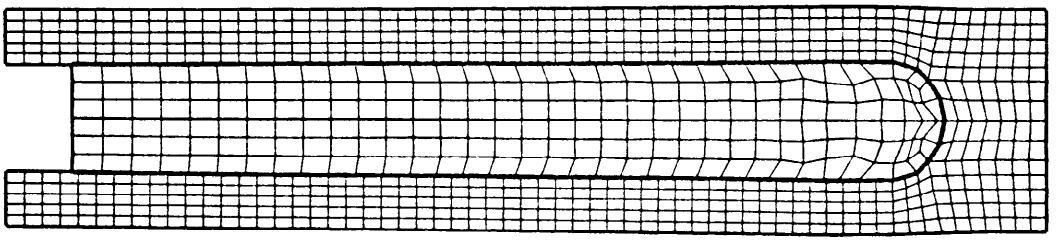

FIGURE 6. Deformed Shapes of Magnesium Projectile Models With Work Hardening ($E_p/E = 0.1$).

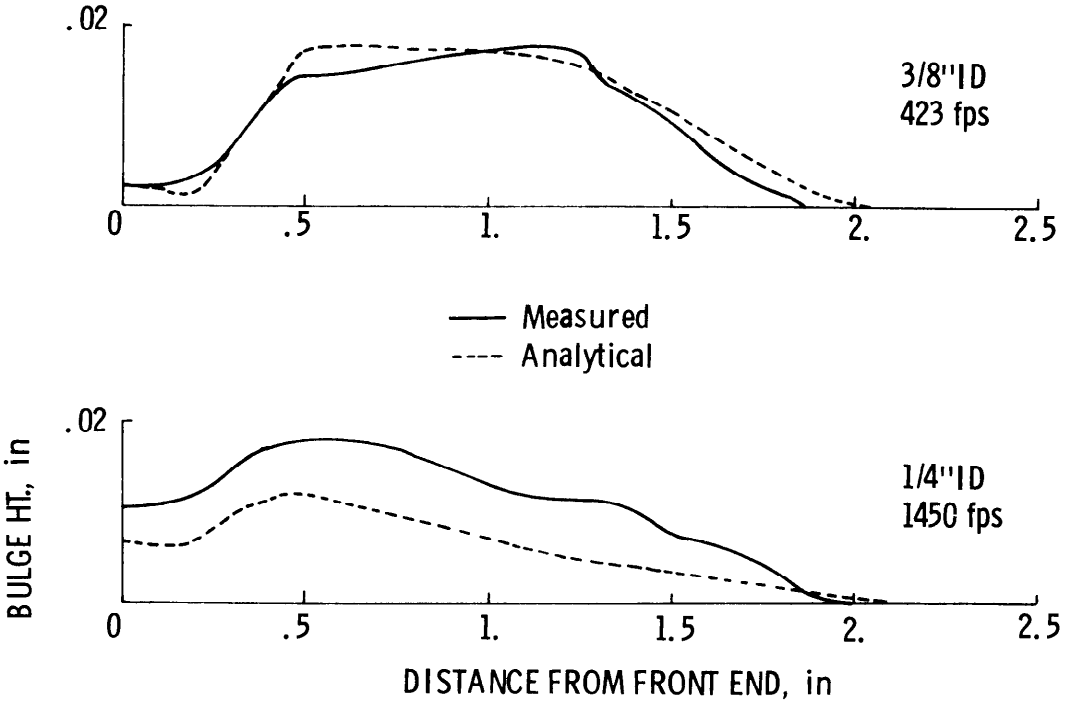

FIGURE 7. Analytical and Measured Bulge Heights for Magnesium Projectiles.

METALLURGY

Metallurgical studies were conducted on selected impacted specimens. These studies consisted of (1) examination of fracture surfaces with variable power (10-70X), binocular microscope to establish failure modes, (2) surface hardness measurements using a Rockwell tester to map out strain hardened areas, (3) macroetching of one virgin specimen to determine basic flow structure patterns in the material, and (4) spectrographic analysis to verify alloy composition.

The test specimens were machined from a single 2 1/2-inch diameter bar of extruded ZK60A magnesium alloy. This alloy was confirmed through spectrographic analysis, while its microstructural condition was tentatively classified as "F" (as fabricated).

Impacted specimens fractured in two areas: along the outer edge of the nose and in the cavity wall. Fracturing in the nose caused the removal of wedge-shaped chips (Figure 2b and c). Fracturing in the cavity wall occurred largely at an angle of ±60 degrees to the longitudinal axis resulting in the formation of spiral cracks (Figure 2e, f, and h). Wall

material to the rear of the fracture surface (away from the impacted end) tended to move outwards as evidenced by the increased level of abrasion on the exterior surface in these localities. A few longitudinal and circumferential fractures were also found.

The surfaces of the spiral cracks were deeply grooved in the direction of movement and had a smeared, shiny appearance as shown in the macrograph of Figure 8. These features are suggestive of a shear mode of failure, although they might also represent secondary damage masking some other initial failure mode. Minor longitudinal cup-and-cone-type tensile fractures were also found in the cavity wall of the 3/8-inch-ID specimens. Tensile fracture formation was possibly influenced by the larger hoop stresses in the wall resulting from the presence of filler material.

FIGURE 8. Macrograph of Surface of Spiral Fracture.

Flow lines in a virgin specimen, as revealed by macroetching in dilute nitric acid, were aligned uniformly along the longitudinal axis, and reflected the flow structure of the extruded bar stock from which they were cut. No direct connection was discerned between any of the fracture systems and flow structure patterns in the material as a result of prior extrusion or fabrication processes.

Rockwell hardness measurements were made along the length of selected impacted specimens. Increased impact speeds produced higher hardness levels and tended to spread the region of increased hardness over a greater distance along the side. There was no obvious relationship between hardness trends and either post-impact cavity diameter measurements or the onset of wall fracturing. However, changes in surface hardness levels due to abrasion by contact with target material may have obscured such effects.

CONCLUSIONS

In this study normal incidence firings of small magnesium projectiles against simulated concrete targets were made to learn more about the behavior of magnesium under impact conditions. The main findings are:

1. The magnesium projectiles exhibited deformation and fracture behavior significantly different from similar-geometry steel projectiles tested previously. Bulging in the cavity extended for a considerable distance in the axial direction rather than being limited to the front of the cavity as was the case for steel projectiles. Spiral cracks inclined at an angle of ±60 degrees to the longitudinal axis occurred in the case wall. These cracks were not observed in steel projectiles. It is possible that the bulging and spiral cracks are related in the sense that a region of uniform bulging may be required to allow the cracks to propagate. Such a region was lacking in the steel projectiles.

2. Inclusion of a suitable plastic modulus in the material representation for magnesium is necessary for accurate finite element modeling of magnesium projectile structural behavior. In the absence of work hardening (elastic, perfectly plastic material) the extended bulging of the case wall is not reproduced. Work leading to the obtainment of more accurate property values for magnesium would be desirable.

3. Spiral fractures in the cavity wall took place by an apparent shear process, with separation involving motion along a curved path across the thickness of the wall. No correspondence was found between failure patterns and prior flow structure resulting from extrusion and fabrication. Thus, these failure processes are believed to be an intrinsic property of the magnesium under the loading conditions and in the sample geometry of this study.

ACKNOWLEDGEMENT

This study was accomplished under the Air-to-Surface Missile Warhead and Fuze Technology Program and was sponsored by the Naval Air Systems Command. The authors would like to thank Mark Alexander for his guidance and support in the conduct of this work.

REFERENCES

1. R. L. Woodward. "Penetration resistance of a magnesium casting alloy." *Journal of Materials Science,* Vol. 15, 1980, pp. 2117-2120.

2. R. M. Orgorkiewicz. "Armor materials for combat vehicles." *Machine Design,* Vol. 41, No. 27, November 27, 1969, pp. 36-41.

3. W. C. Stronge and J. C. Schulz. "Projectile impact damage analysis." In *Papers presented at the Symposium on Computational Methods in Non-linear Structural and Solid Mechanics,* Arlington, Virginia, October 1980, edited by Ahmed K. Noor and Harvey G. McComb, Jr., Pergamon Press, New York, 1981. (Also published as special issue of *Journal of Computers and Structures,* Vol. 13, No. 1-2, 1981, pp. 287-294.)

4. W. Goldsmith and S. A. Finnegan. "Penetration and perforation processes in metal targets at and above ballistic velocities." *International Journal of Mechanical Sciences,* Vol. 13 (1977), pp. 843-866.

5. R. S. Bernard and D. C. Creighton. *Projectile Penetration in Earth Materials: Theory and Computer Analysis.* Defense Nuclear Agency, Washington, D.C., November 1977. (Contract Report S-76-13), publication UNCLASSIFIED.)

6. S. W. Key, Z. E. Beisinger, and R. D. Krieg. *HONDO II, a Finite Element Computer Program for the Large Deformation Dynamic of Axisymmetric Solids.* Albuquerque, N.M., Sandia Laboratories, 1978. (SAMD78-0422).

7. P. E. Senseny, J. Duffy and R. H. Hawley. "Experiments on strain rate history and temperature effects during plastic deformation of close-packed metals." *Journal of Applied Mechanics,* Vol. 45, No. 1, 1978, pp. 60-66.

BLAST RESPONSE OF A HARDENED ARMY ISO SHELTER

Roger W. Milligan, Kaman AviDyne
Allen Lush, Kaman AviDyne
William L. Crenshaw, U.S. Army Natick
Research and Development Laboratories

Permission from higher authorities was not obtained in time to include the manuscript of this paper (pages 44 to 65) in these proceedings.

SHOCKS IN SATURATED SAND

BRIAN M. LEMPRIERE
The Boeing Aerospace Company
Seattle, WA., 98124

ABSTRACT

The response of saturated sand to strong shock waves was determined from plate impact experiments and used to predict the environment experienced by a missile capsule buried in a sand-filled shaft under a surface blast.

Sand samples contained in aluminum or acrylic cups were impacted by aluminum or acrylic discs in a gas gun. Data were obtained for impact and transmitted stress, shock velocity, and relief wave velocity by manganin gauges buried in the sand and on the aluminum or acrylic, and for impact velocity by contact pins. The data were interpreted through numerical models as representing a fluid mixture of quartz and water. They exhibited a small degree of porous crush in the relationship between the pressure dependent loading and unloading velocities, and a small degree of viscosity in shock attenuation at short distances.

The numerical models were used in the WONDY computer program to verify their efficacy in representing the experimental data, and in TOODY to analyze waves propagating down a sand shaft in a tuff or a granite host. These calculations showed that oblique shocks were driven into the sand by the plane wave in the host, and under some conditions, led to large pressure excursions on the axis of the shaft. The reflection of oblique shocks was analyzed using an extension of gas dynamics theory to examine these excursions.

INTRODUCTION

The survival of a deeply buried missile capsule in a sand shaft was being evaluated during the development of a Boeing-patented basing concept for survivability with quick egress (Ref. 1). The capsule would float to the surface after attack when the sand was fluidized by opening the trap door to a large water tank. The sand was to be kept saturated before fluidizing, leading to a concern for its response to shock loading. This prompted an experimental study and numerical evaluation of shock environments. This paper reviews the data and presents conclusions on the behavior of saturated sand, as well as on oblique shock environments.

DYNAMIC RESPONSE OF STATURATED SAND

A series of gas-gun flyer-plate impact tests was conducted on saturated sand in the Boeing Shock Physics Laboratory using methods conventional for this facility (Ref. 2). The impactor consisted of a disc of aluminum, lucite or steel mounted on an aluminum projectile. The target

consisted of a lucite or aluminum cup containing water-saturated sand with a face plate of aluminum, lucite or steel. Extreme care was exercised to ensure a fully saturated condition of the sand, and resulted in a density of 2.07 gr/cc, estimated to be close to 100% saturated. The basic experimental arrangement is shown in Figure 1.

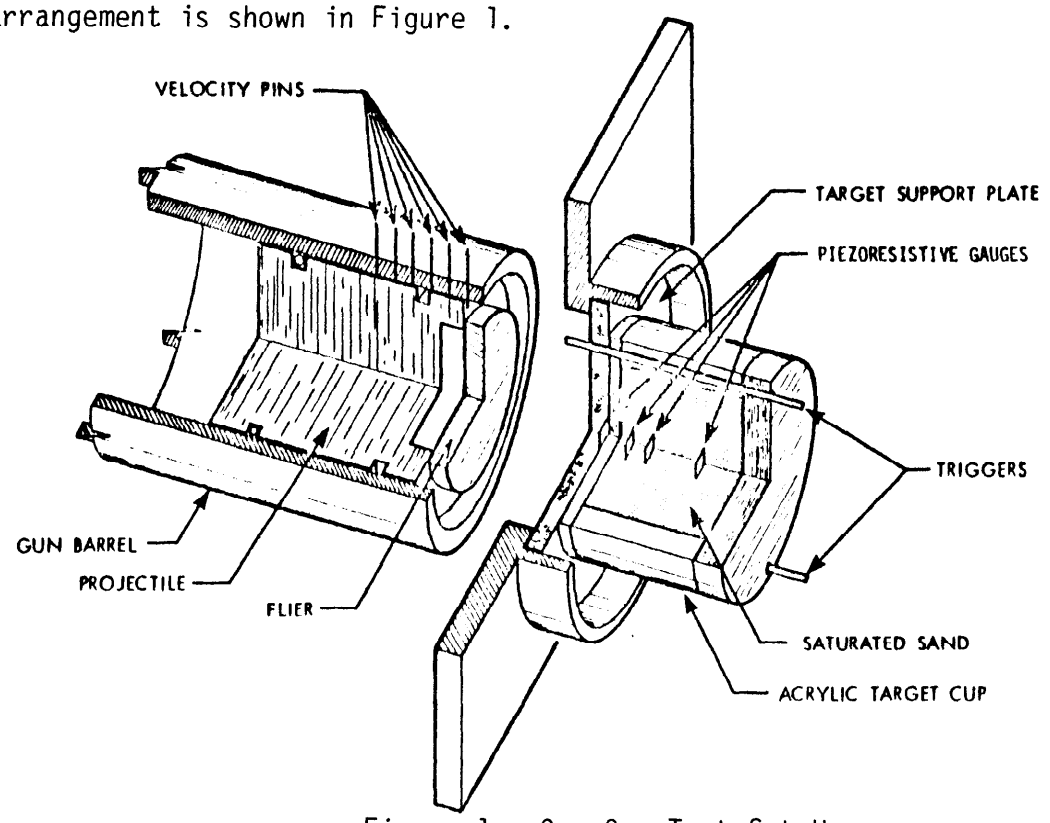

Figure 1. Gas Gun Test Set-Up

Impact conditions were defined by measurement of the impact velocity using contact pins in the barrel and by the piezo-resistive gauge located in the target plate. The propagating wave profile in the saturated sand was measured by carbon or manganin gauges located in the sand and by a gauge in the backing plate of the assembly. Testing showed that it was necessary to sandwich the manganin gauges between 0.010-inch Mylar to maintain the integrity of the gauge in the sand.

The measurements of impact stress σ, were determined directly from oscilloscope traces for the target plate gauge using well-known calibration factors (Ref. 3). Particle velocity u_p was obtained using known characteristics of the target plate (allowing for plasticity effects in the aluminum) (e.g., Ref. 4).

Shock speeds were determined from arrival times of the leading edge of the pulse and relief speeds from the first drop from the pulse peak. Volumetric strain η (where $\eta = 1 - \rho_0/\rho$ and ρ is density) and shock velocity U_s were determined from the condition of conservation of mass and momentum across a shock (the Hugoniot conditions) (e.g., Ref. 5). The simplified form of these equations for a single shock was used as all recordings displayed single shocks.

a) The Hugoniot and Compression Characteristics

The Hugoniot characteristic of saturated sand in the σ - u_p plane is shown in Figure 2, and the compressibility p - η curve in Figure 3.

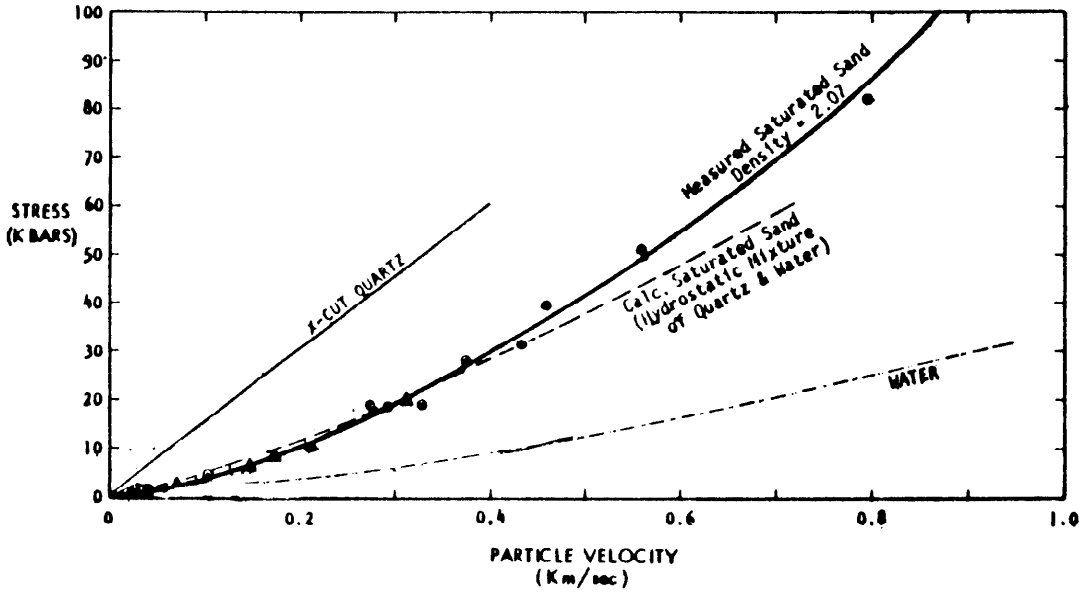

Figure 2. Hugoniot of Saturated Sand and Related Materials

The experimental data provide evidence for a one-wave response implying that shear strength is very small in saturated sand. Thus, stress and pressure are equivalent. It is probable that dry sand would provide a shear strength especially when compacted at moderate pressures.

Theoretical estimates of the behavior of saturated sand were made assuming a simple hydrodynamic mixture. In this analysis, the compression of the mixture was taken to be a volume average of the compressions of the constituents.

Data on unloading wave speed were estimated from the times of onset of a drop in the waveforms at the various gauges. These relief wave speeds are shown in Figure 4. They have been used to determine an unloading characteristic under the assumption that unloading speed is determined by the tangent to the compression curve (Ref. 5):

$$u_r = (\partial p/\partial \rho)^{1/2} \tag{1}$$

so that the unloading curve is given by

$$\eta = \rho/\rho_o - 1 = \int_o^p dp/\rho_o u^2 \tag{2}$$

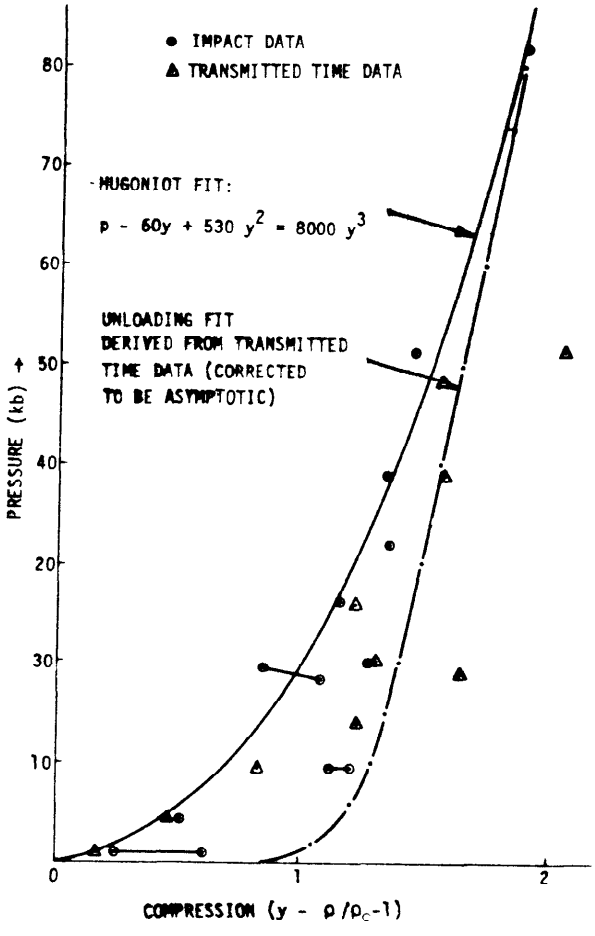

Figure 3. Compression Characteristics of Saturated Sand

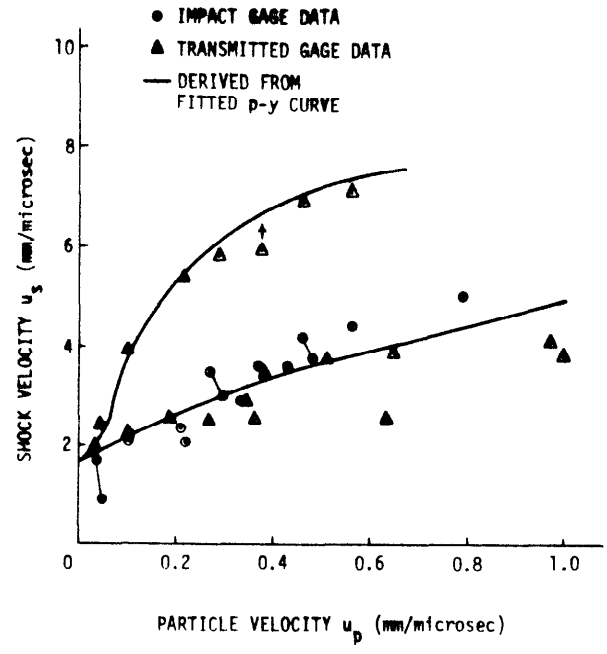

Figure 4. Shock-Particle Velocity Curves for Saturated Sand

This unloading curve is shown in Figure 3, with a shift forcing it to be tangent to the compression curve at high stress and with a corresponding correction to ρ_0. These two curves exhibit a porosity crush behavior in which loading causes permanent volume changes so that unloading generates a hysteresis loop. Such crush behavior was represented by a p - α model relating porosity to pressure (Ref. 6):

$$\alpha(p) = V(p)/V_S(p) = 1 + 0.077 \exp(-0.0486\ p) \qquad (3)$$

(where V is the volume of distended material at pressure p and V_S is the volume of the solid at the same pressure.

b) Attenuation Characteristics

The attenuation of the stress pulse as a function of impact stress and distance, obtained from transmitted pulse measurements, is shown in Figure 5. For a simple viscoelastic material of the Maxwell type (Ref. 5),

$$\dot{\varepsilon} = (1/E)\ (\dot{\sigma} + \sigma/\tau) = \dot{\sigma}/E + \mu\sigma \qquad (4)$$

(where ε is strain, σ is stress, E is the elastic constant, μ is the viscosity coefficient, τ is the relaxation time $1/\mu E$, and a dot denotes the time derivative).

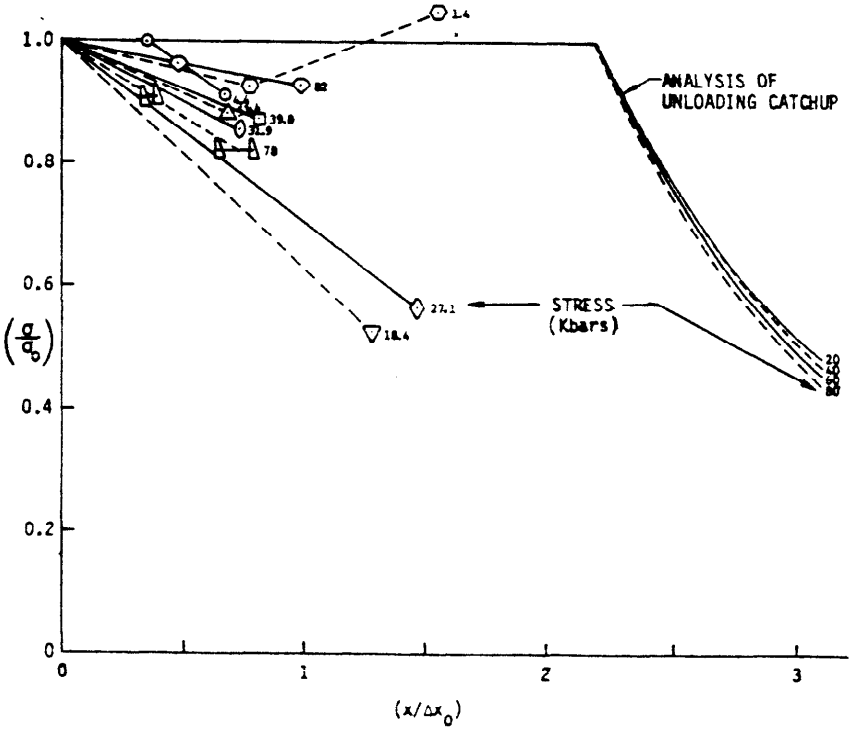

Figure 5. Attenuation of a square wave in Saturated Sand

Attenuation in such a material is independent of the stress and is given by the formula

$$(\sigma/\sigma_0) = \exp\ (-t/2\tau) = \exp\ (-\rho\mu cx/2) \qquad (5)$$

For the experimental data of Figure 5, however, the attenuation is not independent of stress, although within the scatter it could be construed that a stress ratio of 0.8 at 4 microsec (1.3 pulse lengths of about 3 microsec), representing a relaxation time of about 10 microsec, fits the data.

Attenuation by catch-up is a consequence of the nonlinearity of the response, in which unloading waves in highly stressed material move faster than loading waves traveling into undisturbed material. At the catch-up time t_c, the front reaches a distance $x_c = U_s\, t_c$. The relief wave, starting at the time $t_r = \Delta x_o/U_s$ where Δx_o is initial pulse length, reaches the same distance:

$$x_c = U_s t_c = U_r\,(t_c - t_r) = U_r\,(t_c - \Delta x_o/U_s) \qquad (6)$$

From these equations, the catch-up distance, normalized to the pulse length, can be expressed in terms of the wave speed ratio:

$$x_c/\Delta x_o = 1/\,1-((U_s/U_r) \quad = 2.2 \qquad (7)$$

since according to the data of Figure 4, $U_s \simeq 0.55\, U_r$. From these data relating wave speeds to stress, values of the relief wave speed ratio corresponding to various stress ratios have been calculated, and also the propagated distance. The results are given as an attenuation curve in Figure 5. Evidently, catch-up is not responsible for the attenuation observed in the experiments as this occurred at distances shorter than catchup distances. Viscous or porous attenuation is therefore present.

c) Numerical Evaluation of Models

The above models were used in the WONDY computerized finite difference wave propagation code (Ref. 5) in three forms. In the first two, no viscosity was considered, and the material was regarded as a non-linearly elastic material governed by the compressibility curve of Figure 3 or a porous material described by Eq. 3. In the third, the standard viscoelastic solid was used in the form

$$\sigma + \tau_\varepsilon \dot{\sigma} = E_r\,(\eta + \tau_\sigma \dot{\eta}) \qquad (8)$$

with the constant-strain relaxation time $\tau_\varepsilon = \tau$, and the constant-stress (or creep) relaxation time $\tau_\sigma = (U_s/c)^2\,\tau$. The relaxation modulus is $E_r = \rho_o c^2$. Using shock speeds of 3 to 5 mm/microsec over the range from 20 to 80 kbar in which the observed relaxation time was 2 to 20 microsec, and a sound speed between 1.5 and 1.7 mm/microsec leads to a strain relaxation

time of 1 to 2 microsecs when the wave propagation attenuation is regarded as constant-stress relaxation. The value of 1 microsec for the strain relaxation time was used in the calculations.

Predicted histories of stress at the gauge locations for a selected experiment configuration have been extracted from the analyses, and superimposed on the measured traces of stress. Examples of two cases (with and without porosity) are shown in Figure 6.

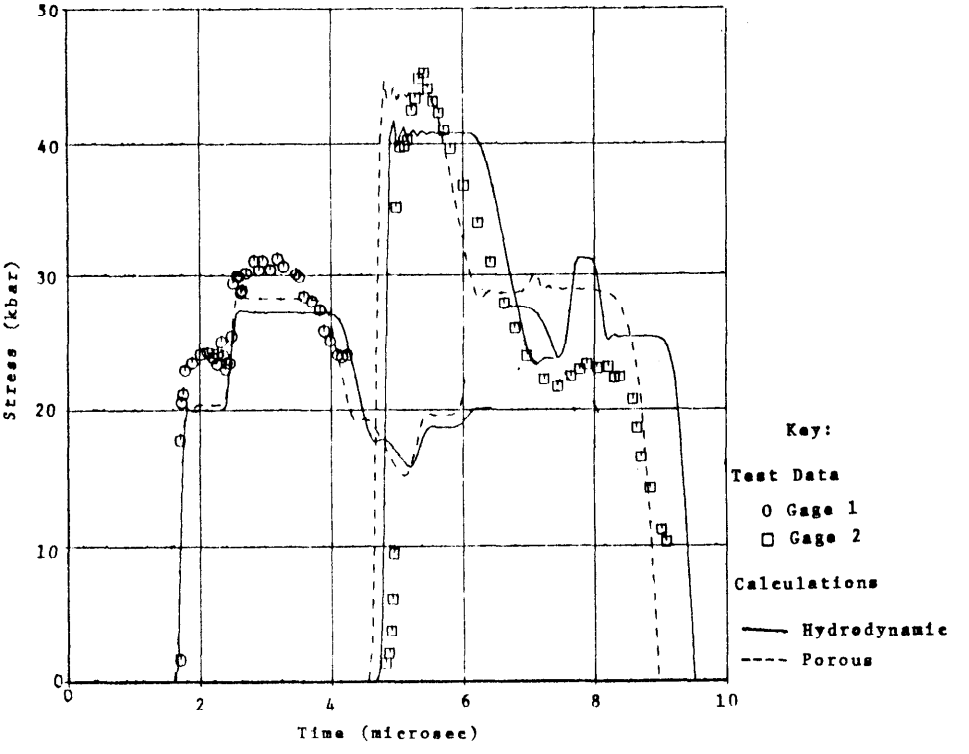

Figure 6. Recorded and Calculated Wave Shapes

The calculations show little difference between the hydrodynamic and porous models except at late times during or after unloading, as to be expected. The test data are better represented by the porous model in general. For those experiments with thick sand specimens, the calculations showed that viscous effects were considerable.

PULSE PROPAGATION ANALYSIS

In the design of a deep-buried egress system, detailed analyses of shock propagation down a sand shaft and into the sand from its host surroundings were required. Various phenomena that could occur in the configuration of a sand shaft embedded in rock or tuff were of concern. These included a form of water-hammer or waveguide effect, entrainment of a shock in the column by that in the rock, and attenuation effects in the sand. The value of using conventional finite-difference wave-propagation codes to analyze the effects was in question. As a consequence of the calculations, the effects produced by the interaction of oblique shocks and the possibility of developing a Mach stem effect were analyzed using oblique shock theory.

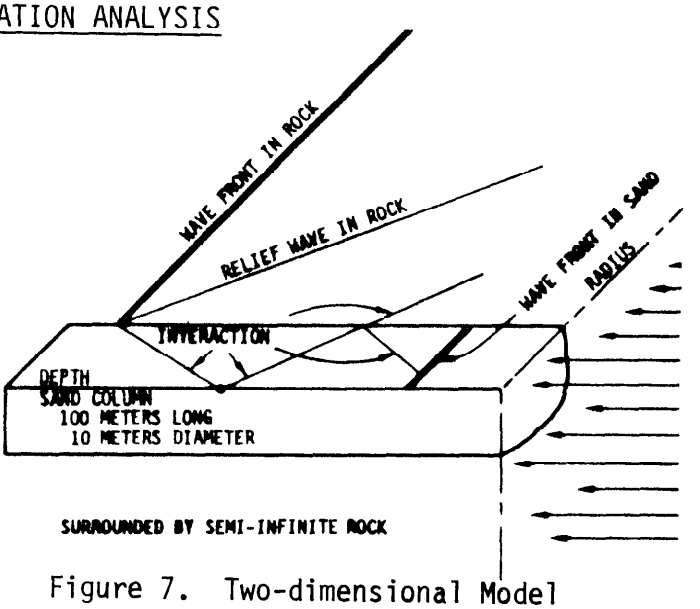

Figure 7. Two-dimensional Model

a) Numerical Calculations Using TOODY Code

Two-dimensional axisymmetric configurations representing a vertical sand column in rock or tuff with an imposed pressure pulse depicted in Figure 7 were modeled with the TOODY code (Ref. 6). The problem was configured as a half-space with a graded mesh and a uniform boundary pressure.

Results of calculations for a step pulse are shown in Figure 8 as an isometric plot of stress on a two-dimensional base, together with a contour map for pressure. Both plots represent wavefronts at 20 ms after application of the step pulse. The column centerline is along the bottom of the figure, and depth increases to the left. Both plots display a plane wave in the host and a pattern of disturbances entrained in

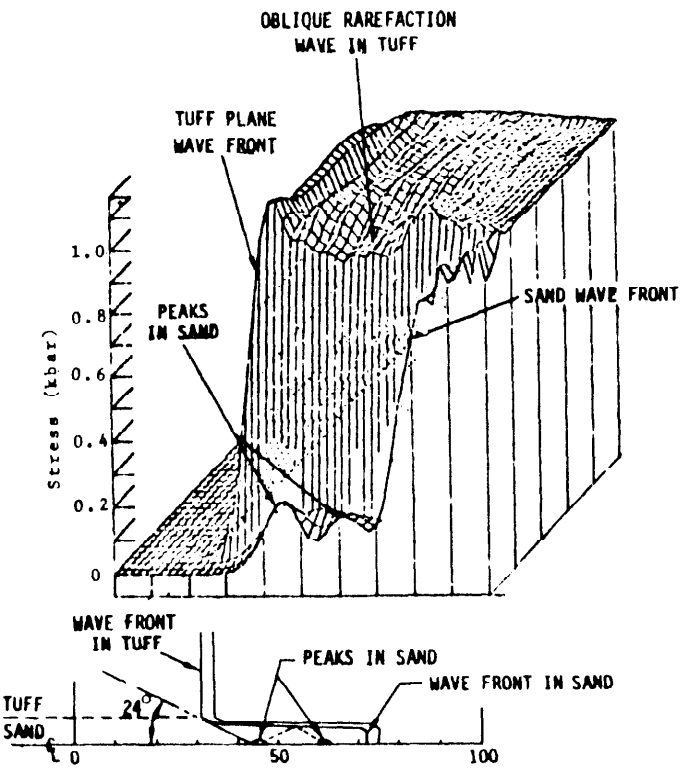

Figure 8. Wave Profile in Tuff and Sand Column

the column. The plane wave in the column, driven by the surface loading follows far behind that in the host. The entrained waves in the sand take a diamond pattern forming peaks on the axis.

To examine the wavefront details a sand column in a quartz host was analyzed to exaggerate the material mismatch and to simulate a hard-rock site. The loading was a 50-kbar square pulse, lasting for one cycle. These calculations showed that oblique wave patterns emanated from the quartz plane wave interaction with the interface both into the sand and back into the quartz, as shown in Figure 9.

A peak motion and pressure occurred in the sand where the oblique wave converged on the axis.

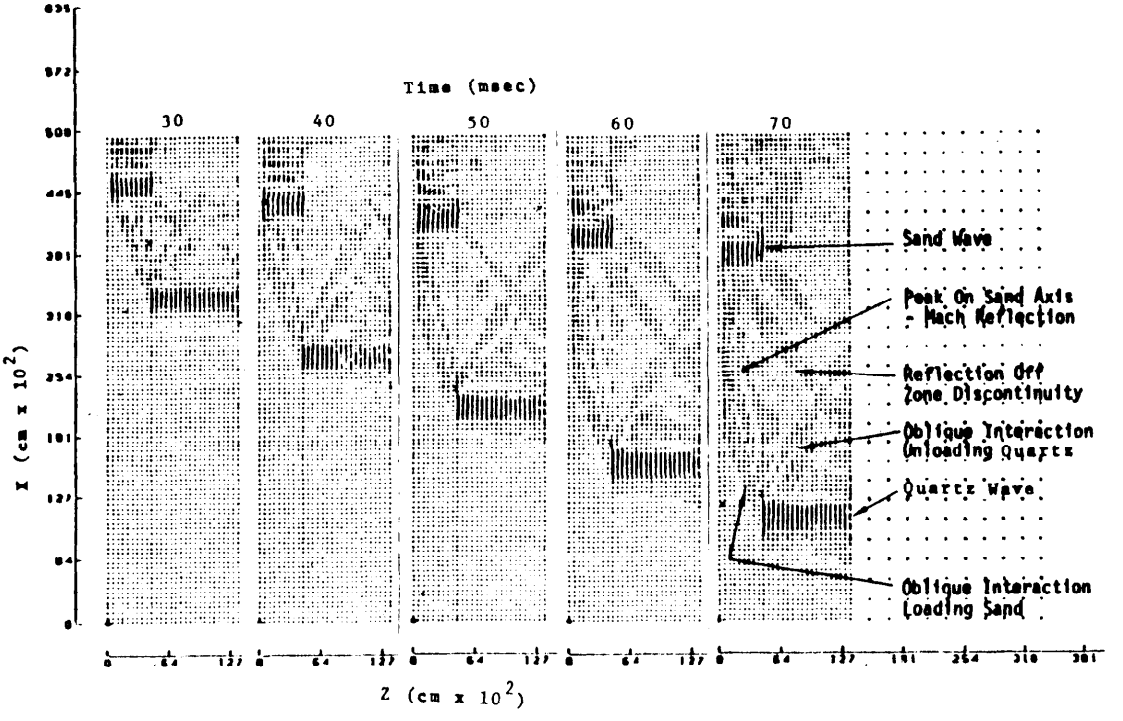

Figure 9. Narrow Pulse Propagation Depicting Wave Patterns

b) Oblique Shocks in Fluids

In the flow of gases, the intersection of certain oblique shocks leads to flow situations which cannot subsist, and an alternate flow pattern is set up: a new shock configuration is established in which a normal shock

develops in place of the oblique shocks, called a Mach stem (Ref. 7). Significantly enhanced pressures can arise in these cases. The analysis method available for oblique shocks and the Mach stem in gases does not allow for an important feature of fluids (such as saturated sand) or solids, namely zero pressure ahead of a shock. The additional complexity associated with solids defined as materials capable of sustaining shear forces is not taken up here. However, at very high stresses, many times in excess of their shear strength solids behave like fluids and shear effects can be ignored.

The analysis of a shock moving with a velocity V_S into a stationary material is analyzed as a stationary shock set up by material moving with the opposite velocity, as sketched in Figure 10. The analysis assumes that the tangential component of velocity is not changed and changes in the normal components satisfy the Rankine-Hugoniot jump conditions on mass, momentum and energy. For solids, shear forces can be set up tangential to the shock and introduce changes in momentum which must be considered separately. For a solid or fluid, shock behavior is commonly described by a linear empirical relationship between shock and particle velocities in a normal shock moving through undisturbed material (Ref. 5):

$$U_s = c_o + Su_p \tag{9}$$

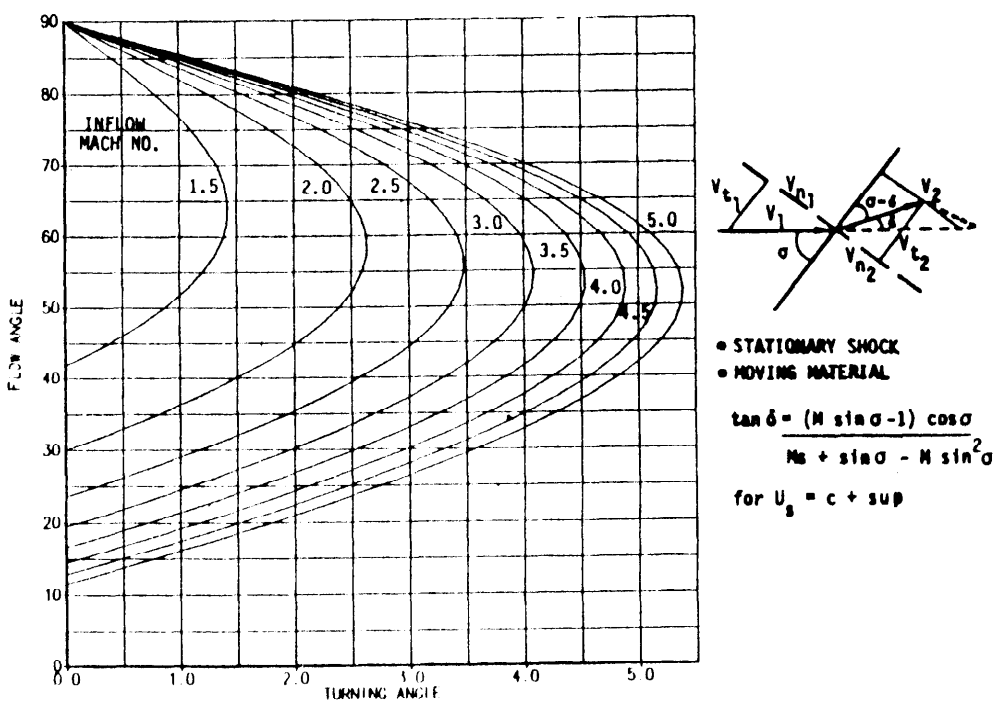

Figure 10. Shock Angle for Turning Flow of Saturated Sand

Equating tangential components on either side of the shock and substituting normal components into this empirical formula allows the flow angle to be expressed in terms of the shock angle and the inflow Mach number $M_1 = V_1/c$ as shown in Figure 10.

$$\delta = \tan^{-1} [(M_1 \sin \sigma - 1) \cos \sigma / (M_1 S + \sin\sigma - M_1 \sin^2\sigma)] \quad (10)$$

All remaining shock parameters can then be expressed in terms of these three as follows:

$$M_2 = M_1 \cos \sigma / \cos (\sigma - \delta)$$

$$\rho_2/\rho_1 = \tan \sigma / \tan (\sigma - \delta)$$

$$\Delta p/\rho_1 c_0^2 = M_1^2 \sin^2 \sigma (1 - \tan (\sigma - \delta)/\tan \delta)$$

Curves of pressure rise across oblique shocks in saturated sand are shown in Figure 11 using $c_0 = 2.07$ and $s = 4.3$. Each curve of shock states (e.g., for outflow pressure p_2 or velocity V_2) for two fixed initial parameters (e.g., inflow pressure p and velocity V_1) has two possible values. The branches of these curves which result in high pressures and large velocity reductions are referred to as strong shocks, and are close to normal shocks. The other branches which produce low pressures and small velocity reductions are weak shocks, essentially flow characteristics or Mach waves. Each curve also exhibits a maximum turning angle beyond which flow at that Mach number is not possible. The maximum turning occurs with shock angles given by the expression

$$\sigma_{max} = \sin^{-1} \frac{(S-2) + [4M^2 S(2S-1) + S(S+4)]^{1/2}}{2M(2S-1)}$$

Maximum turning angles can be calculated using this formula together with the first one above. Note that as

$$M \to 1,\ \sigma_{max} \to \sin^{-1}(1/M)$$

and $\delta_{max} \to 0$, while as $M \to \infty, \sigma_{max} \to \sin [S/(2S-1)]^{1/2}$ and $\delta_{max} \to 1/2\ [S9S-1)]^{1}$

When an oblique shock intersects a surface parallel to the inflow, a reflection must be set up to deflect the flow behind the first shock so that behind the second shock it remains parallel to the surface. Thus, the turning angle for both incident and reflected shocks is the same. The inflow velocity for the second shock is the outflow of the first. When, however, these conditions represent a forbidden state for the reflection (i.e., too great a turning angle for the inflow Mach number), no reflection is possible. Then, a new flow regime involving shock curvature is set up. These conditions are illustrated in Figure 12 for several values of the material shock parameters.

When a normal shock propagates in a host along an interface between dissimilar materials, an oblique reflection arises and an oblique shock is driven into the second material if it has a slower propagation velocity. Analysis of these two oblique shocks follows by requiring the flow deflection to be the same for both, the pressure behind the oblique reflection (dropped from that behind the incident normal shock) to be the same as that behind the driver oblique shock (raised from zero), the inflow velocity of reflection to be the outflow velocity of the normal shock, and the inflow of driven oblique to be the same as of the normal.

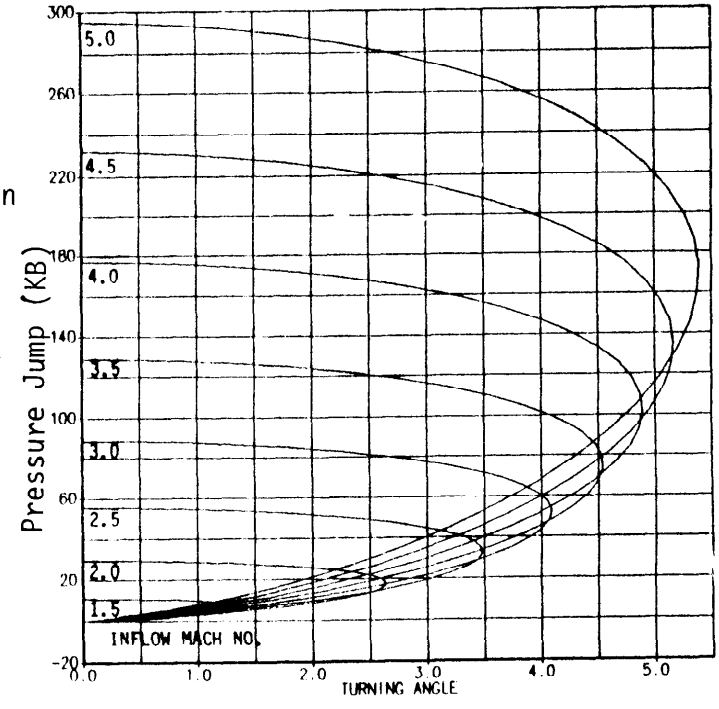

Figure 11. Shock Polar of Pressure for Flow of Saturated Sand

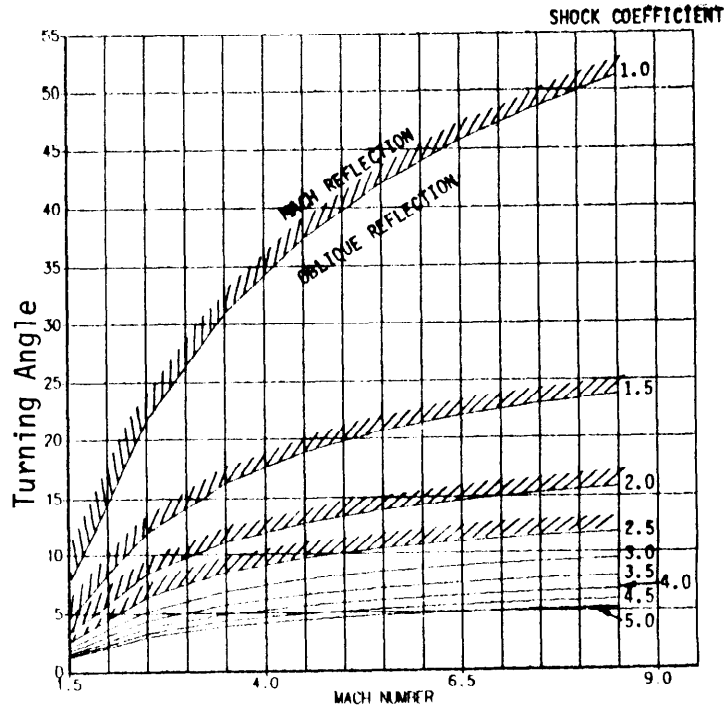

Figure 12. Regions of Oblique Shock Reflection and Mach Reflection

Using the properties of saturated sand described above, and of tuff in the form (Ref. 8)

$$u_s = 2.8 + 1.01\ u_p, \text{ with } \rho = 2.2 \qquad (11)$$

curves were constructed for analyzing the response of a sand column in a tuff medium. The solution is shown in Figure 13 for a range of normal shocks from 0 to 5 kbar. Because these are rather low pressures, the solution is almost linear and the various parameters are proportional to each other as indicated by the common curve for various scales.

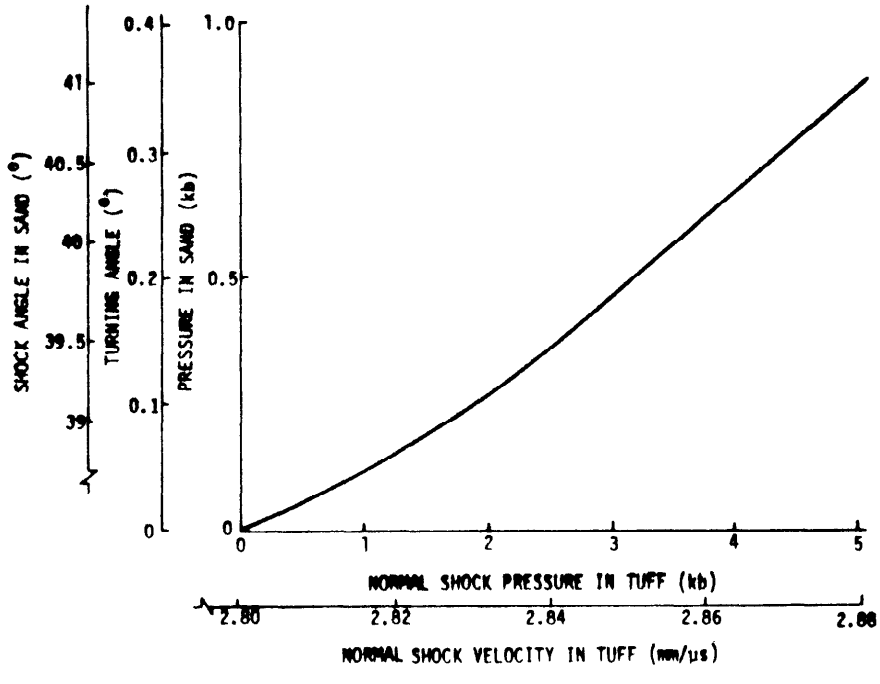

Figure 13. Oblique Shock Characteristics Driven Into Sand by Normal Shock in Tuff

For an incident shock of 1 kbar in the tuff, the sand pressure is about 0.1 kbar behind a 39° shock. The analysis of comparable case shown in Figure 8 leads to 0.2 kbar at 24°. The difference is probably due to conical effects in the latter, as evident from the nonuniformity of pressure in the sand.

CONCLUSIONS

The behavior of saturated sand under shock loading is described as exhibiting porous crush, viscoelasticity, and non-linear compressibility but with no shear capability.

Analysis of oblique shocks in saturated sand as a fluid can be made using adaptations of gas-dynamic methods, and using numerical analyses.

REFERENCES

1. U.S. Patent No. 3,981,152

2. Schmidt, R. M., Davies, F. W., and Shrader, J. E., "The Material Behavior of High Temperature Tungsten," Proceedings of the Fourth Symposium on Nuclear Survivability of Propulsion and Ordnance Systems, Seattle, Washington, April 1974.

3. Graham, R. A., and Ingram, G. E., J. Appl. Phys. 43, 826 (1972).

4. Kohn, B. J., "Compilaton of Hugoniot Equations of State," Air Force Weapons Laboratory, AFWL-TR-69-38, April 1969.

5. Lawrence, R. J., and Mason D. S., "WONDY IV - A Computer Program for One-Dimensional Wave Propagation with Rezoning," Sandia Labs, SC-RR-710284, Aug. 1971.

6. Swegle, J. W., "TOODY IV - A Computer Program for Two-Dimensional Wave Propagation," Sandia Labs, SAND-78-0552, Sept. 1978.

7. Liepman, H. W., and Roshko, A., "Elements of Gasdynamics," John Wiley and Sons, N.Y., 1957.

8. Bass, R. C., Hawk, H. L., and Chabai, A. J., "Hugoniot Data for Some Geologic Materials," Sandia Labs, Research Report SC-4903, June 1963.

THEORETICAL AND EXPERIMENTAL STUDY OF THE RESPONSE OF CLAMPED ROLLED HOMOGENEOUS STEEL ARMOR PLATES TO CLOSE-IN BLAST LOADING

ABDUL R. KIWAN
Mathematician
USA ARRADCOM/Ballistic Research Laboratory
Aberdeen Proving Ground, Maryland 21005

ABSTRACT

A combined experimental and theoretical study of the response of clamped rolled homogeneous steel armor (RHA) plates to close-in blast loading was conducted. The study covered a range of nominal armor thicknesses of 3/16 inches (4.76 mm) to 3/4 inches (19.05 mm) and nominal charge weights of two pounds (0.91 kg) to eight pounds (3.63 kg). Experimental data of vertical deflections and hole areas were used to derive a set of formulae which give a measure of the response of the RHA plates to close-in blast loading. The functional forms used were arrived at through similitude theory and dimensional analysis. A formula was also derived to describe the inception of material failure. The derived set of formulae provide a quick response predictions of damage to RHA plates for system vulnerability or survivablity evaluation.

INTRODUCTION

The requirement for predicting weapon effects on lightly armored vehicle structures leads directly to the study of the response of clamped rolled homogeneous steel armor plates (RHA) to severe transient impulsive loads. The plastic response and failure of light armor to close-in blast loading is the problem of present interest. It is desirable to be able to predict the maximum deformation of armor plates from this type of loading, and to predict the conditions under which an armor plate will fail, and the extent of the failure. The ability to make quick quantitative predictions of the resultant damage from close-in blast loading is of paramount importance for vulnerability and survivability evaluation. Large continuum mechanics finite difference or finite element computer codes are not suitable for such purposes. Approximate analytical methods, on the other hand, are far more useful in this case for design and safety considerations as well as from a system and vulnerability analysis point of view.

Blast measurements and prediction techniques have been historically confined to the far field region [1]. There are no available blast pressure data or simple analytical predictive methods for the close-in blast region. Since our interest is in the response of armor plates and not in characterizing the close-in blast, we intend to characterize the response in terms of the explosive charge weight, its standoff distance, target thickness, and other target parameters. This approach avoids the difficulties of close-in blast measurements and characterization.

Similar structural response studies of cantilever beams to air blast from spherical Pentolite charges were made by Baker et al. [2]. Ewing and Hanna [3] had earlier proposed the use of the response of cantilever beams as a measure of the blast load. More recently, Huffington and Wortman [4] studied the response of fixed cylindrical shells to an assumed frontal cosine impulsive loading. Their study is based on data obtained from a finite difference calculation using the REPSIL code. They employed dimensional analysis to study the properties of the solution. Their solution assumed an elastic-perfectly plastic constitutive equation and the material was assumed to have infinite ductility. They developed an empirical model by fitting the computed data to an assumed functional form. Kiwan and Goodman [5] presented an experimental study and data on the response of rolled homogeneous steel armor (RHA) plates to blast loading. Kiwan [6] used similitude theory and dimensional analysis to give a measure of the response for failed test plates. The present study develops a set of analytical formulae that give a measure of the response of an armor plate to close-in blast when the response is plastic or when material failure occurs. Furthermore, we derive the threshold conditions that determine the inception of material failure.

EXPERIMENT AND DATA

An experimental study was made of the plastic response of light armor plates to close-in blast loading from bare spherical Pentolite charges. The study covered nominal armor thicknesses of 3/16 inch (4.76 mm), 3/8 inch (9.53 mm), and 3/4 inch (19.05 mm) and nominal charge weights of two pounds (0.91 kg), five pounds (2.27 kg), and eight pounds (3.63 kg) at standoffs of less than four charge radii, except for one data point at six charge radii. The test plates were cut as squares with a side of four feet (1219.2 mm) long. The plates were placed on a table constructed of heavy armor and bolted down with 1.25 inch (31.75 mm) bolts. Sixteen holes were burned through each test plate around its perimeter to match similar holes in a table stand to accommodate the bolts. The center of each hole was three inches (76.2 mm) from the edge of the plate. The unsupported part of each test plate was a square of 3 ft. x 3 ft. (914.4 mm x 914.4 mm). The charges were suspended above the geometric center of the plate and detonated with an electric J2 Engineer's Special Cap. Figure 1 gives a schematic cross-sectional view through the center of the plate and the test setup. Vertical deflections were measured at predrawn grid points of a mesh two inches (50.8 mm) apart. Reduction in the thickness of the plate was measured at alternate grid points. For ruptured test plates, the area of the hole was measured and an estimate of the projection of the hole area on the original plane of the test plate was made. The critical rupture threshold standoffs were determined for the nine combinations of plate thicknesses and charge sizes covered in the study. Table 1 gives the critical standoffs so determined.

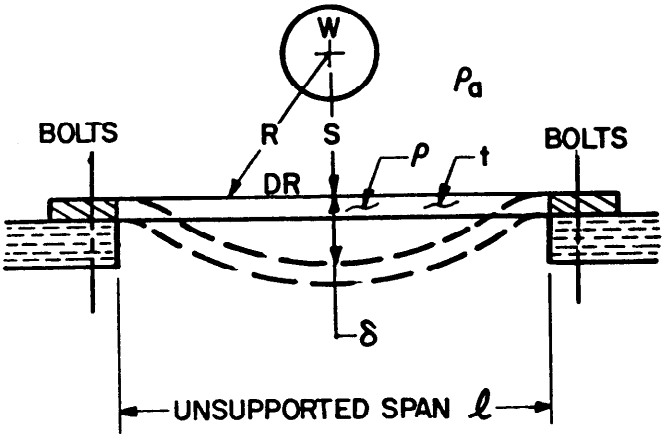

Figure 1 Schematic Cross-Sectional View of Test Setup, Through the Center of the Plate.

Table 1 Critical Threshold Standoff (mm) for RHA Plates as a Function of Thickness and Explosive Charge Weight

Chg. Wt.	Plate Thickness (mm)		
(kg)	5.05	9.83	19.14
0.91	95.25	66.68	50.50
2.27	152.40	98.43	76.4
3.68	196.85	123.83	107.95

Kiwan and Goodman [5] reported the entire set of data obtained from these tests, and gave a preliminary analysis of their experimental results.

DIMENSIONAL ANALYSIS

Dimensional analysis provides a means of studying the possible functional relationships among the various physical variables of our experiment in a framework independent of the physical units of measurement. An insight can be gained by taking cross-sectional cuts of the functional space, for instance, by holding some of the dimensionless variables constant and studying the functional dependence among the remaining variables. Here we consider two cases of interest:

ELASTIC-PLASTIC CASE:

In this case, we take the maximum vertical deformation (deflection) δ, of a plate, which occurs at its geometric center as our measure of the plate's response. The functional dependence of δ on other physical variables can be expressed as

$$\delta = f(t, \ell, \sigma_o, \rho, S, E, \rho_a) \quad , \tag{1}$$

where t, ℓ, ρ, and σ_o denote the plate's thickness, its unsupported span, its material density, and its uniaxial yield stress respectively. The variables E and S denote the total explosive energy of the charge, and its standoff distance as measured from the charge center to the surface of the plate. ρ_a denotes the density of the atmosphere. There are eight variables involving three fundamental units so that our functional relationship (1) can be reduced to an equation involving five nondimensional π-quantities, i.e.,

$$\pi_1 = g(\pi_2, \pi_3, \pi_4, \pi_5) \quad , \tag{2}$$

where $\pi_1 = \delta/\ell$, the nondimensional maximum vertical deflection

$\pi_2 = t/\ell$, the nondimensional thickness

$\pi_3 = S/\ell$, the nondimensional standoff of the charge

$\pi_4 = \ell^3\sigma_o/E$, a parameter representing nondimensional work

$\pi_5 = \rho/\rho_a$, the nondimensional density.

The above set of π-terms is not unique although it constitutes an independent set of variables. The solution represented by Eq. (2) can be visualized as defining a hypersurface in a five-dimensional space as adumbrated in Figure 2. It would be an enormous task to derive a mathematical equation for this surface which is valid over the entire range of values for the four parameters π_2, π_3, π_4, and π_5. Instead, we take cuts through the hypersurface by holding some of the π-variables constant and derive an analytical submodel by using the experimental test data referred to in the second section. The resulting model can then be used for predictions within the range of validity of the

variables included in the submodel, or can be used in sensitivity studies for the variation of the response as a function of the variations of some variable while holding the other variables constant.

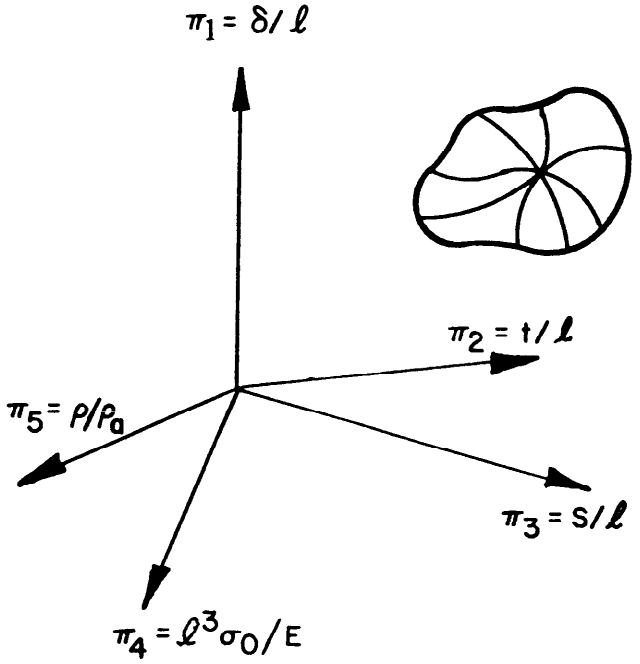

Figure 2 Response Surface Representation in Five-Dimensional Space

FAILURE CASE:

For this case, we choose the radius of the hole generated in the plate DR, as our measure for the extent of failure, or the plate's response. No implication is intended here that a plate's failure patterns are circular in fact. DR is simply defined to be the radius of the circle of equal area as the projection of the hole area produced in the plate onto the original plane of the plate as represented in Figure 1. If one defines R as

$$R = \sqrt{DR^2 + S^2} \quad , \tag{3}$$

then R can be considered to be a function of the other physical variables and can be expressed as

$$R = h(t, \ell, \sigma_1, \rho, S, E, \rho_a) \quad , \tag{4}$$

where σ_1 is the ultimate stress of plate's material. Arguments similar to those used in the elastic-plastic case yield the following π-quantities:

$\pi_1 = R/\ell$, the nondimensional response-standoff measure

$\pi_4 = \ell^3\sigma_1/E$, a parameter representing nondimensional work

and π_2, π_3, and π_5 remain as before. Again this set of π-terms is not unique and other equivalent sets can be taken as will be done subsequently.

MODEL DERIVATION

The experimental data described in the second section above are limited to RHA. Since ρ_a is assumed to be constant, hence π_5 = constant. Furthermore, for the available data ℓ, σ_o, and σ_1 are constant. The remaining set of π-quantities in Eq. (2) can, therefore, be replaced by the equivalent set of variables

$$\hat{\pi}_1 = \pi_1 \cdot \pi_4^{1/3} = \delta\, \sigma_o^{1/3}/E^{1/3} \quad ,$$

$$\hat{\pi}_2 = \pi_2 \cdot \pi_4^{1/3} = t\, \sigma_o^{1/3}/E^{1/3} \quad ,$$

$$\hat{\pi}_3 = \pi_3 \cdot \pi_4^{1/3} = S\, \sigma_o^{1/3}/E^{1/3} \quad ,$$

$$\hat{\pi}_4 = \pi_4^{1/3} = \ell\, \sigma_o^{1/3}/E^{1/3} \quad . \qquad (5)$$

The total energy E is proportional to the explosive charge weight W, hence, interchanging those quantities in Eq. (5) and dropping the variables ℓ, σ_o, and σ_1 that are held constant, Eq. (2) reduces to the relation:

$$\delta/W^{1/3} = F\left(t/W^{1/3},\ S/W^{1/3},\ 1/W^{1/3}\right) \quad . \tag{6}$$

Assuming

$$\delta/W^{1/3} = a\left(t/W^{1/3}\right)^{b}\ \left(S/W^{1/3}\right)^{c}\ \left(1/W^{1/3}\right)^{d} \quad , \tag{7}$$

and then fitting this functional form to the experimental data in a least square sense we find that

$$a = 27392697,\quad b = -1.8796,\quad c = -2.0580,\ \text{and}\ d = 0.0015 \quad . \tag{8}$$

Since $W^{-d/3} \approx 1$, it follows that $\delta/W^{1/3}$ is a function of two scaled terms only and is independent of the third variable in Eq. (7). Eq. (7) reduces to:

$$\delta/W^{1/3} = \frac{27392697}{\left(t/W^{1/3}\right)^{1.8796}\ \left(S/W^{1/3}\right)^{2.0580}} \quad , \tag{9}$$

or equivalently

$$\delta = \frac{27392697\ W^{1.6458}}{t^{1.8796}\ S^{2.0580}} \quad . \tag{10}$$

Eqs. (9) and (10) will be used for parametric studies later on and their predictions will be compared to the experimental data. The units to be used in Eqs. (9) and (10) are millimeters for δ, t and S, and kilograms for W.

Analogous dimensional analysis consideration in the failure case leads to the relation:

$$R/W^{1/3} = G\left(t/W^{1/3},\ S/W^{1/3},\ 1/W^{1/3}\right) \tag{11}$$

Assuming again that

$$R/W^{1/3} = a\left(t/W^{1/3}\right)^{b}\left(S/W^{1/3}\right)^{c}\left(1/W^{1/3}\right)^{d} \quad , \tag{12}$$

and fitting this functional form in a least square sense to the experimentally measured data for failed test plates yields the equation

$$R/W^{1/3} = a/\left[\left(t/W^{1/3}\right)^{2.4116}\left(S/W^{1/3}\right)^{3.6834}\left(1/W^{1/3}\right)^{0.6623}\right] \quad , \tag{13}$$

where a = 2.0317 when the inch and pound are used for units of length and mass, and a = 1.4478×10^{11} when the millimeter and kilogram are used as units. Squaring Eq. (13), then using Eq. (3), and solving for DR we get

$$DR = \left[a^{2} \cdot W^{5.1716}/\left(S^{7.3669} \cdot t^{4.8233}\right) - S^{2}\right]^{1/2} \quad . \tag{14}$$

Eq. (14) gives a measure of the extent of the damage when the response of the plate goes beyond the plastic regime. The plate starts to fail when the expression inside the square bracket vanishes, i.e.,

$$S_{c} = a^{0.2135}\, W^{0.5521}/t^{0.5149} \tag{15}$$

or

$$S_{c} = 241.551\, W^{0.5521}/t^{0.5149} \tag{16}$$

when the metric system of units is used. Eq. (16) can be solved for t, to give

$$t_c = 42471.686\ W^{1.0722}/S^{1.9420} \qquad (17)$$

Eq. (16) gives the critical value of the standoff at which an RHA plate of thickness, t, will fail when loaded by the blast from a Pentolite charge, W. Eq. (17) gives the critical RHA thickness which will fail when blast loaded by a Pentolite charge, W, at standoff S. Using Eq. (17) to eliminate t from Eq. (10), we get:

$$\delta_c = 0.0548\ S^{1.5922}/W^{0.3695} \quad . \qquad (18)$$

Eq. (18) represents a failure surface in three-dimensional space. δ_c represents the critical deformation at which failure starts.

MODEL APPLICATION

Predictions of maximum vertical deflection of the plate made with Eq. (10) compared well with experimental data. Such a comparison can be seen in Figure 3. The various sets of experimental data are plotted using different symbols. The curves plotted were calculated from Eq. (10). Each plotted curve shows the maximum deflection δ, as a function of the standoff S, and corresponds to constant values of t and W. The values chosen for t and W correspond in each case to the average values of a set of data points. The curves are seen to fit the data reasonably well. Figure 4 shows the variation of scaled deformation as a function of scaled standoff. The plotted curves are level curves corresponding to constant values of $t/W^{1/3}$. These curves were computed from Eq. (9). The constant value of $t/W^{1/3}$ for each curve corresponds to the average value for one set of data points. The agreement with the data is again seen to be good.

Eq. (18) for the failure surface can be written as:

$$\delta_c/W^{1/3} = 0.0548\ \left(S/W^{1/3}\right)^{1.5922}/W^{0.1722} \quad . \qquad (19)$$

$$t_c = 42471.686\ W^{1.0722}/S^{1.9420} \qquad (17)$$

Eq. (16) gives the critical value of the standoff at which an RHA plate of thickness, t, will fail when loaded by the blast from a Pentolite charge, W. Eq. (17) gives the critical RHA thickness which will fail when blast loaded by a Pentolite charge, W, at standoff S. Using Eq. (17) to eliminate t from Eq. (10), we get:

$$\delta_c = 0.0548\ S^{1.5922}/W^{0.3695} \quad . \qquad (18)$$

Eq. (18) represents a failure surface in three-dimensional space. δ_c represents the critical deformation at which failure starts.

MODEL APPLICATION

Predictions of maximum vertical deflection of the plate made with Eq. (10) compared well with experimental data. Such a comparison can be seen in Figure 3. The various sets of experimental data are plotted using different symbols. The curves plotted were calculated from Eq. (10). Each plotted curve shows the maximum deflection δ, as a function of the standoff S, and corresponds to constant values of t and W. The values chosen for t and W correspond in each case to the average values of a set of data points. The curves are seen to fit the data reasonably well. Figure 4 shows the variation of scaled deformation as a function of scaled standoff. The plotted curves are level curves corresponding to constant values of $t/W^{1/3}$. These curves were computed from Eq. (9). The constant value of $t/W^{1/3}$ for each curve corresponds to the average value for one set of data points. The agreement of the predictions with the experimental data is again seen to be good.

Eq. (18) for the failure surface can be written as:

$$\delta_c/W^{1/3} = 0.0548\ \ S/W^{1/3\ 1.5922}/W^{0.1722} \quad . \qquad (19)$$

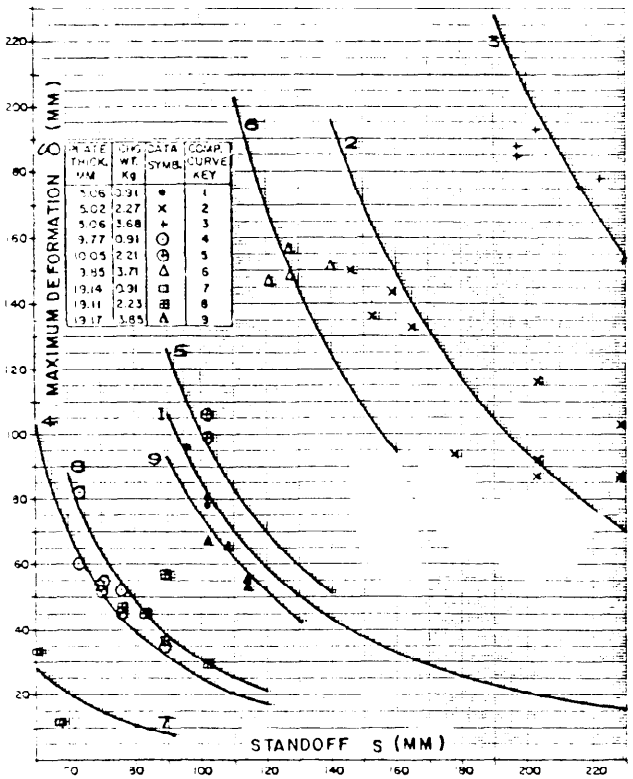

Figure 3 Experimental and Computed Maximum Deformation as a Function of Standoff for RHA Plates

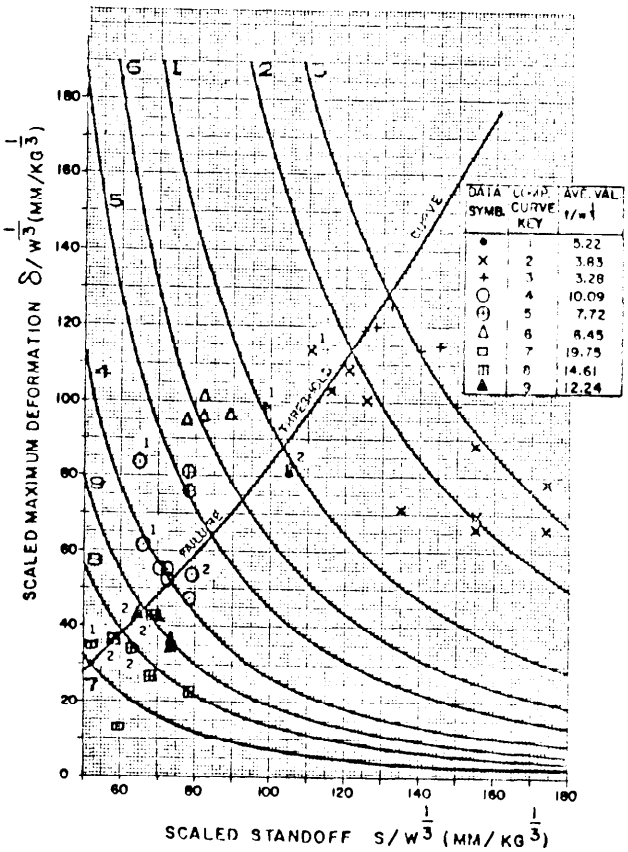

Figure 4 Comparison of Computed and Experimental Scaled Maximum Deformation vs. Scaled Standoff

Since $W^{0.1722} \approx 1$, it can be neglected in comparison with the value of $(S/W^{1/3})^{1.5922}$, Eq. (19) can be approximated by the equation:

$$\delta_c/W^{1/3} = 0.0548 \quad S/W^{1/3})^{1.5922} \quad . \qquad (20)$$

Eq. (20) represents the FAILURE THRESHOLD CURVE in the plane of $(S/W^{1/3}, \delta/W^{1/3})$. This curve which is shown in Figure 4 intersecting the level curves divides the plane into two regions: (a) a Plastic Deformation Region below the threshold curve and (b) a Failure Region. Examination of the individual experimental data points revealed that data points marked with 1 correspond to cases where the test plates had actually failed and had sizable

cracks. All that data is seen to lie in the failure region. Data points marked with 2 correspond to cases where delamination occurred at the geometric center of the plate and inhibited after test thickness measurement at that location. It is believed that delamination indicates the inception of failure. All that data lies close around the threshold curve.

Examination of the data points on curves 5 and 6 of Figure 4 revealed that the six plates represented by these data points did not fail in the tests representing the data points. However, these data points lie in the failure region. A similar situation arises with three of the data points on curve 4. All the data on curves 4, 5, and 6 represent plates of 3/8 inch (9.53 mm) nominal thickness. These observations implied that those test plates exhibited greater ductility before failure. Small samples were recently obtained from these test plates, analyzed metallurgically, and tested for hardness and mechanical properties. Preliminary results from these tests are contained in Table 2 [7].

Table2 Preliminary Results of Hardness Tests

Thickness (Inch)	3/4	3/8A	3/8B	3/16
Average RC	51.0	37.5	36.2	41.5
Equivalent BHN	496	347	334	388
Yield Stress (Ksi)	220	152	147	176
Ultimate Stress (Ksi)	256	163	158	190
Elongation (%)	12	18	18	15

The last three rows of Table 2 were estimated on the basis of the properties of 4340 steel. Table 2 reveals the greater ductility of the 3/8 inch samples as anticipated. The tests also revealed that the 3/4 inch sample tested was contrary to expectation harder than the other samples and was the least ductile.

SUMMARY OF RESULTS AND CONCLUSIONS

Table 1 contains the experimentally determined critical threshold standoffs. Those standoffs were determined on the basis of experience gained that the plates will fail at such standoffs and develop cracks of appreciable length, without massive failure. The information contained in Table 1 is repeated in the first three columns of Table 3. Column 4 contains the corresponding deformations as computed from Eq. (10). Columns 5 and 6 of Table 3 contain scaled standoffs and deformations.

Table 3 Computed Deformations Corresponding to Experimental Critical Threshold Standoffs

W (kg)	t (mm)	S_c (mm)	δ (mm)	$S_c/W^{1/3}$ (mm/kg$^{1/3}$)	$\delta/W^{1/3}$ (mm/kg$^{1/3}$)
0.91	5.05	95.25	94.60	98.29	97.62
2.27	5.05	152.40	161.81	115.96	123.12
3.68	5.05	196.85	211.59	127.50	137.05
0.91	9.83	66.68	56.35	68.81	58.15
2.27	9.83	98.43	113.77	74.90	86.57
3.68	9.83	123.83	157.06	80.21	101.73
0.91	19.14	50.50	28.53	52.11	29.45
2.27	19.14	76.40	54.77	58.13	41.67
3.68	19.14	107.95	59.54	69.92	38.56

Figure 5 contains the nine data points represented by Columns 5 and 6 of Table 3. The curve labelled 1, is the failure threshold curve of Figure 4 which is represented by Eq. (20). It is seen that seven of the data points lie in the failure region as they should. One of the 3/4 inch (19.05 mm) data points lies on the curve and another lies below the curve. Curve 2 in Figure 5 was arrived at by fitting, in a least square sense, the critical standoff S_c of Table 3 as a function of t and W, which gave

$$S_c = 237.55\ W^{0.5509}/t^{0.5075} \quad . \tag{21}$$

Solving Eq. (21) for t one gets

$$t_c = 48024.66\ W^{1.0855}/S^{1.9705} \quad . \tag{22}$$

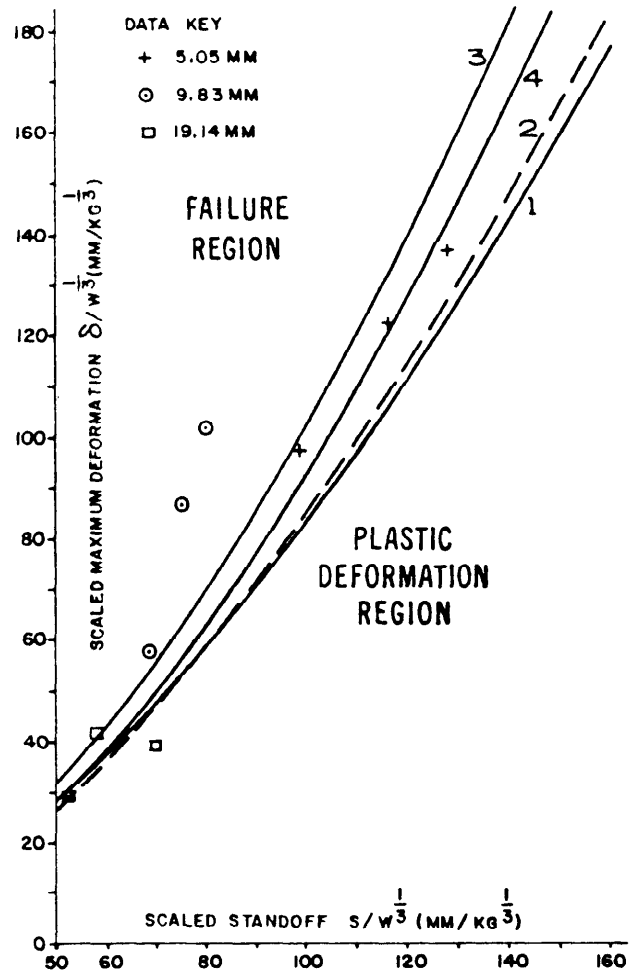

Figure 5 Comparison of Computed Threshold Curves and Threshold Data.

Substituting for t, from Eq. (22) into Eq. (10)

$$\delta_c = 0.0435\ S^{1.6458}/W^{0.3945} \qquad (23)$$

or

$$\delta_c/W^{1/3} = 0.0435 \left(S/W^{1/3}\right)^{1.6458}/W^{0.1792} \quad . \tag{24}$$

Again, since $\left(S/W^{1/3}\right)^{1.6458} \gg W^{0.1792} \approx 1$, Eq. (24) can be approximated by

$$\delta_c/W^{1/3} = 0.0435 \left(S/W^{1/3}\right)^{1.6458} \quad . \tag{25}$$

Eq. (25) is represented by curve 2 in Figure 5. Curve 3 was obtained by a least square fit of Columns 5 and 6 of Table 3, while curve 4 was obtained by fitting the six data points in Columns 5 and 6 representing the 5.05 mm and 19.14 mm thickness data. Curves 3 and 4 are represented by Eqs. (26) and (27), respectively:

$$\delta/W^{1/3} = 0.0448 \left(S/W^{1/3}\right)^{1.6801} \quad , \tag{26}$$

$$\delta/W^{1/3} = 0.0292 \left(S/W^{1/3}\right)^{1.7494} \quad . \tag{27}$$

Eqs. (21) and (22) are to be compared with Eqs. (16) and (17) which were determined in the previous analysis.

The preceding analysis produces a set of formulae which can be used to give a measure of the response of an armor plate to close-in blast loading. Eq. (10) gives a measure of this response in terms of the maximum vertical deflection when the plate responds plastically. Eq. (14) gives a measure of the response when failure occurs and holes are generated. The response in this case is measured in terms of the radius DR of the circle of equal area as the projection of hole area generated onto the original plane. This statement does not have any implication about the type or patterns of plate failures. Finally, Eq. (20) gives the equation of the failure threshold curve shown in Figures 4 and 5. The above set of formulae can find utility in vulnerability assessment codes and can be used for design and safety purposes.

The model presented here is based upon the results of statically detonated bare spherical Pentolite charges near RHA plates. Our ultimate goal, of course, is to be able to predict the effects of HE projectile impacts

on actual vehicle structures. The tests reported here are not claimed as representative of real projectile impacts, nevertheless, we feel that the experiment and derived models are a significant step towards this ultimate goal. The knowledge gained from this work will serve to guide additional efforts. We hope to be able to expand our model to include other parameters such as (1) charge shape, (2) type and degree of confinement, (3) striking velocity, (4) obliquity of impact, (5) dimensions of unsupported span, and (6) armor material.

REFERENCES

1. Goodman, H.J., "Compiled Free-Air Blast Data on Bare Spherical Pentolite," Ballistic Research Laboratories, Report No. 1092, 1960.

2. Baker, W.R., Ewing, Jr., W.O., Hanna, J.W., and Bunnewith, G.E., "The Elastic and Plastic Response of Cantilevers to Air Blast Loading," Ballistic Research Laboratories, Report No. 1121, 1960.

3. Ewing, W.O. and Hanna, J.W., "A Cantilever for Measuring Air Blast," Ballistic Research Laboratories, Technical Report No. 1139, 1957.

4. Huffington, Jr., N.J. and Wortman, J.D., "Parametric Influences on the Response of Strucutral Shells," Trans. of ASME, J. of Eng. Ind., 1975, 1313.

5. Kiwan, A.R. and Goodman, H.J., "The Response of Rolled Homogeneous Steel Armor Plates to Explosive Blast Loading," US Army Armament Research and Development Command/Ballistic Research Laboratory, ARBRL-TR-2393, 1982.

6. Kiwan, A.R., "Predicting the Blast Hole Size in Rolled Homogeneous Steel Armor Plates," US Army Armament Research and Development Command/Ballistic Research Laboratory, ARBRL-TR-2378, 1981.

7. Golaski, S.K., private communication, Ballistic Research Laboratory, 1982.

SIMULATIONS OF BALLISTIC IMPACT SITUATIONS INVOLVING DEEP PENETRATION AND PERFORATION OF TARGETS WITH A LAGRANGIAN IMPACT CODE

BARBARA E. RINGERS
Mathematician
US Army Ballistic Research Laboratory
US Army Armament Research and Development Command
Aberdeen Proving Ground, Maryland 21005

ABSTRACT

A major enhancement to the capabilities of EPIC-2, a Lagrangian finite element impact code, has been developed and implemented enabling the modeling of deep penetration and/or perforation of targets. This paper presents the techniques which were developed to handle dynamic relocation of sliding surfaces and the automatic addition of new sliding surfaces. These techniques were first applied to the modeling of axisymmetric ballistic impact situations involving kinetic energy penetrators versus targets which fail by plugging due to high strains. The criteria which were required for target failure to begin and proceed "naturally", ultimately resulting in perforation when warranted, are discussed. A parametric study is presented of a steel cylinder versus a pure titanium target at normal obliquity. Only the striking velocity and the critical level of equivalent strain necessary to mandate failure were varied. The results are demonstrated to be consistent between calculations; furthermore, no rezoning or manual intervention was involved in any of the calculations.

I. INTRODUCTION

The capability to model deep penetration and/or perforation of targets with the Lagrangian impact code, EPIC-2 [1] has been implemented. Techniques were developed to handle dynamic relocation of sliding surfaces and the automatic addition of new sliding surfaces when necessary. These techniques were utilized in attempts to model a specific impact situation where the primary mode of target failure was plugging.

This paper discusses the criteria utilized and critical levels of such criteria which were required for target failure to begin and proceed "naturally", ultimately resulting in perforation when warranted.

A parametric study is presented of a ballistic situation wherein a hardened, roller bearing steel cylinder impacted a pure titanium (Ti 125) target at normal obliquity and target failure was considered to be the result of plugging due to high strains. Only the striking velocity and the critical level of equivalent strain utilized to enable failure were varied. The results are demonstrated to be consistent; furthermore, no rezoning or manual intervention was involved in any of the calculations.

Some discussion is included of a second impact situation similar to the first except that the target was a titanium alloy, Ti 318 (6%Al,4%V). The plugging failure in this situation was considered to be the result of adiabatic shear. It is shown that this case can not be successfully modeled if only the equivalent strain criterion is utilized to predict failure without consideration being given to possible thermal softening in the equations involved.

II. SLIDING SURFACE TECHNIQUES

In papers by Mos: [2] and Zener and Hollomon [3] describing the results of punching experiments, the thicknesses of the shear bands measured were in thousandths of an inch; the velocities involved were in tens-of-feet/sec. Johnson [4] noted that "the faster a punching operation is, the higher the strain rate and the larger the flow stress but the narrower the shear zone."

In modeling ballistic impacts with EPIC-2, triangular element sizes are measured in tenths or hundredths of an inch. Therefore, in order to simulate the shearing in a region at least an order of magnitude smaller, it was decided to let splitting occur between elements when an element reached a particular criterion. Provision was also made to "totally fail" elements, including master and slave elements, when they reached another, as yet unspecified, failure criterion. In the original version of EPIC-2 [1], material fracture is handled by failing elements in two possible ways: 1) failure in shear and tension if the element exceeds specified equivalent or volumetric strain levels, 2) total failure if the element exceeds a specified equivalent strain level. In the first case the element is still able to withstand hydrostatic compression while in the second case all stresses including pressure are set equal to zero.

The rationale in this study was that the shearing involved should be initiated in an area by splitting between elements and eventually the levels of equivalent strain suffered by some elements would possibly require total failure of those elements.

The original version of EPIC-2 [1] utilizes sliding surfaces comprised of master and slave nodes to keep projectile and target materials separate. For each time increment, the equations of motion are applied to the master nodes (usually the target frontal surface) and the slave nodes (usually those on the projectile surface likely to interact with the target). Although elements with three slave nodes can be totally failed, simulating erosion, the master sliding surface must remain intact. Therefore only relatively moderate penetration problems can be handled before severe grid deformation essentially halts a calculation. The sliding surface routines did not include a double pass, the necessity for which is discussed in Reference 5. Sliding surface routines written by Lambert [6] which included a double pass for interference - slave nodes versus master surfaces, then master nodes versus slave surfaces - were therefore utilized. If there is interference in the first case the slave node is placed on the master surface in a direction normal to the master surface. Similarly an interfering master node is placed on the

slave surface. Ensuring that translational and rotational momenta are conserved, the velocities of the interfering node and the two nodes comprising the surface involved are updated. Due to the excessive stiffness of triangular elements in the two-triangle arrangement [7], the geometry generator for the "crossed" triangle (four triangular elements within a quadrilateral) arrangement was utilized in this work.

For the new sliding surface techniques developed it was assumed that the slave surface is the projectile exterior and the master surface is the frontal target surface. (This is arbitrary and modifications can readily be made to accommodate the reverse situation.) When an element attains Criterion 1* indicating that fracture is to occur, a node is essentially split in two (Figures 1a, 1b). The initial "split" node, that meeting Criterion 2*, also must be a master node or the element involved is rejected as causing splitting. The direction of the split, determined by a third criterion*, establishes the "next" node from which further splitting must occur. Both the "next" node and "new" node are inserted in the master surface after the original "split" node (Figure 2a), thereby dynamically relocating this sliding surface. The "new" node is assigned the same coordinates, velocities and restraint properties as the "split" node. The masses assigned to the "split" and "new" nodes are based on which elements now share each node. The forces assigned each are then based on the ratios of the newly assigned nodal masses to the original pre-split nodal mass.

Besides interference between the projectile and target, there must be concern about possible interference between the two sides of the split developing in the target. This is handled by establishing another set of master and slave surfaces between the developing plug and remaining target material whose mutual interference is checked identically to the first set (Figure 2b).

Splitting continues until the projectile velocity reaches zero or perforation occurs. Perforation is enabled by a complete break in the first master surface. Both master/slave surface relationships continue to be checked for mutual interference with consideration given the possible discontinuity due to perforation until the projectile is no longer affected by the remaining (non-plug) target material. For a more detailed discussion of the sliding surface techniques developed see Reference 8.

III. IMPACT SITUATION TO BE MODELED

Two experimental impact situations served as a basis for this study and were conducted and discussed by Woodward [9]. Both impact situations involved a blunt, hardened, roller bearing steel cylinder impacting titanium targets at 0^0 obliquity. In the first case the titanium target was 99% pure titanium (Ti 125) and target failure was considered to be the result of plugging due to high strains. (See Table 1 for specifics on impact situation.) In the second case the target was a titanium alloy, Ti 318 (6%Al,4%V) and target failure was the result of plugging due to adiabatic shear.

* These criteria are defined and discussed in Section IV.

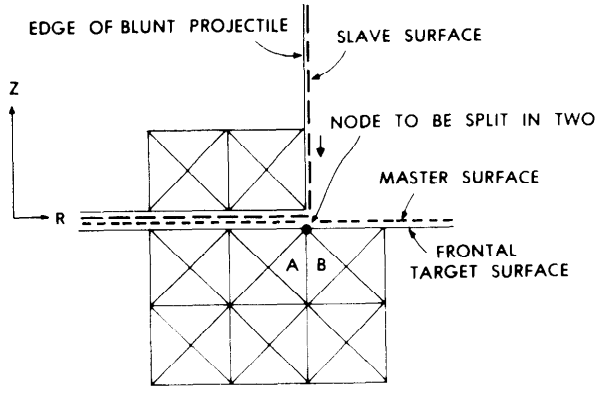

FIGURE 1a. ELEMENT A OR B MEETS CRITERION 1

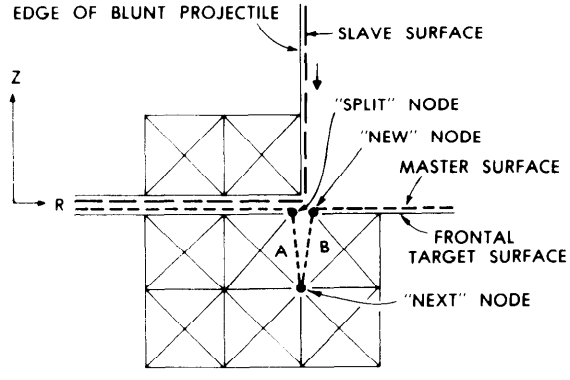

FIGURE 1b. "SPLIT" NODE MET CRITERION 2 SPLIT WILL BE FURTHERED FROM NEXT NODE

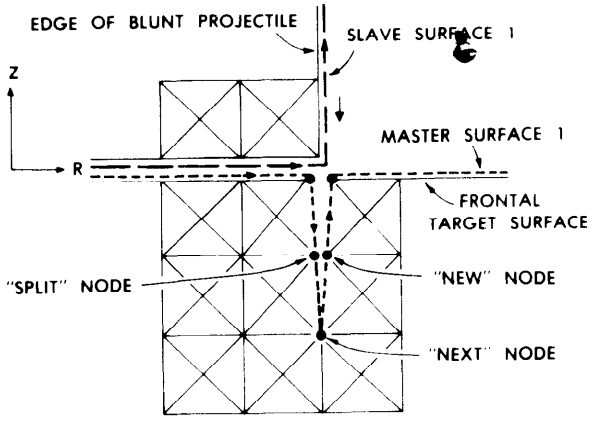

FIGURE 2a. SLIDING SURFACE 1 INTERACTIONS

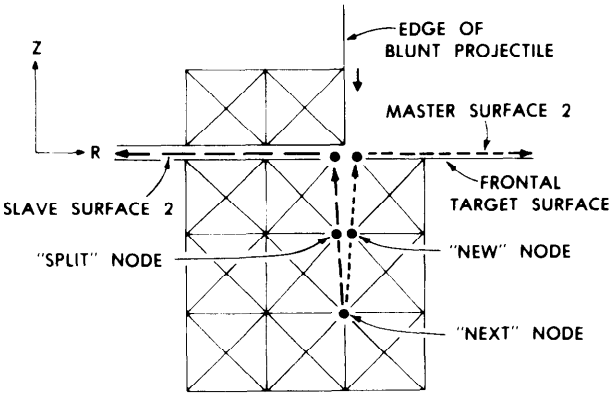

FIGURE 2b. SLIDING SURFACE 2 INTERACTIONS

TABLE 1 PROJECTILE AND TARGET PROPERTIES

	PROJECTILE	*TARGET 1 (Ti 125)*	*TARGET 2 (Ti 318)*
MATERIAL	HARDENED, ROLLER BEARING STEEL	ROLLED & ANNEALED 99% PURE Ti	Ti WITH 6% Al, 4% V
SHAPE	BLUNT	50 mm SQUARE	50 mm SQUARE
MASS	3.34 g	—	—
LENGTH	25.4 mm THICK	6.35 mm	6.35 mm
DIAMETER	4.76 mm	—	—
DENSITY	7.39×10^3 kg/m^3	4.51×10^3 kg/m^3	4.43×10^3 kg/m^3
YIELD σ_Y	2290 MPa	522.5 MPa	1029 MPa
UTL σ_U	2500 MPa	600 MPa	1209 MPa
ε_U	∞	.45 - .5	.2
SPEC HEAT	4.6×10^2 J/kg °K	5.1916×10^2 J/kg °K	5.65×10^2 J/kg °K
YOUNGS MOD	1.93×10^5 MPa	1.158×10^5 MPa	1.158×10^5 MPa

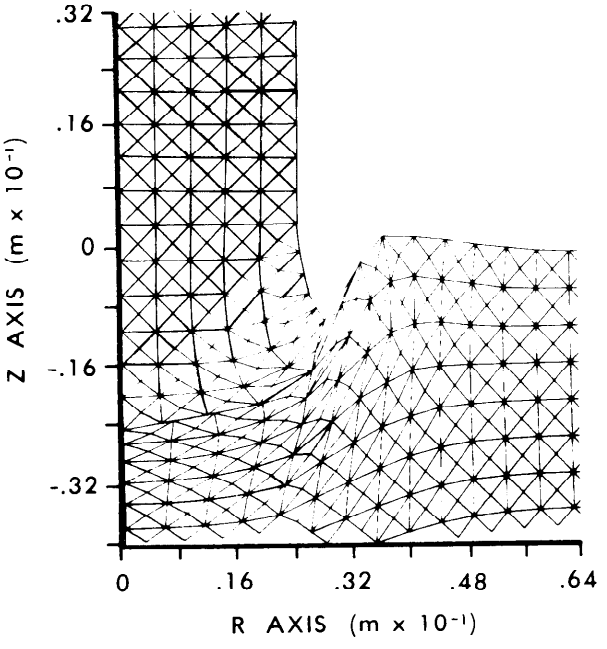

INCIPIENT SHEAR BAND BY 10 μs

FIGURE 3a. STEEL CYLINDER VS. Ti 125 TARGET

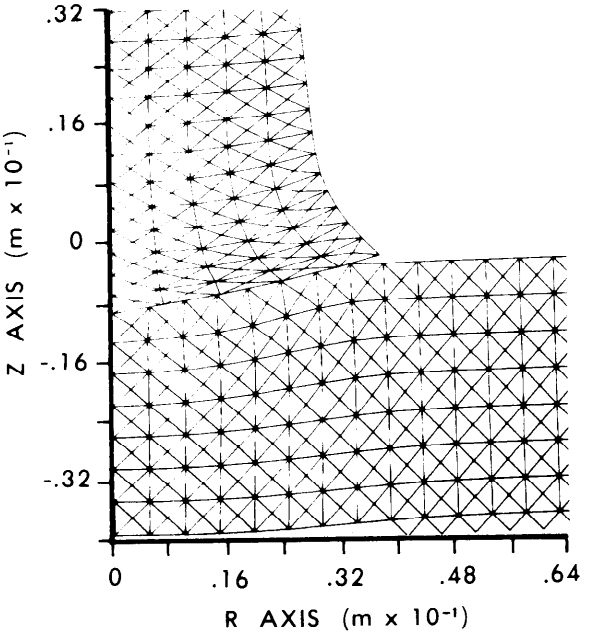

NO SIGN OF SHEAR BAND BY 10 μs

FIGURE 3b. STEEL CYLINDER VS. Ti 318 TARGET

The first case is the basis for the parametric study presented. The expected energy to accomplish perforation of the Ti 125 target with a blunt cylinder was estimated to be 148 joules (Reference 9) implying a critical velocity of approximately 300 m/s.

Prior to enabling splitting, the simulation was attempted with a striking velocity of 350 m/s to assure perforation; this was run for 10 μs, the deformation pattern of which is shown in Figure 3a, indicating the formation of an incipient shear band. The deformed target elements around the projectile periphery suffered an equivalent strain of 300% by 10 μs.

Contrast these results with those for the simulation of the second case, the target material being Ti 318 (Figure 3b). There is no sign of a shear band by 10 μs. The highest strain suffered by an element in the top layer was 88%, the highest second layer element having reached only 13% strain. Clearly, adiabatic shear can not be successfully modeled without the addition of mathematical formulation to include thermal softening. Ti 125 has a far lower strength and a higher strain hardening rate than Ti 318. This would seem to be in agreement with Recht's criterion [10] that a high shear yield stress and low strain hardening rate are conducive to adiabatic shear.

IV. EVOLUTION OF CRITERIA MANDATING TARGET FAILURE

Once the modifications described in Section II were implemented, the issue became that of choosing criteria to initiate and further splitting. A criterion which remained constant during this study was the start and continuation of a split past an element having attained a critical level of equivalent strain ($\bar{\varepsilon}$) (Criterion 1).

According to Crandall, Dahl, and Lardner [11], describing the yielding tendency in terms of equivalent stress and equivalent plastic strain appears to correlate well with data when the ratios of the principal stresses remain constant during the test and appreciable anisotropy is not developed during straining. "The components of strain derived from the Mises yield criterion are much closer to physical observations than those found from the maximum shear-stress criterion." [11]

Another criterion (Criterion 2) which remained constant was the choice of the initial "split" node. The node suffering the highest force associated with the first element meeting Criterion 1 was selected to be the initial "split" node. It was also required that this node be a master node or the element would be rejected as one enabling split to occur. After splitting was initiated, only those elements associated with the "next" node were considered for possible furthering of the split. Since the primary objective of this effort was to model target failure, and little projectile deformation was expected in the case of the Ti 125 target impact, the projectile elements were not allowed to fail.

The direction of the split (Criterion 3), the critical level of Criterion 1, and amendments to Criterion 1 varied during the solutions attempted and are

described in detail in Reference 8. The following is a summary of the principal approaches taken and the results of each. 1) Require only a specific level of $\bar{\varepsilon}$ for an element to cause splitting. Results: a) surface elements not contiguous to the projectile periphery suffered sufficient compression to attain $\bar{\varepsilon}$ first and b) splitting would proceed in one direction while the thrust of the problem proceeded in another. 2) Require relatively high levels of $\bar{\varepsilon}$ (ie. 300%) for an element to cause splitting. Results: calculation took far too long with only slight penetration predicted for an experimental situation in which perforation resulted. 3) Base the direction of the split on nodal forces. Results: nodal forces fluctuated widely; the split proceeded in one direction while thrust of the problem proceeded in another. 4) Let the split close up if the thrust of the problem went in a different direction, enabling the split to be furthered from a node other than the "next" node. Results: intractable.

The following criteria which resulted in natural and pleasing results consistent with the thrust of the impact and consistent between problems were utilized in the parametric investigation of the impact situation described in Section III.

Criterion 1: An element initiates or furthers a split
1) when its equivalent strain reaches a specified critical level, and
2) if furthering a split, is associated with the "next" node, and
3) its shear stress is greater than its axial or radial deviator stress, and
4) the direction of the split(Criterion 3) does not change by 90^0 or more.

Criterion 2: The node at which initial splitting occurs
1) must belong to the element meeting Criterion 1 and
2) must suffer the highest force of all three nodes belonging to the same element, and
3) must be a master node.

Criterion 3: The direction of the split is determined by the strain of the element meeting Criterion 1. If the axial strain is greater than the radial strain, splitting is to the nearer radial node. Otherwise, splitting is to the nearer axial node.

A discussion of some of the criteria is in order. Obviously, every attempt was made to ensure the workability of an equivalent strain criterion. It does not seem unreasonable to require the line of major fracture to continue from the "next" node and without a major (90^0) change in direction. However, the requirement that the shear stress be greater than the axial and radial

deviator stresses may not be satisfying in a continuum mechanics sense. This may, in essence, be invoking a maximum shear stress criterion.

$$\text{Maximum Shear Stress} = \tau_{MAX} = \frac{1}{2}\sqrt{(\sigma_r - \sigma_z)^2 + 4\tau_{rz}^2}$$

$$\text{where the radial stress } \sigma_r = \bar{\sigma}_r + \frac{\sigma_r + \sigma_z + \sigma_\theta}{3},$$

$$\text{the axial stress } \sigma_z = \bar{\sigma}_z + \frac{\sigma_r + \sigma_z + \sigma_\theta}{3},$$

τ_{rz} is the shear stress acting on the axial-radial plane, and $\bar{\sigma}_r$, $\bar{\sigma}_z$ are the radial and axial deviator stresses and the expression $(\sigma_r + \sigma_z + \sigma_\theta)/3$ is the hydrostatic stress.

Therefore

$$\tau_{MAX} = \frac{1}{2}\sqrt{(\sigma_r - \sigma_z)^2 + 4\,\tau_{rz}^2}$$

Both the radial and axial deviator stresses have the same sign (-) so this expression reduces the effect of both, making the shear stress the crucial parameter. However, in redoing the first calculation for 30 μs and determining the maximum shear stress, it appears that some of the top elements modeling the target surface suffer sufficient compression to make the maximum shear stress calculated very close to that for the first element at the projectile periphery which was allowed to start splitting. Future work includes attempting to utilize a maximum shear stress criterion for an element to cause splitting and the angle of the plane of maximum shear to determine the direction of splitting (instead of element strains).

With regard to failing elements, the conservative position was taken that elements would only be totally failed when a minimum time increment violation occurred.

V. RESULTS OF PARAMETRIC STUDY

Four variations on the first ballistic impact situation, a hardened, roller bearing steel cylinder versus a Ti 125 (99% titanium) target, are presented. The projectile and target properties remain the same for each (projectile and target 1 properties in Table 1).

The first calculation was made primarily to test out the techniques developed enabling splitting. A striking velocity of 500 m/s and a critical $\bar{\varepsilon}$ = 100% were utilized to ensure a relatively fast calculation and one assuredly resulting in perforation. At 35.6 μs perforation did occur. This was the only calculation in which a minimum time increment violation occurred (at 44.7 μs) in a highly stressed element to the right of the plug.

Modifications were subsequently made to automatically enable the element to be totally failed for a minimum time increment violation and the calculation was continued, primarily to prove that the procedure worked. By 45 μs the projectile was no longer affected by the remaining target material and the residual velocity had settled to 237 m/s. If this were a multiple target situation, this would be the appropriate time to discard the first target (except for the plug) and add a second target. This could be done relatively easily and automatically because the velocities of the plug nodes were an order of magnitude greater than the nodes representing the remaining target material. The deformation plots detailing the progress are shown in Figure 4. The pattern of elements which initiated and furthered splitting and the times at which they did so are shown in Figure 5a.

For the second through fourth calculations, a striking velocity of 350 m/s was utilized as it was closer to the experimental situation being modeled.

A critical $\bar{\varepsilon}$ of 100% was utilized for the second calculation, as with the first calculation. The projectile penetrated 5.08 mm before rebounding at 40 μs; splitting past six elements and layers had occurred. This calculation was allowed to continue until the rebound velocity stabilized at 27.4 m/s by approximately 70 μs. The deformation plots showing its progress are shown in Figure 6.

The critical $\bar{\varepsilon}$ was reduced to .75 for the third calculation in an effort to obtain perforation at 350 m/s. The projectile penetrated further, to 5.49 mm before rebounding at approximately 45 μs, reaching a rebound velocity of 20 m/s by 50 μs. In this calculation, splitting had occurred past nine elements (layers) before rebound occurred.

For the fourth and last calculation critical $\bar{\varepsilon}$ was reduced to .5, the rationale for the possible validity of such a low level being that the ultimate strain for the target material is .45-.5. This time perforation did occur, at 28.8 μs. The deformation plots showing its progress through 70 μs are shown in Figure 7. The pattern of elements which initiated and furthered splitting are shown in Figure 5b. This is perhaps the most interesting case in that perforation occurred, a plug was completely formed, yet there was not sufficient energy for the penetrator and plug to continue past the remaining target. Instead, the projectile finally rebounded and, at 70 μs, had a rebound velocity of 7 m/s while the plug was still moving in the opposite direction past the remaining target material at 24 m/s. By 90 μs the plug was essentially stuck in the target.

For all four calculations the projectile speed histories are shown in Figure 8; the depth of penetration histories are shown in Figure 9. In all calculations there was no manual intervention or rezoning involved as the problems progressed. Clearly, the results are consistent between calculations, a higher striking velocity producing perforation and a free-flying projectile and plug whereas the lower velocity resulted in projectile rebound. A lower level of critical $\bar{\varepsilon}$ enabled complete formation of a plug and perforation whereas higher levels of critical $\bar{\varepsilon}$ resulted in considerable penetration but

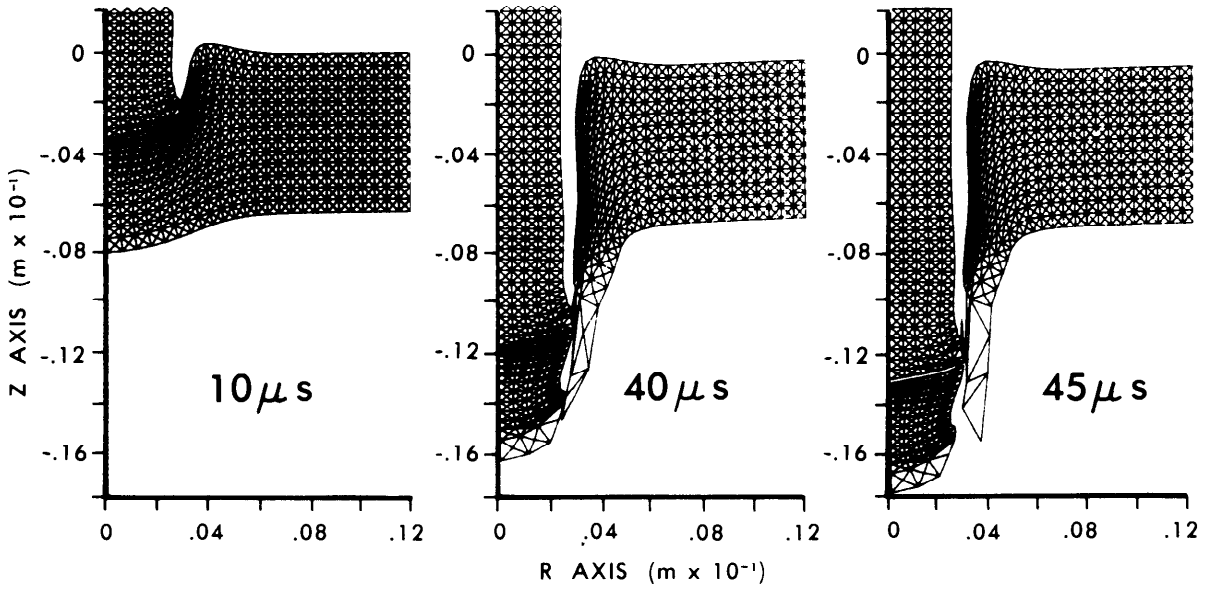

V_S = 500 m/s

$\bar{\epsilon}$ = 1

PERFORATION @ 35.6 μs

V_R = 237 m/s

FIGURE 4 DEFORMATION PLOTS – CALCULATION 1

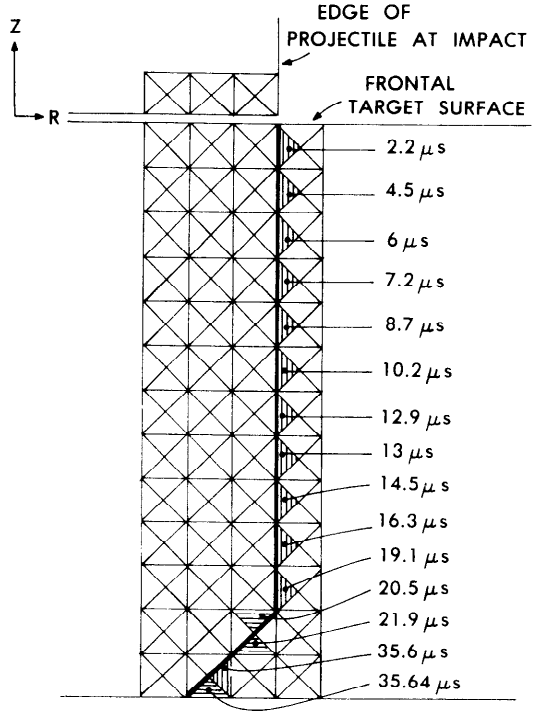

FIGURE 5a. PATTERN OF ELEMENTS INITIATING OR FURTHERING SPLIT (V_S = 500 m/s, $\bar{\epsilon}$ = 1)

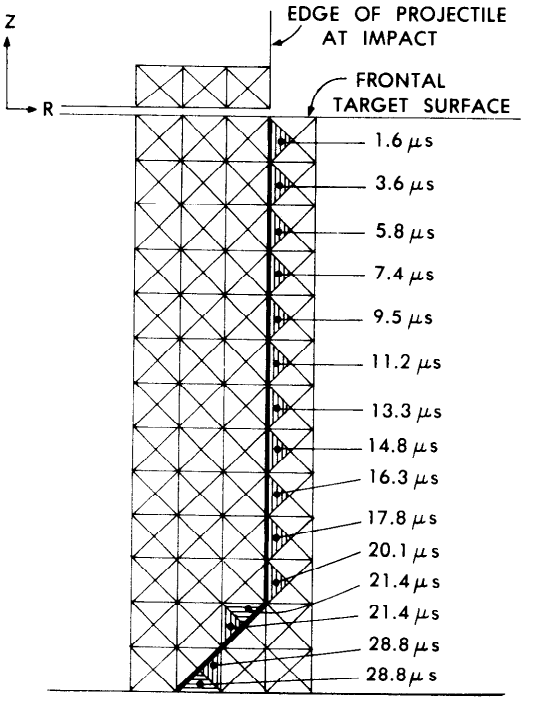

FIGURE 5b. PATTERN OF ELEMENTS INITIATING OR FURTHERING SPLIT (V_S = 350 m/s, $\bar{\epsilon}$ = .5)

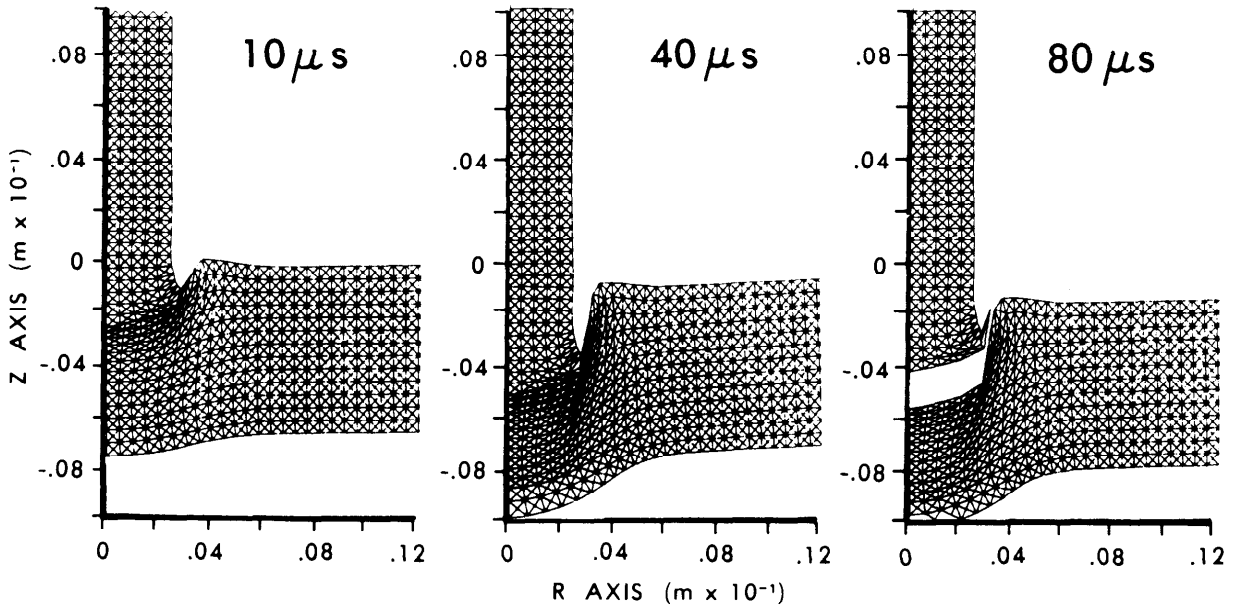

V_S = 350 m/s

$\bar{\epsilon}$ = 1

SPLIT THROUGH 6 LAYERS

REBOUND @ 40 μs

V_{REB} = 27.4 m/s

DEPTH OF PENETRATION = 5.08 mm

FIGURE 6 DEFORMATION PLOTS - CALCULATION 2

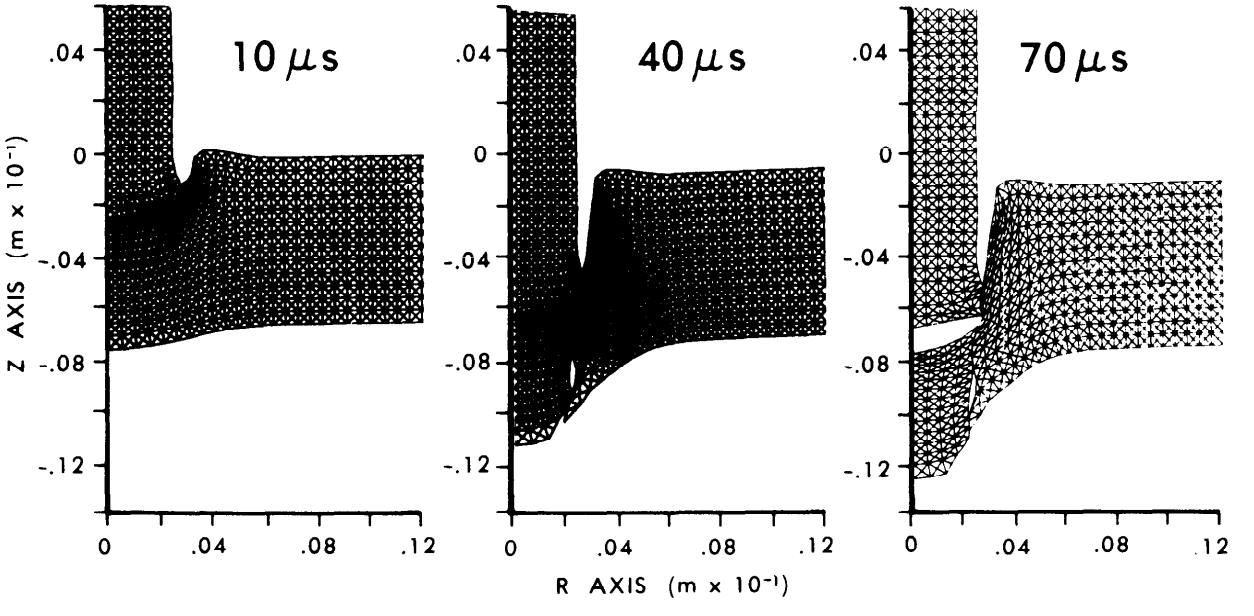

V_S = 350 m/s

$\bar{\epsilon}$ = .5

PERFORATION AT 28.8 μs

REBOUND @ 60 μs

V_{REB} = 7 m/s @ 70 μs

V_{PLUG} = 24 m/s

FIGURE 7 DEFORMATION PLOTS - CALCULATION 4

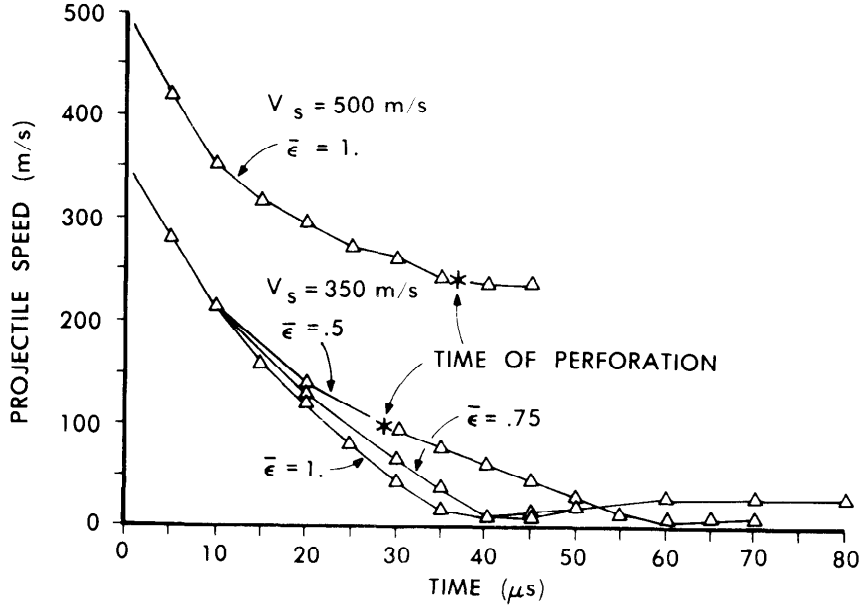

FIGURE 8 PROJECTILE SPEED HISTORY - CALCULATIONS 1-4

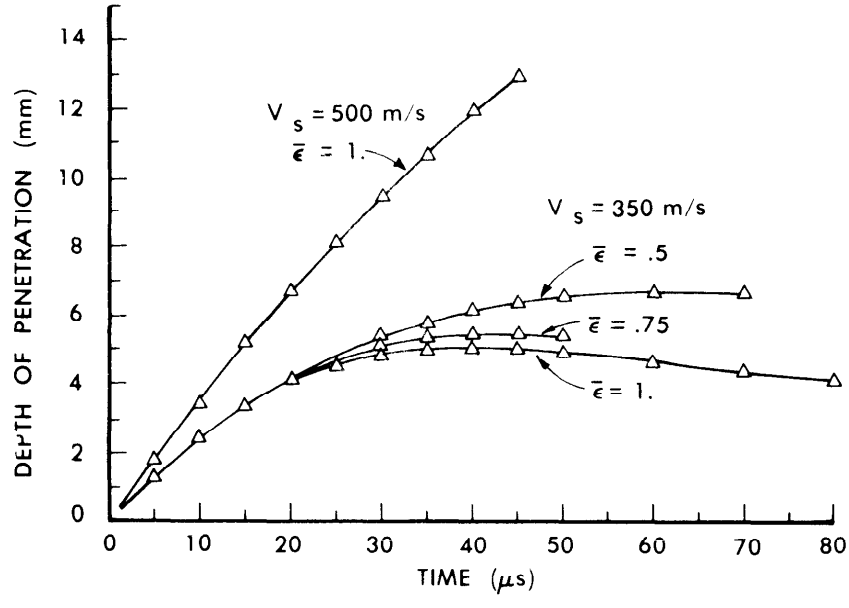

FIGURE 9 PROJECTILE DEPTH-OF-PENETRATION HISTORY - CALCULATIONS 1-4

no perforation.

All of the deformation plots indicate large volumetric strains for the distal target elements at 20 μs and later. This is due to a buildup of hydrostatic tension in the last layer of target elements. This phenomenon might be interpreted as a prediction of spallation; however, the tensile stress was limited to one-third the ultimate stress in the calculation. Such a limitation is considered to be too low for tensile failure resulting in spallation. It is therefore planned to attempt the problem with a higher limit. Then a buildup of hydrostatic tension might be more meaningful with regard to predicting spallation.

VI. CONCLUSIONS

Techniques were described which were developed for EPIC-2 and utilized to model target plugging failure which results from high strains. The evolution of criteria which determined the occurrence of fracture "naturally" as well as a parametric study of a normal impact situation involving plugging failure were presented. Future work includes utilizing these techniques in attempting to model plugging due to adiabatic shear, the extrapolation of these techniques to model other target failure situations such as piercing, plane strain simulations, and the marriage of splitting and erosion techniques.

VII. ACKNOWLEDGMENTS

The author gratefully acknowledges helpful discussions with G. R. Johnson of Honeywell, Inc., R. L. Woodward of Materials Research Laboratories, Australia, and J. M. Santiago, Ballistic Research Laboratory.

VIII. REFERENCES

1. Johnson, G. R., "EPIC-2, A Computer Program For Elastic-Plastic Impact Computations in 2 Dimensions Plus Spin," US Army BRL Contract Report ARBRL-CR-00373, June 1978.

2. Moss, G. L., "Shear Strains, Strain Rates and Temperature Changes in Adiabatic Shear Bands," US Army BRL Report ARBRL-TR-02242, May 1980.

3. Zener C., Hollomon, J. H., "Effect of Strain Rate Upon Plastic Flow of Steel," J. Appl. Phys., V. 15, 1944, 22.

4. Johnson, W., "Impact Strength of Materials," Edward Arnold Ltd., 1972.

5. Johnson, G. R., "Dynamic Analysis of Explosive-Metal Interaction in Three Dimensions," J. Appl. Mech., V. 103, No. 1, March 1981.

6. Lambert, J. P., Private Communication.

7. Johnson, G. R., "Triangular Element Arrangement For EPIC-2," Internal Memorandum, July 1979.

8. Ringers, B. E., "New Sliding Surface Techniques Enable the Modeling of Target Plugging Failure," Ballistic Research Laboratory Report, to be published.

9. Woodward, R. L., "The Penetration of Metal Targets Which Fail By Adiabatic Shear Plugging," Int. J. Mech. Sci., V. 20, 1978, 599-607.

10. Recht, R. F., "Catastrophic Thermoplastic Shear," J. Appl. Mech. Trans., ASME31E, 1964, 189.

11. Crandall, S. H., Dahl, N. C., and Lardner, T. J., "An Introduction to The Mechanics of Solids," McGraw-Hill, 1978.

LABORATORY TESTING OF LONG ROD PENETRATOR AND SABOT COMPONENTS

M. A. Scavullo and J. H. Underwood
U.S. Army Armament Research and Development Command
Large Caliber Weapon Systems Laboratory
Benet Weapons Laboratory
Watervliet, NY 12189

ABSTRACT

Laboratory testing apparatus is described which can be used to simulate the launch loading of penetrator and sabot components from kinetic energy penetrator rounds. Load and deflection to failure of production components has been measured and compared for different materials and configurations.

Results are described from penetrators made from a uranium alloy and two tungsten alloys. Results from sections of sabots are described, including two aluminum alloys and different configurations.

INTRODUCTION

A kinetic energy penetrator is, in basic form, a rod with a high length-to-diameter ratio which is manufactured from high density material and launched from a gun tube. The launching is achieved by mechanically coupling the penetrator to a sabot, which fits the gun tube bore diameter, and which is discarded upon exit from the gun tube. Figure 1 shows a photograph of a typical kinetic energy projectile, Figure 1a, along with a sketch of the basic components and loading of the projectile, Figure 1b. The firing pressure on the sabot causes high acceleration of the projectile, and this leads to the classic F = ma type of loading. Particularly near the junction of the unsupported sections of the penetrator with the sabot, high axial normal stresses develop in the penetrator and high shear stresses develop in both components. The tensile stresses at the rear of the penetrator are of particular concern here, because they could lead to a brittle fracture of a penetrator during launch. Such a failure occurred early in the development of Army kinetic energy penetrator rounds at the rear of the interconnection between sabot and penetrator. Figure 2 shows the mechanical interconnection, a series of lugs and grooves, in detail. They are termed lugs because they have no helix advance as in a thread. The profile of the lug is that of a buttress thread which has long proven its ability to transmit load in a single axial direction. The lugs and grooves act as stress concentrators for the body forces and lug forces which are applied by the sabot. A laboratory test that could simulate the lug loading, and also apply tensile stresses to a finish-machined penetrator would allow the structural integrity of the penetrators to be determined at a lower cost and in a shorter time than would firing tests. In addition, load, deflection, and failure mechanism information can be determined in the laboratory tests, whereas such information generally cannot be obtained from firing tests. This report describes a laboratory launch-simulation test system for kinetic energy

projectiles. It describes test results from uranium and tungsten penetrators and from two aluminum alloys for sabots. In addition, the load carrying capability of the buttress lug profile was investigated by loading to failure sabot sections with varying numbers of lugs.

Figure 1a Typical Kinetic Energy Penetrator Round With One Sabot Section Removed

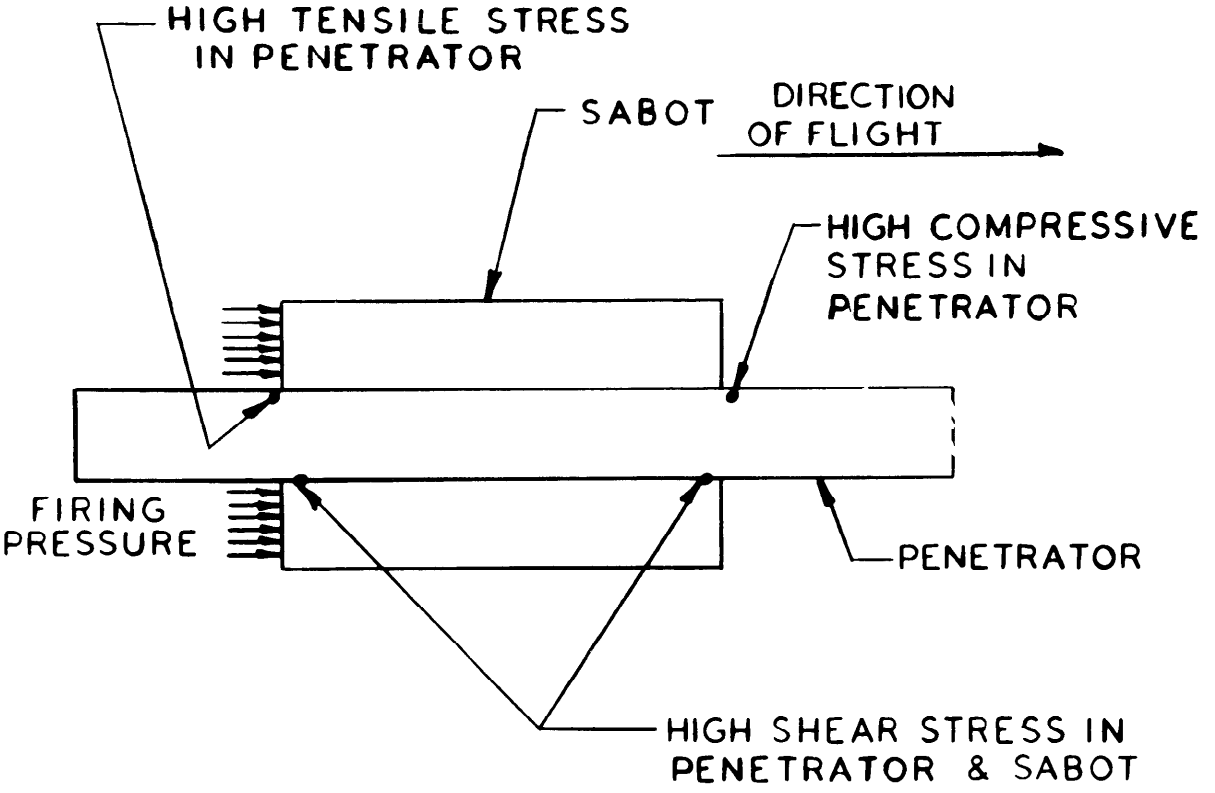

Figure 1b Sketch of Typical Kinetic Energy Penetrator

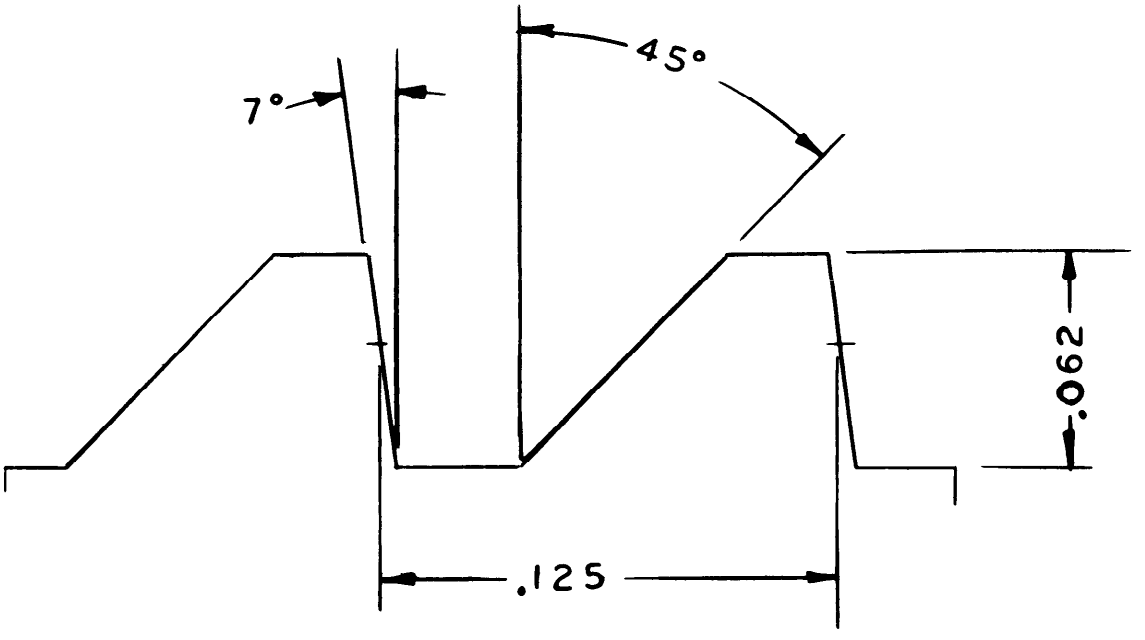

Figure 2 Sketch of Lug Profile

SIMULATION TEST APPARATUS

The launch simulation test equipment was described in a prior report [1]. A few details are given here. Figure 3 is a photograph of the simulation test equipment capable of applying 200,000 lbs. of tensile load to a penetrator or a sabot section. The hydraulic cylinder mounted on the base moves a load frame assembly as a unit. The tensile load is applied between the movable upper load frame (small columns) and the stationary lower load frame (large columns). The load is applied to the specimen assembly (not shown) through the rods and end caps shown near the top of the photograph. A 200,000 lb. load cell mounted between the hydraulic cylinder and upper load frame provides the load measurements.

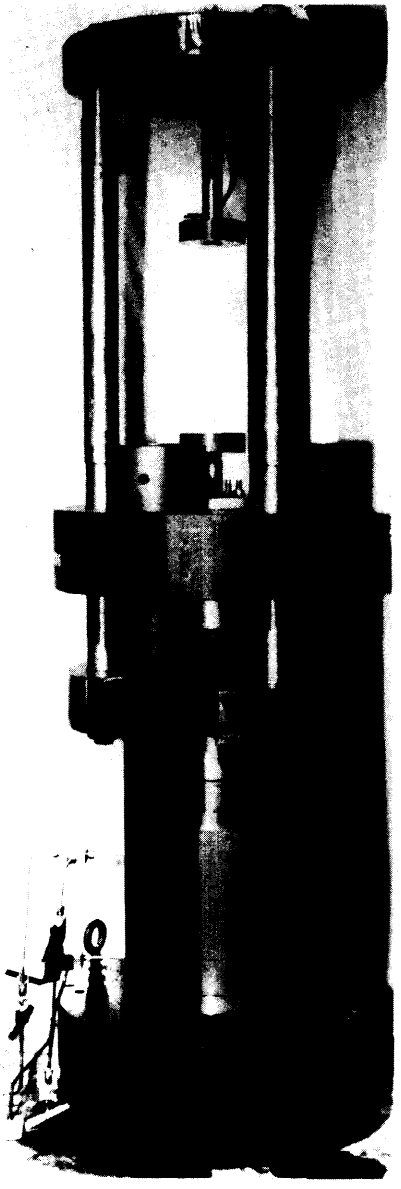

Figure 3 Two Hundred Thousand Pound Launch Simulation Test System For Kinetic Energy Penetrator Rounds

Figure 4 shows the specimen assembly which is mounted in the simulation equipment. The loading rods and end caps apply the tensile load through the fixture to the sabot segments. The forward sabot segment (on the right) transmits the load to the thread-like lugs on the penetrator in the same general way as in the launch of the projectile, the load being applied to the 7° faces of the lugs. The rear sabot segment is loaded on the 45° face and in the direction opposite to that of launch. Figure 5 shows this in more detail. Based on the work of Pflegl et al [2] the concentrated stress at the root of the lug fillet is expected to be lower when the lug is loaded on the 45° face than when it is loaded on the 7° face. In simplified concept, the reason for the lower fillet stress is that the radial compressive component of the force on the penetrator is much larger for the 45° face than for the 7° face. This compressive force tends to lower the tensile fillet stress, so that any failure of the penetrator would be expected at the fillet of the first forward loaded lug on the penetrator, point A shown in Figure 5.

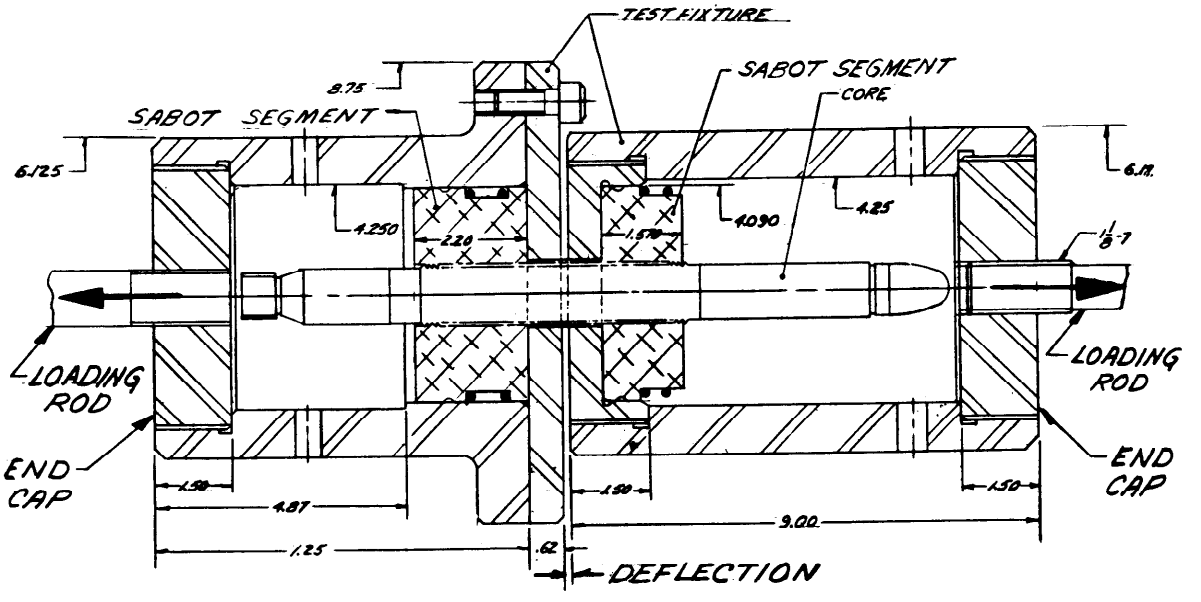

Figure 4 Specimen Assembly For Launch Simulation Test System

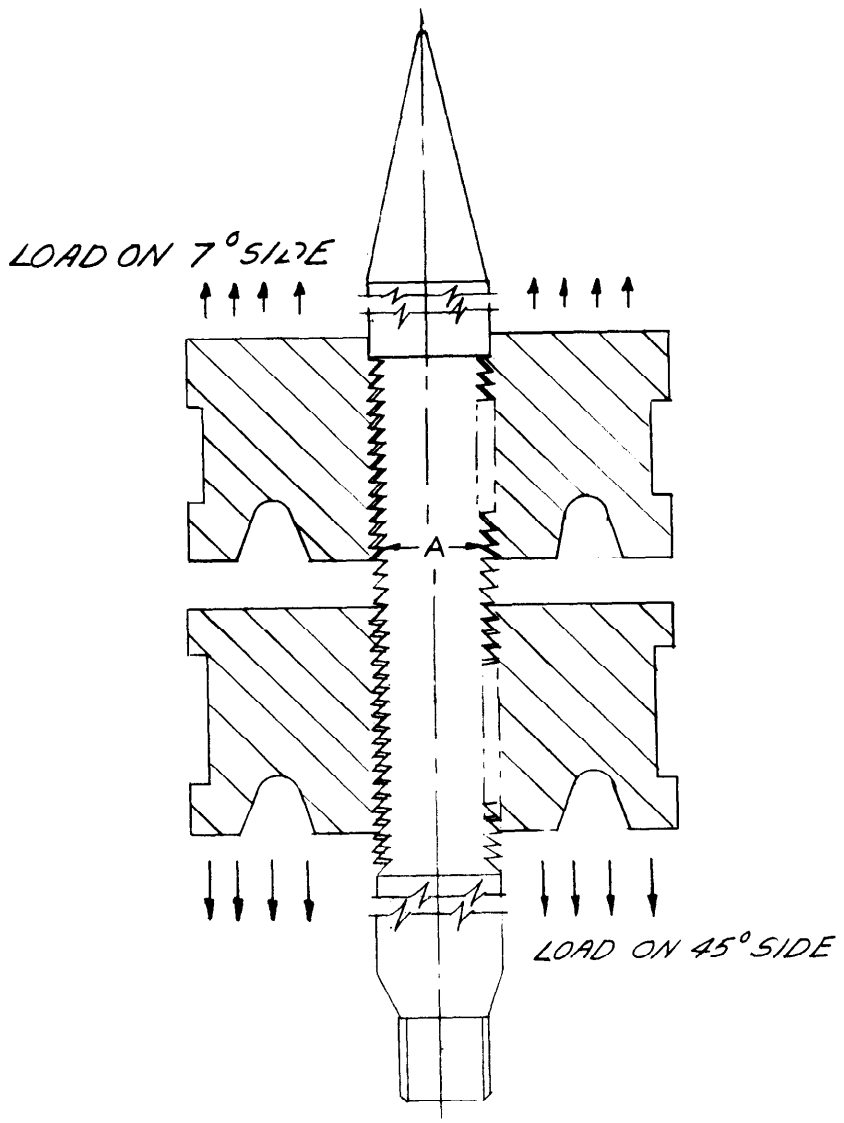

Figure 5 Sketch of Tensile Loading of Complete Penetrator Using Segments of Sabots

PENETRATOR TEST RESULTS

The loading of a penetrator through sabot segments causes a tensile stress field in the penetrator which is concentrated by the lugs and grooves. The lugs are also directly loaded. This combined loading of the penetrator is the same type as that during launch. Further, by using a finish-machined penetrator the same stress concentration factor is obtained in the laboratory as that in service. Table I presents the data for tensile failure of full size penetrators tested in the lug loaded condition using maraging steel sabot segments. Also shown in Table I are typical yield and ultimate tensile strengths for the materials from manufacturers data. The depleted uranium-.75 percent titanium alloy is a solution treated and aged material with nominal solution treatment and aging temperatures of 800-850°C and 350°C respectively. The tungsten materials are proprietary commercial alloys produced using powder metallurgy processes. The average stress at failure is close to the ultimate strength of the material in the cases of the uranium and 90 percent tungsten materials; whereas the 97 percent tungsten failed at a somewhat lower level of stress relative to its ultimate strength. The test specimens were 1.02 in. (26 mm) in diameter with .062 in. (1.6 mm) grooves, as in Figure 2. Some specimens were complete penetrators, as shown in Figures 4 and 5; some were grooved sections only. For the purposes of the test here, there was no difference. The failure appearance of the 90 percent tungsten and uranium materials were typically flat failure surfaces across the root of the lug as shown in Figure 6. The 97 percent tungsten material, rather than failing by a flat break across the root of the lug, failed in cup and cone fashion as shown in Figure 7. In the cup section a crack was seen at the root diameter coinciding in depth with the bottom of the cup. In addition, cracks were noted at adjacent lug roots. The additional cracking suggests that as the failure load is approached, cracks initiate at the lug roots and one crack grows to critical size and results in failure.

Figure 8 shows the load deflection curves for the three penetrator materials studied. The deflection measured is that shown in Figure 4 and is the result of all the elasticity in the system not just the elongation of the penetrator material. However, the slopes of the lines are generally indicative of the elastic moduli of the material; uranium has the lowest modulus and the lowest slope, and so forth. The plastic deformation shown for the 90 percent tungsten and uranium materials indicate their notch toughness in comparison to the 97 percent tungsten material which shows virtually none. The important implications of this measure of notch toughness will be discussed further in Summary and Conclusions.

TABLE I. Tensile Failure Load of Penetrators of Three Materials

Material	Material Strength; ksi (MPa)		Load to Failure; k lb. (kN)	Average Stress to Failure; ksi (MPa)	Failure Stress as a % of Ultimate Stress
Uranium-0.75% Titanium	Yield	120 (827)	156 (694) 157 (699)		
	Ultimate	210 (1448)	154 (685) 154 (685)	189 (1303)	90%
Tungsten-3% Binder	Yield	166 (1145)	98 (436)		
	Ultimate	167 (1151)	98 (436)	119 (820)	71%
Tungsten-10% Binder	Yield	- -	154 (685)	189 (1303)	107%
	Ultimate	176 (1214)	155 (690)		

Figure 6 Macrophotograph of Fracture Surface of Uranium Penetrator at Root of Rearmost of Loaded Lug

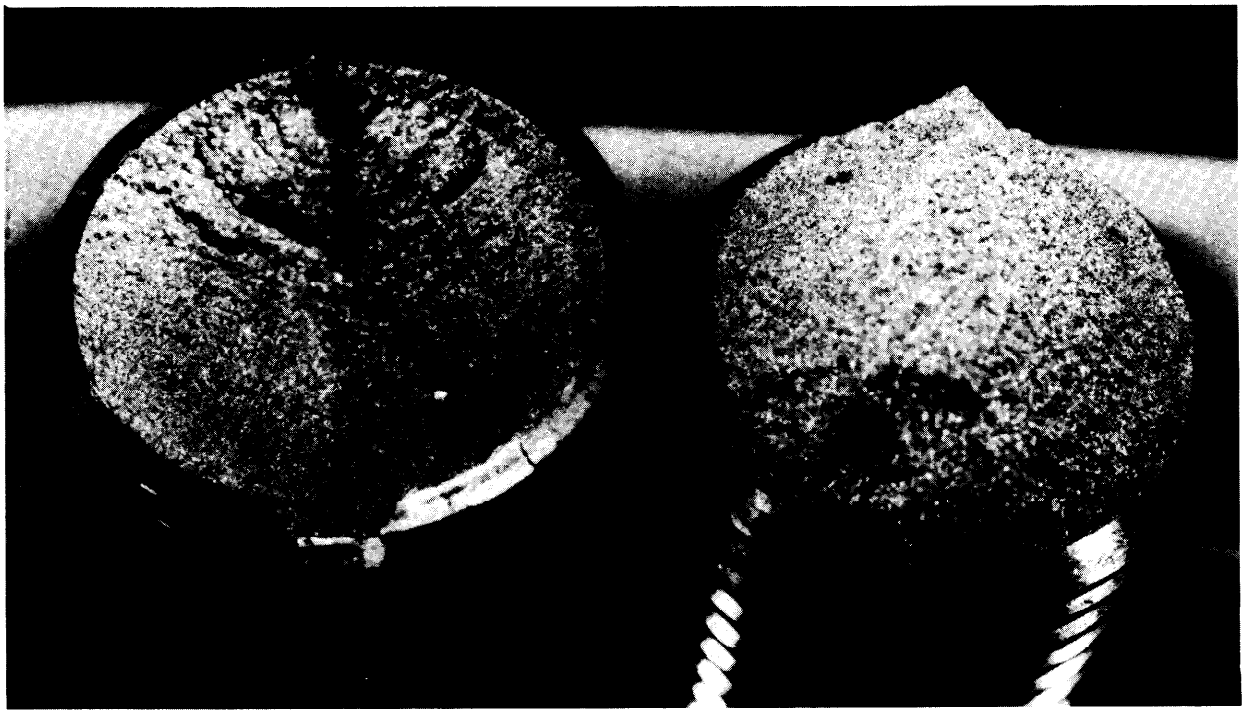

Figure 7 Macrophotograph of Fracture Surface of 97 Percent Tungsten Penetrator at Root of Rearmost Loaded Lug

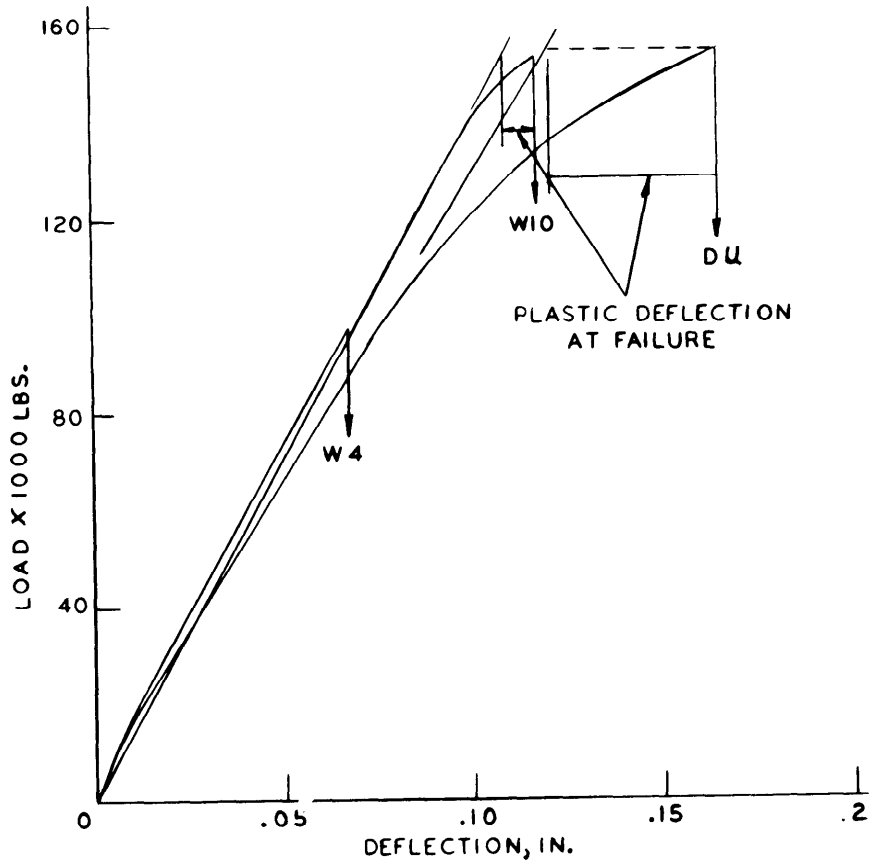

Figure 8 Load Deflection Curves For Three Penetrator Materials

Table II presents the results of notched tension tests conducted on 90 percent tungsten material. Smooth specimens having a diameter of .250 in. (6.4 mm) were tested and compared with notched specimens with .375 in. (9.5 mm) outer diameter, .250 in. (6.4 mm) notch diameter, and .0075 in. (0.19 mm) root radius, 60° notch. The results show the material to be notch ductile, because the failure stress of notched specimens was greater than that of the unnotched specimens, significantly greater in this case, 138 percent on average. Also, it should be noted that the average ultimate tensile strength of the unnotched specimens, 168 Ksi (1158 MPa), is in good agreement with the average manufacturers result from the center of the penetrator blanks, 167 Ksi (1151 MPa).

TABLE II. Failure Stress of Notched and Unnotched 90% Tungsten Tension Specimens; 0.25 in. (6.4 mm) Diameter

Unnotched		Notched	
ksi	(MPa)	ksi	(MPa)
169	(1165)	224	(1545)
167	(1152)	232	(1601)
		230	(1587)
		246	(1699)
		230	(1587)

SABOT TEST RESULTS

ALLOY COMPARISON

Sabot sections were made from 7075 T6 and 7075 T73 aluminum alloy; the T6 condition is that used for sabots and the T73 condition is under consideration because of its increased resistance to stress corrosion cracking. The sections have a basic inner diameter of 1.02 in. (26 mm), have 11 lugs, a length of 1.38 in. (35 mm), and a shear area of 3.45 in.^{2} (2230 mm^2). Table III presents the data obtained when testing these sections with a 250 maraging steel penetrator as previously described in relation to Figures 3 and 4. The short transverse orientation was tested, that is, the shear plane in the tests was normal to short transverse direction, which is the radial direction for sabot segments. As expected the T73 material fails at a lower load. The average failure load and corresponding shear stress for the T73 tests was 89 percent of that of the T6 tests. This is in reasonable agreement with the comparison of ultimate shear strengths, in which the strength for T73 is 85 percent of that for the T6 material. Comparison of the data in Table III shows the T73 failure to be slightly less variable; additional testing would be required to determine if this is generally true. This consistency would of course help in a statistical determination of acceptable strength. Figure 9 is a load vs. deflection curve for sabot sections of T73 and T6 material. The T73 exhibits some increase in ductility which also may be a help in the present application.

TABLE III. Shear Failure of Lugs of Aluminum Sabot Section; Short Transverse Orientation

Material	Ultimate Strength in Shear, ST Orientation; ksi (MPa)	Load to Failure k lb. (kN)	Average Shear Stress at Failure ksi (MPa)
7075-T6 Aluminum	43.4 (299)	144 (641) 151 (672) 145 (645)	42.5 (293)
7075-T73 Aluminum	40.3 (278)	131 (583) 130 (579) 131 (583)	37.8 (261)

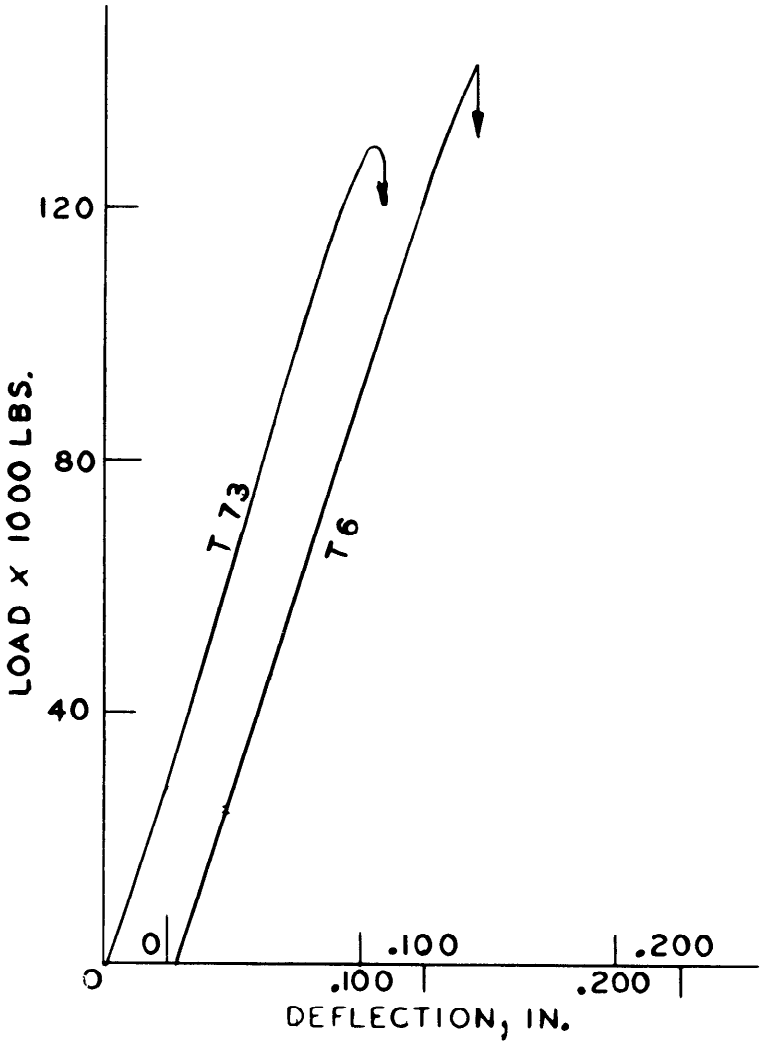

Figure 9 Load Deflection Curves For Two Sabot Materials

SHEAR AREA COMPARISON

Figure 10 shows the results of testing 7075 T6 alloy sabot sections of various lengths. The sabot sections had 11, 8, and 5 lugs; lengths of 1.38 in. (35 mm), 1.00 in. (25 mm), and 0.63 in. (16 mm); and shear areas of 3.45 in.^{2} (2230 mm^2), 2.50 in.^{2} (1610 mm^2), and 1.55 in.^{2} (1000 mm^2), respectively. The plotted points are the three tests conducted for each case and the line is calculated from the measured ultimate shear strength of the T6 material in Table III. The shear strength was measured in the short transverse orientation so that the failure would occur in the same plane as in service conditions; the measurement of shear strength was made according to ASTM Method B565-76. Figure 11 shows the direction in which the shear specimen was taken from a sabot segment and also the test fixture used to generate the strength data. The experimental results are in good agreement with the expected result in Figure 10. This indicates that no one lug will fail until they all fail in unison at about the ultimate shear strength of the material.

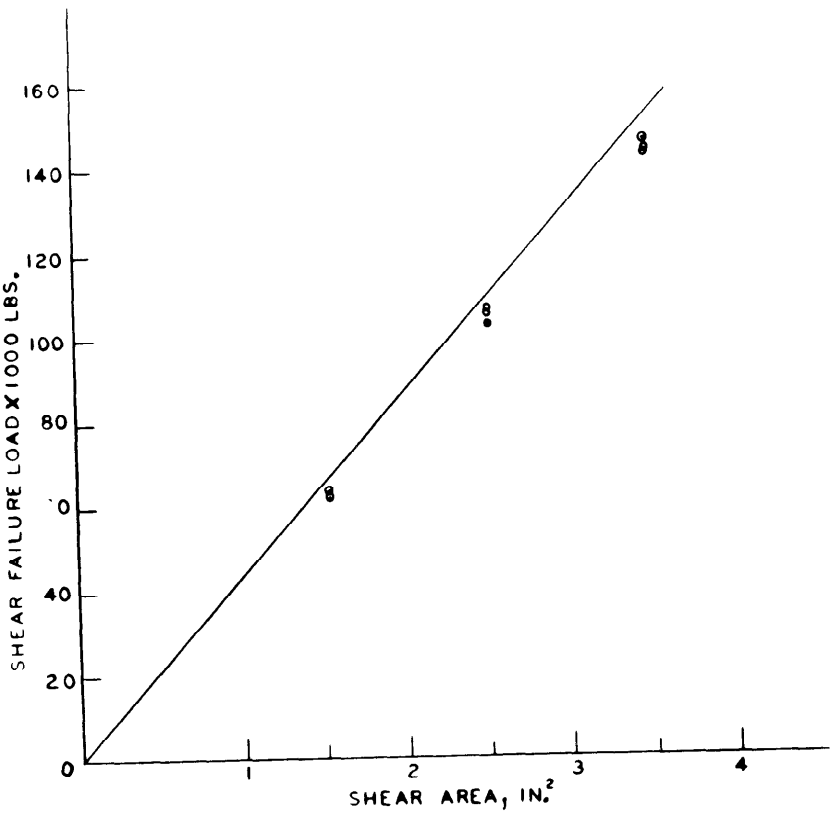

Figure 10. Shear Failure Load Versus Shear Area For Sabot Specimens

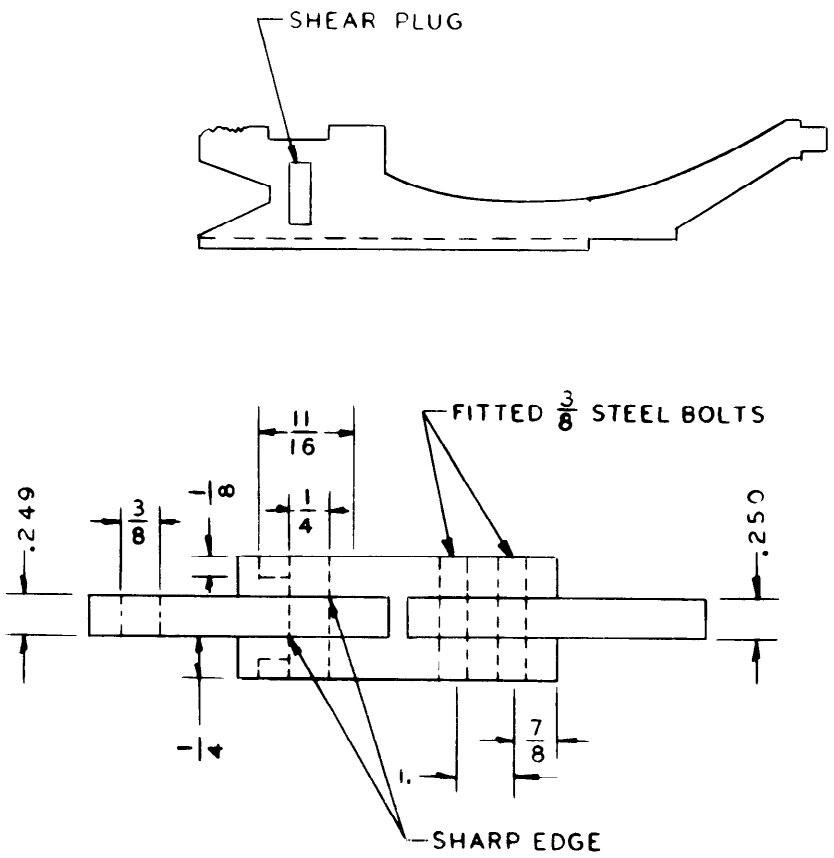

Figure 11 Shear Test Fixture and Orientation and Location of Shear Test Specimen

This is further confirmed by the uniformly rising load deflection curve and a direct fall off to zero load after the peak load has been reached. Further work in this area should be conducted using a uranium penetrator to determine if its material yield strength or elastic modulus changes this result.

SUMMARY AND CONCLUSIONS

A laboratory test apparatus has been developed which can provide a quantitative measure of the structural integrity of a kinetic energy penetrator during launch. The same apparatus can also be used to determine sabot lug integrity during launch. The system is suitable for making material comparisons for both the penetrator and sabot and may be used to determine if different material treatments or service histories have any effect on material and component strength. In addition, the following particular conclusions may be drawn from the testing described above.

1. Based on simulation test failure load, the 90 percent tungsten and uranium penetrators have a similar, high capability of surviving launch while the 97 percent tungsten penetrator is considerably less likely to survive. Based on simulation test plastic deformation, uranium penetrators have much higher capability of surviving launch than tungsten penetrators.

2. The failure stress of 90 percent tungsten penetrators is above the ultimate tensile strength of the material, and the failure stress in notched tension tests of the material is above the ultimate tensile strength. These results indicate that relatively simple notched tension tests can be used to predict the failure of penetrators. Tests in other materials are required to confirm this.

3. The substitution of 7075 T73 for 7075 T6 aluminum alloy, for increased stress corrosion cracking resistance, results in an 11 percent loss in load carrying ability of the sabot lugs. The smaller scatter shown in the T73 results may indicate that the loss in strength in a statistical sense is less than 11 percent; however, further testing is required to verify this.

4. The failure process for the sabot lugs in a series of simulation tests is one in which all lugs fail at once. This was demonstrated by the linear relationship between load to failure and the total shear area of the specimen. This same simultaneous failure would be expected to occur in a launch failure of sabot lugs, at least for the rearmost 11 sabot lugs.

Consideration of the results here along with some prior results can lead to recommendations of critical measures of survivability of penetrator and sabot during launch.

For sabots it is now quite clear that the ultimate shear strength in the short transverse orientation is the most important measure of likelihood for a lug shear failure during launch. The short transverse ultimate shear strength is often about half of the more easily measured longitudinal ultimate tensile strength, but measurements should be made to determine the exact relation between shear and tensile properties for each given material.

For penetrators the situation is not so clear. The comparison of test results in Table IV may help to clarify which test is the best measure of penetrator survivability during service loading. The first listed test result, the average failure stress in launch simulation tests, is certainly a direct measure of survivability; applied stress above this value causes failure. So any test which is proposed as the best measure of survivability must give results consistent with launch simulation failure stress. The difficulty with launch simulation failure stress is that it does not separate uranium from 90 percent tungsten. Ultimate tensile strength can not be relied upon to separate the various materials because it would predict nearly as good properties for the 97 percent tungsten as those for the 90 percent tungsten, and the launch simulation failure stresses do not support this prediction.

TABLE IV. Comparison of Test Results Which Relate to the Survivability of Penetrators

Material	Launch Simulation Failure Stress; ksi	(MPa)	Ultimate Tensile Strength ksi	(MPa)	Plane-Strain Fracture Toughness $ksi \cdot in.^{1/2}$	$(MPa \cdot in.^{1/2})$	Launch Simulation Failure Energy; ft-lb	(Nm)
Uranium - 0.75% Titanium	189	(1303)	210	(1448)	35	(38)	1280	(1741)
Tungsten - 3% Binder	119	(820)	167	(1151)	65	(71)	280	(381)
Tungsten - 10% Binder	189	(1303)	176	(121-)	60	(66)	800	(1088)

The plane-strain fracture toughness results shown in Table IV are a representative value from recent material acceptance tests of uranium and, for the two tungsten materials, the average of five tests each from the same group of penetrators used in launch simulation tests. These results can not be relied upon to properly separate the materials because they also would predict good properties for the 97 percent tungsten, and again, the launch simulation failure stresses do not support this.

The last listed test results in Table IV, launch simulation failure energy, are believed to be the most significant. The lowest failure energy corresponds to the lowest failure stress, and, in addition, failure energy clearly separates the uranium and 90 percent tungsten materials. The failure energies are calculated simply by measuring the area up to failure under the load-deflection curves of Figure 8. Inspection of these curves shows that it is primarily the greater amount of plastic deformation of uranium which increases its failure energy relative to that of 90 percent tungsten. The two materials fail at the same stress in launch simulation tests, so it is the larger plastic deformation of uranium which is believed to increase its survivability during launch.

It is proposed that failure energy in a notched failure test, such as the launch simulation test, is a critical measure of survivability during launch, provided that a fracture toughness controlled fracture does not occur, that is, provided that the fracture toughness is above a critical minimum and defects are smaller than a critical maximum size. To the extent that the loading during target impact is similar in nature to that of the launch simulation test, notched failure energy would also be a critical measure of survivability of a penetrator during target impact. We recommend that notched failure energy be investigated as a proposed critical measure of penetrator survivability for both launch and impact service loading.

ACKNOWLEDGEMENT

We are pleased to credit Mr. J. J. Zalinka for the experimental set-up and testing described in this report. We also wish to thank A. W. Gross for his careful preparation of the sabot models.

REFERENCES

1. Scavullo, M. A. and Underwood, J. H., "Service Simulation Test System For Kinetic Energy Penetrator Projectiles," USA ARRADCOM Technical Report No. ARLCB-TR-81007, Benet Weapons Laboratory, Watervliet, NY, February 1981.

2. Pflegl, G. A., Underwood, J. H., and O'Hara, G. P., "Structural Analysis of a Kinetic Energy Projectile During Launch," USA ARRADCOM Technical Report No. ARLCB-TR-81028, Benet Weapons Laboratory, Watervliet, NY, July 1981.

SESSION II: FATIGUE AND FRACTURE

Chairman: R. M. Bader
Assistant Chief, Structures and Dynamics Division
Air Force Wright Aeronautical Laboratories

ENERGY DENSITY THRESHOLDS ASSOCIATED WITH A MOVING HEAT SOURCE . . 129

G. C. Sih, Lehigh University, and
C. I. Chang, Naval Research Laboratory

ANALYSIS OF MIXED MODE CRACK GROWTH IN SHIP HULL MATERIAL UNDER DYNAMIC LOADING 143

C. R. Barnes, J. Ahmad, and
M. F. Kanninen, Battelle Columbus Laboratories

FATIGUE AND FRACTURE EVALUATION OF THE A-7E ARRESTING GEAR DRAG LINK 159

D. L. Merkord, C. E. Dumesnil, and T. D. Gray
Vought Corporation

A NONLINEAR FRACTURE MECHANICS PREDICTIVE PROCEDURE FOR THE SHORT CRACK EFFECT IN FATIGUE 177

J. Ahmad, A. T. Hopper, M. F. Kanninen,
B. N. Leis, and V. Papaspyropoulos
Battelle Columbus Laboratories

ELASTIC-PLASTIC FRACTURE MECHANICS ANALYSIS OF SMALL CRACKS 203

G. G. Trantina and H. G. deLorenzi
General Electric Company

APPLICATION OF AN ELASTIC-PLASTIC METHODOLOGY TO STRUCTURAL INTEGRITY EVALUATION 215

H. A. Ernst and J. D. Landes
Westinghouse R&D Center

FLAW DETECTION RELIABILITY ASSESSMENT AND ANALYSIS 238

W. D. Rummel and R. A. Rathke
Martin Marietta Corporation

ENERGY DENSITY THRESHOLDS ASSOCIATED WITH A MOVING HEAT SOURCE

GEORGE C. SIH
Lehigh University
Bethlehem, Pennsylvania 18015

C. I. CHANG
Naval Research Laboratory
Washington, D.C. 20375

ABSTRACT

High concentrations of energy can affect the local material properties and cause irreversible material damage in the form of excessive deformation and/or fracture. Considered in this communication is a traveling heat source along a line such that transient thermal stresses are created. Depending on the intensity and speed of the traveling heat source and material properties, material damage threshold is assessed by examining the stored energy causing the local elements to change shape as well as volume. To this end, the proportion of the energy density associated with distortion and dilatation is considered to be important. Their individual contribution is weighed automatically by taking the stationary values of the energy density function with respect to the polar angle that locates the direction of yielding and fracture. It is shown that for a sufficiently powerful heat source, it is possible to cause damage of the material by yielding and fracture with or without the addition of mechanical load. Results are reported for the 2024-T3 aluminum material and are useful for developing a methodology to quantitatively assessed material damage of systems subjected to high energy sources.

INTRODUCTION

For the prediction of failure in structures designed to operate under specified conditions, the traditional approach is to select appropriate quantitative criteria that permit an assessment of the entire structure's behavior from data of simple laboratory tests on small specimens. The implementation of such a procedure, however, involves many uncertainties ranging from the lack of a precise knowledge of loading data to a viable failure criterion. Different criteria are frequently employed to explain different failure modes. In the case of brittle fracture, the theory of linear elastic fracture mechanics (LEFM) has been used in the design against catastrophic fracture. Structural components can also fail by plastic collapse with or without crack growth should the net section stress approach yield at which point gross deformation can occur. A consistent treatment of failure modes is no easy task and requires a rational approach for analyzing material damage.

From the viewpoint of continuum mechanics, material damage can be described by yielding and fracture [1]. The former corresponds to excessive deformation where the material distorts and no longer returns to its original shape. The latter occurs when a material encounters excessive volume change resulting in fracture by crack growth. The rate at which energy is dissipated

by these two damage processes depends on geometry, material and, of course, the rate of input energy. Unless this combined effect is considered in a design methodology [2], no confidence can be placed in the translation of small specimen data to the design of actual structures. In this respect, the stored energy per unit volume that varies from point to point in a system plays an important role since it governs the amount dissipated due to distortion and dilatation at the threshold level of the material [3]. Such a quantity known as the strain energy density function dW/dV will be employed subsequently for analyzing possible material damage around a moving energy source. The effects of the intensity and speed of the energy source are examined in terms of the distortional component $(dW/dV)_d$ and dilatational component $(dW/dV)_v$ of dW/dV. Their individual contributions are determined by the stationary values of dW/dV [4] and provide information on failure by yielding and fracture.

MOVING HEAT SOURCE: TRANSIENT THERMOELASTIC STRESSES

The thermoelastic problem of a moving heat source has been considered in [5,6]. Only a brief account of it will be given. Referring to Figure 1, a

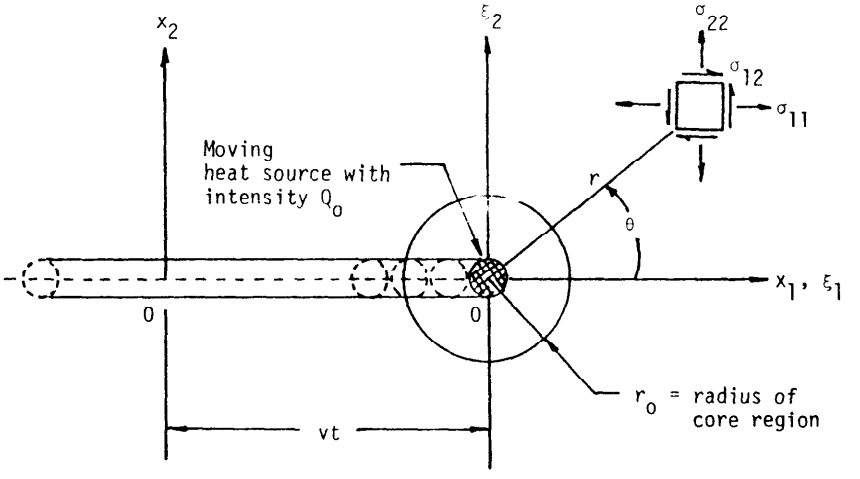

Figure 1 Stress Element Ahead of a Moving Heat Source

heat source with intensity $Q(x_i,t)$ being a constant Q_0 moves at a constant speed v in the horizontal direction. The coordinate axes x_j (j = 1,2) are fixed while ξ_j (j = 1,2) travel with the heat source such that

$$x_1 = \xi_1 + vt, \quad x_2 = \xi_2 \tag{1}$$

The domain of consideration extends to infinity in both the x_1 and x_2 direction while no variation in temperature takes place in the x_3 direction. The material around the heat source experiences a time varying temperature field $T(x_i,t)$ and stress state $\sigma_{ij}(x_i,t)$. At distances sufficiently far away from

the source, say as $x_i \to \infty$, both the heat flow or temperature gradients $\partial T/\partial x_i$ and stresses σ_{ij} are assumed to vanish. The governing equation for the temperature field is

$$\kappa \nabla^2 T(x_i,t) - \dot{T}(x_i,t) = Q(x_i,t), \quad i = 1,2 \tag{2}$$

where $\nabla^2 = \partial^2/\partial x_1^2 + \partial^2/\partial x_2^2$ and $\dot{T} = \partial T/\partial t$. The thermal diffusivity denoted by $\kappa = k/\rho C$ with k being the coefficient of thermal conductivity, ρ mass density and C the specific heat.

A thermoelastic potential $\Phi(x_i,t)$ is introduced such that [7] the displacements $u_i(x_i,t)$ can be written as

$$u_i(x_i,t) = \Phi_{,i} \tag{3}$$

where $\Phi_{,i} = \partial\Phi/\partial x_i$. The potential $\Phi(x_i,t)$ satisfies the equation

$$\nabla^2 \Phi = m_0 T \tag{4}$$

such that m_0 equals $\alpha(1+\nu)/(1-\nu)$ for plane strain and α is the coefficient of thermal expansion. It follows that the thermoelastic stresses become

$$\sigma_{ij}(x_i,t) = 2\mu(\Phi_{,ij} - \delta_{ij}\nabla^2\Phi), \quad i,j = 1,2 \tag{5}$$

and

$$\sigma_{33}(x_i,t) = -2\mu\nabla^2\Phi \tag{6}$$

In equations (5) and (6), μ is the shear modulus of elasticity.

Temperature Distribution. For a constant speed heat source with intensity Q_o, equation (2) can be expressed in the moving coordinate system by means of equations (1). The result is

$$\kappa \nabla_1^2 T(\xi_i) + 2c\kappa T_{,1} = -Q_o \delta(\xi_1)\delta(\xi_2) \tag{7}$$

in which $\nabla_1^2 = \partial^2/\partial\xi_1^2 + \partial^2/\partial\xi_2^2$, $T_{,i} = \partial T/\partial\xi_i$, $2c = v/\kappa$ and $\delta(\xi_i)$ is the Dirac delta function. Without going into details, the solution of equation (7) is

given by [8]:

$$T(\xi_i) = \frac{Q_o}{2\pi K} \exp(-c\xi_1) K_o(cr) \tag{8}$$

The modified Bessel function of the second kind of order zero is $K_o(cr)$ with $r = (\xi_1^2+\xi_2^2)^{\frac{1}{2}}$.

Thermal Stresses. Referring to the moving coordinates ξ_i (i = 1,2), equation (8) may be differentiated with respect to ξ_1. With the aid of equation (7), the following expression is found:

$$\nabla_1^2 \Phi_{,1} = - \frac{m_o}{2c} \nabla_1^2 (T+\Phi_o) \tag{9}$$

in which

$$\Phi_o(\xi_i) = \frac{Q_o}{2\pi K} \log r \tag{10}$$

Use was made of the relation

$$\delta(\xi_1)\delta(\xi_2) = \frac{1}{2\pi} \log r \tag{11}$$

Equation (9) yields the particular solution

$$\Phi_{,1} = - \frac{m_o}{2c} (T+\Phi_o) \tag{12}$$

that satisfies the stress vanishing condition at infinity. The stresses referred to ξ_i take the forms

$$\begin{aligned}
\sigma_{11}(\xi_i) &= -N\{[K_o(cr) - \frac{\xi_1}{r} K_1(cr)]\exp(-c\xi_1) + \frac{\xi_1}{cr^2}\} \\
\sigma_{22}(\xi_i) &= -N\{[K_o(cr) + \frac{\xi_1}{r} K_1(cr)]\exp(-c\xi_1) - \frac{\xi_1}{cr^2}\} \\
\sigma_{12}(\xi_i) &= N[K_1(cr)\exp(-c\xi_1) - \frac{1}{cr}] \cdot \frac{\xi_2}{r}
\end{aligned} \tag{13}$$

The quantity N stands for

$$N = \frac{\mu m_o Q_o}{2\pi\kappa} \tag{14}$$

For plane strain, the transverse normal stress component σ_{33} takes the form

$$\sigma_{33}(\xi_i) = -2NK_o(cr)\exp(-c\xi_1) \tag{15}$$

It is interesting to note that the stresses possess a logarithmic singularity in terms of the radial distance r measured from the source as shown in Figure 1.

Numerical Results. Along the path of heat source $\xi_2 = 0$, the shear stress $\sigma_{12}(\xi_i)$ vanishes because of symmetry as indicated by the third of equations (13). The normal stresses $\sigma_{11}(\xi_i)$ and $\sigma_{22}(\xi_i)$ can be calculated and plotted as a function of the dimensionless argument $c\xi_1$ of the modified Bessel functions. The results expressed in dimensionless form are displayed graphically in Figures 2 and 3 for the 2024-T3 aluminum alloy with the following material properties:

$$\begin{aligned} &\alpha = 42.55 \times 10^{-6}\ \text{m/m/°C}, \quad && \nu = 0.33 \\ &k = 1.903 \times 10^{2}\ \text{w/m°K}, \quad && \mu = 2.748 \times 10^{4}\ \text{MPa} \\ &C = 9.623 \times 10^{2}\ \text{J/Kg°K}, \quad && \rho = 2.770 \times 10^{3}\ \text{kg/m} \end{aligned} \tag{16}$$

Note that regardless of the value cx, $\sigma_{11}(\xi_1,0)$ in Figure 2 is always compressive while $\sigma_{22}(\xi_2,0)$ in Figure 3 is partially compressive for small values of $c\xi_1$ and becomes tensile reaching a peak prior to decaying in magnitude. This means that for a fixed distance ξ_1 from the heat source, the stress component σ_{22} changes from compression to tension as the speed v being directly proportional to c is increased. For small values of c or v and ξ_1, both σ_{11} and σ_{22} are compressive. This is illustrated in Figures 4 and 5 for v = 1.0 cm/sec and r = 10^{-2} cm in which $\sigma_{11}(\xi_i)$ and $\sigma_{22}(\xi_i)$ are plotted as a function of the polar angle θ. The curves are not symmetric with respect to $\theta = 90°$ because of the motion of the heat source in the ξ_1 direction. They tend to become axisymmetric as the distance r is made to approach zero.

STRAIN ENERGY DENSITY CRITERION

The fluctuation of the strain energy density function dW/dV in a solid is fundamental because it can be related to material damage* by yielding and frac-

*The unique character of dW/dV possessing maxima and minima in the neighborhood of any point in a solid system prevails also for material undergoing creep and/or fatigue.

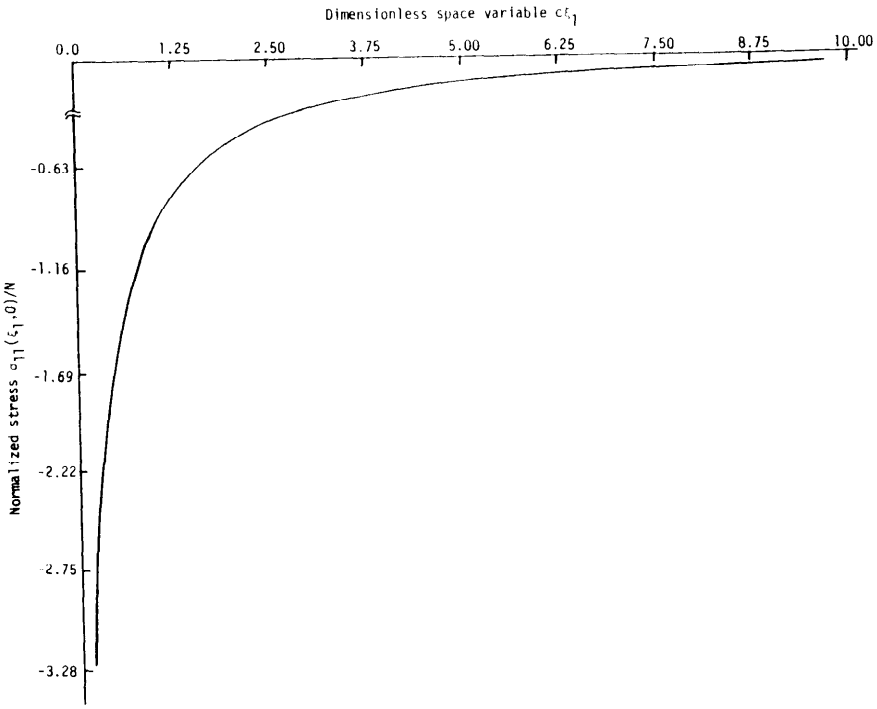

Figure 2 Normalized Stress σ_{11}/N Versus Dimensionless Distance $c\xi_1$ For $\xi_2 = 0$

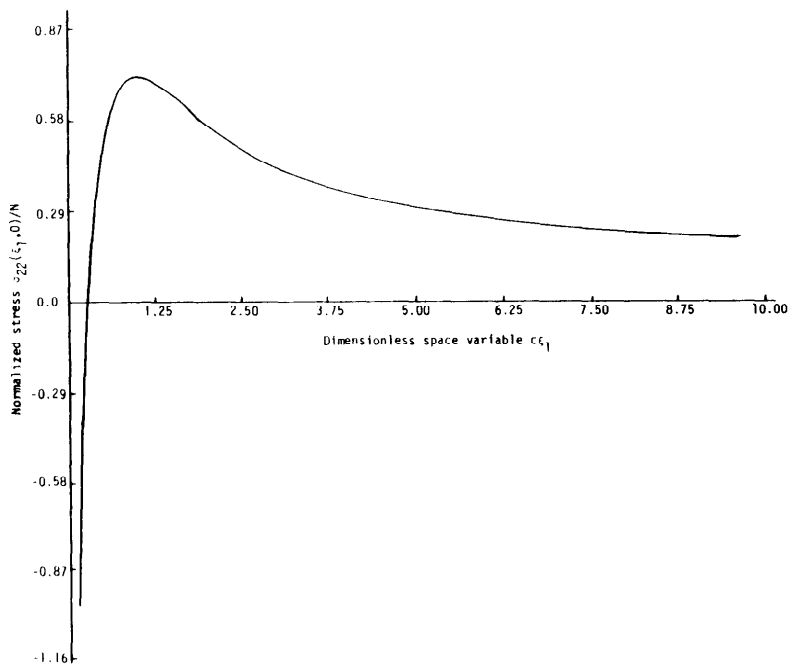

Figure 3 Normalized Stress σ_{22}/N Versus Dimensionless Distance $c\xi_1$ For $\xi_2 = 0$

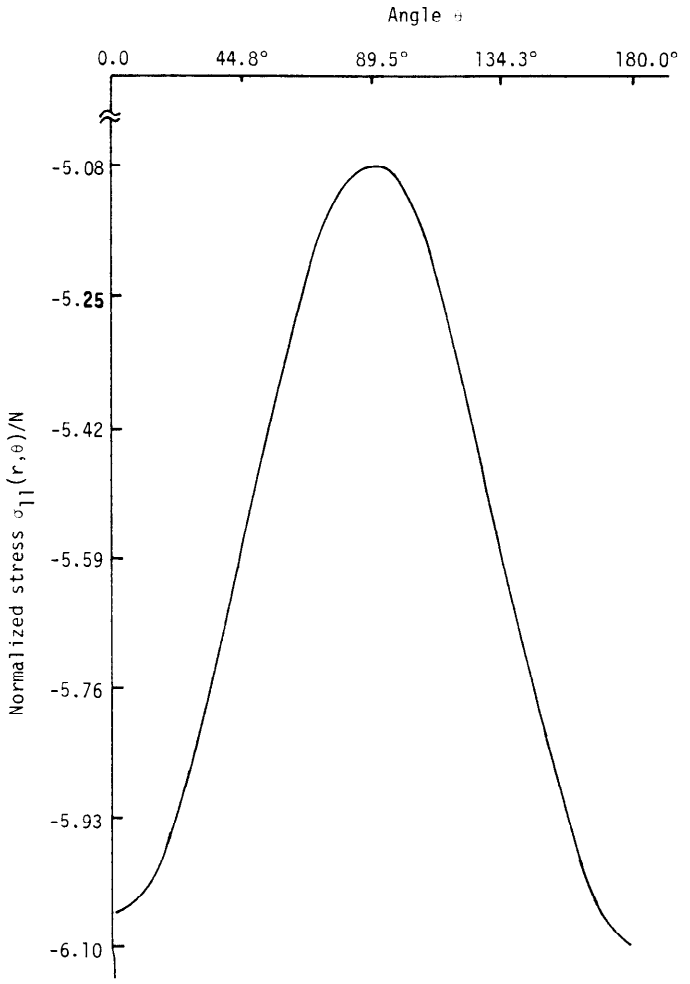

Figure 4 Variations of σ_{11}/N With Angle θ For v = 1.0 cm/sec and r = 10^{-2} cm

ture. The peaks (or maxima) can be associated with the locations of yielding where the material distorted excessively and the troughs (or minima) with fracture corresponding to excessive volume change. The proportion of energy for these two processes is determined by taking the stationary values of dW/dV with reference to the coordinates that locate the possible failure sites. This leads to $(dW/dV)_{max}$ and $(dW/dV)_{min}$ whose threshold values, say $(dW/dV)_o$ and $(dW/dV)_c$, are assumed to denote the initiation of yielding and fracture, respectively. Such an interpretation has had much success in explaining the failure of engineering structural components [2].

Strain Energy Density. For a nonlinear material, the computation of dW/dV requires a knowledge of both the stresses and strains in the body. If the material is linearly elastic, it suffices to know the stresses or strains. Suppose that the system is in a state of plane strain, then

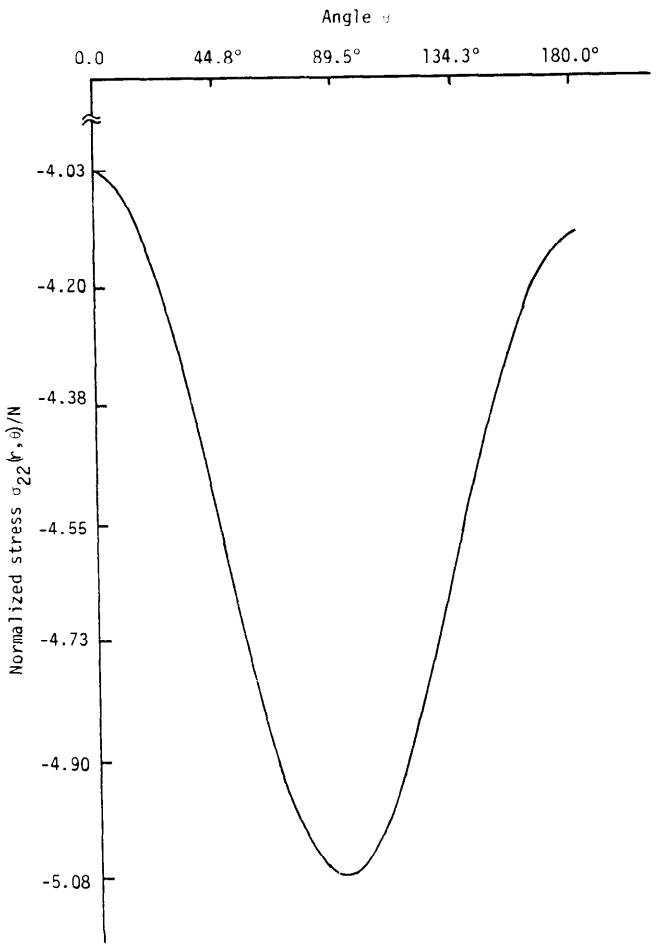

Figure 5 Variations of σ_{22}/N With Angle θ For v = 1.0 cm/sec and r = 10^{-2} cm

$$\frac{dW}{dV} = \frac{1}{4\mu}\left[(1-\nu)(\sigma_{11}+\sigma_{22})^2 - 2(\sigma_{11}\sigma_{22}-\sigma_{12}^2)\right] + (1+\nu)(\sigma_{11}+\sigma_{22})\alpha T + \frac{2\mu(1+\nu)^2}{1-2\nu}(\alpha T)^2 \qquad (17)$$

Referring to Figure 6, the normalized strain energy density function is plotted as a function of the dimensionless variable $c\xi_1$ for the 2024-T3 aluminum. Note that the curve descends rapidly as $c\xi_1$ is increased. The actual values of dW/dV at a specific location depend on the speed of the traveling heat source. The application of the strain energy density criterion [4] to predict possible sites of failure by yielding and fracture will be discussed in the section to follow.

Dilatational and Distortional Component. Additional insight into the strain energy density criterion may be gained by resolving dW/dV into two components:

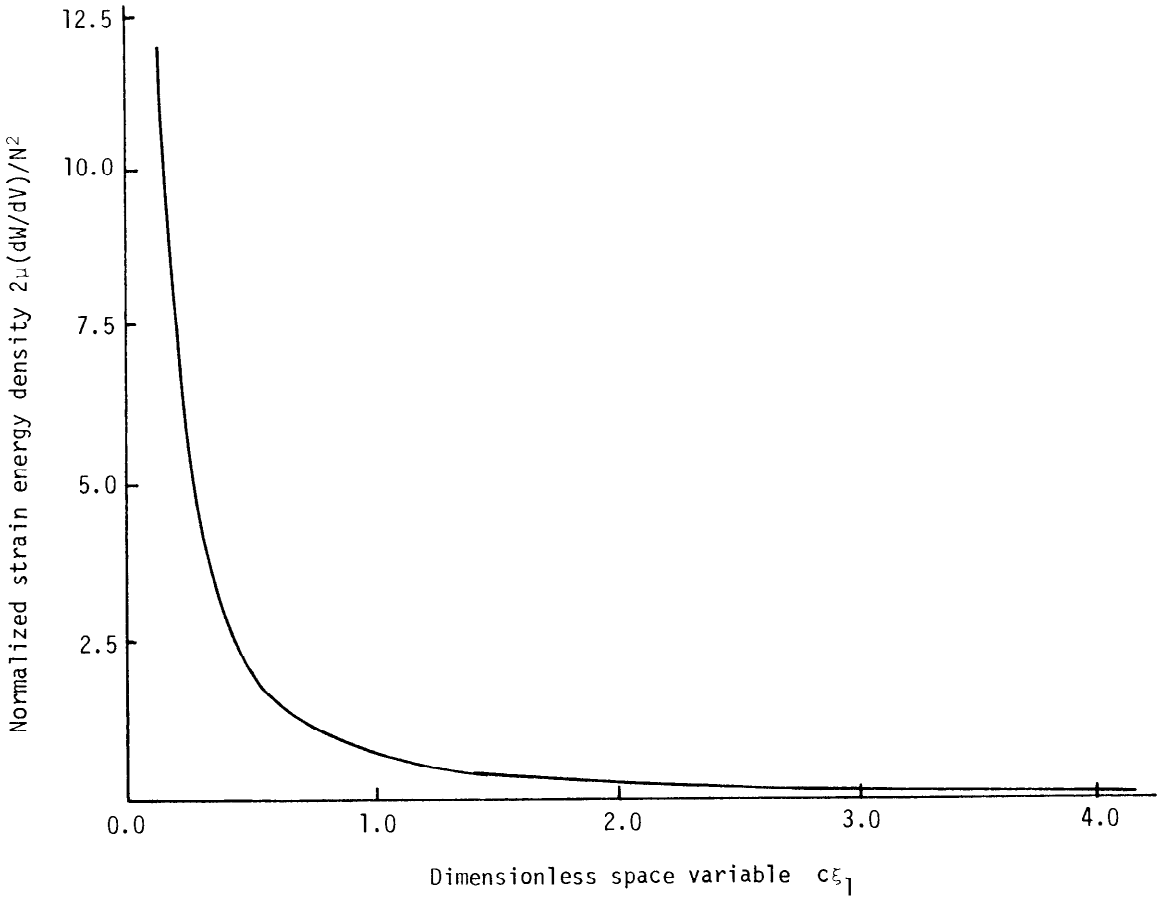

Figure 6 Normalized Strain Energy Density Versus $c\xi_1$ For 2024-T3 Aluminum

$$\frac{dW}{dV} = \left(\frac{dW}{dV}\right)_v + \left(\frac{dW}{dV}\right)_d \tag{18}$$

where $(dW/dV)_v$ and $(dW/dV)_d$ are identified respectively as the energy density component associated with volume change and shape change. Their relative magnitude that may be weighed by the ratio $(dW/dV)_v/(dW/dV)_d$ gives a measure of the proportion of yielding and fracture.

In order to be more specific, Figure 7 gives a plot of $2\mu(dW/dV)/N^2$ versus the angle θ for v = 1.0 cm/sec and r = 10^{-2} cm. It shows that $2\mu(dW/dV)_{max}/N^2 = 77.86$ occurred behind the source at $\theta = 180°$ while $2\mu(dW/dV)_{min}/N^2 = 75.56$ occurred to both sides at $\theta = \pm 59°$. Figure 8 displays the variations of the normalized dilatational strain energy density $2\mu(dW/dV)_v/N$ as a function of θ. The curve attains a minimum of $2\mu(dW/dV)_v^{min}/N^2 = 66.29$ at $\theta = 0°$ and rises monotonically to a maximum of $2\mu(dW/dv)_v^{max}/N^2 = 68.17$ at $\theta = 180°$. In contrast, the distortional stress energy density component $2\mu(dW/dV)_d/N^2$ variation with θ is non-monotonic. Figure 9 shows that $2\mu(dW/dV)_d^{max}/N^2 = 9.68$ is at $\theta = 0°$ and $2\mu(dW/dV)_d^{min}/N^2 = 8.59$ at $\theta = 91°$. The curve then rises again for $\theta > 91°$.

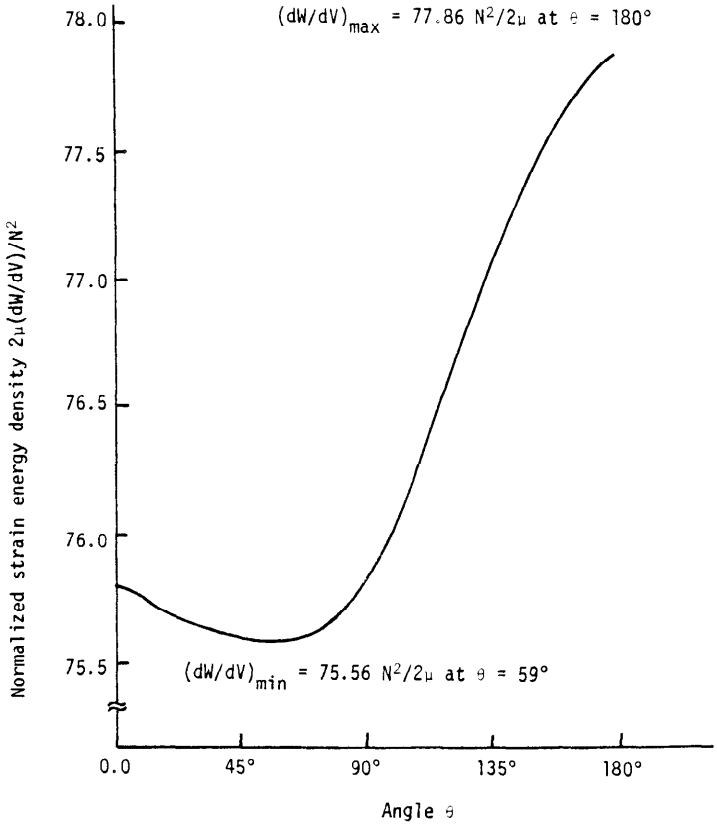

Figure 7 Normalized Strain Energy Density Function Versus θ For v = 1.0 cm/sec and r = 10^{-2} cm

As it is expected, there will be less time available for the system to absorb energy if the heat source speed were increased. This is indeed the case. For v = 10.0 cm/sec and r = 10^{-2} cm, dW/dV is decreased significantly. The value of $2\mu(dW/dV)_{max}/N^2$ and $2\mu(dW/dV)_{min}/N^2$ are smaller than those shown in Figure 7 for v = 1.0 cm/sec.

Threshold Values. Prior to discussing possible failure sites by yielding and fracture, it is worthwhile to have an idea of the stress state and energy density field on elements around the traveling heat source. Figure 10 displays the magnitude and direction of the stresses on elements positioned at $\theta = \pm 59°$ and 180° as they correspond to the locations of $(dW/dV)_{min}$ and $(dW/dV)_{max}$ shown in Figure 11. The element at $\theta = 0°$ is also included for reference purpose. The normal stresses σ_{11} and σ_{22} are all compressive and their magnitudes are nearly the same. In this case, there is no one stress component that tends to dominate and a criterion such as the maximum normal stress is not suitable.

The strain energy density criterion revealed a relative maximum at $\theta = 180°$ and two relative minima at $\theta = \pm 59°$. To be kept in mind is that the initiation of yielding determined by $(dW/dV)_{max} = (dW/dV)_o$ and fracture by $(dW/dV)_{min} = (dW/dV)_c$ occur at different locations around the heat source,

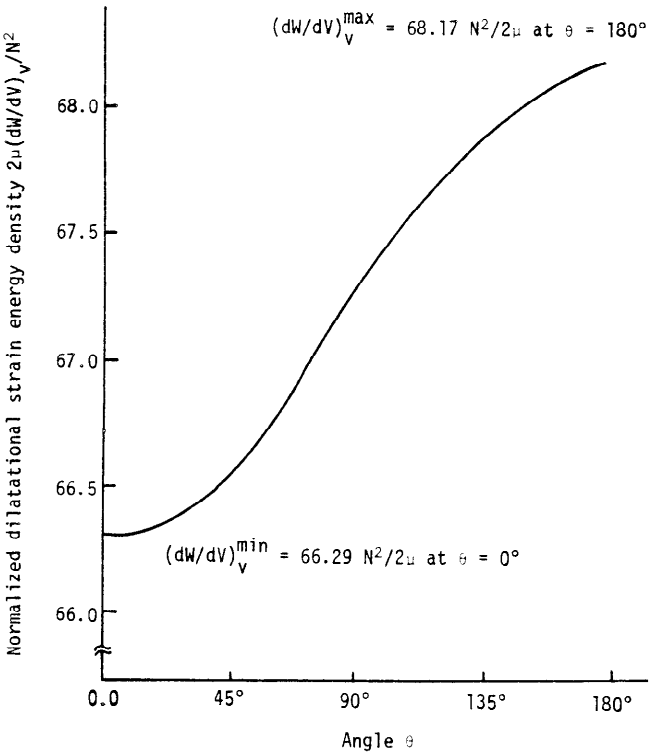

Figure 8 Normalized Dilatational Strain Energy Density Versus θ For v = 1.0 cm/sec and r = 10^{-2} cm

Figure 11. More specifically, the threshold values $(dW/dV)_0$ and $(dW/dV)_c$ refer to the areas under the true stress and strain curve. Refer to [2-4] for more details on the physical meaning of the strain energy density criterion. Even though the same material properties are assumed to prevail for all elements, the energy density field in terms of the proportion of $(dW/dV)_v$ to $(dW/dV)_d$ is different for each element. For instance, the ratio $(dW/dV)_v/(dW/dV)_d$ at $\theta = \pm 59°$ where $(dW/dV)_{min}$ occurred is 7.567 while at $\theta = 180°$ where $(dW/dV)_{max}$ occurred is 7.042. Dilatation is therefore seen to dominate at $\theta = \pm 59°$ while distortion is more pronounced at $\theta = 180°$. The physical interpretation is that yielding will first take place behind the heat source before fracture can initiate from the sides. Once yielding occurs, the elasticity solution is obviously no longer valid as a redistribution of the energy density within the system takes place and this alters the $(dW/dV)_c$ value for fracture initiation [1]. Nevertheless, the elasticity results do illustrate the interaction of $(dW/dV)_v$ and $(dW/dV)_d$ and renders information on the initiation of yielding and fracture.

CONCLUDING REMARKS

When energy is transferred to a solid by a traveling heat source, the trailing material is nearly in a state of hydrostatic compression. Examined is the dilatational and distortional component of the strain energy density

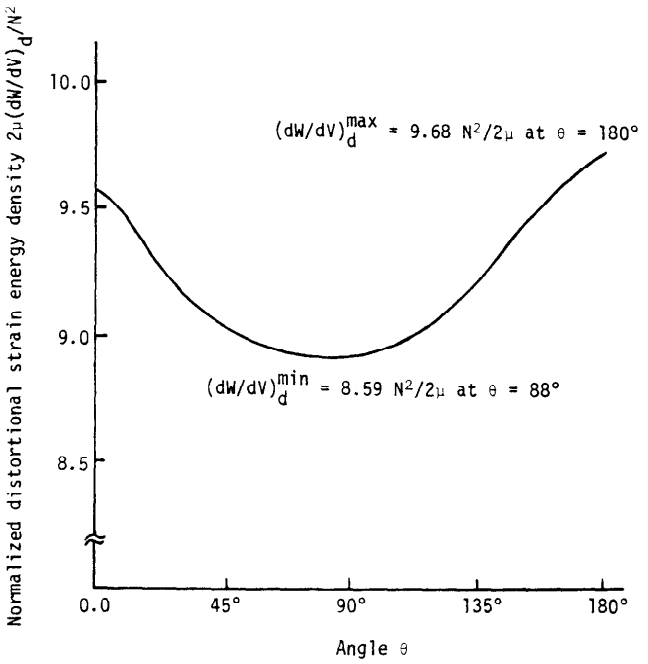

Figure 9 Normalized Distortional Strain Energy Density Versus For v = 1.9 cm/sec and r = 10^{-2} cm

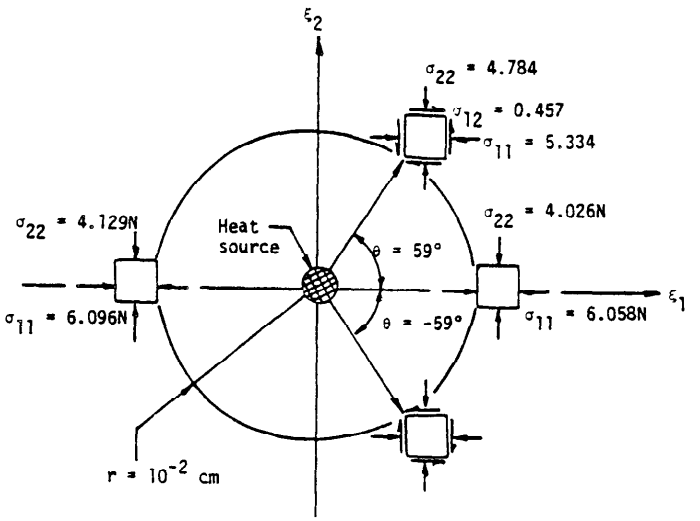

Figure 10 Stress State Around Heat Source For v = 1.0 cm/sec and r = 10

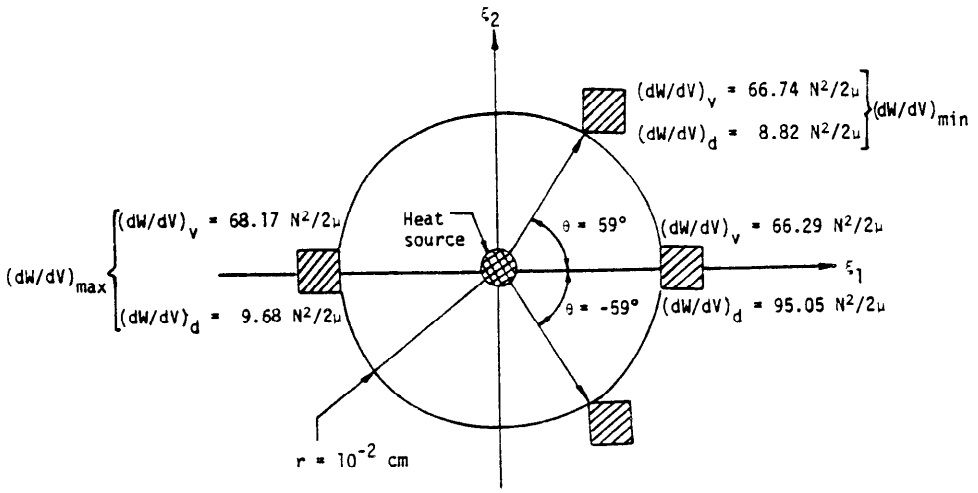

Figure 11 Energy Density Field Around Heat Source For v = 1.0 cm/sec and r = 10^{-2} cm

around the heat source. For sufficiently high intensity and low velocity of energy input, the material can damage by a combined process of yielding and fracture. The threshold levels of dW/dV determining yielding and fracture initiation will depend on the material properties, and other parameters governing the geometry and loading.

The application of external mechanical loads will also affect the results and conclusion. An all-around tensile load tends to compensate the hydrostatic compressive stresses and lower the energy density field. Hence, the influence of energy source can either enhance or damage the material depending on the interacting effects produced by the heat source and mechanical loading or initial stress state.

REFERENCES

1. Sih, G. C., "Mechanics of Ductile Fracture", Fracture Mechanics and Technology, Vol. II, edited by G. C. Sih and C. L. Chow, Sijthoff and Noordhoff International Publishing, The Netherlands, 1977, pp. 767-784.

2. Sih, G. C., "The Role of Fracture Mechanics in Design Technology", ASME, Journal of Engineering for Industry, Vol. 98. 1976, pp. 1243-1249.

3. Sih, G. C., "Experimental Fracture Mechanics: Strain Energy Density Criterion", Mechanics of Fracture, Vol. 7: Experimental Evaluation of Stress Concentration and Intensity Factors, edited by G. C. Sih, Martinus Nijhoff Publishers, The Netherlands, 1981, pp. XVII-LVI.

4. Sih, G. C., "A Special Theory of Crack Propagation", Mechanics of Fracture, Vol. 1: Methods of Analysis and Solutions of Crack Problems, edited by G. C. Sih, Noordhoff International Publishers, The Netherlands, 1973, pp. XXI-XLV.

5. Nowacki, W., Thermoelasticity, Pergamon Press, PWN, 1962.

6. Parkus, H., Instationäre Wärmespannungen, 1959, pp. 76-87.

7. Goodier, J. N., "On the Integration of the Thermo-Elastic Equations", Phil. Mag., Vol. 23, 1937, pp. 1017-1032.

8. Carslaw, H. S. and Jaeger, J. C., Conduction of Heat in Solids, Oxford University Press, 1959.

ACKNOWLEDGEMENT

This research was supported by the Naval Research Laboratory under Contract N00014-82-K-2006 with the Institute of Fracture and Solid Mechanics at Lehigh University, Bethlehem, Pennsylvania.

ANALYSIS OF MIXED MODE CRACK GROWTH IN A SHIP HULL MATERIAL UNDER DYNAMIC LOADING

C. R. BARNES
J. AHMAD
M. F. KANNINEN

Stress Analysis and Fracture Section
Battelle, Columbus Laboratories

ABSTRACT

Research on fracture in HY-100 steel under mixed mode (Modes I and II), dynamic, elastic-plastic loading conditions is described. A combined experimental and finite element analysis effort was pursued. The analysis employed the $\hat{J}$ criterion for fracture; a criterion which effectively generalizes the conventional J-integral to mixed mode and dynamic loading conditions. The experiments were performed with inclined-notch three-point-bend specimens of HY-100 steel. By coupling the experiments and finite element analyses, a fracture criterion based on a critical $\hat{J}$ value was devised and verified.

INTRODUCTION

The fracture mechanics techniques needed for materials that fracture in a highly ductile manner must give explicit attention to the extensive plastic deformation surrounding the crack tip. Extensive crack tip plasticity has two effects. First, because of crack tip blunting, crack growth initiation requires greater loads than are predicted by linear elastic fracture mechanics analyses. Second, significant amounts of stable crack growth under rising load can precede fracture instability. To cope with these essentially inelastic processes, elastic-plastic fracture mechanics techniques are now being widely pursued [1]. This research builds upon these developments to provide the basis for fracture mechanics treatments under the more general conditions of concern to ship structures.

Current work in elastic-plastic fracture mechanics is largely confined to quasi-static loading conditions and to crack growth in the opening mode (Mode I). Yet, in an impact loaded ship structure, crack initiation could occur under dynamic conditions with a combination of both the opening mode and the sliding mode (Mode II). Thus, it is necessary to obtain a quantitative understanding of crack growth initiation, propagation and arrest under initial combined mode dynamic loading conditions. The research described here is aimed at developing this understanding through a program of integrated experimental and finite element analysis work. The objective is to provide the basis for the more general inelastic-dynamic fracture mechanics approach that is needed for Navy applications.

THE GENERAL APPROACH

In a critical survey of progress on elastic-plastic fracture mechanics, Kanninen, et al [1] found that most efforts are focused on the J-resistance

curve approach. Despite the fact that such approaches are inherently limited to small amounts of crack growth prior to fracture instability, they do provide a significant improvement over the conventional linear elastic fracture mechanics techniques. However, the current approaches are restricted to Mode I conditions under quasi-static loading. While a generalization of the J-integral valid for mixed mode and dynamic loading conditions exists, it has not previously been critically examined. Nevertheless, in view of the success that has been achieved with J and the complete lack of a viable alternative, this parameter, known as the $\hat{J}$-integral, was selected for use in this study. The mathematical basis for $\hat{J}$ and the manner in which it can be applied to elastoplastic dynamic fracture problems can be found in references [2], [3], and [4].

The experimental portion of the research described in this paper employed HY-100 steel three-point-bend specimens with slant edge cracks. The specimen configuration is shown in Figure 1. This configuration has a number of advantages for this research. First, crack initiation and propagation can be obtained for both quasi-static and dynamic loading in the same specimen geometry. Second, by varying the crack angle and the crack length, a range of Mode I and Mode II combinations can be achieved. Third, this specimen can be economically analyzed with a finite element method. Fourth, because of the constraint that arises in bending, the J-resistance curves obtained may be lower bound values that will provide conservative predictions when utilized for structural integrity assessments [1].

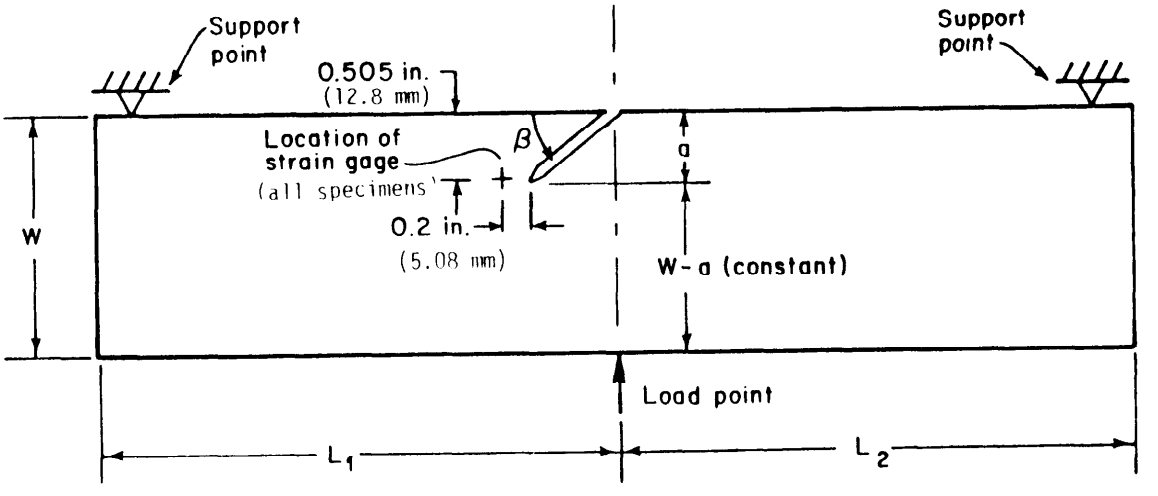

FIGURE 1. THREE-POINT-BEND SPECIMEN WITH A SLANT EDGE CRACK

A dynamic elastic-plastic finite element analysis was used in the analysis portion of the research. The objective was to learn if crack growth initiation in HY-100 steel is governed by critical values of $\hat{J}$. The $\hat{J}$ values were determined by finite element analyses of the experiments. In essence, by calculating the vectorial components of $\hat{J}$ (i.e., $\hat{J}_1$ and $\hat{J}_2$) as a function of load, and using the load level at initiation, critical values for

experiments performed with each different crack angle were determined. This provided a tentative elastic-plastic mixed mode fracture criterion in terms of a single material parameter.

Analyses were also performed for impact loading. Here, the fracture criterion deduced under quasi-static loading was used as input to a finite element simulation of the impact loaded experiment. In this way a prediction of the initiation time was made for comparison with an experiment. The quite reasonable accuracy of this prediction then gave an indication of the usefulness of the approach for the general conditions of interest in this research.

THE EXPERIMENTAL RESEARCH

Quasi-Static Loading Experiments

The specimen type used in this research was shown in Figure 1. Specimen blanks were cut from HY-100 steel plate. The chemical analysis and mechanical properties are shown in Tables 1 and 2. The specimen blanks were oriented such that the crack propagation direction for the specimens with $\beta = 90°$ (see Figure 1) was parallel to the plate rolling direction. Crack propagation in specimens with $\beta = 30°$ and $\beta = 45°$ was at 60° and 45°, respectively, to the rolling direction.

The general specimen configuration conformed with the ANSI/ASTM E604-77 Standard for Dynamic Tear Specimens except for the thickness and notch treatment. While the ANSI/ASTM standard [5] requires a thickness of 0.625 inch, 1.15-inch thick specimens (full plate thickness) were used in this investigation to promote plane strain behavior at the notch tip. The standard also requires that the notch root be sharpened by pressing a preformed tool into the notch root. However, past experience at Battelle has demonstrated that many otherwise ductile materials fail either partially or totally by cleavage when specimens containing the ANSI/ASTM specified notch are impact tested.

TABLE 1. HY-100 CHEMICAL COMPOSITION
(Average of Three Samples)

	C	Mn	P	S	Cu	Si	Ni	Cr	Mo	V	Ti
PLATE	.17	.30	.011	.017	.15	.28	2.76	1.51	.39	.003	.002
MII (a) SPEC.	.12 to .20	.10 to .40	MAX. of .025	MAX. of .025	MAX. of .25	.15 to .35	2.25 to 3.50	1.00 to 1.80	.20 to .60	MAX. of .020	MAX. of .030

(a) Military Specification, Steel Plate, Alloy, Structural, High Yield Strength

(HY-80 and HY-100), MIL-S-1621H (SHIPS), (15 March 1972)

TABLE 2. HY-100 MECHANICAL PROPERTIES

Specimen Orientation	2% Offset Yield Strength (ksi)	Ultimate Tensile Strength (ksi)	Elongation (%)	Reduction of Area (%)	Modulus (10^6 psi)
Longitudinal (T-L)	107.6 (742Mpa)	121.3 (836Mpa)	20	72.4	31.8 (219Gpa)
Transverse (L-T)	108.1 (745Mpa)	121.8 (840Mpa)	20	70.3	31.1 (214Gpa)

(One such material is HY-100 steel). In addition, the specimen configuration precluded the use of fatigue to sharpen the notch root (as used in the ASTM standard for K_{Ic} specimens). Consequently, the notch was sharpened using a jeweler's saw that produced a root radius of about 3.25 mils. It was anticipated that this relatively blunt notch would store enough energy to promote rapid unstable crack propagation in the impact tests that are described later.

Table 3 lists the specimens tested under quasi-static loading conditions. Tests were performed using a Baldwin-Tate Emery Test Machine having a load capacity of 60,000 lbs. The loading rate was adjusted such that the load-point displacement (LPD) was 0.01 inch min^{-1}. The loading was interrupted at preselected points on the load-displacement curve to fill the notch with a silicone rubber compound. This procedure was used to determine the load at crack initiation. It was determined that the cracks initiated internally and tunnelled for a distance roughly equal to the shear lip width (0.2 to 0.3 inch) before reaching the surface.

TABLE 3. QUASI-STATIC LOADING EXPERIMENTS

Specimen Number	Crack Position	β	Maximum Load (lbs)
102S	Mid-Point	90°	39,000 (173.5 kN)
101S	"	45°	42,500 (189 kN)
103S	"	30°	43,000 (173.9 kN)

Specimen 101S ($\beta = 45°$) was further instrumented to determine strain versus load by means of a strain gage rosette. A crude verification of the strains was provided by a coarse grid applied to the specimen's opposite face. A photographic record of this grid was made at each load-strain increment. An identical grid was also applied to Specimen 103S ($\beta = 30°$) and photographically recorded. Figure 2 shows a montage of Specimen 103S from zero load to fracture. Figure 3 shows the fracture surfaces of all three specimens tested under quasi-static loading.

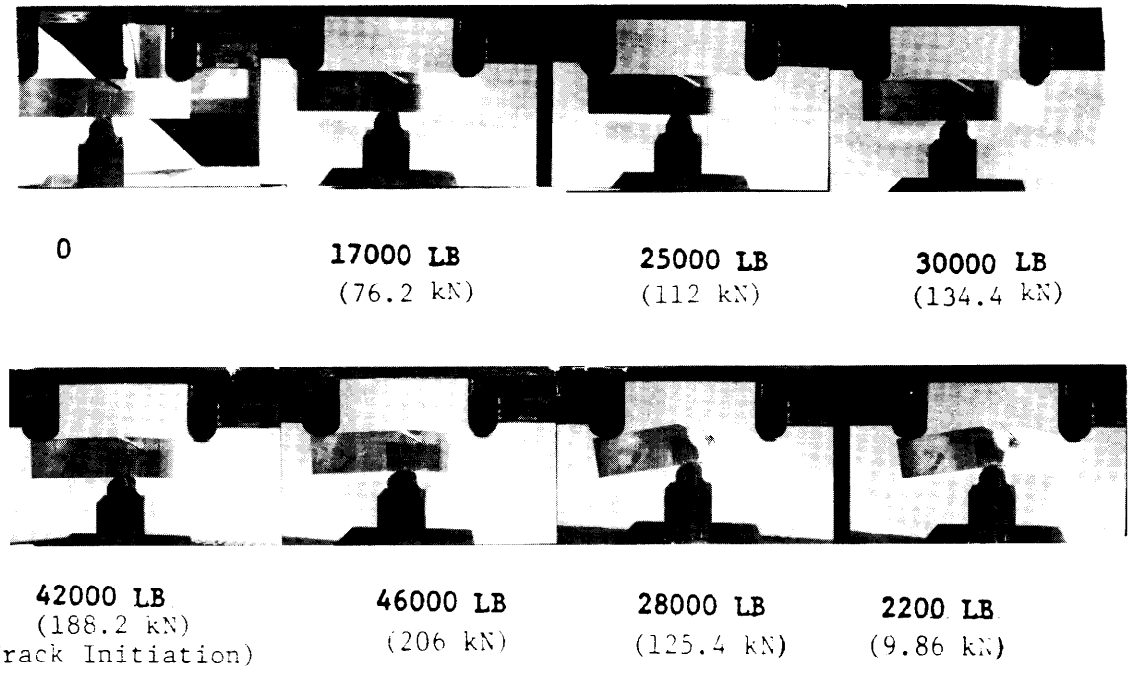

FIGURE 2. SPECIMEN 103S FROM ZERO LOAD TO FRACTURE

The experimental data from the three quasi-statically loaded specimens indicate the following. First, a plot of load versus load-point displacement (LPD) shows good agreement from specimen to specimen (Figure 4). The plot also indicates that lower values of β have higher values of the LPD at crack initiation. Second, the crack-tip-opening displacement (CTOD) at crack initiation was comparable in all specimens even though considerable data scatter was evident at lower loads (Figure 5). The source of this scatter was possibly caused by deformation zones observed about 4 mm from the crack tip.

$\beta = 30^{\circ}$ $\beta = 45^{\circ}$ $\beta = 90^{\circ}$

FIGURE 3. FRACTURE SURFACES OF THE QUASI-STATICALLY LOADED SPECIMENS

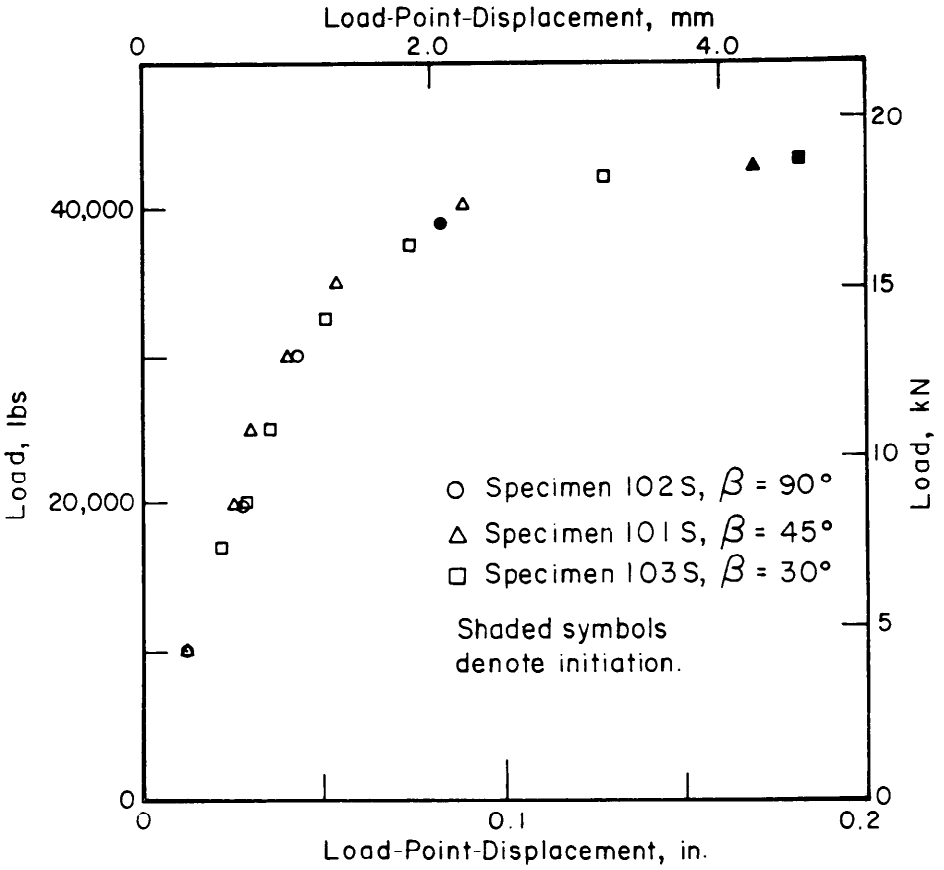

FIGURE 4. LOAD AS A FUNCTION OF LOAD-POINT-DISPLACEMENT FOR THE QUASI-STATIC LOADING EXPERIMENTS

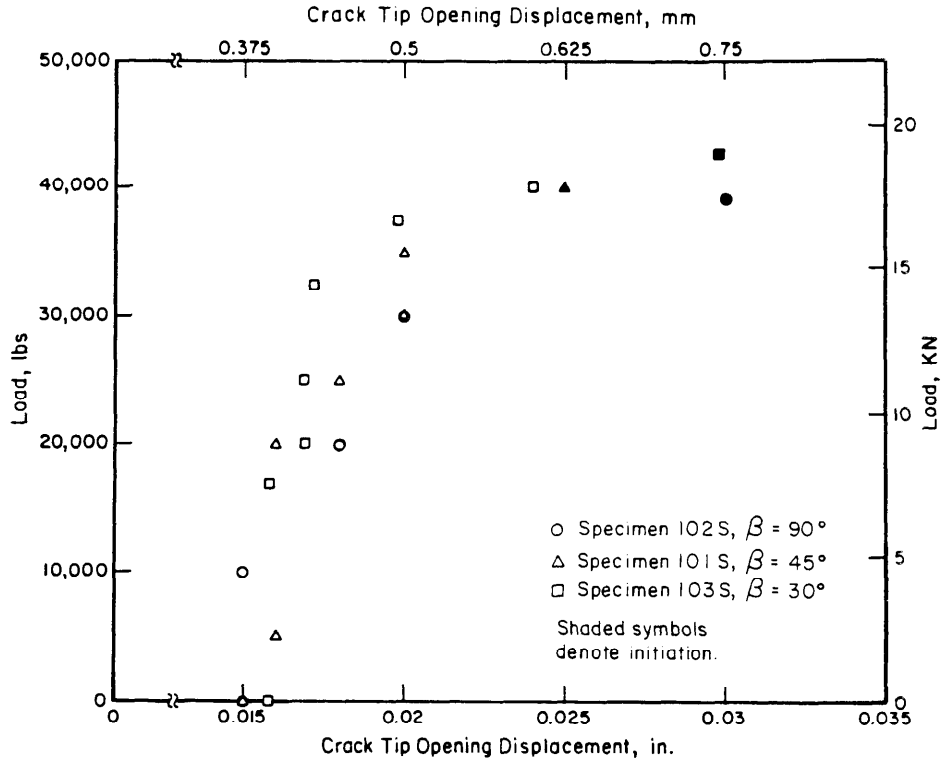

FIGURE 5. LOAD AS A FUNCTION OF CRACK TIP OPENING DISPLACEMENT FOR THE QUASI-STATIC LOADING EXPERIMENTS

Dynamic Loading Experiments

A Battelle designed and built machine, similar in concept to a Charpy machine, was used to conduct the impact tests. It is a multipurpose pendulum-type machine with a total impact energy of approximately 16,000 ft-lbs. A variety of specimen geometries can be accommodated by changing the bolt-on supports. Figure 6 shows a photograph of the specimen loading arrangement used in the tests.

To assess the practicality of determining crack initiation and crack propagation speeds in HY-100 steels, a crack monitoring gage was deposited upon a trial specimen surface according to the procedure given by Kanninen, et al [6]. This technique involves the vapor deposition of an electrically conducting grid upon a thin epoxy layer bonded to the test specimen surface. A strain gage was also applied to the specimen at the locations shown in Figure 7. In addition, the impact machine was electrically wired to indicate the time of the tup-specimen contact. The tup contact switch and output from

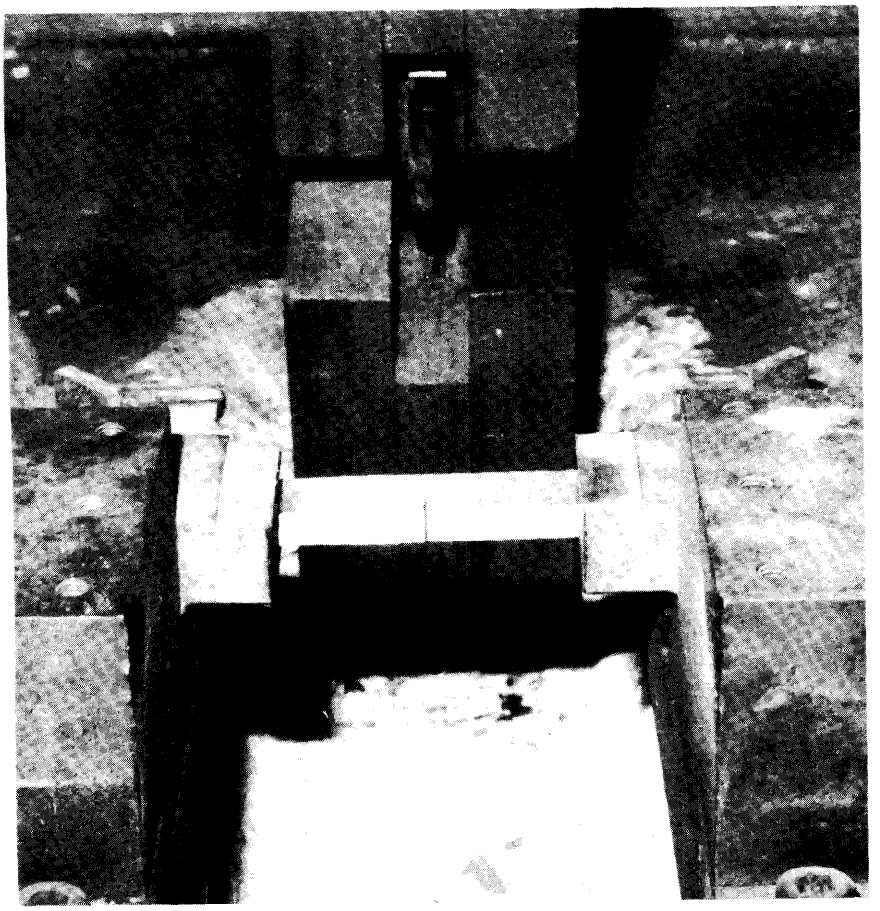

FIGURE 6. IMPACT LOADING ARRANGEMENT

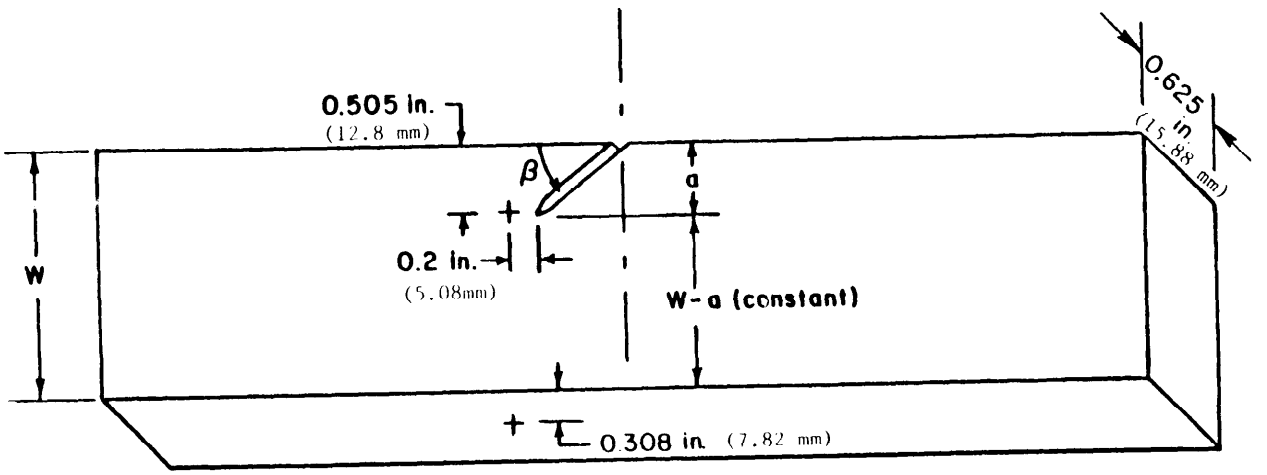

FIGURE 7. FEASIBILITY TEST SPECIMEN SHOWING STRAIN GAGE LOCATION

the crack monitoring gage were recorded simultaneously by a Biomation 8100 transient recorder and an FM tape recorder. The strain gage outputs were recorded on two adjacent tape channels.

Although the data from this feasibility test indicated that the dynamic initiation could be deduced (Figure 8), the crack speed record was less definitive. This was probably caused by the large plastic zone generated at the crack tip which resulted in epoxy-specimen separation. This condition rendered the speed measurement suspect since past experience has shown that it is essential that no epoxy-specimen debonding occurs for reliable crack speed determination. This, coupled with the suspicion that crack tunneling posed similar problems in determining the instant of crack initiation, prompted specimen modification for the impact tests. Accordingly, three specimens were prepared (one each with β = 90°, 45° and 30°) in which the notch configuration was altered as shown in Figure 9.

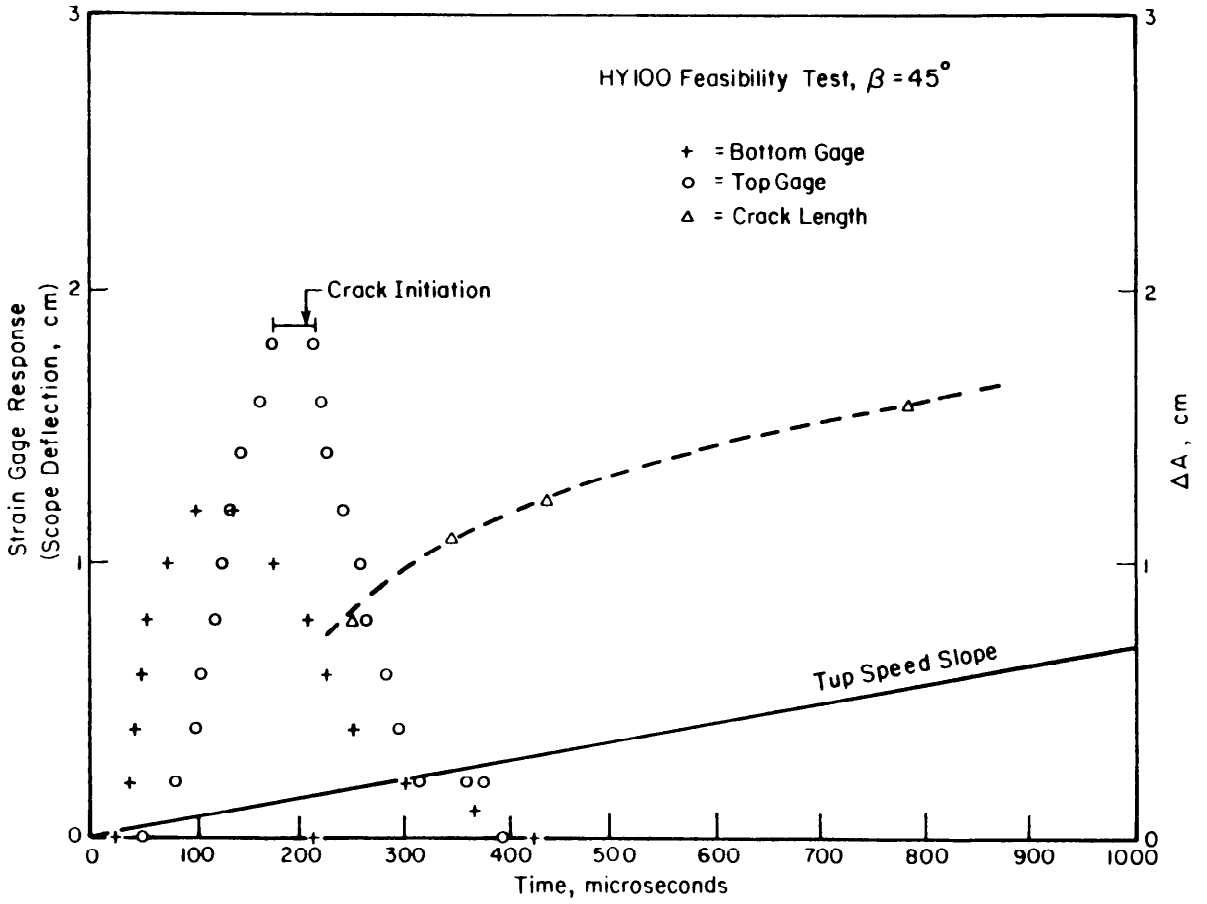

FIGURE 8. RESULTS OF IMPACT LOADED FEASIBILITY EXPERIMENT WITH β = 45° (Time 0 = tup contact)

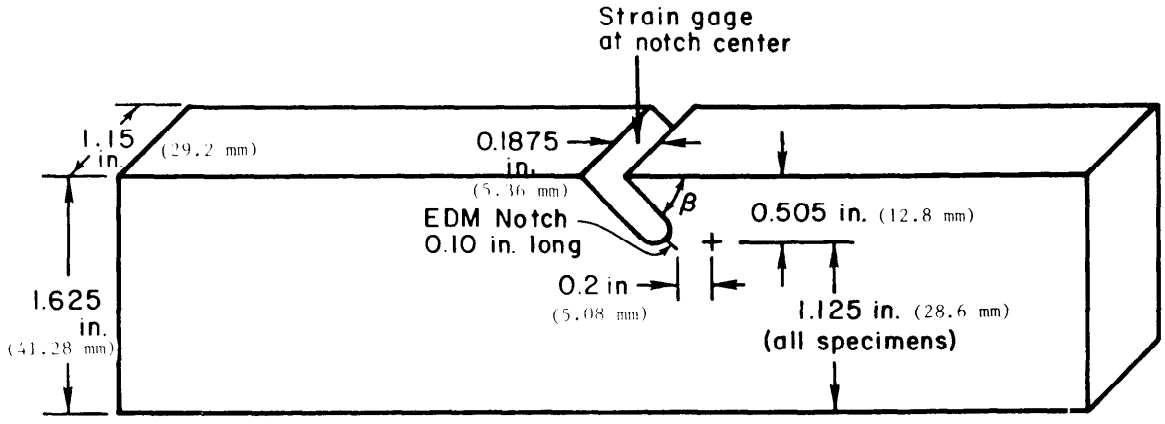

FIGURE 9. IMPACT SPECIMENS WITH CRACK STARTER NOTCH STRAIN GAGE APPLICATION

The notch geometry shown in Figure 9 was adopted so that a strain gage could be applied in the notch center. This indicates crack initiation more precisely than would a gage placed upon the specimen surface. Another gage was positioned at the side of the sharpened notch as in previous specimens. This gage was used to detect the time at which the internally initiated crack surfaced. As will be shown later, the crack initiation data agreed very well with the data from the feasibility test, which indicated that the crack surfaced at about 200 μsec. The surface crack initiation times for $\beta = 90°$, 45° and 30° were 230, 222, and 250 μsec, respectively. Note, however, that the feasibility test was conducted on a thinner specimen. Table 4 lists the three test specimens and the energy required to fracture them.

TABLE 4. IMPACT LOADED EXPERIMENTS

Specimen Number	Crack Position	β	Impact Energy (ft-lbs)
112D	Mid-Point	90°	1479 (2006 J)
113D	Mid-Point	45°	1982 (2688 J)
114D	Mid-Point	30°	1845 (2502 J)

THE ANALYSIS RESEARCH

The analysis effort in this research involved performing elastoplastic, quasi-static and dynamic finite element analyses of the experiments. The quasi-static analyses were performed to compute the $\hat{J}$ integral values corresponding to the experimentally determined loads at crack growth initiation. Using the $\hat{J}$ values at initiation under quasi-static loading conditions,

a crack initiation criterion was devised and used in the dynamic analyses for the prediction of crack initiation in impact loading.

All finite element analyses were performed using Battelle's elasto-plastic dynamic finite element fracture analysis computer code. The finite element meshes used in the analyses are shown in Figure 10. The numbered dotted lines in Figure 10 indicate the three contours used for computing the $\hat{J}$-integrals. The values obtained using the three contours were found to be fairly path independent [4]. The results of the quasi-static analyses summarized in Table 5 represent the average of the three contours at initiation load.

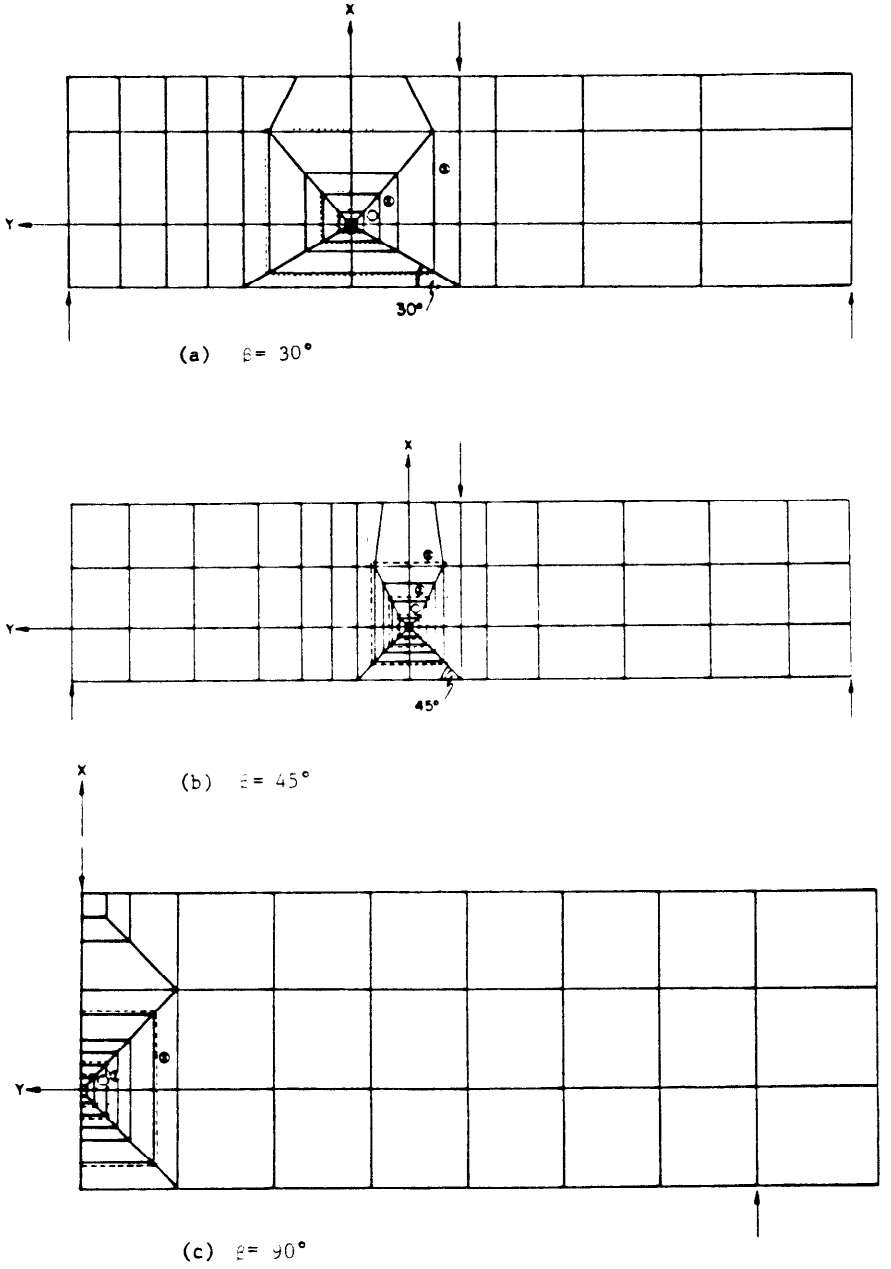

FIGURE 10. FINITE ELEMENT MESH FOR 30°, 45°, and 90° SPECIMENS

TABLE 5. $\hat{J}_1$ and $\hat{J}_2$ AT INITIATION FOR QUASI-STATIC LOADING

β	$\hat{J}_{1c}$ N/m	$-\hat{J}_{2c}$ N/m
30°	6.26×10^4	10.99×10^4
45°	12.84×10^4	12.5×10^4
90°	25.4×10^4	-

Using the results of Table 5 a plot of crack angle (β) vs. the $\hat{J}_1$ at initiation ($\hat{J}_{1c}$) was made. This is shown in Figure 11. An empirical fit of these data suggested that initiation occurs when

$$\hat{J}_1 = J_c \sin^2\beta \tag{1}$$

where J_c is the critical value of $\hat{J}$ at $\beta = 90°$. Note that within the deformation theory of plasticity assumption, J_c coincides exactly with the $\hat{J}$-integral value at crack initiation.

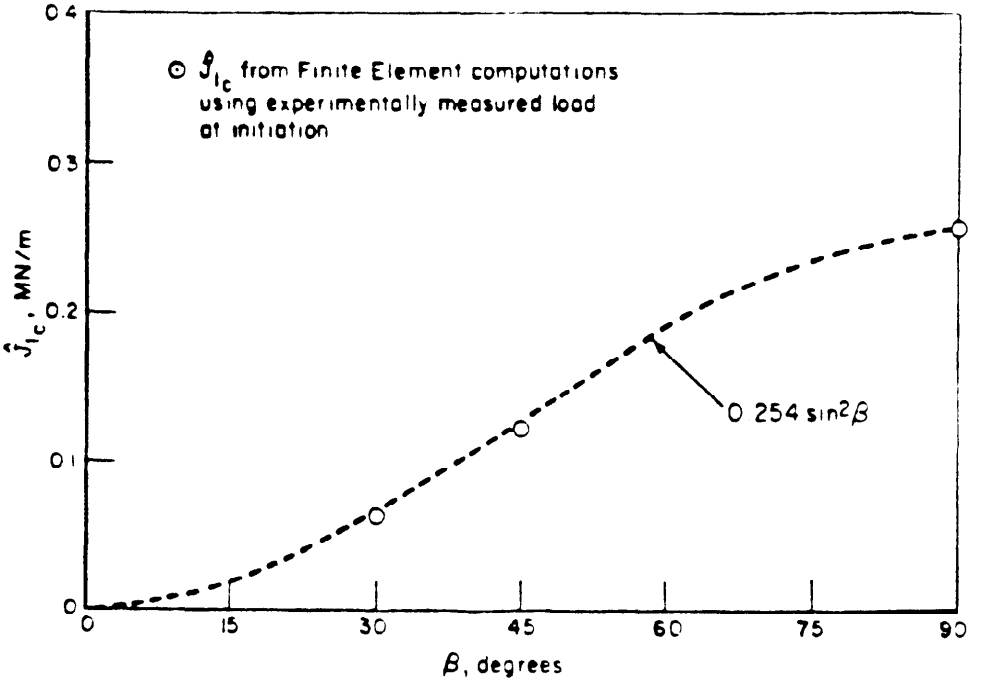

FIGURE 11. VARIATION OF $\hat{J}_{1c}$ WITH NOTCH ANGLE IN QUASI-STATIC LOADING

Turning now to impact loading conditions, a dynamic generalization of Equation (1) would be given by

$$\hat{J}_1 = DJ_c \sin^2\beta \tag{2}$$

where $\hat{J}_1$ now contains inertia effects while D is a rate-dependent material constant. If the loading rate effect is small, then $D \simeq 1$. The assumption will be made here on the basis that it is consistent with the use of the static stress-strain curve in finite element calculations. Therefore, strain-rate effects are omitted from both sides of Equation (2). Now, using Equation (2) and the results of dynamic finite element computations, a prediction of the time at which crack growth will initiate can be made. A comparison of these predictions with the experimentally measured time at initiation is contained in Figure 12. It can be seen that the prediction is quite reasonable.

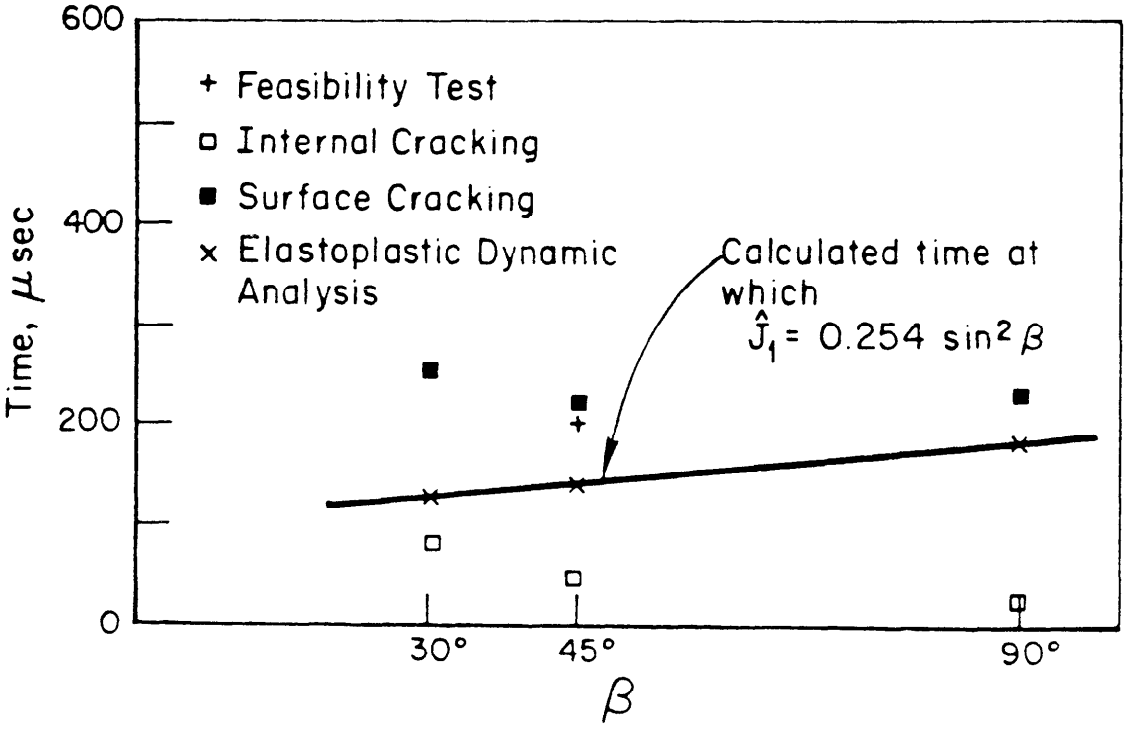

FIGURE 12. COMPARISON OF PREDICTED AND EXPERIMENTALLY MEASURED TIME AT INITIATION IN IMPACT LOADING

DISCUSSION OF RESULTS

The crack initiation criterion suggested by Equation (1) is based on fitting a curve through only four data points (three experimental results together with the origin). To explore the possibility that some other

function of β could provide just as good a fit, the problem depicted in Figure 13 was considered. This is an infinite plate containing a crack of length 2a that is subjected to a remote uniaxial applied stress whose direction makes an angle β with the crack line. The linear elastic solution of this problem gives [7]:

$$K_I = \sigma(\pi a)^{1/2} \sin^2\beta$$

and

$$K_{II} = \sigma(\pi a)^{1/2} \sin\beta\cos\beta. \tag{3}$$

The relation between $\hat{J}_1$ and the stress intensity factors K_I and K_{II} will give

$$\hat{J}_1 = \left\{\frac{k+1}{8}\sigma(\pi a)^{1/2}\right\}\sin^2\beta \tag{4}$$

where μ is the shear modulus, and $k = 3-4\nu$ for plane stress and $k = (3-\nu)/(1+\nu)$ for plane strain.

The expression within the brackets is the energy release rate G which, in a linear elastic problem, is just J. Therefore, Equation (4) can be written as

$$\hat{J}_1 = J \sin^2\beta \tag{5}$$

Now if fracture occurs when J achieves a critical value that is independent of β, then Equation (5) will be identical to Equation (1).

Despite their similarity, there is a significant difference between the origins of Equations (1) and (5). Specifically, Equation (5) contains $\hat{J}_1$ found by taking the material to be linear elastic and assuming a fracture criterion; i.e., $J = J_c$ for all β values. In contrast, Equation (1) was obtained by computing $\hat{J}_1$ by elastic-plastic finite element computations and using actual fracture data. Two conclusions can tentatively be drawn. First, the functional relationship between $\hat{J}_1$ and J in the linear elastic case may remain unaffected by plasticity. Second, this criterion may be geometry-independent. If indeed this is the case, the problem of predicting crack initiation reduces simply to knowing J_{1c} for the material and performing a linear elastic analysis of the problem to determine the relationship between J and $\hat{J}_1$. These implications present intriguing possibilities which must be further explored.

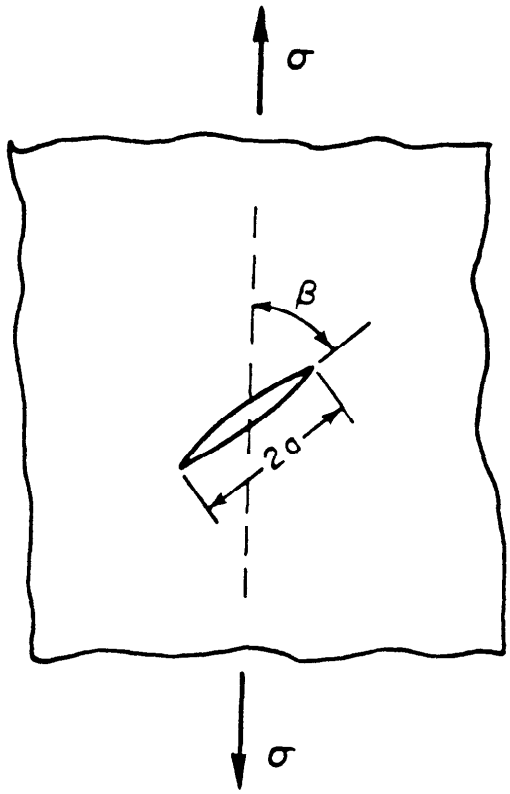

FIGURE 13. INFINITE PLATE WITH INCLINED CRACK

In regard to the prediction of crack initiation in impact loading, Figure 12 shows quite reasonable agreement. However, the significance of this observation is not certain at this time. The fact that the predicted time at initiation in all three cases lies within the measured time interval from the instant when the crack initiation was detected below the surface of the specimen to the instant when it appeared at the surface is very encouraging. That is, since the two-dimensional finite element analyses used in the prediction do not model crack tunnelling, the predicted time should be comparable to some instant inside the measured interval. While it can therefore be claimed that the experiments do provide data that are comparable to the analysis predictions, more experiments are needed to draw any decisive conclusions.

CONCLUSIONS

The results described in this paper indicate that the $\hat{J}$ parameter can be used as an effective criterion for crack initiation in elastic-plastic mixed mode loading conditions. Because a reasonable prediction was made for impact loading using quasi-statically-based values, it appears that the effect of loading rate may not be too important in HY-100 steel. Finally, the results suggest the intriguing possibility that the geometric influences on mixed mode loading under elastic-plastic conditions may be identical to those arising in linear elastic conditions.

ACKNOWLEDGEMENT

This work was performed for t'_ Naval Sea Systems Command via David Taylor Naval Ship Research and Development Center, Contract Number N00167-80-C-0253. The authors would like to express their appreciation to Nash Gifford and Archie Wiggs of DTS NRDC for their support and encouragement of this work.

REFERENCES

[1] Kanninen, M. F., Popelar, C. H., and Broek, D., "A Critical Survey on the Applications of Plastic Fracture Mechanics to Nuclear Pressure Vessels and Piping", Nuclear Engineering and Design, 67, 27-55, 1981.

[2] Kishomoto, K., Aoki, S., and Sakata, M., "On the Path Independent Integral J", Engineering Fracture Mechanics, Vol. 13, 841-850, 1980.

[3] Jung, J., Ahmad, J., Kanninen, M. F., and Popelar, C. H., "Finite Element Analysis of Dynamic Crack Propagation", Failure Prevention and Reliability - 1981, F.T.C. Loo, Editor, ASME, 1981.

[4] Ahmad, J., Jung, J., Barnes, C. R., and Kanninen, M. F., "The Development of a Dynamic Elastoplastic Finite Element Analysis for Fast Fracture Under Impact Loading", To appear in Engineering Fracture Mechanics.

[5] "Test for Dynamic Tear Energy of Metallic Materials", Annual Book of ASTM Standards, Part 10, Philadelphia, 1981.

[6] Kanninen, M. F., et al, "Dynamic Crack Propagation Under Impact Loading", Nonlinear and Dynamic Fracture Mechanics AMD, Vol. 35, N. Perrone and S. N. Atluri, Editors, The American Society of Mechanical Engineers, New York, 1979.

[7] Paris, P. C. and Sih, G. C., "Stress Analysis of Cracks", ASTM STP 381, p. 30, 1965.

FATIGUE AND FRACTURE EVALUATION OF THE A-7E ARRESTING GEAR DRAG LINK

D. L. MERKORD
Engineering Specialist

C. E. DUMESNIL
Technical Project Manager

T. D. GRAY
Manager, Structures Development
Vought Corporation
Dallas, Texas 75265

ABSTRACT

The primary objective of this program was to establish a proof load criteria for the A-7E drag link that is comparable to that of the hook shank. Twenty-three drag links were tested under realistic load and environment (3.5% salt solution) conditions. Critical locations, fatigue lives, residual strength and crack growth rates were determined and a proof load criteria was developed and verified. Even though a proof load criteria comparable to that of the hook shank could not be obtained, this technique used the crack growth data and nondestructive inspection (NDI) capabilities. An interval identical to that of the hook shank was found which gave a high probability of flaw detection. Vought recommended this second option as the most economic and efficient method of inspection.

This paper describes the results of a test and evaluation program conducted for the Naval Air Systems Command [1].

INTRODUCTION

The A-7E arresting gear is attached to the lower keel structure at fuselage station 590.0, as shown in Figure 1. The arresting gear assembly consists of a hook point, hook shank and a drag link. The assembly is presently removed from the airplane after every 100 arrestments for inspection; the hook shank is proof loaded and the drag link is magnetic particle inspected. Drag links are retired from service after 750 arrestments. In September 1978, Vought presented an ongoing case study of the A-7E hook shank at this symposium. At the completion of the program [2] Vought recommended a 175 kip (0.778 MN) axial proof load to be applied at a 550 arrestment interval. The primary objective of this follow-on program was to establish a proof load criteria for the drag link that is comparable to that of the hook shank.

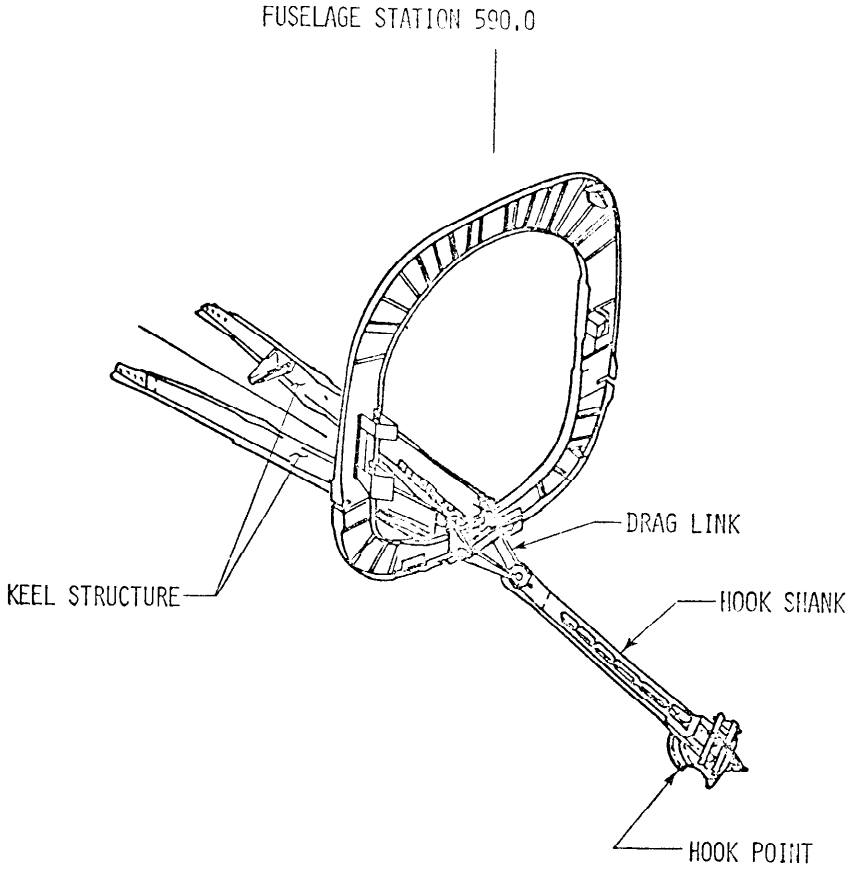

Figure 1. A-7E Arresting Gear

COMPONENT DESCRIPTION

The drag link is made from a 4340 steel die forging heat treated to 200 ksi (1379 MPa) ultimate tensile strength (see Figure 2). It is a triangular structure consisting of a heavy lug to which the hook shank is attached, two side legs of C channel construction and a transverse link member or torque tube to which a dashpot arm is integrally attached.

TECHNICAL APPROACH

The conventional proof test technique for qualifying a structural component takes on added significance when fracture mechanics theory is applied. To assess the condition of a component in terms of existing flaws, nondestructive inspection (NDI) procedures are generally relied upon. The proof test, however, can be considered one of the most positive inspection procedures available. A successful proof test actually defines the maximum possible flaw size that can exist in the structure. This results from the functional relationship between applied stress and flaw size as defined by the crack tip stress intensity factor, K,

$$K = f(\sigma\sqrt{a}) \qquad (1)$$

where "σ" is the stress level and "a" represents the crack size. Fracture occurs when the stress and crack size are such that $K = K_c$, which is the critical stress intensity factor or the material fracture toughness. Therefore, fracture data generated from test can relate stress or load at failure to flaw size. This is presented schematically in Figure 3a. It is seen that if a proof load, which is "α" times greater than the operating load, is successfully applied, then the maximum flaw which can exist in the part is a_i. If the critical flaw size under operating loads is determined as a_{cr}, then there exists a minimum flaw growth potential as shown.

In order to associate remaining life with the flaw growth potential, it is necessary to determine how long it takes a crack to grow from a_i to a_{cr} under operating conditions. One of the most predominate types of subcritical flaw growth is fatigue crack growth resulting from cyclic stresses. The methods used for predicting fatigue crack growth make use of flaw growth testing and the stress intensity concept.

It has been shown by Tiffany and Masters [3] that the number of cycles to failure at a given stress level depends on the initial stress intensity, K_i, compared to the critical stress intensity, K_c. Therefore,

$$N = f\left(\frac{K_i}{K_c}\right) \qquad (2)$$

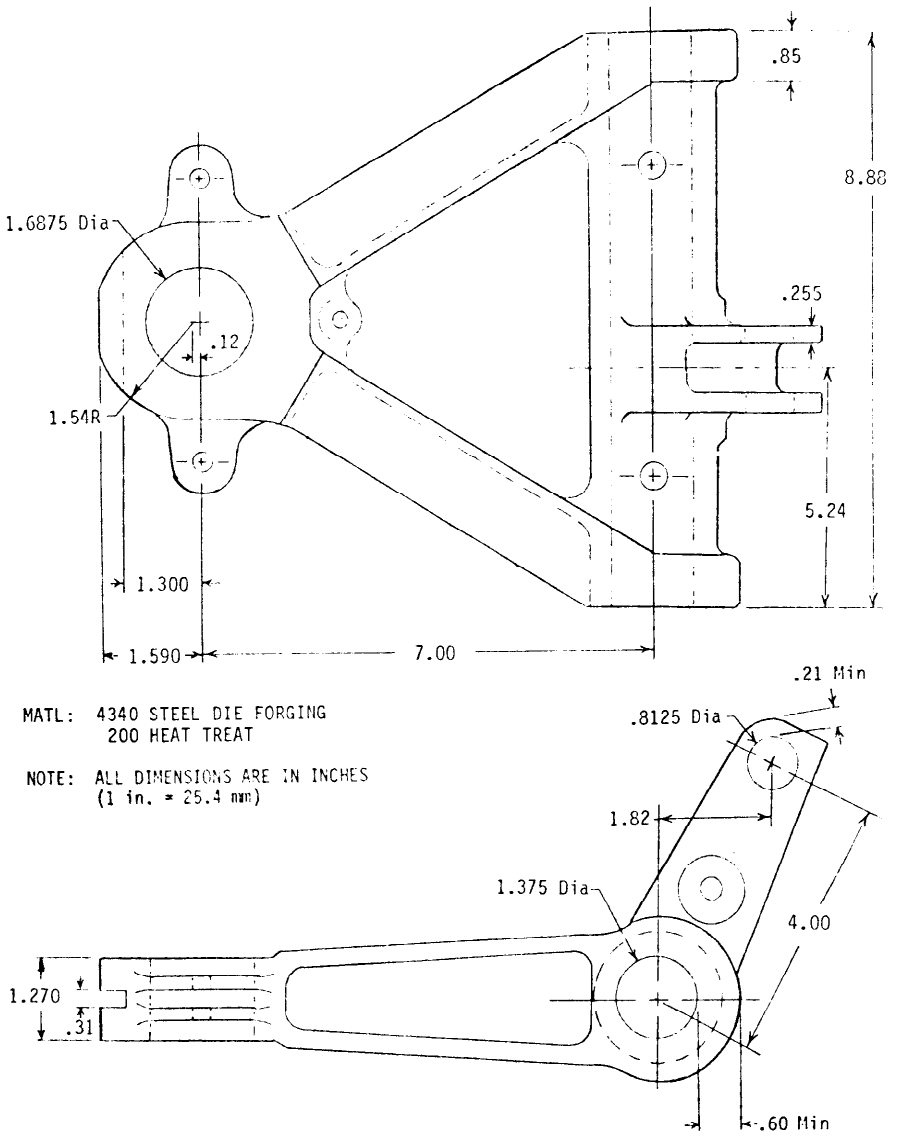

Figure 2. Physical Dimensions of A-7E Drag Link

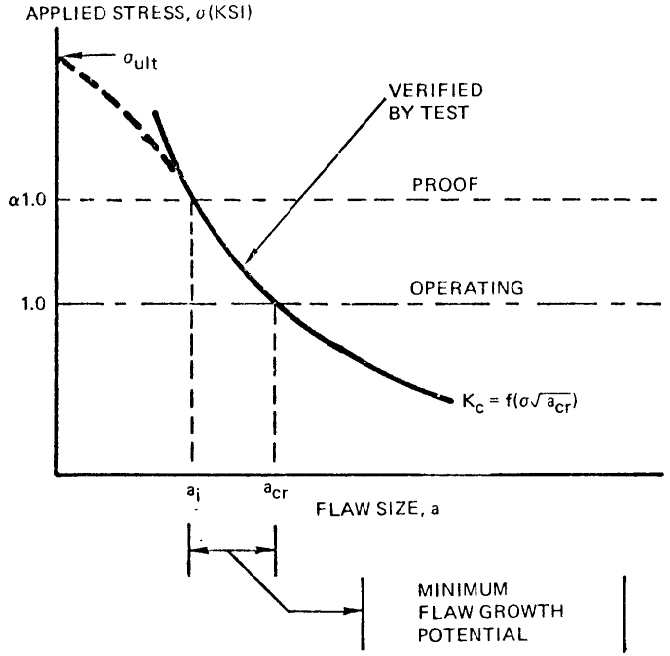

a) Stress vs Flaw Size Relationship

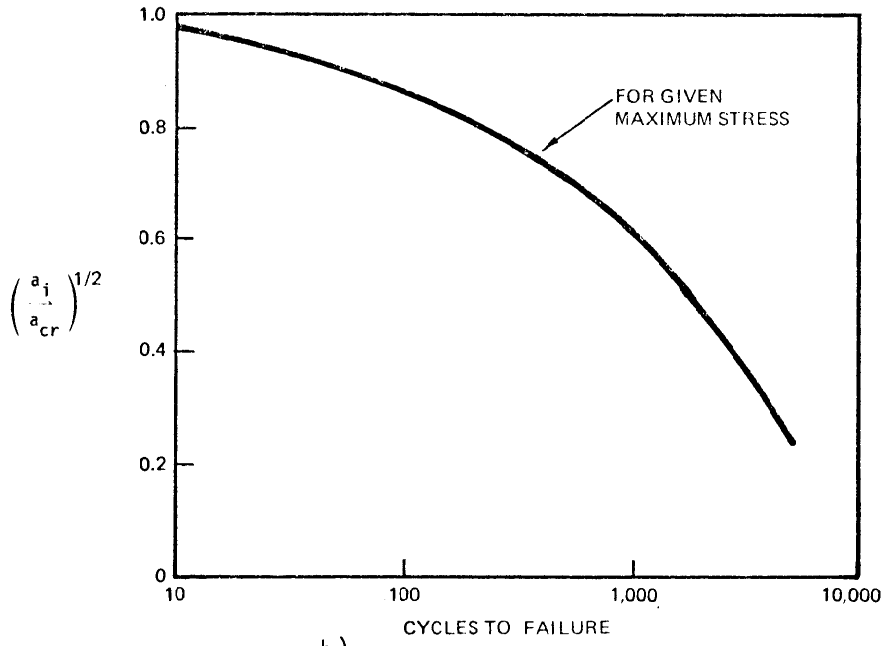

b) Flaw Size Ratio vs Cycles to Failure

Figure 3. Proof Load Development

where N is the number of cycles to failure. It is also seen that the stress intensity ratio is related to the ratio of initial flaw size to critical flaw size as follows

$$\left(\frac{K_i}{K_c}\right) = \left(\frac{a_i}{a_{cr}}\right)^{1/2} \qquad (3)$$

Thus, test data can be used to develop the relationship between the flaw size ratio and the number of cycles to failure. This data may be presented in a form shown graphically in Figure 3b. With this type of data, the cycles required for any given flaw to grow to critical size can be predicted.

Conversely, for a given life requirement, the maximum allowable initial flaw size can be determined. Knowing the maximum allowable initial flaw size for a required remaining life, data represented in Figure 3a can be used to establish the necessary proof load.

With this background information, the technical approach for the fatigue and fracture evaluation of the drag link can be divided into five phases as outlined in Table I.

EXPERIMENTAL PROCEDURE

The test program for the A-7E drag link was designed to provide data necessary for establishing fatigue life, crack growth rates, critical flaw sizes, environmental effects, residual strength, and verification of proof load criteria for the drag link component. The test program involved the structural testing of 22 government-furnished retired A-7E drag links and one Vought furnished drag link for a total of 23 components. The drag links were stripped, cleaned and subjected to close visual and magnetic particle inspection prior to test. No service induced flaws were detected.

TEST FIXTURE AND SPECIMEN CONFIGURATION

The test assembly consisted of the drag link component and a specially fabricated steel dummy hook shank joined by a solid pin. Testing of assemblies joined by production pins and nuts were not conducted since a test program being performed concurrently had shown the production pins as not critical under normal operating arrestment loading.

Specially machined steel pins were used to attach the drag link to a

Table I. Technical Approach

PHASE	PURPOSE	TEST DESCRIPTION
I	• Determine Critical Locations • Determine Fatigue Life	• No Intentional Flaws • Lab Air Environment • Cycle to Failure Under Normal Operating Load
II	• Determine Critical Crack Lengths • Determine Remaining Service Life as a Function of Initial Crack Size Under Normal Operating Load	• Preflawed at Critical Locations • Lab Air Environment and 3.5% Salt Solution Environment • Cycle to Failure Under Normal Operating Load
III	• Determine Residual Strength as a Function of Crack Size and Obtain Fracture Toughness Values	• Preflawed at Critical Locations • Lab Air Environmnnt and 3.5% Salt Solution Environment • Cycle to Various Crack Sizes Under Normal Operating Load • Static Test to Failure
IV	• Determine the Effect of Proof Loads to the Growth Rate Determined in Phase II	• Preflawed at Critical Locations • 3.5% Salt Solution Environment • Cycle to Failure Under Normal Operating Loads with Proof Loads Every "x" Cycles
V	• Verification Test Using Proof Load Criteria	• Preflawed in Critical Locations • 3.5% Salt Solution Environment • Cycle to Failure Under Normal Operating Load with Proof Loads Every "x" Cycles

vertical test frame. Axial load was applied to the assembly by a 175 kip (0.778 MN) servo jack. A 30 kip (0.133 MN) servo jack was used to apply side load (both positive and negative) at the drag link lug and a 30 kip (0.133 MN) servo jack was used to apply the dashpot load. The assembly was constrained and loads applied such that realistic arrestment loads could be introduced into the drag link.

APPLIED LOADS

There are two separate and distinct loading conditions in an arrestment sequence, as shown in Figure 4. At the beginning of an arrestment the hook point bounces from the deck and initial contact is made with the cable. The hook bounce is reacted by the dashpot through the dashpot arm and introduces bending into the hook shank and drag link. Initial contact with the cable introduces a small axial load into the components. As the dashpot load dampens out the axial load increases to a peak which describes the axial loading condition. Due to off angle and off centered arrestments this load is seen by the drag link as both an axial component and a side component. A statistical analysis was performed on previous data and loads were introduced into the drag link by the test fixture such that 90% of the time average loads were applied and 10% of the time average plus two standard devition loads were applied. Data was not available to determine the small axial load associated with the dashpot loading so the design limit load was applied 100% of the time.

TESTING ENVIRONMENT

Some specimens were tested in a lab air environment and some in a 3.5% salt solution environment. This salt environment was obtained by wrapping portions of the drag link in saturated gauze. The solution was applied at intervals to maintain saturation. Crack growth in locations other than that wrapped in gauze were considered as a lab air crack environment.

INSPECTION DURING TESTING

In order to monitor crack growth, the tests were stopped at intervals and the salt water gauze, if any, removed to expose the critical area. The cracks were visually measured using a mounted 20 power tele-microscope and a portable light source. In order to make the cracks easier to see, local areas were cleaned and polished prior to test, and a small axial load applied during inspection.

PREFLAWING THE SPECIMEN

Provisions were made to preflaw specimens so that cracks would initiate at previously observed critical locations with a minimum amount of cyclic test time. These preflaws were mechanically induced using a diamond wire to cut a 45^{0} corner notch measuring approximately 0.030 inch (0.762 mm) x 0.030 inch (0.762 mm).

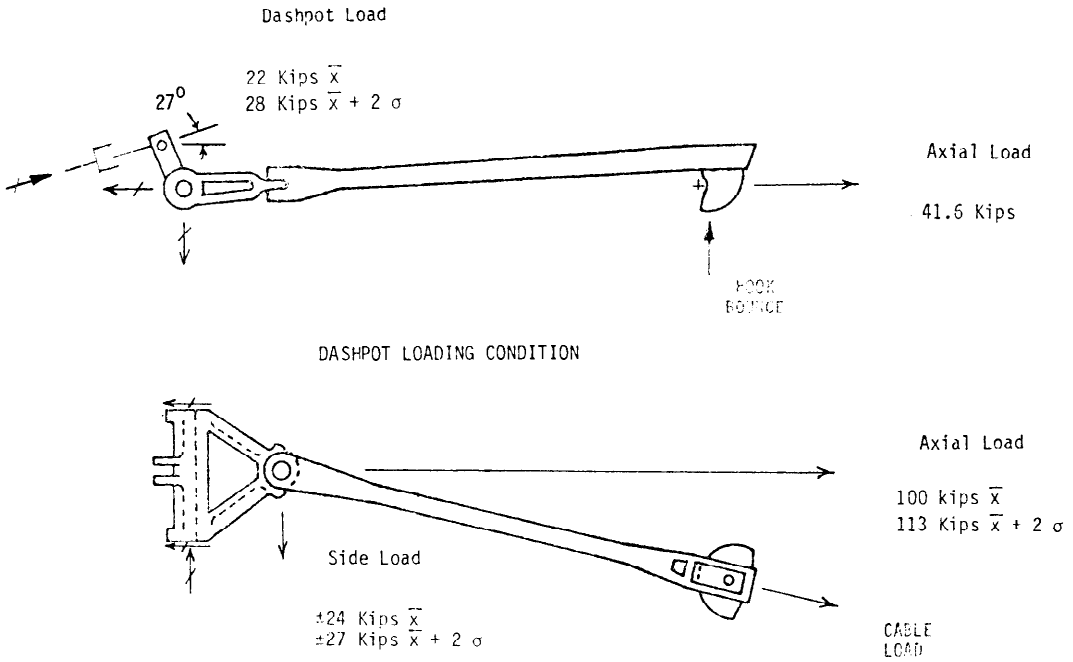

NOTE: 1 kip = 0.04448 MN

Figure 4. Arrestment Sequence Loading

ANALYSIS OF TEST DATA

PHASE I - CRITICAL LOCATIONS AND FATIGUE LIVES

The primary critical location where cracks initiate, propagate and result in drag link failure is the inside corner of either the upper or lower flange of the C-channel where transition is made into the lug, as shown in Figure 5. This is denoted as a C-Section failure.

For those specimens cycled to failure under normal operating load, the fatigue lives can be easily determined. For the specimens in which the cycling was stopped and the part statically failed for residual strength data, the fatigue lives can be predicted with the use of fracture mechanics theory. These lives are shown in Table II. The average life of the drag link in a lab air environment is 10,306 arrestments and in a salt water environment the life is reduced to 6,288 arrestments; a reduction of 39%.

PHASE II - CRACK GROWTH BEHAVIOR UNDER NORMAL OPERATING LOAD

Post test fracture examination was conducted to determine crack growth behavior (see Figure 6). Examination shows that after initiation the flaw grows in plane strain as a quarter-circular to quarter-elliptical flaw shape. As this corner crack approaches the flange thickness of approximately 0.27 inches (6.858 mm), a shear lip develops and the flaw, now growing in a mixed mode, transitions from a corner crack into a through crack. After transition, the crack grows in plane stress until it reaches a critical flaw size of approximately 0.95 inches (24.130 mm). Crack growth data is plotted in Figure 7 and curves were best fit through the points. From this curve the remaining life for any initial flaw size can be determined.

PHASE III - RESIDUAL STRENGTH

The cycling of several drag links was stopped at various flaw sizes and statically loaded to failure to determine the relationship between residual strength and flaw size (see Figure 8). Cracks propagating in a mixed mode exhibit a smaller toughness than those propagating in plane stress. It should be noted that for a given flaw size it will require a larger load to "proof out" a part if the flaw has transitioned into plane stress. When developing a proof load criteria it must be conservatively assumed this transition has taken place.

PHASE IV - EFFECT OF PROOF LOADS

Large intermittent proof loads can blunt the crack tip and retard crack growth. However, growth during the application of the proof load can negate this effect and even accelerate the growth rate. To determine this effect on drag link cracks approximately 200 kips (0.890 MN) of axial load was applied to drag links at intervals of 200 arrestments. Crack growth data is shown in Figure 9. Although these points fall within a scatter

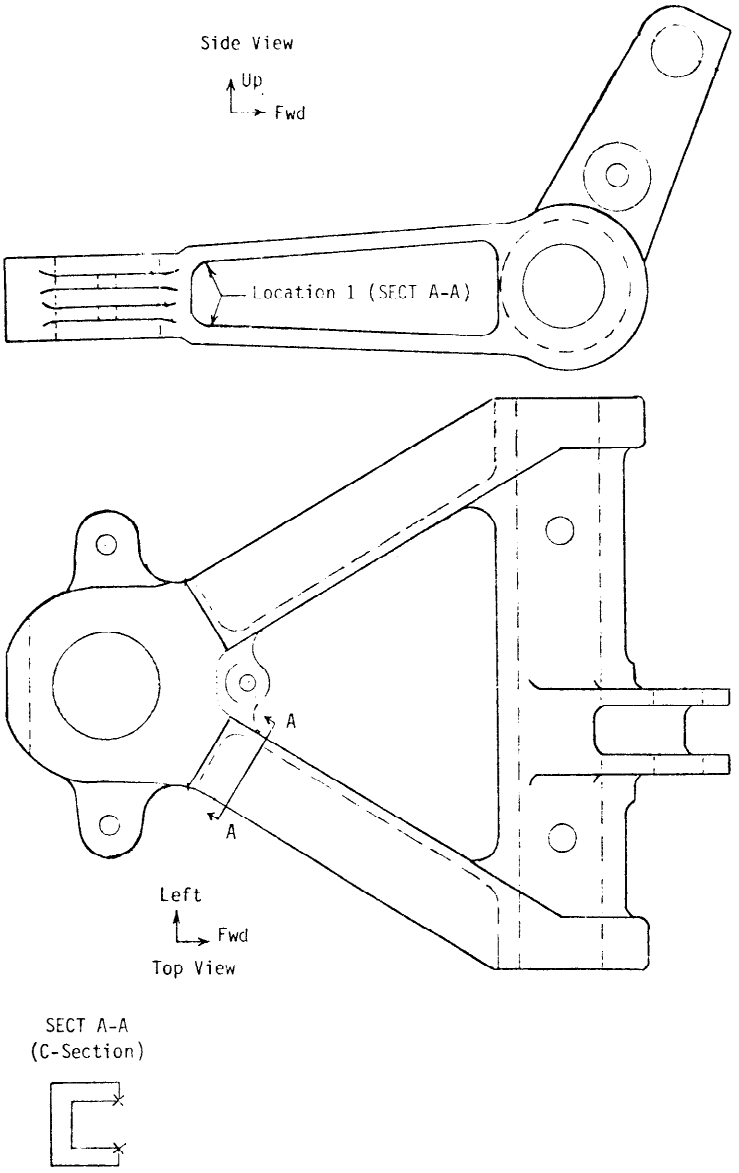

Figure 5. Critical Location

Table II. Fatigue Lives

	C-SECTION			
	3.5% SALT SOL.		LAB AIR	
	TEST NO.	LIFE (ARREST)	TEST NO.	LIFE (ARREST)
SPECIMEN TAKEN TO FAILURE	7	3490	2	7730
	8	6909	5	12538
	9	2802	6	10649
	12	8904		
	15	9030		
PREDICTED FROM RESIDUAL STRENGTH SPECIMEN	10	5920		
	11	9462		
	14	3786		
AVERAGE		6288		10306
STAND. DEV.		2704		2422

REDUCTION IN C-SECT. AVG. LIFE DUE TO 3.5% SALT SOL. = 39%

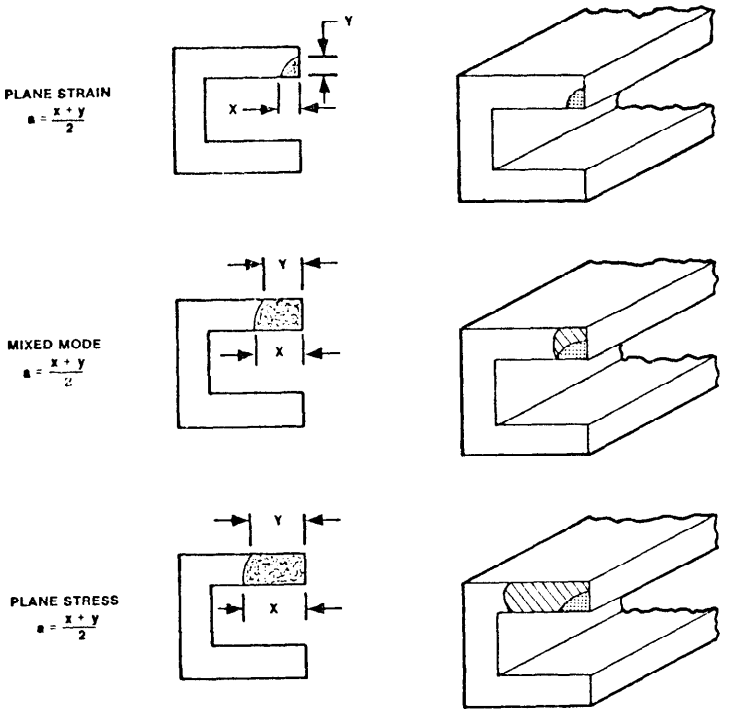

Figure 6. C-Section Crack Propagation

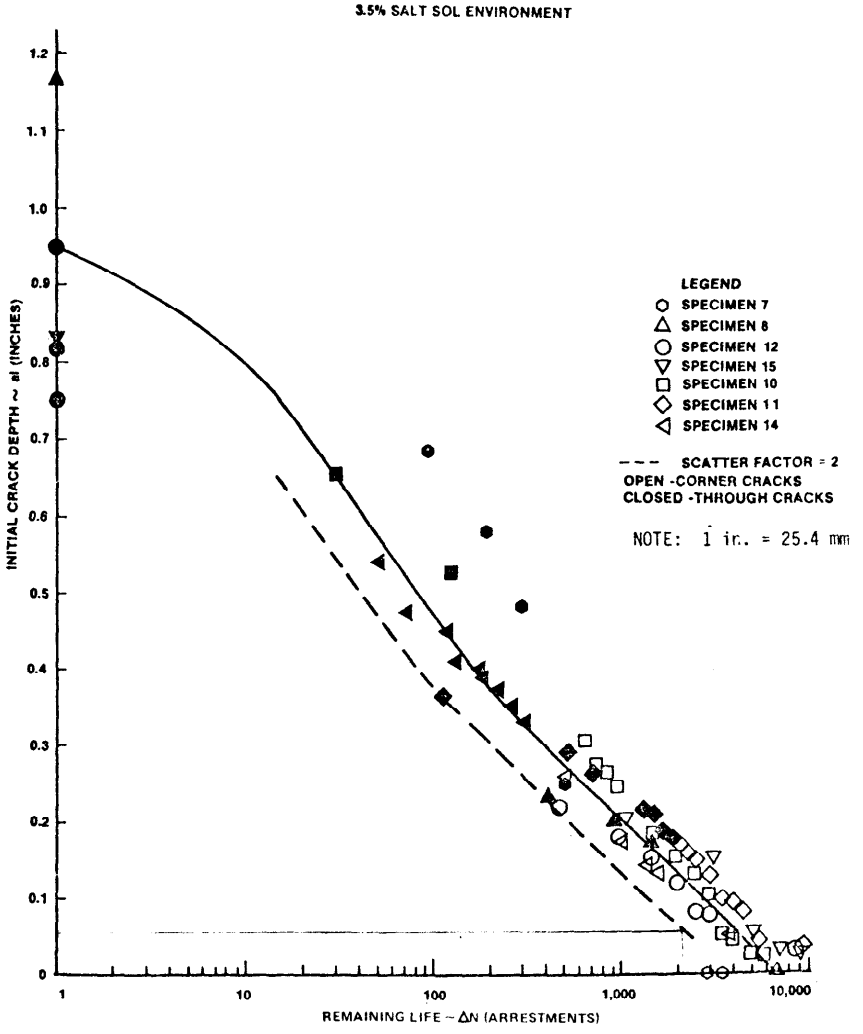

Figure 7. Remaining Life for Drag Links With C-Section Cracks

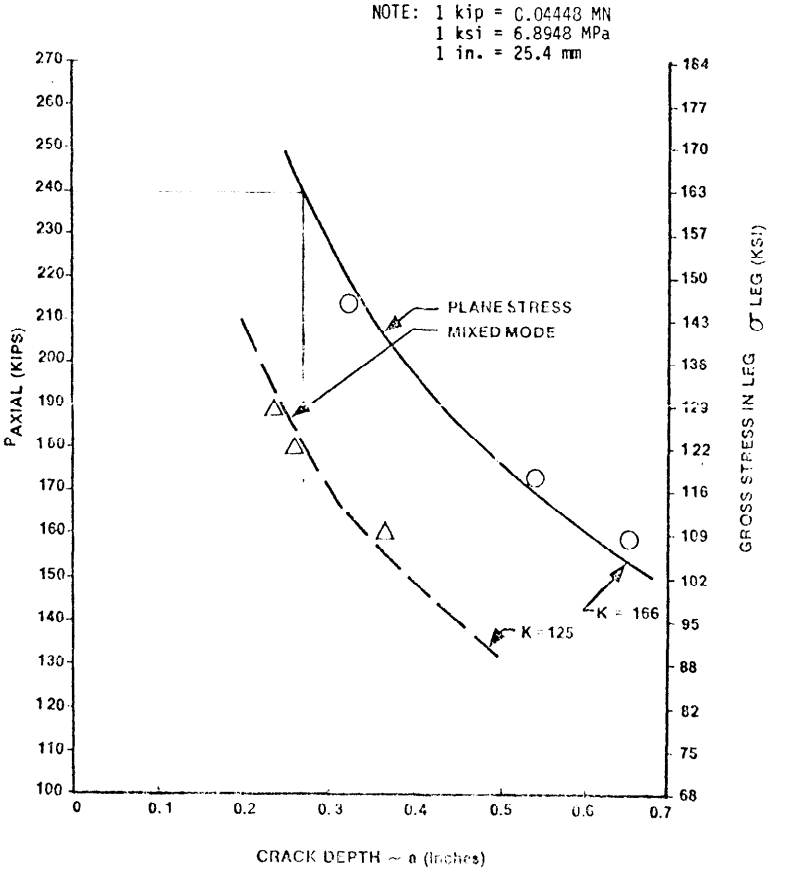

Figure 8. Residual Strength

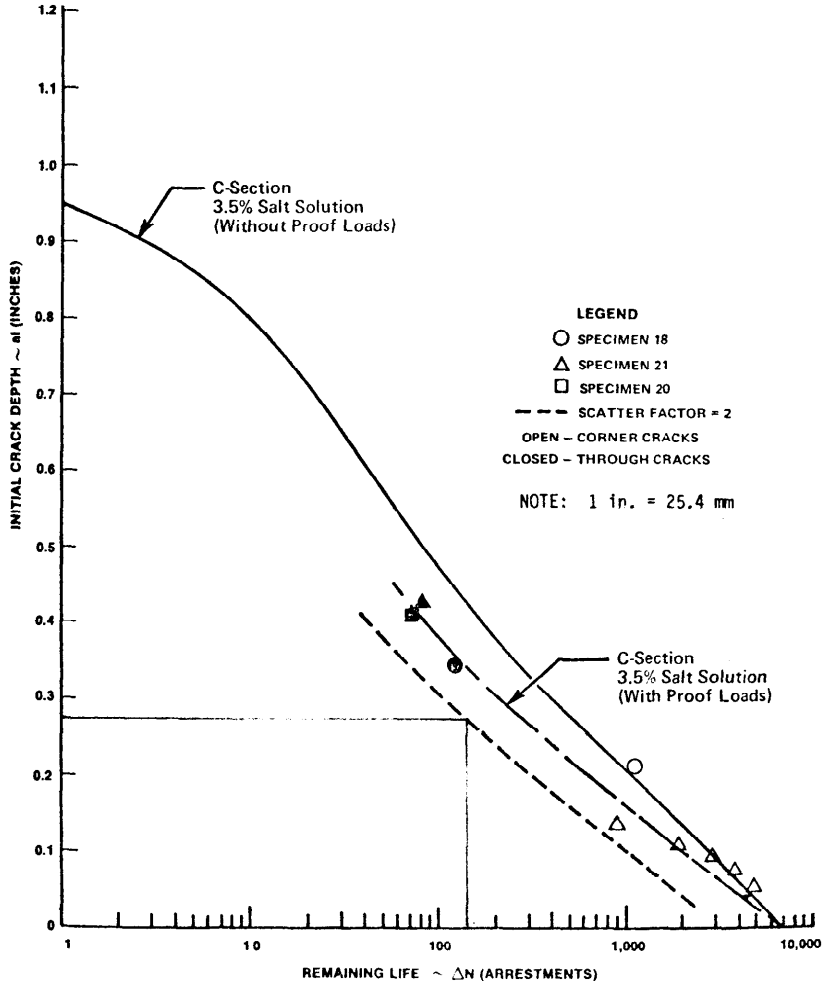

Figure 9. Effect of Proof Loads on Crack Growth

factor of 2 of normal crack growth, conservatively this must be considered as an increased growth rate.

PHASE V - VERIFICATION OF PROOF LOAD CRITERIA

An axial load of 240 kips (1.068 MN) is the largest load that can be applied to the drag link before local yielding occurs. From the residual strength curves in Figure 8 (conservatively assuming a plane stress mode of crack propagation) it is determined that a 240 kip (1.068 MN) applied load will "proof out" cracks that are 0.27 inches (6.858 mm) or greater. The crack growth curves in Figure 9, which contain the effects of proof loads, illustrate that a drag link with a C-Section crack of this size still has an average remaining life of 280 arrestments. Applying a factor of 2 to cover scatter, the proof load should be applied every 140 arrestments. The proof load criteria, therefore, is to apply a 240 kip (1.068 MN) axial load every 140 arrestments. To verify this two drag links were tested and both failed during the application of the proof load. This provides only a small increase over the present inspection interval of 100 arrestments. Criteria comparable to that of the hook shank [175 kips (0.778 MN) applied at a 550 arrestment interval] could not be obtained.

NONDESTRUCTIVE INSPECTION CRITERIA

Nondestructive inspection techniques such as fluorescent penetrant or magnetic particle inspections are viable methods of detecting cracks. This, coupled with exact locations of inspection, can provide a high probability of flaw detection. Assuming that a magnetic particle inspection can confidently detect a flaw size of 0.05 inches (1.270 mm)[4] and using the crack growth curve of Figure 7, an inspection interval of greater than 2,000 arrestments is obtained. This includes a scatter factor of 2. A magnetic particle inspection performed at 550 arrestment intervals (same as that recommended for the hook shank) would make the probability of missing a flaw virtually zero.

CONCLUSIONS

There are two viable options that will insure the structural integrity of the drag link for an additional number of carrier arrestments. These are:

(1) A proof load of 240 kips (1.068 MN) axial load applied at an interval of 140 arrestments, and

(2) A magnetic particle inspection of critical locations at 550 arrestment intervals; at any sign of cracking the part should be rejected.

Vought recommends option 2 as the most economic and efficient method in that it provides a high probability of detecting flaws with confidence and the inspection interval coincides with the recommended proof test

interval for the hook shank. Since the method of inspection is consistent with current requirements, no fleet procedural changes should be necessary. This, coupled with the fact that retired drag links passing this inspection may be returned to service, can create a significant cost savings for the Navy.

ACKNOWLEDGEMENT

This investigation was conducted at Vought Corporation, Dallas, Texas by the Structural Life Assurance Group of the Structures Development Section for the Naval Air Systems Command, Washington, D. C., under contract number N00019-80-C-0313.

REFERENCES

1. Merkord, D. L. and Dumesnil, C. E., "Fatigue and Fracture Evaluation of the A-7E Arresting Gear Drag Link," Vought Report No. 2-51220/1R-52874, September 1981.

2. Ellis, J. R., "Fatigue and Fracture Evaluation of A-7E Arresting Gear Hook Shank," Vought Report No. 2-30400/9R-52133, May 1979.

3. Tiffany, C. F. and Masters, J. N., "Applied Fracture Mechanics," Fracture Toughness Testing and Its Applications, ASTM STP 381, American Society for Testing and Materials, 1965, 249.

4. Moore, J. F., Tsang, S., Thompson, D. O. and Hoenig, S. A. "Nondestructive Detection of Structural Damage Uniquely Associated With Fatigue," Rockwell International Corporation, AFML-TR-74-131, July 1974.

A NONLINEAR FRACTURE MECHANICS PREDICTIVE PROCEDURE FOR THE SHORT CRACK EFFECT IN FATIGUE

J. Ahmad, A. T. Hopper, M. F. Kanninen
B. N. Leis, and V. Papaspyropoulos

BATTELLE
Columbus Laboratories
505 King Avenue
Columbus, Ohio 43201

ABSTRACT

When the predictive techniques of linear elastic fracture mechanics (LEFM) are applied to physically short fatigue cracks, it is often found that the actual crack growth rate is considerably underestimated. This means that damage tolerance and other fracture control methods that rely on accurate crack growth rate predictions could be quite nonconservative. Consequently, considerable attention has been devoted to identifying the causes of the accelerated growth rates and on ways of improving upon the currently available predictions. Virtually all of these have been based exclusively upon LEFM considerations. In contrast, this paper addresses the short crack problem from the point of view that an elastic-plastic fracture mechanics parameter may offer the basis for a resolution of the dilema. The specific approach that is taken is one that focusses on the crack-tip crack-opening displacement (CTOD) as a characterizing parameter. The use of CTOD is at least as general as current LEFM procedures. Of equal importance, the CTOD may possibly be valid where LEFM is not. An illustrative example is used to show the nonlinear character of this approach.

An experiment was undertaken to generate short crack growth rate data that could be directly compared to predictions. An uncracked specimen with a circular hole was cycled under constant amplitude load control conditions. Two cracks were observed to initiate and grow. The crack region was photographed periodically and the film record used to measure the crack growth data. The first crack to initiate showed the short crack effect. The second crack apepared after the first crack was nearly 0.2 inch long and did not show the short crack growth rate effect. Both cracks evolved from corner cracks. This experiment serves as a vehicle for a quantitative comparison of the CTOD based approach with the LEFM based approach. The comparison shows that the nonconservations of the LEFM predictions can be overcome with the CTOD predictions.

INTRODUCTION

When fatigue crack growth rate data for short cracks is plotted on the usual linear elastic fracture mechanics (LEFM) coordinates of crack growth rate and stress intensity factor range, two anomalies have often been observed. First, an unusually large number of data points do not lie near the LEFM crack growth rate trend line. Second, this nonconsolidation of data is

not random. When it occurs, it nearly always shows that the growth rate, early in the propagating life of the crack, is higher than would be expected from the LEFM predictions. These two anomalies are referred to as the short crack effect. Because LEFM models tend to underestimate the growth rate, of small cracks, the short crack effect has a direct impact on damage tolerance and fracture control methods that rely on conservative crack growth rate predictions.

A basic premise of LEFM is that all inelastic deformations are contained in a region immediately ahead of the crack tip that has dimensions much smaller than the length of the crack. Depending upon the severity with which this basic premise is violated, LEFM will provide an increasingly inaccurate description of the crack tip environment. The purpose of the research reported in this paper is to test the importance of the basic LEFM premise by considering a model which begins to account for the plastic zone ahead of the crack, albeit in a linear sense, to see whether or not it offers an improvement in predictive capability.

BACKGROUND

Several researchers have recognized the inability of LEFM to cope with the short crack problem. However, little progress has been made in developing an improved predictive model. El Haddad et. al., [1], for example, have suggested the addition of a small pseudo crack length ℓ_o to the actual crack length in evaluating the stress intensity factors. For a given set of experimental data one may find such a constant ℓ_o which will provide crack growth rates consistent with those experiments. However, it is difficult to accept the notion that ℓ_o may serve as a generally applicable material constant to account for the short crack effect.

It is argued that ℓ_o can be related to the threshold stress intensity and the fatigue limit. If this interpretation is correct, the physical meaning of ℓ_o must be that of an inherent defect length in the material which dominates the specimen response when the artificial crack length is of the order of ℓ_o. But, too much is expected of such defects for them to be both non-interacting and always located so as to increase the artificial crack length. While it would be permissible to limit the smallest crack length to ℓ_o, it cannot logically be incorporated as an additive term.

On a practical basis, the approach of El Haddad et. al., similarly appears to be wanting. Figure 1 (reproduced from Reference 2) shows the failure of their approach to consolidate the short crack data for mild steel developed by Leis and Forte [3]. This version of the El Haddad et. al., approach is based upon the use of the J-integral, as originally suggested by Dowling [4], in an effort to formulate an elastic-plastic fracture mechanics (EPFM) formalism. It can be clearly seen in Figure 1 that the pseudo crack length concept, even when enhanced by the use of J, is not in correspondence to these data. Similar negative results for other J-based approaches have been obtained by Leis [2].

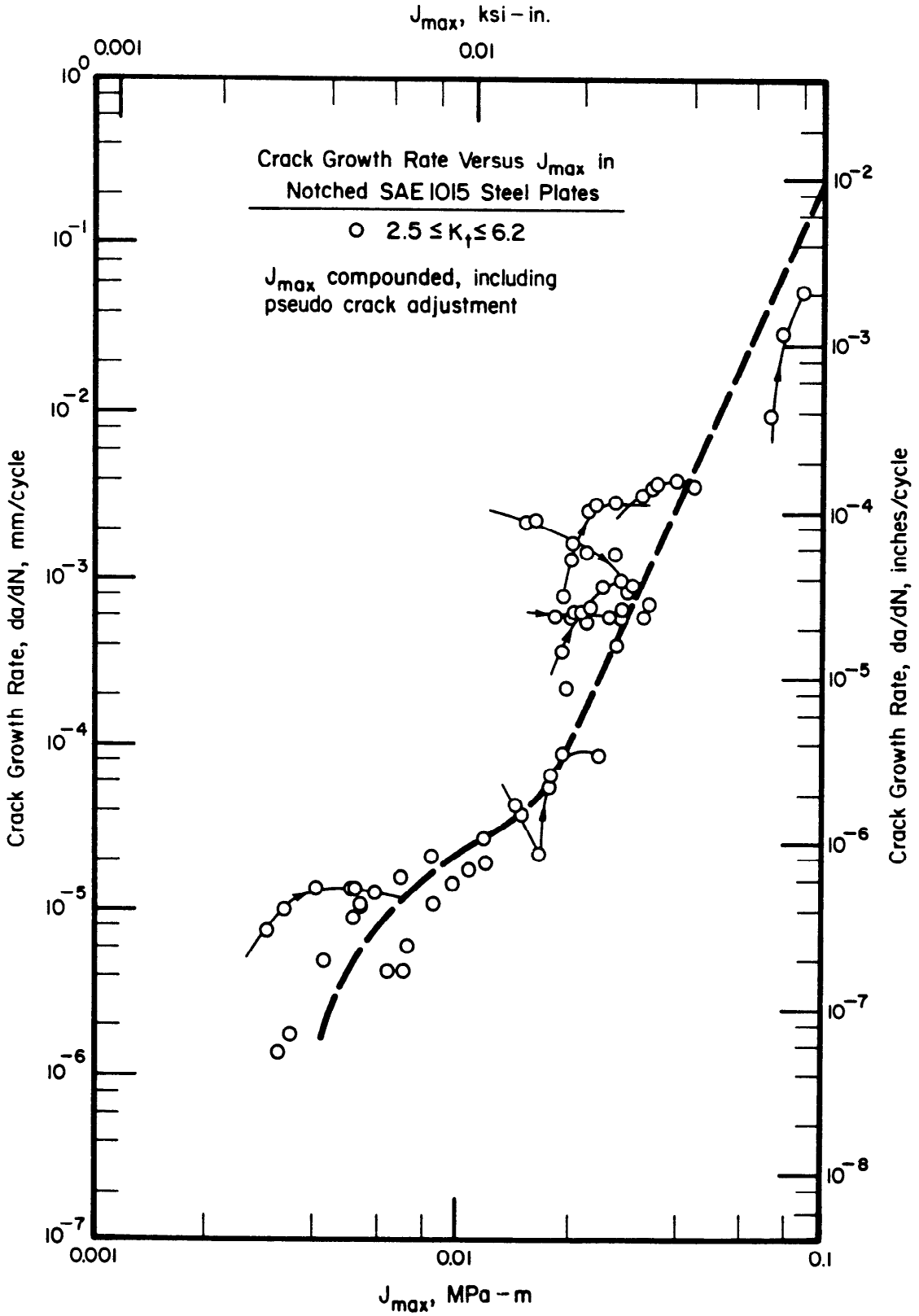

FIGURE 1. FAILURE TO CONSOLIDATE SHORT CRACK DATA USING A J-BASED APPROACH AND THE PSEUDO CRACK CONCEPT OF EL HADDAD ET AL

While the J-integral (unlike ℓ_o) has a rigorous mathematical definition as well a definite physical meaning, it also must satisfy certain restrictive conditions. Since the J-integral is based on the deformation theory of plasticity, it is inherently unsuitable for FCG studies where both cyclic loading and crack growth result in elastic unloading of the material.

A parameter which we feel provides a better description of the crack tip environment is the crack tip crack opening displacement (CTOD). Recent research on crack growth in ductile materials by Kanninen [5], and an extensive critical review of existing EPFM concepts by Kanninen, Popelar, and Broek [6] clearly suggest that stable crack propagation tends to occur with a constant value of CTOD. Therefore, it is worthwhile exploring if subcritical crack growth could also be related to CTOD, an idea that may not only contain an explanation for the short crack effect but could also influence FCG analyses in general.

The idea of using FCG models based on CTOD is not new. As discussed by Broek [7], several such approaches exist in the literature. However, in a recent paper Kanninen, Ahmad, and Leis [8] showed that by using a nonlinear relation between CTOD and crack advance (Δa) instead of the linear relation most often employed by others, the short crack effect can be qualitatively explained. Using heuristic calculations, they demonstrated that for zero-R values and ignoring any closure effects, a nonlinear CTOD based FCG model predicts much higher crack growth rates for short cracks than for longer cracks at the same applied maximum stress intensity factor K_{max}. The key result of Reference 8 is reproduced in Figure 2.

Unfortunately, due to the lack of detailed information necessary for analyzing the short crack experimental results available in the literature, a direct quantitative evaluation of the approach of Reference 8 could not be performed. The present paper constitutes an attempt to quantitatively judge the nonlinear CTOD based FCG model by directly comparing its predictions with experimental results obtained during the course of this research. The details are as follows.

EXPERIMENTAL PROCEDURES

Evaluation of the utility of CTOD in characterizing the crack driving force in fatigue can be accomplished by direct simultaneous measurement of both crack advance, Δa, and CTOD. Sufficient resolution for these measurements requires the use of scanning electron microscopy (SEM) in conjunction with a dynamic loading stage which permits direct observation of both Δa and CTOD. The results of such experiments show that Δa and CTOD are uniquely related, provided that crack closure is accounted for [9,10]. The relationship between Δa and CTOD can also be examined indirectly, in a less fundamental manner, by exploring the correlation between fatigue crack growth rate and an analytical estimate of CTOD. To this end the fatigue crack growth rate has been measured in a thin sheet specimen containing a centrally located circular hole.

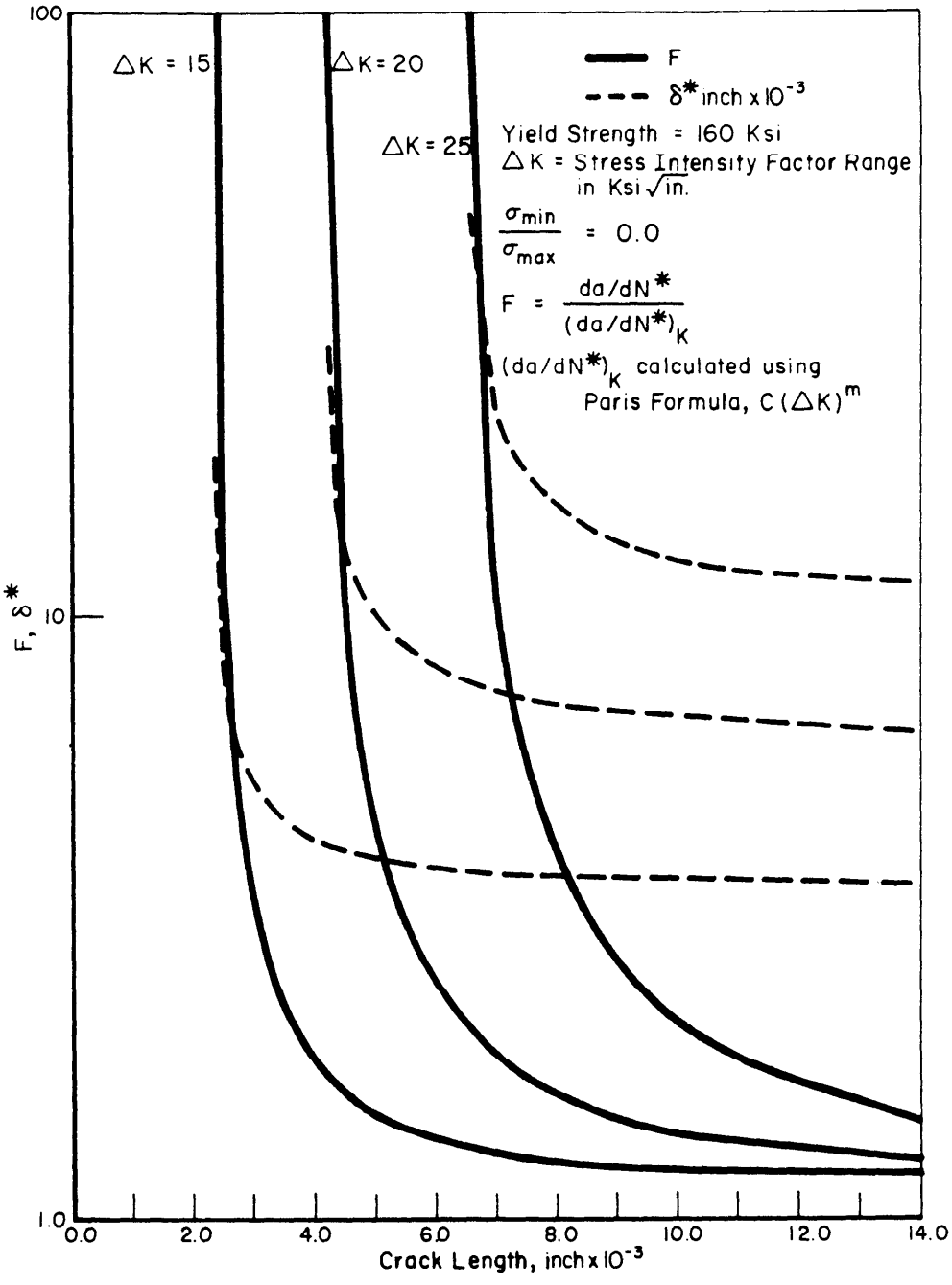

FIGURE 2. USE OF THE CTOD CRITERION FOR SHORT-CRACK BEHAVIOR

The geometry chosen was a plate 7.62 cm (3 inch) wide by 15.25 cm (6 inch) long containing a hole 1.25 cm (0.5 inch) in diameter. The sheet thickness was 0.23 cm (0.09 inch). A three dimensional elasticity solution [11] and elastic-plastic finite element analyses [12] indicated that the notch root is essentially subjected to plane stress conditions. Analyses indicated a value of $K_t = 2.50$ while experiments developed a value of $K_t = 2.56$.

The material investigated was part of a pedigreed heat of 2024 series aluminum alloy. Using current nomenclature the designation would be 2024-T351. Further details can be found in References 12 and 13.

Crack length was periodically measured using high resolution, long focal length, 35 mm cameras designed to track the growth of short cracks [14,15]. The cracking vicinity was photographed at every tenth load peak to capture the initiation and short crack growth process. The crack length was determined by tracking easily observed macrocracks back in time to their point of origin. A high resolution of the crack tip was achieved by a two step magnification process. The dioptric lens and optics provide 5 times magnification at the film plane so that fine grained 35 mm film permits interrogation of a large area of material. Interpretation of the film is made via an enlarger, which provides for up to 20 times further magnification without the expense of printing the film. For the present study a total of 40X magnification was found to be adequate.

The experiment was performed in axial load control. Data were developed from constant amplitude zero-tension cycling at a gross section stress of 186.6 MPa (27 ksi). This stress level was chosen to develop significant, but still confined, notch root plasticity. Finite element analyses [12] indicates that a notch plastic field develops to a distance equal to 0.17 cm (0.068 inch) along the transverse net section, beyond the notch root. Data developed in this study represent two microcracks. These results are similar to that for 27 microcracks developed for this same combination of material and geometry, results for which have been reported in an earlier study [16].

EXPERIMENTAL RESULTS

The experiment generated an increment in crack advance a over the time interval between photographs which involves an integral number of cycles ΔN. Results of this type can be plotted on coordinates of crack length and cycles as shown in Figure 3. Observe that one crack initiates at one notch root well in advance of the second crack at the remaining notch root. The desire here is to assess the viability of CTOD in terms of short cracks, and the application of ASTM Standard E647 to the data analysis would tend to smooth any anomalous data trends previously associated with short cracks. Further, the minimum crack advance of 2.5 mm between readings would limit the amount of data available. For this reason, the ASTM minimum Δa is not enforced. The data reported represent results developed from readings spaced by cycle intervals, not crack advance. Instead of a seven point incremental polynomial, crack growth rate has been obtained using a simple slope technique and a 3 point divided difference scheme.

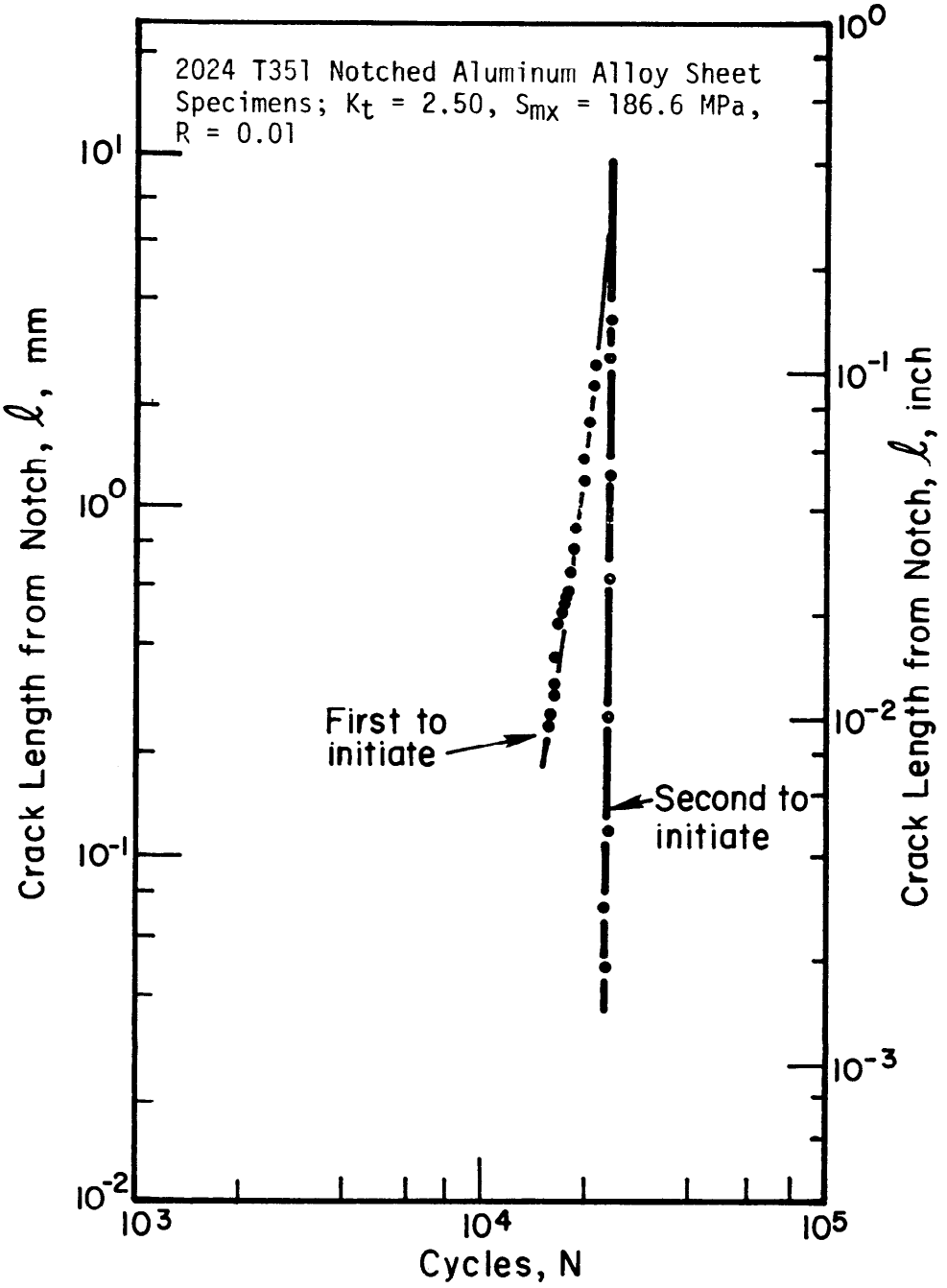

FIGURE 3. CRACK LENGTH AS A FUNCTION OF CYCLES

Figure 4 presents the simple slope crack growth rate as a function of crack length. Note from the figure that two separate trends are presented. One is labelled "first to initiate", the other "second to initiate". Detailed SEM studies indicated that both cracks initiated and grew essentially as corner cracks before a plane fronted crack developed. After plane fronted growth developed, growth occurred at more or less comparable rates along a skewed plane front. The transition from corner to plane fronted growth was completed after about 0.1 cm (0.04 inch) for the first to initiate crack and after about 0.2 cm (0.08 inch) for the second to initiate crack. For the first to initiate crack, cracking on the face where Δa was measured led cracking on the rear face by about 0.05 cm (0.02 inch) after transition. In contrast, the crack on the face where Δa was measured for the second to initiate crack trailed that on the rear face by about 0.1 cm (0.04 inch) after transition. Microscopy indicated that crack growth rates from striation counts are comparable to those based on measurements of Δa over ΔN.

Figure 4 indicates that growth rate for the first to initiate crack initially increases, then decreases, then increases again. The initial data trend appears to be well defined. However, once the data trend to increasing growth rate with crack length is established there is extensive scatter. Note that the corner cracking behavior for the first to initiate crack was tracked for this crack. In contrast, even though the observed crack length for the second to initiate crack is plotted in terms of a physically small crack, the growth rate behavior is associated with a well developed corner crack about 0.18 cm (0.072 inch) long. Not surprisingly, the initial growth rate for the second to initiate crack is similar to that for the first to initiate crack once it is about 0.2 cm (0.08 inch) long.

Figure 5 presents the crack growth rate behavior on coordinates of growth rate and maximum stress intensity factor, K. Because K increases monotonically with crack length, the data of Figure 4 for the first to initiate crack result in an increasing, then decreasing, then increasing, trend. This indicates that K does not consolidate the short crack behavior. However, as the crack becomes longer, the data blend into other "long crack" data for this specific material. Data for the second to initiate crack are not shown in Figure 5 because, as noted in the discussion of Figure 4, the measured crack lengths are not a true indication of the actual corner crack length. The K solution used in developing Figure 5 assumes plane fronted cracks whereas the data are for a corner orientation.

ANALYSIS PROCEDURE

To explore the use of CTOD as a governing parameter, consider that a valid long crack FCG relation is of the commonly used form

$$\frac{da}{dN} = CK^m \qquad (1$$

where $K = K_{max}$, and $K_{min} = 0$.

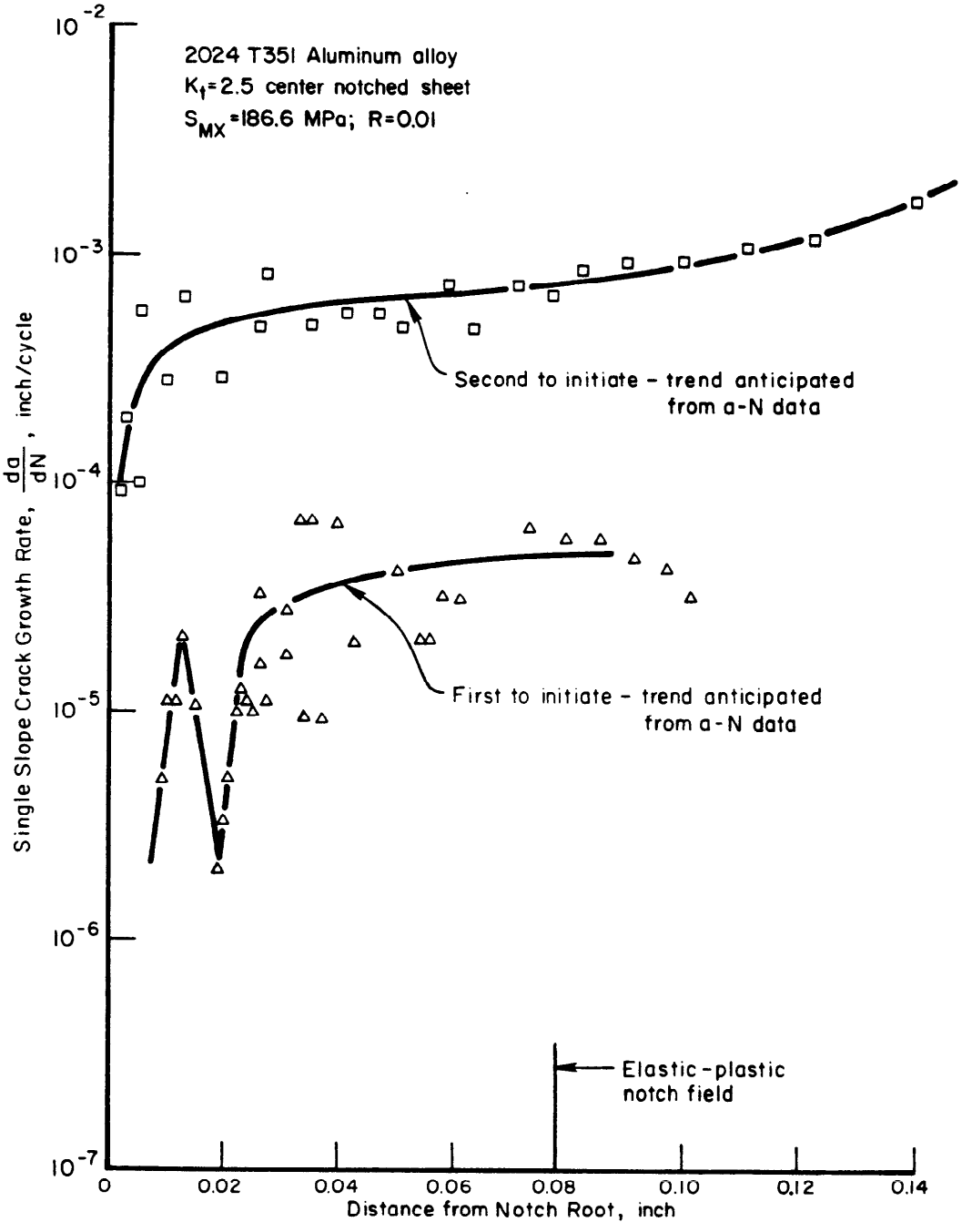

FIGURE 4. FATIGUE CRACK GROWTH RATE AS A FUNCTION OF CRACK LENGTH

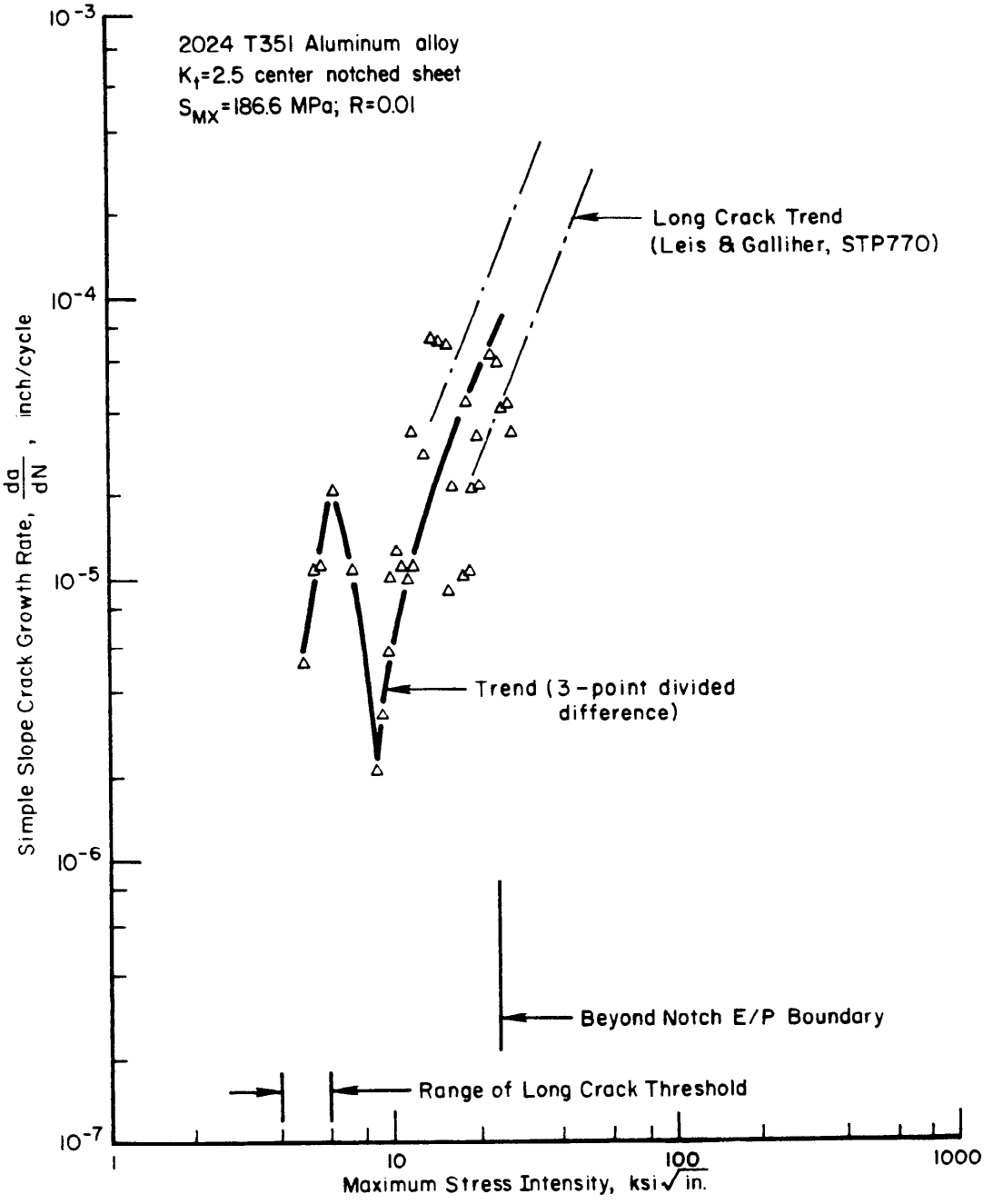

FIGURE 5. FATIGUE CRACK GROWTH RATE AS A FUNCTION OF MAXIMUM STRESS INTENSITY FACTOR

Note that any other valid form of FCG model containing K or J would serve just as well for the purpose of the development that follows. This is because under small scale yielding conditions both K and J are related to CTOD. These relations are [17,18]

$$\delta = \alpha \frac{K^2}{E\sigma_o} \tag{2}$$

$$\delta = d_n \frac{J}{\sigma_o} \tag{3}$$

where δ = CTOD
E = Elastic modulus
σ_o = Yield strength
α = A numerical constant of order unity
d_n = A function of strain hardening exponent and stress state.

Equation (3) will not be used in the following but is shown to suggest that the procedure could equally well be based upon J. Equations (1) and (2) can be combined to obtain

$$\frac{da}{dN} = C'\delta^{m/2} \tag{4}$$

where $C' = C\left(\frac{E\sigma_o}{\alpha}\right)^{m/2}$

It can be hypothesized that equation (4) derived on the basis of the LEFM relationship of equation (2), is valid beyond the small scale yielding regime. This assumption has a basis in the work of Kanninen et al. [5] in which it was shown (although under a different cracking mechanism) that even when accepted elastic plastic fracture mechanics parameters--e.g., the J-integral--become invalid, CTOD remained an acceptable crack growth parameter.

The inevitable question then is how does one use a crack growth model such as equation (4) since CTOD cannot be really measured in the laboratory with sufficient precision. This argument has persistently been used against all CTOD based models. The irony in such an argument lies in the fact that K, the commonly used parameter in FCG studies, cannot be measured either. It can only be inferred using experimental measurements via some analysis. CTOD can be found in a similar manner except that the analysis in this case is more involved and generally applicable handbook solutions are not as readily available.

A simple way of obtaining an estimate of CTOD is via a Dugdale model [19] which is a special case of a more general pseudoplastic modelling approach discussed by Atkinson and Kanninen [17]. For geometries other than simple

center-cracked panels or edge-cracked panels Dugdale solutions are not readily available in the literature. However, any linear elastic solution procedure, numerical or exact, which can be applied to a given geometry to obtain stress intensity factors with constant traction applied over any given portion of the crack surface can also be used to perform the Dugdale analysis. This, of course, is because the Dugdale model is obtained by simple superposition of such linear elastic solutions. Some of the techniques commonly used are the weight function approach used by Petroski [20] and Chell [21], the boundary point least-square collocation procedure used by Hulbert et al. [22], and the linear elastic finite element method used by Hayes and Williams [23] and by Fenner [24].

For the specimen geometry chosen for this work, compliance functions necessary for performing a weight function analysis were not available. Therefore, this method could not be used. The next choice was the boundary point least square collocation method of Hulbert et al. [22] which is much less expensive to run on the computer than the finite element method. While the method provided accurate solutions for relatively long crack lengths, for small crack lengths the accuracy of solutions deteriorated considerably. Therefore, all analyses were performed using a finite element method employing planar eight noded isoparametric elements in conjunction with quarter point elements [25] to model the crack tip stress singularity.

The superposition principle used in the Dugdale analysis is illustrated in Figure 6. The analysis first involves determination of K for problem 1. Then, a series of solutions for Problem 2 is obtained with varying distance X over which traction equal to the yield strength of the material is applied. When the length X becomes such that the K value of problem 2 is equal to the K of problem 1, superposition of the two problems provides the zero K required for the Dugdale model. The "singularity cancelling" value of X is the Dugdale plastic zone ℓ for a physical crack length $a = (c - \ell)$. The CTOD is found by superimposing the vertical displacements of the two problems at $X = \ell$ as shown in Figure 6.

The above procedure is repeated for different values of c so that a variation of CTOD vs. a required for using the FCG model of equation (4) can be obtained. The entire procedure may involve hundreds of individual finite element solutions. However, a finite element computer program developed specifically for Dugdale analysis and which follows the flow chart shown in Figure 7 can perform the required computations quite economically. The stiffness matrix of the structure in this scheme needs to be reformulated and inverted only as many times as the crack length dimension c is changed. The set of force vectors F_i represent nodal forces consistent with the crack face traction.

ANALYSIS RESULTS

The specimen geometry used in the experiments is symmetric with respect to both the horizontal and the vertical axes passing through the center of the hole. If the cracks also grew symmetrically on both sides of the hole, the

COLINEAR STRIP YIELD MODELING

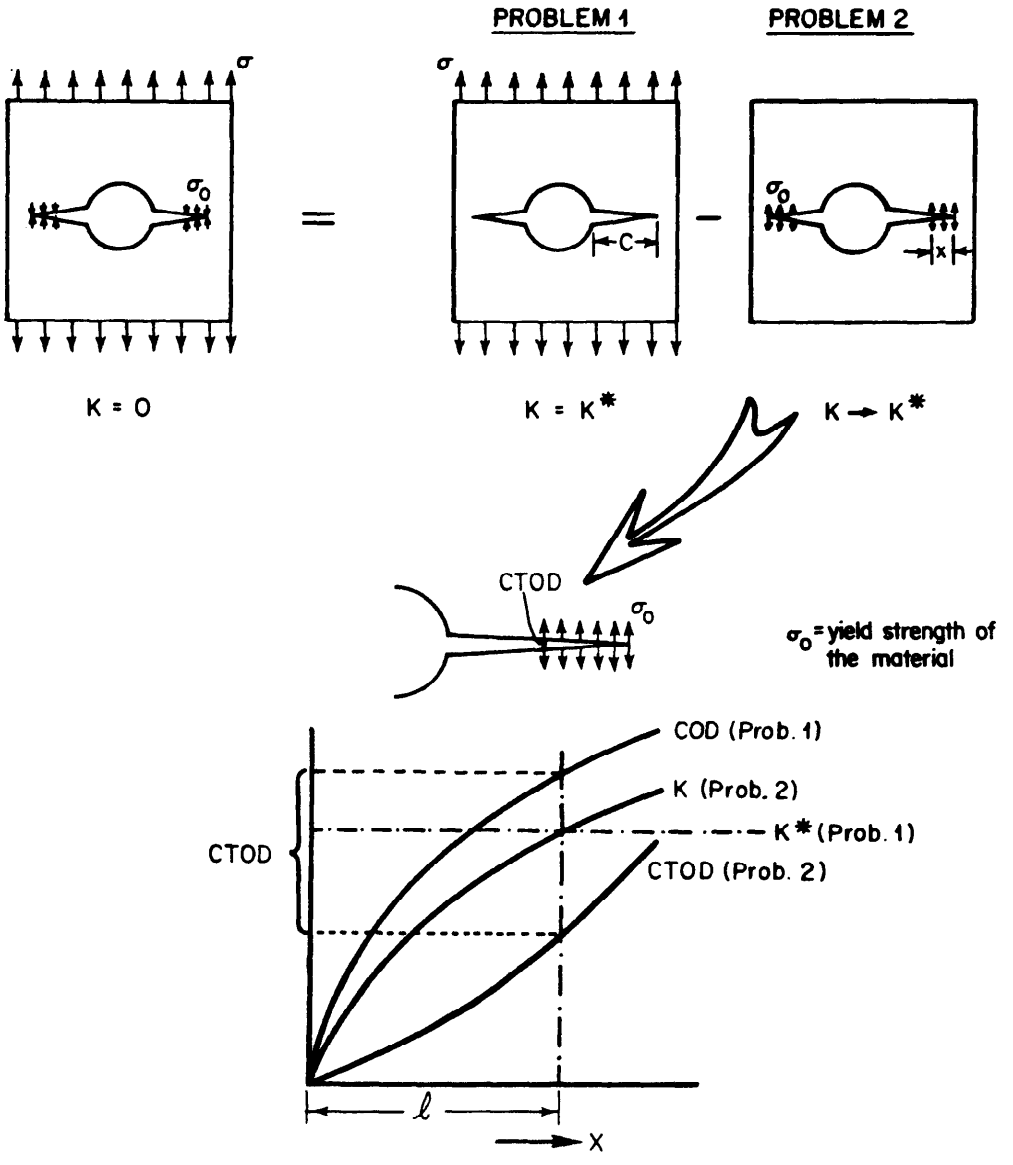

FIGURE 6. FCG RATE PREDICTIONS USING CTOD AND COMPARISON WITH EXPERIMENT AS WELL AS LEFM PREDICTIONS

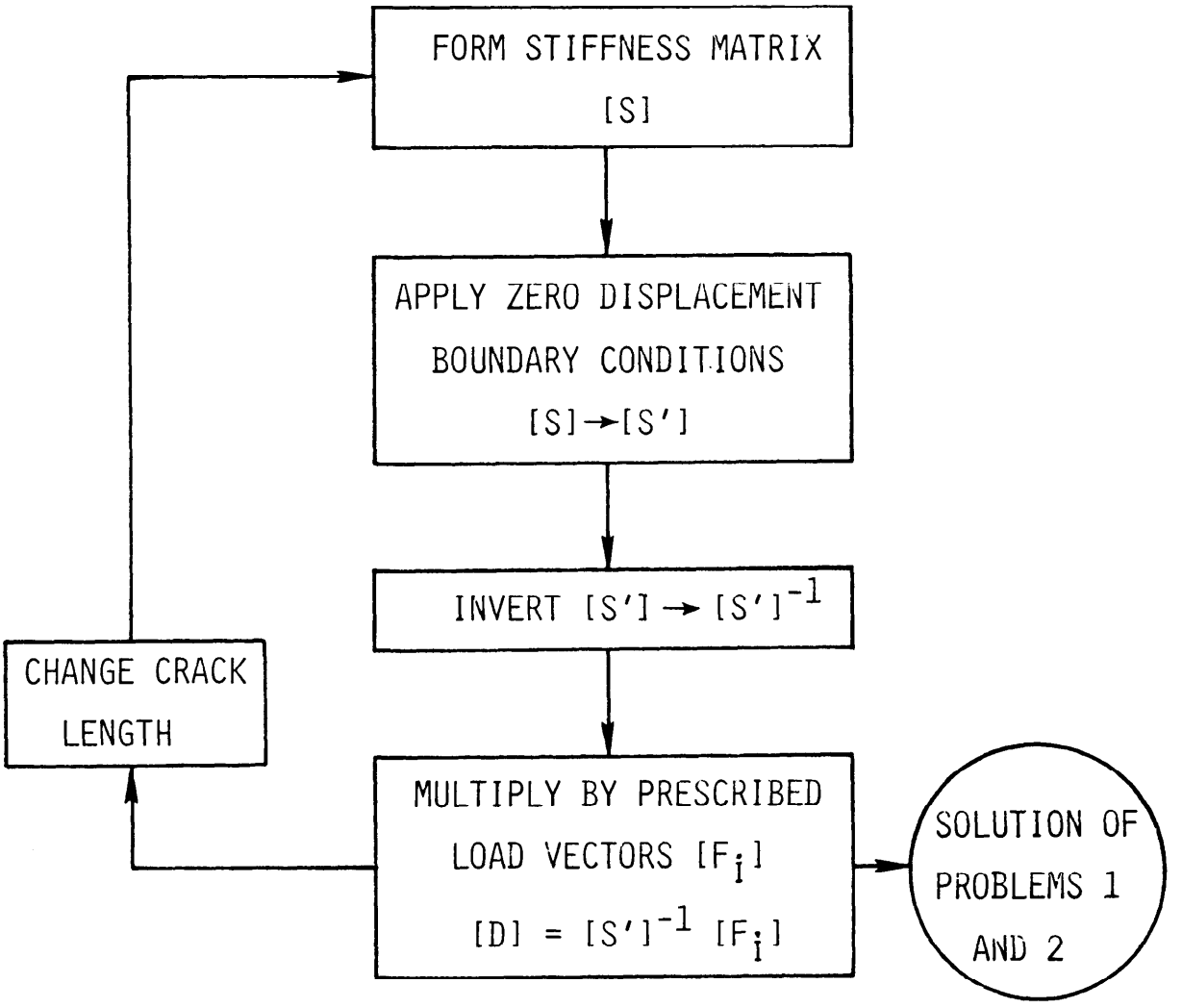

FIGURE 7. ALGORITHM FOR COLINEAR STRIP YIELD MODELING BY FINITE ELEMENT METHOD

analysis could be performed using only one quarter of the domain (as shown in Figure 8a) by imposing appropriate symmetry boundary conditions. This analysis was performed and is referred to as case (A) in the numerical results which follow. However, in the actual experiment one of the cracks initiated and grew to approximately 5.08 mm (0.2 in) before the second crack appeared. Therefore, until the two cracks became of equal length, the geometry was only symmetric about the horizontal axis. Consequently, analyses using this geometry (Case B) were performed using one-half of the domain as shown in Figure 8b.

A typical result of the analyses performed for Case A is shown in Figure 9 for c = 12.7 mm (0.5 in). Results were obtained for c ranging between 3.81 mm (0.15 in) to 20.32 mm (0.8 in). Figure 10 shows the computed CTOD, plastic zone size (P.Z.), and the crack mouth opening displacement (CMOD) as they vary with the physical crack length a. Following the same procedure as in Case A, a typical result for Case B for c = 7.62 mm (0.3 in) is shown in Figure 11. The variation of CTOD and K with crack length for this case are shown in Figures 12a and 12b.

Having obtained the results shown in Figures 10 and 12a and 12b, crack growth rate prediction using equation (4) is straightforward. All that is needed are the values of the constants C and m. These were taken to be

$$C = 9.1 \times 10^{-9}$$

$$m = 2.62$$

The FCG rate predictions made using the results of analyses of cases A and B, along with the experimental results, are shown in Figure 13. It can clearly be seen from these results that the CTOD-based analysis procedure developed here gives a significantly better prediction of the experimental results than does the LEFM-based procedure. Of more significance, the nonconservative nature of the conventional approach is removed.

DISCUSSION AND CONCLUSIONS

The short crack effect in fatigue results from the inability of linear elastic fracture mechanics (LEFM) procedures to predict the growth rate of physically small cracks. Several different possible reasons exist for this effect. It is entirely conceivable, for example, that very small cracks are influenced by microstructural features of the material that are not addressed by the conventional continuum-based LEFM techniques. In addition, three-dimensional effects (as arise in conjunction with corner cracks) exist to compound the problem. In view of these difficulties, it is not likely that predictive techniques can soon be devised to address very small cracks. Nonetheless, it is likely that an intermediate regime exists where progress can be made. The crack sizes for this regime lie just below the limit of validity for LEFM and above that were heterogeneity on the micromechanical scale strongly influences the crack growth process. In this regime an elastic-plastic fracture mechanics approach to fatigue can be effective. By pursuing

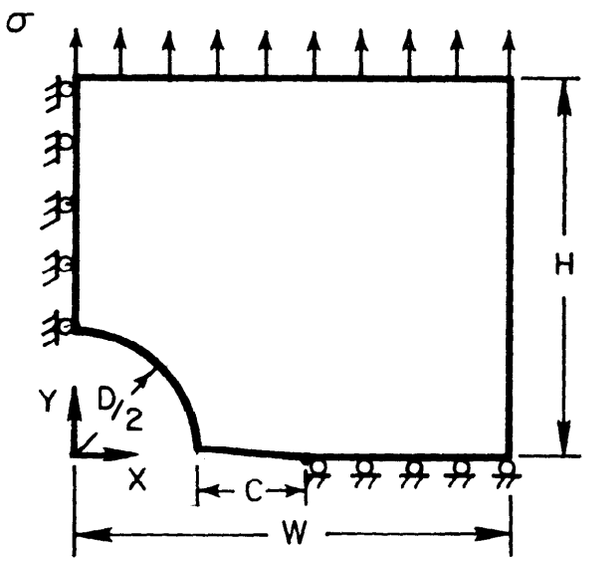

(a) One Quarter of Domain for Case A

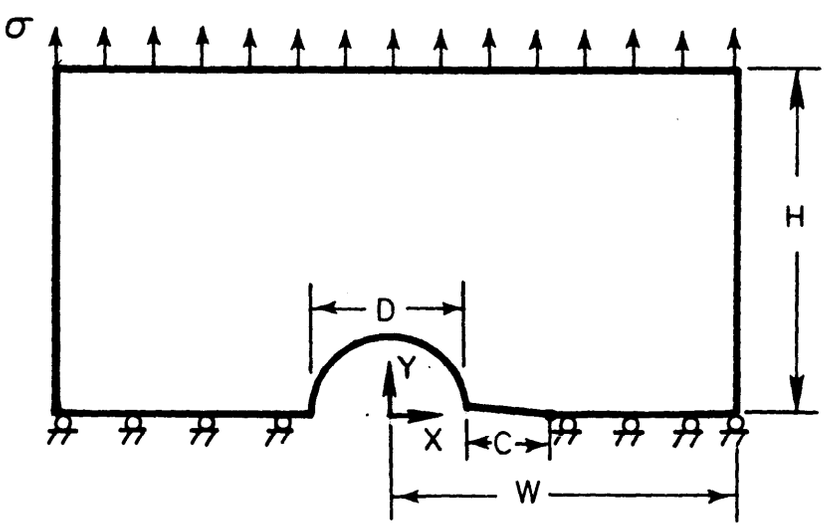

(b) One Half of Domain for Case B

FIGURE 8. THE GEOMETRICAL CONFIGURATIONS FOR ANALYSIS (σ = 27.08 KSI, W = 1.5 IN., H = 1.25 IN., D = 0.5 IN.)

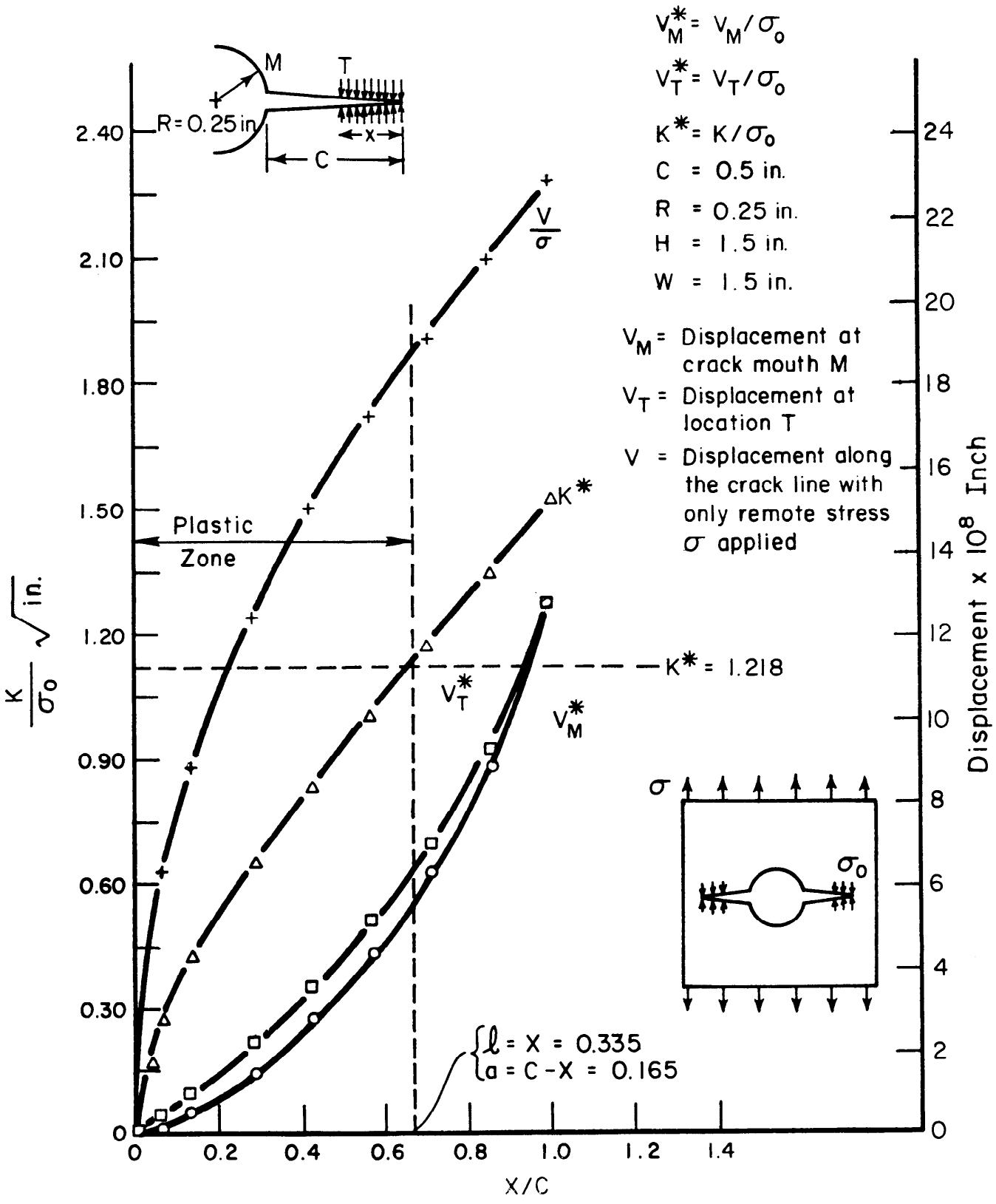

FIGURE 9. RESULTS FOR C = 12.7 MM (0.5 IN.) FOR CASE A

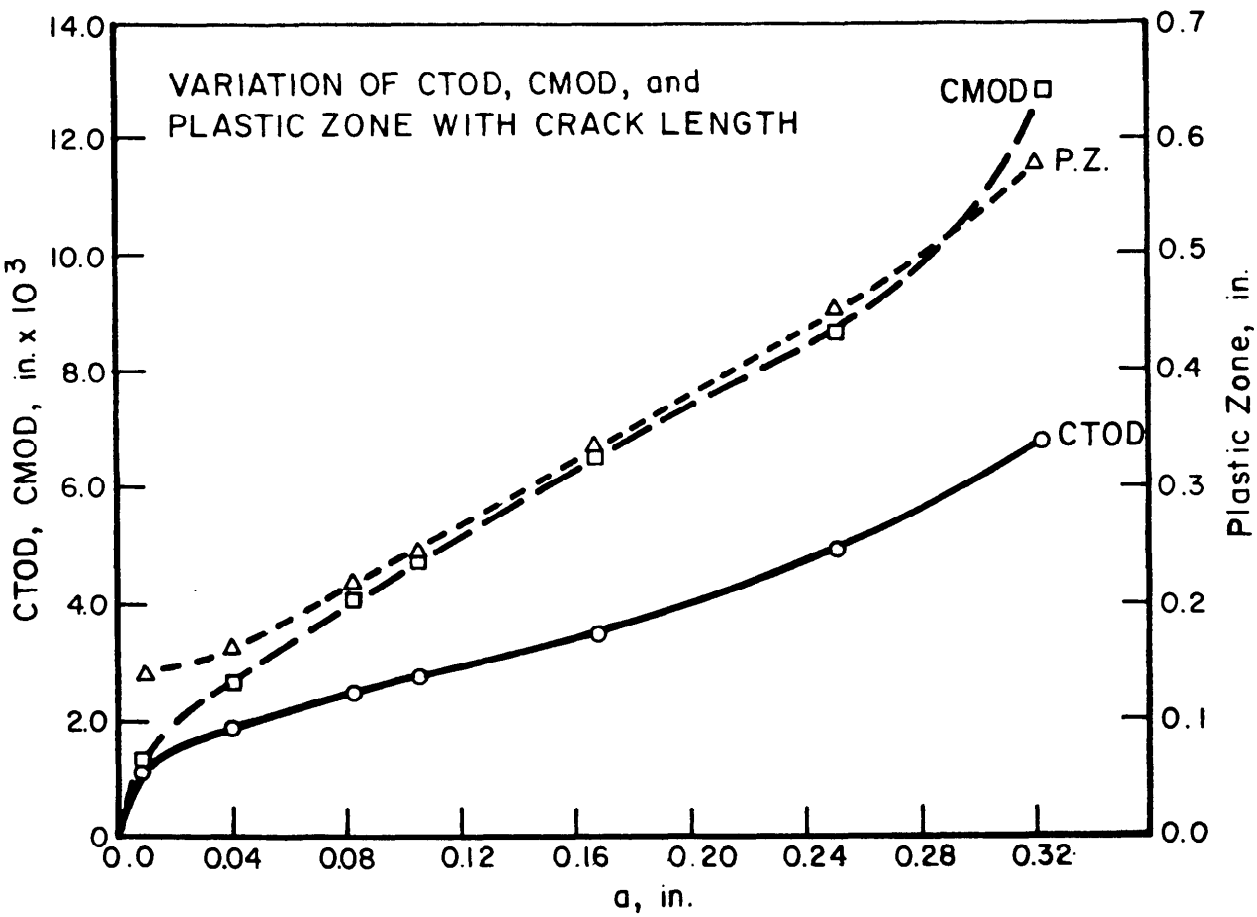

FIGURE 10. RESULTS OF CASE A

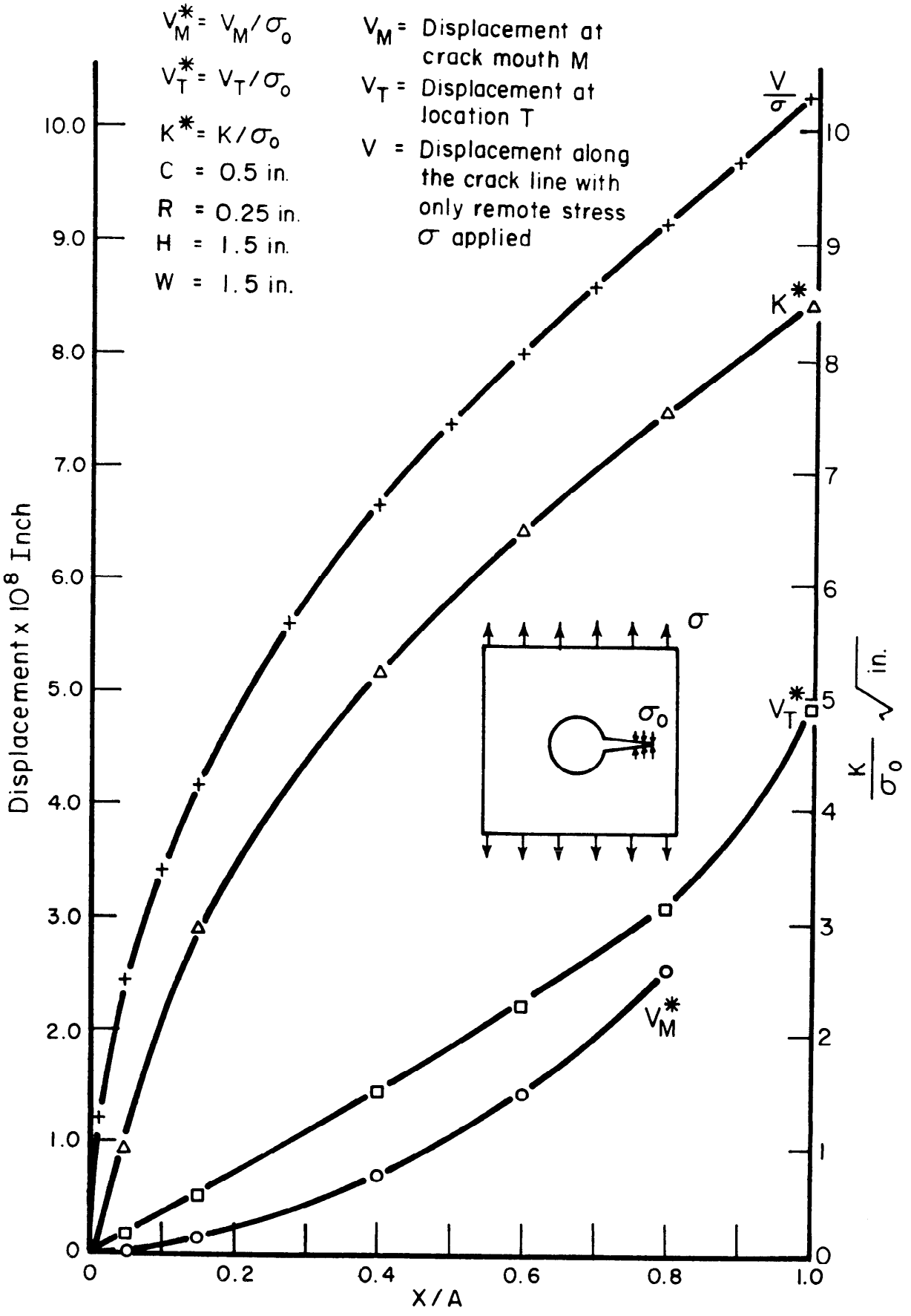

FIGURE 11. RESULTS FOR C = 7.62 MM (0.3 IN.) FOR CASE B

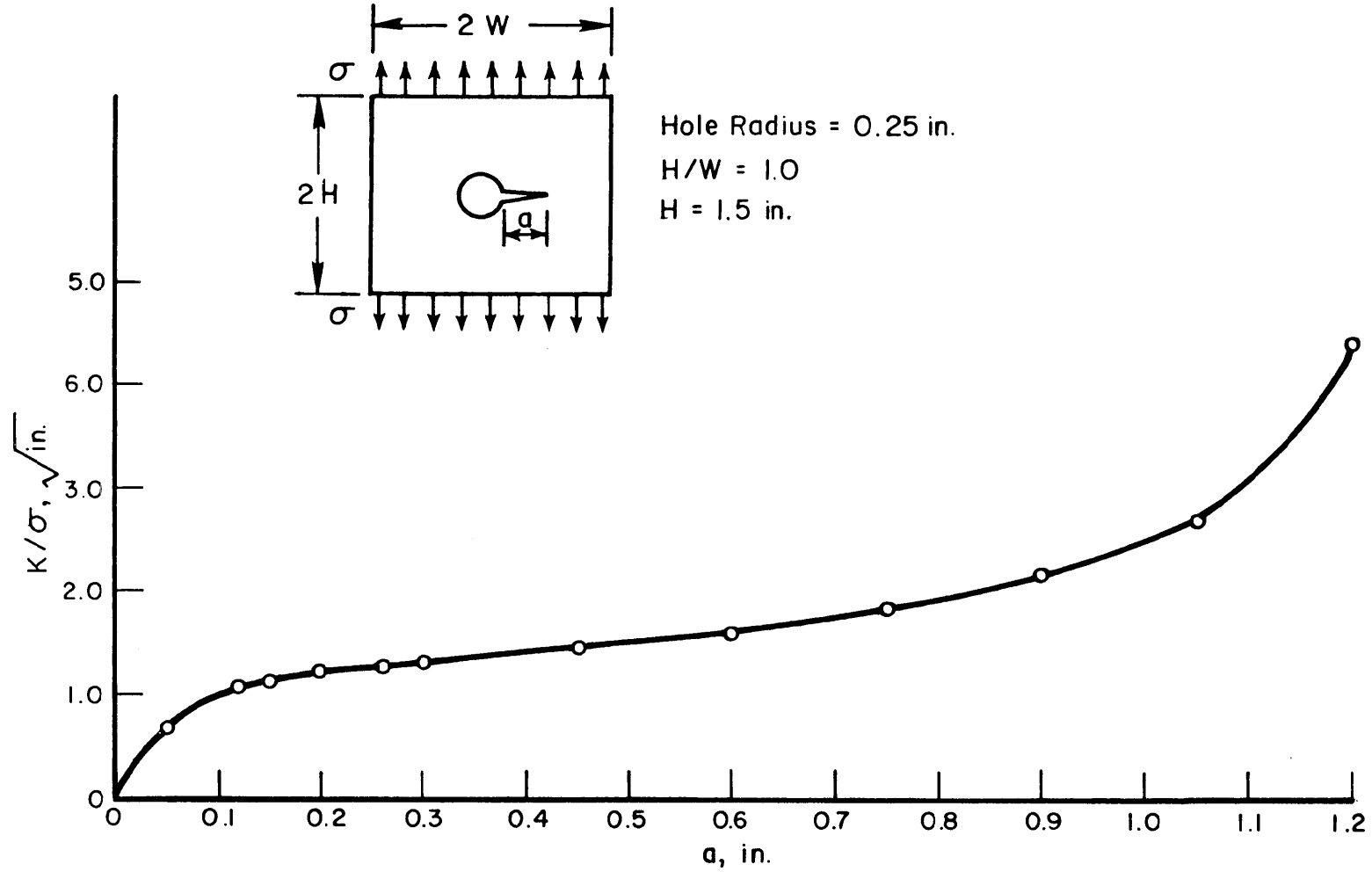

FIGURE 12a. VARIATION OF K WITH CRACK LENGTH FOR CASE B

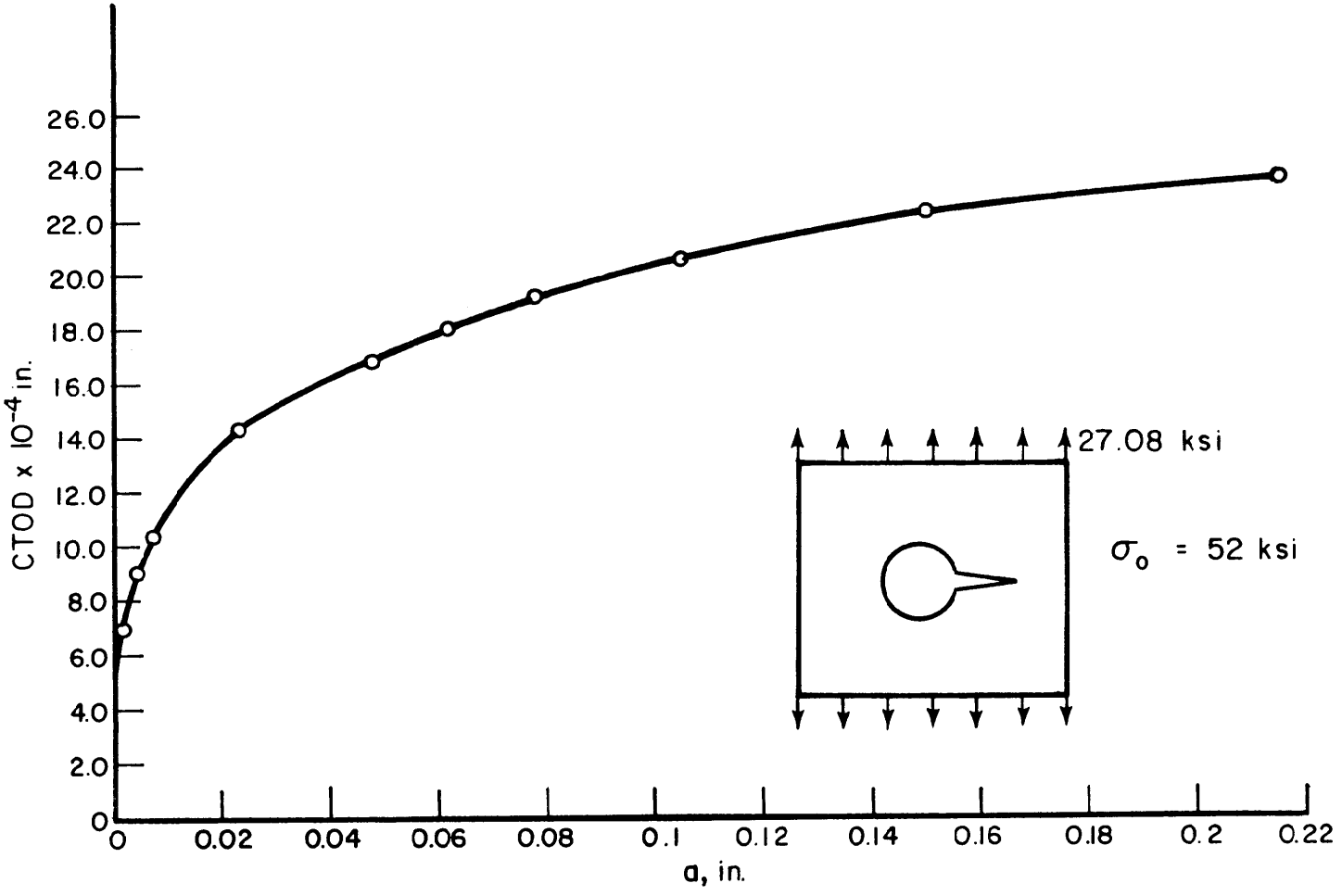

FIGURE 12b. VARIATION OF CTOD WITH CRACK LENGTH FOR CASE B

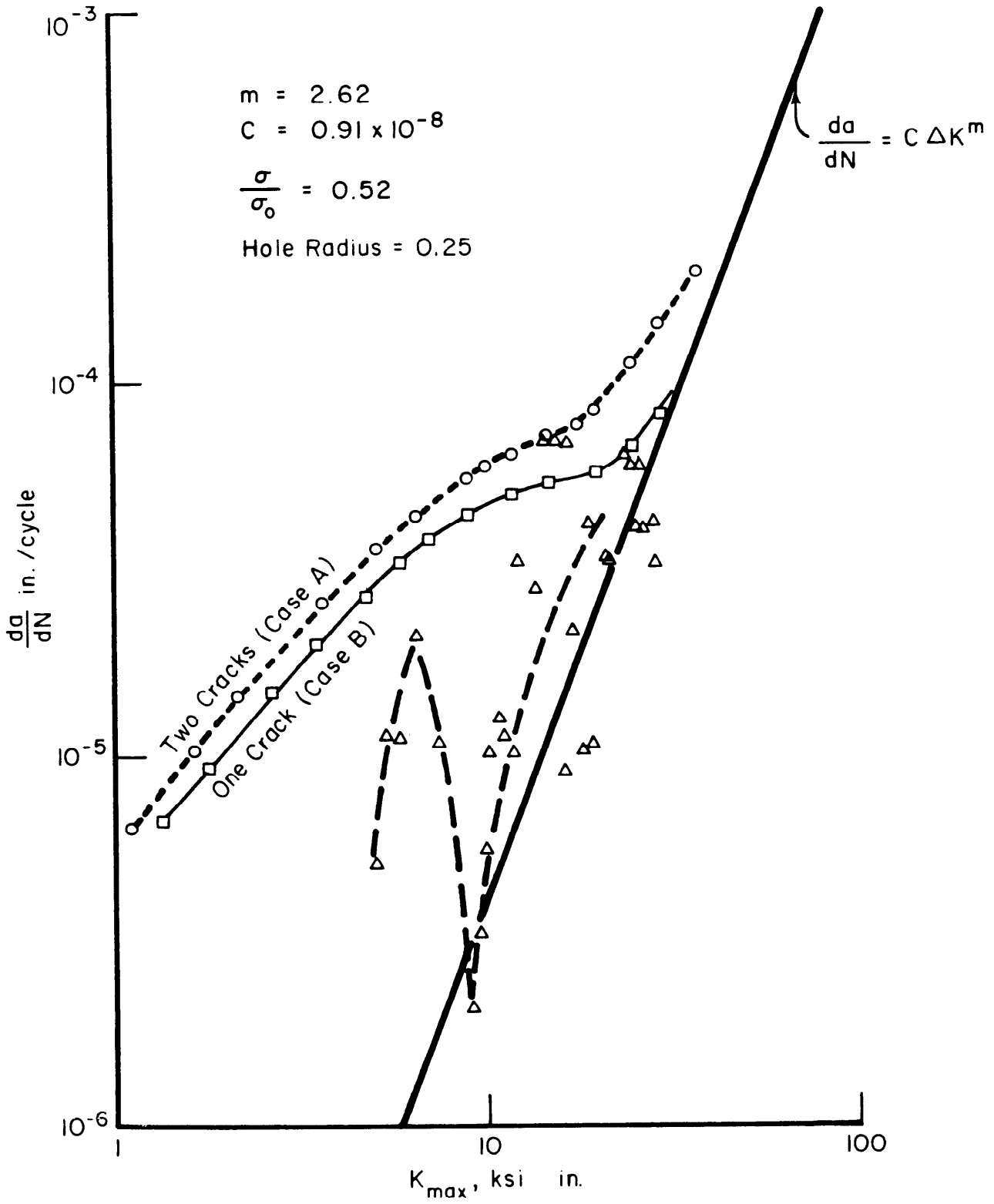

FIGURE 13. CRACK GROWTH RATE PREDICTIONS AND EXPERIMENTAL RESULT

such an approach, therefore, the authors are not expecting to completely erase the short crack effect. Rather, they expect simply to shift the short crack demarcation point downwards by broadening the applicability to the limit of a contiunum mechanics approach.

Considerable experience has been obtained in the past few years with elastic-plastic fracture mechanics--see, for example, Reference 6. This work has revealed the distinctive role played by the crack tip opening displacement (CTOD) during crack growth. While comparable results have not been obtained for subcritical cracking processes, it is tempting indeed to suppose that the CTOD may also serve as a rate controlling parameter there. This supposition is buttressed by the fact that, because of the relation that exists between CTOD and K under LEFM conditions (cf, Equation (2) above), all K-based fatigue crack growth relations can be equally well expressed in terms of CTOD. If LEFM conditions are not violated, there would be no difference between the two. But, when LEFM conditions are not met, if the two approaches differ, on the basis of the elastic-plastic work, it is likely that the CTOD-based is the more correct. For lack of an alternative at present, it was so taken here.

Having devised a CTOD-based fatigue crack growth approach for elastic-plastic conditions, it is necessary quantitatively to determine CTOD values for various conditions. A Dugdale crack model offers appropriate results in a convenient way. Hence, it was adopted for the work described in this paper. The results obtained using this model strongly indicate that the basic approach that has been adopted is correct. Specifically, as shown in Figure 14, there is a distinct difference between the EPFM and the LEFM predictions and, more importantly, that the nonconservatism of the latter has been overcome. Nevertheless, it should be clear that the use of a Dugdale model is merely an expedient selected for a preliminary test of the approach. The general approach will not rely upon the use of the Dugdale model, per se.

It should be recognized that the Dugdale model, as used in this paper, is entirely within the domain of linear elasticity. While nonlinear effects could be incorporated (e.g., by modeling the residual plasticity in the wake of this crack), this has not yet been done. Accordingly, the analysis effort described here should be considered as a first step only. The success that has so far been achieved indicates that the effort, focusing as it does on the CTOD, is aimed in the right direction. Further work to take into account crack closure and other nonlinear effects, therefore, can be expected to further resolve the short crack effect; to at least the extent that the continuum fracture mechanics approaches can do so.

ACKNOWLEDGEMENT

This research is supported by the Air Force under Contract Number F-33615-81-C-5051.

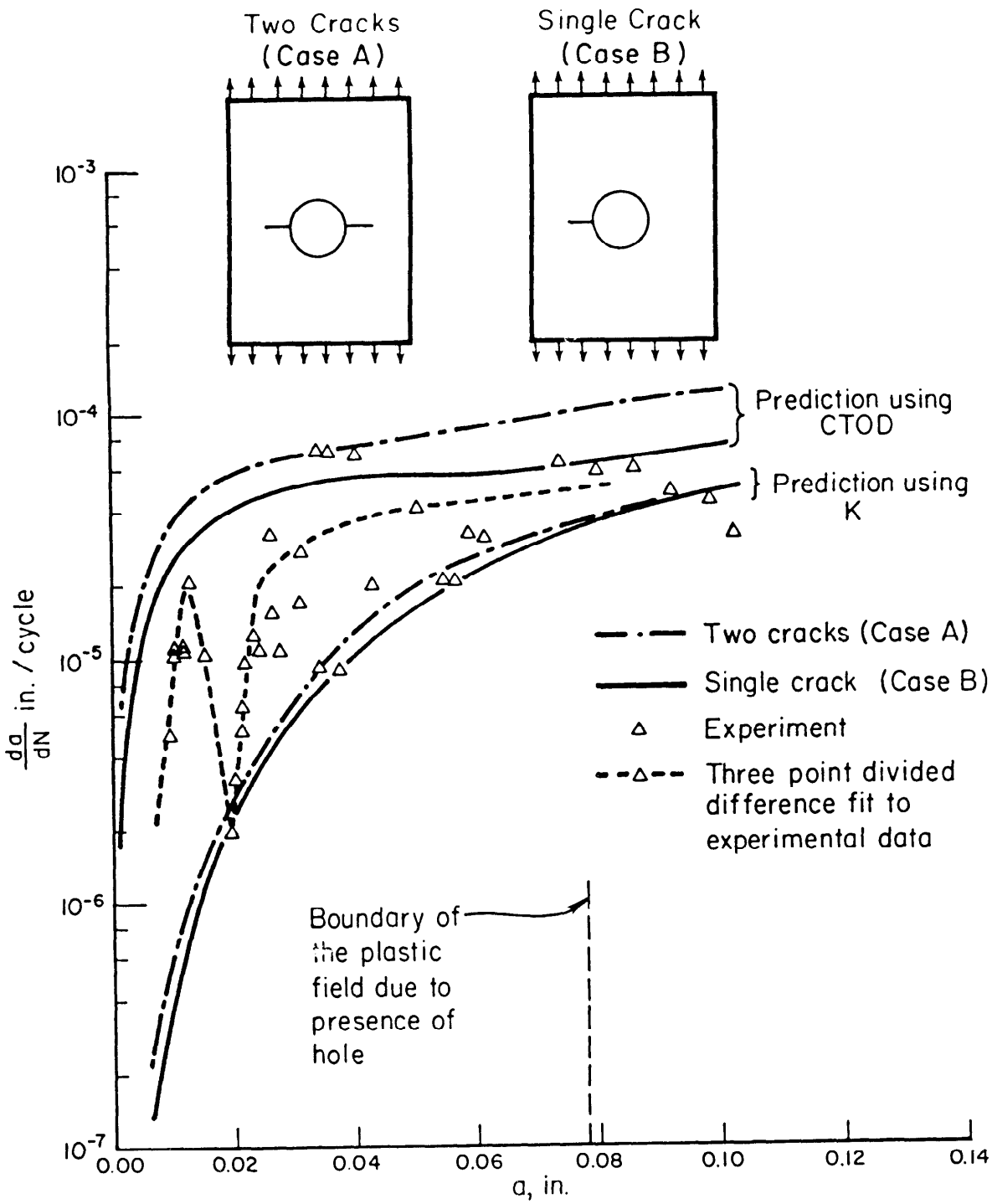

FIGURE 14. SUMMARY OF ANALYTICAL PREDICTIONS AND EXPERIMENTAL DATA

REFERENCES

1. El Haddad, M. H. and Topper, T. H., "Fracture Mechanics Relations for Short Fatigue Cracks", Risk and Failure Analysis for Improved Performance and Reliability, edited by J. Burke and V. Weiss, Plenum Press, New York, 1980, pp 121-140.

2. Leis, B. N., "Fatigue Crack Propagation Through Inelastic Gradient Fields", Int. J. Pressure Vessels and Piping, Vol. 10, 1982, pp 141-158.

3. Leis, B. N. and Forte, T. P., "Fatigue Crack Growth of Initially Physically Short Cracks in Notched Aluminum and Steel Plates", Proceedings 13th National Fracture Symposium, ASTM STP 743, 1981, pp 100-124.

4. Dowling, N. E., "Crack Growth During Low Cycle Fatigue of Smooth Axial Specimens", ASTM STP 637, 1977, pp 97-121.

5. Kanninen, M. F., et al, The Development of a Plastic Fracture Methodology, Battelle-Columbus Laboratories Final Report to the Electric Power Research Institute on RP601-1, NUREG/CR-2110, December, 1980.

6. Kanninen, M. F., Popelar, C. H., and Broek, D., A Critical Survey on the Application of Plastic Fracture Mechanics to Nuclear Pressure Vessels and Piping, Battelle-Columbus Laboratories Report to the U.S. Nuclear Regulatory Commission, January, 1981.

7. Broek, D., Elementary Engineering Fracture Mechanics, Sijthoff and Noordhoff, The Netherlands, 1978, pp 242-243.

8. Neumann, P., "The Geometry of Slip Processes at a Propagating Fatigue Crack", Acta Metallurgica, Vol. 22, 1974, p 1167.

9. Kikukawa, M., Jono, M. and Adachi, M., "Direct Observation and Mechanism of Fatigue Crack Propagation", Fatigue Mechanisms, (J. T. Fong, editor), ASTM STP 675, p 234, May 1978.

10. Nisitani, H., and Kage, M., "Observation of Crack Closure Phenomena at the Tip of a Fatigue Crack by Electron Microscopy", Fracture, 1977, Vol. 2, ICF4, Waterloo, Canada, June 19-24, 1977.

11. Sternberg, E. and Sadowsky, M. A., "Three Dimensional Solutions for Stress Concentration Around a Circular Hole in a Plate of Arbitrary Thickness", J. Appl. Mech., Trans. ASME, March, 1949.

12. Leis, B. N. and Sampath, S. G., "Development of an Improved Method of Consolidating Fatigue Life Data", NASA CR 145312, August 1977.

13. Leis, B. N., and Frey, N. D., "Cyclic Inelastic Deformation and Fatigue Resistance Behavior of Notched Aluminum Plates", Experimental Mechanics, SESA, in press.

14. Leis, B. N., Forte, T. P., Galliher, R. D., and Rungta, R., "Fatigue of Great Lakes Ships (Phase II)", Final Report to American Bureau of Shipping from Battelle's Columbus Laboratories, March 1981.

15. Leis, B. N., "Fatigue Microcrack Initiation and Growth in a Rail Steel", Interim Report on Item 13, DOT/TSC Contract 1663, Report to Transportation Systems Center, Department of Transportation from Battelle's Columbus Laboratories, February 1982.

16. Leis, B. N., and Galliher, R. D., "Growth of Physically Short Corner Cracks at Circular Notches", Low Cycle Fatigue and Life Prediction, ASTM STP, 770, 1982, pp 399-421.

17. Atkinson, C. and Kanninen, M. F., "A Simple Representation of Crack Tip Plasticity: The Inclined Strip Yield Superdislocation Model", International Journal of Fracture, Vol. 13, 151, 1977.

18. Shih, C. F., "Relationships Between the J-Integral and COD for Stationary and Extending Cracks", Journal of the Mechanics and Physics of Solids, to appear 1981.

19. Dugdale, D. S., "Yielding of Steel Sheets Containing Slits", Journal of the Mechanics and Physics of Solids, 8, 100., 1960.

20. Petroski, H. J., "Dugdale Plastic Zone Sizes for Edge Cracks", International Journal of Fracture, Vol. 15, 217, 1979.

21. Chell, G. G., "The Stress Intensity Factors and Crack Profiles for Center and Edge Cracks in Plates Subject to Arbitrary Stresses, Int. J. Fract., Vol. 12, 1, 1976, p 33.

22. Hulbert, L. E., Hahn, G. T., Rosenfield, A. R., and Kanninen, M. F., "An Elastic-Plastic Analysis of a Crack in a Plate of Finite Size", Applied Mechanics, Springer-Verlag, 1969, p 221.

23. Hayes, D. J. and Williams, J. G., "A Practical Method for Determining Dugdale Model Solutions for Cracked Bodies of Arbitrary Shape", Int. J. Fract. Mech., Vol. 8, No. 3 (1972), pp 239-256.

24. Fenner, D. N., "Dugdale Model Solutions for a Single Edge Cracked Plate", Int. J. Fract., Vol. , No. 1, March 1974.

25. Barsoum, R. S., "On the Use of Isoparametric Finite Elements In Linear Fracture Mechanics", Int. J. for Num. Meth. in Engrg., Vol. 10, 25-37, 1976.

ELASTIC-PLASTIC FRACTURE MECHANICS ANALYSIS OF SMALL CRACKS

G. G. Trantina
H. G. deLorenzi
General Electric Corporate Research and Development
Schenectady, New York 12301

ABSTRACT

For many materials the fracture strength and fatigue lifetime is controlled by small cracks that can grow at sizes and applied stress levels which are below those predicted from data for long cracks. The objective of this paper is to describe how elastic-plastic fracture mechanics analysis can be used to interpret small crack behavior. The results of the elastic-plastic analysis indicate that deviations from LEFM begin at about 0.7 of the yield stress and that the trend of the small crack data can be predicted. The results of 3-D elastic-plastic analysis of a surface crack show a unique variation of the crack driving force along the crack front. This information is used to predict crack shapes during cyclic crack growth.

INTRODUCTION

Predictions of fracture strength and fatigue lifetimes of components fabricated with high strength materials require accurate representation of the crack driving force for small cracks. In addition, an understanding of short crack behavior is necessary for proper interpretation of test specimen behavior in fatigue and cyclic crack growth rate testing. For short cracks, crack geometry and material nonlinearity must be considered along with the three-dimensional nature of the surface crack. The objectives of this paper are to describe the fracture mechanics analysis procedure and the results of two- and three-dimensional finite element analysis of small surface cracks. The finite element analysis procedure involves the use of the deformation theory of plasticity, crack tip elements with blunting, and J-integral calculations by contour integrals and virtual crack extension. The results of elastic and elastic-plastic analysis of small surface cracks provide an indication of the limitations of linear elastic fracture mechanics (LEFM) and some techniques to modify the stress intensity factor for elastic-plastic conditions. The results of the analysis are used to interpret the fatigue growth threshold for small cracks and to predict crack growth shapes for small surface cracks.

Small crack behavior and the prediction of fatigue life has been reviewed recently by Hudak [1]. There are many observations that small cracks behave differently than large cracks. Small cracks can grow at sizes and applied stress levels which are below those predicted from threshold data for large cracks. Small cracks grow at faster rates than predicted from crack growth rate data for large cracks. Interpretation of the crack growth rate data from specimens with small cracks [2] and the prediction of growth of small intrinsic defects in specimens and components require proper representations of the crack tip stress field. The purpose of this paper is to demonstrate how

elastic-plastic fracture mechanics analysis can help to interpret the behavior of small cracks.

ANALYSIS TECHNIQUES

Plastic flow can be described by a total strain theory where the strain is given as a function of the actual stress state. The deformation theory of plasticity is a total strain theory and since the strains only depend on the final stresses, the strain state is independent of any particular loading path. In the uniaxial case the stress-strain law for this theory can be described by the Ramberg-Osgood law

$$\varepsilon/\varepsilon_y = \sigma/\sigma_y + \alpha(\sigma/\sigma_y)^n \qquad (1)$$

where ε_y is the yield strain, σ_y the yield stress ($\sigma_y = E\,\varepsilon_y$), α a material constant, and n the power hardening exponent. It is generally accepted that the deformation theory of plasticity does not model the path-dependent behavior of materials for radical departures from proportional loading (i.e., all stress components increase proportionally during loading). In applications where unloading and strong deviation from proportional loading is restricted to a small region of the structure, deformation theory is valid. For the analysis of small cracks described in this paper, unloading is not considered and thus deformation theory is used.

It has been shown that appropriate singularities can be induced in the isoparametric finite elements if the node points are arranged in an appropriate manner. Several authors have employed the 8-noded 2-D and 20-noded 3-D isoparametric elements in near tip modeling of 2- and 3-dimensional cracks. Henshell and Shaw [3] and Barsoum [4] pointed out that when the mid-side nodes in these elements are placed at the quarter-point position the elements will have a $1/\sqrt{r}$ singularity in the strain fields at the neighboring corner node, where r is the distance from the crack tip. This kind of element can, therefore, effectively be used around the crack tip in an elastic analysis. In the present investigation an elastic-plastic analysis was employed. The stress and strain singularity for a perfectly plastic material is 1/r and it has been shown by Barsoum [5] that the 8-noded 2-D and the 20-noded 3-D elements have the 1/r singularity when two corner nodes and a mid-side node are collapsed such that they initially are at the same location, but are allowed to separate when the elements deform.

For a power hardening material which is loaded into the plastic range, neither the $1/\sqrt{r}$ nor the 1/r singularity is theoretically the proper singularity to use. However, when collapsed elements are used at the crack tip in an elastic analysis, even the elastic stress intensity factors are determined very accurately. Since these elements lead to accurate results in the elastic and perfectly plastic limits, it is also believed that they will model the crack tip behavior accurately for a power hardening material in the entire elastic-plastic regime. These elements were therefore chosen for the crack

tip modeling in the finite element models. When the collapsed elements are used several nodes share the same location in the undeformed configuration. When the model is loaded, the crack tip elements will start to deform and the node points at the crack tip will start to separate. This will cause the crack tip to blunt and give a realistic modeling of the real crack tip behavior.

During the last few years, the J-integral has been used increasingly to characterize crack initiation and crack growth in the elastic-plastic regime. In the context of linear elasticity and deformation theory of plasticity, the J-integral simply denotes the energy released by a unit increase in crack area. The J-integral can be calculated by different techniques. In the 2-D analyses the J-integral was calculated from the path independent integral [6]

$$J = \int_C \{ (W - \sigma_{11} \frac{\partial U_x}{\partial X} - \sigma_{21} \frac{\partial U_y}{\partial X}) dy + (\sigma_{12} \frac{\partial U_x}{\partial X} + \sigma_{22} \frac{\partial U_y}{\partial X}) dx \} ds \qquad (2)$$

where W is the strain energy density, σ the stress tensor, and U the displacement vector. It has been shown [6] that when this integration is performed along a path around the crack tip, the integral is independent of the particular path both for elastic materials and for materials following the deformation theory of plasticity.

In the 3-D analyses the J-integral was calculated by the virtual crack extension method. With this technique the J-integral at a certain point on the crack front is found from the local energy release rate at this point. The J-integral can now be calculated by advancing the crack front a small amount at the point of interest as schematically shown in Figure 1a. This will increase the cracked area by the amount A. The J-integral is then defined as the total energy released by this crack advance divided by the area A. In a finite element model the local crack advance can be introduced by shifting the nodes near the crack tip as shown in Figure 1b. This leads to a virtual crack extension at that particular point and the change in energy in the surrounding elements can then be calculated. A detailed description of this method of calculating the J-integral is given in reference [7].

RESULTS AND DISCUSSION

Two-Dimensional Analysis

The 2-D analysis was performed to evaluate the effect of elastic-plastic material behavior on the stress intensity factor for a short crack. The Ramberg-Osgood representation of the stress-strain curve was used with a power hardening exponent (n) of 10. The finite element analysis of a tension-loaded double-edge crack plate was performed by using the mesh shown in Figure 2. This model, consisting of 8-noded isoparametric elements, represents one-quarter of the plate (Figure 3) and a crack length to plate width ratio (a/W) of 0.1. An a/W of 0.01 was also analyzed by adding 40 elements to the top and right side of the model. The results for these two cases were essentially the same indicating no significant effect of the plate width. Therefore, the

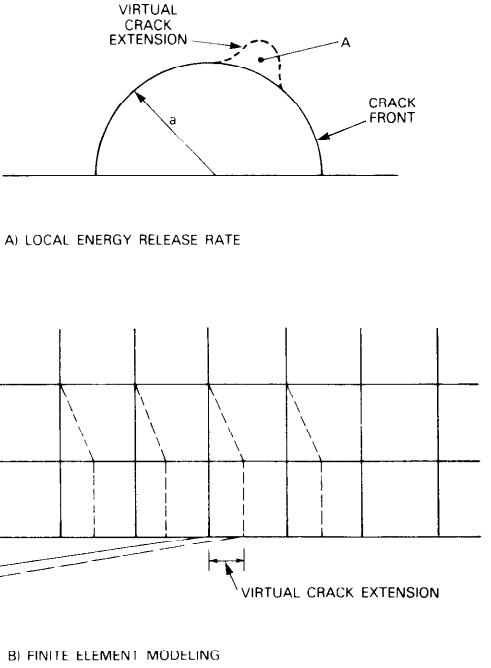

Figure 1. J-integral calculation by virtual crack extension.

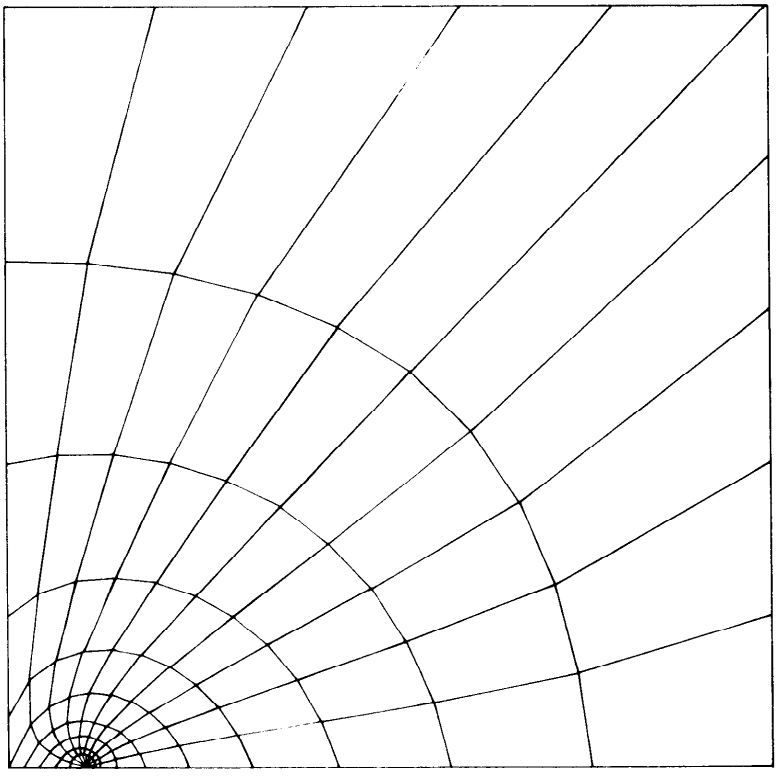

Figure 2. Finite element mesh for double-edge crack plate with a/W of 0.1.

crack behaves as a small crack in an infinite medium. The elastic-plastic analysis (deformation theory) was performed in 4 steps. The plastic zones (effective stress = yield stress) for the last three steps of a plane strain analysis are shown in Figure 3. The development of the plastic zone follows the expected pattern for plane strain and does not seem to be affected by the free surface in this small displacement analysis.

The J-integral for a plane stress finite element analysis is computed by contour integrals and the stress intensity factor is computed as

$$K = \sqrt{EJ} \tag{3}$$

where E is the elastic modulus. These results are plotted in Figure 4 by normalizing the elastic stress intensity factor by

$$K = 1.12\ \sigma\sqrt{\pi a} \tag{4}$$

for an edge crack where σ is the applied stress and a is the crack length. Significant deviations from LEFM occur as σ/σ_Y increases with about a 5% deviation for $\sigma/\sigma_Y = 0.7$.

The J-integral can be estimated [8] from $J = J_e + J_p$ where J_e is the elastic part and J_p is the plastic part. The elastic J is computed by combining Eqs. (3) and (4) and adding a plastic zone size correction where

$$J_e = (1.12)^2\ (\sigma^2/E)\ \pi(a + r_Y) \tag{5}$$

and the plastic zone size correction for plane strain [9] is

$$r_Y = \frac{1}{6\pi}\ (K/\sigma_Y)^2 \tag{6}$$

The plastic J solution is given by

$$J_p = (1.12)^2\ f(n)\ \varepsilon_p\ \sigma\ a \tag{7}$$

where ε_p is the applied plastic strain and

$$f(n) = 3.85\ \sqrt{n}\ (1 - 1/n) + \pi/n \tag{8}$$

where f(n) = 11.3 for n = 10. With this estimation scheme the J-integral can be calculated and converted to K (Eq. (3)) to compare with the elastic solution and the finite element results (Figure 4). The estimated K's are very close to the values computed from the finite element results.

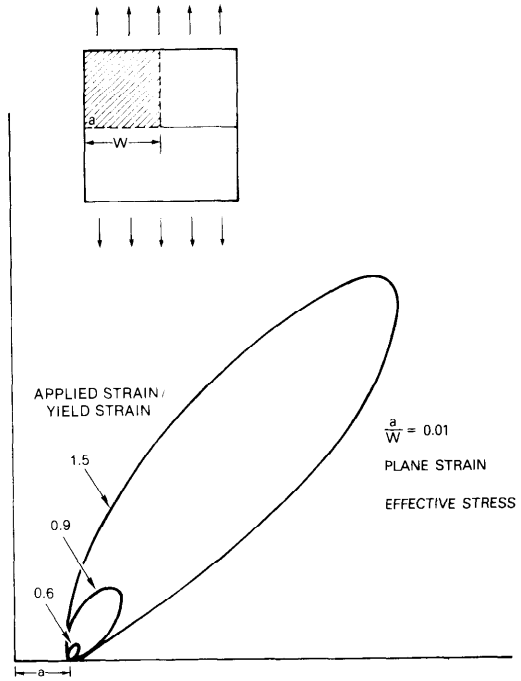

Figure 3. Plastic zone size as a function of applied strain.

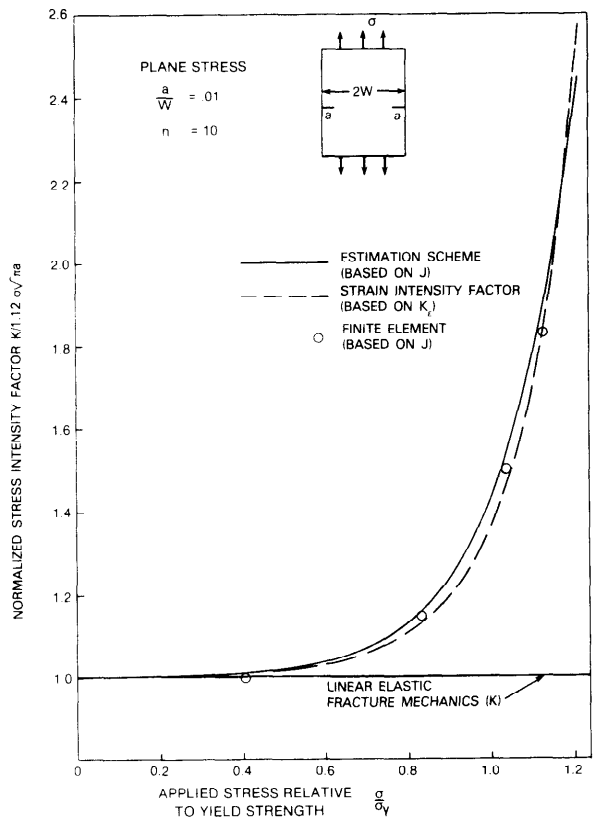

Figure 4. Effective stress intensity factors for double-edge crack plate.

Computing the stress intensity factor in terms of the applied strain rather than stress is a simple means of incorporating nonlinear effects in the crack tip parameter. This "strain intensity factor" is expressed as

$$K = 1.12\ E\ \varepsilon \sqrt{\pi(a + r_Y)} \tag{9}$$

where ε is the applied strain. The results with this simple method agree well with the finite element results as illustrated in Figure 4.

There has been an extensive amount of experimental data published concerning the cyclic crack growth rate behavior of small cracks. These experiments all indicate a deviation from LEFM behavior for small cracks. The data usually involves a plot of the cyclic stress ($\Delta\sigma$) required to propagate a crack versus the crack size. For large cracks the data follows the line predicted by LEFM ($\Delta\sigma\sqrt{a}$ = constant) while for short cracks $\Delta\sigma$ is less than predicted by LEFM. By normalizing the crack length by the plastic zone size (Eq. (6)), LEFM and the elastic-plastic fracture mechanics (EPFM) results in Figure 4 can be displayed as in Figure 5. The LEFM line is dependent only on the crack geometry (1.12) while the EPFM line is dependent on the power hardening exponent (n). Deviations between LEFM and EPFM begin when the applied stress is about 70% of the yield strength and the plastic zone size is about 10% of the crack length (Figure 5). This suggests that experimental data for the threshold of cyclic crack growth of small cracks should be treated with EPFM. A compilation of much of this data [10] is used here to demonstrate the use of EPFM to interpret the small crack behavior. The threshold value of the stress is normalized by the fatigue limit of a smooth specimen and plotted as a function of the crack length divided by the intrinsic crack length for the smooth specimen (Figure 6). The intrinsic crack length is defined by the LEFM relationship (Eq. (4)) where K is the threshold stress intensity factor and σ is the fatigue limit. The LEFM prediction fits the long crack data while for short cracks the threshold stress is considerably less than predicted (Figure 6). The EPFM prediction produced by using the results in Figure 4 and the assumption that the fatigue limit is 1.2 times the yield stress, fits the general trend of the data for long and short cracks. The data in Figure 6 represents a wide variety of steels, copper, and aluminum [10]. A power hardening exponent of 10, which is typical of many metals, was used for the EPFM prediction. However, a more precise prediction of the individual data points could probably be obtained by using the specific power hardening exponents for each of the materials.

Three-Dimensional Analysis

Many small surface cracks in test bars, crack growth rate specimens, and components are of a semicircular or semielliptical shape. These two-dimensional crack surfaces require a three-dimensional stress analysis. A 3-D finite element analysis of a small semicircular surface crack in a semi-infinite body has been performed. The actual 3-D mesh consists of a crack with a length equal to 0.1 of the radius of a half-cylinder which represents the semi-infinite body. The mesh has 340 20-noded isoparametric elements and

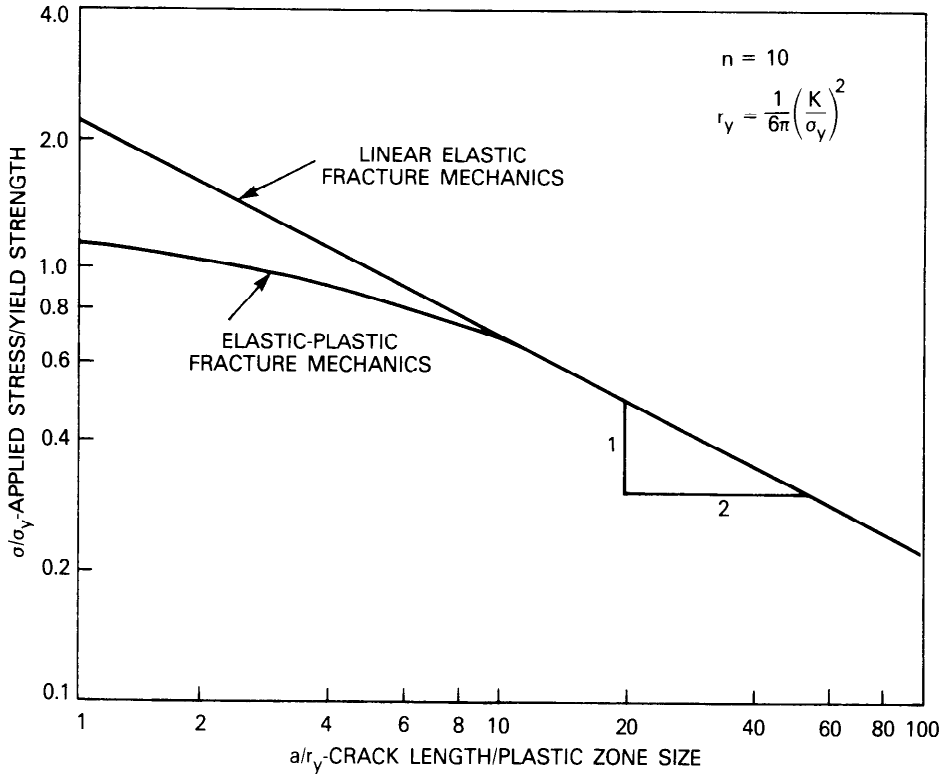

Figure 5. Difference in elastic-plastic and linear elastic fracture mechanics for small cracks.

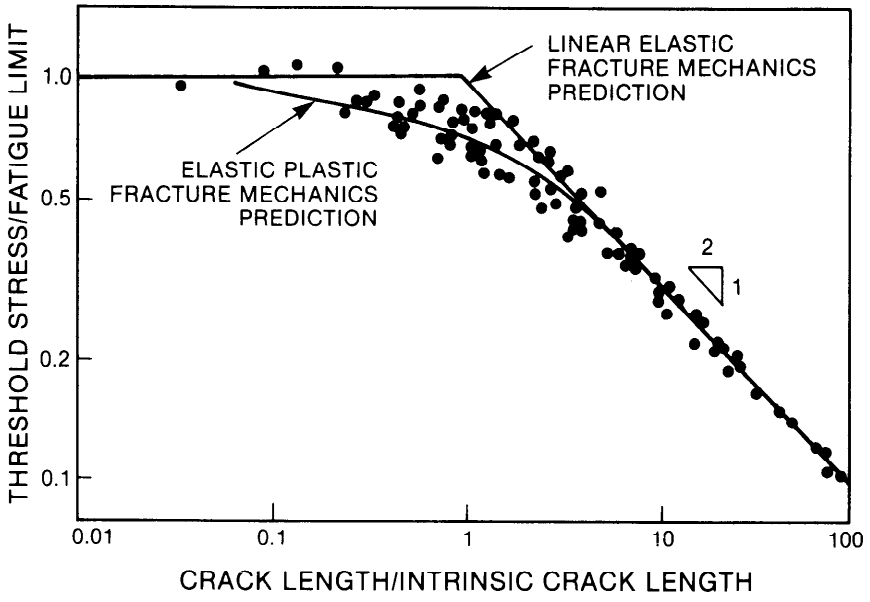

Figure 6. Threshold stress for cyclic crack growth data for various steels, copper, and aluminum [10].

1864 nodes. The known stress intensity factor for a semicircular surface crack is given by [11]

$$K = F(2/\pi)\ \sigma\sqrt{\pi a} \tag{10}$$

where σ is the stress applied perpendicular to the crack, a is the crack length, and F is a geometry factor. For a small surface crack the average value of F from other solutions [11] is 1.19 at the surface and 1.03 at the maximum depth point (90^0 from the surface). By using the virtual crack extension technique, the J-integral was calculated at 11 positions along the crack front. The J values were converted to K values by the relationships $K = \sqrt{JE/(1 - \nu^2)}$ (Figure 7). These computed values at the surface and the maximum depth point were almost exactly the same as the average of the other solutions. This provides confidence in the finite element mesh and the computation of the J-integral for small 3-D surface cracks. These results for the elastic analysis show a smooth variation of F along the crack front. The small oscillations in the computed values (Figure 7) result from a piecewise linear model of the curved crack front.

An elastic-plastic analysis of the small, semicircular, surface crack was performed using the deformation theory of plasticity. One step to an applied stress of 0.7 of the yield stress was taken. The virtual crack extension technique was used to compute J and K as in the elastic analysis. The results show a unique variation of F along the crack front (Figure 7). For $\theta > 15^0$ the stress intensity is beginning to increase due to elastic-plastic effects. This is consistent with the 2-D analysis. However, where the crack intersects the free surface ($\theta = 0$), the stress intensity has decreased. This effect is due to increased yielding at the free surface due to a lack of constraint. The region below the free surface, where there is plane strain constraint, carries a larger portion of the load. This variation in constraint along the crack front produces a plastic zone which is smaller in the interior than on the free surface.

An example of the use of this 3-D analysis in predicting crack shapes for cyclic crack growth is shown in Figure 8. The computed variation of K along the crack front is incorporated into a cyclic crack growth rate computation by using the power law crack growth rate relation. This expression can be integrated to compute the crack length as a function of cycles. One-half of four surface cracks is shown in Figure 8. In Figures 8a and 8b the initial surface crack is semicircular while in Figures 8c and 8d the depth-to-length ratio is 2.0 and 0.5, respectively. The crack shape is plotted when the crack has grown in the depth direction by an increment equal to 10% of the original depth (10% of the original surface length for Figure 8d). Figure 8a shows the growth of a crack for LEFM conditions while Figures 8b, c, and d include EPFM considerations as illustrated in Figure 7. The decreased amount of crack growth on the surface for the elastic-plastic conditions is a result of the decrease in the crack driving force on the surface and the increase in the crack driving force below the surface with increased plasticity (Figure 7). This prediction is consistent with experimental observations and empirical

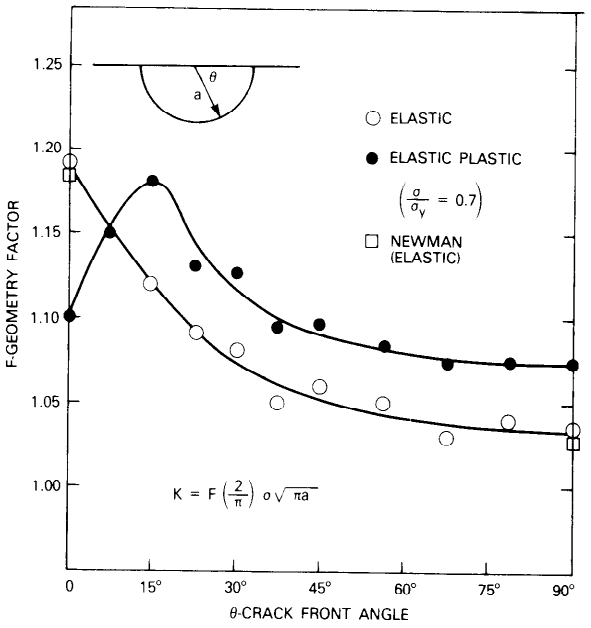

Figure 7. Stress intensity factor for semicircular surface crack for elastic and elastic-plastic loading.

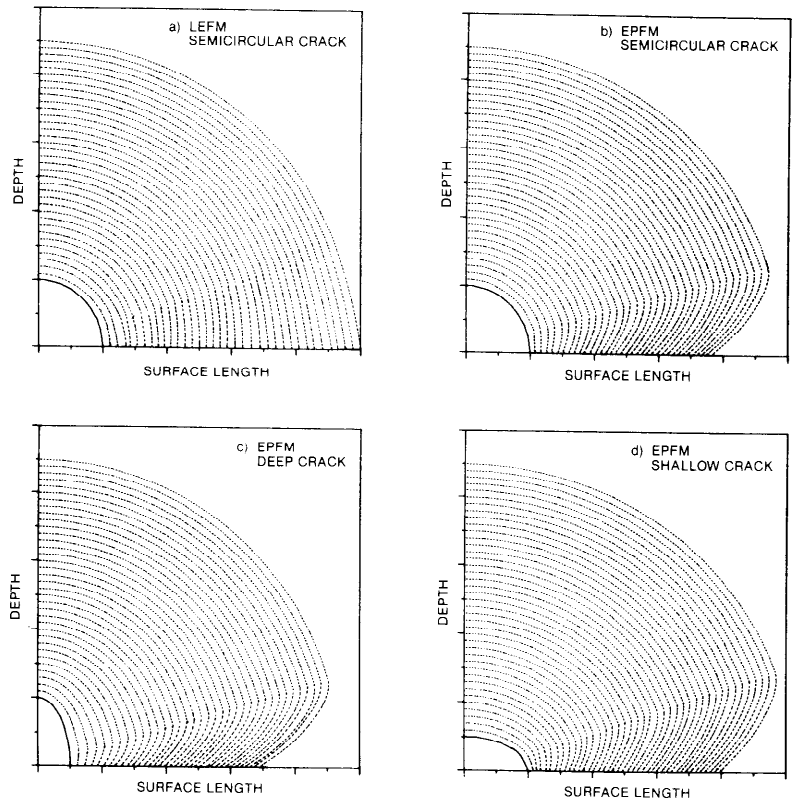

Figure 8. Crack shape predictions for cyclic crack growth.

adjustments to LEFM calculations [12]. In Figures 8c and d stress intensity factors for elliptical surface cracks [11] are combined with corrections for elastic-plastic conditions to show how deep and shallow cracks propagate to crack shapes that are nearly the same.

CONCLUSIONS

Predictions of fatigue lifetimes of components and test specimens and the interpretation of cyclic crack growth rate data require accurate representation of the crack driving force for small cracks. Results of two-dimensional analysis of an edge crack indicate that variations from LEFM begin at an applied stress of about 0.7 of the yield strength where the plastic zone size is about 0.1 of the crack length. Above this level an effective K can be calculated with the J-integral from finite element analysis or the J-integral estimation scheme or with a strain intensity factor. The trend of the small crack data for the threshold stress for cyclic crack growth can be predicted by EPFM techniques. The results of 3-D elastic-plastic analysis of a small surface crack show a unique variation of the crack driving force along the crack front with a decrease in the crack driving force at the surface and an increase in the crack driving force below the surface with increasing plasticity. This information was used to predict crack shapes for cyclic growth that are in general agreement with the observed trend of reduced crack growth on the surface.

REFERENCES

1. Hudak, S. J., Jr., "Small Crack Behavior and the Prediction of Fatigue Life," J. Eng. Mat. and Tech., v. 103, January 1981, 26-35.

2. Gangloff, R. P., "Electrical Potential Monitoring of Crack Formation and Subcritical Growth from Small Defects," Fat. of Eng. Mat., v. 4, no. 1, 1981, 15-33.

3. Henshell, R. D. and Shaw, K. G., "Crack Tip Elements are Unnecessary," Int. J. Num. Meth. Eng., v. 9, 1975, 495-507.

4. Barsoum, R. S., "On the Use of Isoparametric Finite Elements in Linear Fracture Mechanics," Int. J. Num. Meth. Eng., v. 10, 1976, 25-37.

5. Barsoum, R. S., "Triangular Quarter-Point Elements as Elastic and Perfectly Plastic Crack Tip Elements," Int. J. Num. Meth. Eng., v. 11, 1977, 85-98.

6. Rice, J. R., "A Path Independent Integral and the Approximate Analysis of Strain Concentration by Notches and Cracks," J. Appl. Mech., June 1968, 379.

7. deLorenzi, H. G., "Energy Release Rate Calculations by the Finite Element Method," to be published.

8. Shih, C. F. and Hutchinson, J. W., "Fully Plastic Solutions and Large-Scale Yielding Estimates for Plane Stress Crack Problems," J. Eng. Mat. and Tech., v. 98, October 1976, 289-295.

9. Irwin, G. R., "Plastic Zone Near a Crack and Fracture Toughness," Proceedings, Seventh Sagamore Conference, 1960, IV.63.

10. Tanaka, K., Nakai, Y., and Tamashita, M., "Fatigue Growth Threshold of Small Cracks," Int. J. Fract., v. 17, no. 5, October 1981, 519-533.

11. Newman, J. C., Jr., "A Review and Assessment of the Stress-Intensity Factors for Surface Cracks," in Part-Through Crack Fatigue Life Prediction, ASTM STP 687, J. B. Chang, Ed., American Society of Testing and Materials, 1979, 16-42.

12. Newman, J. C., Jr. and Raju, I. S., "An Empirical Stress Intensity Factor Equation for the Surface Crack," Eng. Fract. Mech., v. 15, no. 1-2, 1981, 185-192.

APPLICATION OF AN ELASTIC-PLASTIC METHODOLOGY TO STRUCTURAL INTEGRITY EVALUATION

Prepared for the Army Symposium on Solid Mechanics

H. A. Ernst
Senior Research Engineer

J. D. Landes
Advisory Engineer

Materials Engineering Department
Westinghouse R&D Center
Pittsburgh, PA 15235

ABSTRACT

The elastic plastic fracture mechanics (EPFM) technology has advanced to the point where it can be used to make a realistic assessment of the structural integrity of components containing crack like defects. This evaluation is based on the ductile cracking character of the material as described in an R curve format where J (or a similar parameter) is plotted as a function of ductile crack extension, Δa. The R curve is used along with the principles of tearing instability to predict the fracture behavior of the structure.

This paper describes a methodology for incorporating the new concepts of EPFM into a structural stability evaluation. The structure is modeled as a cracked test specimen either in series or parallel with a spring. Both the deformation properties of this specimen as given by tensile test results and the crack growth properties as given by the R curve are combined to make the stability evaluation. The evaluation is straight forward when the model for the cracked structural component is nearly identical to the laboratory test specimen used to generate the material R curve. When the model of the structure has a different geometry from the test specimen, special procedures are needed both to develop the deformation character and the cracking character of the structural model. These procedures are described in this paper along with a complete description of the steps needed to apply the methodology.

1. INTRODUCTION

The assurance of safe and reliable structural performance of critical components, structures,and equipment subjected to adverse loading conditions has always been a matter of vital concern. The capability to conduct appropriate structural integrity analyses takes on an added importance when new equipment, designs, materials, inspection and fabrication procedures are concerned.

In these situations there is little or no service experience to rely upon; hence, a thorough structural integrity analysis, incorporating all of the interacting factors must be included as a major element in the overall plan. Such analyses should take advantage of the most advanced technology areas that are applicable to the situation of concern; in this case modern fracture mechanics technology offers a unique and directly applicable capability.

Early developments of fracture mechanics focused on plane strain - that is, essentially linear-elastic fracture mechanics (LEFM) - and on the relatively high-strength brittle materials used for aircraft structures, gun tubes, missile cases, etc. Attention was concentrated on K_{Ic} and K_{Id} values, which relate well to instability conditions for materials which exhibit relatively brittle fracture behavior. However, for a broader structural reliability spectrum of applications and materials - such as lower strength, higher toughness materials; thinner sections; higher localized stress regions - in many cases, large scale plasticity will develop prior to fracture. Hence, elastic-plastic and fully plastic analyses will be required.

Elastic-plastic fracture mechanics (EPFM) was developed in response to needs that were not met by LEFM. Specifically, many structural alloys were used in temperature regimes where the fracture did not develop before significant yielding occurred. Fracture toughness values were large and could not be measured for these alloys on test specimen sizes which would meet the requirements of the linear elastic, plane strain K_{Ic} test. Often it was assumed that when fracture toughness was very large, a quantitative assessment of toughness was unnecessary. As requirements for structural integrity evaluation became more demanding, this assumption became unacceptable and a quantitative evaluation of toughness was deemed necessary.

1.1 The J Integral

Recognizing that the applicability of LEFM was necessarily limited, researchers in fracture mechanics endeavored to extend the technology to encompass situations involving considerably more plasticity than is characteristic of LEFM. The breakthrough came in the form of the path independent J-integral,[1] a field parameter analogous to K in LEFM. As a direct extension of linear-elastic behavior, J can be regarded as the strength of the stress-strain fields near the crack tip for nonlinear elastic materials.[2,3,4,5] Figure 1 illustrates the crack tip stress-strain field with J as the single parameter characterizing the strength of that field.

The ductile fracture can be divided into separate steps, Figure 2a. Each step can be represented on a plot of J versus ductile crack extension, Δa, which is labeled the R curve, Figure 2b. The point on the R curve where a blunted crack tip begins to tear in a stable manner has been labeled J_{Ic}. J_{Ic} marks the initiation of the ductile cracking behavior in a material and has been labeled as a material property. J_{Ic} is limited in use

Dwg. 6446A72

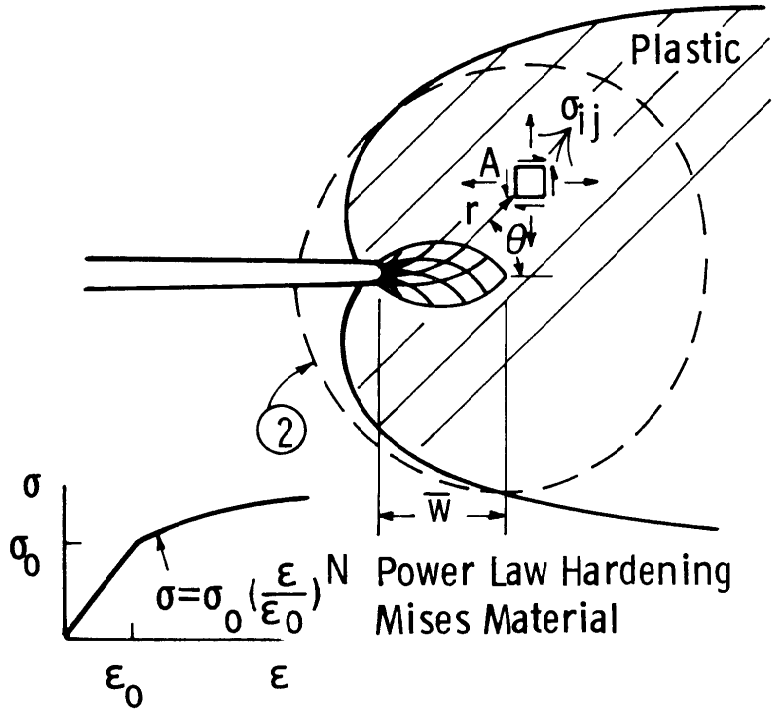

$$\sigma_{ij} = \sigma_0 \left(\frac{J}{r\,\sigma_0\,\varepsilon_0}\right)^{\frac{N}{1+N}} \bar{\Sigma}_{ij}(r, \theta, N)$$

$$\varepsilon_{ij} = \varepsilon_0 \left(\frac{J}{r\,\sigma_0\,\varepsilon_0}\right)^{\frac{1}{1+N}} \bar{E}_{ij}(r, \theta, N)$$

if $\bar{w} < r << $ planar dimensions

then: J is the intensity of the plastic field surrounding the crack tip

further: For the elastic case, $N = 1$, the above field equations give the same results as view (1), where $J = G = \frac{K^2}{E}$

Fig. 1 Plastic crack tip field characterization

a. Four steps in ductile fracture process

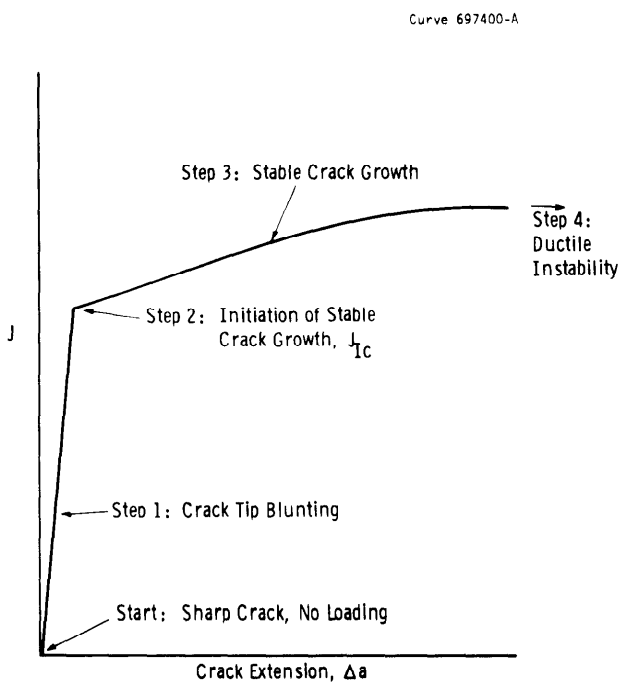

b. Four steps of ductile fracture process on an R-curve

Fig. 2.

for structural fracture evaluation in that it often provides a too conservative evaluation of toughness. The stable crack advance shown in the R curve of Figure 2b, often provides useful structural life well beyond the J_{Ic} point. The R curve then becomes the representation of fracture toughness most useful for evaluating structural behavior.

1.2 R Curve

The concept of a crack growth resistance curve -- the R curve -- provides a useful general framework for understanding the relationship between specimen geometry effects and material behavior. This concept may be explained in the following manner: Consider a cracked body being monotonically loaded. Any fracture mechanics parameter -- such as G, J, K, crack opening displacement (COD), or crack opening angle (COA) -- can be chosen to characterize the generalized crack driving force. The crack may start to grow in a slow-stable manner above a certain applied crack drive level. The R-curve represents a locus of equilibrium conditions where the crack will remain stable if the loading is stopped, and where the applied crack driving force is equal to the crack growth resistance of the material; i.e., G_I or $J = R(MN\text{-}m/m^2)$ or $K_I = KR(MPa/m^{1/2})$. Unstable crack growth develops when the crack driving force increases at a greater rate than the crack growth resistance.

The R-curve concept has been successfully developed for use in the linear-elastic range, and the characterizing crack drive can be either K_I or G_I. Experiments have shown that in the dominant elastic/small-scale-plastic range, a crack growth resistance curve can be considered a material property. In stating this, the R-curve is proven to be independent of specimen geometry effects such as initial crack size, specimen width, or specimen type. Observed effects are dependent on the material thickness and test temperature, since these variables affect the basic material toughness behavior.

The first step in considering elastic-plastic and fully plastic R-curves is the choice of a suitable parameter to characterize the generalized crack driving force. J-integral and COD concepts were designed specifically for use up to the crack growth initiation point. After significant slow stable crack growth has developed, the use of these elastic-plastic methods must be justified. Hutchinson and Paris[6] showed that J can be used to characterize the crack growth process if the remaining ligament, b, in a J test specimen is large enough so that a region of proportional strain field easily encompasses the local crack tip nonproportional strain field. They defined a material based length parameter, D, which they expressed as a function of the R-curve slope and J itself; that is, $D = J/(dJ/da)$. And then the size requirement is $b \gg D$ or $\omega = b/D \gg 1$. The required size of the proportional region before J is affected has not yet been well fixed.

The R curve based on J as the characterizing parameter is justified through the analysis of Hutchinson and Paris. It can therefore be used to assess the fracture stability of structural components; this analysis of structural stability is discussed in the following section.

2. STABILITY

Although the J-R curve concept is growing in acceptance and its use becoming more common, the question of whether a crack will grow stable or unstable remained unresolved until very recently. It was recognized that instability results from a lack of balance between the rate of increase of the applied drive force and that one of the material resistance to crack growth.

Recently, the basic implications of this concept were further explored by Paris et al.[7-8] and, as a result, it was demonstrated that the overall characteristics of the structure play a major role in instability and its effects have to be included in the rate balance mentioned. In this work, they introduced a non-dimensional quantity called the tearing modulus, T, that in general has the form:

$$T = \frac{E}{\sigma_o^2} \frac{dJ}{da} \qquad (1)$$

where E is the elastic modulus and σ_o is the flow stress. If Equation (1) is evaluated using the J-Resistance curve of the material, the resulting T is the material tearing modulus T_{mat}. If instead, dJ/da in Equation (1) is calculated as the rate of change of crack drive or the applied J, per unit virtual crack extension, with the condition of total displacement, δ_{tot}, kept constant (or other similar conditions specified), the resulting T is the applied tearing modulus T_{app}. And so following References[7-8], instability will occur when:

$$T_{app} \geq T_{mat} \qquad (2)$$

Using the condition of total displacement constant, the compliance of the structure, C_M, is introduced into the analysis the T_{app} becomes a function of C_M. Consequently, according to the theory, Equation (2), instability is predicted provided the values of T_{mat} and expressions for T_{app} are known. In their original work, Paris et al. developed formulae for T_{app} for different configurations assuming perfect plasticity and that the crack grew under limit load conditions. They also performed the first experimental evaluation of the theory. In tests of three point bend specimens loaded in series with a spring bar of adjustable length, the compliance of the system, C_M, was varied from test to test, producing stable or unstable behavior in complete agreement with the theory.

The results were originally shown in a T_{mat} vs T_{app} plot, Figure 3. Each test is represented by its T_{mat} and T_{app} values. Open points correspond to unstable crack growth while filled points correspond to stable crack growth. Ideally, according to the theory, all open points (unstable) should lie to the right of the 45° line (region where $T_{app} > T_{mat}$), while the filled points (stable) should lie at the left of the 45° line (region where $T_{mat} > T_{app}$). The excellent agreement shown in Figure 3 was the first experimental verification of the tearing instability theory.

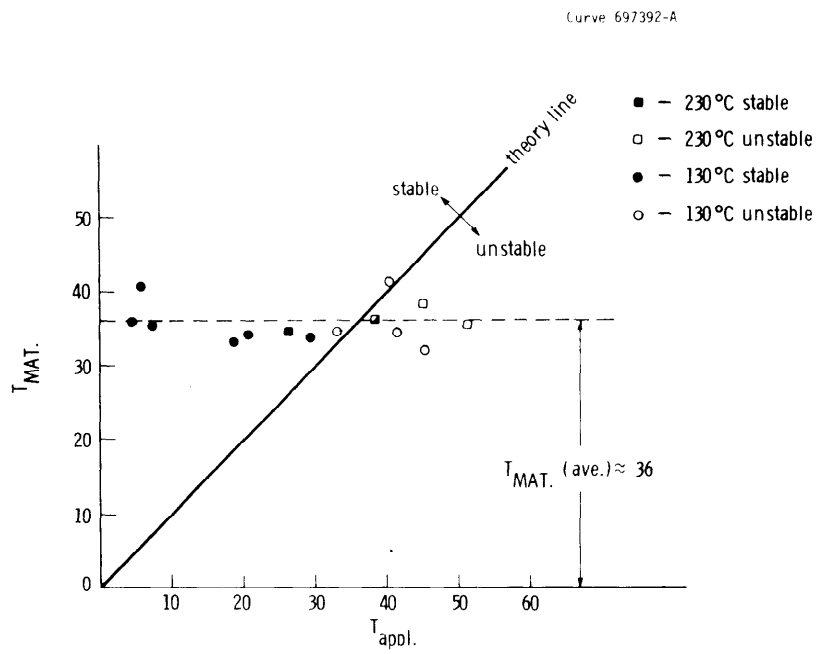

Fig. 3 Experimental results from instability studies on 3 point bend bars T_{mat} vs T_{app}. after Paris, et al.

2.1 Specimen in Series with a Spring Displacement Controlled Conditions

Since this first work, significant effort was devoted to extend the same concepts in different directions. To better illustrate these concepts consider the example shown in Figure 4. A specimen is loaded in series with a linear spring of constant $K_M = C_M^{-1}$, simulating the structure, in a displacement controlled test.

Hutchinson and Paris developed a general expression for T_{app} for this configuration

$$T_{app} = \frac{E}{\sigma_o^2} \left| \left[\frac{\partial J}{\partial a} \Big|_\delta - \frac{\partial J}{\partial \delta} \Big|_a \frac{\partial \delta}{\partial a} \Big|_P \frac{1}{\left[C_M + \frac{\partial \delta}{\partial P} \Big|_a \right]} \right] \right| \qquad (3)$$

where δ is the displacement due to the crack and C_M is the compliance of the spring. All the terms appearing in the above equation are calibration functions, i.e., they don't bear any information regarding the material response to crack growth. These functions can be obtained from finite element analysis or experimentally from blunt notch specimen tests, and no

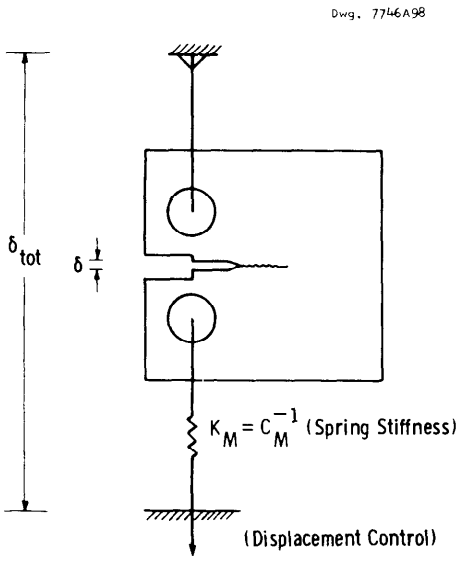

Fig. 4 Displacement controlled test of a bend specimen in series with a spring bar

"real" crack growth test is needed for their determination. This scheme has been used[7-8] to obtain T_{app} for different configurations of practical interest and, as was mentioned, instability can be predicted by comparing the value of T_{app} obtained from Equation (2) with the experimentally obtained T_{mat}.

Recently Ernst et al.[9,10,11] developed general formulae to evaluate both T_{mat} and T_{app} directly from a load-displacement (P-δ) test record giving, for the above case, respectively

$$T_{mat} = \frac{E}{\sigma_o^2}\left[\frac{\partial J}{\partial a}\bigg|_{\delta} - \frac{\partial J}{\partial \delta}\bigg|_{a}\frac{\partial P}{\partial a}\bigg|_{\delta}\left(\frac{1}{\frac{\partial P}{\partial \delta}\big|_{a} - \frac{dP}{da}}\right)\right] \tag{4}$$

$$T_{app} = \frac{E}{\sigma_o^2}\left[\frac{\partial J}{\delta a}\bigg|_{\delta} - \frac{\partial J}{\partial \delta}\bigg|_{a}\frac{1}{\frac{\partial P}{\partial \delta}\big|_{a} + K_M}\right] \tag{5}$$

This formulation allows a direct comparison between the T_{mat} vs T_{app} values. The instability condition can now be found directly defining

$$\Delta T = T_{mat} - T_{app} \tag{6}$$

Instability will result when

$$\Delta T < 0 \tag{7}$$

or using Equations (4) and (5).

$$\Delta T = -\frac{E}{\sigma_o^2}\left|\frac{\partial P}{\partial a}\Big|_\delta \frac{\partial J}{\partial \delta}\Big|_a \left(\frac{1}{\frac{\partial P}{\partial \delta}\Big|_a - \frac{dP}{d\delta}} - \frac{1}{\frac{\partial P}{\partial \delta}\Big|_a + K_M}\right)\right| < 0 \qquad (8)$$

noting that

$$\frac{\partial P}{\partial a}\Big|_\delta < 0$$

$$\Delta T < 0 \text{ if and only if} \qquad (9)$$

$$-dP/d\delta > K_M \text{ for the instability condition}$$

Thus according to the theory, instability will ensure when $\Delta T < 0$ and that will happen if and only if $-dP/d\delta > K_M$.

2.2 Alternate Physical Interpretation of the Instability Condition

The condition for instability can be obtained using a different approach.

Consider the P-δ record of a bend specimen tested under displacement control, and the correponding calibration (nongrowing crack) curves as shown in Figure 5a.

It is assumed that the fracture process is described in terms of the J-R curve; that is, every point in the P-δ record has associated a value of J, J_i and a value of a, a_i which are connected according to the J-R curve.

Suppose now that an identical specimen (same a/W) is tested, this time in series with a spring (as described before), Figure 5b. It can be seen that the effect of the spring on the calibration functions is just to shift every point in Figure 5a to the right by an amount

$$\delta_M = PC_M$$

or

$$\delta_{A'} = \delta_A + P_A C_M \qquad (10)$$

$$\delta_{B'} = \delta_B + P_B C_M \qquad (11)$$

where P_A and P_B are the loads at Points [A-A'] and [B-B'], respectively. Note that corresponding points, [A-A'], [B-B'], etc., have the same value of

Fig. 5 P-δ record of a specimen a) without and b) with spring in series

J(J depending on a/W and displacement only due to the crack, δ). Thus the resulting test record is expected to go through these corresponding points [A'],[B'], etc. in order to follow the J-R curve as before. Combining Equations (10) and (11) gives

$$\delta_{B'} - \delta_{A'} = \delta_B - \delta_A + C_M(P_B - P_A) \tag{12}$$

is important to note that for the portion of the test record where $P_B - P_A < 0$ (dropping part), the relative distance of subsequent points is diminished by the addition of the spring

$$\delta_B - \delta_A > \delta_{B'} - \delta_{A'} \text{ if } P_B < P_A \tag{13}$$

In fact, if enough compliance is added, this relative distance can even turn out to be negative; that is, Point [B'] lying to the left of [A']. If this is the case the test record would have to go backwards (in δ) to pass through [B'] in order to follow the J-R curve. But this is not compatible with the boundary condition, which asks for a monotonically increasing displacement. Thus, the test record gets as near to Point [B'] as it is allowed to (vertical drop), corresponding to unstable growth.

The conditions for stability can be then expressed as

$$\delta_{B'} - \delta_{A'} < 0 \text{ unstable}$$

$$\delta_{B'} - \delta_{A'} > 0 \text{ stable} \tag{14}$$

Replacing Equations (10) and (11) in the preceding expression gives

$$\delta_{B'} - \delta_{A'} = \delta_B - \delta_A + (P_B - P_A)\, C_M < 0$$

$$\frac{\Delta\delta}{\Delta P} < - C_M \qquad (15)$$

$$C_M^{-1} = K_M < - dP/d\delta \text{ for instability}$$

This condition was found on a completely general basis with no need to mention J or even crack length. It is exactly the same as that one of Equation (9) found from tearing instability theory. As a result the condition $\Delta T < 0$ is a necessary and sufficient one for instability. Thus, the tearing instability theory has been proven to be always valid.

2.3 Specimen in Parallel with Spring Load-Controlled Conditions

It is well recognized that the structural member is normally constrained by the structure in such a way, that neither an exclusively load-controlled, nor a displacement-controlled situation is realistic, but more likely a mixed one where the stiffness of the rest of the structure K_M has to be taken into account. In the last section it was shown that by adding a spring in series with the specimen in a displacement controlled test, the structure can be simulated and in fact, the whole range from load control to displacement control can be covered by just changing the stiffness of the spring K_M. Nevertheless, that is not the only possible way of ranging from one end to the other. In fact, there are situations where the structure is in an intermediate loading condition which cannot be represented by the above mentioned model. Namely redundant structures where several members are sharing the overall applied load: stiffened plates or pipes, set of structural supporters, cables, etc. The stability of crack growth problem for this type of structures was the subject of a recent paper by Paris et al[12], where they developed the so-called Fracture Proof Design Concept. According to this concept structural parts can be designed in such a way as to guarantee stable crack growth even under load-controlled conditions. To better illustrate these concepts consider a specimen in parallel with a spring of constant K_M simulating the structure, subjected to load controlled conditions, as shown in Figure 6. For this case Ernst[11] obtained the expression for T_{mat} and T_{app}.

$$T_{mat} = \frac{E}{\sigma_o^2} \left| \frac{\partial J}{\partial a}\bigg|_\delta - \frac{\partial J}{\partial \delta}\bigg|_a \frac{\frac{\partial P}{\partial a}\Big|_\delta}{\left(\frac{\partial P}{\partial \delta}\Big|_a - \frac{dP}{d\delta}\right)} \right| \qquad (16)$$

$$T_{app} = \frac{E}{\sigma_o^2}\left[\left.\frac{\partial J}{\partial a}\right|_{\delta} - \left.\frac{\partial J}{\partial \delta}\right|_{a} \frac{\left.\frac{\partial P}{\partial \delta}\right|_{\delta}}{\left.\frac{\partial P}{\partial \delta}\right|_{a} + K_M}\right]_a \qquad (17)$$

This equation is the general expression for T_{app} for a specimen in parallel with a spring (structure) under load controlled conditions. The instability condition can be obtained by comparing Equations (16) and (17) giving

$$\Delta T = T_{Mat} - T_{app} < 0 \qquad (18)$$

if and only

$-dP/d\delta > K_M$

for instability

Dwg. 7740A44

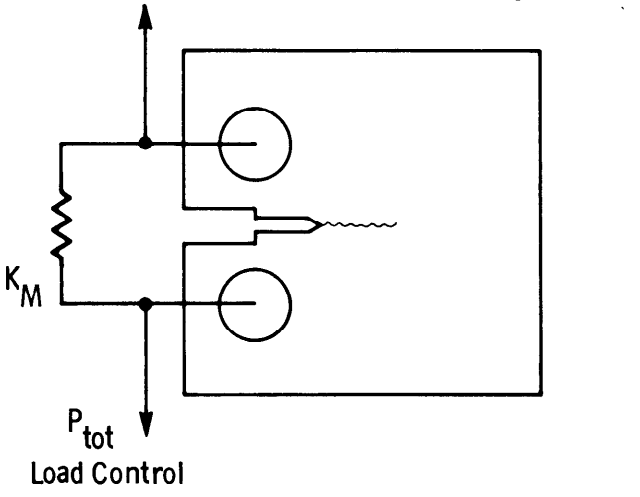

Fig. 6 Specimen in parallel with a spring in a load controlled test

Following a similar line to the last section, the instability condition can be obtained from the P-δ record itself.

Consider the P-δ record of a specimen tested under displacement control as shown in Figure 7a. Suppose now that an identical specimen is tested in parallel with a spring of compliance C_M (or stiffness $K_M = C_M^{-1}$). The displacement underwent by the specimen, and that one of the spring δ_M are the same

$$\delta = \delta_M \qquad (19)$$

On the other hand, according to the principle of equilibrium, the load held by the specimen, P, plus the load held by the spring P_M, give the total externally applied displacement P_{tot}

$$P_{tot} = P + P_M \tag{20}$$

As a consequence, the second specimen test record (P_{tot}, δ) shown in Fig. 7b, will be just the result of shifting every point of the original P-δ record up in load by an amount

$$P_M = K_M \delta \tag{20b}$$

As before, if two generic points A and B in Fig. 7a are considered, with coordinates (δ_A, P_A) and (δ_B, P_B) respectively, the addition of the spring will shift them to (δ_A, P_A') and (δ_B, P_B'), with

$$\begin{aligned} P_A' &= P_A + K_M \delta_A \\ P_B' &= P_B + K_M \delta_B \end{aligned} \tag{21}$$

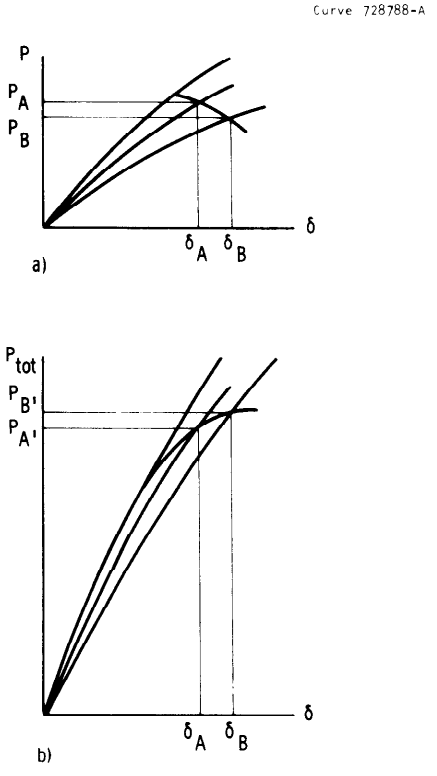

Fig. 7 P-δ record of a specimen a) without and b) with a spring in parallel

Combining the above equations one gets Equation (22) here

$$(P_{B'} - P_{A'}) = (P_B - P_A) + K_M (\delta_B - \delta_A) \tag{22}$$

The above expression can be regarded as the fundamental instability equation for load controlled systems. If points A and B were in the raising portion of the P-δ record ($P_A > P_B$) the addition of the spring causes an increase in the load difference due to the fact that the second term in the right hand side of Equation (22) is positive.

$$(P_{B'} - P_{A'}) > (P_A - P_B) \tag{23}$$

If the points A and B were in the dropping portion of the P-δ record ($P_A > P_B$), the addition will also cause an increase in the load difference for the same reason as before.

$$(P_{B'} - P_{A'}) > (P_B - P_A) \tag{24}$$

In fact, if the second term in the right hand side of Equation (22) is big enough the relative difference in load can turn to be positive $P_{B'} - P_{A'} > 0$, and that means an always increasing curve in load. The required value of K_M to produce this behavior can be obtained from Equation (22)

$$(P_{B'} - P_{A'}) = (P_B - P_A) + K_M (\delta_B - \delta_A) > 0$$

$$-\frac{P_B - P_A}{\delta_B - \delta_A} < K_M \tag{25}$$

$$-dP/d\delta < K_M$$

to produce a monotonically increasing curve.

Note that if the resulting $P_{tot} - \delta$ record is a monotonically increasing curve, it is irrelevant whether the test is run under load or displacement controlled conditions i.e., the test will be stable regardless of these conditions. Thus, Equation (25) represents the fundamental condition for stable behavior under load controlled conditions, and the minimum value of K_M that satisfies it, is the minimum value of stiffness required to produce a monotonically increasing curve and thus prevent instability. As a result the instability conditions are

$$\begin{aligned} -dP/d\delta &< K_M \quad \text{stable} \\ -dP/d\delta &> K_M \quad \text{unstable} \end{aligned} \tag{26}$$

Note that this condition is exactly the same as that one of Equation (18) derived for a completely different situation; in both cases stable behavior will be guaranteed if and only if

$$-dP/d\delta < K_M \qquad (27)$$

As in the last section, note that this condition is completely general and agrees with that one obtained from the tearing instability theory. This condition obtained from the tearing instability theory agrees with Equation (18) obtained on a completely general basis, based on nothing else but the principle of equilibrium. As a result, the tearing instability theory has proven to be always valid for load controlled conditions in the sense that instability will occur if and only if $\Delta T < 0$. Note that as before, if any other parameter $X = X(\delta, a)$ was used instead of J, the resulting X-based tearing moduli, T_{matX} and T_{appX}, will provide an automatically validated tearing instability condition.

Finally, it is to be noted that Equations (15) and (27) are the same although they represent completely different situations. The former was obtained for a specimen in series with the spring under displacement control, while the latter was obtained for a specimen in parallel with the spring under load controlled conditions.

2.4 J-T Diagrams

In the last sections attention was devoted to the development of formula for T_{app} for different situations. Although since the original work of Paris et al.[7-8], significant effort was also devoted to experimentally verify the tearing instability theory. Joyce et al.[13], Vassilaros et al.[14] and Kamimen et al.[15] among others conducted several experimental programs to do this. The basic philosophy has been the same as that one of the initial work of Paris et al.[7-8]; select a certain material-specimen geometry combination and run a series of displacement controlled tests of specimens in series with a spring whose compliance could be changed from test to test. Values of T_{mat} were obtained as the normalized slope of the J-R curves and T_{app} values were obtained using some of the different schemes[6-11,16].

As was mentioned earlier at the beginning, the results were reported in a T_{mat} vs T_{app} plot similar to that of Figure 3, but later on, it was realized that in general neither T_{mat} nor T_{app} were constant in a given test. As a consequence, the results were shown in a J-T plot as shown in Figure 8. Slopes of the J-R curves were obtained at different J levels and after normalized replotted in a J vs T_{mat} frame. At the same time, using some of the schemes mentioned above values of T_{app} were obtained for different J levels and also plotted in the J-T frame. Every time that the two curves intercepted, instability was expected to occur at the intersection of the two curves; if the test were stable, the two curves should not intersect. If that was the case, instability was properly

predicted by the tearing instability theory and thus the latter was said to be validated. The results, as predicted by the last section analyses, have proven to always validate the tearing instability theory.

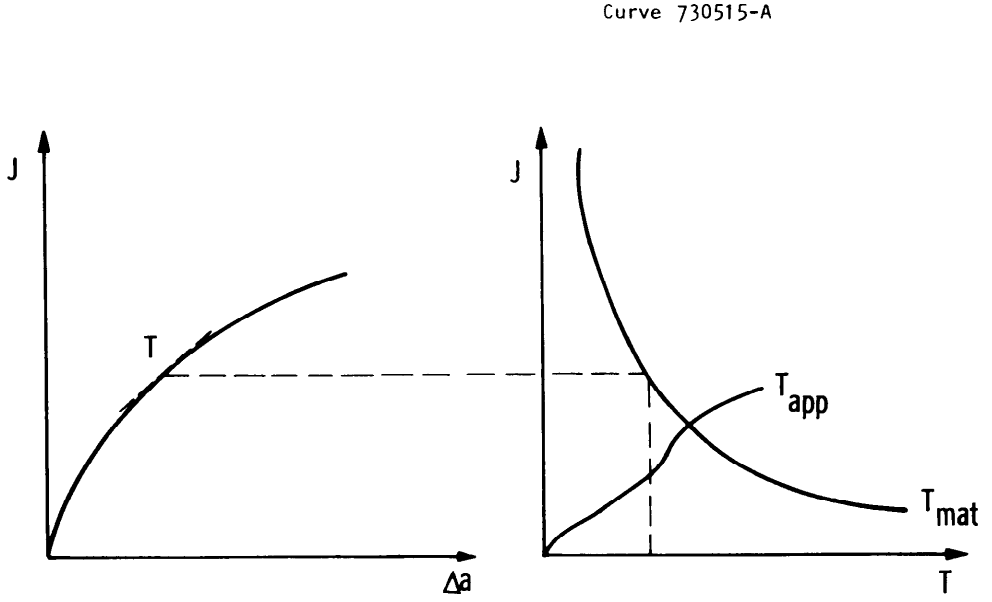

Fig. 8 J-T Diagram

3. METHODOLOGY FOR STRUCTURAL ANALYSIS

In the previous section the solution to the ductile fracture stability problem in a structure was given with the model of a test specimen in series or parallel with a spring. The test specimen represents a cracked component in a structure. It provides the resistance to increased crack extension. The spring in series represents the driving force tending to pull the structure to instability in a displacement limited structure. The spring in parallel represented redundant components resisting instability in a structure under applied loading. The problem of predicting instability in the structure is simple if the cracked component is identical in geometry to the laboratory specimen used to generate fracture resistant R curves. The problem to be solved in providing a methodology for structural analysis is that of predicting stability when the cracked component represents a different geometry from that of the test specimen. This problem can be solved without conducting a test for each new geometry if two sets of information can be generated for that new cracked geometry. They are the calibration functions for the geometry which relate load, displacement and J as a function of crack growth. The second piece of information is the materials resistance to crack extension which is given by the R curve for the cracked structural geometry.

Experimental data obtained in a program for the Electric Power Research Institute were used to show the adequacy of this approach. The program is described in detail in References[21-22]. Basically, it consisted of the R-curve testing of compact tension specimens (CT) of different planar sizes, thickness B and crack aspect ratio a/W, of a A508 Class 2 steel at 400°F.

Out of the large test matrix some specimens were selected for this study. These specimens were geometrically similar. All of them had an a/W = 0.6 and the thickness B was half of the total width W in all cases. The overall size ranged from 1/2T (W = 1 in) to 10T (W = 20 in). The resulting J-R curves showed consistency at the early stages but, as expected, the different curves start deviating when the crack length increment Δa was significant compared to the ligament b.

The J-Δa curves were then converted to J-T plots. The result is shown in Figure 9. Here the differences between specimens are more obvious than in the regular J-R curve plot. It can be seen for lower T_{mat} (higher J) the "peeling off" of the smaller specimen curves occur. In fact, as was mentioned before for some specimens, T_{mat} is close to zero (even negative for the 1/2T ones). The same data were replotted using the J_M in a J_M-T_{Mmat} frame. Using for J_M and T_M

$$J_M = J_D + \int_{a_o}^{a} (1 + 0.76\ b/W)\ \frac{J_{pl}}{b}\ da \qquad (28)$$

$$T_{Mmat} = \frac{E}{\sigma_o^2}\ \frac{dJ_M}{da} = T_{mat} + \frac{E}{\sigma_o^2}\left(\frac{1 + 0.76\ b/W}{b}\right) J_{pl} \qquad (29)$$

As can be seen in Figure 10, all the curves collapse into one when J_M and T_{Mmat} are used, even for the last points of the smallest specimens. This basically means that J_M is correlating data for situations well beyond the so-called J controlled crack growth and crack extension up to 30% of the initial remaining ligament. This basically means that J_M is a better parameter to use for describing the material resistance to significant crack growth, and that its use for R curve representation makes maximum meaningful use of the information obtained from small specimens, well beyond the J controlled crack growth regime with no unnecessary reduction in the predicted toughness capability.

3.3 Methodology

When the two components needed in applying the methodology are determined (the calibration curves and the R curve for the cracked geometry representing the structure) the complete response of that structure to an applied loading can be determined. From this response load versus displacement plots or J versus T diagrams can be determined. The stability of the structure or maximum load capacity can be assessed.

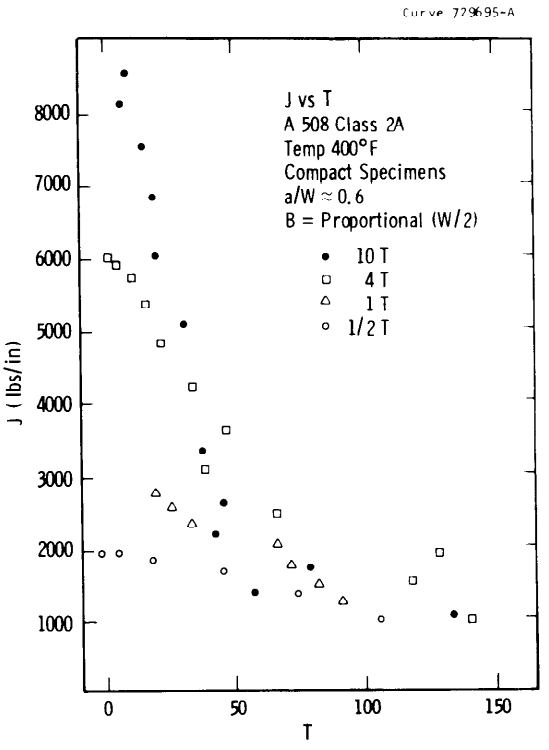

Fig. 9 J vs T, based on deformation theory of plasticity

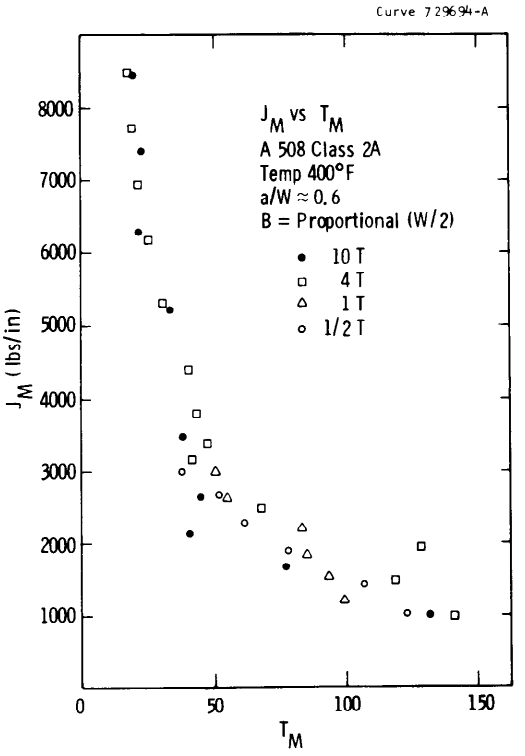

Fig. 10 Modified J vs modified tearing modulus

The complete methodology is represented by a flow diagram in Figure 11. The structural cracked geometry model is taken with the material tensile properties to determine the calibration functions for that geometry. The R curve determined from a laboratory test specimen is represented in the J_M versus Δa format. This represents the geometry independent material property needed to assess the resistance to crack growth in the structural cracked geometry. The calibration curves and the R curve are then combined to produce load versus displacement or J-T curves for the model geometry. From these maximum load bearing capacity and stability of the structure are assessed. These can then be compared with the design requirements for the structure to determine whether the material toughness is adequate. Inadequate toughness would require that some point in the initial input be changed. This could be a modification of design requirements, the selection of a material with superior toughness or even a reanalysis of the structure using a more refined model for the cracked component in the structure.

3.4 Discussion

The methodology presented here represents in principle a complete approach to assessing the load bearing capacity and stability characteristics of any cracked structural geometry. In practice there are many steps in the methodology which need further assessment and development.

3.1 Calibration Curves

The calibration functions can be obtained from the load versus displacement behavior for the non-growing crack. One method for obtaining the calibration curves for a given cracked geometry is by the Shih-Hutchinson estimation procedures.[17-18] This procedure allows displacement and J to be calculated as a function of load and crack length. Inputs needed for this estimation procedure are the tensile properties of the material including the elastic modulus, E, the strain hardening exponent, n, and the proportionality constant, α, in the Ramberg-Osgood representation of hardening behavior. All of the constants can be obtained from a tensile test which measures the true stress-strain behavior.

The Shih-Hutchinson estimation procedure has been applied to a number of different cracked geometries using the finite element calculation method. The results of these calculations are summarized in a Handbook published by the Electric Power Research Institute.[19] Although this Handbook does not cover all possible geometries of interest and the accuracy of the estimation procedure itself has not been assessed experimentally, it does represent a viable method for obtaining calibration curves for many different types of cracked geometries.

The first part needed to apply the methodology, that of determining calibration curves for the cracked structure, has been solved by the estimation procedure. The results are available in handbook form and can be used by a competent engineer.

3.2 R Curve

The second piece of information needed to apply the methodology is the R curve for the material and cracked geometry used in modelling the structure. This is a more difficult piece of information to obtain. It is known that R curves may be geometry dependent so that one determined from a laboratory test specimen may not be appropriate the cracked geometry which represents the structure. What is needed is a way to represent the R curve as truly a material property independent of all specimen geometry considerations. One step toward establishing the R curve as a material property was taken in specifying limitations for J controlled crack growth.[6] This approach stated that a geometry independent R curve can be developed on a laboratory test specimen which is appropriate for the cracked structural geometry if certain limitations can be met for both the laboratory specimen geometry and the cracked structural geometry.

Unfortunately, the limitations are not often met for typical materials used in building structures. A significant step in developing a geometry independent R curve came from the work of Ernst[20] in which he suggested a modified J parameter, J_M, which could be used to characterize the R curve behavior. R curves plotted with J_M were not subject to the same limitations imposed on the traditional deformation J-R curve representation.

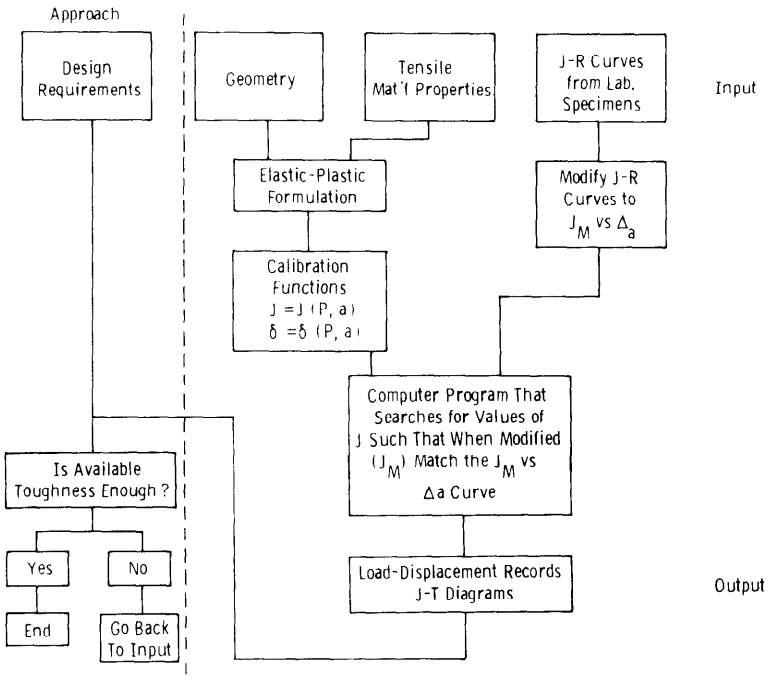

Fig. 11 Elastic plastic methodology

The determination of the calibration functions is the most advanced part of the method. The Handbook[19] containing the Shih-Hutchinson estimation procedure solutions provides the information needed to develop calibration curves. However, the number of solutions in the Handbook is presently limited and may not exist for a given structural model. Methods for adapting a solution to a different geometry or combining solutions to best fit a structural model have not been developed. Also the solutions in the handbook were developed by finite element computations and their accuracy has not been verified independently by another method such as an experimental evaluation. Nevertheless, these Handbook solutions represent the best approach presently available for developing calibration curves for models of cracked structural components.

The R curve evaluation for the structural model represents the most difficult part of applying the methodology. The method developed by Ernst[20] representing the R curve with the modified J, J_M, is the most promising approach to developing a geometry independent material property. However, this approach is still in the early stages of development and cannot be applied with complete confidence. Certainly this approach would have inherent limitations and these have not been determined.

This methodology does present a complete approach for evaluating a cracked structure. The present limitations and uncertainties involved in the method suggest areas where further work is needed to develop confidence in this approach.

4. SUMMARY

A methodology is described in this paper for assessing the structural stability of a cracked component. The method incorporates new EPFM concepts through the use of a J based R curve and tearing instability analysis. The central feature of the methodology is a model of the cracked structural geometry which is combined with a spring in series or parallel for the stability analysis. The method is based on the analysis of the response of the structural to deformation, labeled the calibration curves, and the response of the material and structure to crack advance, the R curve.

The calibration curves are evaluated through the Shih-Hutchinson estimation procedure. Results for this procedure are available in an EPRI published Handbook. The R curve is evaluated as a geometry independent material property using the modified J_M approach developed by Ernst. By combining the R curve and the calibration curves a complete description of the fracture behavior can be given for the structural model. Such things as maximum load bearing capability and structural stability can be assessed.

The methodology is complete and in principle can apply to any structural geometry. However, some of the more practical details of the approach need further development.

5. ACKNOWLEDGMENT

The authors acknowledge the support of the Office of Naval Research through Contract N00014-80-C-0655. Dr. O. Arora of DTNSRDC, Annapolis is the contract monitor.

6. REFERENCES

1. J. R. Rice, "A Path Independent Integral and the Approximate Analysis of Strain Concentration by Notches and Cracks," Journal of Applied Mechanics, 35: 379-386 (1968).

2. J. W. Hutchinson, "Singular Behavior at the End of Tensile Crack in a Hardening Material," Journal of the Mechanics and Physics of Solids, 16 (1): 13-31 (1968).

3. J. R. Rice and C. F. Rosengren, "Plane Strain Deformation Near a Crack Tip in a Power Law Hardening Material," Journal of the Mechanics and Physics of Solids, 16 (1): 1-12 (1968).

4. J. A. Begley and J. D. Landes, "The J Integral as a Fracture Criterion," Fracture Toughness, ASTM STP 514, pp. 1-23 (1972).

5. J. D. Landes and J. A. Begley, "The Effect of Specimen Geometry on J_{Ic}," Fracture Toughness, ASTM STP 514, pp. 24-39, (1972).

6. J. W. Hutchinson and P. C. Paris, "Stability Analysis of J-Controlled Crack Growth," Elastic-Plastic Fracture, ASTM STP 668, pp. 37-64 (1979).

7. P. C. Paris, H. Tada, A. Zahoor, and H. A. Ernst, "The Theory of Instability of the Tearing Mode of Elastic-Plastic Crack Growth," Elastic-Plastic Fracture, ASTM STP 668, pp. 5-36 (1979).

8. P. C. Paris, H. Tada, H. A. Ernst and A. Zahoor, "An Initial Experimental Investigation of Tearing Instability Theory," Elastic-Plastic Fracture, ASTM STP 668, pp. 251-265 (1979).

9. H. A. Ernst and P. C. Paris, "Techniques of Analysis of Load Displacement Records by J-Integral Methods", Nuclear Regulatory Commission NUREG/CR-1222, January 1980; also available as H. A. Ernst, PhD Thesis, Department of Mechanical Engineering, Washington University (St. Louis, MO), December 1979.

10. H. A. Ernst, P. C. Paris, and J. D. Landes, "Estimation on J-Integral and Tearing Modulus T from a Single Specimen Test Record," Fracture Mechanics: Thirteenth Conference, ASTM STP 743, Richard Roberts Ed, American Society for Testing and Materials, 1981, pp. 476-502.

11. H. A. Ernst, "Some Salient Features of the Tearing Instability Theory," presented at the Second International Symposium on Elastic-Plastic Fracture Mechanics, ASTM, Philadelphia, October 1981.

12. Paris, P. C., Tada, H. and Baldini, S. E., "Fracture Proof Design" CSNI Specialists Meeting on Plastic Tearing Instability held at the Center for Fracture Mechanics, Washington University, St. Louis, MO., September 25-27, 1979. U.S. Nuclear Regulatory Commission Report, Nureg CP-0010, January 1980.

13. J. A. Joyce and M. G. Vassilaros, "An Experimental Evaluation of Tearing Instability Using the Compact Specimen," 13th National Symposium on Fracture Mechanics, American Society for Testing and Materials, 1981.

14. M. G. Vassilaros, J. A. Joyce and J. P. Gudas, "Experimental Verification of the Tearing Instability Phenomena for Structural Materials," presented at the 14th National Symposium on Fracture Mechanics, Los Angeles, CA, July 1981.

15. Kanninen, M. F., Zahoor, A., Wilkowski, G. M., Abou-Sayed, I. S., Marschall, C. W., Broek, D., Sampath, S. G., Rhee, H. D., and Ahmad, J., "Instability Predictions for Circumferentially Cracked Type 304 Stainless Steel Pipes Under Dynamic Loading," Battelle's Columbus Laboratories Final Report to the Electric Power Research Institute on T118-2, in preparation, June, 1981.

16. Zahoor, A., "Tearing Instability of Elastic-Plastic Crack Growth", Ph.D. Dissertation, Washington University, St. Louis, MO, August 1978.

17. Hutchinson, J. W., Needleman, A. and Shih, C. F., "Fully Plastic Problems in Bending and Tension", to be published in the Proceedings of an ONR International Symposium on Fracture Mechanics, Washington, DC, September 1978.

18. Shih, C. F., "J Integral Estimates for Strain Hardening Materials in Antiplane Shear Using Fully Plastic Solution," Mechanics of Crack Growth, ASTM STP 590, American Society for Testing and Materials, 1976, pp. 3-26.

19. Kumar, V., German, M. D., Shih, C. F., "An Engineering Approach for Elastic-Plastic Fracture Analysis," Electric Power Research Institute, NP1931, July 1981.

20. Ernst, H. A., "Material Resistance and Instability Beyond J Controlled Crack Growth," to be presented at the Second International Symposium on Elastic Plastic Fracture Mechanics, October 1981, Philadelphia, PA.

21. McCabe, D. E., Landes, J. D., "J_R Curve Testing of Large Compact Specimens", presented at the Second International Symposium on Elastic Plastic Fracture Mechanics, Philadelphia, October 1981.

22. McCabe, D. E., Landes, J. D., Ernst, H. A., "An Evaluation of the J_R Curve Method for Fracture Toughness Characterization", presented at the Second International Symposium on Elastic Plastic Fracture Mechanics, Philadelphia, PA, October 1981.

FLAW DETECTION RELIABILITY ASSESSMENT AND ANALYSIS

by Ward D. Rummel
Manager Advanced Quality Technology
and
Richard A. Rathke
Staff Quality Engineer
Martin Marietta Corporation
Denver Aerospace

ABSTRACT

The assessment of nondestructive flaw detection reliability is complex in character due to the varied engineering and scientific disciplines involved. The evolution of nondestructive flaw detection reliability demonstration and assessment has involved varied efforts by workers in various industries, applications and environments. A significant data base has been established and has contributed to a general understanding of the elements of inspection reliability. A considerable number of analyses have been performed to effect a better understanding of the problem and to identify critical factors in both the inspection process performance and in reliability assessment.

This paper reviews principle factors in nondestructive flaw detection process performance and suggests an alternative approach to the analysis of performance data. The approach includes consideration of the conditional probability character of flaw detection and consideration for predictive modeling based on signal and noise analyses of flaw detection by instrumental techniques and by human operators.

INTRODUCTION

Nondestructive inspection has been incorporated as an integral part of modern engineering structures design in both critical and non-critical applications. The assessment of nondestructive flaw detection reliability is complex in character due to the number of parameters that must be accounted for and to the varied disciplines involved. For critical applications, the reliability of inspection processes must be assured to provide confidence in the functional integrity and performance of critical materials, structures or components. Measurement and assessment of nondestructive inspection reliability requires multi-parameter assessment and documentation under controlled conditions. Indeed, much of the reliability data and data analyses that have been generated are confusing and appear to be contradictory. The following discussion provides an approach to the understanding and modeling of nondestructive inspection processes with respect to overall process reliability.

THE NATURE OF INSPECTION RELIABILITY ASSESSMENT

The task of measuring inspection reliability differs from that of initial inspection selection by a shift in emphasis from the smallest flaw detected to the largest flaw missed. An inspection process constitutes an exercise in conditional probability as opposed to joint probability due to the interdependence of inspection stimuli and inspection responses. A schematic presentation of such interdependence is shown in the following:

		STIMULI	
		POS a	NEG n
RESPONSE	POS A	M(Aa) T.P. P(A,a)	M(An) F.P. P(A,n)
	NEG N	M(Na) F.N. P(N,a)	M(Nn) T.N. P(N,n)

The outcome of the inspection test may be:

TRUE POSITIVE (T.P.),
where M(Aa) is the total number of T.P. calls;
and P(A,a) is the probability of T.P. calls.

FALSE POSITIVE (F.P.),
Where M(An) is the total number of F.P. calls;
and P(A,n) is the probability of F.P. calls.

FALSE NEGATIVE (F.N.),
where M(Na) is the total number of F.N. calls;
and P(N,a) is the probability of F.N. calls.

TRUE NEGATIVE (T.N.),
where M(Nn) is the total number of T.N. calls;
and P(N,n) is the probability of T.N. calls.

Interdependence of the matrix quantities is denoted by:

T.P. + F.N. = Total opportunities for positive calls.
F.P. + T.N. = Total opportunities for negative calls.

Therefore, only two independent probabilities must be considered in alternative inspection / decision tasks.

The SPECIFICITY of the technique or the PROBABILITY OF DETECTION of flaws may be expressed as:

$$POD = \frac{T.P.}{T.P. + F.N.} \text{ or } \frac{\text{total positive calls}}{\text{opportunities for positive calls}}$$

Likewise, the NONSPECIFICITY of the technique of the PROBABILITY OF FALSE ALARMS may be expressed as:

$$POFA = \frac{F.P.}{T.N. + F.P.} \text{ or } \frac{\text{total false alarms}}{\text{opportunities for false alarms}}$$

Confidence limits for the probability of detection value may be calculated from standard tables for a given sample size and calculated value from experimental sample data. This technique establishes an estimate for performance at one flaw size value, calibration level and acceptance criteria level. Data of most interest to the design engineer, nondestructive inspection engineer and systems manager is plotted as a composite of the discrete values calculated for individual operating points.

PROBABILITY OF DETECTION (POD) CURVES

The established method of assessing and presenting inspection reliability data is by means of a probability of detection or POD curve as shown in FIGURE 1. A POD curve is generated by passing a series of specimens that contain a large number of flaws of varying flaw sizes, through a nondestructive inspection process and documenting the success in detecting all flaws. Flaws are then ordered from large to small in terms of decreasing flaw size and are grouped to provide a statistically significant sample size for analysis. Sampling to provide a 95% confidence level (MIL Handbook No. 5, B values) is attained by grouping samples into lots of 60 observations (REF 1). The point estimate of detection for the sample group is calculated by dividing the total number of opportunities for the sample group into the total number of successes (flaws detected). The point estimate (probability of detection) is plotted at the largest flaw size in the sample group. The process is repeated to generate a curve that denotes the probability of detection as a function of flaw size (FIGURE 1). This method of data presentation was introduced by Rummel et al (REF 2) in 1971 and has been adopted as the standard method for inspection reliability data presentation. The method has been used by various investigators to plot both controlled experimental data sets and uncontrolled experimental data sets. A measure of the capability of a specific inspection technique for flaw detection can be derived when the method is used to analyze controlled experimental data. A measure to the overall baseline capability for a facility, organization, etc. can be derived when the method is applied to unlike (uncontrolled) inspection operations.

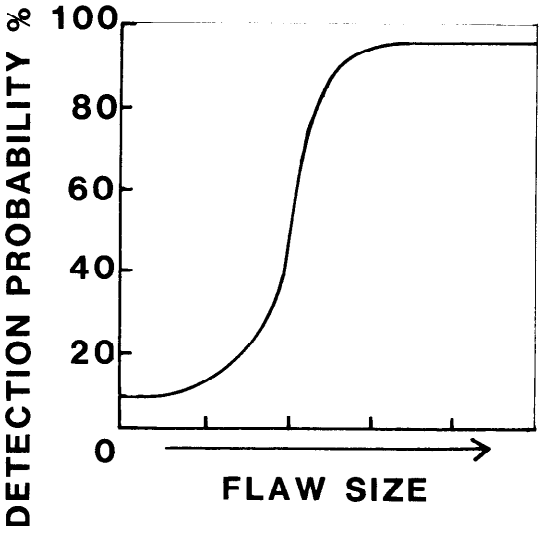

Figure 1 Typical Form of a Probability of Detection (POD) Curve

The shape of the POD curve provides a qualitative basis for assessment of the degree of control for a given data set and by the criteria for grouping of similar data sets. FIGURE 2, illustrates the POD curves for the data sets generated under varying condition of control. Curve A is typical of an inspection process that is under control and that is discriminatory (specific) to the desired output. Curve B is typical of a process that is approaching control. The mode and type of variance denote the influence of factors not accounted for in the direct correlation of process performance with flaw size. Curve C is typical of a process that is out of control but whose performance is influenced by flaw size. Curve A is worthy of further statistical rigor. Curve B is worthy of further analyses to ascertain the nature of secondary variances. Curve C is worthy of further analyses to improve the process or to provide a measure of inspection discrimination by sampling. Flaw size is a secondary variance in Curve C at the operating point for the inspection. Identification and control of the primary variance will change the nature of the data set, the specificity of the technique and the resultant POD curve.

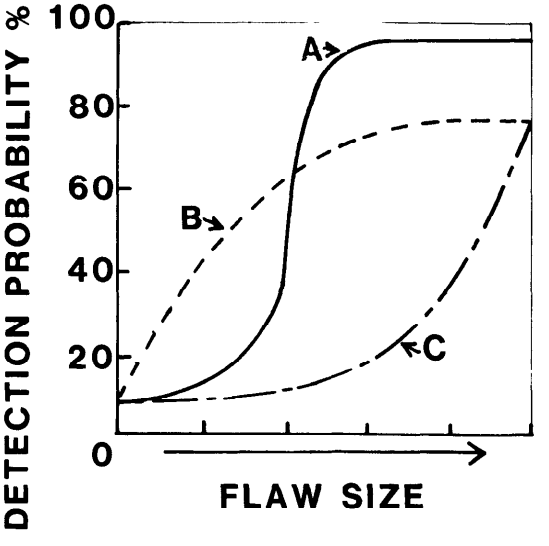

Figure 2 Typical Probability of Detection (POD) Curve Under Varying Conditions of Process Control

Each POD curve is unique to the specificity of the inspection process, the degree of control effected in the inspection process and to the nature and distribution of flaws being assessed. Rigorous use of the data in specific applications is limited to the specific process, control and flaw distribution conditions used in data generation. The cost of generation, precision in data collection and the discipline required for specific applications have fostered many attempts to generalize and model POD curve prediction. To date, no satisfactory model has been developed and some modeling attempts have contributed to the confusion in application and in data generation. Since many critical inspections are currently performed by skilled operators using manual techniques, human factors are most frequently cited as the source of unreliability. Although human factors are a primary contributor to unreliability, nondestructive test engineering and engineering management (selection and control of the right tool for the job) are proposed by the authors to be greater sources of unreliability in general applications. Such errors will not be alleviated by the automation of inspection processes. An understanding of the nature and character of inspection processes is necessary to predict and to effect improvements. Automation without understanding will only lead to multiplication of errors.

CONSIDERATIONS FOR MODELING OF INSPECTION PROCESSES

The POD curve provides a convenient method for comparison of inspection process performance. It provides visualization of the discrimination capability of a given technique in a form that communicates to the designer, the system manager and to the nondestructive inspection engineer. The POD curve does not, however, provide an indication of the calibration performed to establish the baseline process, the acceptance criteria imposed on the process or the level of incorrect rejections (false calls) inherent to the process / application.

Selecting an exact operating point from the POD curve is difficult and has not proven to be meaningful in many applications. Variation in a point on the curve is due to variation in response of the system and variation in the reproducibility of the inspection process application. For example, flaw size measurement by nondestructive inspection processes has been shown to be variable within a technique and between techniques (REF 3,4). The distribution of response of an interrogating energy field accounts for variation in flaw sizing by nondestructive inspection processes and to part of the variation in POD curve generation. This "third dimension" of analysis must be accounted for in an inspection model. Variation in response along a POD curve is shown schematically in FIGURE 3.

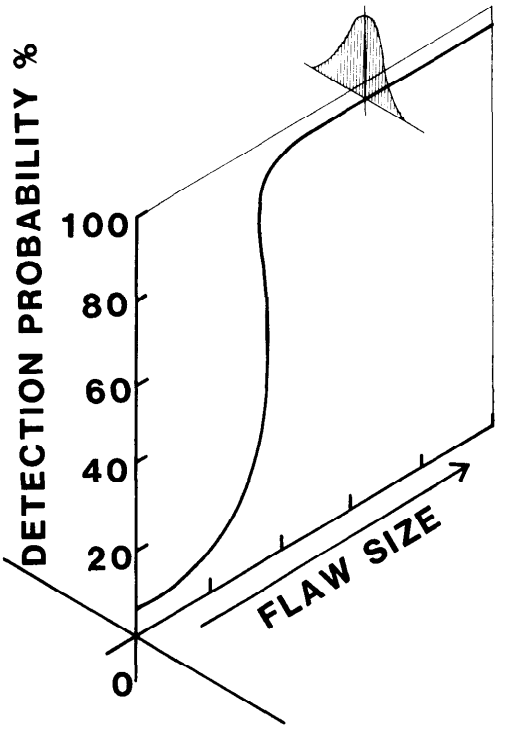

Figure 3 Interaction of the Probability of Detection (POD) Curve with the Distribution of Flaw Response

SIGNAL / NOISE VARIATIONS AND THE POD CURVE

Consider a case where the response (signal) from a flaw is "Gaussian" in nature and where process noise is well separated from the signal (FIGURE 4). Such an inspection has high specificity for discrimination of signals that are due to flaw responses from background or process noise signals that are inherent to the process.

Consider a second case where the response (signal) from a flaw is "Gaussian" in nature with process noise signals overlapping the flaw response envelope (FIGURE 5). A threshold (signal) discrimination level may be set for this process to provide a degree of separation of flaw responses from inherent process noise. Some flaws will be missed by such a system and some false calls (rejections) will be inherent to the process. The lack of specificity will cloud the use of the process as a final discriminator.

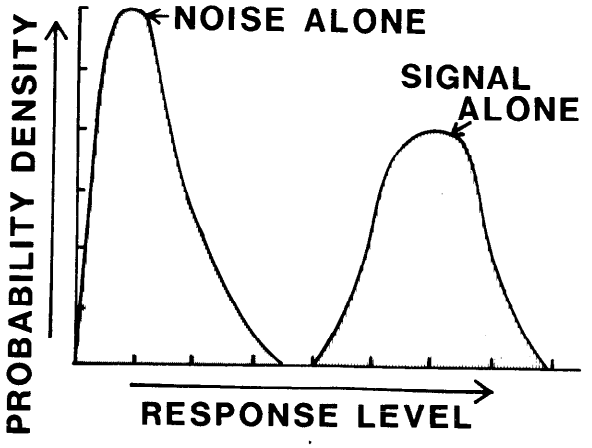

Figure 4 Signal / Noise Response for Discrimination with a High Degree of Specificity

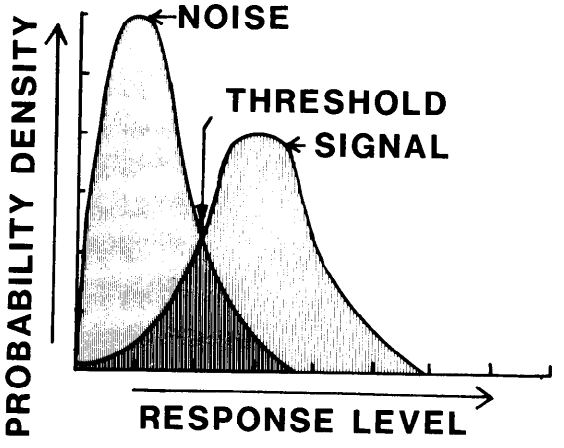

Figure 5 Signal / Noise Response for Discrimination with Overlapping Signal and Noise Stimuli

Consider a third case where the response (signal) from a flaw is coincident with the process noise signals (FIGURE 6). Such a process provides a random discrimination of flaws and is not considered to be a valid process. Indeed, better separation is likely by simple coin flipping.

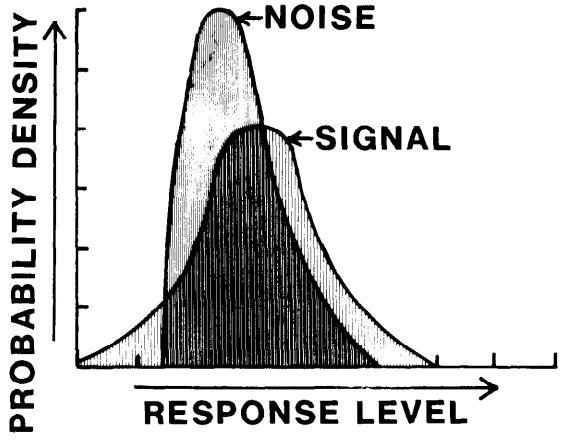

Figure 6 Signal / Noise Response for Coincident Stimuli

A POD curve typically reflects all of the variations in signal / noise response and discrimination levels as shown schematically in FIGURE 7. A continuing variation in signal / noise response is reflected by variation in the discrimination level along the POD curve. The signal / noise response and the discrimination level appear to be "common denominators" for all inspection processes and hence all POD curves generated for respective processes.

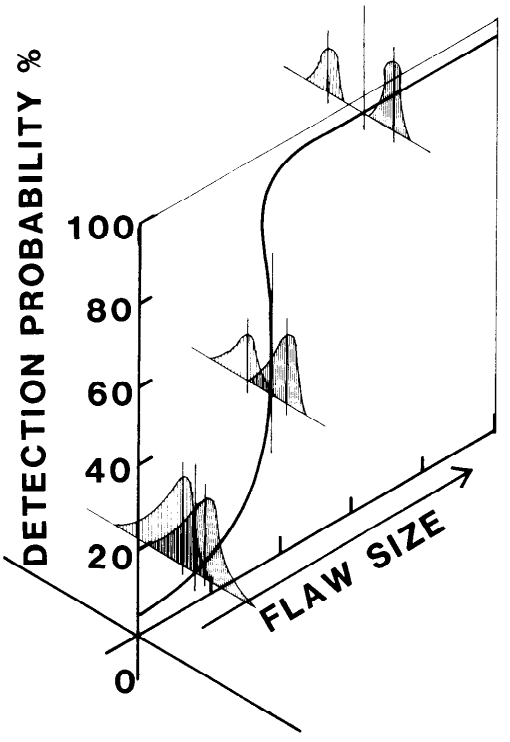

Figure 7 Interaction of Signal / Noise Discrimination with the Probability of Detection (POD)

CRITERIA DISCRIMINATION RESPONSE AND THE POD CURVE

A second factor (common denominator) that may be shown to affect the mode and specificity of an inspection process is the criteria level selected. Consider an inspection process with a measurable separation in noise and flaw signal responses as shown in FIGURE 8. If the acceptance (discrimination) criteria level for this inspection (indicated by the vertical arrow) is set too high, some flaws will be accepted (missed) by application of the process and "EVERYBODY WILL BE UNHAPPY". If the acceptance criteria is set at a level that provides clear separation of noise signal from flaw signal, all flaws will be rejected, few false calls (rejections) will occur and "EVERYBODY WILL BE HAPPY". If the acceptance criteria is set too low, all flaws will be rejected, some false calls (rejections) will occur and "MANAGEMENT WILL BE UNHAPPY".

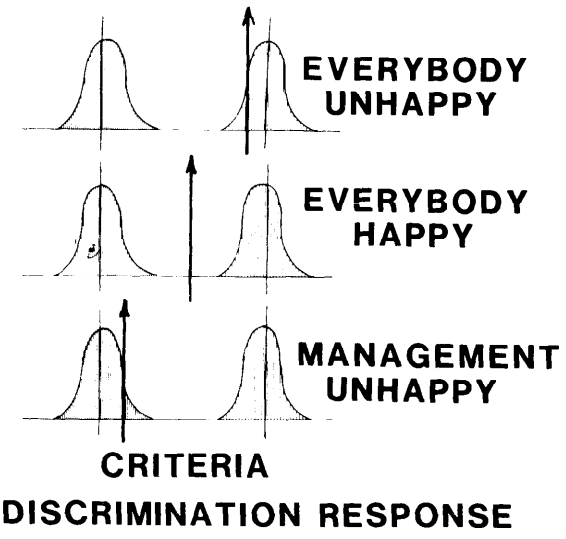

Figure 8 Influence of Acceptance Criteria Level (Vertical Arrow) on Process Discrimination (Specificity)

The process specificity and hence its POD curve may be affected by changes in the acceptance criteria level. FIGURE 9 illustrates the effects of varying levels of criteria discrimination levels on performance as denoted by the POD curve. It is important to note that the criteria discrimination level is a function not only of the rejection level imposed on an inspection process but also of the calibration reference standards and criteria used to set-up and validate inspection process performance.

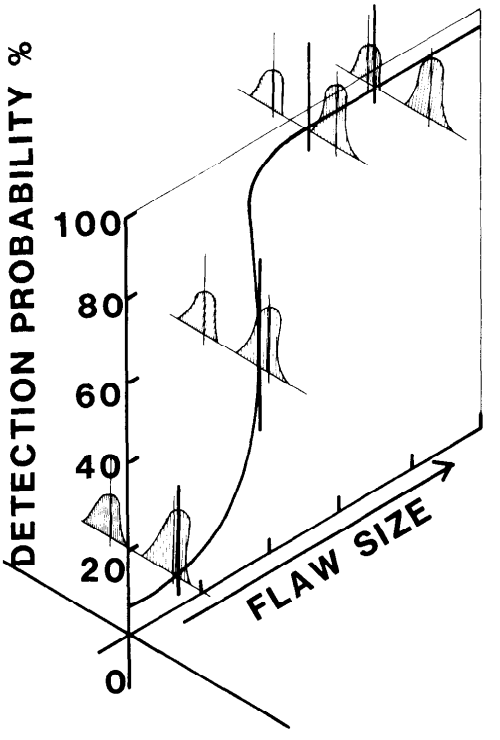

Figure 9 Interaction of Acceptance Criteria with the Probability of Detection (POD)

INSPECTION FACTORS AND SIGNAL / NOISE RESPONSE

Variations in the condition of the flaws to be interrogated and variations in inspection conditions will affect the signal / noise function of the inspection process and its resultant discrimination level. FIGURE 1Ø illustrates some known and projected variations in flaws and process applications on the signal / noise response. Experimental data on the effects of variation of a single parameter on the overall signal response have been documented by various investigators. (REF 5,6) It is now clear that documentation of the calibration technique and the process noise for the inspection is necessary to account for parameter variations in a predictive model.

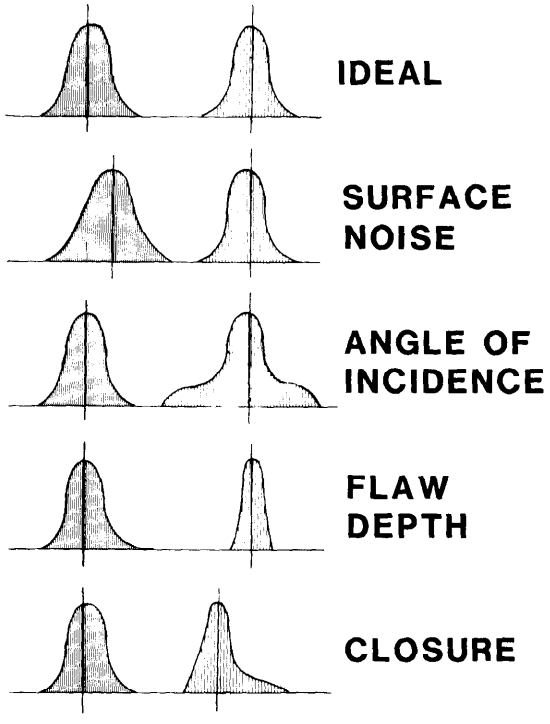

Figure 1Ø Interaction of Flaw Condition with Signal / Noise Discrimination

PREDICTIVE MODELING OF INSPECTION PROCESS PERFORMANCE

Generation of POD curves and qualification of inspection processes are tedious, time consuming and expensive. At present, POD curves are unique to the inspection process and process application and cannot be used for a second process or process application. For critical applications, experimental qualification and validation are required and must be completed for each process and process application.

Current work is under way to approach predictive modeling based on "first principles" to calculate behavior and interaction of an energy field in a given application (REF 7). The approach and emphasis of this important work will provide a prediction of the performance level (POD) for an inspection process for calibration and validation at a given signal / noise level. Ultrasonic (REF 8) and eddy current (REF 9) models have been initiated as first steps in providing the engineering tools for future nondestructive process applications.

Predictive modeling would be of significant advantage in both the qualification of additional inspection processes and in reconsideration of current processes. Consider the case of cracks emanating from a radius area in a slot as shown in FIGURE 11. An eddy current inspection had been developed and qualified for cracks emanating from the center of the radius. The inspection consisted of inserting an eddy current probe, with a small ferrite core, into the radius area such that it touched the center of the radius in a plane passing through the center of curvature of the radius. After qualification and validation, crack intiation was discovered at both points of tangency of the radius area. Predictive modeling / analysis tools could have been used to calculate the size of cracks that could be reasonably detected by the center probe technique. Actual requalification and validation were necessary to establish the performance level with the analysis tools that are currently available.

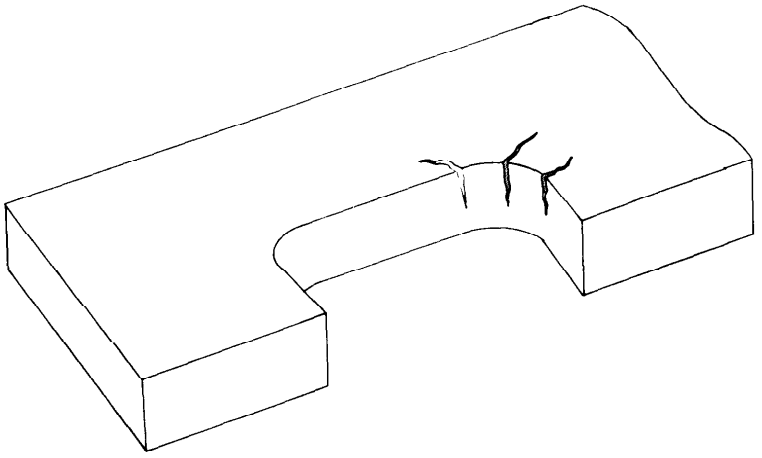

Figure 11 Variation in Location of Service Cracks in Typical Engineering Hardware

HUMAN FACTORS VARIATIONS ON INSPECTION RELIABILITY

The impact of human factors on inspection reliability have been discussed by various investigators and have been considered to be a primary factor in "unreliability" of a given inspection process. It is therefore important to separate and measure human factors response and variations in application of inspection processes. Recent work by Swets and Pickett (REF 12) provide a logical basis for assessment of the human factors variable in an inspection process. The technique consists of establishing an inspection process with known variation in signal response and known discrimination response criteria. By repetitive measurement of human response / discrimination to the signal stimulus, a performance level may be established and used in prediction for a variety of applications. Swets and Pickett propose development of a "RELATIVE OPERATING CHARACTERISTICS (ROC)" curve (FIGURE 12) as the method of displaying and analyzing human factors data. This curve visualizes the human factors contribution at an established signal / noise level, and various discrimination levels, for a single point on the POD curve. The primary advantages of this method are the use of signal / noise and discrimination criteria as factors in assessment, and in previous use of the method in similar inspection / detection processes.

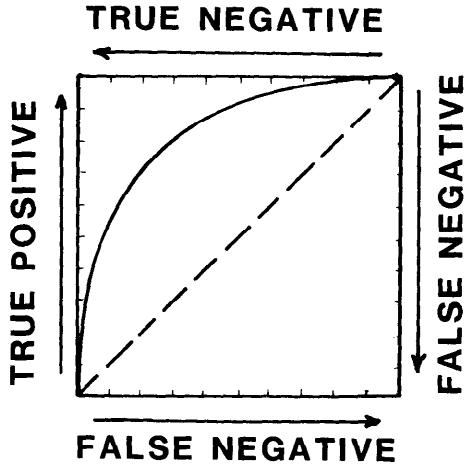

Figure 12 Typical Relative Operating Characteristic (ROC) Curve (REF 10)

CONCLUSIONS

Flaw detection reliability assessment is indeed a complex process that requires consideration of many factors in both application processes and in assessment. Signal / noise response at a given discrimination (criteria) level have been introduced as "common denominators" to both characteristic inspection process performance and human factors performance. The combined performance levels may be summarized by plotting a probability of detection curve (POD) curve for the inspection process and application. The human factors contribution to the output must be minimized for "controlled data" that is used for assessment of the capability of a process.

Reliable flaw detection may be effected by knowledge of the nature and boundary conditions for signal response in a given inspection task. Such analysis is necessary to provide the nondestructive inspection engineering that is necessary for application to critical inspection processes. Experience by the authors has shown that inspection process qualification is probable for those applications where a consistent response is obtained at a minimum signal to noise response of 3 to 1 for flaws one-half the minimum size required by design acceptance criteria.

Progress is being made for predictive inspection modeling based on "first principles" of energy interaction and scattering. Such techniques will be a primary tool for all future nondestructive inspection engineering analyses. Process modeling, together with human factors modeling will provide the necessary tools for improvement of productivity and for automation of inspection processes in future applications.

REFERENCES

1. Beyer, W.H., Handbook of Tables for Probability and Statistics, 2nd Edition, CRC Press, Inc., Boca Raton, Florida, 1966.

2. Rummel, W.D., Todd, P.H. Jr., Frecska, S.A. and Rathke, R.A., "The Detection of Fatigue Cracks by Nondestructive Testing Methods", NASA CR-2369, February 1974.

3. Rummel, W.D. and Rathke, R.A., "Detection and Measurement of Fatigue Cracks in Aluminum Alloy Sheet by Nondestructive Evaluation Techniques," Transactions, Second Annual ASM Materials/Design Forum on Prevention of Structural Failure, April 9-11, Port St. Lucie, Florida.

4. Knorr, E., "Reliability of the Detection of Flaws and of the Determination of Flaw Size", AGARD Fracture Mechanics Survey, AGARD - AG - 176, January, 1974.

5. Martin, B.G. and Adams, C.J.,"Detection of Lack-of-Fusion in Aluminum Weldments by Ultrasonic Shear Waves," Materials Research and Standards, v.6, no. 9, September, 1966, 440-442.

6. Corbly, D.M., Packman, P.F., and Pearson, H.S., "The Accuracy and Precision of Ultrasonic Shear Wave Flaw Measurements As a Function of Stress on the Flaw", Materials Evaluation, v. 30, no.5, May 1970, 104-110.

7. Thompson, D.O., Review of Progress in Quantitative NDE, Ames Laboratory, Iowa State University, August 1982.

8. Fertig, K. Jr. and Richardson, J.M., "Computer Simulation of Probability of Detection", Review of Progress of Quantitative NDE, Ames Laboratory, Iowa State University, August 1982, 20-21.

9. Bahr, A.J. and Cooley, D.W., "Analysis and Design of Eddy Current Measurement Systems", Review of Progress of Quantitative NDE, Ames Laboratory, Iowa State University, August 1982, 28-29.

10. Swets, J.A. and Pickett, R.M., Evaluation of Diagnositic Systems, Academic Press, New York, 1982, 19-26.

SESSION III: COMPOSITE STRUCTURES

Chairman: T. E. Hess
Supervisor, Structures Research and Development Branch
Naval Air Development Center

COMPOSITE MATERIAL STRUCTURES FOR TACTICAL SHELTERS: A COST/WEIGHT STUDY 257

J. P. Fanucci, Kaman AviDyne

FAILURE ANALYSIS OF COMPOSITE LAMINATES USING A TENSOR POLYNOMIAL STRENGTH CRITERION 271

R. C. Tennyson, G. Elliott, and J. S. Hansen, University of Toronto

STATIC INDENTATION TESTS ON COMPOSITE PLATES FOR IMPACT SUSCEPTABILITY EVALUATION 288

G. M. Bostaph, Army Aviation R&D Command, and W. Elber, NASA-Langley Research Center

MECHANICS PROBLEMS IN COMPOSITE MAIN ROTOR BLADE DESIGN 318

R. L. Foye and D. J. Baker, Army Aviation R&D Command, and S. P. Petrie and A. O. King, Army Materials and Mechanics Research Center

AN EFFICIENT METHOD FOR DETERMINING THE "A" AND "B" DESIGN ALLOWABLES 343

D. M. Neal and L. Spiridigliozzi, Army Materials and Mechanics Research Center

DESIGN AND FABRICATION OF LOW COST COMPOSITE COMPRESSOR BLADES 380

C. D. Houghton, W. W. Houghton, and M. E. Roylance, Army Materials and Mechanics Research Center, and J. A. McElman, University of Lowell

EFFECTS OF SIMULATED LIGHTNING ON COMPOSITE AND METAL JOINTS 400

W. E. Howell, NASA-Langley Research Center, and J. A. Plumer, Lightning Technologies, Inc.

COMPOSITE MATERIAL STRUCTURES FOR TACTICAL SHELTERS - A COST/WEIGHT STUDY

Jerome Paul Fanucci
Research Scientist
Kaman AviDyne
83 2nd Avenue
Burlington, Massachusetts 02174

ABSTRACT

As part of an overall program sponsored by the U. S. Army Natick Research and Development Laboratories (NLABS) to develop a nuclear hardened, mobile, tactical shelter of minimum weight and cost, the application of three composite materials in future tactical shelters has been investigated. Nine shelter wall panels were designed using various combinations of material and panel cross sectional geometry. Acquisition cost and weight of the individual designs were estimated. The best of the graphite/epoxy configurations resulted in a 50% weight reduction from a baseline aluminum panel. The projected acquisition cost of this graphite panel was 3.3 times higher than the equivalent aluminum design. Predicted weight trends compared favorably with design experience reported by a variety of manufacturers. Aerospace industry pricing of composite versus metal production hardware suggests that predicted shelter panel acquisition costs have been substantially overestimated. Because composite technology is currently in a state of rapid growth and change, reliable cost information is relatively scarce. Evidence suggests that an expected reduction in composite shelter maintenance cost could result in a lower overall life cycle cost for the composite designs. If predictions for superior weight performance and lower life cycle cost are valid, it is probable that future tactical shelters will be fabricated largely from composite material.

INTRODUCTION

Mobile shelters are currently used by all branches of the service to house electronics equipment. These shelters are often required to be hardened against the effects of tactical nuclear weapons. The energy released by the detonation of a nuclear weapon is transmitted to a shelter in a variety forms. A powerful electromagnetic pulse (EMP), intense thermal and ionizing particle radiation, wind induced overturning, and blast overpressure all combine to threaten the integrity of the structure and the equipment it contains.

In most scenarios, blast overpressure loads are by far the most difficult for the structure to survive. Previous analytical and experimental studies [1,2] have shown that it is possible to construct a shelter capable of surviving the overpressure induced dynamic loads using aluminum. Unfortunately, the substantial increase in weight

required to harden a metal design against blast effects reduces usable payload and overtaxes mobilization systems.

The Army's Hardened Tactical Shelter (HATS) program [3] demonstrated that a cost and weight effective system designed to survive the entire spectrum of nuclear weapons effects can be constructed using Kevlar/epoxy composite material. The structural panels used in the HATS program were stiffened sandwich designs similar in configuration to those currently employed in metal shelters. The purpose of the work described in this paper was to systematically investigate the relative cost and weight of designs using graphite, Kevlar and S-glass/epoxy composites in four different structural panel configurations. A hardened 6061-T6 aluminum sandwich design was used to provide baseline values in this study.

A well optimized shelter takes advantage of potentially beneficial synergism in the materials used to harden against the various threats. For example, the aluminum EMP shield in the HATS shelter provided a significant proportion of the inner sandwich skins load carrying capability. This shelter's outer Kevlar thermal barrier supplied additional protection against ballistic penetration. Employment of such multi-function concepts in system design is obviously desirable. For the study described in this paper, however, considerable simplification was achieved by uncoupling the blast overpressure from the rest of the loads on the shelter. Preliminary analysis suggests that trends predicted by considering only overpressure effects will remain valid in a more completely optimized system.

For purposes of the comparison described in the following pages, nine different 220 x 80 inches (5.59 x 2.03 meter) side walls were designed for the International Standards Organization (ISO) shelter (Figure 1). All panels were sized to survive the dynamic structural loads induced by a 10 psi (69.0 kPa) incident blast wave. Composite panels were treated as materially elastic, while aluminum designs were allowed a maximum of 2% strain. A safety factor of 1.5 was used throughout the program. Panel stresses were predicted using a variety of methods ranging from beam theory to dynamic finite element analysis. The design procedure included studies of optimum stiffener spacing, panel depth, and subcomponent buckling and post buckling. Computer codes employed in the structural design included DEPROP (Dynamic Elastic Plastic Response of Panels) [4] and a modified version of ADINA (Automatic Dynamic Incremental Nonlinear Analysis) [5]. The spatially varying blast overpressure versus time history at various points on the panel was predicted using BLOCK [6]. Panel costs were estimated using material in Noton [7,8] and LeBlanc [9,10], as well as from discussions with various panel fabricators.

MATERIAL SELECTION

Shelter wall panels constructed from graphite, Kevlar and S-glass/epoxy composite materials along with 6061-T6 aluminum were

considered. The use of composite material offers several advantages over metal in the design of weight efficient structures. Of primary importance in minimizing the weight of a design are the generally superior specific properties of all the composite materials.

Table 1 compares some important properties of aluminum with the unidirectional form of the various composites. Specific tensile strengths of composites average 7 to 9 times better than 6061-T6, while specific compressive strength indicates 2 to 7 times more load carrying capability per unit weight. Note the relative unbalance between tensile and compressive properties of Kevlar and glass. The comparatively poor compressive performance of these two materials limits their usefulness in applications where large bending loads are expected. Graphite/epoxy exhibits well balanced tensile and compressive properties, as well as a better specific axial modulus. Specific shear carrying capability of these composites, when used as ±45 laminates, is approximately twice that of 6061-T6.

TABLE I. IMPORTANT MATERIAL PROPERTIES

Property[1]	Graphite	Kevlar	Glass	6061-T6
Tensile KSI Strengh (GP_a)	168.9 (1.165)	200.0 (1.379)	226.0 (1.558)	42.0 (0.29)
Compressive KSI Strength (GP_a)	162.0 (1.117)	40.0 (0.276)	85.0 (0.586)	42.0 (0.290)
Axial MSI Modulus (GP_a)	18.5 (127.5)	11.0 (75.8)	7.8 (53.8)	10.0 (68.9)
Shear MSI Modulus (GP_a)	4.85 (33.43)	2.83 (19.50)	2.38 (16.40)	3.80 (26.19)
Density lb/in^3 (gm/cm^3)	0.05 (1.38)	0.05 (1.38)	0.075 (2.08)	0.098 (2.71)
Cost $/lb ($/kg)	30 66	20 44	5 11	2 4.4
Relative Specific Properties[2]				
Tensile Strength	7.86	9.30	7.00	1.00
Compressive Stength	7.53	1.86	2.63	1.00
Shear Strength	1.86	2.04	1.82	1.00
Axial Modulus	3.63	2.16	1.02	1.00
Shear Modulus	2.50	1.46	0.82	1.00

(1) Axial composite properties are for unidirectional laminates, shear properties are for ±45° laminate

(2) $(Property/Density)/(Property/Density)_{Aluminum}$

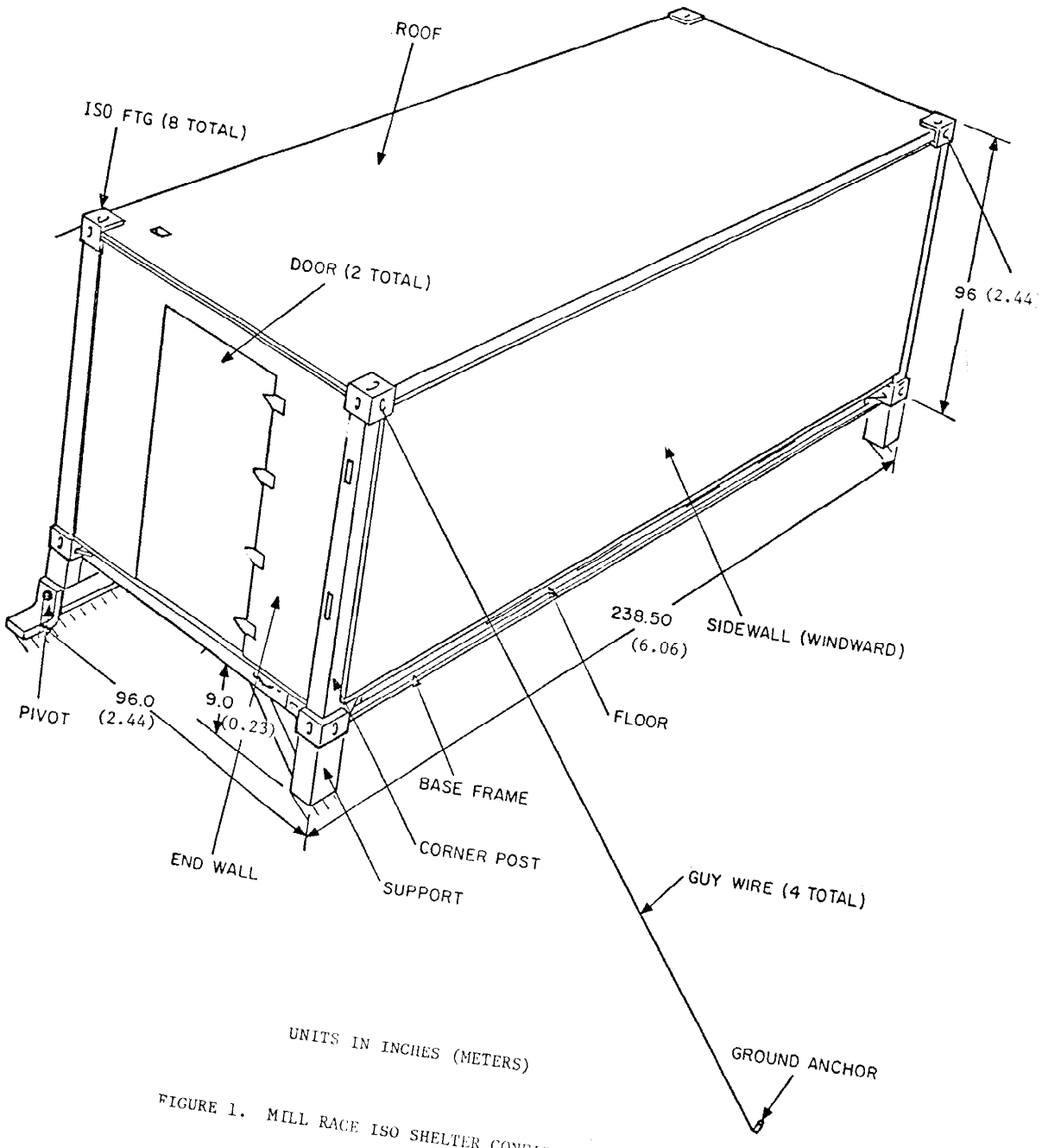

UNITS IN INCHES (METERS)

FIGURE 1. MILL RACE ISO SHELTER CONFIGURATION

Because composite parts are built from thin layers of material, the strength characteristics of a laminate can be tailored to carry any combination of biaxial and inplane shear loads. The ability to construct individualized material properties provides composites with an additional advantage over metals.

DESIGN LOAD DETERMINATION

The BLOCK code [6] was used to calculate the time varying pressure loads induced on the side wall of an ISO shelter by the passage of a 10-psi (69.0-kPa) shock. In this analysis, the shelter's long face was oriented parallel to the approaching wave front. Figure 2 shows the results of the BLOCK calculations for the time period of maximum wall panel response. Reflection of the incident shock results in an initially uniform step rise in surface overpressure to 25.3 psi (174.4 kPa). This load is eventually reduced to approximately 12 psi (82.7 kPa) by clearing waves which form at the shelter's free edge and travel inward toward the center of the wall. The motion of these waves can be tracked in Figure 2 by observing the time of initial pressure drop at various points.

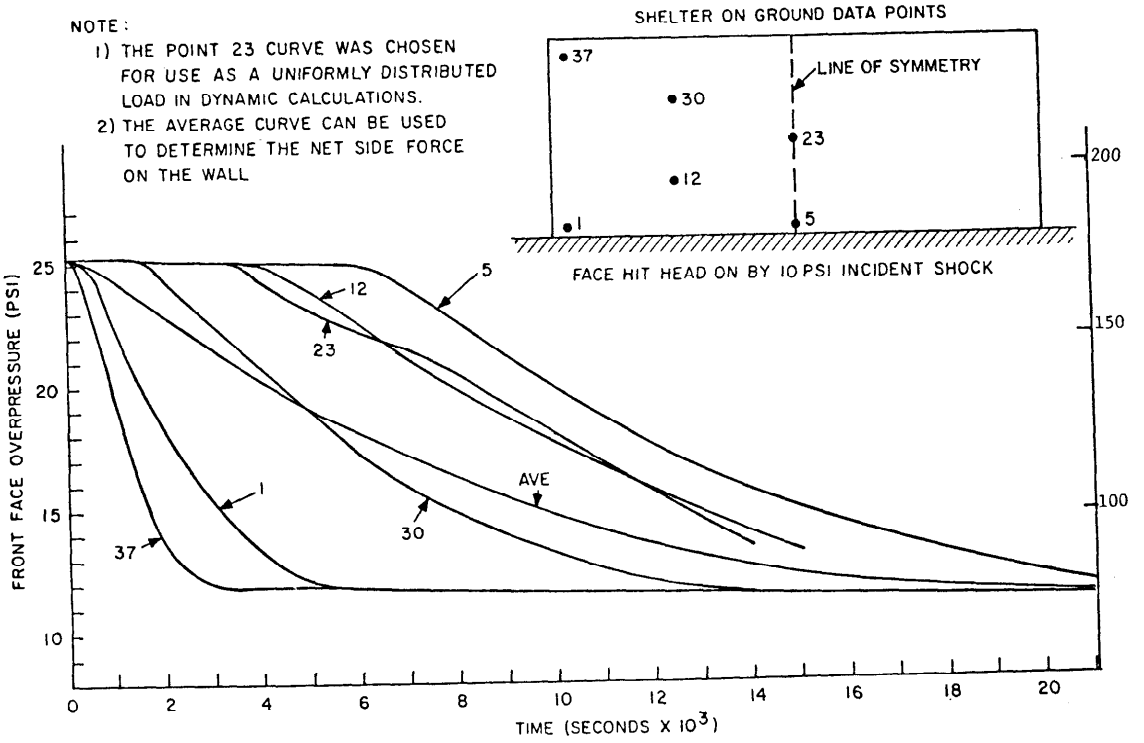

FIGURE 2 ISO WALL PRESSURE-TIME HISTORIES-SHELTER ON GROUND CASE

The curve for point 23, located at the panel's center, was used as a uniformly distributed, time varying pressure load in all later dynamic analyses. Using this pressure loading, a DEPROP [4] dynamic structural analysis was performed for a representative aluminum honeycomb sandwich design. Peak dynamic shear and moment at various points on this panel were determined. These preliminary design loads were used to initially size other panel configurations.

PANEL DETAILS

Many of the tactical shelters currently in service employ 6061-T6 aluminum sandwich panels as structural members. For unhardened shelter applications, inexpensive nonmetallic honeycomb or foam material has sufficient shear strength to survive the comparatively small core shear loads encountered in normal service. The predicted magnitude of the peak dynamic core shear resulting from a nuclear blast encounter, however, exceeds the strength of available foam, paper, and Nomex core material. A major consideration in the design of nuclear-blast-hardened panels was the selection of weight and cost efficient methods of supporting the large transverse shear loads.

The four panel geometries shown in Figure 3 were considered as potential solutions to the shear problem. In the first of these designs, the honeycomb sandwich panel of Figure 3a, the possibility of using a higher strength aluminum core was investigated. In the second panel type, Figure 3b, shear stiffeners were added to the sandwich configuration to reduce the load carried by the relatively weak nonmetallic honeycomb. Although it did continue to support some shear load, the honeycomb's only vital function in shear stiffened panels was the prevention of face sheet buckling. The corrugated core panels shown in Figure 3c were examined as a means of eliminating difficulties associated with the use of honeycomb. In this type of design the honeycomb was entirely removed from the panel, and all the shear load transferred to the corrugation. The hat stiffened panel configurations of Figure 3d carried this procedure one step further by eliminating both the honeycomb and the panel's inner skin. Bending loads, previously carried by the inner face in sandwich panels, were now supported by the caps of the hat stiffeners. Since stiffener bending loads are mainly axial, reinforcement of the cap section with composites is an almost ideal application for the highly orthotropic strength properties of the unidirectional form of these materials. Buckling of the relatively thin face and web components becomes a major concern in the last two configurations.

Figure 3 lists details of the nine panels designed during this program. Note that the inner and outer skins of sandwich panels were allowed to vary in thickness as well as laminate orientation. Four shear stiffened honeycomb sandwich panels, one using each of the materials considered in this study, were designed to allow direct comparison of the three composites with a metal configuration. Two hat

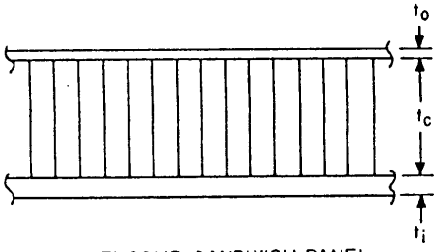

FIGURE 3a HONEYCOMB SANDWICH PANEL

	ALUMINUM SKINS + ALUMINUM HONEYCOMB
t_o IN (CM)	.09 (.23)
t_i IN (CM)	.09 (.23)
t_c IN (CM)	5.5 (14.0)
WEIGHT LBS (KG)	765 (348)

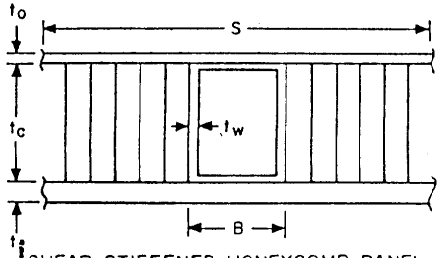

FIGURE 3b SHEAR STIFFENED HONEYCOMB PANEL

	KEVLAR	GLASS	GRAPHITE	ALUMINUM
t_o IN (CM)	.152 (.386)	.104 (.264)	.072 (.183)	.09 (.23)
t_i IN (CM)	.280 (.711)	.168 (.427)	.072 (.183)	.09 (.23)
t_c IN (CM)	5.5 (14.0)	5.5 (14.0)	5.5 (14.0)	5.5 (14.0)
t_w IN (CM)	.152 (.386)	.115 (.292)	.169 (.429)	.16 (.406)
B IN (CM)	2.73 (6.93)	2.73 (6.93)	2.73 (6.93)	2.73 (6.93)
S IN (CM)	16.0 (40.6)	16.0 (40.6)	16.0 (40.6)	16.0 (40.6)
WEIGHT LBS (KG)	610 (277)	605 (275)	369 (168)	673 (306)

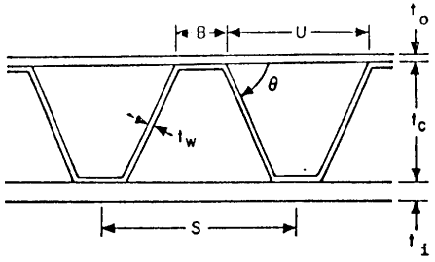

FIGURE 3c CORRUGATED CORE PANEL

	ALUMINUM	GRAPHITE
t_o IN (CM)	.13 (.33)	.084 (.21)
t_c IN (CM)	5.5 (14.0)	4.5 (11.4)
t_i IN (CM)	.19 (.48)	.168 (.43)
t_w IN (CM)	.11 (.28)	.17 (.43)
S IN (CM)	7.0 (17.8)	6.5 (16.5)
B IN (CM)	1.0 (2.5)	1.0 (2.5)
U IN (CM)	6.0 (15.2)	5.5 (14.0)
WEIGHT LBS (KG)	953 (433)	499 (227)

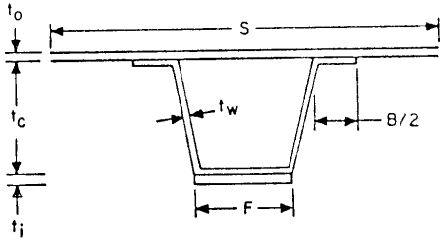

FIGURE 3d SHEET/STIFFENER PANEL

	ALUMINUM + GRAPHITE	GRAPHITE
t_o IN (CM)	.125 (.318)	.126 (.320)
t_i IN (CM)	.200 (.508)	.175 (.445)
t_c IN (CM)	5.5 (14.0)	4.0 (10.2)
t_w IN (CM)	.16 (.41)	.17 (.43)
S IN (CM)	12.0 (30.5)	10.0 (25.4)
B IN (CM)	1.7 (4.1)	2.0 (5.1)
F IN (CM)	3.5 (8.9)	3.0 (7.6)
WEIGHT LBS (KG)	651 (296)	352 (160)

FIGURE 3. PANEL DETAILS

stiffened panels, one constructed of aluminum with a graphite reinforced cap and one built entirely from graphite/epoxy, were also studied. Two all aluminum sandwich panels, one using an 8 pcf (128 kg/m^3) aluminum honeycomb core and the second using a corrugated core, were designed. A graphite corrugated core panel completes the list of configurations investigated.

PANEL COST AND WEIGHT COMPARISON

The estimated acquisition cost of the nine panels described in Figure 3, along with several other representative shelter panel designs, has been plotted versus weight in Figure 4. Cost predictions for the 220 x 80 inch (5.59 x 2.03 meter) side wall panels were based on a production run of 200. By employing methods described in Noton [7,8] and LeBlanc [9,10], fabrication cost associated with recurring and nonrecurring tooling, the layup of composite skin and stiffener components, consolidation of detail parts, vacuum bagging and curing were estimated in terms of standard man hours. The labor costs were converted at a rate of $25/man hour and added to material cost to arrive at the estimated acquisition cost for each design. Graphite, Kevlar, S-glass and aluminum were charged at $30, $20, $5 and $2 per pound respectively, based on predicted 1985 prices for these materials.

As Table II and Figure 4 show, a significant reduction in panel weight was obtained by using composite materials. Hardening the graphite/epoxy designs required only a 60% weight increase over the unhardened aluminum ISO configuration. Hardening to the same load level with aluminum resulted in a weight increase of approximately 200%. Weight reduction in the Kevlar and glass designs was limited by the relatively poor compressive properties of these materials.

TABLE II. ISO SIDE WALL ACQUISITION COST AND WEIGHT

Panel Type	Weight lb (kg)	Acquisition Cost $
Unhardened ISO	218 (99)	2970
Graphite Skin/Stiffener	351 (160)	17644
Shear Stiffened Graphite H/C	369 (168)	15022
Graphite Corrugated Core	499 (227)	24952
Shear Stiffened Glass H/C	605 (275)	9789
Shear Stiffened Kevlar H/C	610 (277)	19289
Aluminum Skin/Stiffener (with Graphite Cap)	651 (296)	5959
Shear Stiffened Aluminum H/C	673 (306)	5374
HAT Panel (7.3 PSI Design)[3]		13846
Aluminum Skin/Aluminum H/C	765 (348)	10722
Aluminum Corrulated Core	953 (433)	12000
MILL RACE Design [1]	1096 (498)	6402

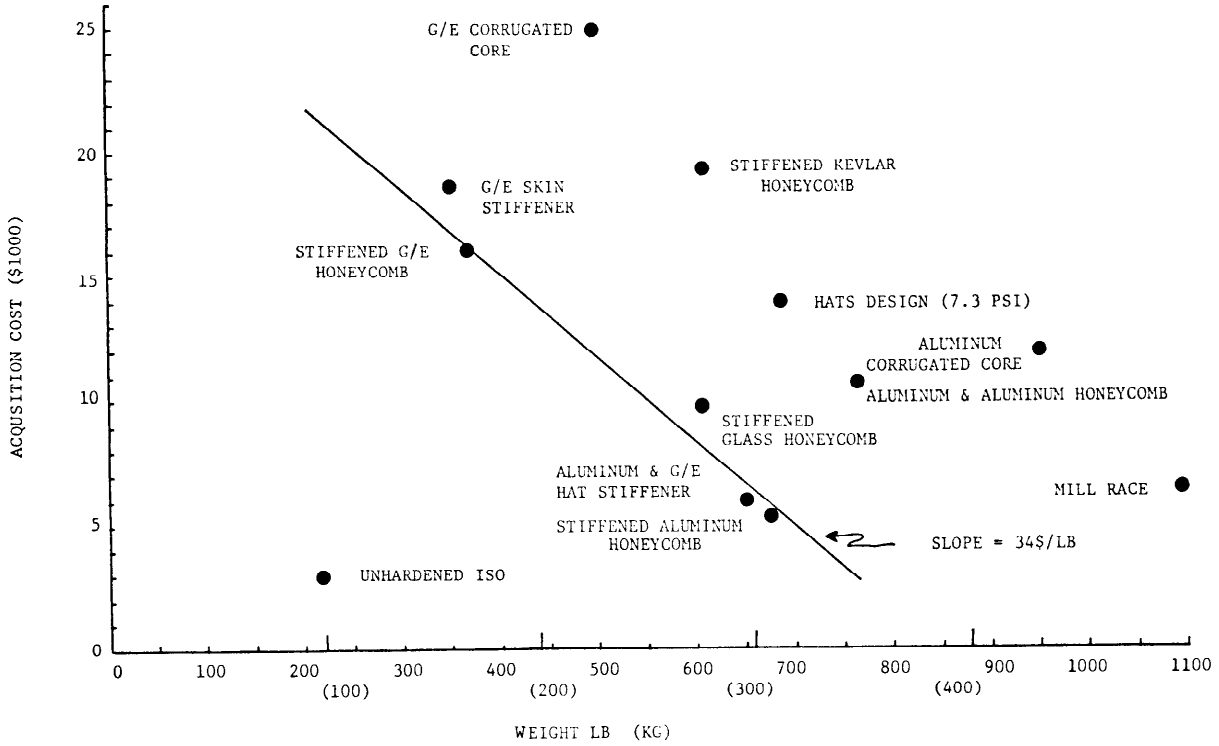

FIGURE 4. ISO SIDE WALL ACQUISITION COST VERSUS WEIGHT

The range in estimated acquisition cost exhibited as much variation as panel weight. The estimated price of the least expensive graphite design was 2.8 times the cost of the hardened aluminum panel. The lightest graphite/epoxy design was 3.3 times as expensive as aluminum. The straight line in Figure 4, a least squares fit of the five most cost effective designs, indicates that weight can be removed from a panel at a cost of $34/lb ($15.50/kg).

Table III presents a sampling of cost and weight trends observed by a variety of aerospace manufacturers when replacing aluminum configurations with composite designs. As expected, the data confirm that large reductions in structural weight are possible. Somewhat surprising, however, are the consistently lower acquisition costs of the composite designs. A large portion of this cost savings results from a reduction in the number of fasteners and individual parts required to build a composite structure. The use of composites also simplifies the manufacture of the curved contours normally found in aircraft parts.

TABLE III. TYPICAL COMPOSITE COST - WEIGHT TRENDS

COMPONENT TYPE (MANUFACTURER)	WEIGHT SAVED (%)	ACQUISITION COST REDUCTION (%)	COMMENTS
AV-8B Forward Fuselage (McDonnell) [11]	25.3	"Reduced"	o Composite has 88 parts, 2450 rivets o Metal has 237 parts, 6440 rivets
Advanced Composite Center Fuselage (Grumman) [12]	26.6	10	o "30% labor cost reduction partially offset by HIGHER material cost"
Advanced Composite AFT Fuselage (Vought) [13]	20.5	12	o 21% labor cost savings o Estimated 75% reduction in maintenance man hours
Advanced Composite L-1011 Aileron [14] (Lockheed)	23.2	"Competitive"	o Cost sensitive commercial application
Graphite/Polyimide Helicopter Transmission Housing (Boeing Vertol and AVRADCOM) [15]	10	10	o Improved MTBR o 450°F Matrix filament wound o Replaces Magnesium
Submarine Mast (Lockheed and Naval Ocean Systems Center) [16]	77	"Considerably Less"	o Replaced Titanium Design for Cost Reasons Alone
L-1011 Vertical Fin (Lockheed) [17]		40	o Many Fewer Fasteners
EF-111A Horizontal Stabilizer Trailing Edge (Grumman) [18]	6.2	29	o 70% Lower Life Cycle Cost
Helicopter Floor Panel (Boeing) [19]	10	"Less Costly"	o Flat, Stiffened Kevlar Panel

While these characteristics can be extremely influential in aerospace applications, they are much less important in the fabrication of the flat stiffened panels used in shelters.

The last entry in Table 3 suggests that cost reductions can also be acheived when producing flat panels from composites. The Kevlar sandwich helicopter floor built by Boeing is similar in configuration to the Kevlar stiffened panel designed for the ISO shelter. The 10% weight reduction reported by Boeing compares favorably with the 6% reduction predicted for the Kevlar shelter panel. However, Boeing's indication that the composite panel is "less costly" than the aluminum design it replaces suggests that the acquisition cost of the Kevlar shelter panel, along with the other composite designs, may have been significantly overestimated. If the data of Table 3 can be regarded as typical, acqusition cost of composite panels should be competitive with equivalent aluminum designs.

OTHER FACTORS INFUENCING COST

Taken alone, panel acquisition cost is not a fair indicator of the advantages and disadvantages of metal versus composite designs. A significant increment of additional cost and weight can be incurred when joining the individual panels to form a closed box structure. Because composite panels are molded, relatively inexpensive fabrication of complex edge shapes is possible. This permits the use of more efficient joint configurations in composite shelters. Because the number of detail parts and fasteners is reduced, composite panel edge connections should be less costly than metal joints of the same fixity.

A variety of sources suggest that the maintenance is by far the largest single expense in a metal shelter's overall life cycle cost [18, 20, 21]. The data in Figure 5, taken from a Grumman report on aircraft tail fabrication [18], compares life cycle cost of an aluminum sandwich panel with two graphite/epoxy designs. Service experience showed that maintenance of the aluminum configuration accounted for 69% of this panel's life cycle cost. In other words, the real price of the aluminum design was over three times its initial acquisition cost. Largely because they did not corrode, maintenance cost of the graphite panels was reduced by 62%. Overall life cycle cost of the graphite panels was predicted to be 70% lower than the original aluminum design.

Maintenance has also been found to be a major expense for aluminum military shelters. It has been estimated that up to 80% of the required maintenance of aluminum designs is related to corrosion [20]. A 1976 Air Force audit cited the average cost of repairing 124 aluminum shelters at $80,000 each. This same document estimated that time between overhauls with non-metallic shelters should at least double [21]. These figures suggest that the employment of composites in tactical shelters may be justified by maintenance savings alone.

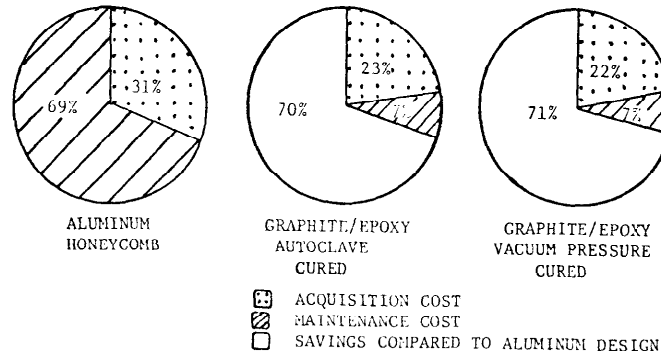

DATA FROM GRUMMAN EF-111A TAIL PANEL STUDY [18]

FIGURE 5. ALUMINUM VERSUS COMPOSITE LIFE CYCLE COST COMPARISON

SUMMARY AND CONCLUSIONS

It has been shown that the use of graphite/epoxy composite panels could substantially reduce the structural weight of blast hardened tactical shelters. In addition, evidence suggests that life cycle cost of composite shelters would be less than equivalent aluminum designs. Effects of thermal, EMP and other loads in a nuclear environment as well as standard ISO requirements for stacking and transportation induced loads must also be investigated. With the possible exception of EMP, none of these additional requirements give any distinct advantage to metal designs. Given composite construction's clear superiority in structural performance and its potential for competitive life cycle cost, it seems likely that future tactical shelters will be fabricated mainly from advanced composites material.

REFERENCES

1. Milligan, Roger. W., Fanucci, Jerome P., Rodal, Jose J.A., and Lawrence J. Mente, "Research and Development of an ISO Rigid Wall Hardened Shelter," Kaman AviDyne Report KA TR-187, July 1981.

2. Crenshaw, William L., Milligan, Roger W., and Jerome P. Fanucci, "Test and Evaluation of a Hardened ISO Shelter at MILL RACE," procedings of the MILL RACE symposium, March 1982.

3. Zartarian, Garabed., Yeghiayan, Raffi P., and Lush, Allen M., "Preliminary Design of Hardened Tactical Shelters - Design Concepts and Test Planning," US Army Research and Development Command, ARBRL-CR-00464, August 1981.

4. Mente, Lawrence J. and William N. Lee., "NOVA-2S, A Stiffened Panel Extension of the NOVA-2 Computer Program," Air Force Weapons Laboratory, Kirtland AFB, AFWL-TR-78-182, December 1978.

5. Klaus-Jurgen Bathe, "ADINA - A Finite Element Program for Automatic Dynamic Incremental Nonlinear Analysis," M.I.T. Report 82448-1, September 1975 (Revised December 1978).

6. Lee, William N. and Garabed Zartarian, "BLOCK - A Digital Computer Program for Calculating the Blast Loadings on Box-like Structures," Kaman AviDyne Report TR-156, January 1979.

7. Noton, Bryan R., "ICAM Manufacturing Cost/Design Guide Volume I: Demonstration Sections," Air Force Wright Aeronautical Laboratories, AFWAL-TR-80-4115, September 1980.

8. Noton, Bryan R., "ICAM Manufacturing Cost/Design Guide Volume II: Appendices to Demonstration Section," Air Force Wright Aeronautical Laboratories, AFWAL-TR-80-4115, September 1980.

9. LeBlanc, Donald J. et. al., "Advanced Compositor Cost Estimating Manual Volume I," Air Force Flight Dynamics Laboratory, AFFDL-TR-76-87, August 1976.

10. LeBlanc, Donald J. et. al., "Advanced Composite Cost Estimating Manual Volume II," Air Force Flight Dynamics Laboratory, AFFDL-TR-76-87, August 1976.

11. Watson, James C. and David L. Ostrodika, "AV-8B Forward Fuselage Development," Proceedings of the Fifth DOD/NASA Conference on Fibrous Composites in Structural Design Volume 1, January 1981, p. I-3.

12. Corvelli, Nicholas and Samuel J. Dastin, "Advanced Composite Center Fuselage Development," Proceedings of the Fifth DOD/NASA Conference on Fibrous Composites in Structural Design Volume 1, January 1981, p. I-83.

13. Forman, Charles R., "Development of Advanced Composite Aft Fuselage Structure for Future Navy Aircraft," Proceedings of the Fifth DOD/NASA Conference on Fibrous Composites in Structural Design Volume 1, January 1981, p. I-101.

14. Griffin, Charles F. and Larry D. Fogg, "Design Development of an Advanced Composite Aileron," Proceedings of the Fifth DOD/NASA Conference on Fibrous Composites in Structural Design Volume 1, January 1981, p. I-135.

15. Lenski, Joseph W. and James Gomez, "Development of Filament - Wound Graphite/Polymide Composite Transmission Housing," Proceedings of the Fifth DOD/NASA Conference on Fibrous Composites in Structural Design Volume 1, January 1981, p. I-465.

16. Jung, Peter and Forrest B. Yarborough, "Development of the Manufacturing Technology for a Graphite/Epoxy Submarine Mast," Procedings of the Fifth DOD/NASA Conference on Fibrous Composites in Structural Design Volume 2, January 1981, p. II-467.

17. Eudaily, R.R., "Assembly of the L-1011 Composite Fin," Proceedings of the Fifth DOD/NASA Conference on Fibrous Composites in Structural Design Volume 2, January 1981, p. II-451.

18. Suarez, J.A., and L.M. Poveromo, "Fabrication of Integrally Stiffened Graphite/Epoxy Components," 11th National SAMPLE Technical Conference, November 13-15, 1979, p. 49.

19. Marchinski, Leonard J. and Robert L. Pinckney, "The Design, Construction, and Performance of Composite Fuselage Components for the Boeing 234 Helicopter," 13th National SAMPLE Technical Conference, October 13-15, 1981, p. 287.

20. Chilcott, William C., Sacramento Air Logistics Center, Personal Communication.

21. Anon., Manufacturing Technology Program Budget Estimate FY1983, Air Force Systems Command, Focal Area 3A-Composite Structural Materials, 17 August 1981.

FAILURE ANALYSIS OF COMPOSITE LAMINATES USING A TENSOR POLYNOMIAL STRENGTH CRITERION

R. C. Tennyson
Professor

G. Elliott
Research Assistant

J. S. Hansen
Associate Professor
University of Toronto
Institute for Aerospace Studies
Toronto, Ontario, Canada

ABSTRACT

This report presents a summary of the work done on the development of the cubic form of the tensor polynomial strength criterion for composite laminates. The capability of this model to accurately predict multi-mode failures for a range of laminates under various load conditions is demonstrated, and the results compared to quadratic model predictions. Both symmetric and nonsymmetric laminates have been considered. Furthermore, the effect of nonlinear shear stress/strain behavior is included to provide some insight as to its role in determining the strength of laminates. Of particular interest is the application of this criterion to the strength analysis of laminates containing circular holes.

NOMENCLATURE

$A_{ij}, B_{ij}, D_{ij} = \int_{-(h/2)}^{h/2} (\bar{Q}_{ij})_k (1, z, z^2) dz$

$[A'] = [A^*] - [B^*][D^*]^{-1}[C^*]$
$[B'] = [B^*][D^*]^{-1}$
$[C'] = -[D^*]^{-1}[C^*]$
$[D'] = [D^*]^{-1}$
$[A^*] = [A]^{-1}$
$[B^*] = -[A]^{-1}[B]$
$[C^*] = [B][A]^{-1}$
$[D^*] = [D] - [B][A]^{-1}[B]$

E_{11}, E_{22} = Orthotropic moduli of elasticity measured in the 1 and 2 directions, respectively
G_{12} = Shear modulus of elasticity measured in 1-2 plane
h = total laminate thickness
K = curvature
$\ell_{T,C,S,B}$ = Characteristic distances for tension, compression, shear and biaxial loading, respectively
$[M]$ = bending moment resultant matrix
$[N]$ = normal stress resultant matrix

$$\bar{Q}_{11} = Q_{11}m^4 + 2(Q_{12} + 2Q_{66})n^2m^2 + Q_{22}n^4$$

$$\bar{Q}_{22} = Q_{11}n^4 + 2(Q_{12} + 2Q_{66})n^2m^2 + Q_{22}m^4$$

$$\bar{Q}_{12} = (Q_{11} + Q_{22} - 4Q_{66})n^2m^2 + Q_{12}(m^4 + n^4)$$

$$\bar{Q}_{66} = (Q_{11} + Q_{22} - 2Q_{12} - 2Q_{66})n^2m^2 + Q_{66}(m^4 + n^4)$$

$$\bar{Q}_{16} = (Q_{11} - Q_{12} - 2Q_{66})nm^3 + (Q_{12} - Q_{22} + 2Q_{66})n^3m$$

$$\bar{Q}_{26} = (Q_{11} - Q_{12} - 2Q_{66})n^3m + (Q_{12} - Q_{22} + 2Q_{66})nm^3$$

$$Q_{11} = E_{11}/(1 - \nu_{12}\nu_{21})$$

$$Q_{22} = E_{22}/(1 - \nu_{12}\nu_{21})$$

$$Q_{12} = \nu_{21}E_{11}/(1 - \nu_{12}\nu_{21})$$

$$Q_{66} = G_{12}$$

S = Shear strength in 1-2 plane

X, X' = Tensile and compressive lamina strengths measured in 1 direction

Y, Y' = Tensile and compressive lamina strengths measured in 2 direction

Subscripts

x, y = Orthogonal in-plane structural axes

$1, 2$ = Lamina material axes parallel and orthogonal to fiber reinforcement

Greek Symbols

γ = Shear strain

ε = Normal strain

θ = Fiber orientation relative to x-axis

ν = Poisson's ratio

σ = Normal stress

τ = Shear stress

1. INTRODUCTION – THE TENSOR POLYNOMIAL STRENGTH CRITERION

In the design of composite laminates for load bearing applications, one of the major difficulties is that of selecting a suitable lamina strength model. The most general failure criterion proposed is the tensor polynomial which was advocated as early as 1966 by Malmeister [1] and developed extensively by Tsai and Wu [2] in quadratic and higher order forms [3,4]. The failure surface in stress space is then described by the equation,

$$F_i\sigma_i + F_{ij}\sigma_i\sigma_j + F_{ijk}\sigma_i\sigma_j\sigma_k + \ldots \qquad (1)$$

$$= f(\sigma) \begin{cases} < 1 & \text{no failure} \\ = 1 & \text{failure} \\ > 1 & \text{exceeded failure} \end{cases}$$

for i, j, k = 1, 2, 3,...6. F_i, F_{ij} and F_{ijk} are strength tensors of the 2nd, 4th and 6th rank, respectively. If one restricts the analysis to a plane stress state and considers only a cubic formulation as being a reasonable representation of the failure surface, then Eq. (1) can be reduced to [3],

$$F_1\sigma_1 + F_2\sigma_2 + F_{11}\sigma_1^2 + F_{22}\sigma_2^2 + F_{66}\sigma_6^2 + 2F_{12}\sigma_1\sigma_2 + 3F_{112}\sigma_1^2\sigma_2$$

$$+ 3F_{221}\sigma_2\sigma_1 + 3F_{166}\sigma_1\sigma_6^2 + 3F_{266}\sigma_2\sigma_6^2 = 1 \qquad (2)$$

Cubic Strength Equation in Terms of External Load Parameters

In general, assume the principal stresses can be described in terms of some variable load parameter λ such that

$$\sigma_1 = C_{11}\lambda + C_{12}, \qquad \sigma_2 = C_{21}\lambda + C_{22}, \qquad \sigma_6 = C_{31}\lambda + C_{32} \qquad (3)$$

where C_{12}, C_{22} and C_{32} represent some additional constant load components. Hence, substituting Eq. (3) into Eq. (2) one obtains

$$a\lambda^3 + b\lambda^2 + c\lambda + d = 0 \qquad (4)$$

where

$$a = 3(F_{112}C_{11}^2C_{21} + F_{122}C_{11}C_{21}^2 + F_{166}C_{11}C_{31}^2 + F_{266}C_{21}C_{31}^2) \qquad (5a)$$

$$b = 3F_{112}(C_{11}^2C_{22} + 2C_{11}C_{12}C_{21}) + 3F_{122}(C_{12}C_{21}^2 + 2C_{11}C_{21}C_{22})$$

$$+ 3F_{166}(C_{12}C_{31}^2 + 2C_{11}C_{31}C_{32}) + 3F_{266}(C_{22}C_{31}^2 + 2C_{21}C_{31}C_{32})$$

$$+ F_{11}C_{11}^2 + F_{22}C_{21}^2 + F_{66}C_{31}^2 + 2F_{12}C_{11}C_{21} \qquad (5b)$$

$$c = 3F_{112}(2C_{11}C_{12}C_{22} + C_{12}^2C_{21}) + 3F_{122}(2C_{12}C_{21}C_{22} + C_{11}C_{22}^2)$$

Continued...

$$+ 3F_{166}(C_{11}C_{32}^2 + 2C_{12}C_{31}C_{32}) + 3F_{266}(C_{21}C_{32}^2 + 2C_{22}C_{31}C_{32}) + 2F_{11}C_{11}C_{12}$$

$$+ 2F_{22}C_{21}C_{22} + 2F_{66}C_{31}C_{32} + 2F_{12}(C_{11}C_{22} + C_{21}C_{12}) + F_1C_{11} + F_2C_{21} \quad (5c)$$

$$d = 3F_{112}C_{12}^2C_{22} + 3F_{122}C_{12}C_{22}^2 + 3F_{166}C_{12}C_{32}^2 + 3F_{266}C_{22}C_{32}^2 + F_{11}C_{12}^2$$

$$+ F_{22}C_{22}^2 + 2F_{12}C_{12}C_{22} + F_{66}C_{32}^2 + F_1C_{12} + F_2C_{22} - 1.0 \quad (5d)$$

Once the coefficients [Eq. (5)] are calculated for a given ply orientation and structural configuration subject to prescribed loads, the solution of Eq. (4) yields the desired failure condition in terms of λ.

The first task of course is to evaluate the tensor polynomial strength parameters. Simple tension, compression and shear tests on 0° and 90° laminates will yield the principal components which are defined by,

$$F_1 = \frac{1}{X} - \frac{1}{X'}, \quad F_2 = \frac{1}{Y} - \frac{1}{Y'}, \quad F_{11} = \frac{1}{XX'}, \quad F_{22} = \frac{1}{YY'}, \quad F_{66} = \frac{1}{S^2} \quad (6)$$

Because of the inordinate amount and complexity of experiments required to accurately evaluate the F_{12} and four F_{ijk} terms retained in the model, a hybrid method can be employed. This approach is based on a biaxial strength test and utilizing four constraint equations. The latter conditions can be derived by setting the discriminant of the cubic polynomial [Eq. (4)] coefficients to zero, thus requiring the failure equation to yield three real roots, two of which must be equal. This satisfies the physical consideration of having only two distinct roots for two colinear loading paths. Further details can be found in [3]. Table I summarizes the strength parameters for the particular graphite/epoxy (3M SP288 T300) used in the experiments.

Selection of Correct Failure Loads from Solution of Cubic Equation

The cubic strength criterion can be described by

$$f(\lambda) = a\lambda^3 + b\lambda^2 + c\lambda + d \quad (7)$$

where failure loads are obtained from solving $f(\lambda) = 0$. For all load values λ such that $f(\lambda) < 0$, the lamina does not fail. As noted above, the interaction parameters were determined by solving constraint equations such that only two real roots of $f(\lambda)$ occurred, one of which was double valued. However, this was performed for a specific load case (internal pressure) and the constraints were imposed only on sufficient ply configurations to yield the required solutions. Since the selection of these cases was rather

Table I(a) Summary of Principal Strength Parameters
Graphite/Epoxy (3M SP-288 T300)

F1	F11	F2	F22	F6	F66
$(KSI)^{-1}$	$(KSI)^{-2}$	$(KSI)^{-1}$	$(KSI)^{-2}$	$(KSI)^{-1}$	$(KSI)^{-2}$
-2.482×10^{-3}	4.239×10^{-5}	1.035×10^{-1}	3.936×10^{-3}	0	8.009×10^{-3}

Table I(b) Summary of Interaction Strength Parameters for Cubic Model

F12	F112	F221	F166	F266
$(KSI)^{-2}$	$(KSI)^{-3}$	$(KSI)^{-3}$	$(KSI)^{-3}$	$(KSI)^{-3}$
-3.855×10^{-4}	3.116×10^{-7}	-5.713×10^{-6}	-4.054×10^{-6}	-2.268×10^{-4}

arbitrary, there is no guarantee that the double real root condition will hold for all other possibilities. Consequently, recourse to plotting the $f(\lambda)$ vs λ curve should be undertaken before selecting the correct failure load. Three particular cases can arise:

(i) two real roots one of which is double valued;
(ii) one real root with two complex roots;
(iii) three real distinct roots.

Case (i)

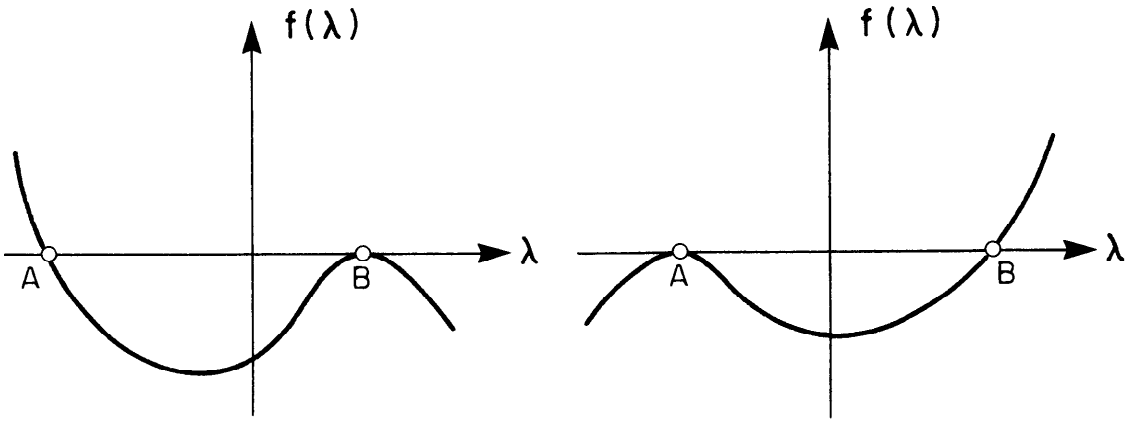

This represents the "ideal" case with only two real roots to consider, A and B. Note that $f(\lambda) < 0$ for $A < \lambda < B$.

Case (ii)

This particular format has been found to occur when the local maximum falls below the load axis (λ), thus failing to yield the expected double root.

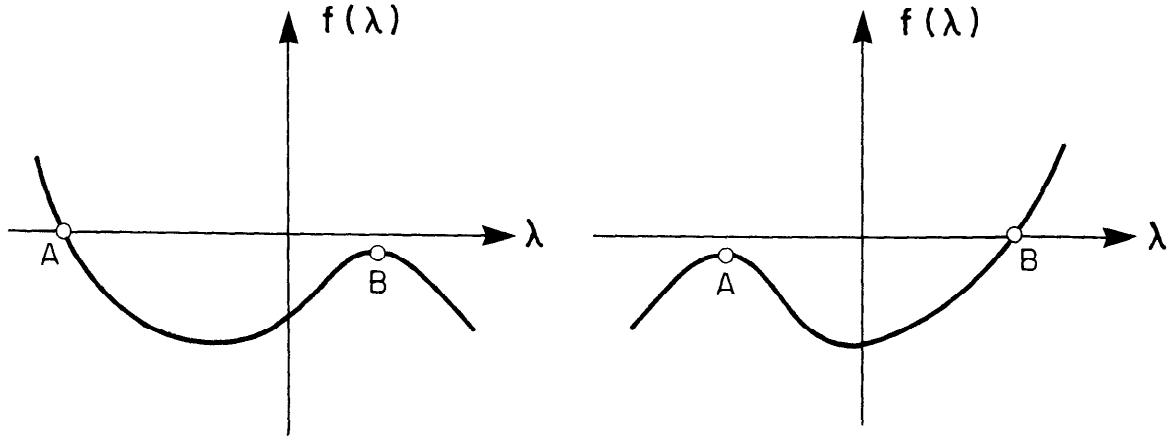

Experience has shown that this maximum together with the real root should be taken as defining the two possible failure loads. Again $f(\lambda) < 0$ for $A < \lambda < B$.

Case (iii)

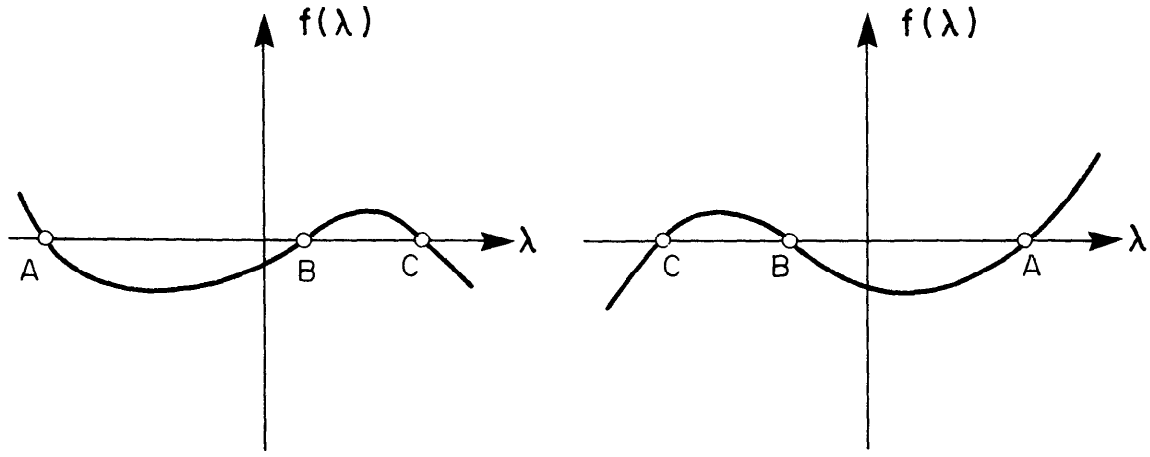

Based on the notion that $f(\lambda) < 0$ between the two possible failure loads, then in the two cases shown above, A and B would be selected since $f(\lambda) > 0$ for λ lying between B and C. From a physical viewpoint, even though three distinct real roots exist, one can argue that the 'correct' values bound the region $f(\lambda) < 0$ in which no failure has occurred.

Clearly from physical considerations, Case (i) is desirable. However, due to inaccuracies in determining the polynomial coefficients, practical experience has demonstrated that Cases (ii) and (iii) frequently arise. Experimental evidence has further shown that the above interpretations will yield accurate estimates for the failure loads.

2. GENERAL LAMINATE STRENGTH ANALYSIS PROCEDURE (MULTI-MODE FAILURE)

In general, when one considers some arbitrary laminate comprised of an assembly of laminae of different material properties and orientations, the failure condition must be individually calculated for each lamina. Assuming a plane stress state and linear elastic behavior, the stress matrix for the k-th lamina a distance Z_k above the mid-plane is given by,

$$\begin{bmatrix} \sigma_x \\ \sigma_y \\ \tau_{xy} \end{bmatrix}_k = [\bar{Q}_{ij}]_k[A'][N] + [\bar{Q}_{ij}]_k[B'][M] + Z_k \left\{[\bar{Q}_{ij}]_k(C'][N] + [\bar{Q}_{ij}][D'][M]\right\} \tag{8}$$

The lamina principal stresses for any ply of θ orientation are then obtained from

$$\begin{bmatrix} \sigma_1 \\ \sigma_2 \\ \sigma_6 \end{bmatrix}_k = [T]_k \begin{bmatrix} \sigma_x \\ \sigma_y \\ \tau_{xy} \end{bmatrix}_k \tag{9}$$

where σ_6 denotes the shear stress in the principal material axes plane 1-2, and

$$[T]_{\pm\theta} = \begin{bmatrix} m^2 & n^2 & \pm 2mn \\ n^2 & m^2 & \mp 2mn \\ \mp mn & \pm mn & (m^2-n^2) \end{bmatrix} \tag{10}$$

Hence, Eq. (9) is evaluated for each lamina and substituted into Eqs. (2) or (4). Having determined which lamina (or laminae) will fail first, one must then obtain modified stiffness matrices. One possible procedure that can be used to assess the overall failure strength of a laminate is outlined in the flow chart of Fig. 1. Several failure modes that are possible include:

(i) matrix crazing or fracture with fiber reinforcement intact;
(ii) fiber/matrix fracture;
(iii) interlamina shear separation from adjacent plies;
(iv) compressive fiber failure in a 'buckling' mode.

Consequently, after initial 'failure', assumptions have to be made regarding the effect of the 'failed' ply (or plies) on the stiffness of the remaining laminate. For case (i) above, one can set $E_{22} = \nu_{12} = G_{12} = 0$ and for (ii), remove the failed laminae altogether. In both instances, if first failure occurs on interior plies, interlaminar separation may result with a consequent loss of shear transfer between adjacent plies. From a design viewpoint, there

would appear to be some merit in arranging the stacking sequence for multi-mode failure configurations such that initial failure occurs in the exterior plies. Such a design might then preclude interlaminar separation due to 'first ply' failures. This statement must be qualified by noting that normal stresses to the plane of the lamina have not been considered and it has been pointed out that they can also lead to interlaminar separation [5,6].

The fourth case involving fiber buckling in a lamina requires modification of the compressive stiffness and/or strength for the fibers.

Nonlinear Effects

In treating nonlinear stress/strain behavior, only shear was considered in the manner of Hahn and Tsai [7], i.e.,

$$\varepsilon_6 = \tilde{S}_{66}\sigma_6 + \tilde{S}_{6666}\sigma_6^3 \tag{11}$$

This results in a modified $[\bar{Q}'_{ij}]_k$ matrix of the form,

$$[\bar{Q}'_{ij}]_k = [\bar{Q}_{ij}]_k + g_k(\varepsilon_x, \varepsilon_y, \gamma_{xy})[f(\theta)]_k \tag{12}$$

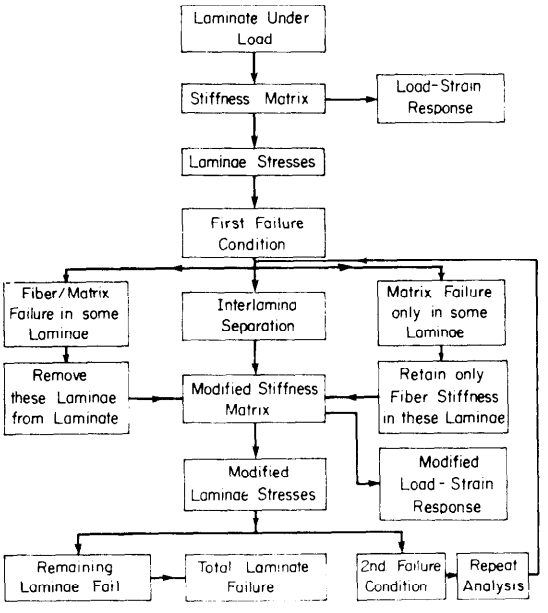

Fig. 1

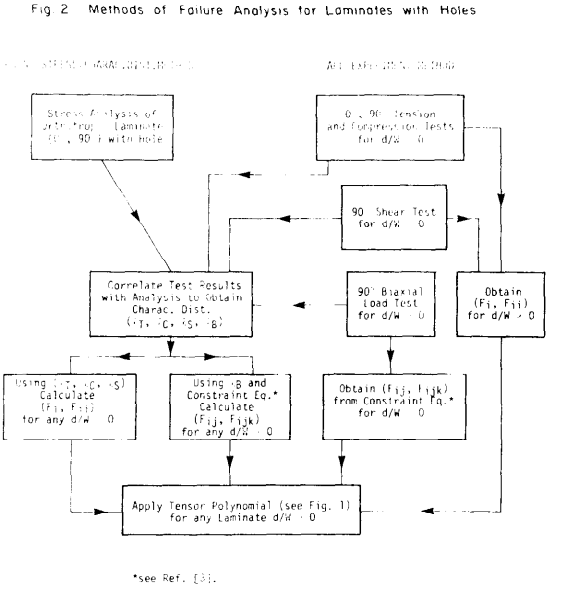

Fig. 2

where

$$[f(\theta)]_k = \frac{1}{2}\begin{bmatrix} (1-\cos 4\theta) & -(1-\cos 4\theta) & -\sin 4\theta \\ & (1-\cos 4\theta) & \sin 4\theta \\ \text{symmetric} & & (1+\cos 4\theta) \end{bmatrix} \tag{13}$$

and $g_k(\varepsilon_x, \varepsilon_y, \gamma_{xy})$ is the real root of

$$y^3 + \frac{3}{\tilde{S}_{66}} y^2 + \left[\frac{3}{\tilde{S}_{66}^2} + \frac{S_{66}}{\tilde{S}_{6666}} \cdot \frac{1}{\varepsilon_6^2} \right] y + \frac{1}{\tilde{S}_{66}^3} = 0 \tag{14}$$

with ε_6^2 replaced by

$$\varepsilon_6^2 = \frac{(1-\cos 4\theta)}{2} (\varepsilon_x - \varepsilon_y)^2 - (\sin 4\theta)(\varepsilon_x - \varepsilon_y)\gamma_{xy} + \frac{(1+\cos 4\theta)}{2} \gamma_{xy}^2 \tag{15}$$

An iterative procedure is then used to solve for failure loads, details of which can be found in [7,8].

3. FAILURE ANALYSIS OF LAMINATES WITH CUTOUTS

Previous failure analyses of laminates containing cutouts or cracks have employed either a 'point stress' or an 'average stress' criterion [see [9], [10] for example). Test data are required to yield 'characteristic distances' which define either evaluation points or integration intervals to be used in conjunction with detailed stress analysis information to predict uniaxial strengths. Although these methods provide reasonably good correlations with the limited test data available, general biaxial loading has not been considered.

An alternative approach is based on the tensor polynomial equation in which the strength parameters can be obtained as a function of d/W (hole diameter/plate width). In this procedure, the laminate is treated as though it had no cutout but with strength properties suitably reduced according to the d/W ratio. If one wishes to avoid a stress analysis of plates-with-holes entirely, then the strength parameters can be experimentally determined as functions of d/W. On the other hand, an orthotropic stress analysis in conjunction with limited strength tests for a given d/W can be employed to ascertain the characteristic distances (ℓ_T, ℓ_C, ℓ_S, ℓ_B). These values can then be utilized to calculate the strength coefficients for varying d/W. Both methods are illustrated in the flow chart of Fig. 2. Table II presents a comparison of the principal strength parameters for d/W = 0.25 using both approaches.

4. APPLICATIONS OF THE TENSOR POLYNOMIAL FAILURE CRITERION

In earlier work [4,8], comparisons between quadratic and cubic model

Table II Summary of Principal Strength Parameters for d/W = 0.25
Glass/Epoxy (3M, 1003)

F1 $(KSI)^{-1}$	F11 $(KSI)^{-2}$	F2 $(KSI)^{-1}$	F22 $(KSI)^{-2}$	F66 $(KSI)^{-2}$
Experiment Only:				
-8.013×10^{-3}	4.045×10^{-4}	0.382	6.090×10^{-2}	8.000×10^{-2}
Point Stress/Characteristic Distances* from Tests:				
-6.520×10^{-3}	3.397×10^{-4}	0.386	7.500×10^{-2}	8.300×10^{-2}

*ℓ_T = 0.07", ℓ_C = 0.09", ℓ_S = 0.10".

strength predictions were presented for tension, compression and shear loading of simple laminates. Although some differences were found, particularly under pure shear, by far the most important case examined was that of biaxial tension for $(\pm \theta)_S$ laminates. This work has been extended to include general biaxial loading.

General In-Plane Biaxial Loading

Consider laminates of $(\pm \theta)_S$ symmetric balanced construction subject to in-plane biaxial loading defined by the stress ratio $\alpha = \pm N_x/\pm N_y$ with $N_{xy} = 0$. Using the strength parameters of Table I, failure loads were calculated for varying θ. From these results it was then possible to plot maximum strengths and optimum fiber angles as a function of α (see Figs. 3-6). Included in these graphs are the quadratic predictions for comparative purposes. It is of interest to note that in Fig. 3, some complex root solutions

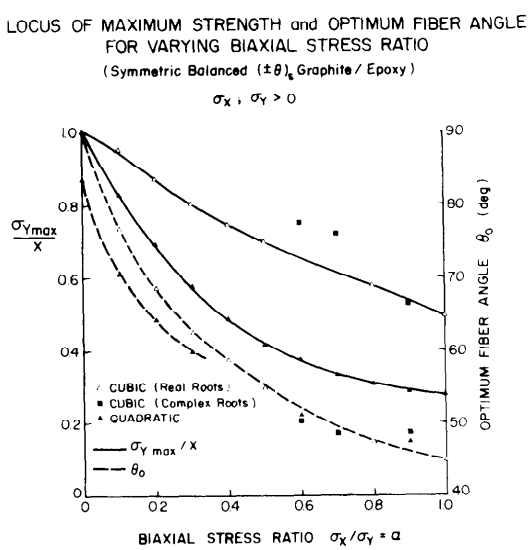

Fig. 3

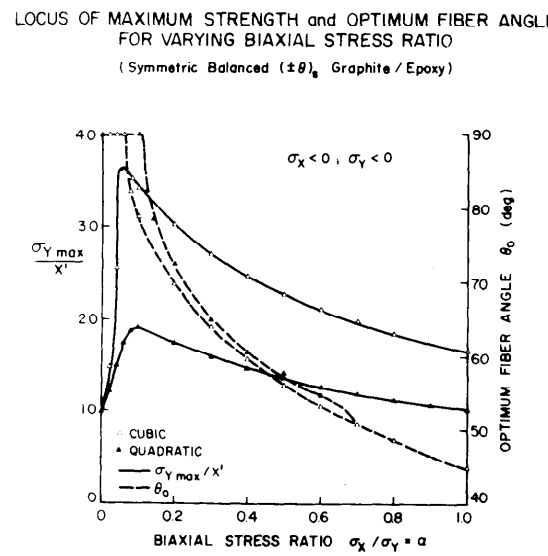

Fig. 4

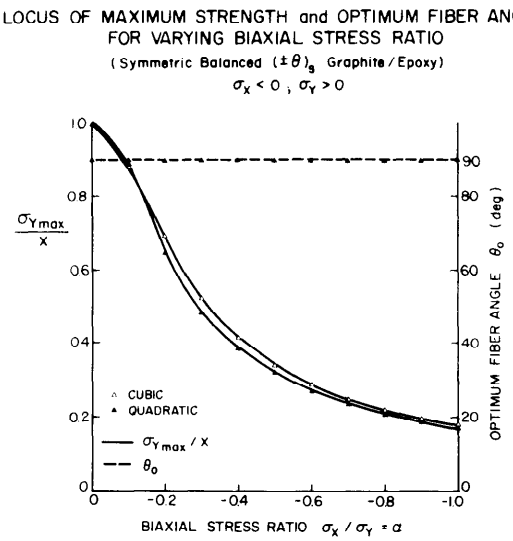

Fig. 5

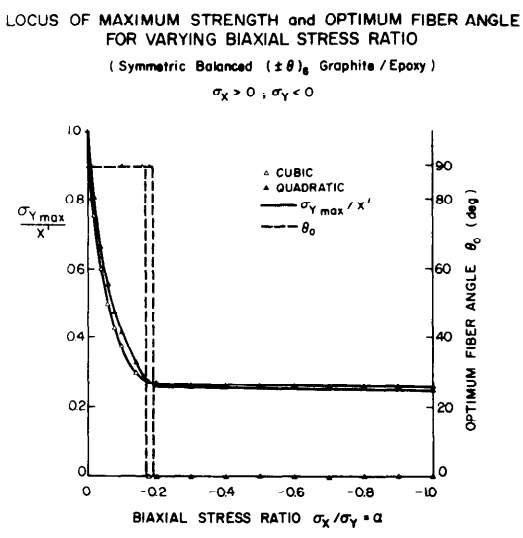

Fig. 6

were obtained for a limited number of cases. However, the general trend of the remaining data can be used to provide an estimate of the failure loads.

It can be seen that for $+\alpha$, large differences in failure loads are predicted (Figs. 3, 4) whereas $-\alpha$ solutions are virtually the same. However, it should be emphasized that the biaxial compression results are preliminary and must await experimental confirmation.

Limited experimental confirmation of the cubic strength criterion was obtained from internal pressure tests conducted on $(\pm\ \theta)_S$ graphite/epoxy tubes [3]. A comparison of the test data with both quadratic and cubic predictions is shown in Fig. 7. It is clear that agreement with the cubic model is quite good while the quadratic formulation substantially underestimates the strength, particularly in the optimum fiber angle range.

The effect of nonlinear shear behavior was also investigated for similar pressure loaded cylinder conditions. Figure 8 demonstrates that the nonlinear corrections are small.

Multi-Mode Failure and Combined Loading

Up to this point we have considered the strength of laminates where failure of all laminae comprising the structure occurred simultaneously. Multi-mode failure of a laminate arises from the progressive failures of laminae that occur at various stages of loading. Since the failure mode of each ply can differ, assumptions have to be made regarding the effect of the "failed" ply (or plies) on the stiffness of the remaining structure, as described earlier.

To demonstrate the application of a lamina failure criterion in predicting both initial and ultimate strengths, let us consider graphite/epoxy tubes of $(0, \pm 60)_S$ symmetric construction. Figure 9 presents a comparison of

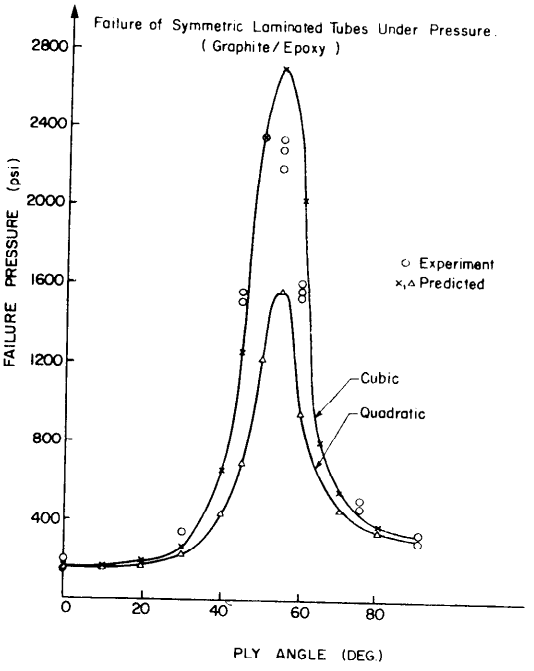

Fig. 7

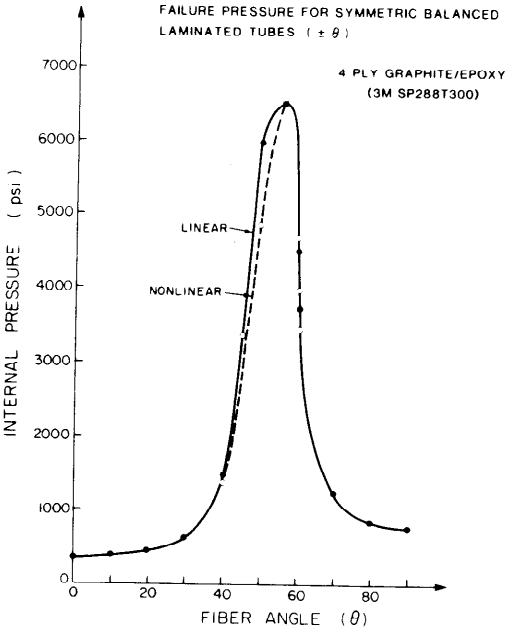

Fig. 8

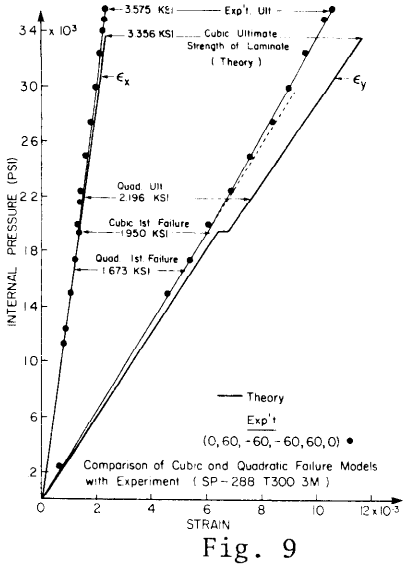

Fig. 9

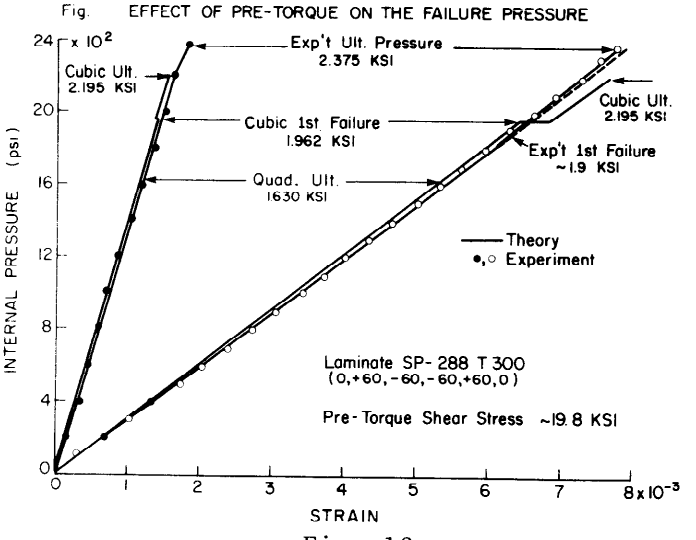

Fig. 10

quadratic and cubic model predictions for internal pressure loading (α = 0.5). Again, quadratic theory substantially underestimates both initial and ultimate failure loads.

In the second experiment, a pre-torque shear stress of $\sim$ 19.8 KSI was applied and the tube subsequently loaded by internal pressure until it fractured. The load/strain curves are shown in Fig. 10 where it can be seen that the agreement between test and predicted results is excellent. In this instance, quadratic theory predicts only one failure load at a value well below the onset of actual initial ply failure.

The third test involved pre-loading the tube with an internal pressure of 1.10 KSI and then torque loading it to failure. Figure 11 contains comparisons of the experimental torque/shear strain data with predictions based on the cubic criterion, which are in quite good agreement. It can be observed that the test sample exhibited nonlinear behavior up to first failure and then followed a different response slope up to final fracture. Although theory predicts a second failure mode, it is too close to the ultimate strength and was not observed experimentally. Note that quadratic estimates in this case exceed the cubic values and this appears to be typical when failure due to torsion loading is involved. Further details on similar tests conducted on other laminates can be found in [4] and [8].

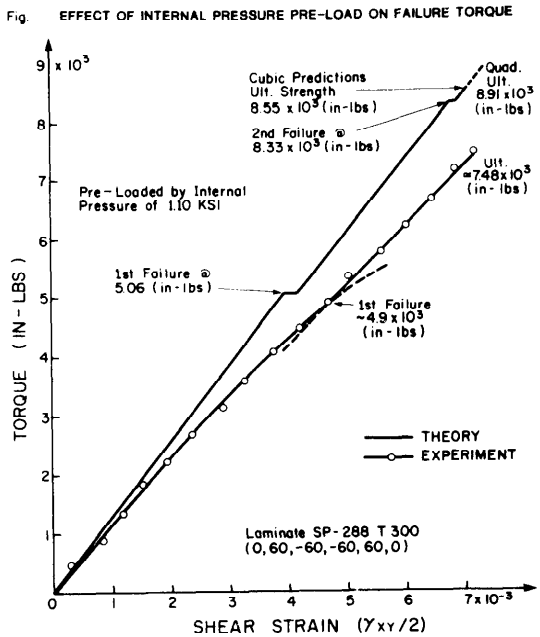

Fig. 11

Effect of Bending Loads

To investigate the effect of bending on the failure of laminates, particularly multi-mode cases when $[B_{ij}] \neq 0$, graphite/epoxy (3M SP 288 T300) plate specimens were subjected to 'pure' M_x loading. This was obtained with a four-point load system acting on a central test section nominally 2" long × 1" wide bounded by two clamped edges and two free sides. Depending on the laminate configuration, clamping produced some M_y and M_{xy} loading due to K_y, K_{xy} curvature constraints. Finite element analysis was used to ascertain the effect of boundary conditions on the test section stresses and these results were compared to biaxial strain gauge measurements on the top and bottom surfaces of the samples.

Table III summarizes the test results for both $(0, 90)_s$ and $(0, \pm45, 90)_s$ laminates together with the cubic and quadratic model predictions. Note that for the orthotropic configuration $(0, 90)_s$, little difference exists between the ultimate failure moments using either a quadratic or cubic analysis, although the predicted failure modes do not agree. It was found that a small increase ($\sim$ 5%) in the 0° compressive strength (X') shifted the mode from compression to tension using the cubic equation, but not for the quadratic model which required more than a 10% change.

The quasi-isotropic laminate $(0, \pm45, 90)_s$ was found to exhibit first ply failure around 80 lbs resulting in matrix cracking in the 0° compression plies. Subsequent analysis with $[B_{ij}] \neq 0$ indicated that the corresponding 0° fibers should fail in compression, but this was not observed. Rather, because of the bending mode distortion, the 0° plies could be regarded as 'buckled'. Thus,

the analysis was continued without permitting these fibers to fracture in compression and the next failure mode was that of the 0° laminae in tension. This constituted 'final failure' of the structure and both the quadratic and cubic models yielded similar values. Experimental observations (based on seven samples) confirmed the final failure as 0°-tension with no 0°-fiber compression fracture evident.

Table III Comparison of Bending Test Results with Failure Predictions (Graphite/Epoxy 3M SP 288 T300)

LAMINATE CONFIGURATION	MODULI USED IN CALC.	M_x-BENDING MOMENT RESULTANT (LBS)						
			PREDICTED					
			$M_y=0$		$M_y=.028\ M_x$		$K_y=0$	
		MEASURED	CUBIC	QUAD.	CUBIC	QUAD.	CUBIC	QUAD.
$(0°,90°)_{2s}$ 16 ply	$E_{11T}=20.5$ $E_{11C}=17.8$	225 0° COMP. 235	184.3	172.2	—	—	184.7	162.1
FAIL.MODE	(MSI)	0° TENSION	0° TENSION	0° COMP.			0° TENSION	0° COMP.
$(0°,\pm45°,90°)_{2s}$ 16 ply	$E_{11T}=20.5$ $E_{11C}=14.7$ (MSI)	129 133 127 137 134 123 133	1st ∿ 70 0° COMP.	1st ∿ 80 0° COMP.	1st ∿ 80 0° COMP.	1st ∿ 90 0° COMP.	Total 143.6	1st 130.5 0° TENSION 2nd 138.1 0° COMP.
			Total	Total	Total	Total		Total
		0° TENSION	127.0	133.4	129.5	134.5		142.8
FAIL.MODE		AVG. 131	0° TENSION	0° TENSION	0°TENSION	0° TENSION	0° TENSION	0° TENSION

Figures 12 and 13 illustrate the moment/strain data obtained from the tension and compression outer surface plies. The various failure loads are also shown. For the quasi-isotropic case, it was established from transverse strain gauge measurements and finite element analysis that the clamped boundary conditions produced an M_y load component given by $M_y = 0.028\ M_x$. However, as can be seen from Table III, this did not produce any significant effect on the failure moments.

Strength of Laminates With Holes

A series of tension tests were carried out on off-axis (θ) and angle-ply ($\pm\ \theta$) glass/epoxy laminates (3M, 1003) containing circular holes with d/W = 0.15, 0.25 and 0.40. Two or three replicates were tested for varying values of θ for both laminate configurations, the results of which are presented in Figs. 14 and 15. Note that 'first failure' was taken as the laminate strength value. This is consistent with the tests conducted on 0° and 90° laminates to determine both the tensor polynomial parameters and the 'characteristic distances' used in the 'point stress' calculations. As noted in Figs. 14 and 15,

the predicted curves are based on 'point stress' calculations of the strength parameters for varying d/W. In Fig. 16, the curves were obtained from the experimentally determined strength coefficients for d/W = 0.25 (given in Table II). One can readily see that both methods provide good agreement with

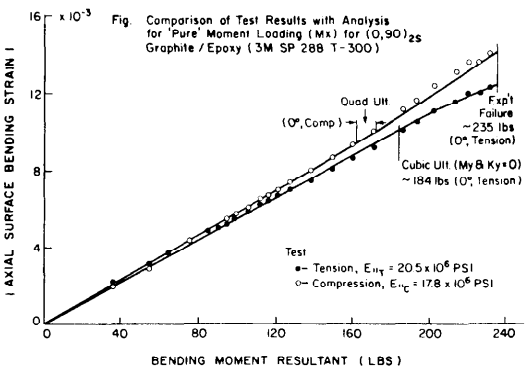

Fig. 12

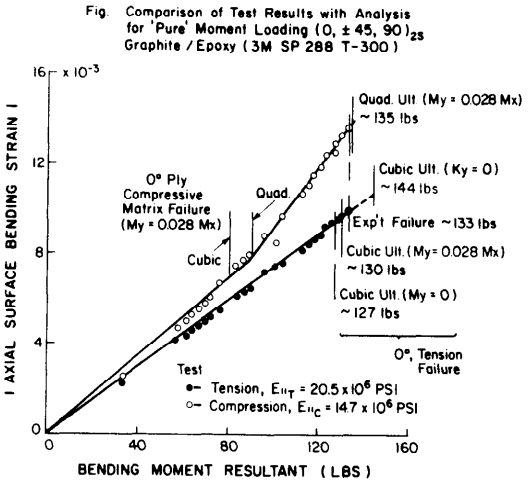

Fig. 13

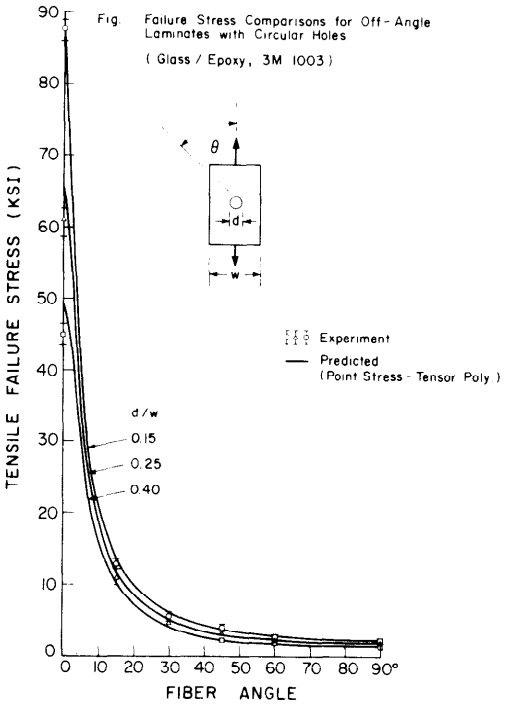

Fig. 14

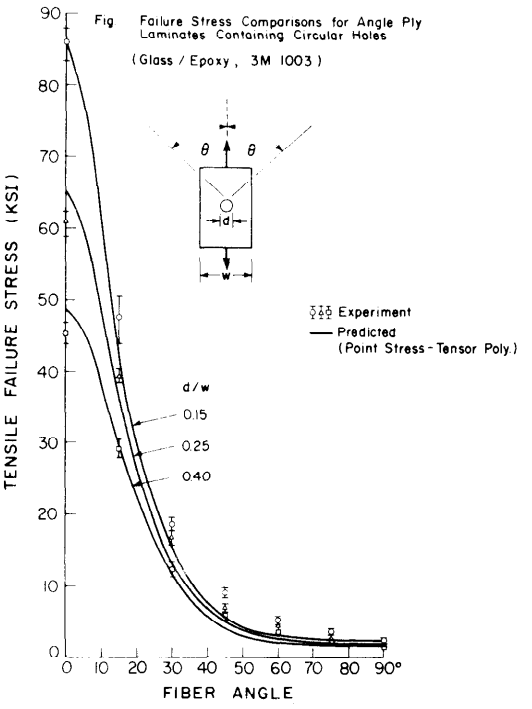

Fig. 15

test data. It now remains to perform the necessary biaxial tests and evaluate the interaction parameters to assess the validity of using the tensor polynomial failure criterion on laminates with holes, subject to general loading conditions.

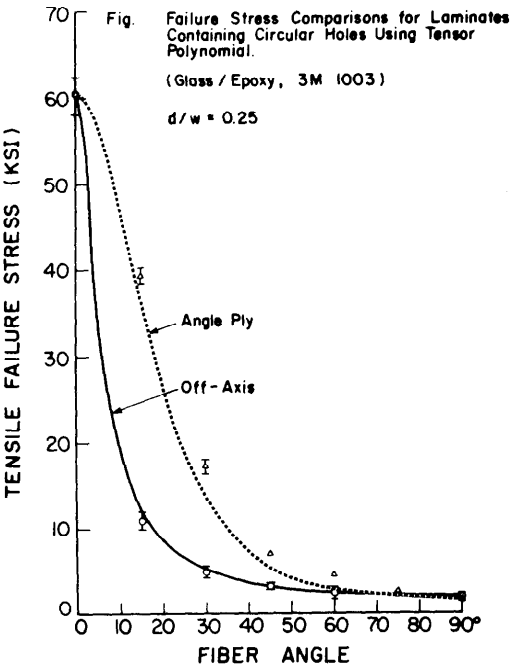

Fig. Failure Stress Comparisons for Laminates Containing Circular Holes Using Tensor Polynomial.
(Glass / Epoxy, 3M 1003)
d/w = 0.25

Fig. 16

5. CONCLUSIONS

Experimental and analytical results have been presented demonstrating the necessity of incorporating a higher order strength criterion than the quadratic form, particularly for biaxial and combined loading. The cubic polynomial form of the strength criterion has been shown to provide good correlation with test data for the range of configurations studied, although care must be exercised for those cases where complex solutions are obtained. There is no doubt that significant differences between the two formulations can exist both in terms of failure stresses and in the selection of optimum ply orientations.

One area of concern that still exists relates to the proper treatment of compressive ply failure. Further effort is necessary to determine the modifications required to account for fiber buckling and delamination.

Finally, application of the tensor polynomial failure criterion to the strength analysis of laminates with holes has been demonstrated for uniaxial loading. Clearly additional experiments must yet be performed to obtain the interaction coefficients and a larger data base for various biaxial load conditions before this model can be used with confidence.

6. ACKNOWLEDGEMENTS

The authors wish to gratefully acknowledge the financial support for this program received from both the National Aeronautics and Space Administration under NASA Grant NSG-7409 and the Natural Sciences and Engineering Research Council of Canada under Grant A-2783. We also wish to note that the laminate cutout experiments and analysis were undertaken by Mr. Qi Rufan, a visiting Chinese scholar from Harbin Shipbuilding Engineering, Harbin, China. Mr. J. A. Zapfe, a research assistant at UTIAS, performed the bending tests and associated analysis.

REFERENCES

1. Malmeister, A. K , "Geometry of Theories of Strength", Mekhanika Polimerov,

Vol. 2, No. 4, 1966.

2. Tsai, S. W. and Wu, E. M., "A General Theory of Strength for Anisotropic Materials", J. Composite Materials, Vol. 5, 1971.

3. Tennyson, R. C., MacDonald, D. and Nanyaro, A. P., "Evaluation of the Tensor Polynomial Failure Criterion for Composite Materials", J. Composite Materials, Vol. 12, 1978.

4. Tennyson, R. C., Nanyaro, A. P. and Wharram, G. E., "Application of the Cubic Polynomial Strength Criterion to the Failure Analysis of Composite Materials", J. Composite Materials Supplement, Vol. 14, 1980.

5. Foye, R. L. and Baker, D. J., "Design of Orthotropic Laminates", presented at the 11th AIAA Structures, Structural Dynamics and Materials Conference, Denver, Colorado, April 1970.

6. Pagano, N. J. and Pipes, R. B., "The Influence of Stacking Sequence on Laminate Strength", J. Composite Materials, Vol. 5, Jan. 1971.

7. Hahn, H. T. and Tsai, S. W., "Nonlinear Elastic Behavior of Unidirectional Composite Laminae", J. Composite Materials, Vol. 7, 1973.

8. Tennyson, R. C., "Application of the Cubic Strength Criterion to the Failure Analysis of Composite Structures", NASA-CR-165712, May 1981.

9. Nuismer, R. J. and Whitney, J. M., "Uniaxial Failure of Composite Laminates Containing Stress Concentrations", Fracture Mechanics of Composites, ASTM STP 593, 1975.

10. Garbo, S. P. and Ogonowski, J. M., "Strength Predictions of Composite Laminates with Unloaded Fastener Holes", J. American Inst. Aeronautics and Astronautics, Vol. 18, No. 5, May 1980.

STATIC INDENTATION TESTS ON COMPOSITE PLATES FOR IMPACT SUSCEPTIBILITY EVALUATION

Gretchen M. Bostaph* and Wolf Elber
NASA Langley Research Center
Hampton, Virginia 23665

SUMMARY

Static indentation tests with spherical steel indenters were conducted on thin composite plates to assess the impact susceptibility of graphite epoxy composites. The data were used to validate an impact strength analysis based on large deflection plate theory. Tests and analysis were in good agreement on both plate stiffness and maximum strain energy at failure. A parametric analysis showed that for brittle matrix composites the matrix dominated the threshold of damage, while in tough matrix composites the fibers dominated the threshold of damage. Penetration was always dominated by large deflection membrane effects.

INTRODUCTION

High modulus fiber reinforced composites have strength to weight ratios that make them attractive for use in aircraft structures. However, the damage tolerance of these materials is limited because, unlike most metals, these fibers have no plastic stress relief capability and can only store energy elastically. Even in normal use an airplane can be subjected to low velocity impact from service equipment or tools. In metal structures such minor incidents may produce surface dents and usually are not reported or investigated, but in composites the damage may be much more serious.

In composite skins, the first level of impact damage occurs as delaminations invisibly inside the skin. The second level of damage, especially in thin skins, occurs (as visible damage) on the back face of the skin only. Visible upper surface damage is normally the most advanced level of impact damage. Current research in impact tolerance of composites is aimed at improving the threshold at which delamination damage occurs by developing stronger and tougher resins [1] and by developing graphite fibers with higher ultimate strains.

The goal of this study was to develop simple analytical techniques for application to the impact problem, and to provide parametric equations suitable for use in material selection. Experimental results for this study were obtained from static plate indentation tests. For the highly elastic materials, such static tests may provide a very reliable substitute for the more expensive impact tests. All tests in this study were conducted on thin (8-ply), quasi-isotropic plates, which are typical of what will first appear in aircraft use, and because the introduction of membrane stretching is simpler in thin laminates.

*Structures Laboratory, U.S. Army Research and Technology Laboratories (AVRADCOM), NASA Langley Research Center.

LIST OF SYMBOLS

A	membrane tension coefficient
a	plate radius, m
b	plate radius less contact radius, m
c	equivalent load radius, m
d_c	membrane deflection under load point, m
d_r	membrane deflection outside load point, m
E	Young's modulus, Pa
E	plate modulus, Pa
H	plate thickness, m
K_F	flexural stiffness, N/m
K_i	indentation stiffness
K_s	shear stiffness, N/m
P	total plate load, N
P_{cr}	critical load, kN
P_{del}	initial delamination load, kN
P_p	flexural plate load, N
P_M	membrane plate load, N
p	contact pressure, Pa
Q	load point radius, m
r	general radius point, m
r_m	radius of uniformly loaded membrane, m
r^*	radius of indentation, m
T	membrane tension force, N
u	radial displacement, m

W_{cr} strain energy at failure, J

δ total membrane displacement, m

δ_{cr} critical displacement, mm

δ_F flexural displacement, m

δ_i indentation displacement, m

δ_s shear displacement, m

δ_T total displacement, m

$\Delta\ell_c$ spherical membrane stretching, m

$\Delta\ell_r$ conical membrane stretching, m

ε_F flexural strain

ε_u ultimate fiber strain

θ membrane slope

σ membrane stress, Pa

τ shear stress, Pa

ν Poisson's ratio

ANALYSIS

Plate Membrane Action

During the failure process of 8-ply laminates, the displacements of the plate exceed the plate thickness for most of the plates tested. Membrane actions due to mid-plane stretching must therefore be analyzed. To model the membrane effects without resorting to expensive finite element solutions the membrane action can be simplified by modelling a one-dimensional membrane.

Figure 1 shows a membrane loaded by a uniform pressure on a radius r_m around its center. With the assumption of one-dimensionality this membrane deforms into a spherical shape underneath the load, and into a conical shape between the load and the support. The two portions of the membrane can be analyzed separately and made compatible at the radius r_m. In the analysis of this membrane, first order approximations will be made, for instance $\theta = \sin\theta$, and the sphere will be considered equivalent to a paraboloid.

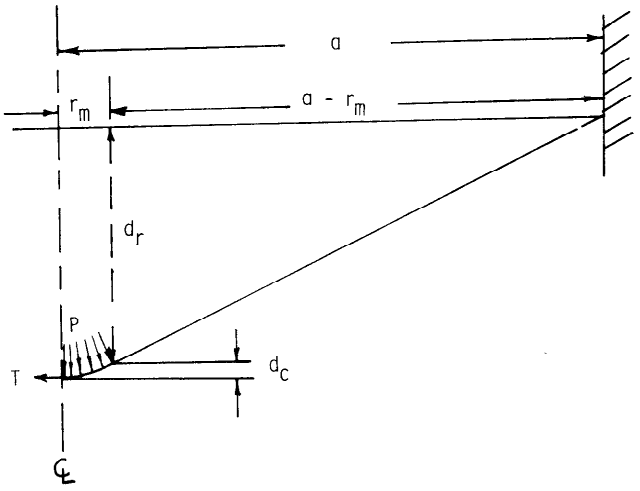

Figure 1. Cross-section of deflected ideal circular membrane.

The spherical membrane will be treated first. For an applied load P, the stress in the membrane is uniform and given by

$$\sigma = \frac{P}{4\pi H d_c}$$

If the membrane junction point r_m has an outward radial displacement u, and a membrane tension force T, we can establish two equations for the stretching of the membrane.

From the displacement condition the first-order approximation for the stretch in the spherical portion is

$$\Delta \ell_c = \frac{d_c^2 + u^2 + 2ur_m}{2r_m}$$

and from the elastic properties

$$\Delta \ell_c = \frac{T}{2\pi H E'}$$

where $E' = E/(1-\nu^2)$, which assumes that the tangential strains are zero. Elimination of $\Delta \ell_c$ results in the membrane equation

$$\frac{d_c^2 + u^2 + 2ur_m}{2r_m} = \frac{T}{2\pi HE^r} \tag{1}$$

The slope of the membrane at the junction point to be used later is

$$\theta = 2\frac{d_c}{r_m} \tag{2}$$

The conical portion of the membrane carries no transverse load. Under the membrane force T the radial stresses vary inversely with the radius

$$\sigma = \frac{T}{2\pi Hr}$$

from which the elastic elongation can be found as

$$\Delta\ell_r = \frac{T}{2\pi HE}\,\ell n\left(\frac{a}{r_m}\right)$$

The radial outward displacement of the junction point is again u, so that the geometric stretch of the membrane is

$$\Delta\ell_r = \frac{d_r^2 + u^2 - 2bu}{2b}$$

where $b = a - r_m$.

For the conical membrane then

$$\frac{d_r^2 + u^2 - 2bu}{2b} = \frac{T}{2\pi HE}\,\ell n\,\frac{a}{r_m} \tag{3}$$

The slope at the junction point is

$$\theta = \frac{d_r}{b} \tag{4}$$

The two displacements of the conical and spherical membranes, d_c and d_r, can be related by equating the slopes in equations (2) and (4), so that

$$d_c = \frac{r_m}{2b} d_r$$

Equations (1) and (3) can be solved simultaneously for the radial displacement u, and the total membrane load P can be determined by back substituting into equation (1) or (3).

Although these solutions can be obtained in complete algebraic form, it is simpler to solve for the radial displacement u and then calculate P.

Most membrane solutions [2] are written around the correlating function

$$\frac{EH\delta^3}{a^2}$$

The membrane load is then

$$P = A \frac{EH\delta^3}{a^2}$$

Figure 2(a) shows the function A. It varies with the parameter r/a, and is independent of the plate displacement. The function approaches $A = 0$ for a point load and $A = 2\pi$ for a load distributed over the full membrane.

In composite plates loaded by a spherical indenter, the indentation causes a small distributed load zone. The radius of the membrane under the spherical indenter is somewhat larger than the radius of the sphere even when the plate is largely delaminated.

It is therefore assumed in this analysis that the effective load distribution radius r_m is

$$r_m = 2H + 0.03\ a$$

to fit the observations in experiments.

Figure 2(b) shows the load-displacement curves for five membrane sizes on the assumption that the plates have lost all flexural stiffness.

By calculating the membrane strain in the spherical portion of the membrane, critical displacements and critical loads can be calculated. The curves in Figure 2(b) are truncated at these critical values.

Plate Flexural Action

For small plate deflections of clamped circular plates the flexural stiffness dominates the plate reaction. For the purpose of this analysis we will assume that the flexural deflections react to the spherical indenter like to a ring load of radius c, where c will be chosen equal to one plate thickness. This approach avoids the stress singularities associated with a point load solution. From reference [2] the center displacement is

$$\delta_F = \frac{3Pa^2}{4\pi E'H^3}\left(2\frac{c^2}{a^2}\ln\frac{c}{a} + 1 - \frac{c^2}{a^2}\right)$$

The curvature inside the ring load is constant and the strain on the bottom surface can be obtained as

$$\varepsilon_F = \frac{3P}{2\pi E'H^2}\left\{\frac{1-\nu}{2}\left(1 - \frac{c^2}{a^2}\right) - (1+\nu)\ln\frac{c}{a}\right\}$$

If $c < 0.03a$, δ_F is within 1% of the point load deflection, so that the strain can be written in terms of the displacement as

$$\varepsilon_F = \frac{2H\delta}{\pi a^2} \times \left\{\frac{1-\nu}{2}\left(1 - \frac{c^2}{a^2}\right) - (1+\nu)\ln\frac{c}{a}\right\}$$

Plate Indentation

A rigid spherical indenter will cause an indentation in the plate. The Hertzian Law [3] relates the indentation depth to the load, where

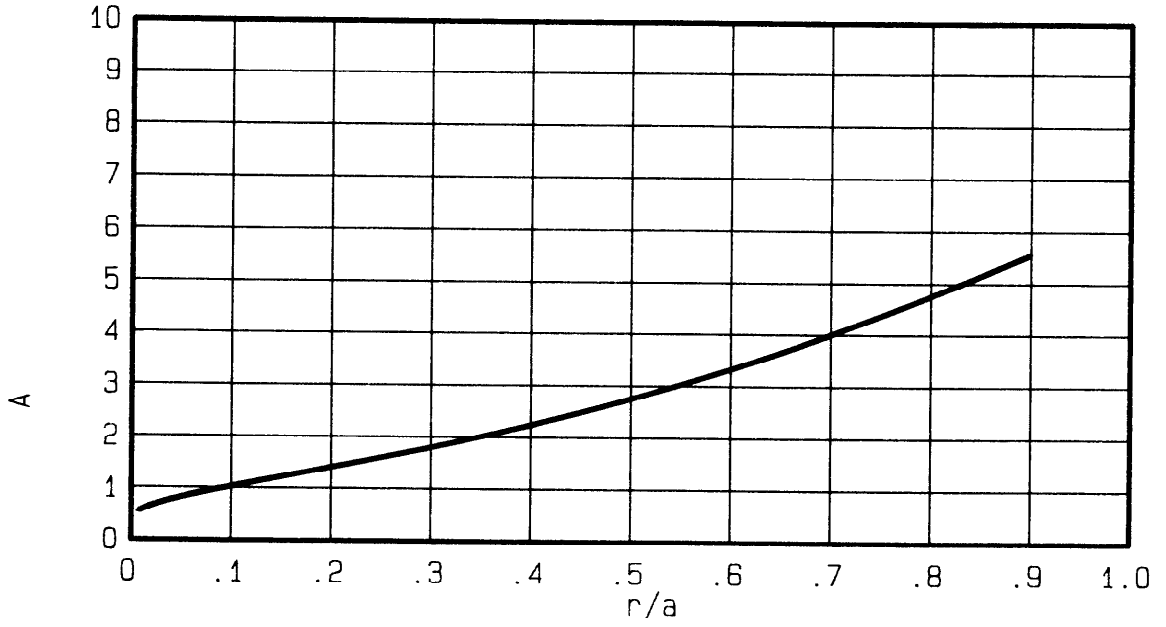

a) Membrane tension coefficient

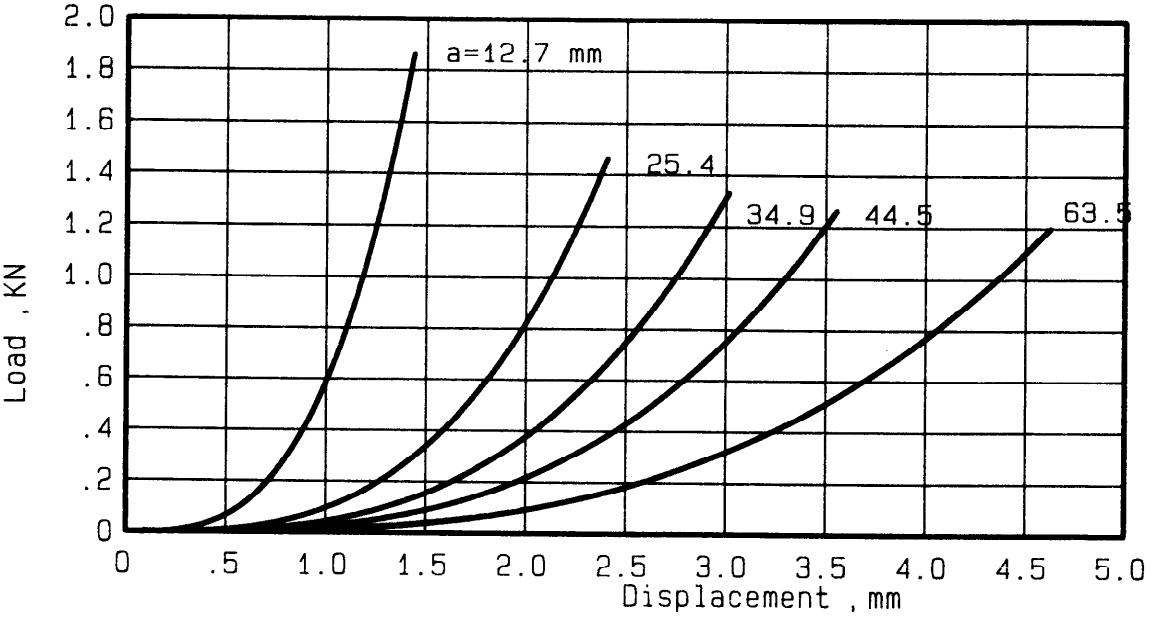

b) Membrane load-displacement curves for aperatures tested.

Figure 2. - Predicted membrane behaviour.

$$\delta_i = \left(\frac{P}{K_i}\right)^{2/3}$$

If the sphere has a radius Q then the radius of the indentation area is

$$r^* = \sqrt{2Q\delta_i}$$

Plate Shear Action

The region of maximum shear stress is the cylinder of radius r^* and height H. This shear stress is given by

$$\tau = \frac{P}{2\pi H r^*}$$

Substituting for r^* and δ_i gives

$$\tau = \frac{K_i^{1/3}}{2\pi H\sqrt{2Q}} P^{2/3}$$

This shear stress will be used in a delamination criterion.

The shear deflections of the plate can be obtained from the integration of shear strains as

$$\delta_s = \frac{P}{2\pi HG} \ell n \frac{a}{r^*}$$

Superposition of Plate and Membrane

The complete plate can be decomposed into two parts: a plate with shear and flexural stiffness but no mid-plane extensional stiffness, and a membrane with mid-plane extensional stiffness, but no shear and flexural stiffness.

For a given displacement δ of the mid-plane the total load is then equal to the sum of the flexural plate reaction and the membrane reaction.

If K_F is the flexural stiffness

$$K_F = \frac{4\pi E' H^3}{3a^2}$$

and K_S is the shear stiffness

$$K_S = \frac{2\pi GH}{\ell n \frac{a}{r^*}}$$

then the plate reaction is

$$P_P = \frac{1}{1/K_F + 1/K_S}\,\delta$$

The membrane reaction is

$$P_M = A\,\frac{EH}{a^2}\,\delta^3$$

so that the total plate load is

$$P = P_M + P_P$$

The surface indentation can now be obtained from

$$\delta_i = \left(\frac{P}{K_i}\right)^{2/3}$$

so that the total plate displacement is

$$\delta_T = \delta + \delta_i$$

Parametric Analysis

Figure 3(a) shows the load displacement plot for a fully laminated 5208/T300 graphite-epoxy plate of aperture $a = 0.0254$ m and thickness $H = 1.05$ mm. This load displacement curve reflects the flexural stiffness in its original slope, but is non-linear even at zero load because of the indentation contribution. At displacements above one-half the thickness the membrane term becomes significant and at high loads dominates the plate stiffness.

The second curve would be the load-dominant curve if the plate lost all its flexural stiffness due to delamination and acted purely as a membrane. The experimental data should be bounded by these two curves, but this analysis does not aim to predict the actual load displacement curve.

Figure 3(b) shows three curves of critical load for 5208/T300 8-ply composite as a function of plate size. The shear criterion shows that for this material the onset of delamination is expected at 400 N. If the shear strength were much higher, then the flexural failure criterion would dominate. A minimum flexural strength is expected at $a = 2.5$ cm. For larger plates a higher fraction of the total load is carried by the membrane action which causes lower strains on the lower surface of the plate.

If delamination does occur first, the flexural failure criterion would not be applicable, and only the membrane failure criterion for the fully delaminated plate controls the penetration failure load for the plate.

The only significant material failure properties used in these criteria are the matrix shear strength (70 MPa), and the fiber ultimate strain ($\varepsilon_u = 0.01$). These simple models can be used to study the influence of changes in shear strength and fiber failure strain on the plate failure load and the maximum strain energy at failure.

EXPERIMENTAL PROCEDURE

Materials

Three different materials were tested in this study. They included 2 composite materials--8-ply quasi-isotropic 5208/T300 graphite/epoxy and 8-ply 5208/T300 quasi-isotropic HX205/C6000, a tough matrix composite. The stacking sequence for both materials was $[0,45,-45,90]_S$. While the 5208/T300 specimens had a thickness of 1.05 mm, the HX205/C6000 was considerably thicker, (almost 10%), with a thickness of 1.15 mm. For comparison of the composite test results with metal behavior, a specimen of 2024-T3 aluminum with a thickness of 1.02 mm, was also tested.

For failure mode analyses transparent 5208/E-glass composite was used. The lay-up was the same as for the graphite test specimens.

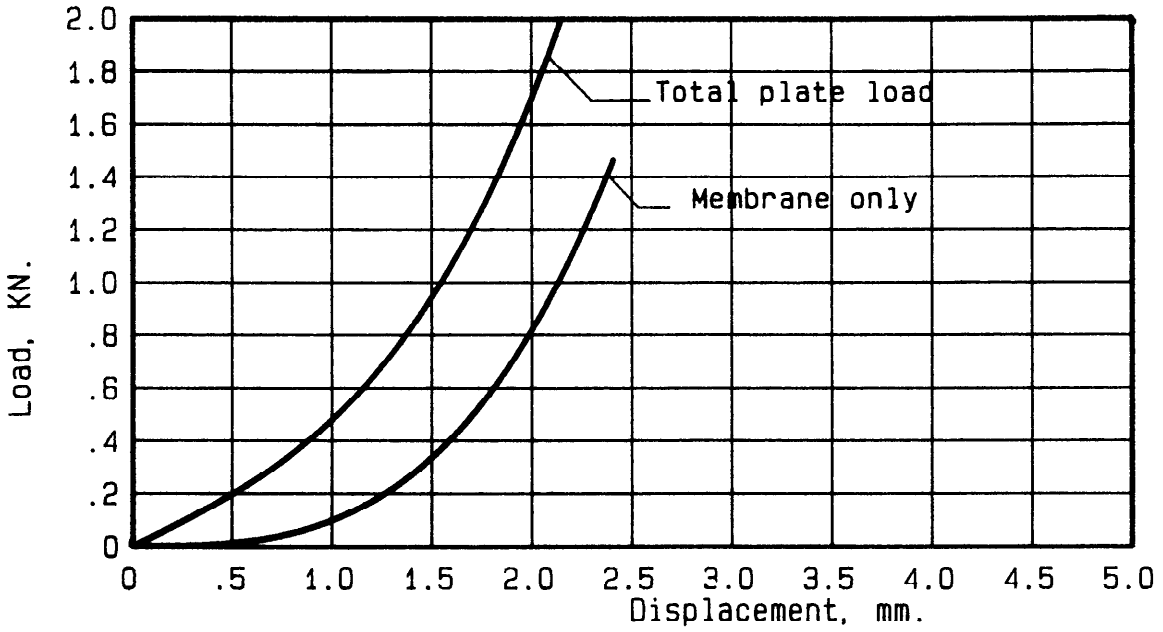

a) Plate flexural reaction and membrane reaction.

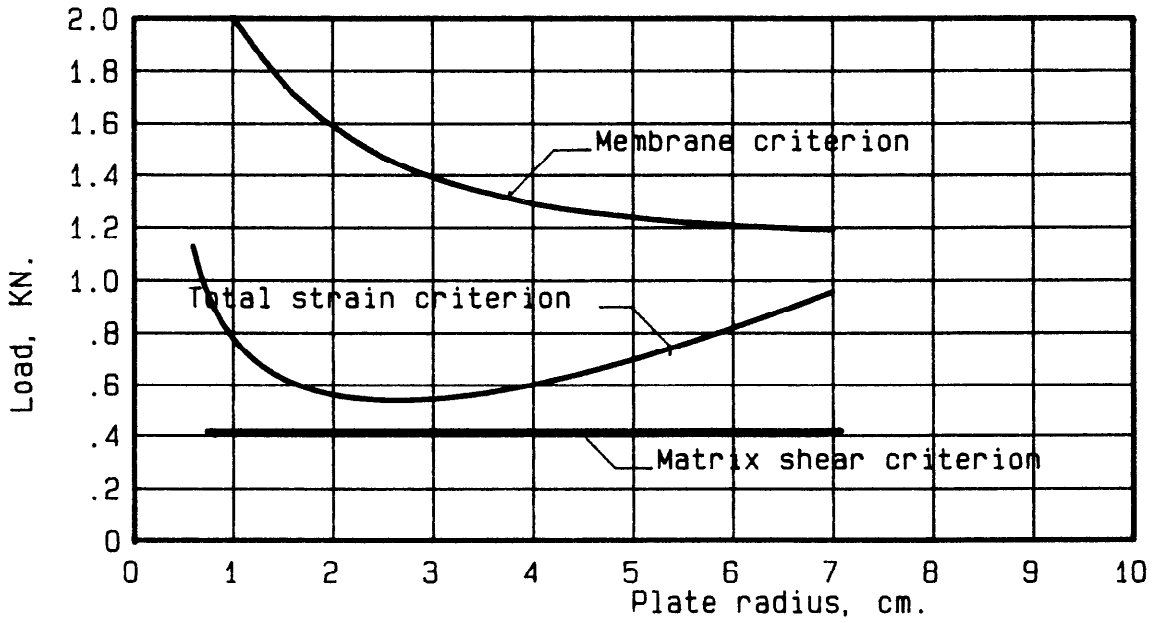

b) Predicted critical loads.

Figure 3.- Predicted Flexural and Membrane Stiffness.

Specimens

For static testing, samples of each of the test materials were bonded between two aluminum plates with various diameter circular apertures. These aluminum plates provide the specimens with fully-supported circular boundary conditions. The 5208/T300 specimens were tested using 6 different aperture sizes, ranging from 6.35 mm to 63.5 mm radius. The HX205/C6000 composite was tested with 6.35 mm and 12.7 mm apertures. The 2024-T3 was tested at only one aperture size, 34.9 mm.

Testing Equipment

The static loading tests were conducted in a servo-hydraulic testing machine. The test specimens were clamped to a platform, shown in Figure 4, which was mounted on the hydraulic ram, and load was applied to the center of the specimen by means of a punch, tipped with a 25.4 mm diameter steel ball. A DCDT displacement gauge was attached to the indenter to measure the plate deflection as the load was applied. The load cell and DCDT had been calibrated previously and found to have an accuracy within 1%. The electrical signals from the load cell and displacement gauge were first processed through a digital data acquisition system, and then through a computer and placed onto cassette tapes to allow direct load-displacement data plotting.

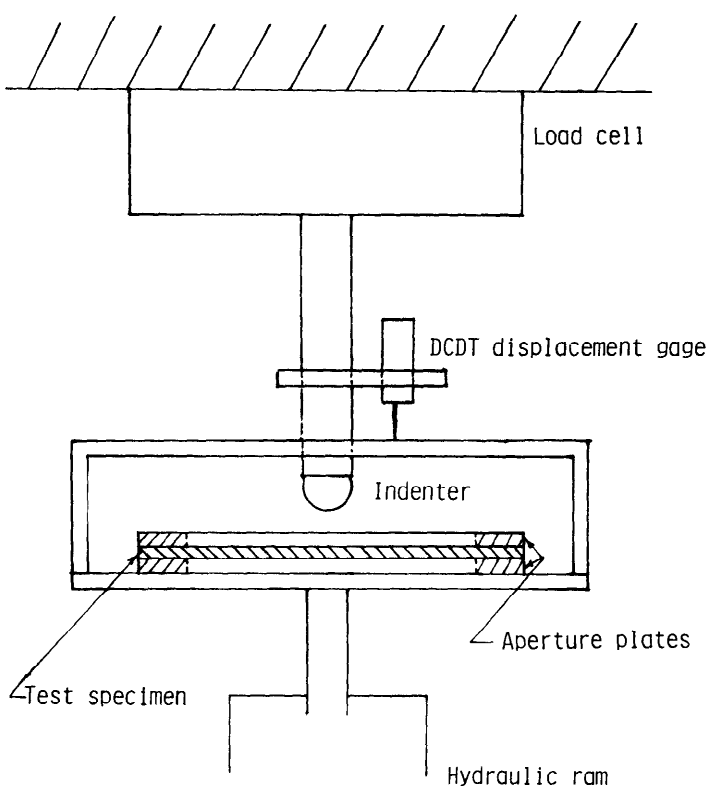

Figure 4. Static indentation test.

RESULTS AND DISCUSSION

Test Data

5208/T300

The 5208/T300 composite was tested with 6 different aperture sizes. Table 1 gives the aperture radius (a), the load at which delamination was first observed (P_{del}), the critical or instability load (P_{cr}), the critical displacement (δ_{cr}), and strain energy at failure (w_{cr}) for each test specimen. Load-displacement curves for each of the aperture sizes are shown in Figures 5-10. The curves for the two smallest apertures, Figures 5 and 6, show that the load displacement curve progresses linearly up to a load of about 400 N, and then the material undergoes a softening, or yielding. This is due to the interlaminar shear stresses causing the material to delaminate. While this delamination becomes audible in the larger aperture plates at approximately the same load level, it is not clearly demonstrated by the load-displacement curves in Figures 7-10. At large deflections, some stiffening of the specimens is apparent. This is an effect of membrane stretching. Under further loading, the material continues to deform until the plate is completely delaminated. Then, as the membrane strains under the indenter reach the critical strain of the fiber, 0.01, penetration failure occurs.

Figure 11 shows calculated values of fiber critical displacement and critical load (versus plate radius), which were determined by calculating the membrane strains in the spherical portion of the membrane. On the same figure, the experimental critical displacements and critical loads measured for each 5208/T300 specimen are plotted. Both plots show reasonable agreement between the calculated curves and the test data, which would indicate that the assumption of the analysis—that membrane forces dominate the plate failure—is valid.

TABLE I. RESULTS OF QUASI-STATIC TESTS OF 5208/T300

Aperture radius, mm	P_{del}, kN	P_{cr}, kN	δ_{cr}, mm	W_{cr}, J
6.35	0.40	1.80	0.90	0.70
12.7	0.40	1.75	1.55	1.19
25.4	0.37	1.59	2.45	1.63
34.9	0.41	1.48	2.90	1.58
44.5	0.42	1.43	3.45	1.85
63.5	0.40	1.30	4.25	1.89

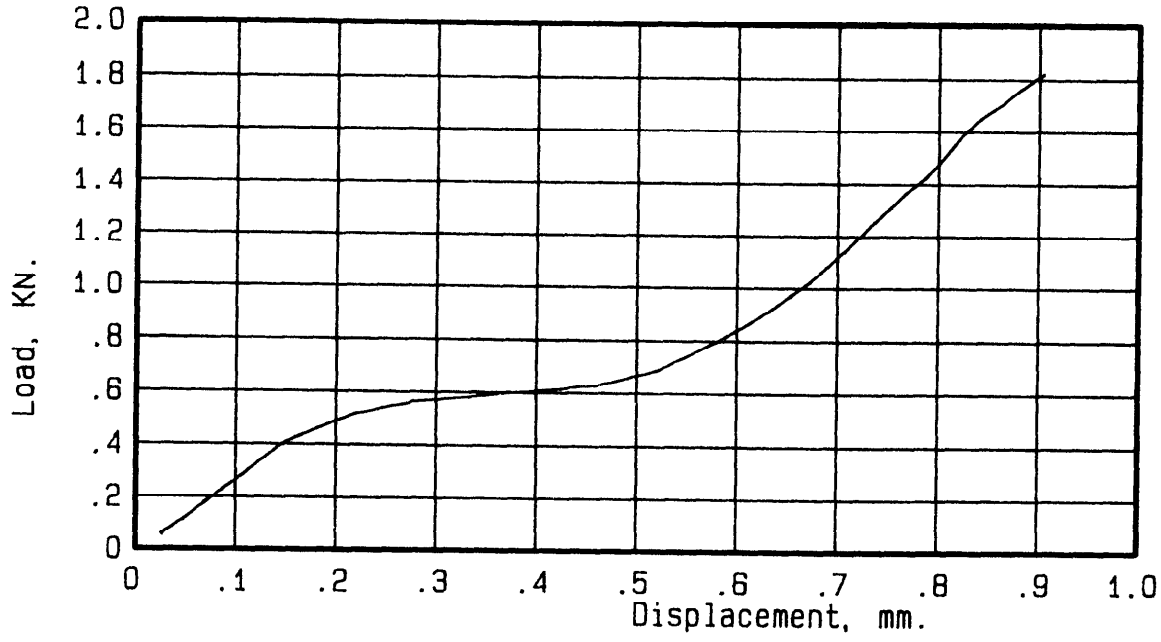

a) Load-displacement data.

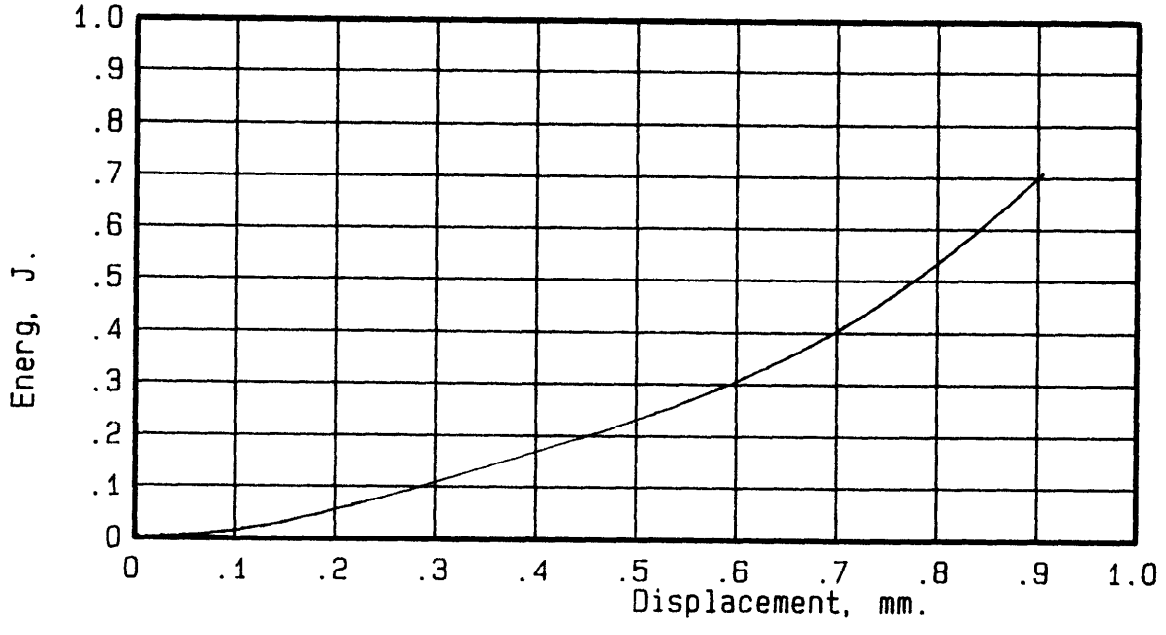

b) Energy-displacement data.

Figure 5.- Plate deformation data for 8-ply 5208/T300 composite plate. Aperture radius = 0.00635 m. Thickness = 0.00105 m.

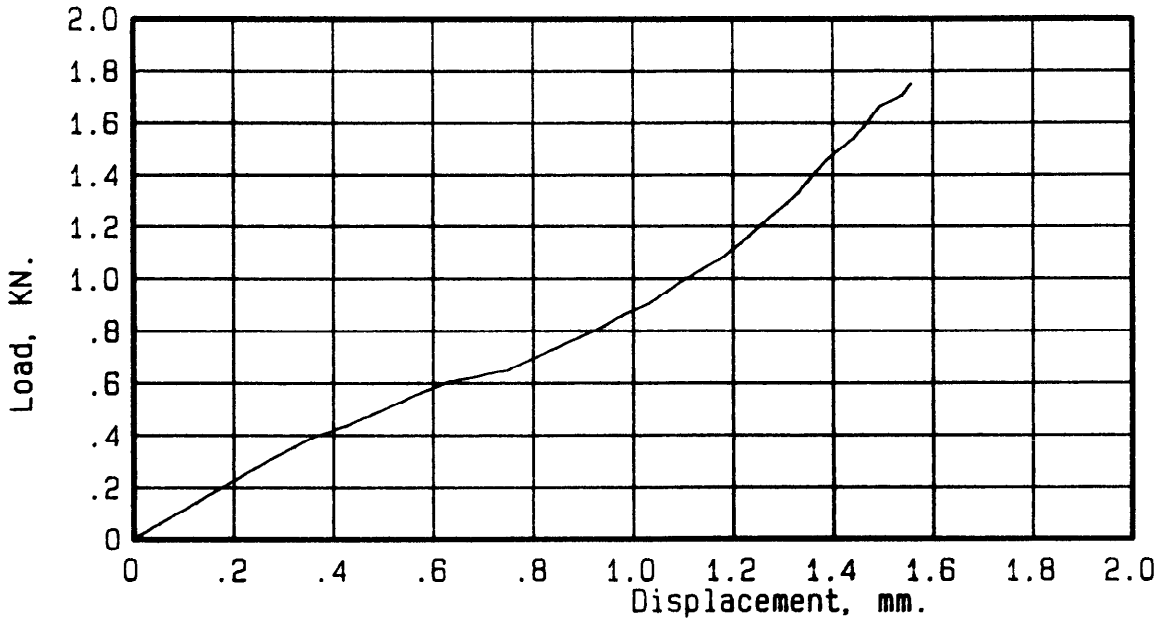

a) Load-displacement data.

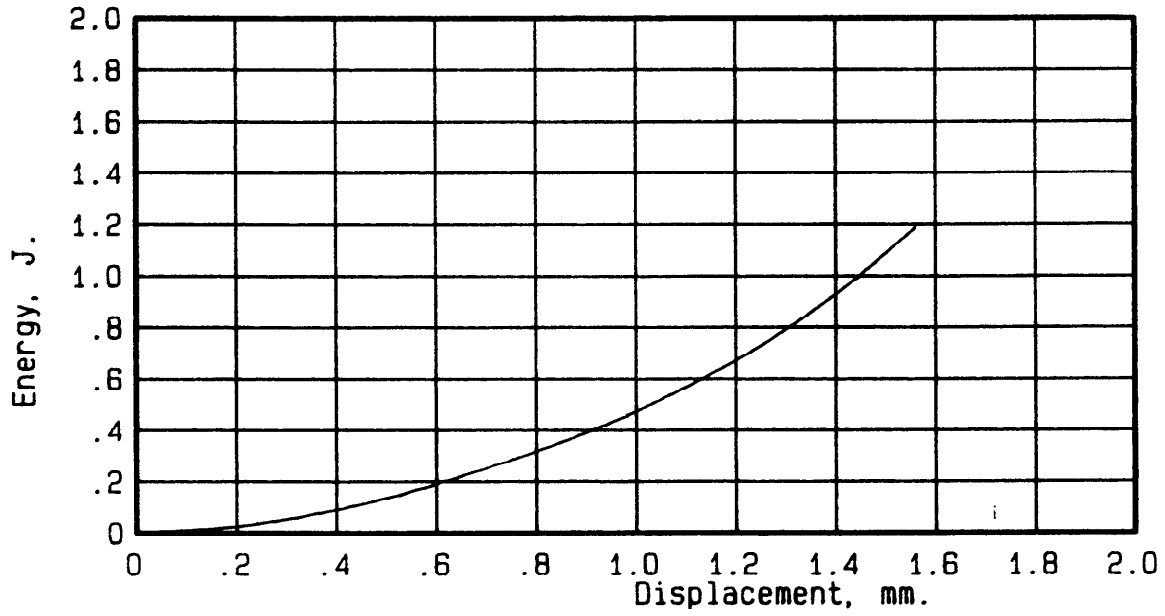

b) Energy-displacement data.

Figure 6.- Plate deformation data for 8-ply 5208/T300 composite plate. Aperture radius = 0.0127 m. Thickness = 0.00105 m.

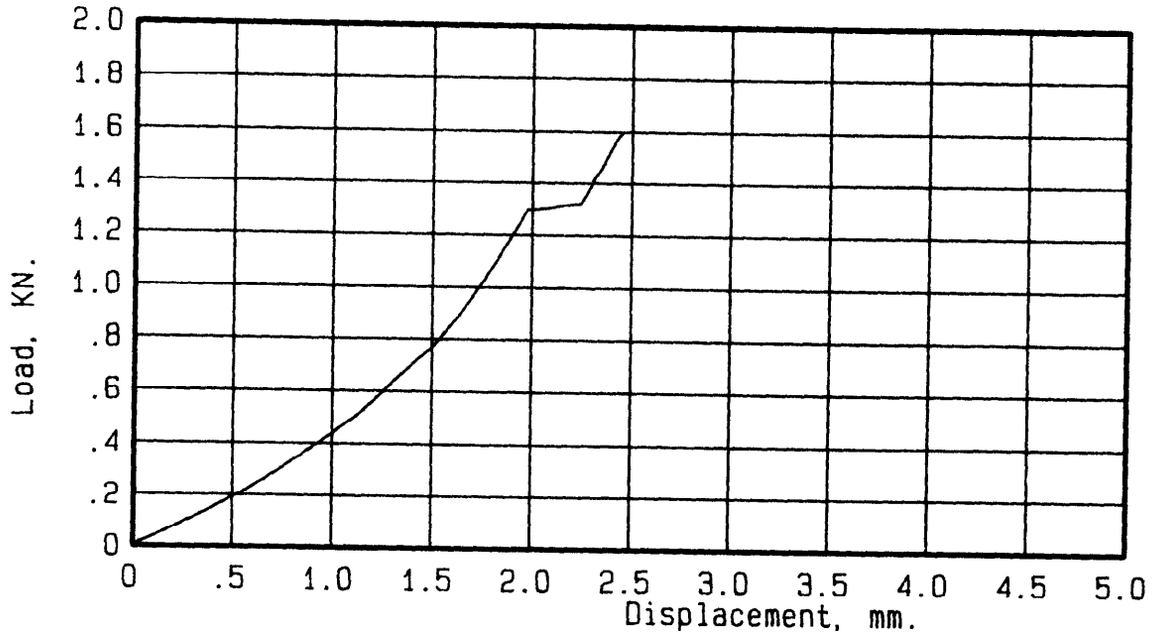

a) Load-displacement data.

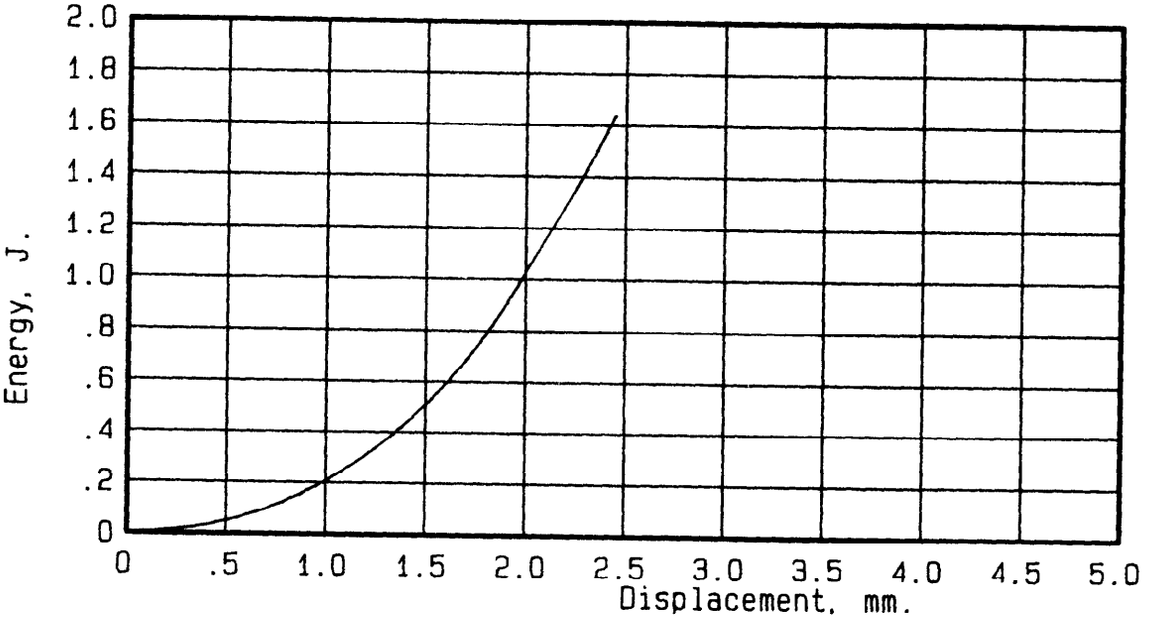

b) Energy-displacement data.

Figure 7.- Plate deformation data for 8-ply 5208/T300 composite plate. Aperture radius = 0.0254 m. Thickness = 0.00105 m.

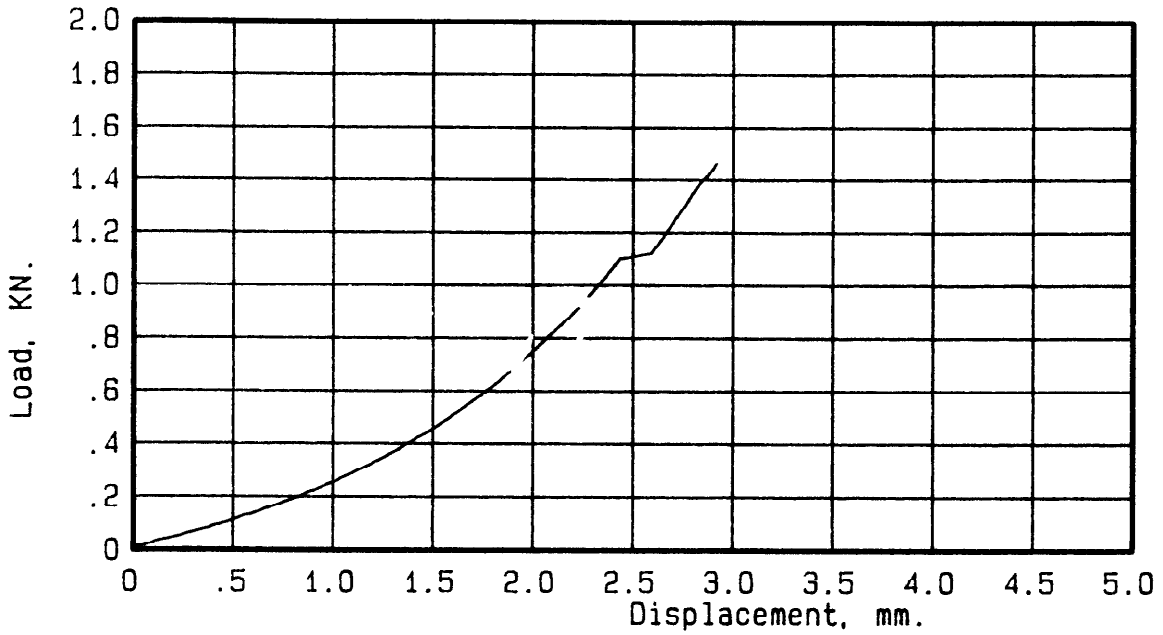

a) Load-displacement data.

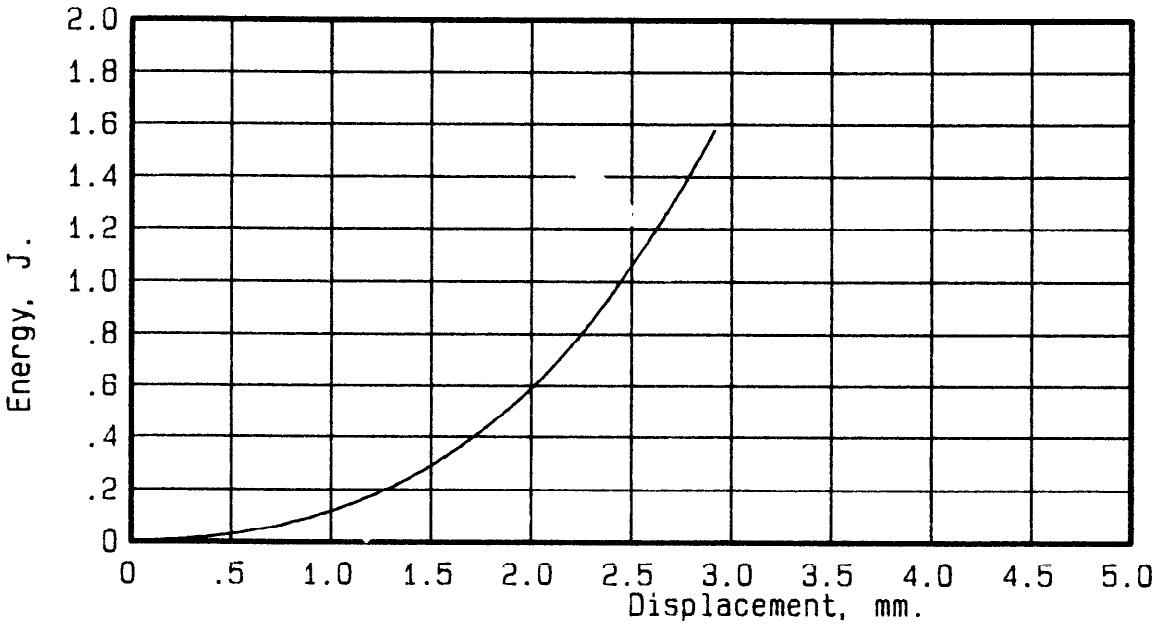

b) Energy-displacement data.

Figure 8.- Plate deformation data for 8-ply 5208/T300 composite plate. Aperture radius = 0.0349 m. Thickness = 0.00105 m.

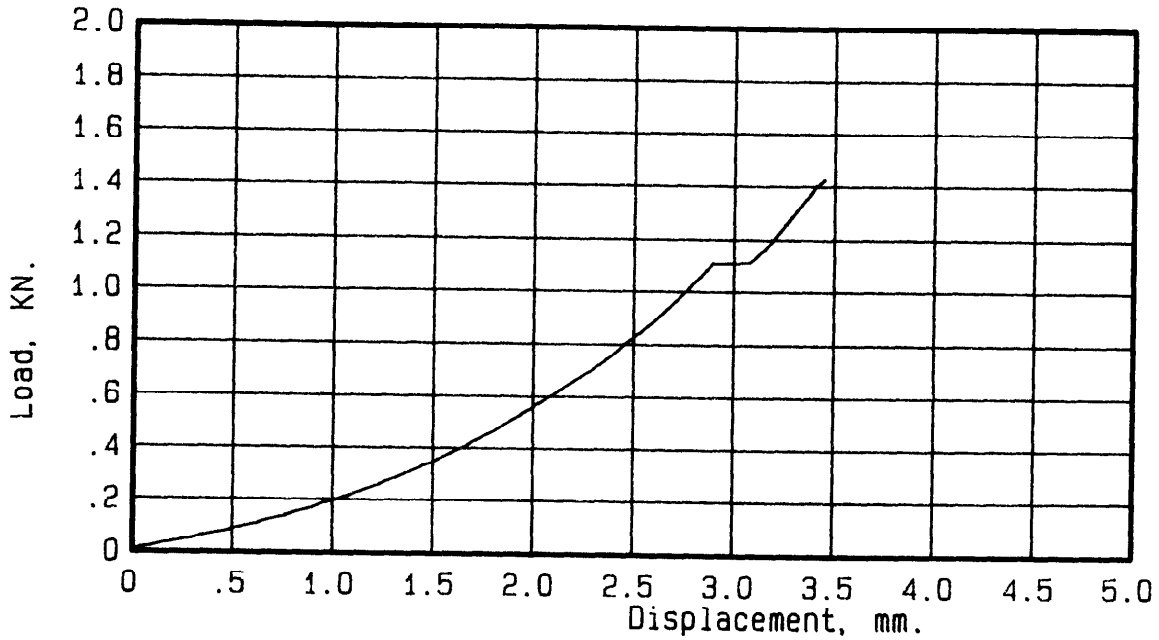

a) Load-displacement data.

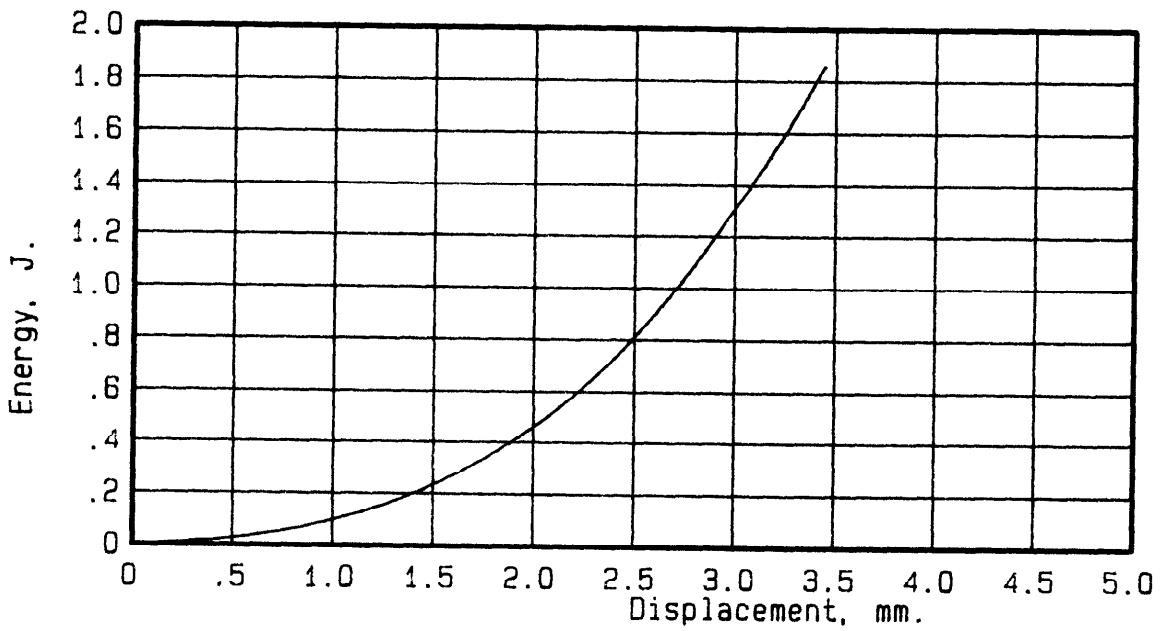

b) Energy-displacement data.

Figure 9.- Plate deformation data for 8-ply 5208/T300 composite plate. Aperture radius = 0.0445 m. Thickness = 0.00105 m.

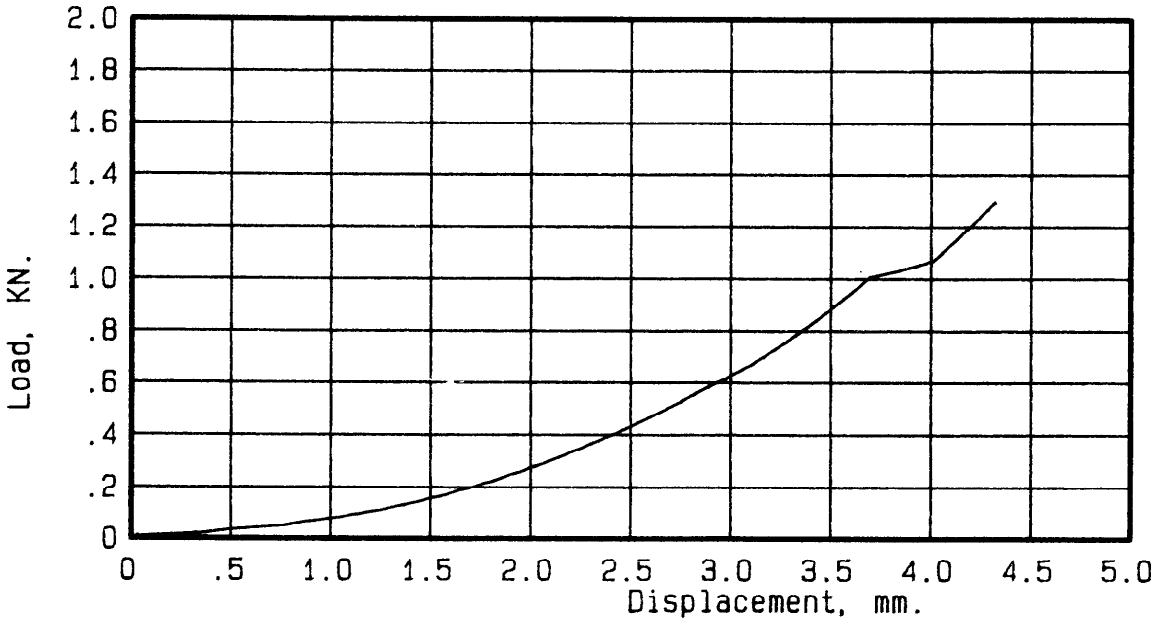

a) Load-displacement data.

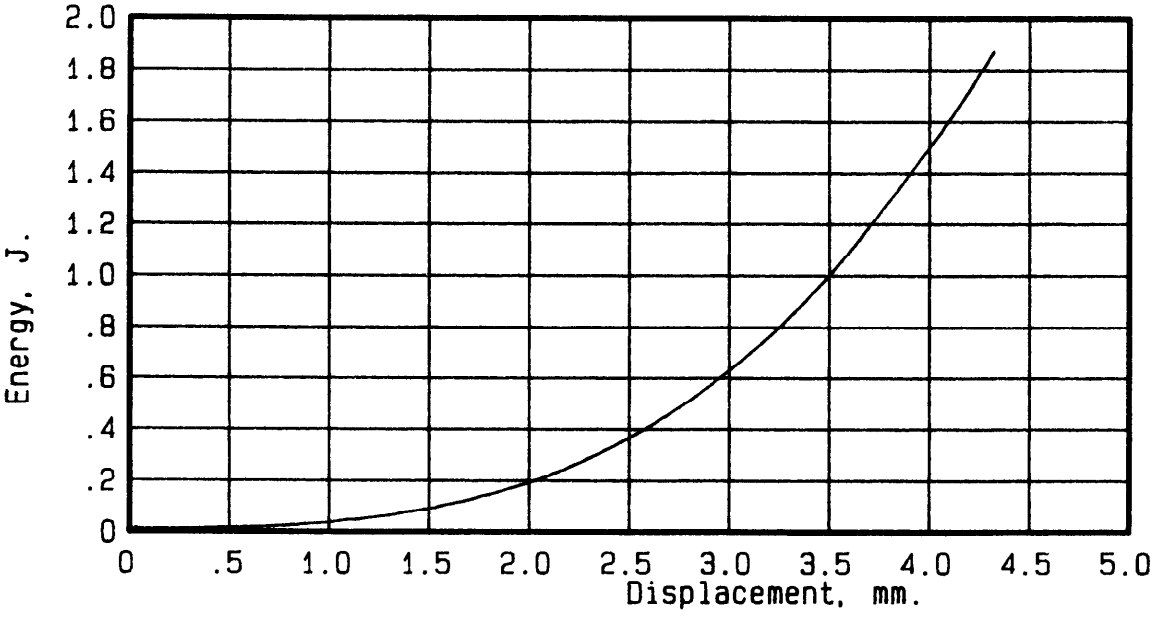

b) Energy-displacement data.

Figure 10.- Plate deformation data for 8-ply 5208/T300 composite plate. Aperture radius = 0.0635 m. Thickness = 0.00105 m.

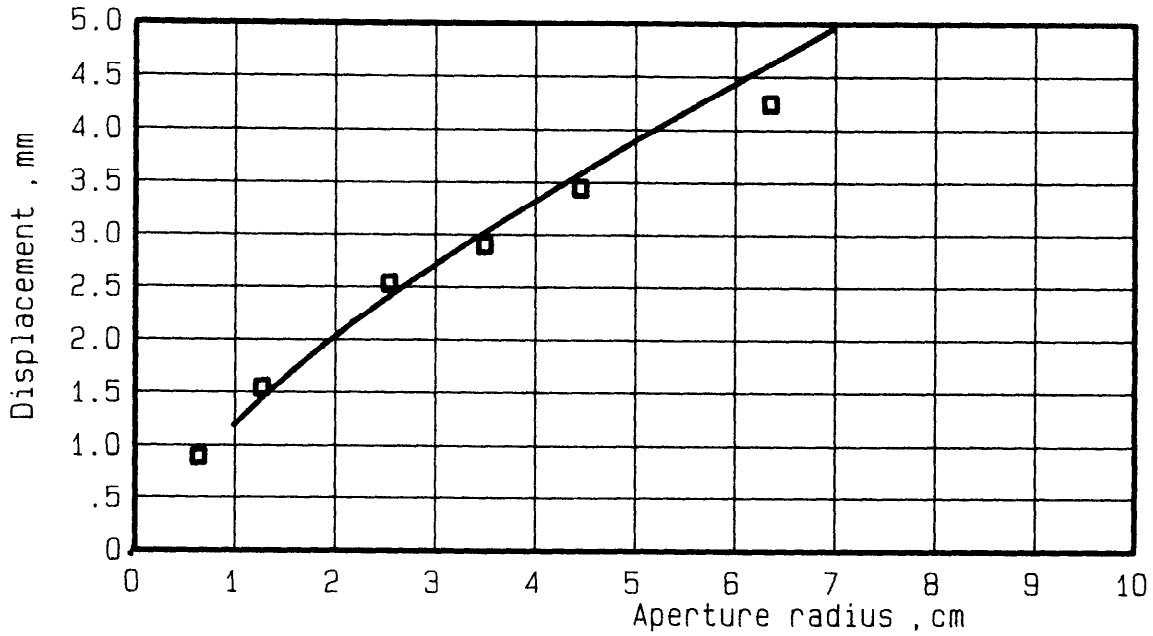

a) Critical displacement data.

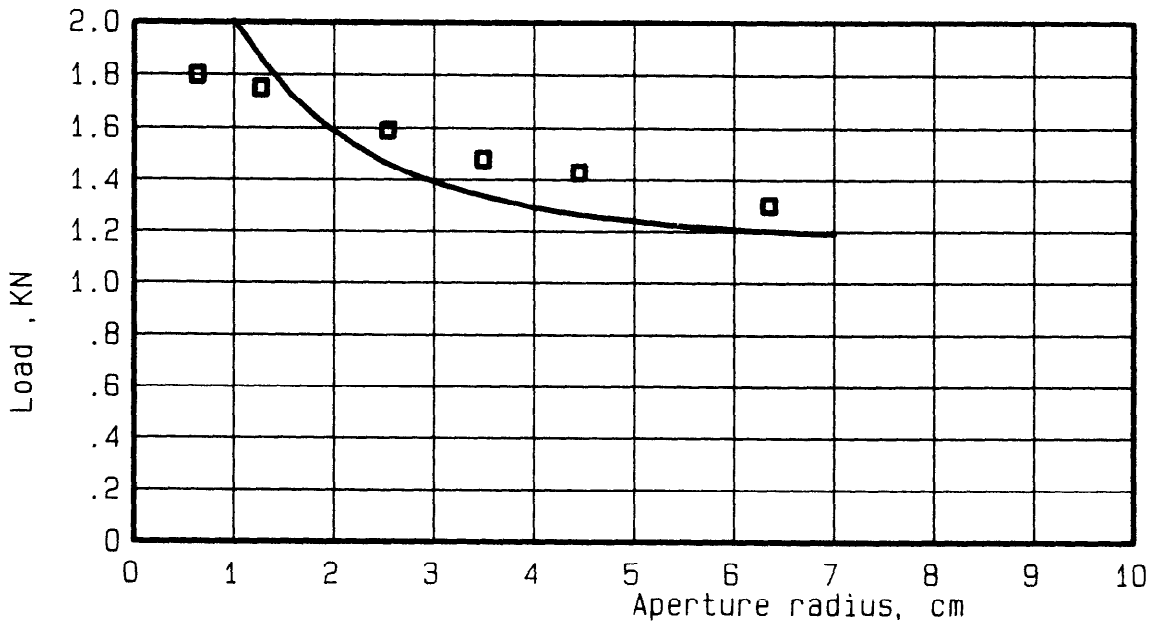

b) Critical load data.

Figure 11. - Membrane failure data for 5208/T300 composite plates.

In Figure 12(a), the load displacement curve for the 25.4 mm specimen is plotted, along with the curves for a fully laminated (full flexural stiffness) plate and a fully delaminated (no flexural stiffness) plate. The plot of the test data follows the predicted fully laminated curve to a load of approximately 400 N, the point where delamination was first detected audibly. The displacements at this load are plotted for each test specimen in Figure 12(b) along with a curve of the expected displacement at initial delamination, versus aperture size, as predicted by the analysis. Both Figures 12(a) and 12(b) show close agreement between the initial behavior of the specimens and behavior predicted by the flexural model.

HX205/C6000

Two specimens of the HX205/C6000 material were tested in this study. They had apertures of 6.35 mm and 12.7 mm radii. Figure 13(a) shows the loading-unloading loop for the smaller plate. As the figure shows, delamination is first apparent as specimen softening at a load of 900 N and a displatement of 0.28 mm. Comparing this to Figure 5 for the same size 5208/T300 specimen, where P_{del} = 400 N and δ_{del} = 0.14 mm, it is obvious that the tougher matrix of the HX205/C6000 can delay the onset of delamination significantly. A comparison of the strain energy versus displacement plots for the two materials shows that the HX205/C6000 has absorbed 0.14 joules before delamination begins, but the 5208/T300 has absorbed only 0.04 joules. Similar comparisons can be made for the 12.7 mm plates. Figures 6 and 14 give results for the 12.7 mm 5208/T300 plate and HX205/C6000 plate, respectively. Although, in Figure 14, the load at which the specimen first delaminates is not as obvious as in Figure 13, it is assumed that this size plate also delaminates first at about 900 N. This is a reasonable assumption, since some delamination was detected audibly at this load. The corresponding displacement and strain energy for the HX205/C6000 were 0.45 mm and .2 joules. Figure 6 shows that the 5208/T300 specimen first delaminates at only 400 N load and 0.35 mm displacement. The 5208/T300 specimen absorbs just 0.08 joules strain energy before the initial delamination occurs.

For both of the HX205/C6000 plates tested in this study, the effect of the tougher matrix was to increase the load necessary for incipient delamination. The amount of strain energy absorbed prior to delamination was also increased by 2-1/2 to 3-1/2 times in the HX205/C6000 specimens. However, Figures 13 and 14 also show that once the load for initial delamination has been reached, under further loading the plate will continue to delaminate in the same manner as the 5208/T300 specimens. Eventually the plate will become fully delaminated, at which point plate failure is again membrane critical and penetration failure depends on the fiber ultimate strain.

2024-T3 aluminum

Only one specimen, with a 34.9 mm radius aperture, of the 2024-T3 aluminum was tested in the study. The load displacement curve is shown in Figure 15. The initial elastic portion of the curve extends to about 800 N load, 1.4 mm displacement, before the first damage occurs. As the bottom

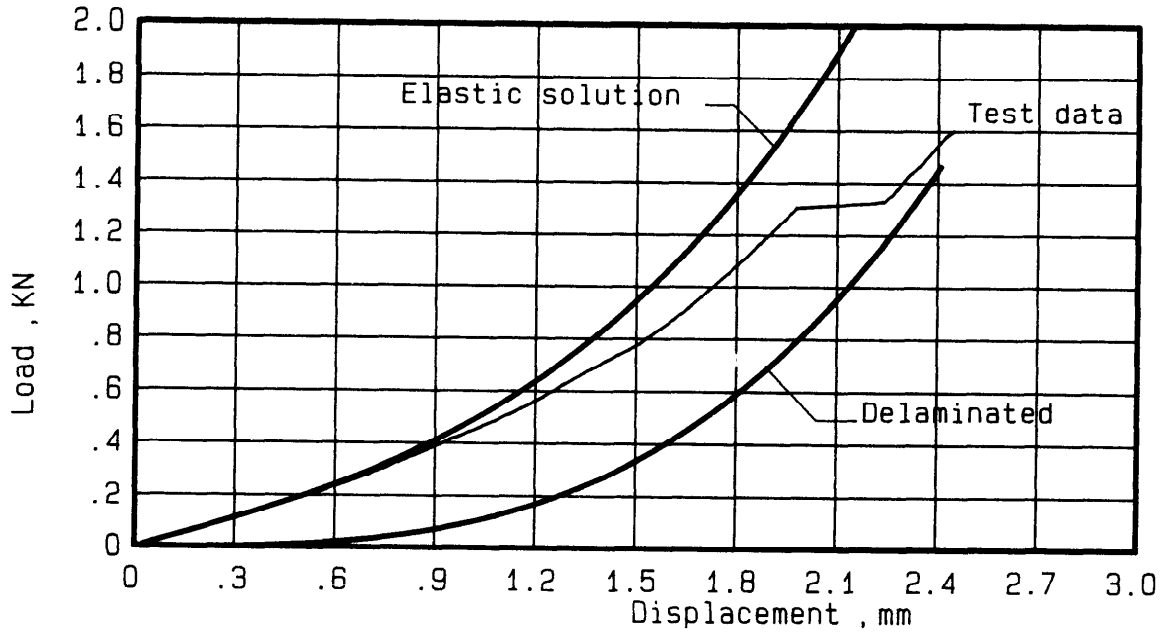

a) Initial delamination for 2.54 cm aperture plate.

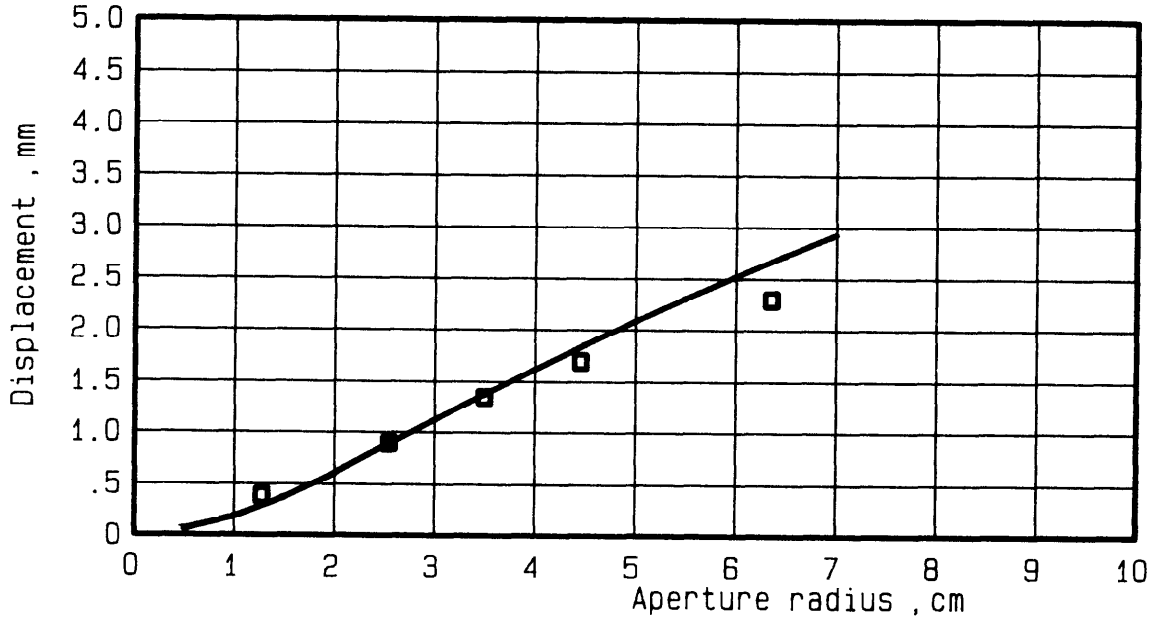

b) Initial delamination displacement for 5208/T300 specimens.

Figure 12. - Initial delamination of 5208/T300 composite plates.

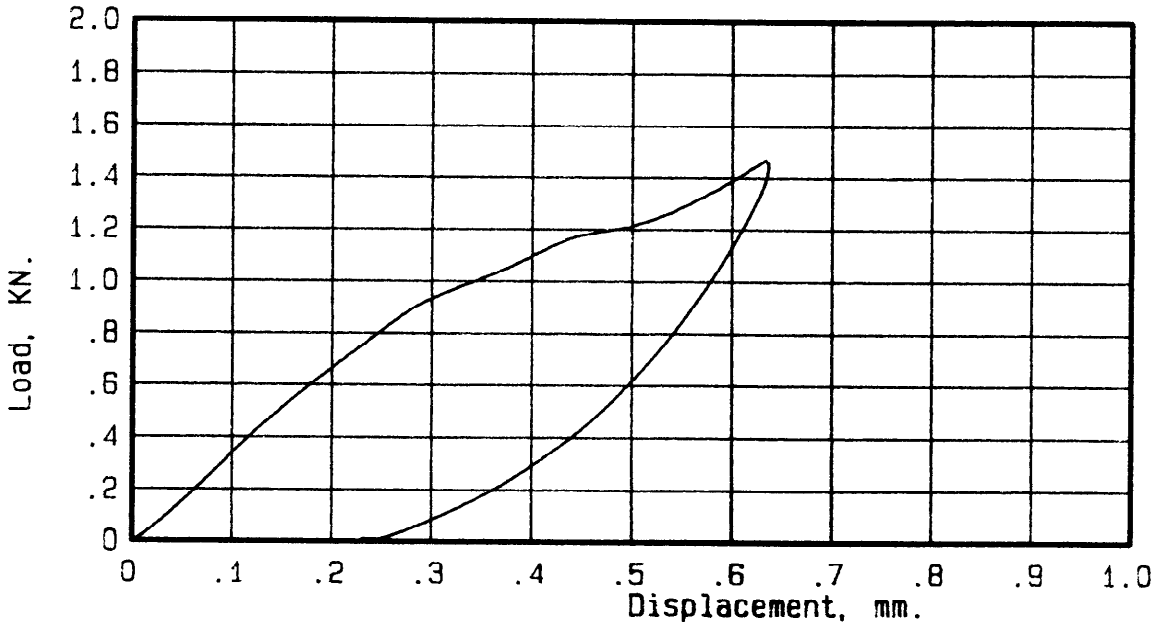

a) Load-displacement data.

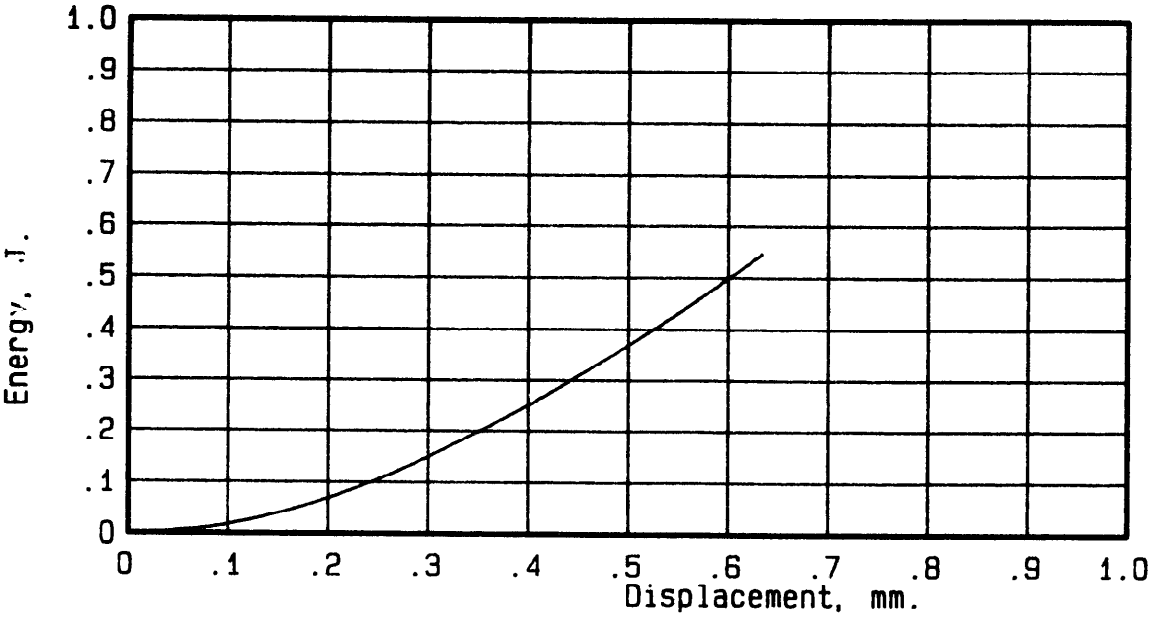

b) Energy-displacement data.

Figure 13.- Plate deformation data for HX205/C6000 composite plate. Aperture radius = 0.00635 m. Thickness = 0.00115 m.

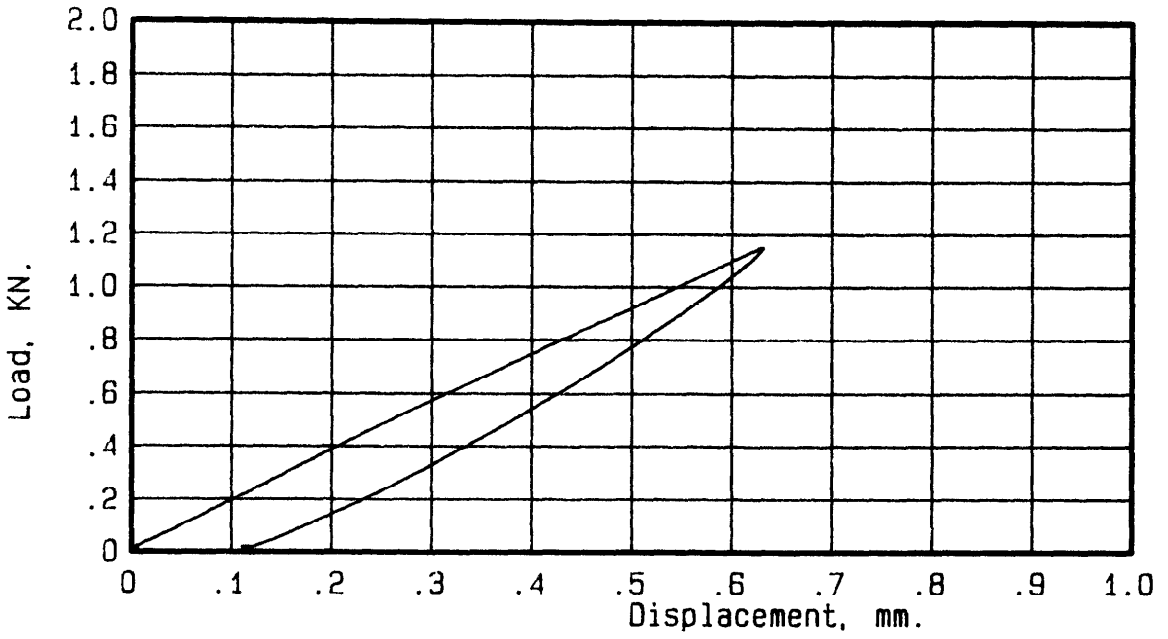

a) Load-displacement data.

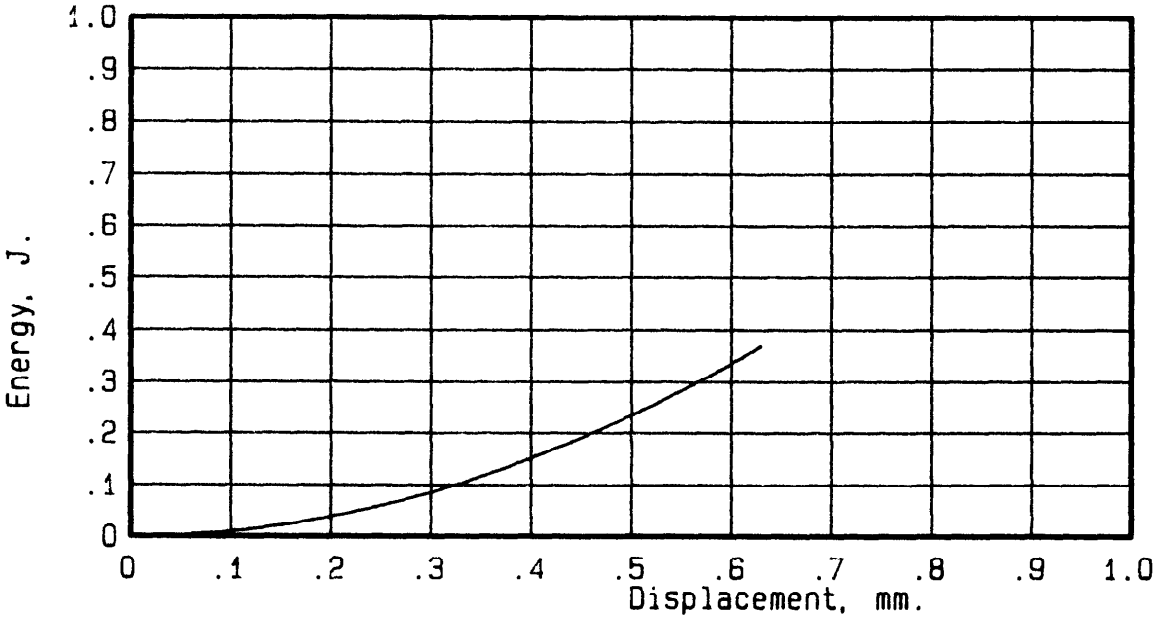

b) Energy-displacement data.

Figure 14.- Plate deformation data for HX205/C6000 composite plate. Aperture radius = 0.0127 m. Thickness = 0.00115 m.

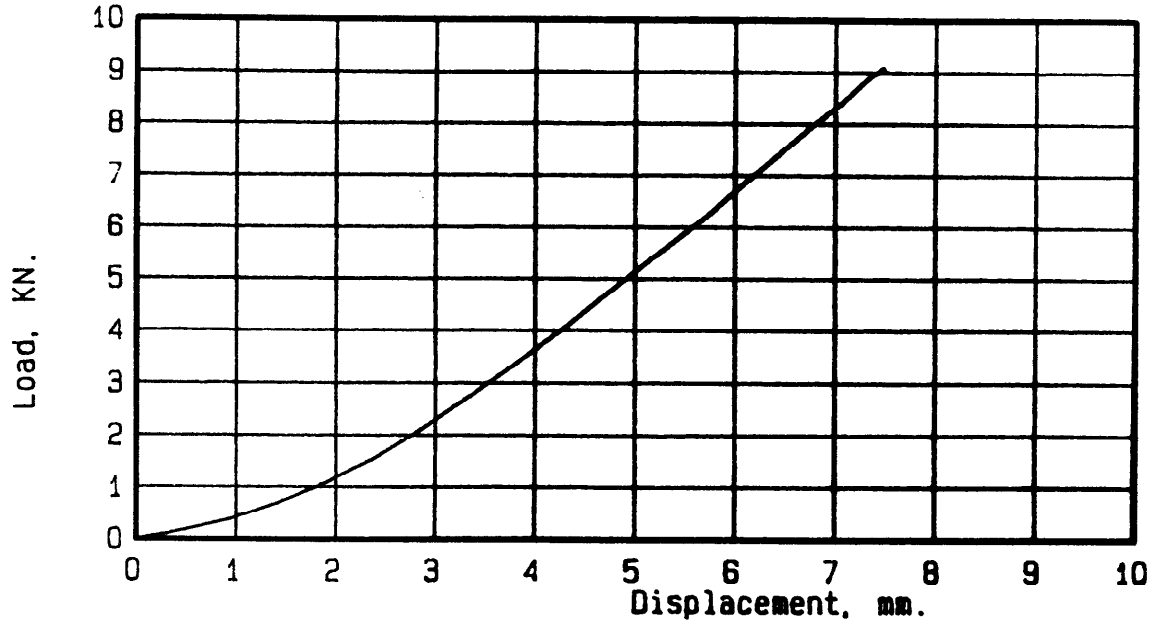

a) Load-displacement data.

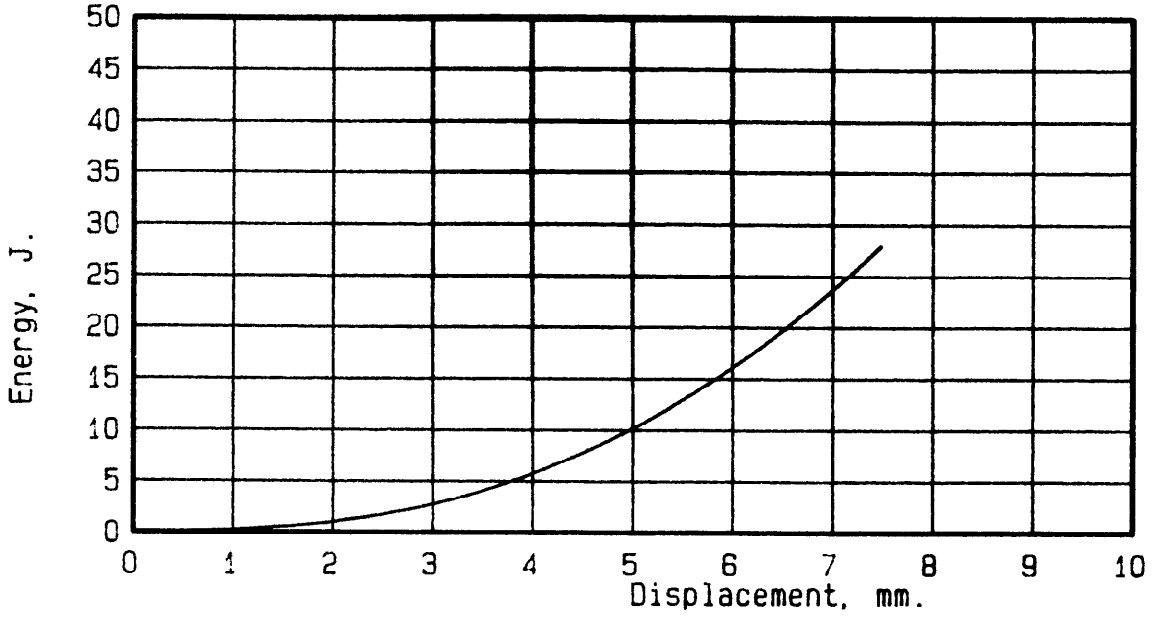

b) Energy-displacement data.

Figure 15.- Plate deformation data for 2024-T3 aluminum plate. Aperture radius = 0.0349 m. Thickness = 0.00102 m.

curve shows, at the initial yielding, the plate has absorbed less than 1 joule of strain energy, but by the time failure occurs, it has absorbed 28 joules. This large increase in strain energy absorbable by the plate after initial damage, is an effect of yielding of the aluminum. Figure 8 shows test results for the same size plate of 5208/T300 material. The composite failed at a considerably smaller load, 1480 N and a strain energy of 1.58 joules.

Maximum Plate Impact Energy

If the occurrence of delamination is eliminated by using a perfectly strong matrix, the load displacement curve would follow the plate equation, or the top curve in Figure 16(a). If the flexural strength criterion is ignored, and it can be assumed that plate failure can be delayed until the membrane becomes critical, then an upper bound on the maximum strain energy which the plate can absorb can be calculated (shaded area). For the 5208/T300, this maximum strain energy is shown as a function of plate radius in Figure 16(b). It shows that for a 1 mm plate, the maximum strain energy, or impact energy, is relatively insensitive to plate size and is of the order of 2 joules. The square data points represent the failure strain energies calculated for the 5208/T300 plate tested in this study. The round data point for the smallest plate represents the HX205/C6000 matrix and indicates that that material, through delayed delamination, approaches the calculated upper bound energy limit. Because this upper limit is only fiber dependent no improvement in the matrix alone can improve the failure impact energy level.

The upper curve in Figure 16(b) represents a similar calculated upper energy limit for a 1 mm thick quasi-isotropic S-glass material. With the flexural modulus of the S-glass assumed to be one-third of the graphite fiber modulus, and the critical strain assumed to be 2.5%, that calculation indicates that even large changes in modulus and ultimate strain produce changes in the upper bound impact energy of only a factor of two.

Failure Mode Progression

The failure mode and failure progression by delamination were investigated using 5208 E-glass specimens in a symmetrical 8-ply quasi-isotropic lay-up. A 25.4 mm diameter plate of the E-glass material was loaded to just beyond the critical delamination. Figure 17(a) shows a light transmission photograph of the specimen. The photograph shows a series of splits in the bottom (0°) ply leading the damage (A). A second family of splits then forms in the +45° ply, spanning the splits in the 0° ply. The spacing of these cracks is very small (B). Closer to the center of indentation, these cracks join and delamination between the zero-degree ply and the 45-degree ply becomes visible (C). Closer still to the center of indentation, splits in the next ply (-45°), and more severe delamination become visible (D). This

leads to the conclusion that, at least in the fiberglass, the damage originates in the bottom ply because of transverse tensile splitting, and that the damage progresses outward and upward into the next highly stressed plies. The damage progression in 5208/T300 should be similar to this sequence, except for the rate sensitivity observed in the 5208 E-glass. Figure 17(b) shows the same specimen after failure. In addition to the penetration damage in the fully blackened area, the photo shows that the lower ply had fully delaminated, and that ply splits and delaminations exist throughout the plate.

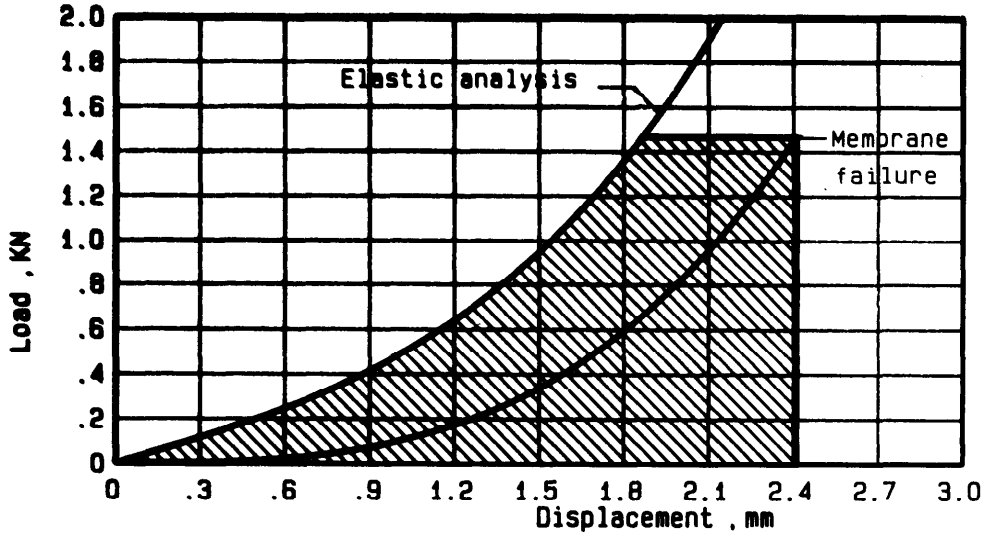

a) Strain energy to failure for a perfectly strong matrix.

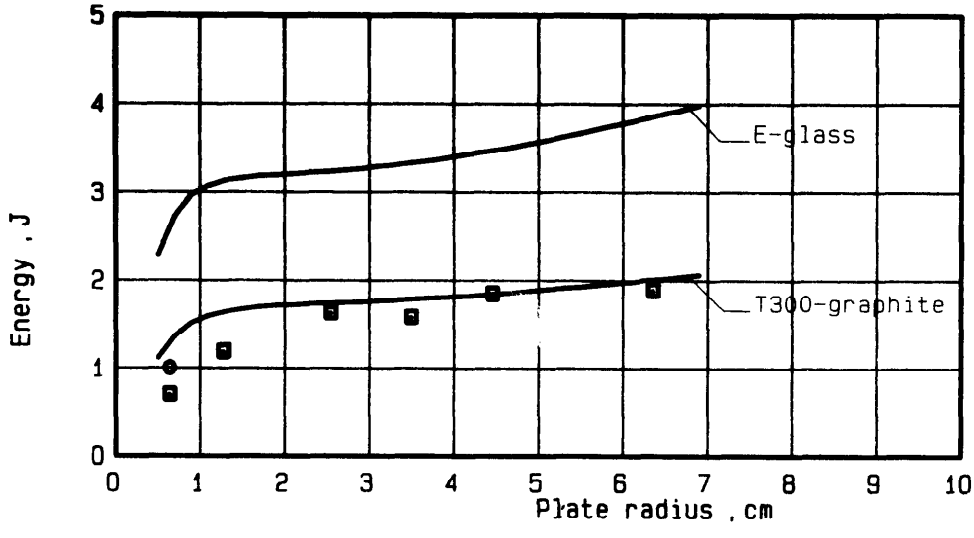

b) Maximum strain energy absorbable.

Figure 16. Maximum plate impact energy.

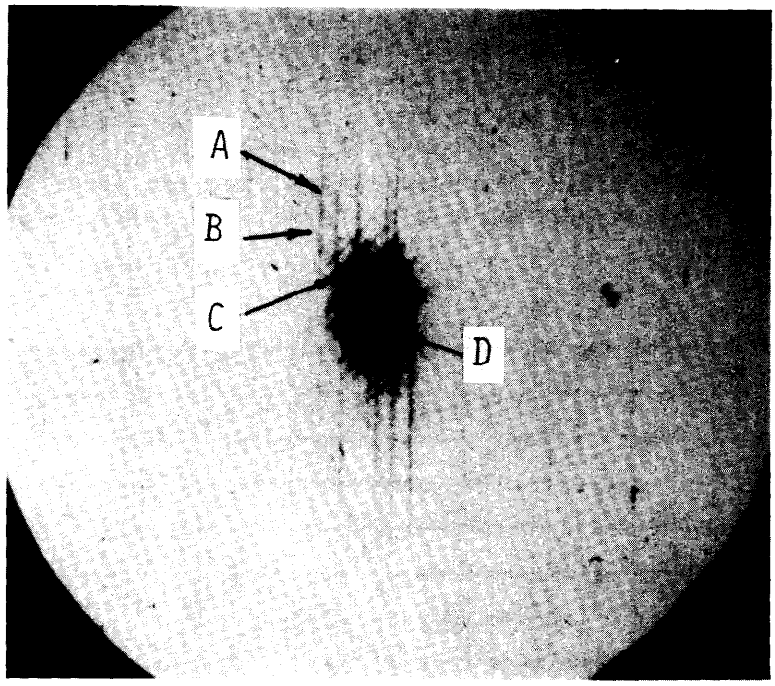

a) Delamination at observed delamination load.

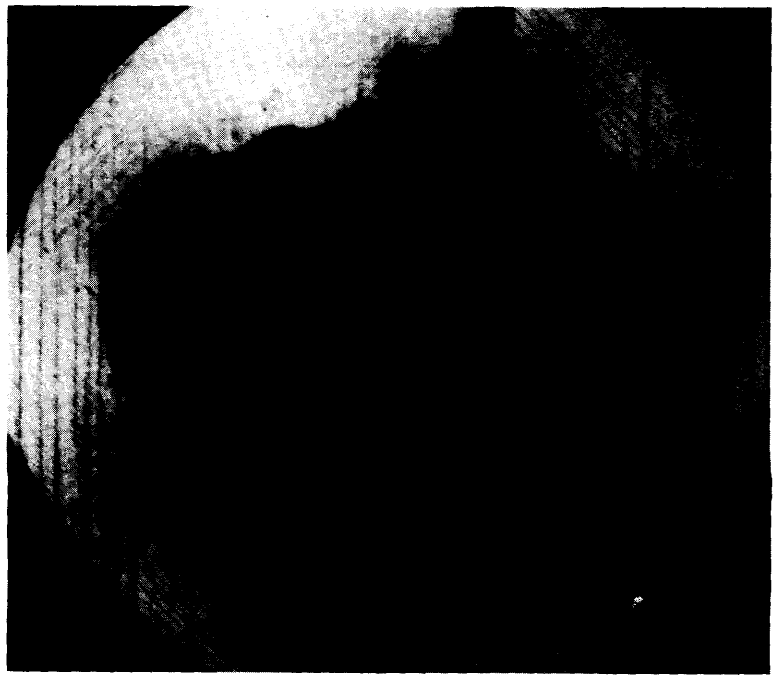

b) Penetration failure.

Figure 17.- Failure progression of 8-ply 5208/E-glass.

CONCLUSIONS

The study of impact resistance through quasi-static testing of 8-ply graphite and glass quasi-isotropic laminates has results in the following conclusions:

1. The initial delamination damage is matrix shear strength dependent and can be delayed or inhibited by use of stronger or tougher matrix materials.

2. Fiber failure from high flexural and mid-plane membrane strains limits the amount of strain energy which can be stored in the plate.

3. The pure membrane failure mode controls plate penetration after delamination.

4. The membrane failure energy depends only on the ultimate fiber strain and fiber modulus and those properties prescribe an upper limit for energy absorption, which is therefore independent of the matrix used.

5. For composites containing T300 fibers, the critical penetration energy under a 25.4 mm diameter steel ball is approximately 2 joules for quasi-isotropic 8-ply plates.

REFERENCES

1. Williams J. G. and Rhodes, M. D., "The Effect of Resin on the Impact Damage Tolerance of Graphite-Epoxy Laminates," NASA Technical Memorandum 83213, October 1981.

2. Timoshenko, S. and Woinowsky-Krieger, S., Theory of Plates and Shells, McGraw-Hill Book Co., New York, 1959, 51-78.

3. Goldsmith, W., Impact, The Theory and Physical Behavior of Colliding Solids, Edward Arnold Publishers Ltd., London, 1960, 82-92.

MECHANICS PROBLEMS IN COMPOSITE MAIN ROTOR BLADE DESIGN

by

R.L. Foye*
D.J. Baker *
S.P. Petrie **
A.O. King **

ABSTRACT

Over 50 all-composite helicopter main rotor blades have been designed to date. More than 15 of these have reached either limited or full production status. Eight others are approaching production. This paper reviews the different design concepts and analyses that have been applied to many of these blades. Various design and analytical solutions to the problems of root end and drag link attachments, spar and blade transition sections, and tip weight and tip cap attachments are described.

INTRODUCTION

Well over 50 different all-composite main rotor blades have been designed to date. About 25 of these have been flight tested and over 15 have progressed to limited or full production status. This paper will be mainly concerned with those designs that have advanced to or beyond flight test status. The emphasis will be on US Army blade designs because of the authors affiliations and the fact that much of the composite blade development work has been US Army sponsored.

There have been about 25 different US Army funded composite rotor blade programs underway since 1970. Six of the blades have reached flight status. They are:

1) the CH-47 Advanced Geometry Blade (1972)
2) the AH-1 Multi Tubular Spar Blade (1975)
3) the CH-47D Composite Blade (1978)
4) the AH-1S Improved Main Rotor Blade (1980)
5) the AH-64 Prototype Blade (1981)
6) the BO-105 Bearingless Main Rotor (1981)

The most significant of these (in the sense of their progression to operational status or promise of such) are the CH-47D, AH-1S, and AH-64

* US Army Aviation R&T Laboratories (AVRADCOM)
** US Army Materials and Mechanics Research Center

blades. This paper will emphasize the features and problem areas of these three designs.

There were other recent and interesting Army composite blade programs. Perhaps the most interesting and ambitious one, by virtue of blade size and load level, was the HLH blade which has been in storage for the last several years.

DESIGN CONCEPTS

This section considers some of the material/structural design concepts that have been used on several of the recent Army composite blades. Figure 1 contains a collection of mid span blade cross sections (drawn to different scales) that illustrate the materials and their distributions and orientations. The D spar has been the most popular concept with C spars a close second. Multi tubular spars have been used in several military designs for improved ballistic tolerance. Full depth honeycomb sandwich afterbodies are the most popular aft blade concept in the US. Foam core sandwich is more prevalent in European designs.

Figure 2 shows some of the different root end and drag link attachment concepts that have been used. The "wrap around lug" concept is the dominant one today. The early "coke bottle" concept of the AGB is uncertain and difficult to reproduce. The only competing root attachment concept is the "bolt through" one of which the H-3 and Sea King designs are typical. There is considerable interest in attaching blades directly to the hub or hub yoke bearings by incorporating the blade flapping element into the blade design. Except for the few bearingless main rotor designs this concept has not been put to use. It poses some practical difficulties when maintainability and blade folding requirements are considered.

Figure 3 shows some of the spar wrap transition concepts wherein the mid span spar material transitions into the root end attachment region. This has been accomplished by twisting a flat segment of the spar pack 90°, wrapping it around a vertical root end lug, and then twisting it back through 90° into the spar cap plane once more. This can also be accomplished either by wrapping around a horizontal root end lug or by simply not twisting the spar pack before it wraps around a vertical lug.

Figure 4 shows some of the concepts for transitioning both the centrifugal force and the twist and drag moments out of the aft blade and trailing edge longos into the root end. This has been done by increasing the afterbody skin thicknesses at the root end, providing a diagonal close out rib, or in some cases carrying the trailing edge longos directly into the drag link attachment lug.

Figure 5 shows some tip weight attachment concepts. These have been held in place by wrapping the spar cap material around them in a continuous manner, entrapping them within tapering spars, wrapping cap material around plugs or knobs on the ends of the tip weights, or bonding or bolting them to

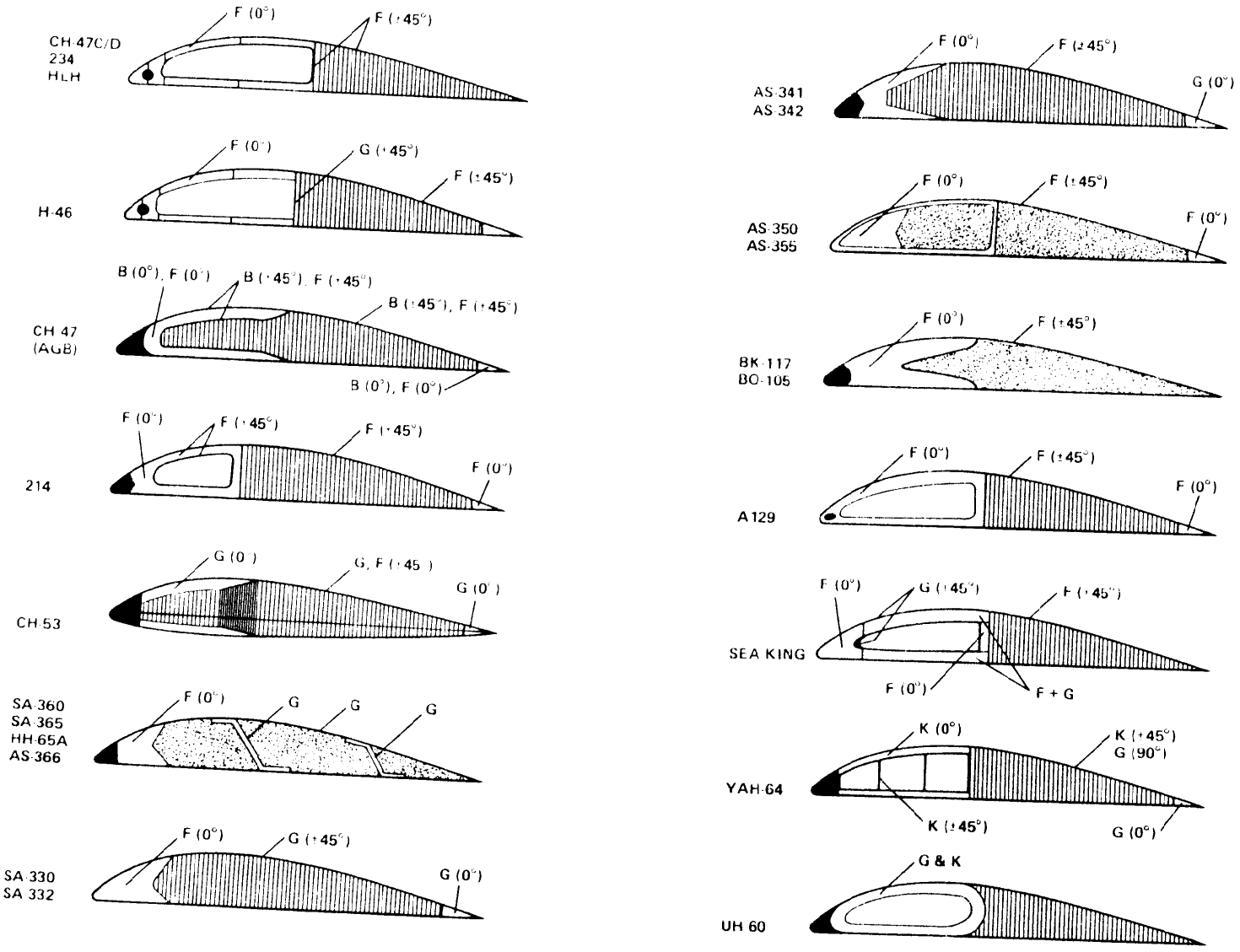

FIGURE 1. BLADE CROSS SECTIONS

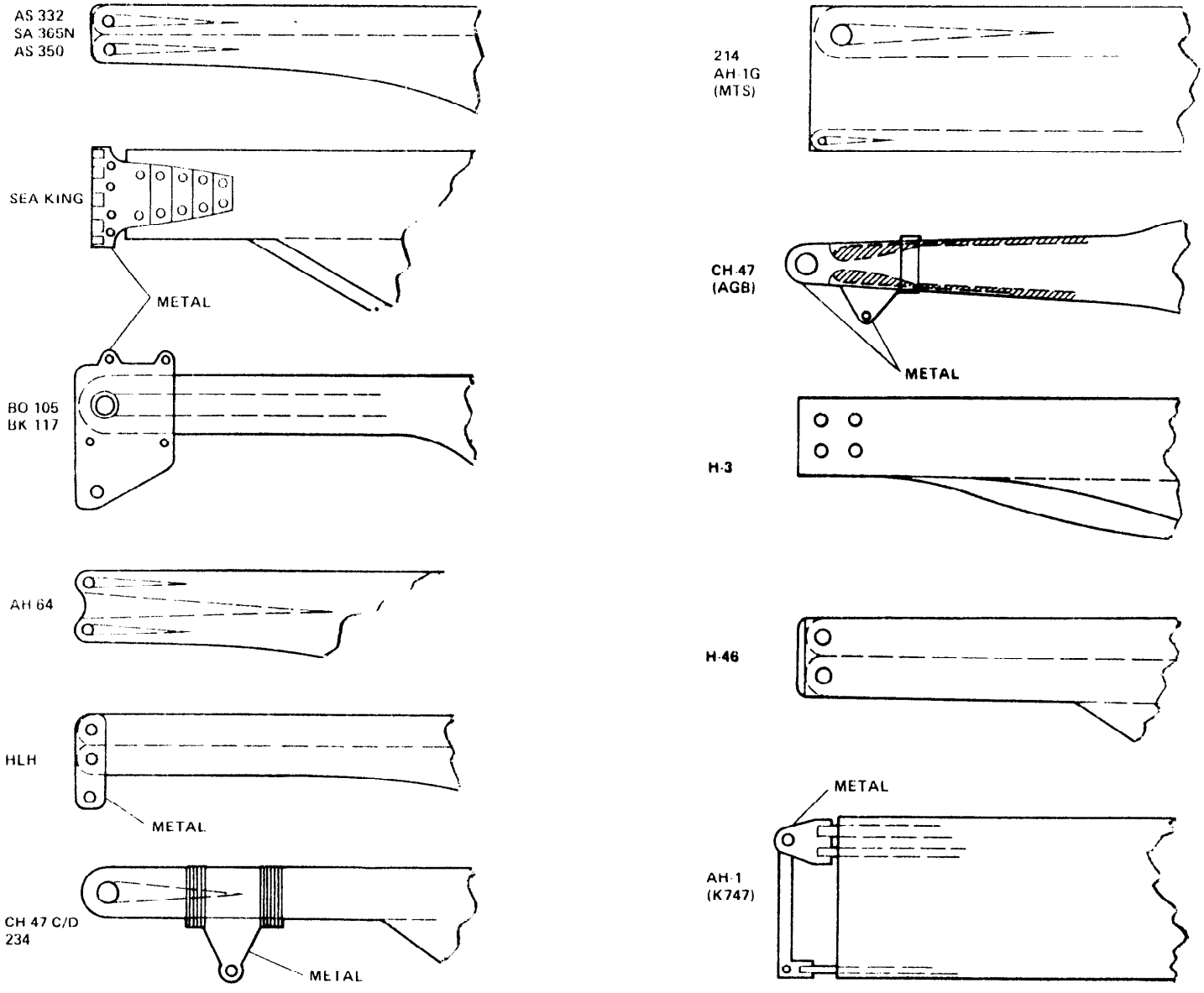

FIGURE 2. ROOT END AND DRAG LINK ATTACHMENTS

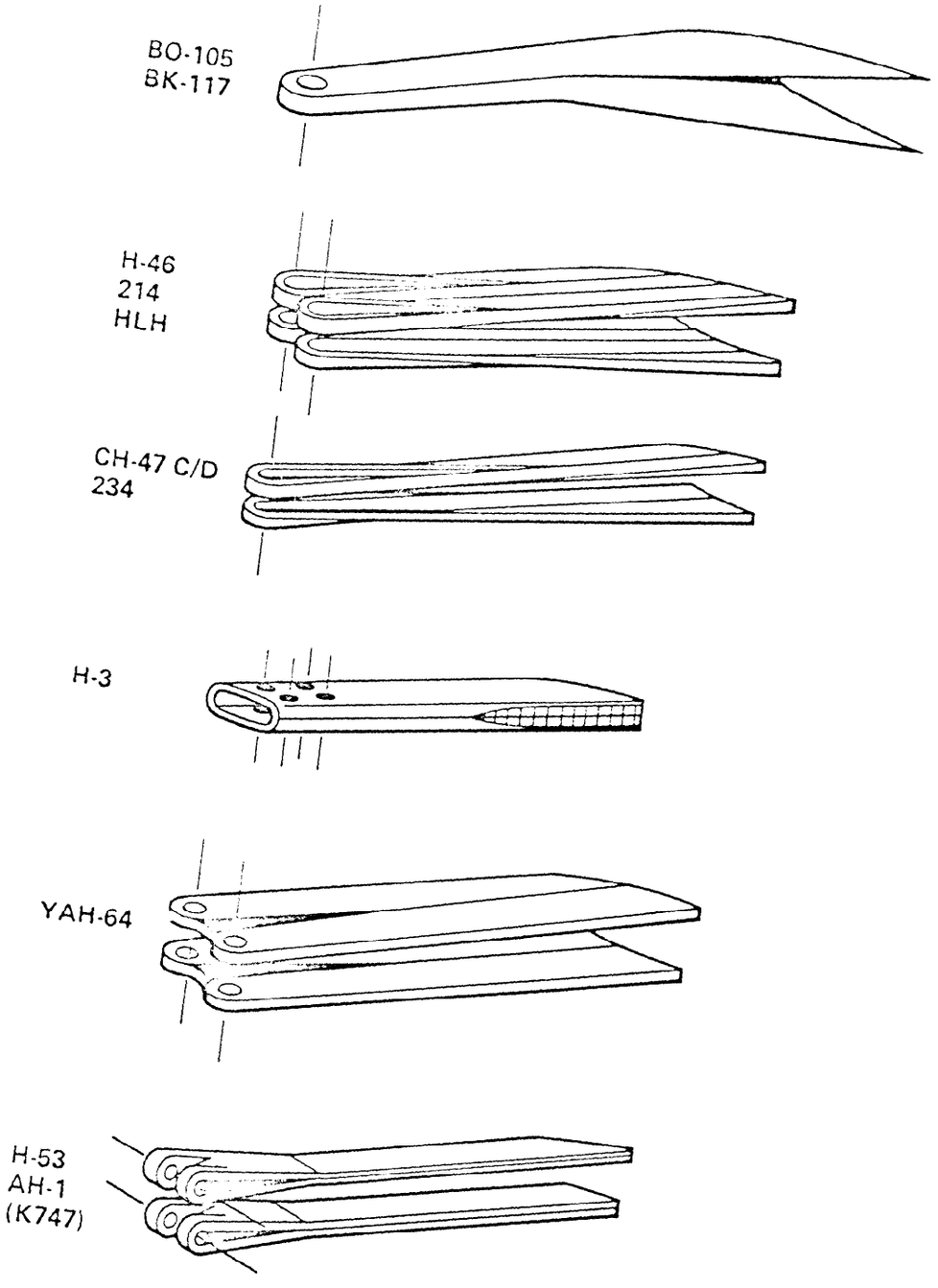

FIGURE 3. SPAR TRANSITION CONCEPTS

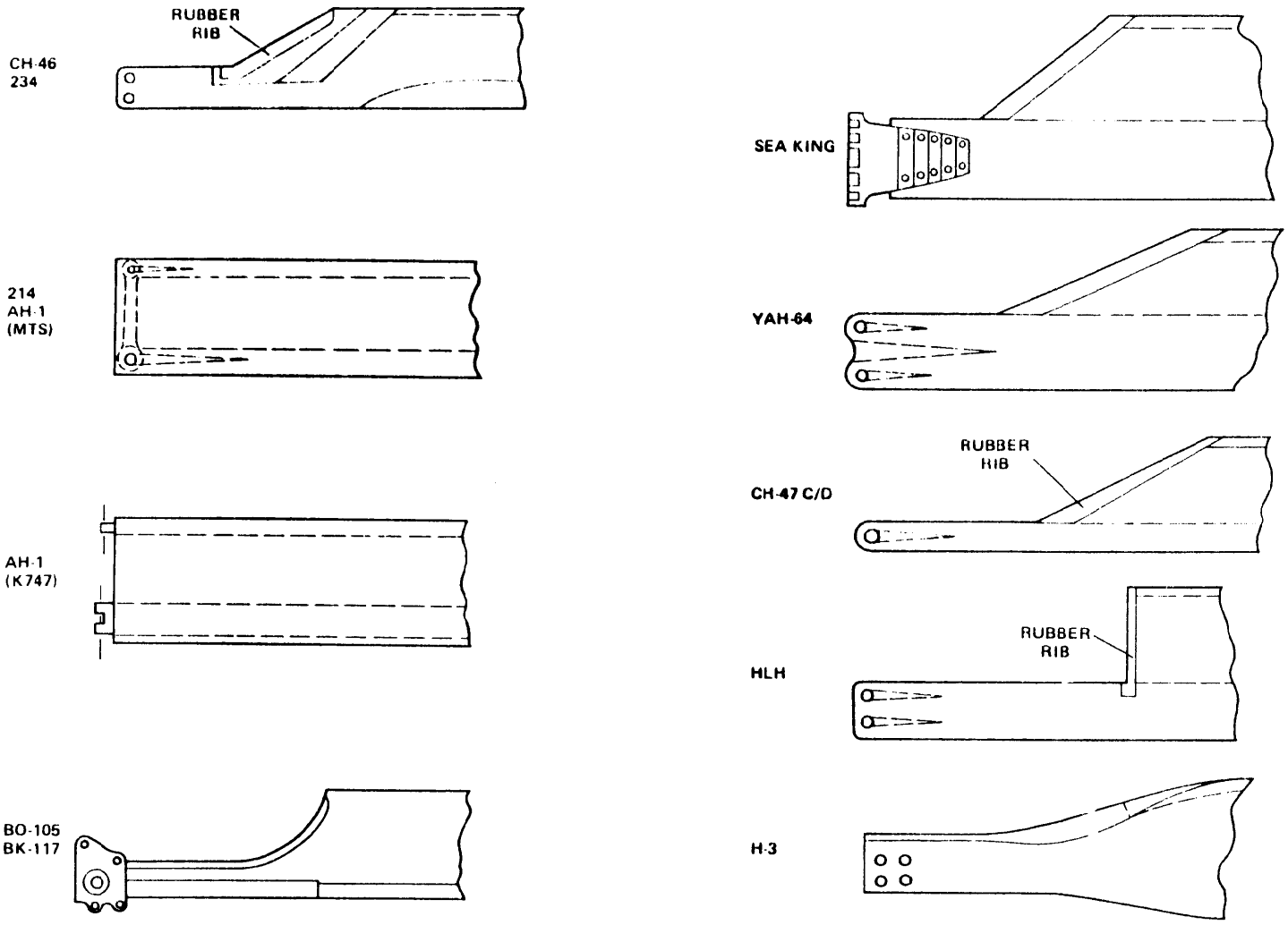

FIGURE 4. BLADE TRANSITION CONCEPTS

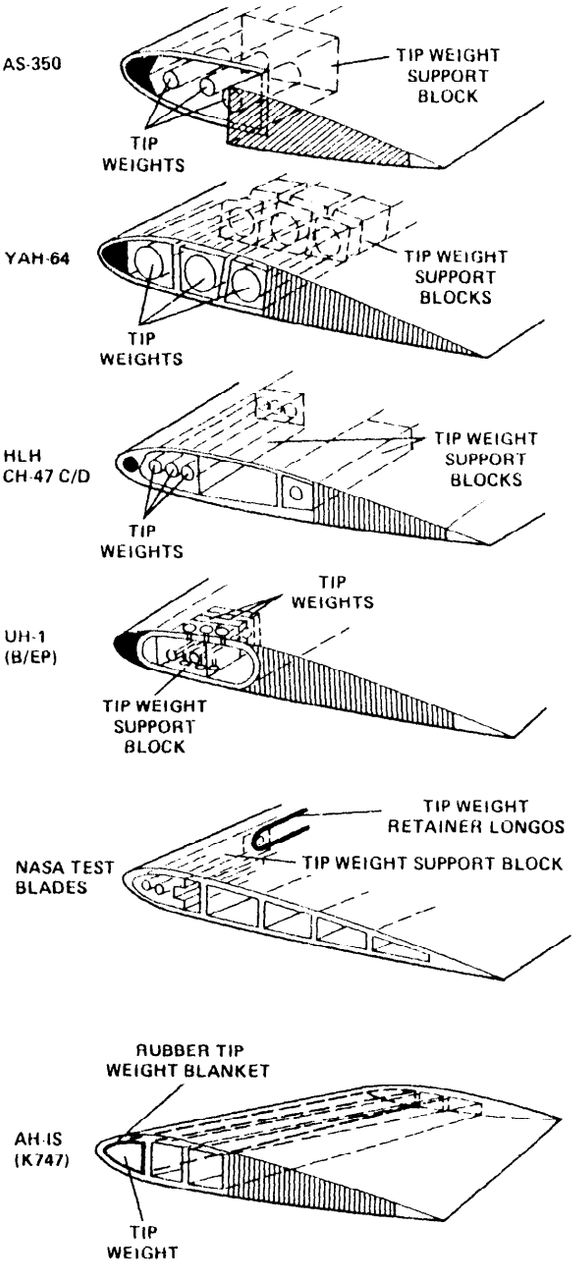

FIGURE 5. TIP WEIGHT ATTACHMENTS

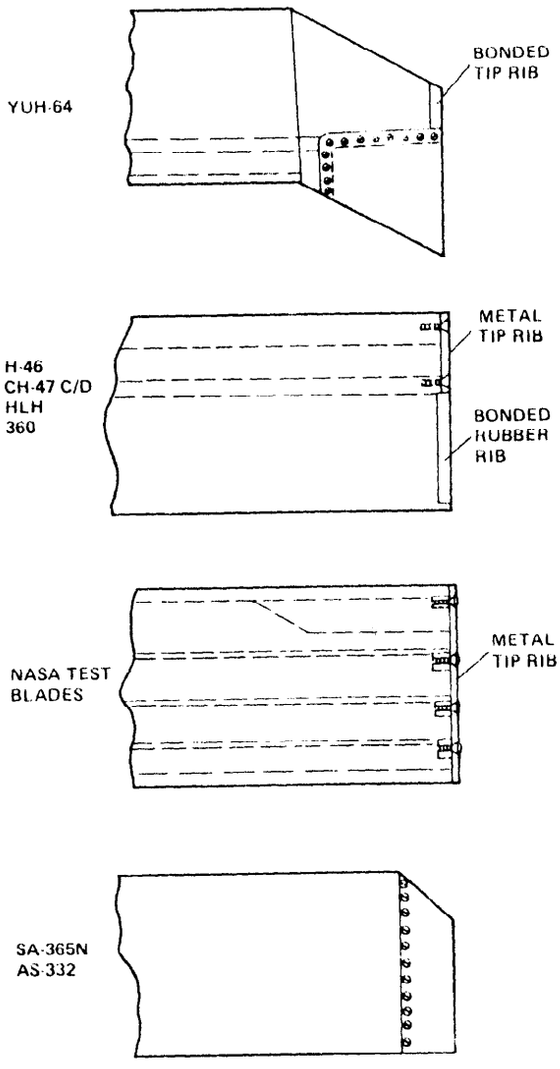

FIGURE 6. TIP CAP ATTACHMENTS

the main spar and outer skin material.

The concepts for attaching the tip cap rib or tip cap fairing to the blade all seem to fall into the category of either bonding or mechanically attaching them to the blade extremity. These are typified by the designs in Figure 6.

PROBLEM AREAS

The center sections of composite main rotor blades have experienced few structural problems. These sections are generally overdesigned with regard to strength and contain no troublesome cutouts, joints or attachments that see large loads. The center section can be analyzed as a beam or rod made from dissimilar materials. The few problems have been in the nature of local delaminations of nose caps, afterbodies or spar/skin bonds.

In contrast, the root end attachment has been the source of several composite blade problems. The production blade on the BO-105 had a bond separation problem between the "wrap around" spar material and the titanium blade retainer (see Figure 2). This led to a lateral stability problem that was termed the "Boelkow Shuffle". Many of these blades have been removed and the fiberglass blades rebonded to their metal retainers using an improved bonding procedure.

The structural analysis of the "bolt through" designs can be accomplished by the conventional treatment of composite to metal joints. Many papers have addressed this class of problem. The "wrap around lug" designs have not received as much general attention. The next section treats the analysis of one such design, the AAH Attack Helicopter prototype blade, which experienced problems in its development.

Single blade retention pin concepts, such as the AH-1 and CH-47 designs, necessitate a drag link to take out the in-plane bending moments at the root (caused by blade drag loads). These attachments have not presented any major problems as yet. The drag induced loads tend to be much lower in magnitude than the centrifugal blade loads, which were as high as 165,000 pounds of force for each of the eight main rotor blades of the HLH design. (The weight of a composite HLH blade was 750 pounds mass.)

Spar transition sections have not been a problem thus far but they do have the potential for producing large delaminations in regions that are often inaccessable by some NDT methods. These transition sections generally contain small angular changes in the spar cap unidirectional fiber paths. It is well known from unidirectional fiber tension tests that small fiber deviations from principal load directions can produce high matrix stresses and longitudinal splitting of the material. Also, it is common for portions of the unidirectional spar packs to terminate short of the root end. Their share of the centrifugal load must be shear lag transferred out of this material at a carefully controlled rate.

Blade transition sections have long represented a difficult but less critical problem area in blade design. In this area the bending and twisting moments that develop in the mid span section must transition into the generally smaller and more compact root end cross section over a relatively short distance along the blade span. The rapid geometry changes rule out the use of most elementary methods of analysis. The next section gives an example of the application of finite element analysis to this complicated area of blade stress analysis.

The tip weight attachment problem is generally considered second only to the blade root end retention problem in criticality. The loss of a tip weight can produce a sudden vibratory force sufficient to damage a helicopter. There have been problems with composite blade tip weight retention designs. The next section will describe one such problem in detail.

The loss of a tip rib or tip cap fairing is an all too common occurrence with helicopters but generally does not lead to a serious safety incident.

The long term degradation of composite mechanical properties due to moisture absorption and ultraviolet radiation has been studied extensively for the last ten years. The general conclusion, for rotor blade applications, is that the overall effects are relatively minor and can be adequately accounted for by adopting modest reductions in the material allowables.

STRUCTURAL ANALYSIS

The root end of the AH-64 prototype blade shown in Figure 2 experienced some premature failures during full scale fatigue testing. Originally the stress concentrations in the longos that wrap around the root end pin (and bushing) had been estimated by using an empirical handbook formula for stresses adjacent to loaded holes. Subsequently, two different finite element analyses were run on the same design. The first, based on the sketch in Figure 7, was a two dimensional analysis using rectangular and triangular elements with membrane, shear, and bending stiffness. Using this analysis the peak stress concentrations in the fiber direction was substantially higher than the empirical factor. A second finite element analysis was done based on the three dimensional model of Figure 7. The three dimensional analysis accounts for pin bending and shear deformations and the resultant secondary distortions of the lug material. The components of stress in the fiber direction did not change significantly but the other stress components did. The magnitudes of the stresses with components normal to the fibers, though low by comparison to the fiber stresses, were high with respect to the transverse strength of the unidirectional material. These off-axis stresses were probable contributors to the premature fatigue failures of the test blades. The empirical lug stress factors used in design were not only unconservative, by a factor of almost two, but were not capable of making any estimate of those stresses having components normal to the fibers. The typical elementary assumption of sinusoidally varying pressure between a lug and a pin was not close to the finite element results for the complex pin

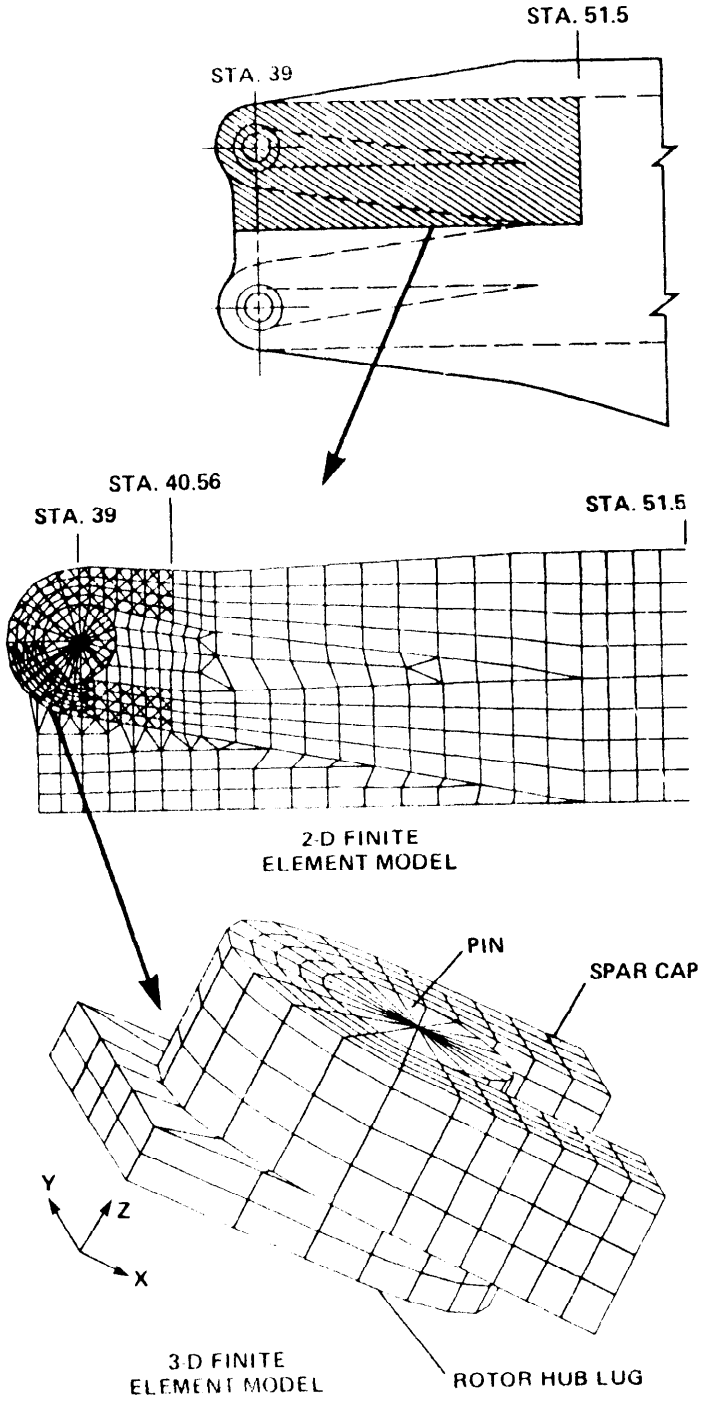

FIGURE 7. FINITE ELEMENT MODELS OF AH-64 ROOT LUG

pressure distribution. A composite design, unlike metals, requires careful attention be given to all the components of multiaxial stress in almost every realistic application. Details of this analysis are given in Appendix A.

The next example of the adequate analytical treatment of a rotor design problem involves the transition section of a composite CH-46/CH-47 type blade as shown in Figure 3. The load in the trailing edge and aft fairing must be transferred into the root end region over a short spanwise distance. Strength of material methods are generally inadequate for this analysis. Shear lag analysis and two dimensional elastic analysis is an improvement but the resulting detailed stress information is still either crude or totally absent. As a result three dimensional NASTRAN analysis has been applied to this problem. Figure 8 shows the finite element idealization of the structure. The elements used are triangular and quadrilateral membranes for the skin and trailing edge materials and hexahedron and wedge elements for the thick spar covers and the honeycomb sandwich. The separate effects of centrifugal force, blade bending moments, and twisting moments on the transition section stresses were resolved in separate runs. For level flight the critical element was at the inboard cover skin at the beginning of the transition section as shown in Figure 8. The margins of safety from the analysis were adequate and verified by subsequent bench and flight tests.

The final example of composite blade analysis involves the AH-1S improved main rotor blade. This composite replacement for an older metal blade ended up weighing considerably less than the metal design, necessitating the addition of a large tip weight to restore the blade rotary inertia. The tip weight attachment concept is shown in Figure 5. The 47 pound brass D shaped tip weight is encased in rubber and molded into the outer portion of the main spar. A two dimensional shear lag analysis of the tip weight bond stress due to centrifugal force (see Figure 9) showed the peak shear stresses in the rubber to be relatively low. Also the outer spar was tapered in order to trap the tip weight in the spar in case the rubber layer failed. Despite these precautions a tip weight was thrown after about 150 hours of operation. Fractographic analysis of the failed parts showed progressive fatigue failure of the rubber around the inboard end of the weight which was probably aggravated by inhomogeniety of the filled rubber material. (See Appendix B for details.) The presence of a sharp leading edge on the tip weight permitted the weight to cut through the spar leading edge. This action was further abetted by a nonuniform layer of rubber which was thinnest at the leading edge. A finite element analysis of the stress distribution around the periphery of the D shaped tip weight (see Figure 10) showed a highly nonuniform normal stress distribution instead of what was tacitly assumed to be uniform. The inadvertent rubber thickness variation also led to a high shear strain concentration at the same location. Microscopic examination showed pulverized rubber particles imbedded deeply between layers of leading edge spar material that had been progressively cut by the sharp edged tip weight before total separation of the weight. This problem was relieved by mechanically attaching the tip weight to the spar caps, rounding off the sharp leading edge of the tip weight, and taking precautions in the

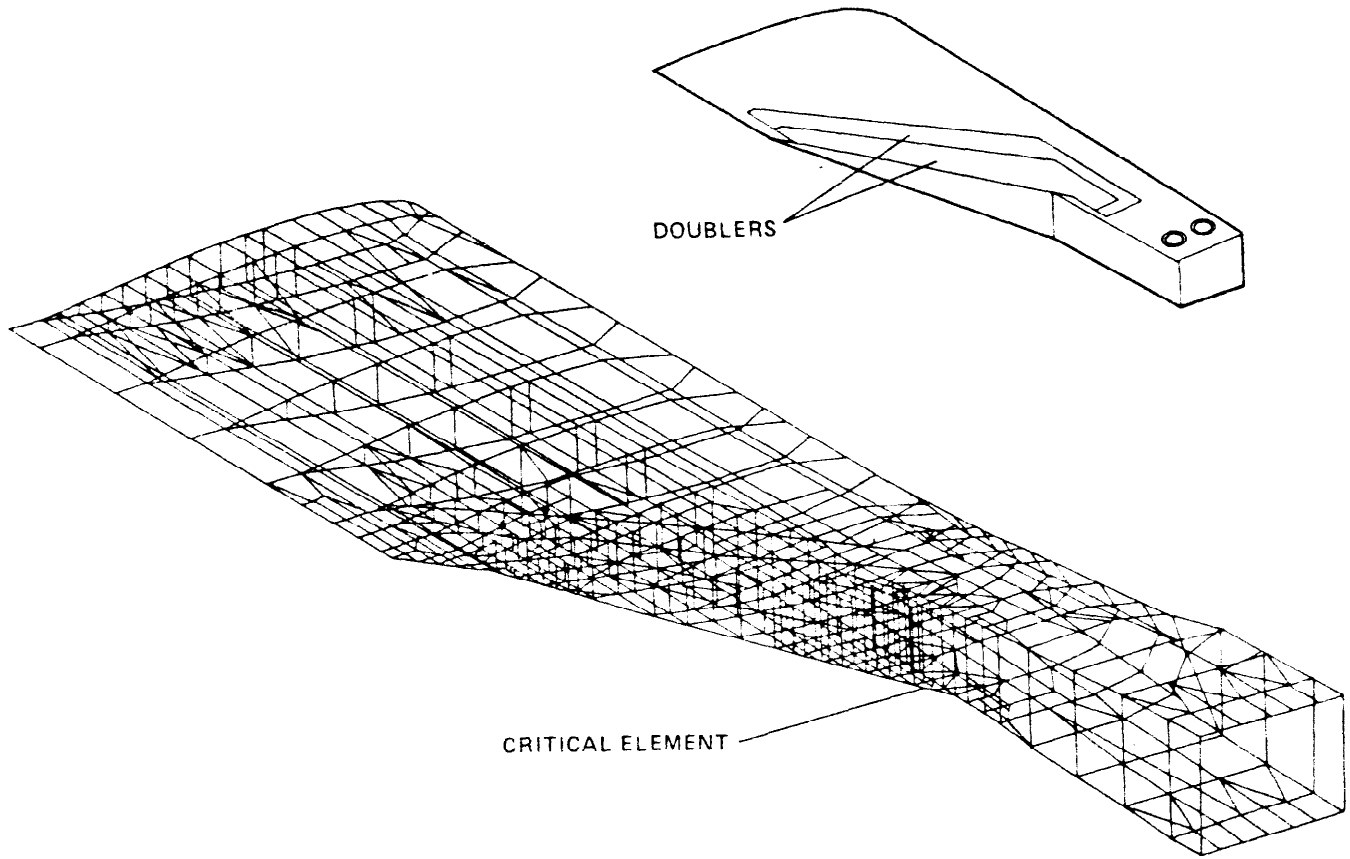

FIGURE 8. FINITE ELEMENT MODEL OF BLADE TRANSITION SECTION

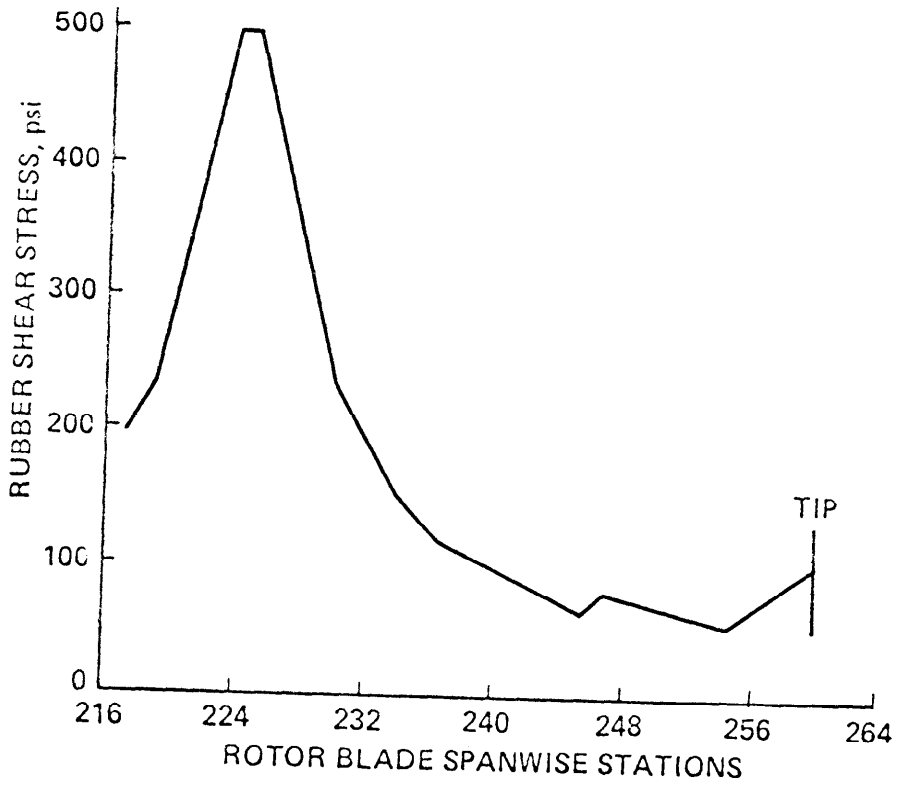

FIGURE 9.

SPANWISE DISTRIBUTION OF SHEAR STRESSES BETWEEN TIP WEIGHT AND BLADE SPAR

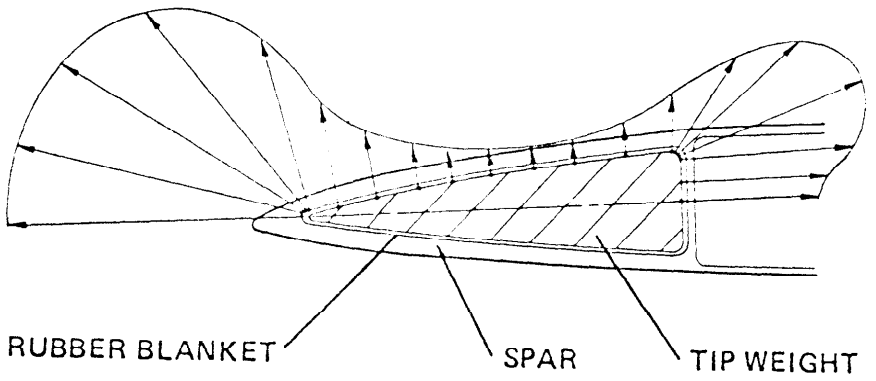

FIGURE 10. NORMAL (PRESSURE) DISTRIBUTION AROUND A TAPERED TIP WEIGHT DUE TO CENTRIFUGAL FORCE

vulcanizing of the rubber weight cover to assure a controlled layer thickness.

This example points out another general lesson to be learned in the analysis of composite or metal structures. There is a mistaken tendency to analyze structures as they are drawn rather than as they are actually being built. Worst cases of manufacturing tolerances and mismatches should be accounted for in the analysis.

CONCLUSIONS

a) The earlier concerns about moisture absorption and solar UV radiation effects on composites have diminished to the level of a minor design problem causing less difficulty than that of corrosion in conventional metal construction.

b) Analytical and test methods that disregard multiaxial and secondary stresses and strains (which designers and analysts have learned to safely apply to blades made of isotropic materials) may not apply to anisotropic materials. All the inherent assumptions must be reevaluated.

c) Damage tolerant and fail safe concepts should not be overlooked in composite blade design because of the popular conception that composites have readily detectable or "soft" failure modes. The disciplined approach of anticipating failures, establishing failure rates by test or analysis, and devising timely detection methods is still necessary to insure "on-condition" design of composite components.

d) Manufacturing tolerances and allowances may be greater and at the same time more critical in composite design. They should be carefully considered in the stress analysis.

e) Material and process specifications must be stringently defined and strictly adhered to.

ACKNOWLEDGEMENTS

The authors wish to acknowledge the contributions of George Thompson of Boeing Vertol and Charles Harderson of Kaman Aerospace for their contributions to the structural analysis.

APPENDIX A - STRESS ANALYSIS OF AAH COMPOSITE MAIN ROTOR BLADE ROOT END LUG

Introduction

Two designs have evolved from the AH-64 composite rotor blade MM&T program. The first design (A) is an all Kevlar/epoxy blade as shown in Figure 1. The second design (B) is similar to design (A) except for graphite/epoxy doublers at each lug surface in lieu of the Kevlar/epoxy skin. The second design was required because element testing of the design (A) root end produced early fatigue failures in the attachment lugs. Stress concentration factors for the lug have been computed for each design using finite element analysis. Results of the finite element analysis are compared to the empirical methods used in the initial design and analysis.

Rotor Blade Description

Primary load carrying members for the AH-64 rotor blade are uni-directional Kevlar/epoxy spar caps (see Figures 2 and 3). Each of the upper and lower spar caps has two bundles that are continuous from the blade tip and are wrapped around steel bushings where the blade attaches to the hub. These uni-directional spar caps are laid on rectangular tubes that form the center or core of the blade as shown in Figure 1. The assembly is overwrapped with $\pm$ 45° Kevlar/epoxy skins of varying thickness. The Kevlar/epoxy skins between the lug end and station 42.5 in design A are replaced with a graphite/ epoxy doubler for design B.

Lug Analysis

The lug analysis was performed using finite elements. A 2-D analysis was performed initially to determine the displacement field near the lug. A 3-D stress analysis was performed in a local area of the lug. Boundary conditions for the 3-D analysis were obtained from the displacement field determined by the 2-D analysis.

The 2-D analysis of the lug was performed using SPAR, Level 14, finite element code. Quadrilateral and triangular elements with combined membrane and bending stiffness were used to obtain the stress distribution. The blade root end has two planes of symmetry and a symmetrically applied load. Therefore only one fourth of the root end was modeled for the analysis. The 2-D finite element model used in this analysis is shown in Figure 7.

Two boundary conditions have been considered which bound the actual condition. Condition I has the root attachment pin fixed in the x-direction and free to move in the y-direction. Condition II has the root attachment pin fixed in both directions.

An axial load (centrifugal force) was applied at Blade Station 51.5. This load was applied by assuming uniform axial displacement at Station 51.5. Failure load can be determined by scaling the applied load in a linear analysis.

The 2-D analysis cannot account for a through the lug thickness effect or the interaction of pin bending with the lug. Material thickness in this lug exceeds that normally used in 2-D thin plate theory. Therefore, a 3-D analysis was performed on a localized area around the pin and lug. The 3-D model shown in Figure 7 uses pentahedron and hexadron elements of the EISI/EAL finite element code. The EISI/EAL finite element code has the same elements as SPAR but has improved solution algorithms. The same symmetry conditions exist for the 3-D analysis as the 2-D model. To introduce a load in this model the 2-D displacements were applied at Station 40.56.

Discussion and Results

The results of the 2-D analysis are shown as stress contours in Figure 11 for design A spar caps (unidirectional Kevlar) only. Each contour level indicates a line of constant stress. The dense concentration of σ_x stress contours in spar caps indicates a high stress gradient leading to the point of maximum stress. The σ_y and τ_{xy} stress are very low (approximately 20% of σ_x). A plot of the stress concentrations across the lug on a line through the point of maximum stress is shown in Figure 12. The stress concentrations equal the stress (σ_θ) at the center of the element divided by the far field stress (σ_o). The maximum stress concentration at the center of the element adjacent to the pin is 4.00 for design (A), and 3.47 for design (B). Some of this reduction results from the center of the element for design (B) being further (approximately 1.0 mm) from the pin axis than the similar element for design (A) because design (B) lug has a slightly larger outside diameter.

The radial stress in the unidirectional Kevlar spar cap adjacent to the pin is shown in Figure 13 for boundary condition II. This radial stress peak is 82 percent of the far field stress and occurs at the point of maximum circumferential stress concentration in the unidirectional fiber.

Manufacturing problems such as low fiber volume fraction and voids reduce the elastic properties of the materials. The elastic stiffness properties of the model for design (A) were reduced 10 and later 35 percent to determine their effect on the stress concentration factor. The reductions had very little effect. This indicates that the stress concentration is primarily a function of lug geometry and insensitive to material properties.

The 3-D stress contours through the lug thickness at the plane of maximum stress are shown in Figure 14. In this figure σ_θ is in the circumferential and σ_R is in the radial direction. The Z-direction is through the lug thickness. The maximum stress concentration in the lug is 3.87. This point of maximum stress is located adjacent to the pin on the lower surface of the lug. The σ_R contours indicate the effect of the

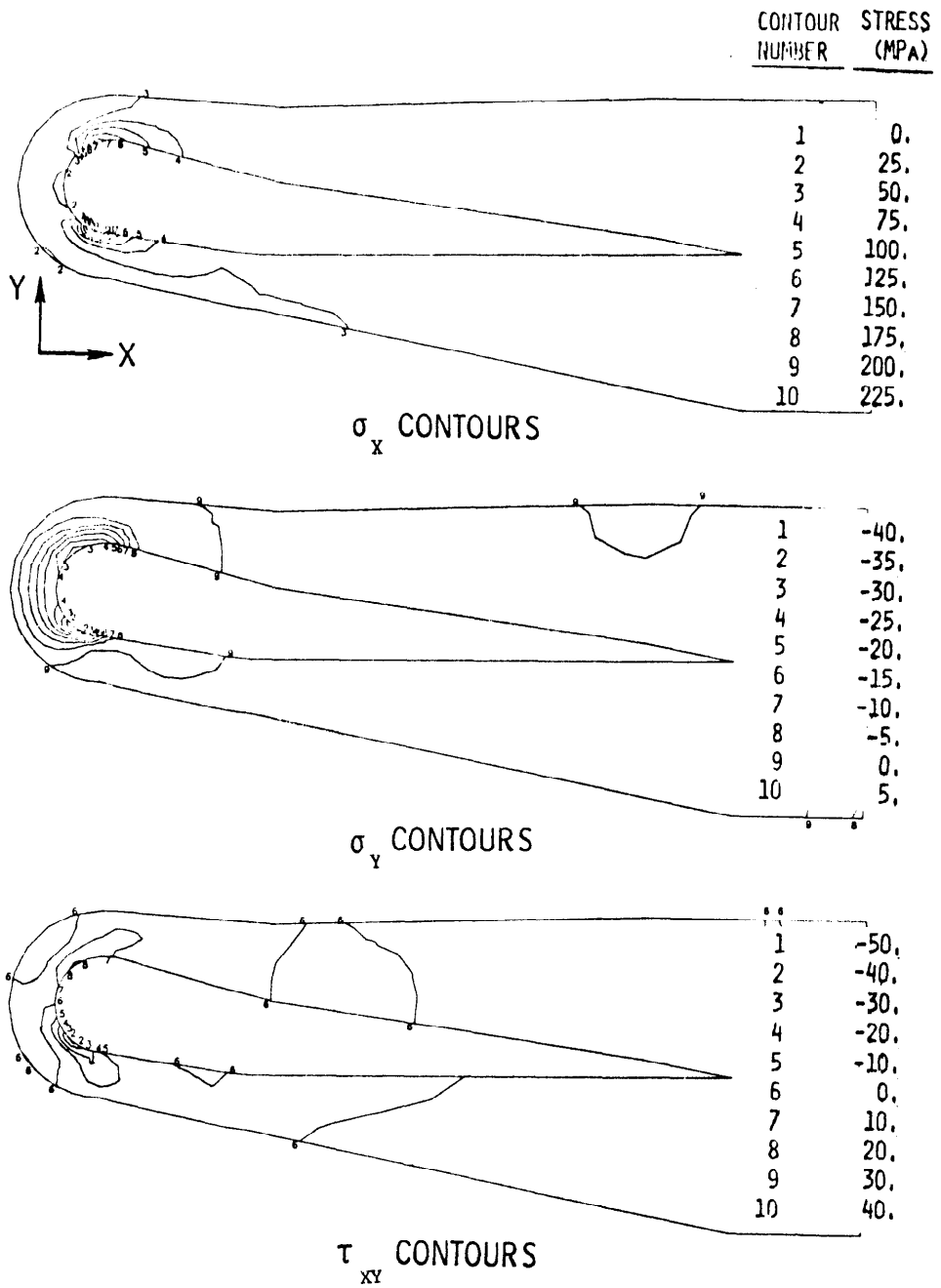

FIGURE 11. STRESS CONTOUR IN SPAR CAPS (BOUNDARY CONDITION II - DESIGN A)

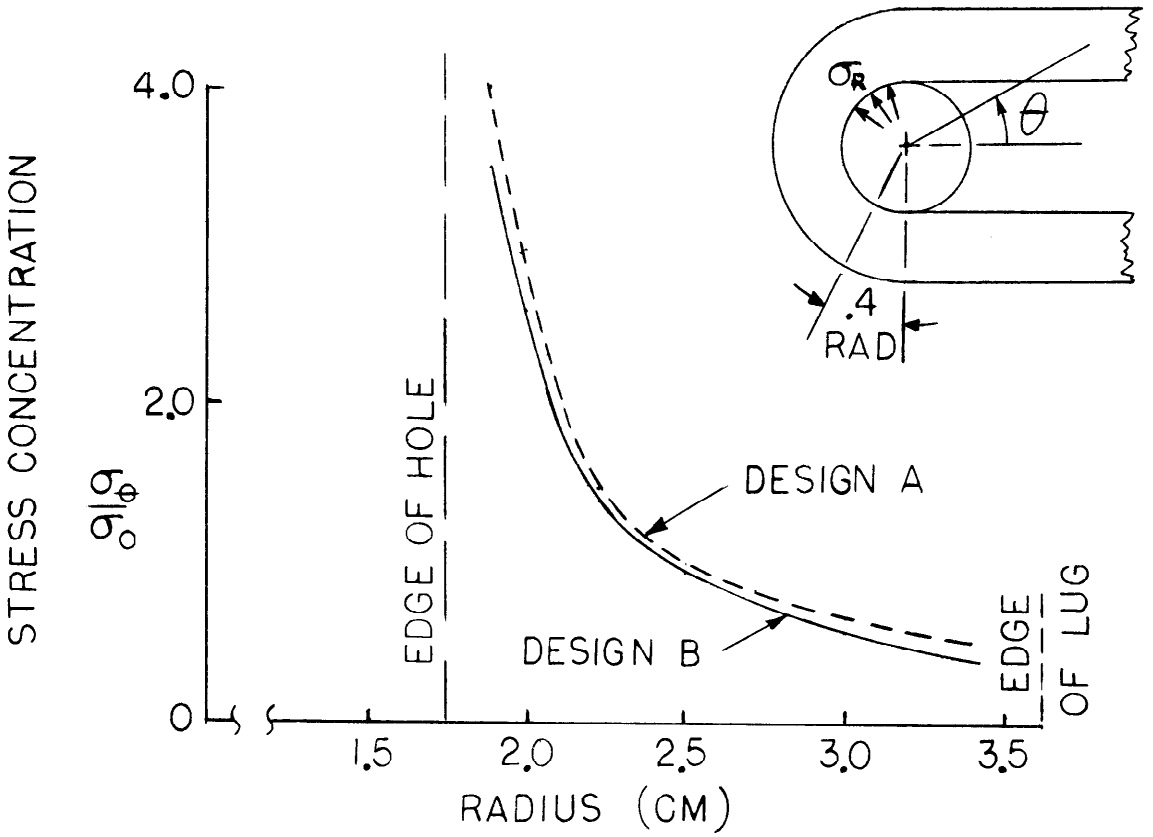

FIGURE 12. STRESS CONCENTRATION IN LUG ON A LINE THRU POINT OF MAXIMUM STRESS (BOUND. COND. II)

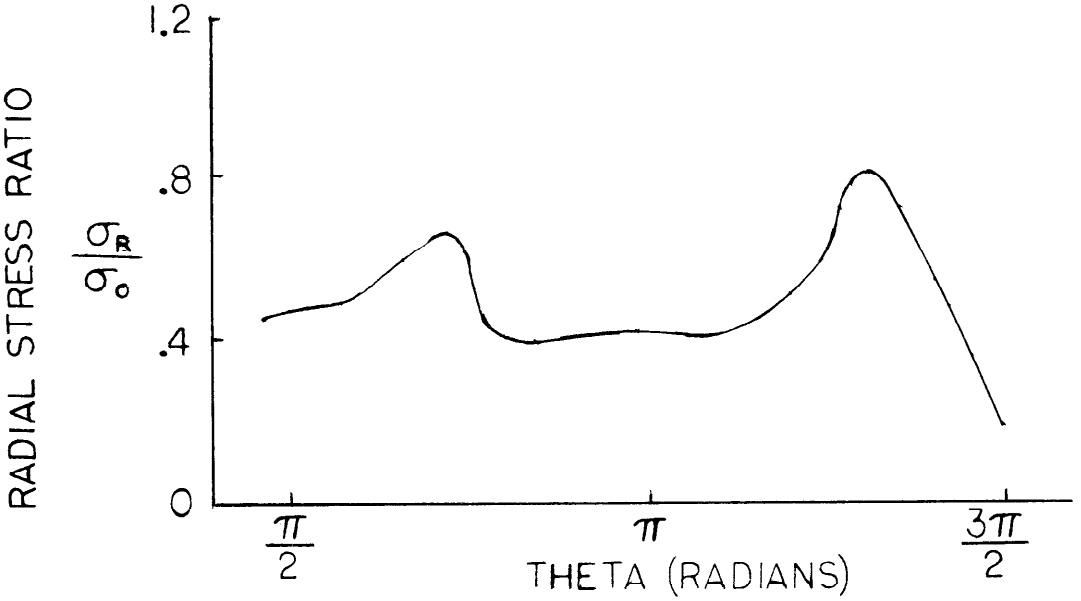

FIGURE 13. RADIAL STRESS IN LUG ADJACENT TO PIN (BOUND COND II - DESIGN A)

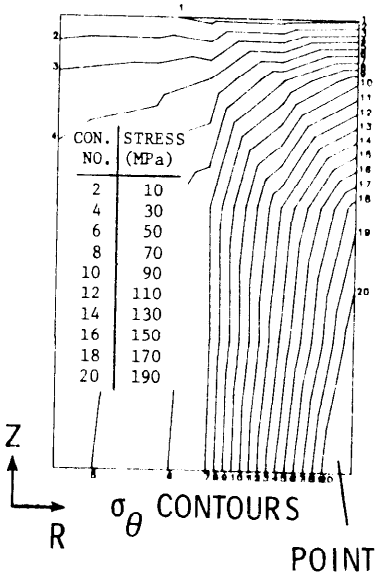

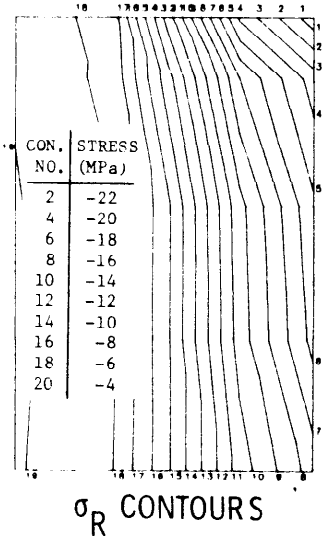

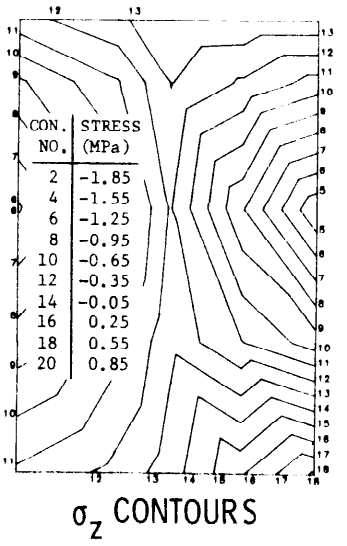

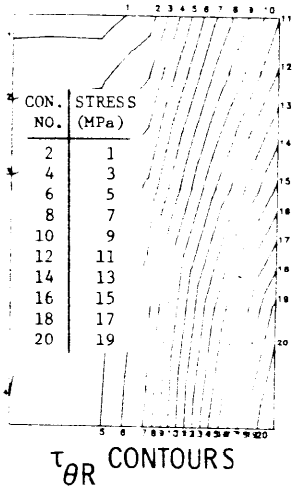

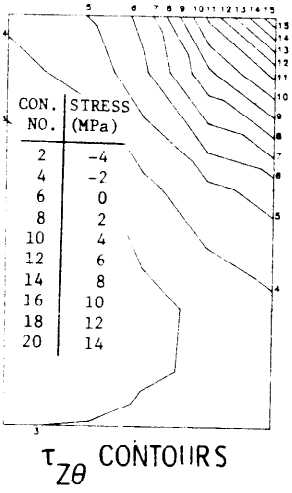

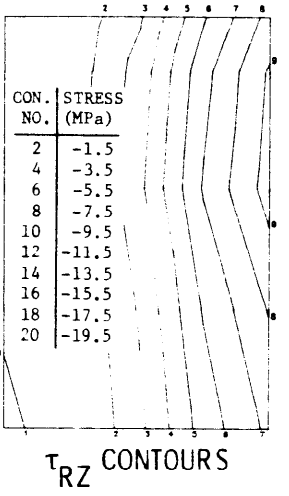

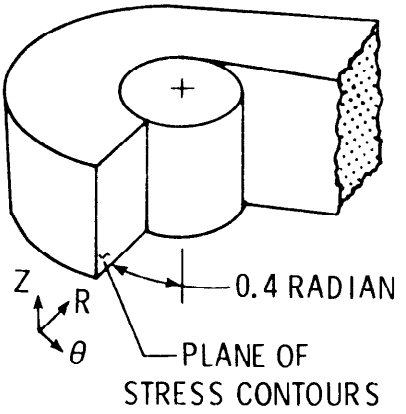

FIGURE 14.

STRESS CONTOURS FROM 3-D ANALYSIS (BOUND. COND. II - DESIGN A)

unidirectional fiber pulling against the pin, and the maximum value equals approximately 10 percent of σ_θ. The effects of Poisson contractions through the thickness of the lug are shown in the σ_z plots. The three shear stress components are less than 10 percent of σ_θ.

Lug Design

The stress report for the initial design and analysis of the composite main rotor blade indicated that the following empirical formula was used to compute the stress concentration factor:

$$K = \frac{1.3(R/r)^2 + 0.7}{(R/r) + 1.0}$$

where R is the outer radius and r is the lug inner radius. This gives K = 1.95 (design A) and 2.01 (design B). The previous equation was obtained by reducing the basic empirical equation:

$$K = \frac{(R/r)^2 + 1}{R/r + 1} + \left(\frac{\nu_{t1}E_1}{E_t}\right)\frac{(R/r)^2 - 1}{R/r + 1}$$

using the assumption the $E_1/E_t = 4$ and $\nu_{t1} = 0.075$. However, for the Kevlar/epoxy $E_1/E_t = 13.75$ and ν_{t1} is approximately 0.05. Substituting these values into the basic equation gives: K = 2.35.

Failure Analysis

The maximum stresses in design B were used to compute the failure load for the lug (using the Tsai-Hill failure theory) with the result that the predicted failure load was 136.07kN. The static test specimen failed at 277.56. Thus the actual failure load is approximately twice the predicted failure load.

The critical stress component, according to the Tsai-Hill criteria,is in the radial direction. The computed transverse strain for the static test specimen is 2.6% which is a typical failure strain for an epoxy matrix system. The transverse strain for the predicted failure load is 1.3%. This lower strain included environmental knockdown factors. The one root end static test indicated a conservative design for static strength. The premature failures occured during cyclic loading. To verify the adequacy of the design in fatigue it is necessary to have transverse compression-compression S-N data. This is not available in the literature.

APPENDIX B - FAILURE ANALYSIS OF THE AH-1S BLADE

Sections of a composite blade that threw a tip weight were examined to determine the extent of damage and mechanism of failure. Figure 15 contains a drawing of the blade tip showing the locations of the samples. The dark rectangular sections I, II, III, and IV were cut from the spar adjacent to the fracture surface. Section I is near the inboard end of the tip weight. Section IV is at the outboard end. Figure 15 also shows two cross sections cut from the spar of another blade.

A preliminary examination was made with an optical microscope to find the origin of failure. With few exceptions the locus of failure appeared to be entirely within the rubber tip weight sheath. A closer examination using sectioning techniques revealed that the undercuts did not extend into the glass/epoxy but were entirely within the rubber. These initial observations also revealed fatigue striations that were most obvious in section I and became increasingly less pronounced in sections II, III, and IV.

To gain more detail, section I was examined using a scanning electron microscope (see Figure 16). The striations running at an angle across the specimen are typical of fatigue failure of rubber. This is also true of the undercutting (indicated by the arrow in the figure). An enlargement of this area (Figure 17) reveals some interesting structural details. Cylindrical rods can be seen throughout the entire undercut area. Some of the rods appear to be protruding from the fracture surface. This indicates that the rods are partially embedded within the rubber matrix. The protruding ends are indicative of a "pullout" mechanism. This is further verified in that some of the fibers are partially wetted by the rubber. Elemental chemical analysis for silicon was performed on the rods using energy dispersive analysis by x-rays (EDAX). This analysis confirmed the presence of all the elements of E glass. The debris in Figure 17 consists of "broken" rods and balled up rubber material (commonly called spall). Spalling is normally associated with a rubber surface which has been abraded by friction.

Figure 18 further illustrates the fracture process. In this figure, a glass fiber can be seen protruding from the fracture surface with cracks radiating from the base of the fiber into the surrounding rubber. It appears that the fiber acted as a stress concentrator and initiated cracks which propagated into the rubber. Pullout due to mechanical fatigue is evident in the striations along the fiber surface.

The manufacturer of the rubber was contacted to determine the nature and composition of the stock material. We were advised that the material consisted entirely of chloroprene rubber and a sample was sent to us for SEM and X-ray analysis. EDAX analysis again showed the same basic elements found in E glass. This led to the conclusion that glass was present as an impurity in the rubber stocks. Wet chemical analysis established the weight percent of E glass at 2 to 7 percent.

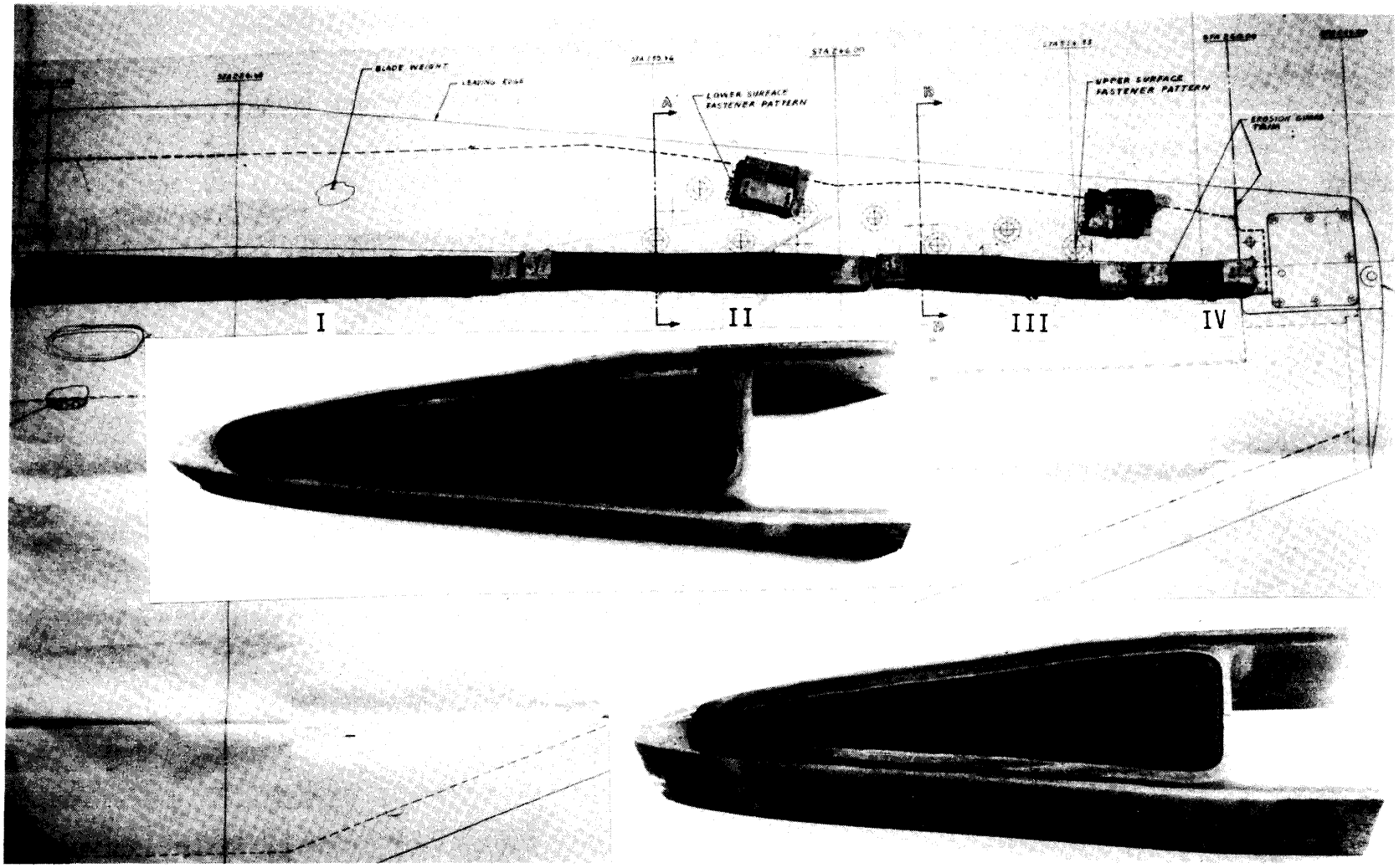

FIGURE 15. DRAWING OF AH-1S HELICOPTER BLADE

FIGURE 16. SAMPLE FROM INBOARD END OF BRASS TIP WEIGHT SHEATH

FIGURE 17. ENLARGEMENT OF FIGURE 16 SHOWING ABRADED UNDERCUT AREA

FIGURE 18. PROTRUDING GLASS FIBER IN RUBBER MATRIX

An Efficient Method for Determining the "A" and "B" Design Allowables

DONALD NEAL AND LUCIANO SPIRIDIGLIOZZI
Army Materials and Mechanics Research Center
Watertown, Massachusetts

ABSTRACT

Suggested statistical procedures for obtaining material "A" and "B" allowables from both complete and censored samples are outlined in this paper. The allowables represent a value determined from a specified probability of survival with a 95% confidence in the assertion. The survival probabilities are .99 for the "A" allowables and .90 for the "B" allowables. Both parametric and non-parametric statistical models are evaluated with respect to their desirability in obtaining the allowables. Exploratory data analysis procedures are introduced in order to determine acceptable distribution functions for representing the data in addition to recognizing outliers (bad data) or multi-modality. It is demonstrated from a variety of materials test data that allowable determinations require prior application of exploratory data analysis procedures in order to assure acceptable results.

The two parameter Weibull, normal, lognormal distribution functions are the proposed statistical models for computing the allowables (where non-parametric methods are not applicable), since they usually will provide a range of possible allowable values. The desirability of the Weibull function application is shown when limited number of probability ranked data values are available in the primary region (lower ranked numbers) of interest in determining the allowables. The required conservatism in this region is satisfied while also satisfying criteria for acceptability of the data representation. The existence of multi-modality or gross outliers in the data set, will in some instances introduce excessively conservative estimates of the allowables when the Weibull function is applied. If the multi-modality case is a reality then a suggested procedures using the Penalized Likelihood Method [1] is used in conjunction with Cramer-Rao lower bound [2] estimate for the 95% confidence values.

Extensive tables for sample sizes (5(100)1) have been made available for computing the allowables using the Weibull function. Use of the Monte Carlo Method in conjunction with maximum likelihood (M. L.) relations describe the procedures used in obtaining the necesssary values in determining the allowables. A simple computer code has been made available so that M. L. estimate of Weibull paramter can be determined thereby resulting in direct computation of the allowables.

Introduction

The work described in this report is part of a continuing effort to provide statistical procedures for determining the "A" and "B" allowables for the MIL-HDBK-17 (Handbook for Composite Material in Aircraft Application). The preparation of handbook is a prime mission of the AMMRC Engineering Standardization Division. The current statistical procedures used in the MIL-5 handbooks is not considered applicable to determination of the allowables for composite materials.

The MIL-5 requirement that data be represented exclusively by a normal or if not applicable by a non-parametric method is not realistic. For example, if an "A" allowable were needed for a specific material and the normal distribution was not adequate in representing data, then 300 test results would be required. This could result in an extremely costly test program, in that, control of environment and manufacturing process for composite material must be very precise. Also when the normal distribution is applied erroneous allowable can be obtained due to incorrect representative of data in lower fail regions. A quote from Hahn and Shapiro [3] which says, "Although many models might appear appropriate within the range of the data, they might well be in error in range for which predictions are desired," adequately summarizes this important issue. The fact that most tests for acceptable representations will accept the assumed distribution, therefore, a model can rarely be proven inadequate on the basis of sample data. This complicates the issue with respect to allowable computations, therefore possibly requiring a extreme value distribution representation which will account the uncertainties in the lower tail region.

Inorder to address the allowable computation problem more rigorously, the authors have examined the relative merits of 4 distinct distribution functions including the Penalized Likelihood Method [1] for multi-modal case. In most instances the 2 parameter Weibull function is recommended. This extreme value function will usually provide acceptable estimates of the allowables. Either very precise, or slightly conservative estimates will be obtained. According to Freudenthal and Gumbel[4], the use of the Weibull distribution to represent the distribution of the breaking strength of materials has been justified by using extreme value theory.

In applying the Weibull distribution it is important to recognize data with outliers in vicinity of higher ordered values in addition to multi-modal behavior. Data contaminated in this manner will usually reduce accuracy in the weibull allowable computation. The Quantile Box Plot [5] was used in determining outliers and multi-modality. This method proved to be more reliable then the conventional robust procedures [6,7,8] currently being suggested for determining outliers. If there is not a rationale for removing outliers then they should remain in data set, otherwise erroneous estimates of the allowables will result. In the multi-modal case, careful examination of test procedures and material

processing should be made prior to acceptance of this phenomena. It is possible that in testing certain composite materials, bimodal behavior could occur. In exploring some recent test results from Kevlar, Graphite and Glass composites in addition to ceramic materials an occasional bimodality has existed. In most cases errors in testing or material conditioning and processing have accounted for this situation.

The following robust method for applying exploratory procedures in the examination of outliers was used primary as verification of the Quantile Box Plot results. The methods singular advantage is that visual inspection is not necessary in recognition of the outliers. The disadvantage results from arbitrariness in selection of scale and the tuning constant.

Robustness Method

The outliers are determined in a formal manner by applying a robust method involving application of the maximum likelihood (M.L.) estimation where the residuals are weighted in a systematic manner. The computed weights describe the relative importance of the data points. For example, a zero weight should indicate exclusion of a point. It should be emphasized that removing outliers without a valid reason is poor practice. Outliers should be examined for errors in testing or possible material defects. The removal of outliers (bad data) will essentially define robust data. The robust procedures applied in this paper involves using both the M-estimating technique of Huber[7] and Andrews[8]. Initially the Huber technique is applied in order to determine a robust location parameter (weighted mean). The Andrew's function is then applied using location parameter estimated from the Huber result. It should be noted that this robust method requires a uni-modal distribution of the data, therefore initial application of the Quantile Box Plot should be made.

The Huber m-estimation technique which involves defining the likelihood function

$$L(\theta) = \prod_{i=1}^{N} f(X_i-\theta), \quad -\infty < \theta < \infty \qquad (1)$$

where f is a contaminated normal distribution,

X_i = data,

θ = location parameter and

N = sample size

By maximizing log $L(\theta)$ such that

$$\Sigma\psi(X_i-\theta) = 0, \qquad (2)$$

where $\psi = f'/f$

then the solution of (2) is M.L. estimate of θ designated as $\hat{\theta}$. In order to represent ψ in scale invariant form, equation (2) can be rewritten as

$$\sum \psi\left(\frac{(X_i - \theta)}{d}\right) = 0 \tag{3}$$

with d equal to the estimate of scale. The scale is often defined as

$$d = \text{median}|X_i - \text{median}(X_i)| \,/.6745$$

$$\text{or simple M.A.D./.6745} \tag{4}$$

This estimate is considerably more robust than using the complete samples which could result in poor representation of the actual scale.

By solving

$$\sum_{i=1}^{N} W_i(X_i - \theta) = 0 \tag{5}$$

where

$$W_i = \psi\left(\frac{X_i - \theta}{d}\right) \Big/ \left(\frac{X_i - \theta}{d}\right)$$

$$\psi = \begin{cases} r & |r| \le c_1 \\ c_1 \text{ sign } (r) & |r| > c_1 \end{cases},$$

c_1 is defined as the tuning constant and

$$r = \left(\frac{X_i - \hat{\theta}}{d}\right)$$

An iterative process is then used in the solution of (5) such that when the differences in W_i become negligible provides the necessary criteria for an acceptable solution for the θ and W_i values. For c_1=1.345 the Huber's ψ function provides a 95% efficiency[3].

With estimate of $\hat{\theta}$ determined from the solution of (2) the iteration is continued where the ψ function is now defined as

$$\psi(r) = \begin{cases} c_1 \sin(r/c_1), & |r| \le \pi c_1 \\ 0, & |r| > \pi c_1 \end{cases} \tag{6}$$

This new function is called the Andrew's wave equation. In order to obtain the desired robust data for this ψ function, the tuning was adjusted to c_1=1.34 and the scale defined as in equation (4).

It should be noted that Andrew's function was selected for its ability to describe outliers as data with essentially zero weights.

Quantile Box Plot

A general description of the Quantile Box Plot is shown in Figure 1. Where the quantile function is defined as

$$Q(u) = F^{-1}(u),\ 0 \leq u \leq 1 \tag{7}$$

that is, if the random variable x with distribution function given by F(x), then the root of $F(x) = u$, $0 \leq u \leq 1$ is the p^{th} quantile of F(x). From the ordered statistic $x_1 \leq x_2 \leq \ldots, x_n$, Q is defined as piece wise linear function with interval (0,1) divided into 2n subintervals. Therefore representing Q as

$$Q\left(\frac{2j-1}{2n}\right) = x_j\ ,\ j = 1, 2, \ldots, n. \tag{8}$$

In order to interpolate

$$u \in \left(\frac{2j-1}{2n}\ ,\ \frac{2j+1}{2n}\right)$$

$$Q(u) = n\left(u - \frac{2j-1}{2n}\right) x_{j+1} + n\left(\frac{2j+1}{2n} - u\right) x_j, \tag{9}$$

where n equals the sample size .

The box boundaries are defined as

Q (.25) to Q (.75)

Q (.125) to Q (.875)

Q (.0625) to Q (.9375)

The Quantile function Q(u) is useful for detecting the presence of outliers, modes and the existence of two populations. Flat slots in Q(u) indicate modes. Sharp rises in Q(u) for u near 0 or 1 suggest outliers; sharp rises in Q(u) within the boxes indicate the existence of two (or more) populations. The obvious bimodality shown in Figure 2 is represented by the Quantile Box Plot displayed in Figure 3. In figure 4 (lowest ordered value) the gross outlier is requested by the extended vertical line at lower left region of graph in figure 5. The results shown in figures (2, 3, 4, 5) are not represented of typical data sets. In many instance multi-modality and outliers are not obvious from routine examination of the data.

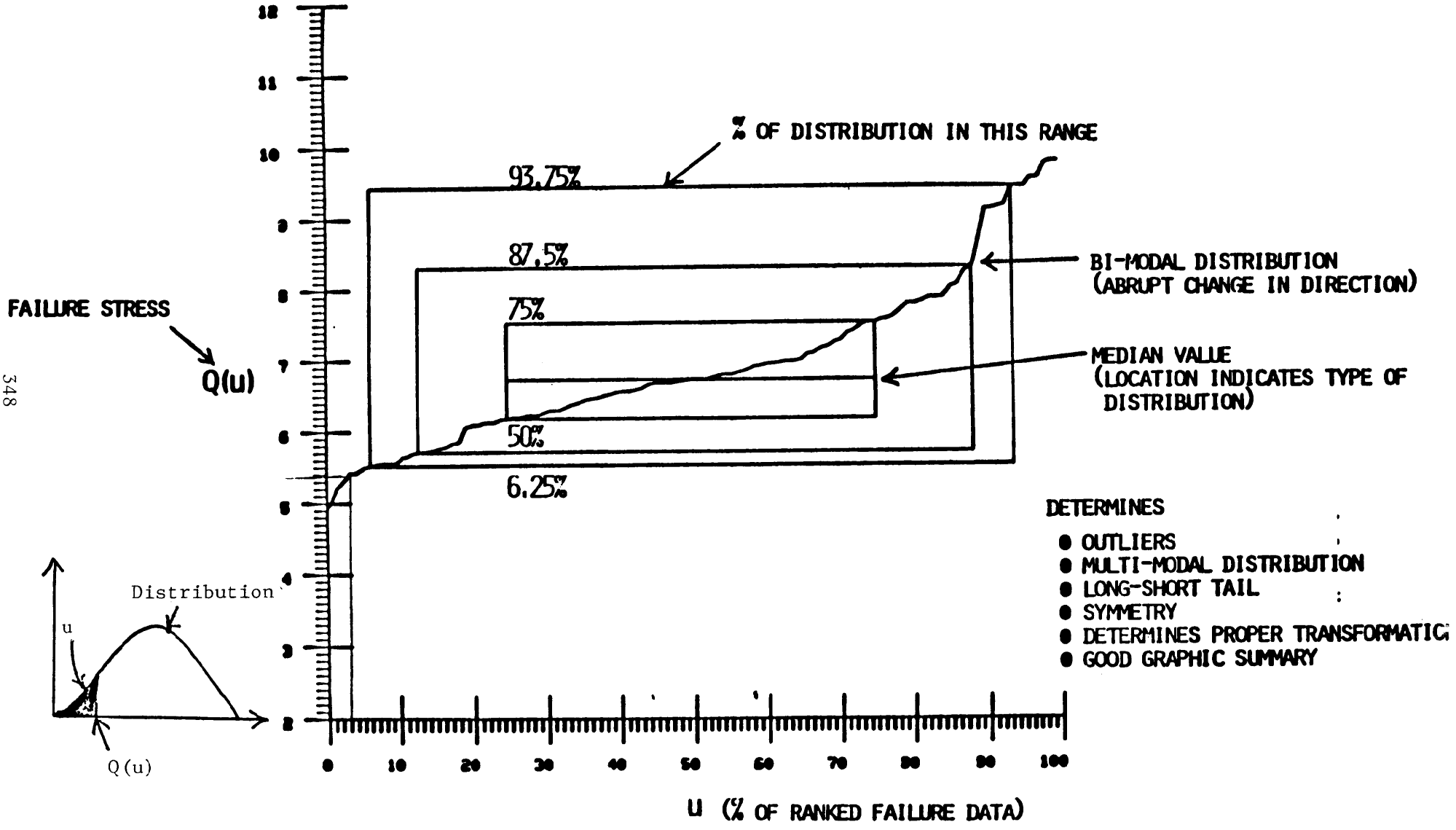

Figure 1 Quantile Box Plot

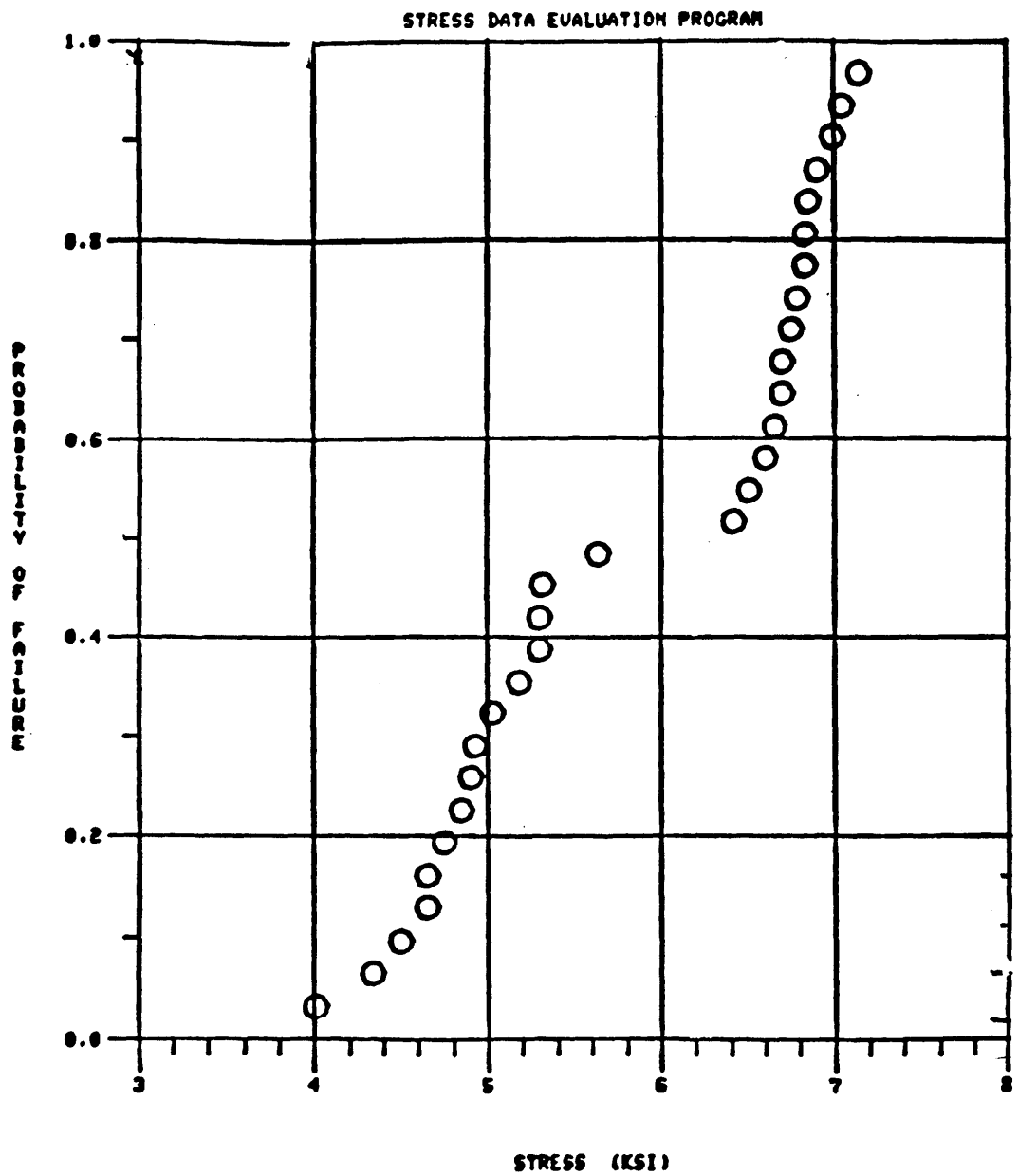

Figure 2 Probability of Failure Vs. Strength

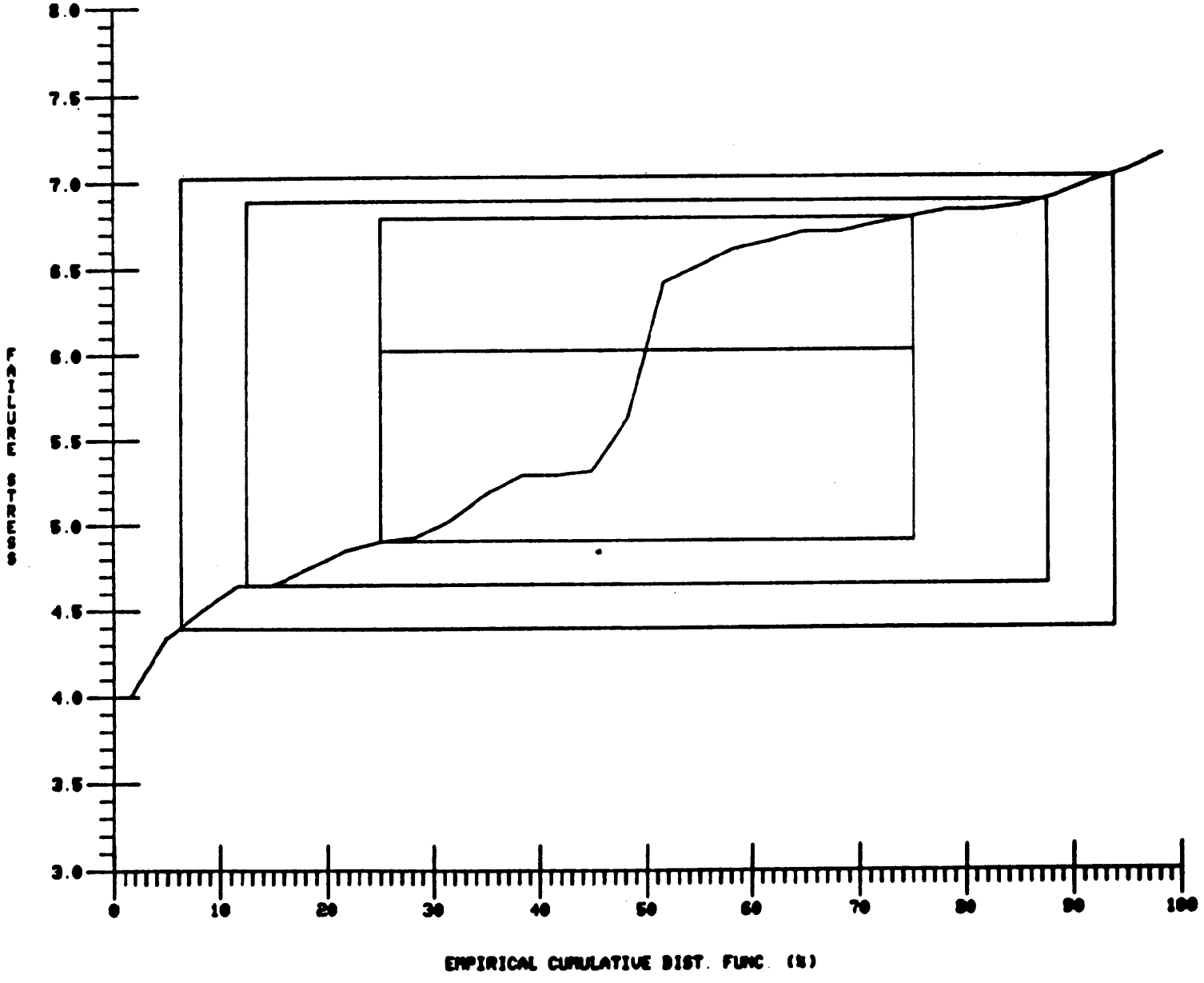
8.0
7.5
7.0
6.5
6.0
5.5
5.0
4.5
4.0
3.5
3.0
FAILURE STRESS
0
10
20
30
40
50
60
70
80
90
100
EMPIRICAL CUMULATIVE DIST. FUNC. (%)

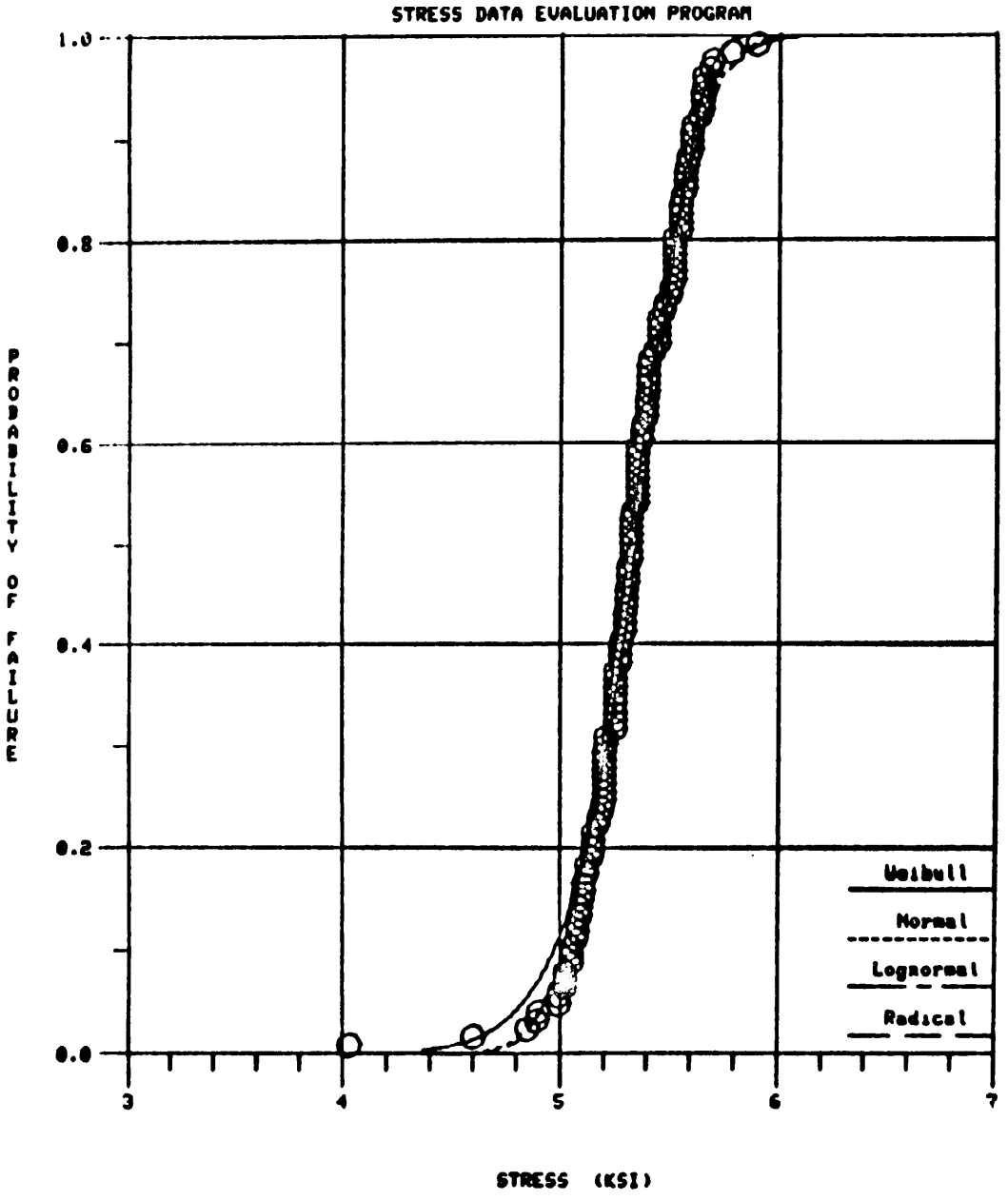

RMS ERROR

	Normal	Lognormal	Weibull	Radical
R1	.0308	.0329	.0393	.0318
R2	.0302	.0323	.0389	.0318
R3	.0293	.0315	.0382	.0317

		90% CONFIDENCE INTERVAL	
MEAN (KSI)=	5.320	5.283	5.357
S DEV (KSI)=	.242	.219	.270

WEIBULL PARAMETERS

		90% CONFIDENCE INTERVAL	
SLOPE M=	25.680	22.887	28.909
CHAR VALUE=	5.426	5.393	5.459
99% ORIGIN=	4.544	4.427	(95% CL)
ORIGIN=	.000		

RADICAL PARAMETERS

A=	4.212	EXP B (N)=	12.000
B=	8.426	EXP(R)=	12.000
C=	-1.226		
SIGI=	2.985	SIGF=	6.637

NON-PARAMETRI SOLN: A AND B ALLOWABLES
OPTIMAL:A(99,95,N=300)B(90,95,N= 30)
GIVEN DATA:
A(99,72,N=125)B(90,88,N=125)

WEIBULL:
DESIGN A= 4.427
DESIGN B= 4.901

NORMAL:
DESIGN A= 4.681
DESIGN B= 4.958

LOGNORMAL:
DESIGN A= 4.692
DESIGN B= 4.952

Figure 4 Statistical Data Evaluation of Kevlar Material (Tension Test)

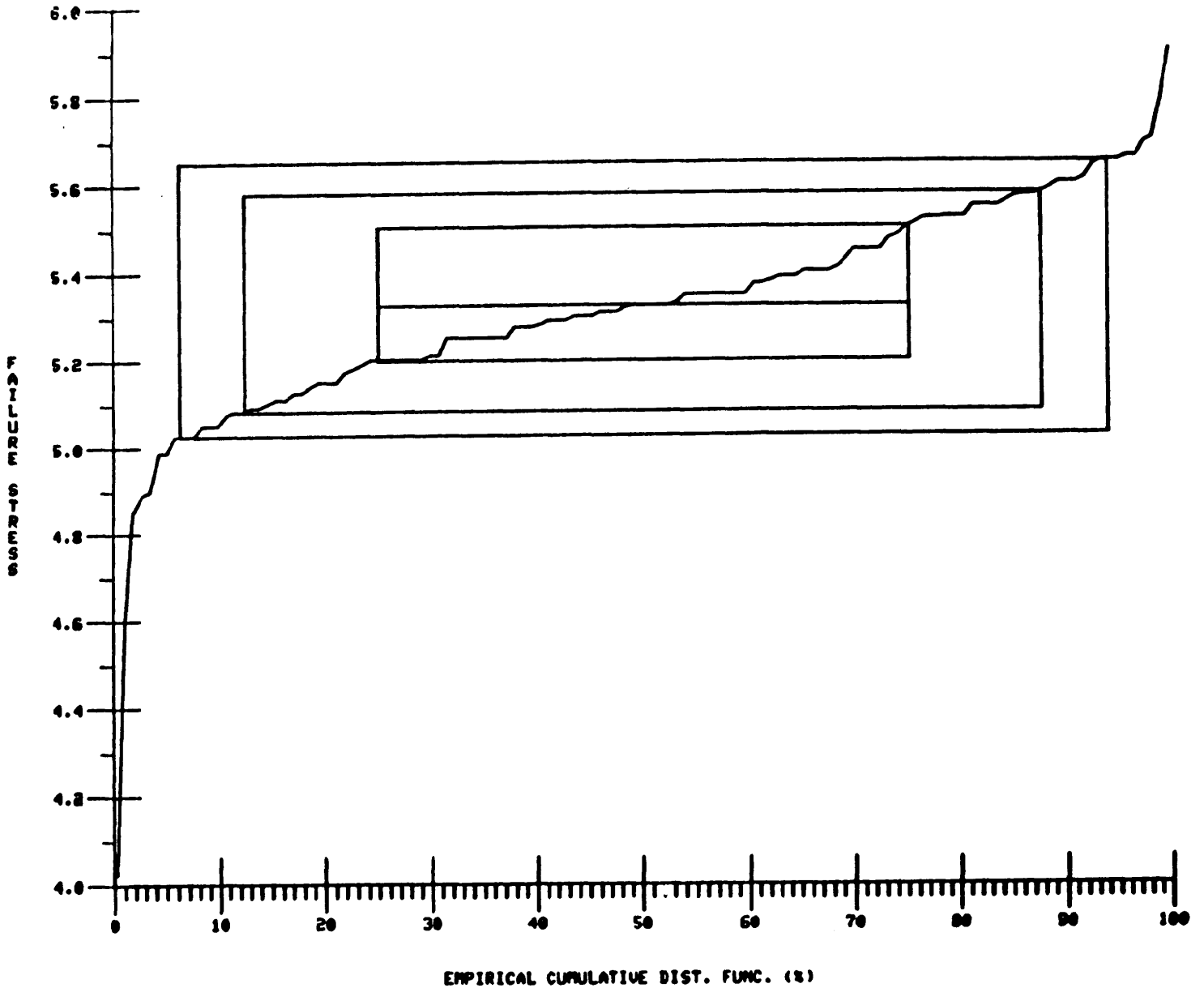

Figure 5 Quantile Box Plot - Kevlar Material

Normal Distribution Function

$$F_x(z) = \frac{1}{\sqrt{2\pi}} \int_{-\infty}^{z} e^{-\frac{1}{2}\nu} \, d\nu$$

$$\text{where } z = \frac{x - m_x}{\sigma_x}$$

and x, m_x and σ_x are strength data, mean value and standard deviation respectively. $F_x(z)$ can be simply and accurately evaluated using the following polynomial representation, [9].

$$F_x(z) = 1 + \frac{1}{2}\left(1 + d_1 z + d_2 z^2 + d_3 z^3 + d_4 z^4 + d_5 z^5 + d_6 z^6\right)^{-16} + E(z) \quad [10]$$

where $E(z) < 1.5 \times 10^{-7}$

and $d_1 = .049867847$

$d_2 = .0211410061$

$d_3 = .0032776263$

$d_4 = .0000380036$

$d_5 = .0000488906$

$d_6 = .000005383$

Lognormal:

The lognormal 2 parameter distribution function is evaluated by using Equation 2, where the maximum likelihood method estimates the mean (m_x) and standard deviation (σ_x),

$$\text{where } m_x = \frac{1}{n} \sum_{i=1}^{n} L_n(X_i)$$

$$\text{and } \hat{\sigma}_x = \left\{ \frac{\sum_{i=1}^{n} L_n(X_i)^2 - M\left(\sum_{i=1}^{n} L_n(X_i)/n\right)^2}{n} \right\}^{1/2} \quad [11]$$

X_i = data values

The unbiased estimate of σ_x is $\left(\left(n/(n-1)\right)\sigma_x^2\right)^{1/2}$

By defining $X_1 = L_n X$, then

$$Z = \frac{X_1 - m_x}{\sigma_x}$$

Weibull Distribution Function

The M.L. method is applied in order to obtain the two parameters of the Weibull function.

$$f(x) = \frac{m}{\mu}\left(\frac{x}{\mu}\right)^{m-1} \exp\left[-\left(\frac{x}{\mu}\right)^{m}\right] \qquad [12]$$

The method requires defining the likelihood function[10]

$$L = N! \prod_{i=1}^{N} \left\{\frac{m}{\mu}\left(\frac{X_i}{\mu}\right)^{m-1} \exp\left[-\left(\frac{X_i}{\mu}\right)\right]^{m-1}\right\} \qquad [13]$$

where X_i = data,

m, μ = shape and normalizing parameter and

N = sample size,

By solving the following log likelihood equations

$$\frac{\partial L_N L}{\partial \mu} = 0 \quad \text{and}$$

$$\frac{L_N L}{\partial m} = 0 \qquad [14]$$

determines the $\hat{m}$ and $\hat{\mu}$ values.

Equation (14) must be solved in an iterative manner by using the computer code listed in Appendix A. The unbiased m and μ and their corresponding confidence intervals are obtained from Tables by [2]. It can be shown that:

$$\sigma_A \text{ or } \sigma_B = \hat{\mu}\left(\ln\left(\frac{1}{P^*_s}\right)\right)^{1/\hat{m}} \qquad [15]$$

where σ_A or σ_B = the allowable, depending on P^*_s.

P^*_s = tolerance limit on P^*_s (probability of survival) determined form application of Monte Carlo method. In tables 1 and 2 the results for A and B allowable and P^*_s computation is tabulated. Parametric determination of three parameter and censored data requires a more elaborate analysis. These procedures will not be outlined in this text, although they have been completed and the results of this analysis will be shown later in t text. The (^) represents a biased estimate.

TABLE 1 P_S^* VS. SAMPLE SIZE N FOR "A" ALLOWABLES

N	P_S^*	N	P_S^*	N	P_S^*	N	P_S^*
5	.999999	29	.998214	53	.996816	77	.995970
6	.999992	30	.998130	54	.996776	78	.995940
7	.999972	31	.998048	55	.996736	79	.995911
8	.999930	32	.997968	56	.996697	80	.995883
9	.999859	33	.997891	57	.996657	81	.995855
10	.999780	34	.997816	58	.996619	82	.995827
11	.999713	35	.997743	59	.996580	83	.995800
12	.999650	36	.997673	60	.996543	84	.995773
13	.999579	37	.997606	61	.996505	85	.995747
14	.999500	38	.997541	62	.996468	86	.995721
15	.999420	39	.997479	63	.996432	87	.995695
16	.999340	40	.997420	64	.996396	88	.995670
17	.999256	41	.997363	65	.996360	89	.995645
18	.999160	42	.997309	66	.996325	90	.995620
19	.999050	43	.997257	67	.996290	91	.995596
20	.998940	44	.997207	68	.996256	92	.995572
21	.998843	45	.997159	69	.996222	93	.995548
22	.998760	46	.997113	70	.996189	94	.995525
23	.998684	47	.997068	71	.996156	95	.995502
24	.998613	48	.997025	72	.996124	96	.995479
25	.998540	49	.996982	73	.996092	97	.995456
26	.998463	50	.996940	74	.996061	98	.995434
27	.998382	51	.996898	75	.996030	99	.995412
28	.998298	52	.996857	76	.996000	100	.995390

TABLE 2 P_S^* VS. SAMPLE SIZE N FOR "B" ALLOWABLES

5.0	.99880	29.0	.95991	53.0	.94499	77.0	.93884
6.0	.99783	30.0	.95930	54.0	.94468	78.0	.93861
7.0	.99651	31.0	.95861	55.0	.94437	79.0	.93838
8.0	.99450	32.0	.95785	56.0	.94407	80.0	.93815
9.0	.99170	33.0	.95703	57.0	.94377	81.0	.93792
10.0	.98900	34.0	.95617	58.0	.94349	82.0	.93769
11.0	.98716	35.0	.95528	59.0	.94321	83.0	.93747
12.0	.98540	36.0	.95438	60.0	.94293	84.0	.93724
13.0	.98287	37.0	.95349	61.0	.94267	85.0	.93702
14.0	.97992	38.0	.95261	62.0	.94241	86.0	.93680
15.0	.97720	39.0	.95178	63.0	.94215	87.0	.93658
16.0	.97517	40.0	.95100	64.0	.94190	88.0	.93636
17.0	.97358	41.0	.95029	65.0	.94165	89.0	.93614
18.0	.97200	42.0	.94963	66.0	.94140	90.0	.93593
19.0	.97013	43.0	.94904	67.0	.94116	91.0	.93572
20.0	.96820	44.0	.94850	68.0	.94092	92.0	.93552
21.0	.96653	45.0	.94800	69.0	.94069	93.0	.93531
22.0	.96514	46.0	.94755	70.0	.94045	94.0	.93511
23.0	.96400	47.0	.94712	71.0	.94022	95.0	.93492
24.0	.96306	48.0	.94673	72.0	.93999	96.0	.93472
25.0	.96228	49.0	.94636	73.0	.93976	97.0	.93454
26.0	.96161	50.0	.94600	74.0	.93953	98.0	.93435
27.0	.96102	51.0	.94566	75.0	.93930	99.0	.93417
28.0	.96047	52.0	.94532	76.0	.93907	100.0	.93400

Non-parametric method. Non-parametric procedures (reference 11) are usually more desirable than parametric ones, since they provide the exact probabilities. In the parametric case, the reliance is on an assumed distribution function which provides extrapolated results for the probability of survival values. The penalty for applying the non-parametric method is the need for relatively large amounts of data (e.g., 29 values for the "B" allowable and 300 for the "A" allowable). The lowest ranked value describes the corresponding allowable. In the case where 100 data values are available, the sixth lowest ranked data value determines the "B" allowable. The use of 100 values in obtaining the "B" allowables prevents any erroneous estimates if lower ordered strength values are incorrect. Table 3 shows which ranked data value should be used for a particular sample size. The importance of using sample sizes greater than the required 29 for the "B" allowable is shown in figure 6: For example, if all data is included, the allowable will be "4"; however, this could be erroneous if data value 4 was an outlier. By removing the outlier, the allowable is 4.6 (a 15% error if first ranked value had been used).

TABLE 3. Ranks, r, of observation, n, for an unknown distribution having the probability and confidence of A and B values.

A Basis		B Basis		B Basis		B Basis	
n	r	n	r	n	r	n	r
300	1	29	1	321	24	1269	110
480	2	46	2	345	26	1376	120
630	3	61	3	368	28	1483	130
780	4	76	4	391	30	1590	140
920	5	89	5	413	32	1696	150
1050	6	103	6	436	34	1803	160
1190	7	116	7	459	36	1909	170
1320	8	129	8	481	38	2015	180
1450	9	142	9	504	40	2120	190
1570	10	154	10	560	45	2230	200
1700	11	167	11	615	50	2330	210
1820	12	179	12	671	55	2430	220
1950	13	191	13	726	60	2530	230
2070	14	203	14	781	65	2630	240
2190	15	215	15	836	70	2730	250
2310	16	227	16	890	75	2830	260
2430	17	239	17	945	80	2930	270
2550	18	251	18	999	85	3000	277
2670	19	263	19	1053	90		
2790	20	275	20	1107	95		
2910	21	298	22	1161	100		

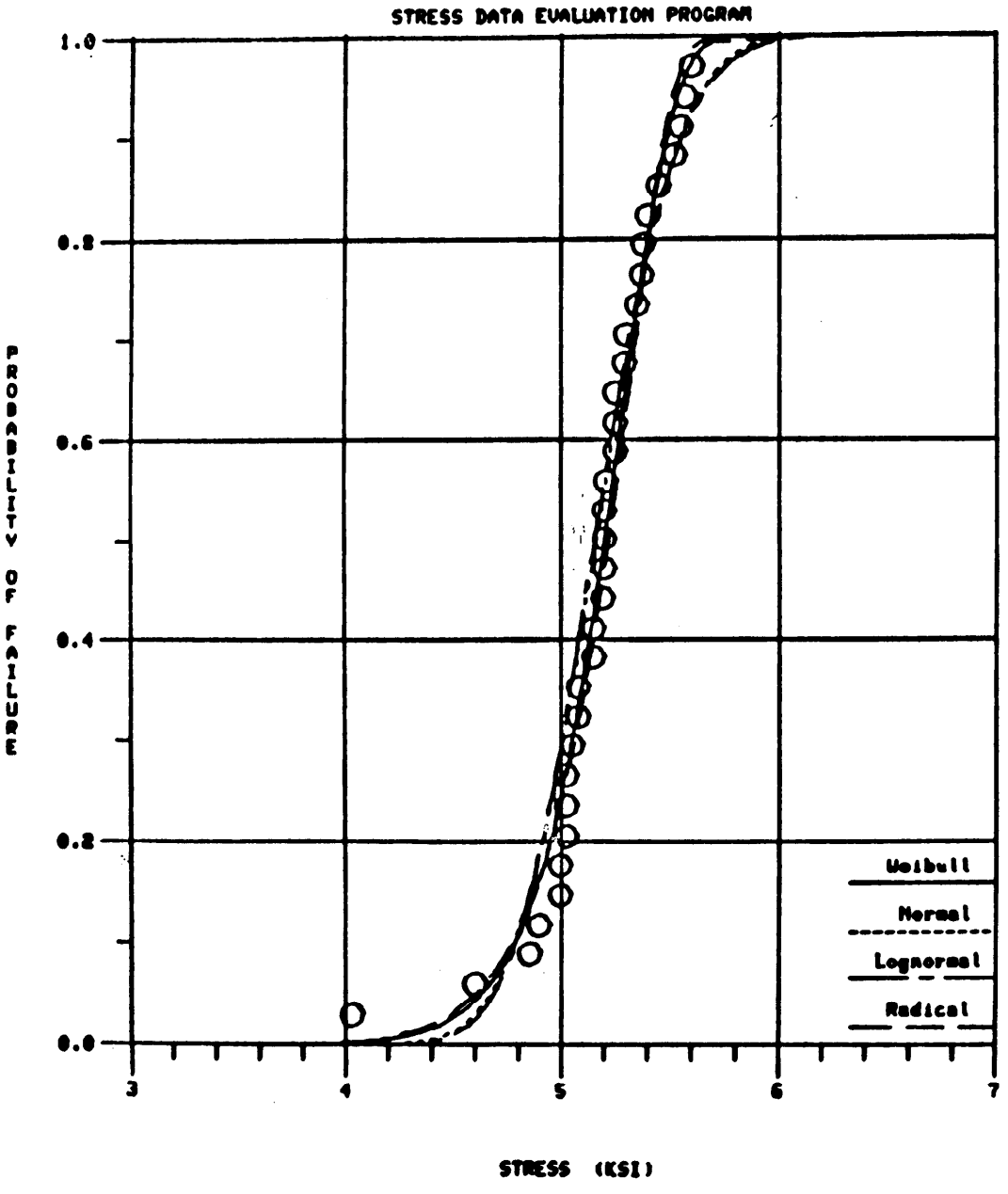

RMS ERROR

	Normal	Lognormal	Weibull	Radical
R1	.0627	.0674	.0420	.0498
R2	.0605	.0653	.0404	.0510
R3	.0574	.0624	.0384	.0626

		90% CONFIDENCE INTERVAL	
MEAN (KSI)=	5.166	5.076	5.256
S DEV (KSI)=	.301	.251	.379

WEIBULL PARAMETERS

		90% CONFIDENCE INTERVAL	
SLOPE M=	22.450	17.829	28.341
CHAR VALUE=	5.288	5.217	5.361
99% ORIGIN=	4.345	4.154	(95% CL)
ORIGIN=	.000		

RADICAL PARAMETERS

A=	2.621	EXP B (N)=	12.000
B=	3.504	EXP(R)=	12.000
C=	-.750		
SIGI=	1.871	SIGF=	6.125

NON-PARAMETRI SOLN: A AND B ALLOWABLES
OPTIMAL:A(99,95,N=300)B(90,95,N= 30)
GIVEN DATA:
A(99,28,N= 33)B(90,97,N= 33)

WEIBULL
DESIGN A= 4.164
DESIGN B= 4.627

CONVAIR HEXCEL TEN. RT 0%RH

2 PAR. WEIBULL

Figure 6. Statistical Data Evaluation of Kevlar (Hexcel)

Multi-Modality. If the bimodality displayed in figures 1, 2 and 3 is a reality, not the result processing or testing errors then the current available parametric procedures usually will not provide acceptable representation of the data. A non-parametric method[11] is suggested having excellent approximation properties, for estimating an unknown probability density function from a random sample $X_1,\ldots,X_N$

The estimator optimizes a criterion function which combines the maximum likelihood principle and a penalty term for smooth (i.e., not bumpy) behavior. The criterion function is a discrete approximation to

$$L(f) = \prod_{i=1}^{N} x(i) \exp\left[-\alpha \int \left|\frac{d^2 f(t)}{dt^2}\right|^2 dt\right] \qquad [16]$$

where f(t) is any probability density function; that is, f(t) is nonnegative and intergrates to 1. Equivalently, we may maximize the $\ln[L(f)]$ which separates into two terms - a log likelihood plus a log penalty term.

The penalty term contains an unknown positive constant α which determines the amount of smoothness in the resulting estimator. Values of α that are "too small" result in bumpy estimates while α "too large" oversmooths. In practice, α as small as possible without introducing excessive bumps. Several values of α that differ by factors of ten should be tried and graphically displayed and compared to a histogram or parametric assumption. For standard normal data, $\alpha = 10$ works well.

Numerical integration determines the cumulative density values (probabilty of survival) for the prescibe percentile, 90 or 99 depending on the desired allowable.

Confidence limit on these estimates ray R_{90} or R_{99} can be determine from the Cramer-Rao lower bound which determine the variance on R. The confidence limit L is determine iteratively from

$$L_i = R - U_\gamma\left[V(L_i - 1)\right]^{\frac{1}{2}}; \; i = 2, 3... \qquad [17]$$

where U_γ is the γ percentage point (95%) of the normal distribution.

Initially, $L_1 = R - U_\gamma[V(R)]^{\frac{1}{2}}$

Where, $V(R) = R^2 (\ln R)^2 \left\{1.109 - .514 \ln(-\ln R) + .608 [\ln(-\ln R)]^2\right\}/n \qquad (18)$

Subsequent interation in equation 16 requires substitution of L_i for R in equation 18.

Pooling of Data. In obtaining the allowables, test data should be obtained from a number manufacturers (e.g. composite materials from various aircraft industry representatives). All test data should be pooled inorder to obtain an allowable consistent with a general population of that specific materials strength values. If a significant difference exist among the manufacturer then an investigation should be made regarding the cause of this situation. The tests recommended for determining significant difference are the conventional t test, and two non-parameter tests for the K - sample case. The Kruskal-Wallis[12] multi-sample test for identical populations is applied such that H is corrected for ties. The null hypothesis (identical populations) is rejected at the 2% level. The other distribution free test suggested, is the Jonckheere's[12] K sample trends test against the ordered alternative. Where ties are removed by applying a randomization process. The null hypothesis of randomness is rejected at 2% level, that is acceptance of difference in samples at this level.

Statistical Evaluation of Data (Graphical Display). In Figure 4, a plot of probability failure (P_f) versus failure stress (see marked circles) of empirical failure data were shown. The P_f values were determined from an R_i ranking. The four candidate functions are listed on the graph with their corresponding line form representations. In addition to obtaining a visual inspection of best fit, the RMS error provides a quantitative evaluation for the three rankings and the density functions. The sample means and standard deviations are tabulated with their corresponding 90% confidence interval. The Weibull shape and normalizing (Char. value) parameters are tabulated with confidence intervals. The 99% a origin represents one percent probability of failure with 95% lower confidence limit for that number. This representation is the A allowable. If one wants to increase or decrease origin percentage, it can be done by applying methods described in (2). The work "origin" will equal zero if two parameter Weibull function was considered, otherwise, three parameter Weibull function was used. In the radical parameter tabulation, A, B and C are coefficients obtained from a least squared fit routine. Exp B (N) and Exp C (R) are the corresponding exponents determined in the fitting of the data. Sig I and Sig F are the two cut-off points. That is, the smallest and largest projected values determined by the function.

In applying the robust procedures, it is important to have a rationale for ignoring the determined outlier, otherwise, erroneous estimates of survival probability computations could result. The robust scheme can be applied to data from relatively samll size specimens, where errors in machining, testing, etc., greatly effect strength determination. The authors have noted considerable improvement in ceramic material failure predictions of large specimens (13 in^3) from knowledge of small specimen (.03125 in^3) strength results when the outliers are removed from the original data. Non-parametrics solutions, as applied to the code (see Figure 4), can provide information regarding confidence levels for A and B allowables, with respect to the number of data points. The code can be altered to include other allowables by using the simple relationships outlined in (11).

Results and Discussion

In figure 4, the results of tension tests on Kevlar composite material (Hexcel Co.) are shown, the allowables are similar for all three functions. This is an ideal situation, since selecting any of the functional results will provide acceptable allowable value, although the Weibull's heavy tail tends to represent the outlying values better. The results shown in figure 7, describe the difficulty arising from outliers existing in vicinity of higher ordered values. See figure 8 display of Box Plot for verification of outliers at 26.5 KSI (vertical line extending from 22 to 26.5). The design B allowable of 10.9 KSI determined from Weibull computation differs from the non-parametric result by 2.1 KSI a 19% difference. The A allowable result, Weibull vs normal, is different by 2.1. Since the non-parametric result is any exact probability then Weibull results are in error by a substantial amount (19%). An error which has produced excessively conservative estimates. The unfortunately, vulnerability of the M. L. method is shown in this example for determining the Weibull parameters. In figure 9, the outlier has been removed from the data displayed in figure 8. Note the substantial increase in Weibull shape parameter from 5.66 to 7.32 because one value was removed from sample size of 30. The Weibull B allowable computation is now in error by less than 8%. The examples shown in figure 7 and 9 demonstrate the need for adequately exploring data prior to applying distribution functions. If the outliers was not removed from data because rationale was not determined for its removal then the normal function allowable values should be considered. In figure 10 the Box Plot is shown with outliers removed for the data.

Figure 11 describes the compression test results for a Kevlar composite material (Hexcel) where three manufacturers data has been pooled. In this example selection of .966 for "A" allowable and 1.020 for the "B" allowable from the normal distribution representation would be adequate additional data was obtained from another manufacturer where the test and material were the same as the other three. This data was pooled with other three samples and is shown in figure 12. This selection of allowables would be .808 for the "A" and .948 for the "B", a 20% difference from results shown in figure 11. There are two fundamental issues involved, one is the need for a substantial number of manufacturers participating in the program to obtain allowables and secondly the need for using an extreme value type distribution (Weibull) inorder to provide an element of conservatism in accounting for the uncertainties existing in limited number of pooled samples in representing the population. Note, in figure 11 the normal function provided adequate representation yet with additional data (figure 12) the Weibull function provides the better representation. This situation introduces complex problem where the questioning of pool or not pooling exists. From statistical tests for significant differences in samples, the fourth manufacturers' test results included in figure 12 were not acceptable for pooling with the other samples (figure 11). Since it is important to provide allowables from a population of specific materials and tests, the authors recommend pooling of all samples inorder to provide a more complete representation of the materials capabilities.

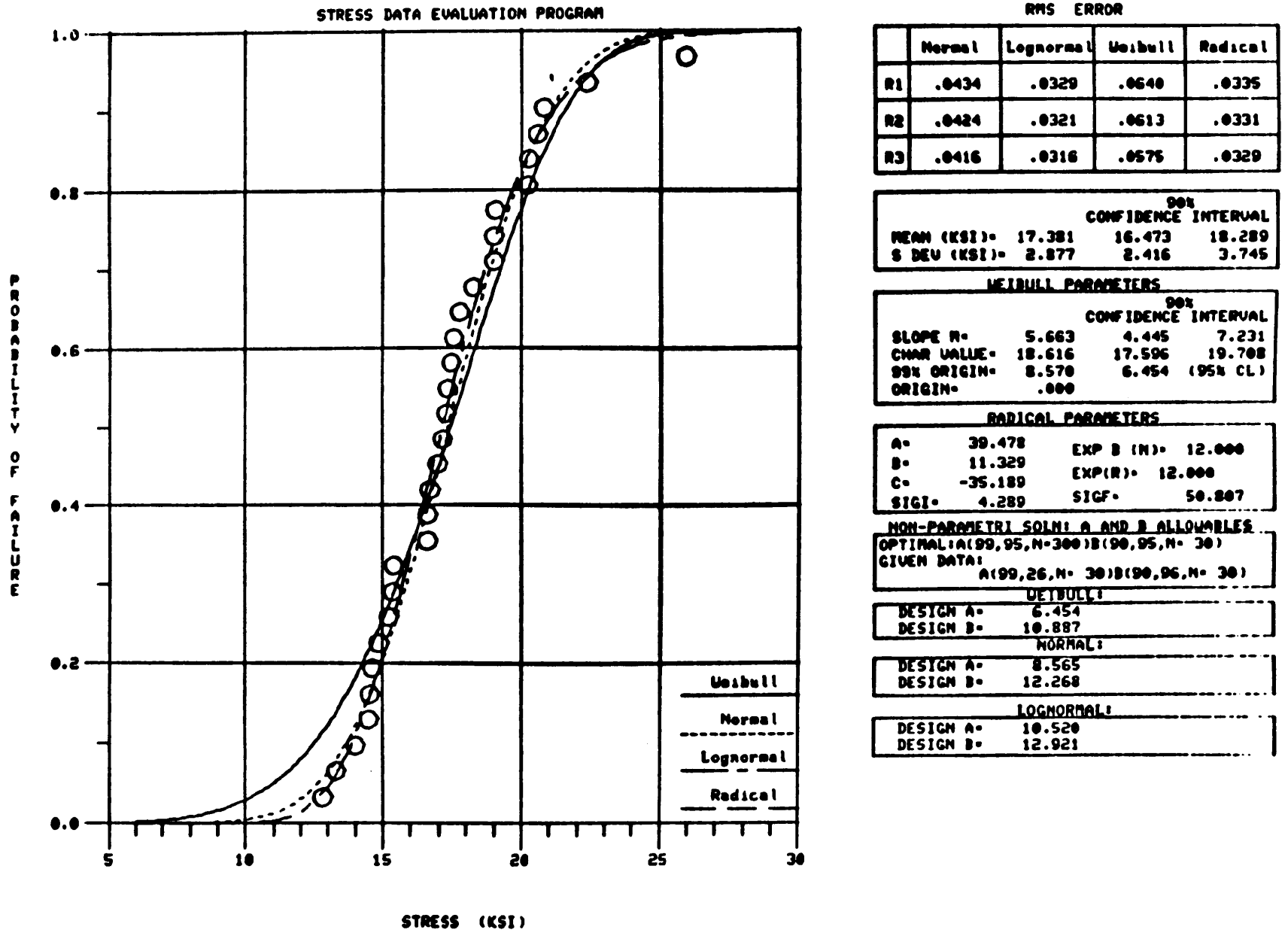

Figure 7 Statistical Data Evaluation Bend Test Results (Ceramics)

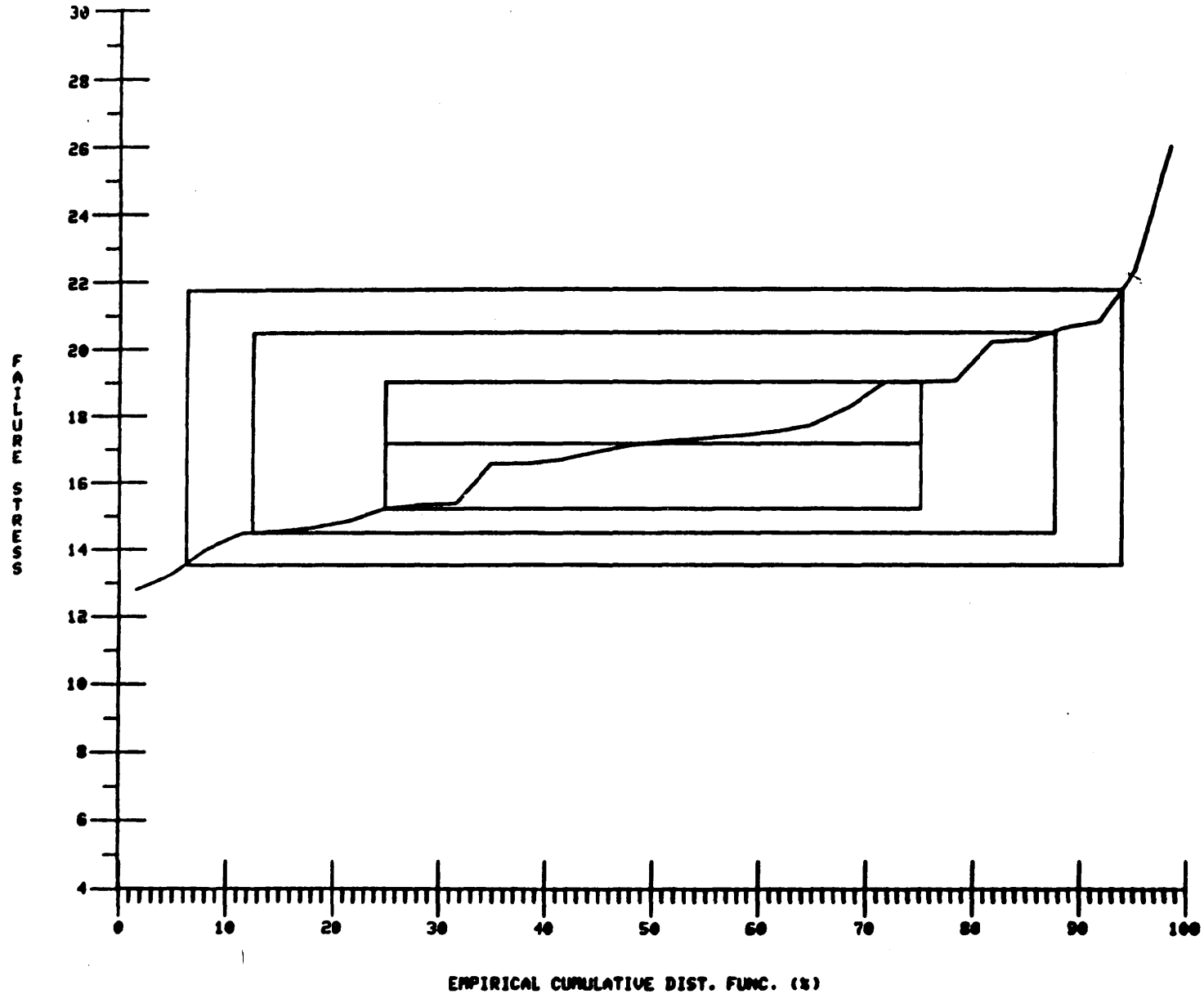

Figure 8 Quantile Box Plot - Bend Test Results

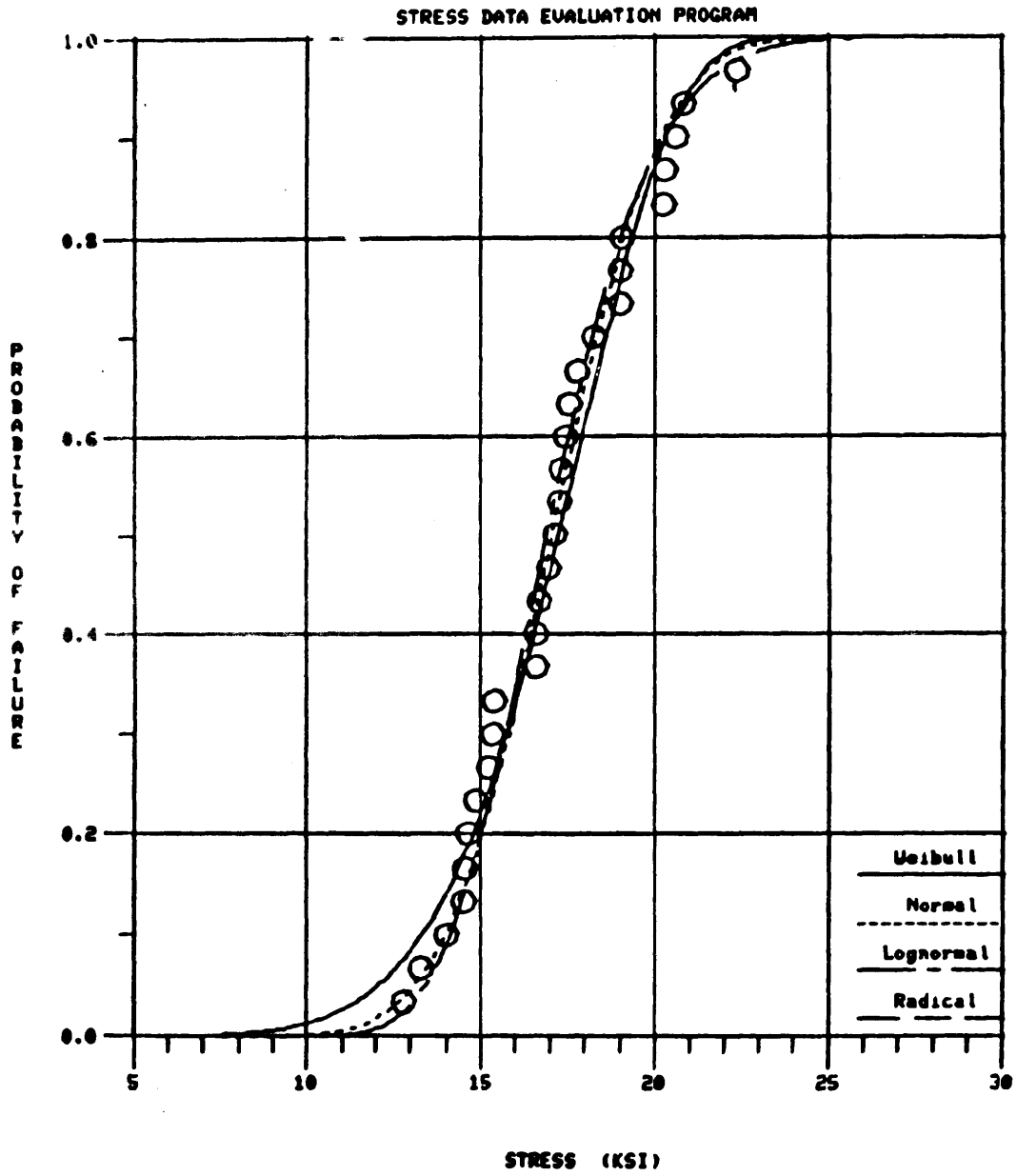

RMS ERROR

	Normal	Lognormal	Weibull	Radical
R1	.0364	.0357	.0448	.0328
R2	.0371	.0366	.0436	.0323
R3	.0387	.0386	.0425	.0324

		90% CONFIDENCE INTERVAL	
MEAN (KSI)=	17.085	16.308	17.863
S DEV (KSI)=	2.419	2.026	3.227

WEIBULL PARAMETERS

		90% CONFIDENCE INTERVAL	
SLOPE M=	7.318	5.718	9.387
CHAR VALUE=	18.135	17.347	18.968
99% ORIGIN=	9.962	7.956	(95% CL)
ORIGIN=	.000		

RADICAL PARAMETERS

A=	29.587	EXP B (N)=	2.000
B=	5.667		
C=	-17.595	EXP(R)=	18.000
SIGI=	11.993	SIGF=	35.255

NON-PARAMETRI SOLN: A AND B ALLOWABLES

OPTIMAL:A(99,95,N=300)B(90,95,N= 30)
GIVEN DATA:
A(99,25,N= 29)B(90,95,N= 29)

WEIBULL:

DESIGN A=	7.956
DESIGN B=	11.961

NORMAL:

DESIGN A=	9.634
DESIGN B=	12.761

LOGNORMAL:

DESIGN A=	10.932
DESIGN B=	13.132

Figure 9 Statistical Data Evaluation-Robust Bend Test Results

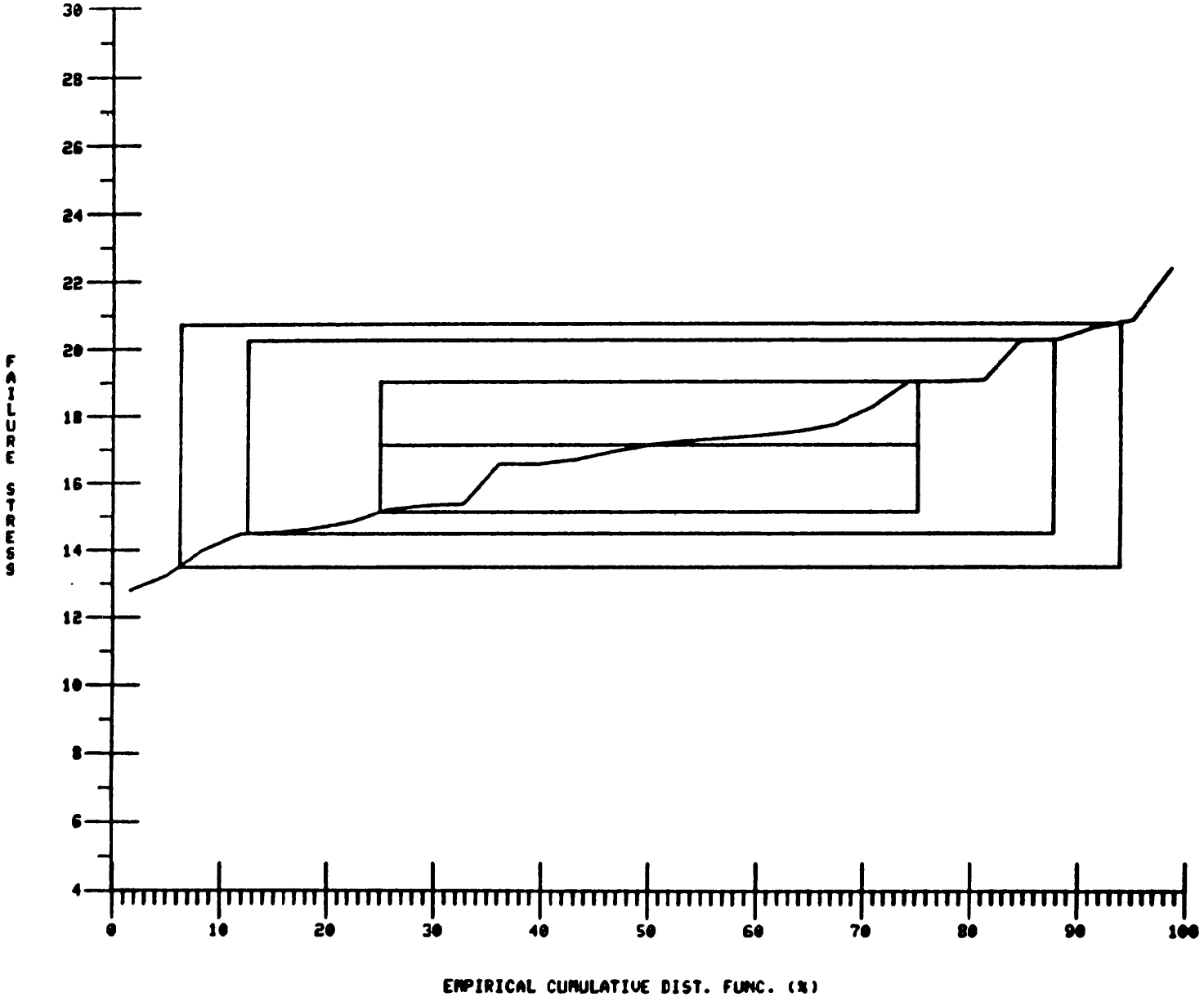

Figure 10 Quantile Box Plot - Robust Bend Test Result

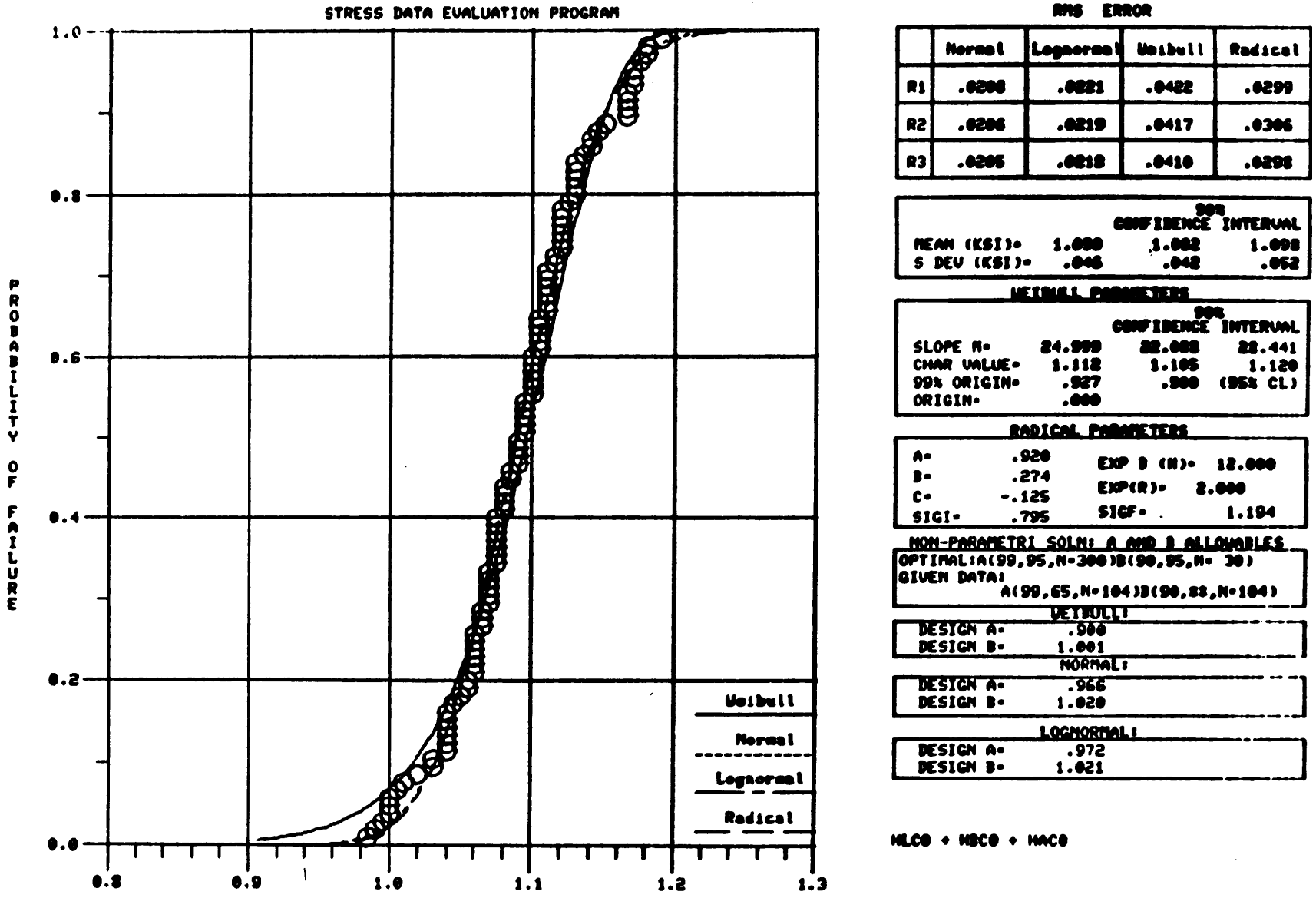

Figure 11 Statistical Data Evaluation Kevlar (Compression Test) Partial Sample

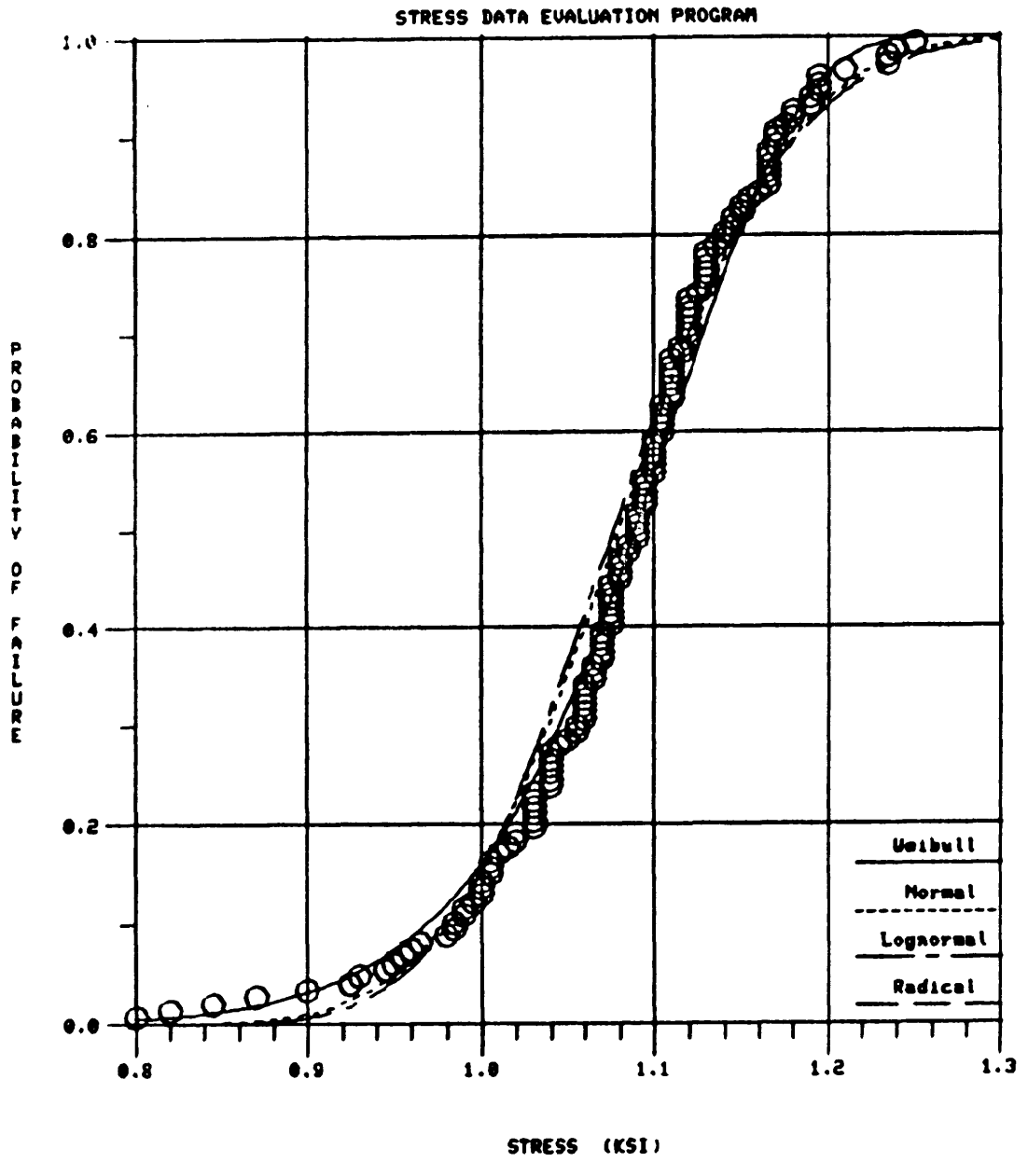

RMS ERROR

	Normal	Lognormal	Weibull	Radical
R1	.0392	.0461	.0305	.0254
R2	.0388	.0458	.0301	.0258
R3	.0383	.0454	.0294	.0266

		90% CONFIDENCE INTERVAL	
MEAN (KSI)=	1.080	1.069	1.091
S DEV (KSI)=	.079	.072	.087

WEIBULL PARAMETERS

		90% CONFIDENCE INTERVAL	
SLOPE M=	16.080	14.313	18.078
CHAR VALUE=	1.115	1.104	1.126
99% ORIGIN=	.839	.808	(95% CL)
ORIGIN=	.000		

RADICAL PARAMETERS

A=	.643	EXP B (N)=	12.000
B=	.826	EXP(R)=	12.000
C=	-.353		
SIGI=	.290	SIGF=	1.470

NON-PARAMETRI SOLN: A AND B ALLOWABLES

OPTIMAL:A(99,95,N=300)B(90,95,N= 30)
GIVEN DATA:
A(99,77,N=146)B(90,88,N=146)

WEIBULL:

DESIGN A=	.808
DESIGN B=	.948

NORMAL:

DESIGN A=	.874
DESIGN B=	.963

LOGNORMAL:

DESIGN A=	.883
DESIGN B=	.963

HAC0 ♦ HLC0 ♦ HBC0 ♦ HCC0

Figure 12 Statistical Data Evaluation Kevlar (Comp. Test) Complete Sample

In figure 13, the higher ordered values appeared to be from a different mode of failure. The Box Plot example shown in figure 1 is a display of this data which essentially confirms the existence of bimodality. It sould be noted in figure 13 that none of the candidate functions adequately represent the ranked data. The allowables are too conservative, particularly for the Weibull and normal representative. The radical function provides an adequate representation but unfortunately does not have allowable computation capability at present. A suggested alternative in determining allowables for this data is the Maximum Penalized Likelihood Method [1] described in text. The results (solid line) are shown in figure 14 showing an excellent representation of the ranked data including the sizable bump. The allowables are 4.99 KSI for the "A" allowable and 5.51 KSI for the "B" allowable. The "B" allowable agrees within .5% of the non-parametric solution. At present, the authors considers this the most acceptable method for determining allowables where multi-modality exists in the data. Examination of other methods, such as; considering lowest mode as censored data and application of the mixed Weibull distributions to the data, proved to be inadequate. The later method may have merit if selected percentiles of the distribution are matched with corresponding ranked values in manner that guaranteed a good fit. In figure 15, another example of bimodality is shown. In this case, location of mode changes provided better fit of data although Weibull shape parameter value of 2.65 is extremely low. The results from MPL method are shown in figure 16 including tabulation of the allowables. Manufacturer of this material has recently indicated that lower mode data was incorrectly added to upper mode data due to different autoclaves used in processing of material.

Figure 17 shows the results from Tension test on Kevlar material (Cycom Co.). The allowable computation are similar for the three function representative (less 7% difference). Allowables determined from Weibull computation would be selected for this material and test. The ability to determine a proper density function to represent fatigue data both censored and uncensored is shown in figure 18. The two and three parameter lognormal and Weibull functions are suggested. The maximum likelihood method determines the functional parameters in order to eliminate acute data dependency problems existing in the more conventional method of moments, graphical procedures, etc. The need for considering all data including censored data is important. An improved P_f computation can be obtained when the total data set is included. Partial probability ranking (graphical) procedures tend to introduce substantial errors in the extrapolation process necessary in obtaining minimum life time estimates of the material. An example of Weibull functions ability to provide an acceptable function for a set of fatigue data is shown in Figure 18. The data was obtained from results of a fatigue test conducted on aircraft engine rotor assembly (see Table 4).

Figure 19, shows data evaluation of Composite graphite material. Note, bimodality displayed in the sample. A rationale has not been available to account for this condition.

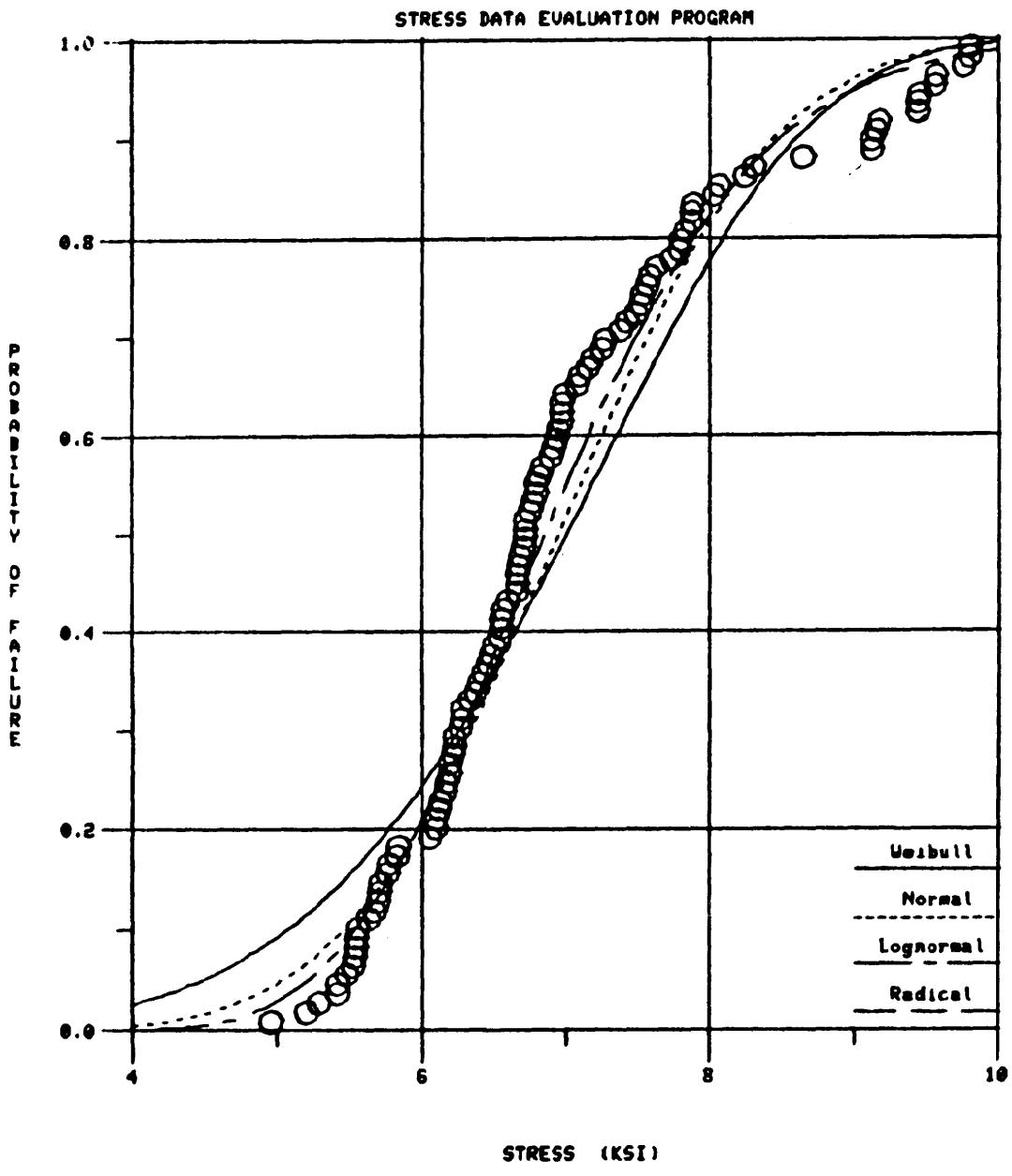

RMS ERROR

	Normal	Lognormal	Weibull	Radical
R1	.0589	.0401	.0765	.0248
R2	.0587	.0398	.0760	.0251
R3	.0584	.0395	.0752	.0257

		90% CONFIDENCE INTERVAL	
MEAN (KSI)=	6.952	6.762	7.143
S DEV (KSI)=	1.162	1.046	1.310

WEIBULL PARAMETERS

		90% CONFIDENCE INTERVAL	
SLOPE M=	5.858	5.187	6.646
CHAR VALUE=	7.459	7.251	7.672
99% ORIGIN=	3.433	3.030	(95% CL)
ORIGIN=	.000		

RADICAL PARAMETERS

A=	16.306	EXP B (N)=	12.000
B=	3.624	EXP(R)=	12.000
C=	-13.746		
SIGI=	2.560	SIGF=	19.930

NON-PARAMETRI SOLN: A AND B ALLOWABLES

OPTIMAL:A(99,95,N=300)B(90,95,N= 30)
GIVEN DATA:
A(99,66,N=108)B(90,88,N=108)

WEIBULL:

DESIGN A=	3.030
DESIGN B=	4.758

NORMAL:

DESIGN A=	3.852
DESIGN B=	5.190

LOGNORMAL:

DESIGN A=	4.477
DESIGN B=	5.383

Figure 13 Statistical Data Evaluation - Ceramics (Bend Test)

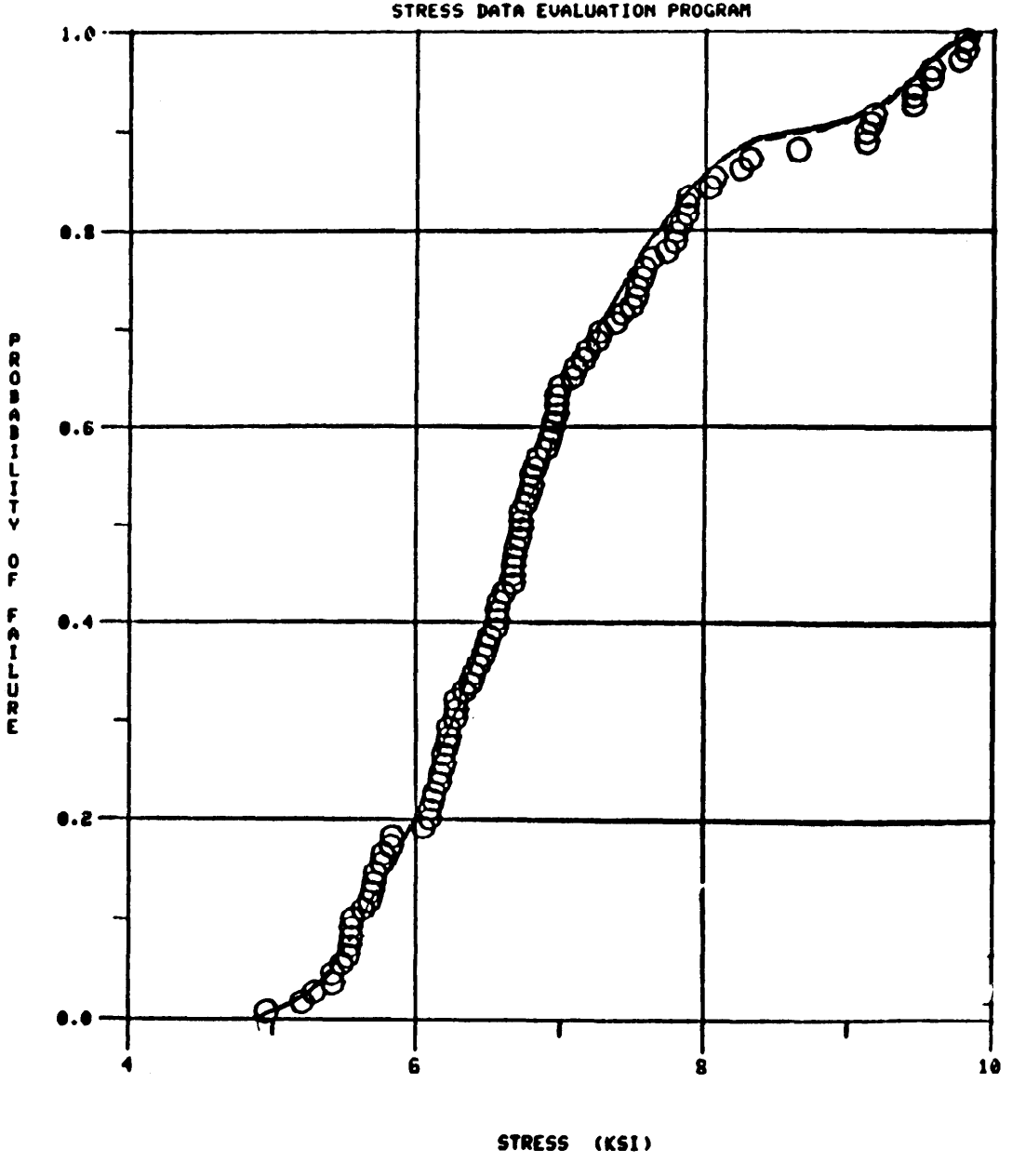

RMS ERROR

	Normal	Lognormal	Weibull	Radical
R1	.0589	.0401	.0765	.0248
R2	.0587	.0398	.0760	.0251
R3	.0584	.0395	.0752	.0257

		90% CONFIDENCE INTERVAL	
MEAN (KSI)=	6.952	6.762	7.143
S DEV (KSI)=	1.162	1.046	1.310

WEIBULL PARAMETERS

		90% CONFIDENCE INTERVAL	
SLOPE M=	5.858	5.187	6.646
CHAR VALUE=	7.459	7.251	7.672
99% ORIGIN=	3.433	3.030	(95% CL)
ORIGIN=	.000		

RADICAL PARAMETERS

A=	16.306	EXP B (N)=	12.000
B=	3.624	EXP(R)=	12.000
C=	-13.746		
SIGI=	2.560	SIGF=	19.930

NON-PARAMETRI SOLN: A AND B ALLOWABLES
OPTIMAL:A(99,95,N=300)B(90,95,N= 30)
GIVEN DATA:
A(99,66,N=108)B(90,88,N=108)

WEIBULL:

DESIGN A=	3.030
DESIGN B=	4.758

NORMAL:

DESIGN A=	3.852
DESIGN B=	5.190

LOGNORMAL:

DESIGN A=	4.477
DESIGN B=	5.383

MPL Method

"A" Allowable = 4.99
"B" Allowable = 5.51

Figure 14 Statistical Ranked Data and MPL Results

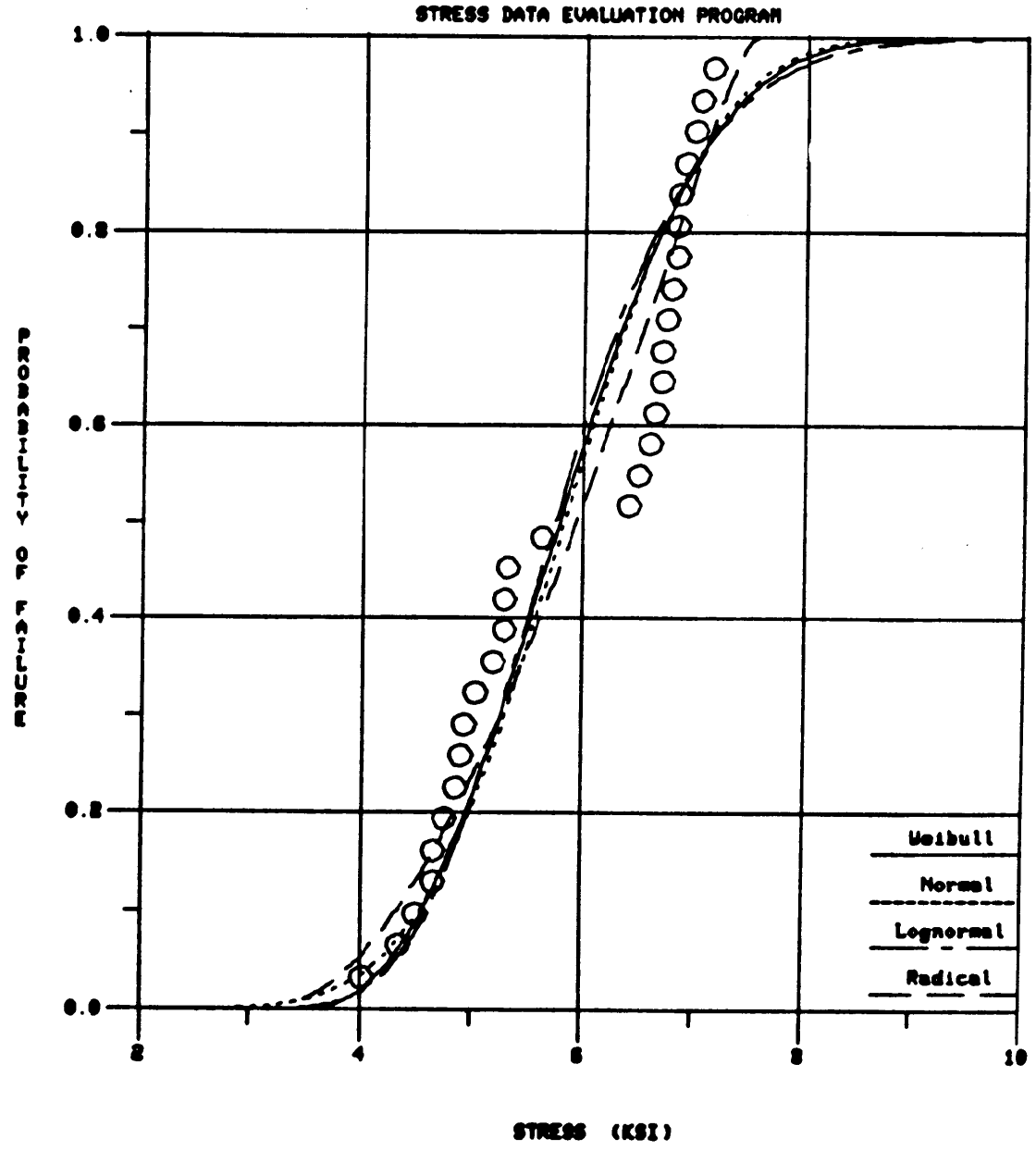

RMS ERROR

	Normal	Lognormal	Weibull	Radical
R1	.1000	.1028	.0971	.0820
R2	.1008	.1038	.0979	.0802
R3	.1022	.1053	.0993	.0778

		90% CONFIDENCE INTERVAL	
MEAN (KSI)=	5.834	5.513	6.154
S DEV (KSI)=	1.016	.853	1.322

WEIBULL PARAMETERS

		90% CONFIDENCE INTERVAL	
SLOPE M=	2.657	2.085	3.398
CHAR VALUE=	2.780	2.085	3.574
99% ORIGIN=	3.895	3.853	(95% CL)
ORIGIN=	3.363		

RADICAL PARAMETERS

A=	3.905	EXP B (N)=	2.000
B=	3.650	EXP(R)=	2.000
C=	-.776		
SIGI=	3.129	SIGF=	7.556

NON-PARAMETRI SOLN: A AND B ALLOWABLES
OPTIMAL:A(99.95,N=300)B(90.95,N= 30)
GIVEN DATA:
A(99.28,N= 30)B(90.86,N= 30)

WEIBULL:

DESIGN A=	3.653
DESIGN B=	4.249

NORMAL:

DESIGN A=	2.721
DESIGN B=	4.028

LOGNORMAL:

DESIGN A=	3.308
DESIGN B=	4.171

Figure 15 Statistical Data Evaluation Composite (S-glass)

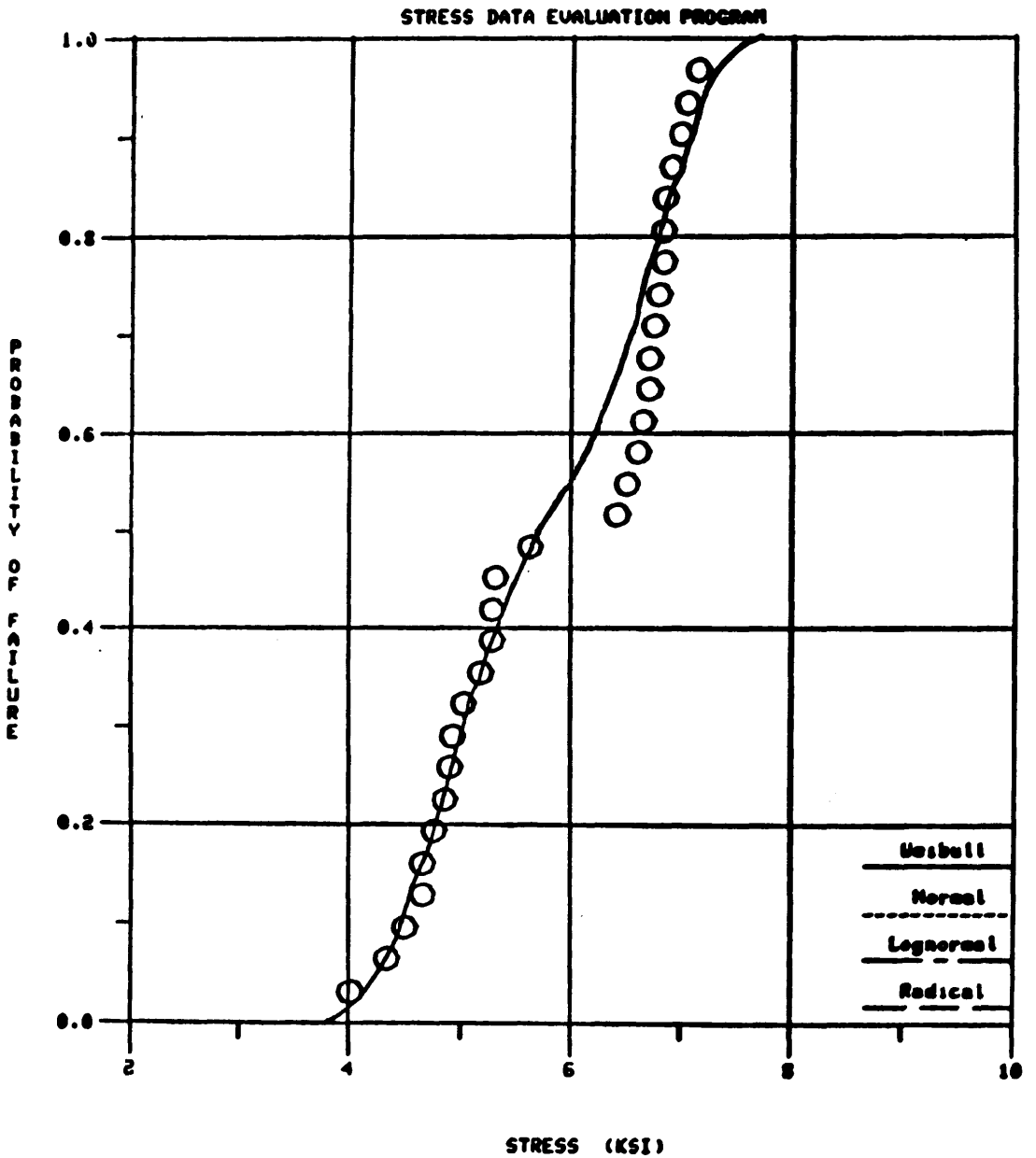

RMS ERROR

	Normal	Lognormal	Weibull	Radical
R1	.1000	.1028	.0997	.0820
R2	.1008	.1038	.1005	.0802
R3	.1022	.1053	.1019	.0776

		90% CONFIDENCE INTERVAL	
MEAN (KSI)=	5.834	5.513	6.154
S DEV (KSI)=	1.016	.853	1.322

WEIBULL PARAMETERS

		90% CONFIDENCE INTERVAL	
SLOPE B=	6.747	5.296	8.616
CHAR VALUE=	6.255	5.966	6.561
99% ORIGIN=	3.262	2.571	(95% CL)
ORIGIN=	.000		

RADICAL PARAMETERS

A=	3.905	EXP B (N)=	2.000
B=	3.650	EXP(R)=	2.000
C=	-.776		
SIGI=	3.129	SIGF=	7.556

NON-PARAMETRI SOLN: A AND B ALLOWABLES

OPTIMAL:A(99,95,N=300)B(90,95,N= 30)
GIVEN DATA:
A(99,26,N= 30)B(90,96,N= 30)

WEIBULL:

DESIGN A=	2.571
DESIGN B=	3.987

NORMAL:

DESIGN A=	2.721
DESIGN B=	4.028

LOGNORMAL:

DESIGN A=	3.308
DESIGN B=	4.171

MPL Method

"A" Allowable = 3.71
"B" Allowable = 4.16

Figure 16 Ranked Data (S-Glass) - MPL Result

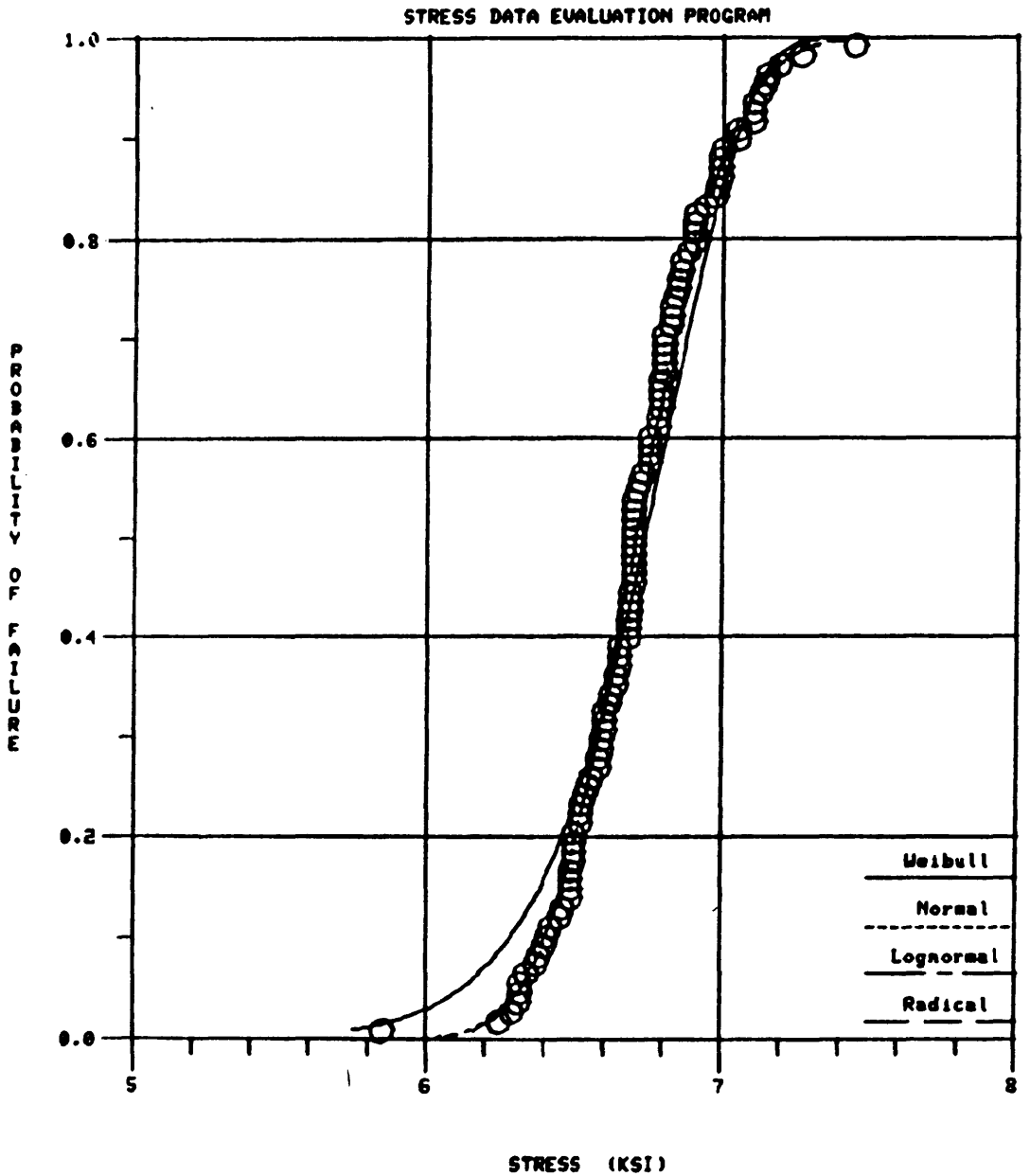

RMS ERROR

	Normal	Lognormal	Weibull	Radical
R1	.0267	.0257	.0584	.0220
R2	.0262	.0252	.0577	.0224
R3	.0256	.0246	.0566	.0232

		90% CONFIDENCE INTERVAL	
MEAN (KSI)=	6.712	6.672	6.752
S DEV (KSI)=	.244	.219	.275

WEIBULL PARAMETERS

		90% CONFIDENCE INTERVAL	
SLOPE M=	27.008	23.893	30.643
CHAR VALUE=	6.829	6.787	6.871
99% ORIGIN=	5.771	5.616	(95% CL)
ORIGIN=	.000		

RADICAL PARAMETERS

A=	6.806	EXP B (N)=	12.000
B=	1.764	EXP(R)=	12.000
C=	-1.867		
SIGI=	4.939	SIGF=	8.571

NON-PARAMETRI SOLN: A AND B ALLOWABLES

OPTIMAL:A(99,95,N=300)B(90,95,N= 30)
GIVEN DATA:
A(99,66,N=107)B(90,88,N=107)

WEIBULL:

DESIGN A=	5.616
DESIGN B=	6.194

NORMAL:

DESIGN A=	6.061
DESIGN B=	6.342

LOGNORMAL:

DESIGN A=	6.086
DESIGN B=	6.347

Figure 17 Statistical Data Evaluation Composite (Kevlar) Tension

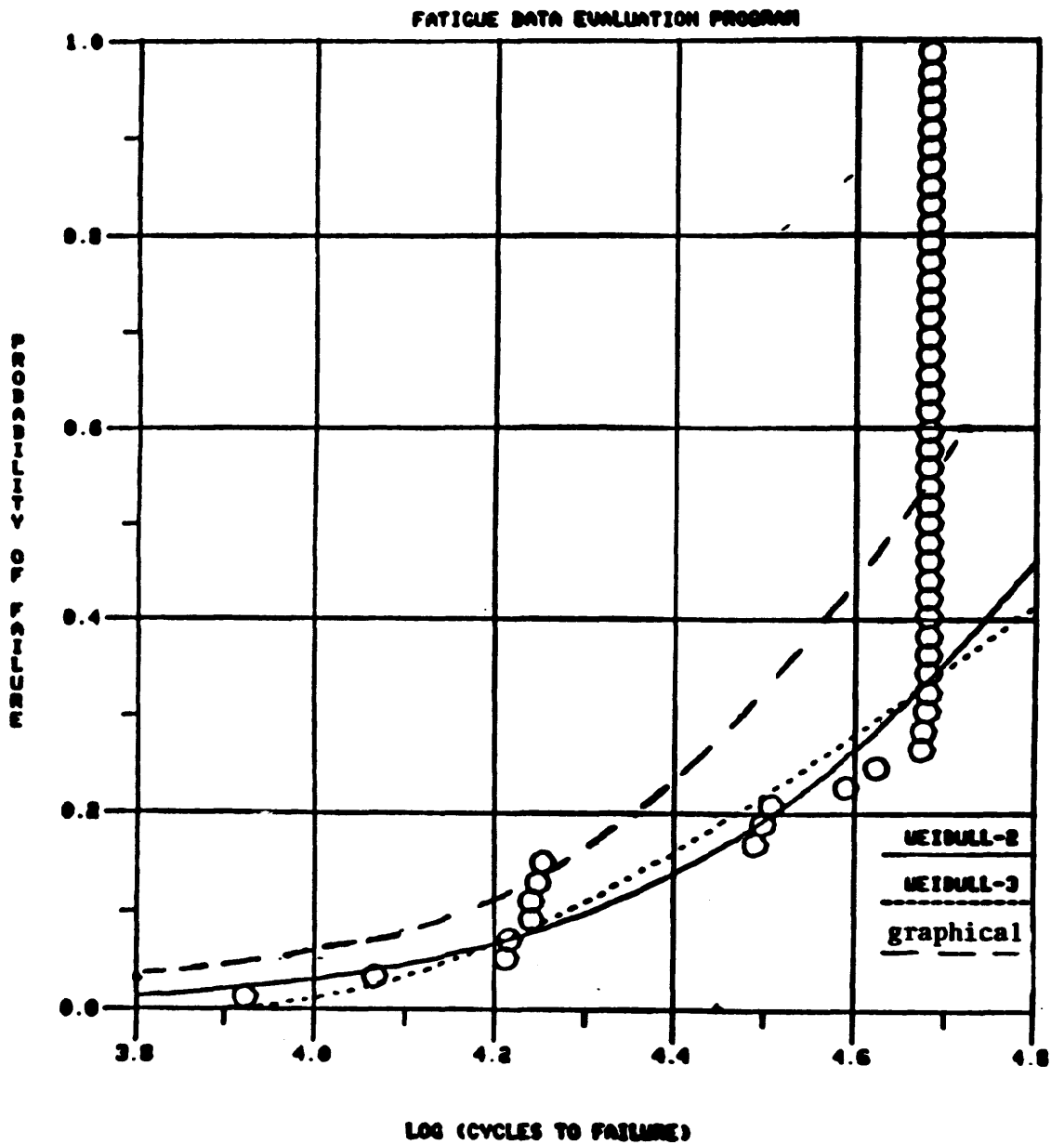

RMS ERROR

	WEIBULL-2	WEIBULL-3	LOGNORM-2	LOGNORM-3
R1	.0194	.0200	.2003	.2003
R2	.0193	.0206	.1987	.1987
R3	.0193	.0203	.1964	.1964

WEIBULL-2 PARAMETERS

		90% CONFIDENCE INTERVAL	
SLOPE M=	16.418	13.689	19.772
CHAR VALUE=	4.941	4.868	5.015
90% ORIGIN=	3.761	3.701	(95% CL)
ORIGIN=	.000		

WEIBULL-3 PARAMETERS

		90% CONFIDENCE INTERVAL	
SLOPE M=	2.058	1.717	2.480
CHAR VALUE=	5.136	4.563	5.785
90% ORIGIN=	3.993	3.906	(95% CL)
ORIGIN=	3.847		

LOGNORMAL-2 PARAMETERS

MU=	**********
SIGMA=	**********
TAU=	.0000

LOGNORMAL-3 PARAMETERS

MU=	**********
SIGMA=	**********
TAU=	.0000

A - ALLOWABLE

GRAPHICAL: 2400 CYCLES

M.L. METHOD: 5011 CYCLES

Figure 18 Censored Data Evaluation

TABLE 4. FATIGUE TEST RESULTS

Rene 95 Powder Metal
Censored Data

i	RANK ($i/N+1$)	CYCLES	LOG CYCLES
1	.019	8368	3.923
2	.038	11651	4.066
3	.058	16281	4.212
4	.077	16428	4.216
5	.076	17413	4.241
6	.115	17434	4.241
7	.135	17761	4.249
8	.154	17958	4.254
9	.173	30866	4.489
10	.192	31454	4.498
11	.212	32103	4.507
12	.213	38356	4.589
13	.250	41982	4.623
14	.269	47177	4.674
15	.288	47309	4.675
16	.327	47900	4.680
17	.346	47978	4.681
↓	↓	↓	↓
51	.981	47978	4.681

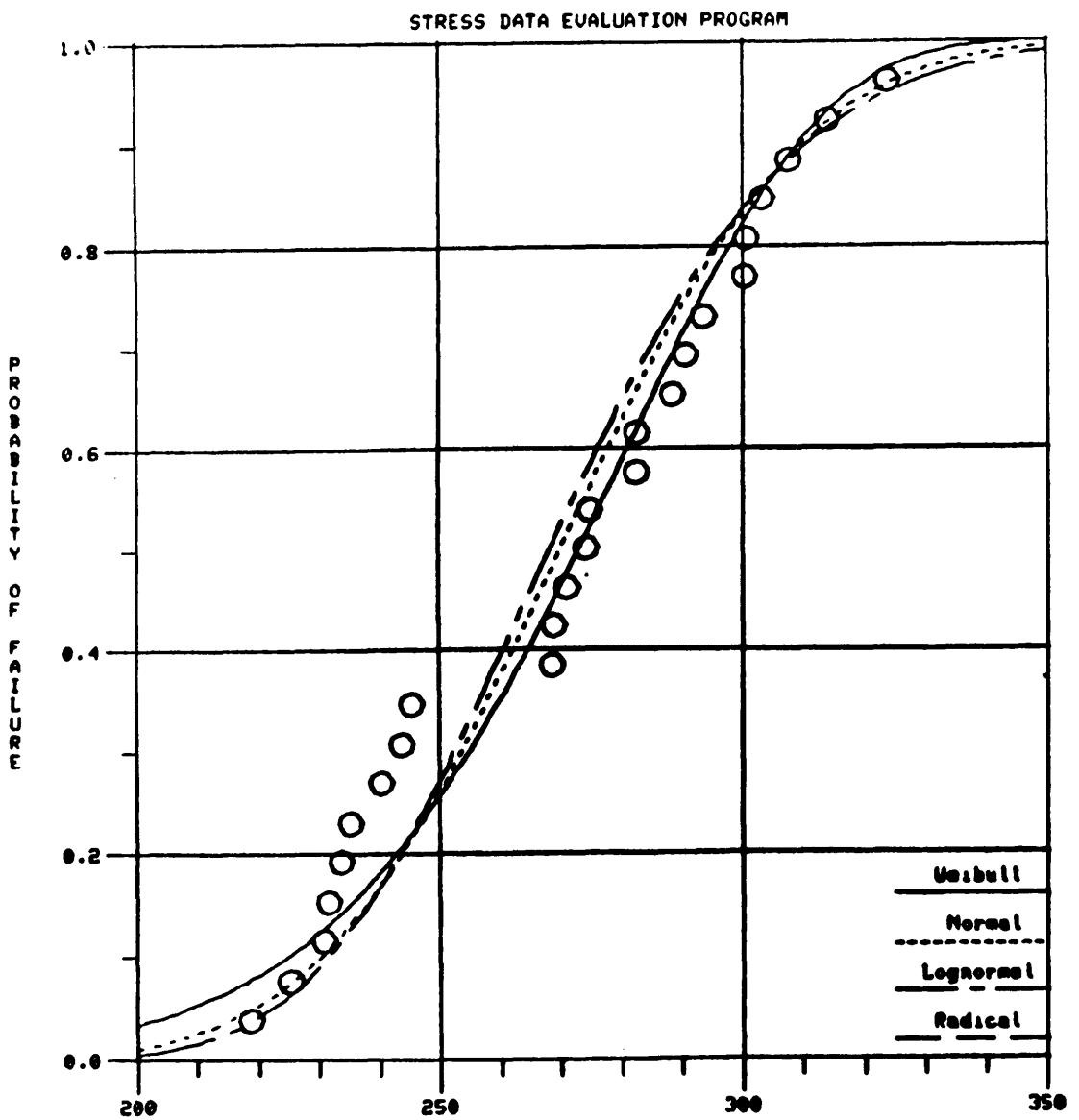

RMS ERROR

	Normal	Lognormal	Weibull	Radical
R1	.0585	.0666	.0455	.0431
R2	.0598	.0679	.0463	.0418
R3	.0623	.0703	.0480	.0409

		90% CONFIDENCE INTERVAL	
MEAN (KSI)=	269.948	259.090	280.806
S DEV (KSI)=	31.090	25.760	41.773

WEIBULL PARAMETERS

		90% CONFIDENCE INTERVAL	
SLOPE M=	9.673	7.412	12.669
CHAR VALUE=	283.527	273.435	294.135
99% ORIGIN=	180.896	149.834	(95% CL)
ORIGIN=	.000		

RADICAL PARAMETERS

A=	317.341	EXP B (N)=	2.000
B=	104.460	EXP(R)=	12.000
C=	-126.725		
SIGI=	190.616	SIGF=	421.801

NON-PARAMETRI SOLN: A AND B ALLOWABLES

OPTIMAL:A(99,95,N=300)B(90,95,N= 30)
GIVEN DATA:
A(99,22,N= 25)B(90,93,N= 25)

WEIBULL:

DESIGN A=	149.834
DESIGN B=	206.233

NORMAL:

DESIGN A=	171.767
DESIGN B=	212.805

LOGNORMAL:

DESIGN A=	185.446
DESIGN B=	216.370

Figure 19 Statistical Data Evaluation (Graphite Composite)

Conclusion

1. Exploratory Data Procedure should be applied prior to acceptance of statistical model used in the allowable computation.

2. Quantile Box Plot provides an excellent summary of test data results in addition to location outliers and multi-modality in the sample.

3. The authors recommend using the Weibull distribution function for obtaining the allowables, if outliers (higher ordered values) or multi-modality, do not exist in data set.

4. An extreme value distribution (Weibull) provides a degree of security if pooled samples do not represent general data population. (a common occurrence).

5. Normal distribution is recommended for allowable computation if outliers exist in data set at upper tail region.

6. In multi-modality case, the Maximum Penalized Likelihood Method is suggested for the allowable determination.

7. At present the authors recommend pooling all samples made available even though significant difference test indicated otherwise. If a sample contains modality then this data set would be excluded.

8. The development of tables 1 and 2 required a considerable amount of effort (most complete tabulation for the Weibull function). With the aid of computer code listed in appendix A and tabulated P^*_S values, the reader should be able to obtain a simple and accurate computation of the allowables when the Weibull function is considered.

Literature Cited

[1] Good, I. J., and Gaskins, R. A., "Density Estimation and Bump - Hunting by the Penalized Likelihood Method Explified by Scattering and Meteorita Data", Journal of the American Statistical Assoc., Vol.75, No.369, March 198

[2] Thoman, D. R., Bain, L. J., Antle, C. E., "Maximum Likelihood Estimation, Exact Confidence Intervals for Reliability and Tolerance Limits in the Weibull Distribution", Technometrics, Vol. 12, May 1970, PP. 363 - 371.

[3] Hahn, G. J., and Shapiro, S. S., "Statistical Models in Engineering", John Wiley and Sons, Inc., New York, London and Sidney, 1967.

[4] Freudenthal, A. M., and Gumbel, E. J., "On the Statistical Interpretation of Fatigue Tests", Proc. Royal Soc. (A) 216, 309, (1953).

[5] Parzen, Emmanuel, "A Density-Quantile Function Perspective on Robust Estimation", Robustness in Statistics, Academic Press, New York 1979.

[6] Huber, P. J., "Robust Estimation of a Location Parameter", Annuals of Mathematical Statistics, 35, 73-101, 1964.

[7] Andrews, D. F.; Bickel, P. J.; Hampel, F. R.; Huber, P. J.; Roger, W. H.: Tukey, J. W., "Robust Estimates of Location", Princeton University Press, 1972.

[8] Tukey, J. W., "Exploratory Data Analysis", Addison-Wesley Publishing Company, 1977.

[9] "Handbook of Mathematical Functions", National Bureau of Standards Applied Mathematics Series 55, June 1964, Edited by M. Abramowitz and Ire e Stegun.

[10] Harter, L. H., and Moore, A. H., "Maximum Likelihood Estimation of the Parameter of the Gamma and Weibull Population from Complete and Censored Samples", Journal of the American Statistical Association, Vol. 61, 1966, PP 842 - 851.

[11] Bradley, James V., "Distribution - Free Statistical Tests", Prentic-Hall, Inc., Englewood Cliffs, NJ.

[12] Walsh, J. E., Handbook of Non-parametric Statistics, Vol. II, D. Van Nostrand Company, Inc., New Jersey, 326.

```
C
C          WEIBULL PARAMETERS M AND U
C
C-------------------------------------------------C
C
C     READS IN AMOUNT OF DATA AND THE DATA
C
           DIMENSION T(200)
           IMPLICIT DOUBLE PRECISION (A-H,O-Z)
           READ(5,1)NPTS                    <-------------Sample Size
           READ(5,1)(T(I), I=1,NPTS)     <---------Data
C
C     DETERMINES M BY MAXIMUM LIKELIHOOD
C
           A=0.0
           N=0.0
           DA=1.0
   2       XNUM=0.0
           XMINUS=0.0
           PROD1=0.0
           PROD2=0.0
           A=A+DA
C
C     SUMATIONS CALCULATED FIRST
C
           DO 10 I=1,NPTS
           XNUM=T(I)**A+XNUM
           XMINUS=T(I)**A*LOG(T(I))+XMINUS
  10       PROD2=LOG(T(I))+PROD2
           A1=NPTS*XNUM/(NPTS*XMINUS-XNUM*PROD2)
           IF(A-A1)2,5,3
   3       N=N+1
           IF(N-5)4,4,5
   4       A=A-DA
           DA=1./10.**N
           A=A-DA
           GO TO 2
   5       WRITE(6,1)A          <-------------m
C
C     DETERMINES U 'HAT'
C
           BSUM=0.0
           DO 6 I=1,NPTS
   6       BSUM=T(I)**A+BSUM
           B=(1./NPTS*BSUM)**(1./A)
           WRITE(6,1)B     <-------------------u
   1       FORMAT( )
           END
```

Appendix A Computer Code for Determining Allowables

DESIGN AND FABRICATION OF LOW COST COMPOSITE COMPRESSOR BLADES

CHARLES D. HOUGHTON
WILLIAM W. HOUGHTON
MARGARET E. ROYLANCE
Army Materials and Mechanics Reseach Center
Watertown, Massachusetts 02172

JOHN A. McELMAN
University of Lowell
Lowell, Massachusetts 01853

ABSTRACT

A simplified technique for fabrication of low cost composite blades has been demonstrated. Sandwich construction was implemented and a two step fabrication technique was developed using a simplified composite design as a test vehicle. The approach used to design and fabricate full scale blades was duplicated using the test blade.

A finite element model was constructed and used to predict blade properties. Test blades were then fabricated using a two step squeeze molding technique. The method was to mold the foam core, release it, apply the skin material, and place the layed up blade back into the same mold for curing. This would compress the core and apply pressure to the skin which is desirable during cure.

These test blades were tested to static deflection and frequency predictions to verify the finite element model. The close correlation between predicted and experimental results support the approach to the design and fabrication techniques applied here and indicate no problems during the eventual fabrication and testing of a full scale blade.

The preliminary composite design using sandwich construction and an aluminum root section resulted in a composite blade design which decreased the major loading by 82%, reduced the weight of the blade by 29%, and was easy to fabricate using the squeeze molding technique described. This reduction in blade weight would decrease the power requirements of the wind tunnel during operation.

The use of a composite design should greatly improve tolerance to impact damage and fatigue loading conditions found within the wind tunnel. The resulting increase in safe operation, decrease in cost of materials, fabrication, and operation of the tunnel, and the possibility of eliminating blade replacement due to repairability and enhanced fatigue life, support the effort to replace the metal compressor blades with those of a composite design using these low cost fabrication techniques.

INTRODUCTION

The fabrication of low cost composite blades has been a recent interest in the design and manufacture of composite windmill, helicopter rotor, and wind tunnel fan blades.

A study has been carried out to design and fabricate a composite replacement for an aluminum wind tunnel blade. This study was divided into several parts: design of a replacement compressor blade entailing an analysis of the present blade and its proposed composite counterpart, selection of materials and fabrication techniques, and verification of the design and fabrication method with test blades.

A concept for fabrication of such low cost blades has been developed using a foam core sandwich construction technique. This method entails a two step squeeze molding technique which utilizes a mold to form the foam core and uses the same mold to bond the composite skin to this core. This produces the finished blade with minimum effort and use of excess materials.

At the time this concept was being developed, NASA-Ames Research Center was investigating the possibility of designing and fabricating composite replacements for the solid aluminum fan blades for one of three wind tunnels in use at Moffett Field. Figure 1 depicts the compressor blade chosen for replacement. The reasons for implementing a composite design were (1) the blades may encounter moving objects (rocks, nuts, bolts) during operation and a composite design would have superior resistance to impact damage as compared to the solid metal blades, (2) a composite design would have better properties under the fatigue loading conditions encountered in the tunnel, (3) the composite blades would weigh less than their all metal counterparts, reducing the power requirements of the tunnel, (4) the blades would be easier to

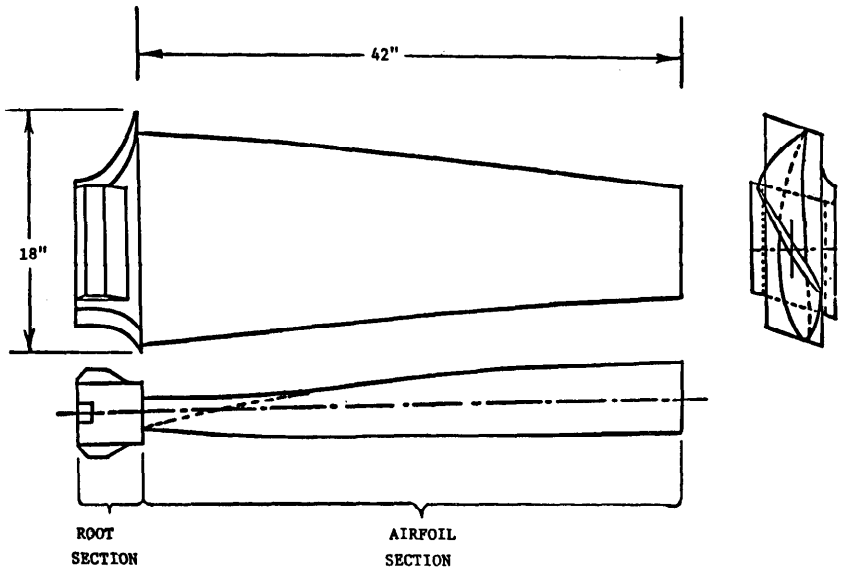

Figure 1. Compressor blade.

fabricate than the all metal blades and (5) with a composite design there exists the potential capability to tune the natural frequency of the blade by changing the fiber type and orientation. This would accomodate tunnel improvements which might present vibration problems with present blades.

Ease of fabrication and the desire to produce a viable replacement for the blades presently in use were considered to be important aspects of the design. When the squeeze molding technique had been chosen, two restrictions were placed on the design. These were that the fabrication method required a design of sandwich construction with a moldable foam core and a fibrous skin material (cloth or filament wound) and the aerodynamic shape of the blade was not to be changed.

Materials for the skin and core had to be chosen to produce the desired properties for the fabrication and design. Kevlar-epoxy was chosen as the skin material for its high impact resistance and excellent properties under fatigue loading. Polyurethane foam was chosen as the core material for its ease in molding and light weight.

The design criteria for the composite blade would be to approach the natural frequency of the present blade and its static stiffness (bending and torsional). Skin thickness, fiber orientation and the incorporation of graphite were variables involved in the design cycle.

After considering a general approach to the design and fabrication, the method of attaching the blades to the rotating hub was evaluated. This is an important aspect because the root is an area of high stresses and the design should be simple to facilitate ease of fabrication. For these reasons it was considered early in the design cycle.

The approach to the design and fabrication was then verified using a smaller simplified composite design.

Finally the design of the composite replacement was undertaken. The final proposed design resulted in an 82% decrease in the centrifugal loading and 29% reduction in the total weight of the blade.

QUALIFICATION OF THE FINITE ELEMENT MODEL

It was proposed to model the sandwich construction using the structural analysis program SAP4a(1). The sandwich design would be simulated using plate elements to model the skin and brick elements to model the foam core. This concept was supported by comparing results from a computer model of a sandwich beam with actual tests.

It was not known whether a finite element model of a foam core sandwich beam could be constructed tying a 3-D solid brick element (modelling the core) to a plate element (modelling the skin). There is a difference between these elements in that the brick has 6 degrees of freedom (x,y,z translation and x,y,z rotations) and the brick has only 3 degrees of freedom (x,y,z translation). Figure 2 illustrates these differences. To determine if this was a

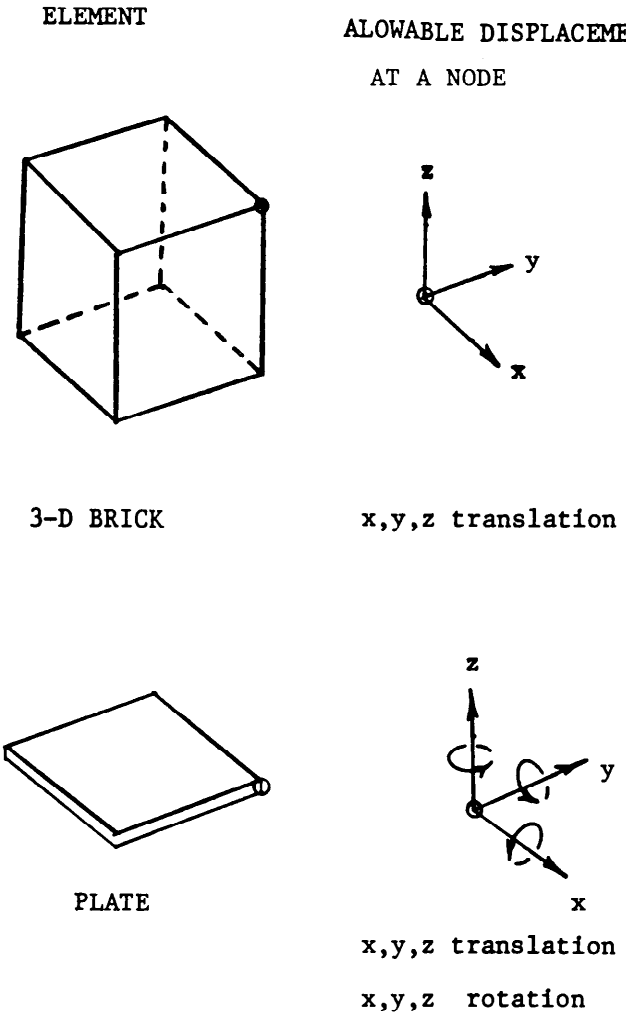

Figure 2. Allowable displacements for brick and plate elements.

viable method to model sandwich construction a finite element model of a 5 inch long cantilevered sandwich beam was constructed using the properties of the foam core and Kevlar skin used in the actual construction of the beam (Figure 3). The actual sandwich beam for comparison was constructed using a foam core 5 inches long with a 1 inch square cross section and epoxying a 0.033 X 1 inch layer of Kevlar to the top and bottom of the foam. The natural frequency of the sandwich beam was found by three methods which were used as a basis for comparison. The finite element model was used to predict the fundamental frequency initially. The second method was to calculate an effective EI for the beam and the use of handbook methods to predict the frequency. The third method was to measure the actual frequency by clamping the root section, placing an accelerometer on the end of the beam, exciting the beam and passing the output through a fast Fourier Transform analyzer.

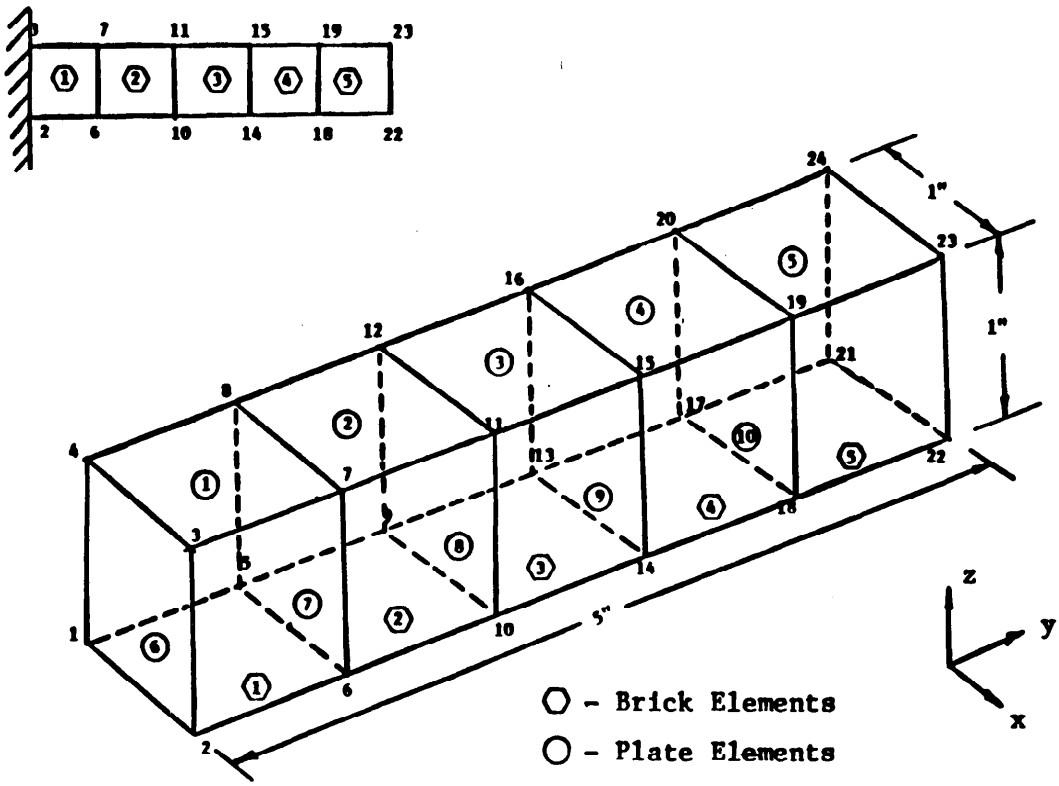

Figure 3. Finite element model of 5"-long test beam (sandwich construction).

The fundamental frequency predicted using the finite element model, 345 Hz, was much lower than the handbook prediction of 1312 Hz (Table I). This could be explained because the handbook does not consider the low shear stiffness of the foam core, which will decrease the overall beam stiffness and reduce the actual frequency.

TABLE I

	Frequencies of Sandwich Beam		
Method	Handbook	SAP IV	Measured
Frequency (Hz)	1312	345	350

The finite element model considers the low shear stiffness of the foam and was expected to predict the correct natural frequency.
This conclusion was verified by experimentally measuring the fundamental frequency of the modeled beam. The actual frequency was measured as 350 Hz. This represents a 1.4% difference from the 345 Hz predicted by the computer model.

Thus it appears that combining the plate and brick elements presents no problems and may be used as a basis to model a sandwich beam.

ANALYSIS OF ALUMINUM COMPRESSOR BLADE

The 11 foot wind tunnel at NASA-Ames Research Center was elected to receive the first composite compressor blade. The primary reasons for its selection were that this tunnel receives the most use at Moffett Field and the compressor blades are 42 inches long and would fit easily into the autoclave at AMMRC during fabrication.

Surface coordinates for the solid aluminum blade were obtained and used to generate nodal coordinates for the model. A finite element model of the blade was constructed using 3-D solid brick elements. The structural program used was SAP 4a. The model contained a total of 229 nodes yielding 90 elements. Figure 4 shows a graphical representation of the model. In order to approximate the restrictions placed on the blade at the root during operation, displacement and rotational boundary conditions were imposed to simulate a cantilevered beam.

STATIC ANALYSIS

Two static analyses were performed on the model to determine the static stiffness of the solid aluminum blade for comparison to the composite design.

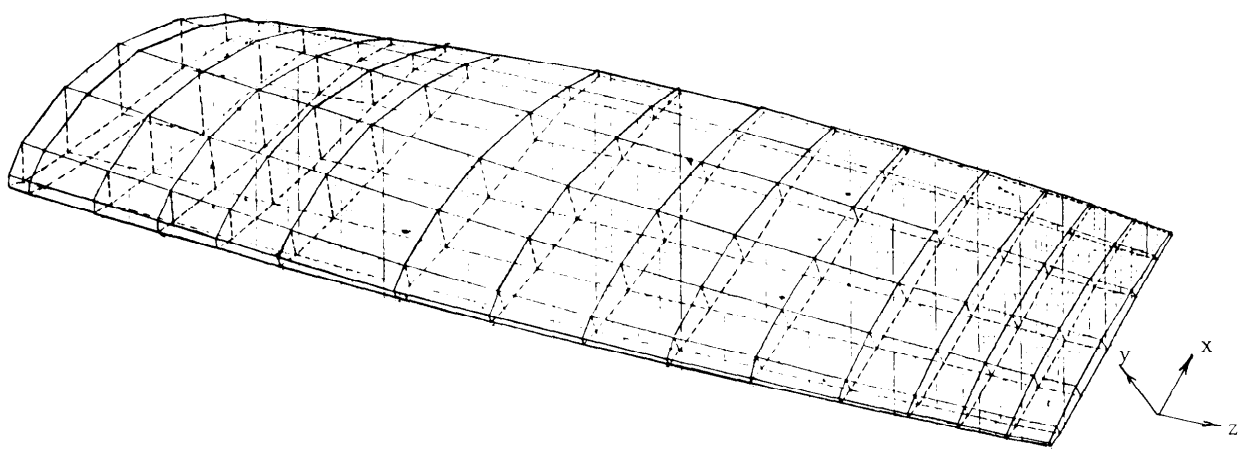

Figure 4. Finite element model of 42" wind tunnel compressor blade.

A one pound distributed load was placed on the end of the blade to determine its static bending stiffness. Next a twisting load was applied to the tip (+1 pound on one corner and -1 pound on the other corner of the tip). Deflections for these two case loads were obtained and shown in Figures 5.a and 5.b.

DYNAMIC ANALYSIS

A modal analysis was also performed using this model to predict the fundamental natural frequency, its harmonics, and the associated mode shapes. These frequencies are tabulated in Table II and the mode shapes and associated frequencies are shown in Figures 6 a, b, c, d.

EXPERIMENTAL MODAL ANALYSIS

The actual natural frequency, harmonics and associated mode shapes of the aluminum blade were determined by an experimental modal analysis. This was performed on the aluminum blade by restraining the root section in a mechanical testing machine under compression, placing an accelerometer on the tip, exciting the blade, and running the accelerometer output directly into a Fast Fourier Transform Analyzer. This determined the range of frequencies to be matched with the composite design and also provided a check of the accuracy of the computer model.

Attachment of the root section in the machine was critical. First testing was carried out using a servohydraulic system (Tinius Olsen). Erroneous results were obtained leading to suspect the system hydraulics may have caused interference in the frequency measurements. Further analysis was performed using a mechanical screw type testing machine (Instron 1127) which produced a more rigid grip of the root section. Total restraint of the root section was accomplished by "shimming" the fixture so that clamping pressure could be distributed over the entire root section.

TABLE II

Comparison of Blade Frequencies-
Predicted and Experimental

	Frequency (hz.)		
Mode	Al.(FEA)	Composite(FEA)	Measured(Al.)
1	51.5	69.62	55
2	158.7	209.9	155
3	266.4	304.1	305
4	340.9	---	395
5	426.5	---	555

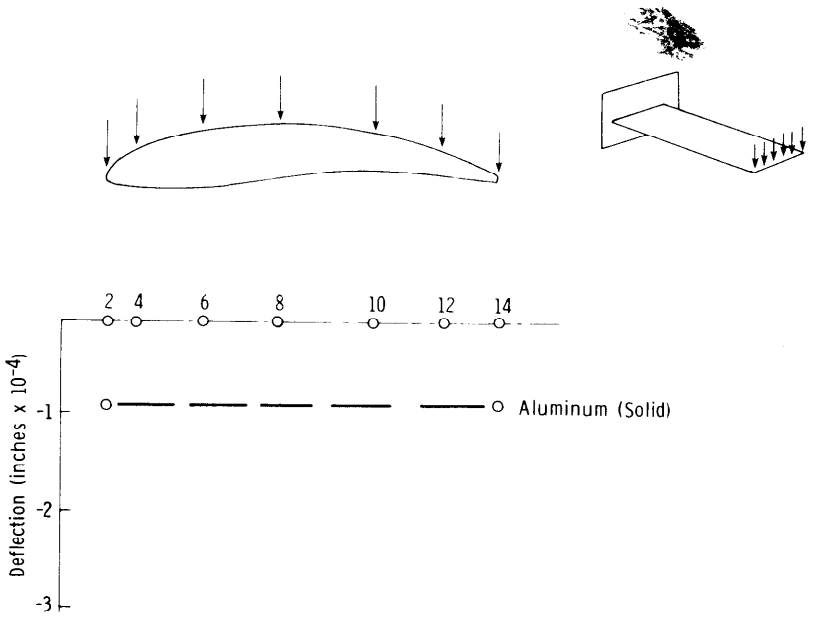

a. Relative tip deflection versus material for distributed unit load at tip.

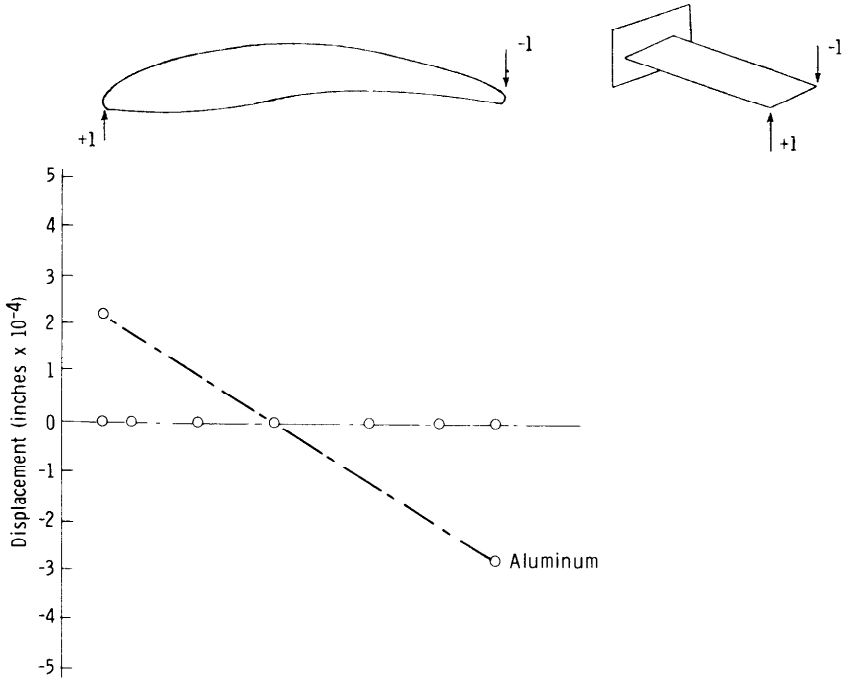

b. Twist at tip for twisting load applied at tip.

Figure 5.

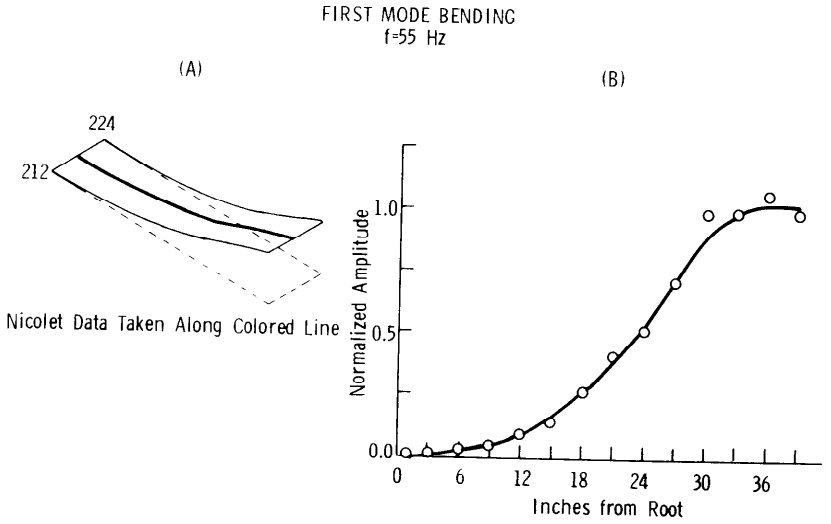

a.

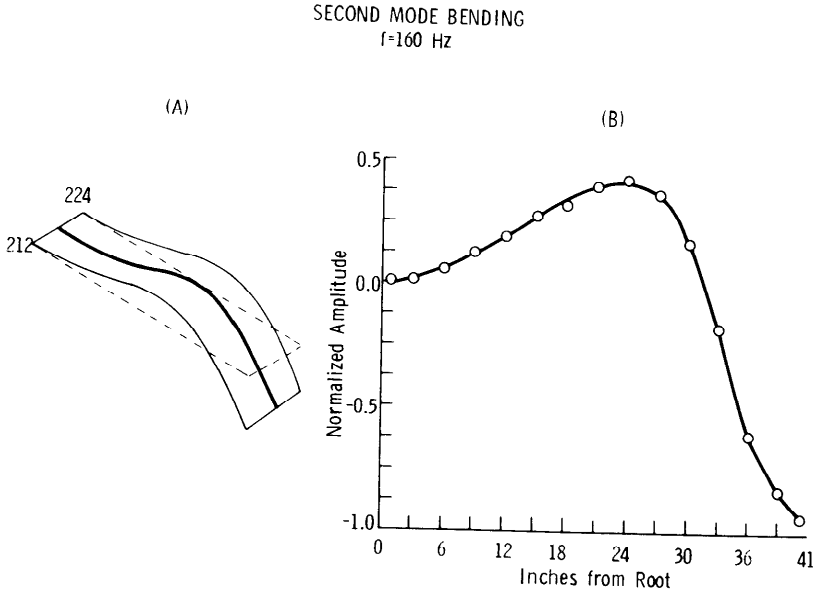

b.

Figure 6. Mode shapes obtained from (A) Finite Element Model, and (B) Nicolet Frequency Analyzer.

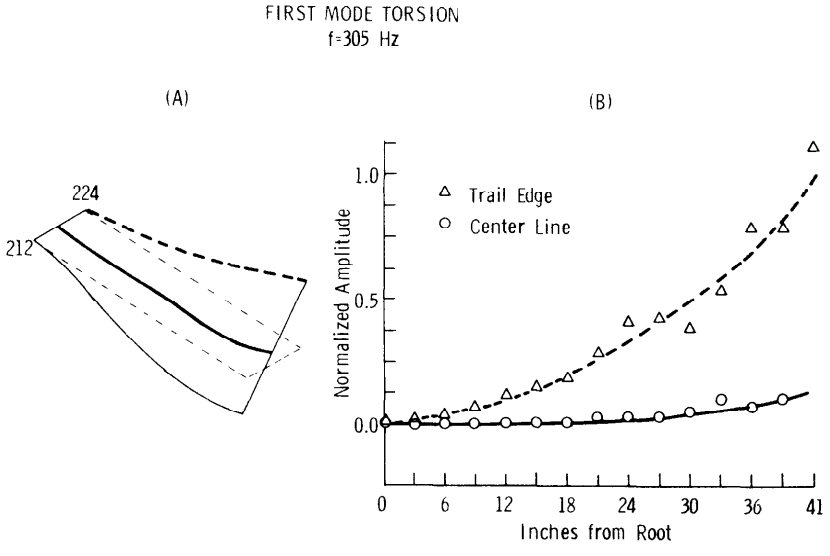

c.

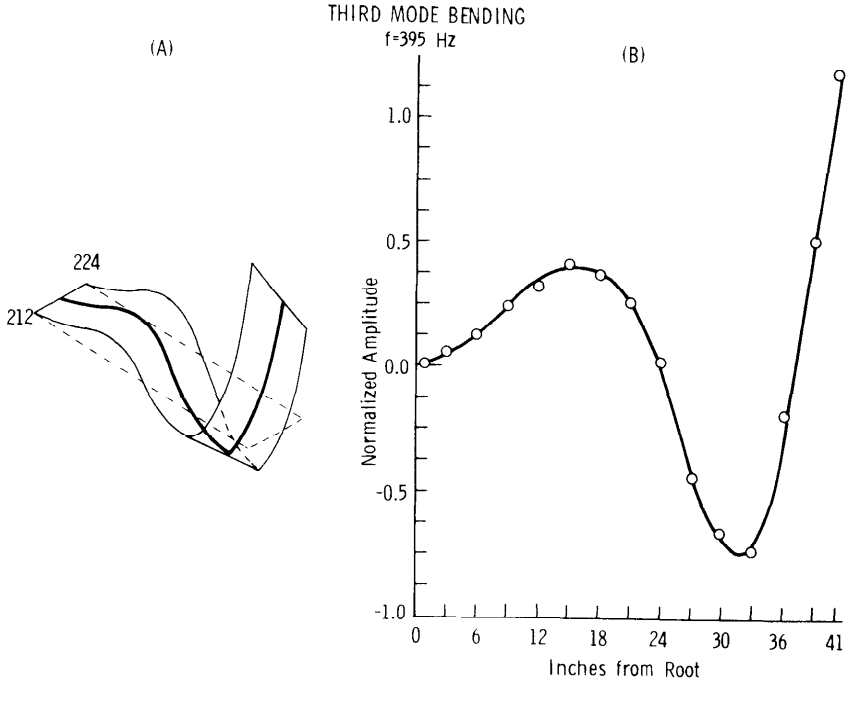

d.

Figure 6. (Cont.)

Frequencies obtained in the modal analysis were related to the clamping pressures. Natural frequency and harmonics were measured at various clamping pressures. Frequencies increased with clamping pressure until levelling off between 15,000 and 20,000 pounds. For the final analysis a clamping pressure of 20,000 pounds was chosen.

Mode shapes were obtained using the same FFT analyzer and the same method of root retention. The approach used to measure the mode shape was to place the transducer at various intervals along the length of the blade. The blade was excited by striking the tip with a hammer and recording the frequency spectrum from the accelerometer. This was repeated four times at each transducer location.

MATERIALS AND DESIGN

Presently the wind tunnel compressor blades are made by milling the shape out of a billet of solid aluminum. In an effort to simplify design and fabrication a preliminary design using sandwich construction[2] was chosen for the composite blade. This method produces very strong and stiff structures which are simple in design and easy to fabricate. Sandwich construction consists of a lightweight core material "sandwiched" between two relatively stiffer and/or stronger outer layers. This skin provides strength and stiffness. The skin is bonded to the core to maintain stiffness and to prevent buckling and skin vibrational modes. Polyurethane foam was chosen as the core material because it is easy to use and has good chemical resistance (it is insoluble in the solution used for cleaning and dewaxing the core material).

The wind tunnels in question are of the racetrack type (air is recirculated) and parts (nuts, bolts, etc.) lost from the model being tested are encountered by the moving compressor blades. This presents a problem for solid metal blades because the objects may cause nicks, initiating crack growth and resulting in possible catastrophic failure. A composite blade will not fail catastrophically (without warning). When a blade is damaged the operator would have time to stop the machine before further damage could occur. If by chance a blade were released the sandwich construction would be so light that there would be minimal damage to surroundings.

Kevlar was chosen as the skin material for two reasons; it has superior resistance to impact damage and excellent properties under fatigue loading conditions[3]. For these reasons it is chosen as the major constituent in most composite helicopter blades.

The static stiffness of the blade became an important factor in the design, therefore, unidirectional graphite fibers were incorporated into the design. Graphite fibers have a much higher stiffness than Kevlar, resulting in an increase in the overall stiffness of the blade. Graphite could be added together with Kevlar to form a hybrid composite skin to obtain the mutually beneficial properties of a high degree of stiffness associated with high strength and toughness.

The resin chosen as the matrix material for the composite skin was EPON 828 with Jeffamine T-403 hardener. This resin was chosen for the preliminary design because it can be cured at room temperature overnight or at high temperature ($200^{o}F$) for one hour. This would eliminate the need for an oven for initial fabrication of test blades. A high cure temperature is associated with a high glass transition temperature which is desirable because of the elevated temperature encountered in the 3 stages of the wind tunnel compressor. The temperature ranges from $150^{o}F$ in the first stage to approximately $180^{o}F$ in the third stage. To maintain the stiffness of the blade, the glass transition temperature of the resin must be above the operating temperatures.

FABRICATION AND TEST OF COMPOSITE VERIFICATION BLADE

The proposed fabrication method consisted of a two step squeeze molding technique molding the foam core in the first step and bonding the skin to this core using the same mold in the second step. Because this was a relatively new technique for the fabrication of blades, the approach was perfected using a simplified composite design as a test vehicle. A finite element model of the test blade was constructed, and used to predict the static stiffness of the blade and its natural frequency. The blade was then constructed and tested to these same criteria and compared with the theoretical predictions.

ROOT DESIGN

A solid aluminum root insert was chosen as a method for attaching the blade to the hub. The solid aluminum root insert obtained from the original blades (Figure 7a) provided the unique opportunity of direct comparison of the performance of aluminum vs. composite for blades apart from the root design. The only difference in the design is the blade section itself. It also offers ease of construction of the new blade in that the complicated root section can be molded into the blade in one step during fabrication. Also the method of restraining the root section for the modal analysis of the blade could be duplicated.

When the 42 inch blade (11 ft. tunnel) was chosen as the blade to be replaced, the solid root insert was chosen as the prototype for several reasons. It could be easily molded into the blade, and presented a direct comparison of old and new designs.

This type of solid insert was used in the fabrication of the test blade to duplicate the eventual manufacture of the full scale compressor blade. Figure 7b shows the design used for root end of the test blade.

FABRICATION OF TEST BLADE

Verification of the proposed construction method was accomplished using a 36 inch long composite blade design of trapezoidal cross section (Figure 8). The mold for this blade was constructed using a two 3/8 inch thick aluminum plates held apart by aluminum spacers which have a 45^{o} bevel cut along one side.

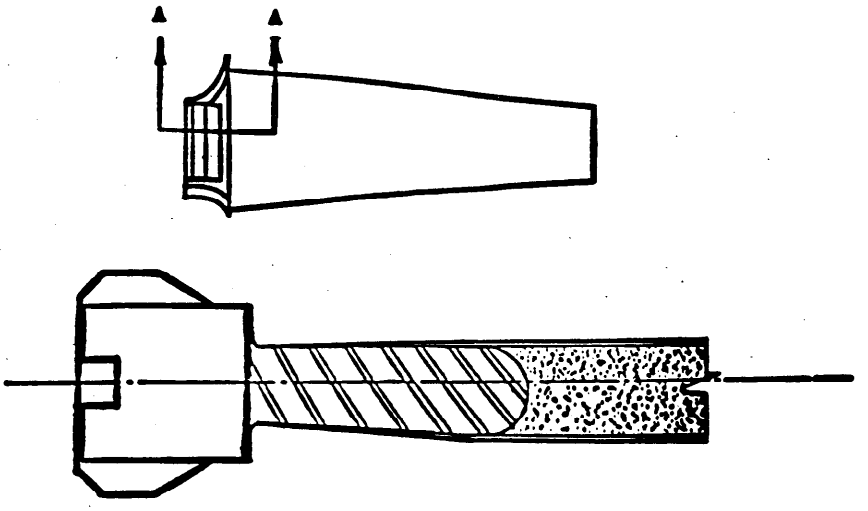

Figure 7a. Solid aluminum root insert for composite blade.

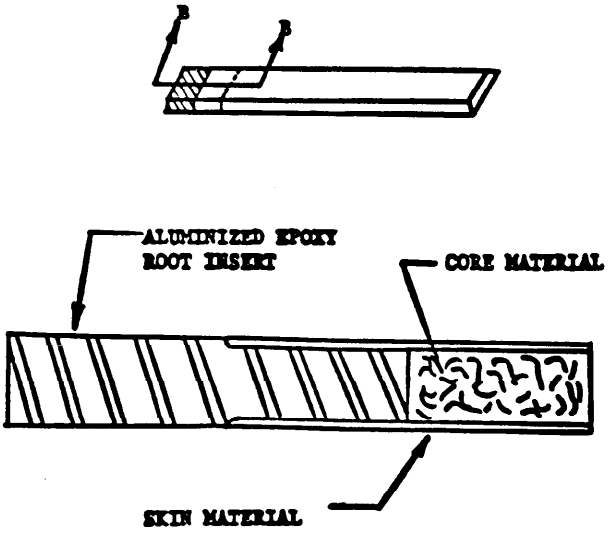

Figure 7b. Solid epoxy root insert for composite test blade.

The mold was held together with 27 1/4-20 steel bolts. the top aluminum plate was removable to provide access into the mold and could be tightened down with nuts to provide clamping pressure during blade fabrication.

To simulate fabrication of the composite compressor blade the test blade was constructed using a Kevlar epoxy skin, polyurethane foam core, and aluminized epoxy root insert. The epoxy root insert provided simulation of the aluminum insert in the compressor blade while decreasing the time required for its fabrication (machining) because it could be cast in place right in the mold. The trapezoidal shape of the blade was chosen for two reasons; it was a slightly more complex shape than a simple box beam, lending itself to a better comparison to the behavior of the aluminum blade, and beveling the edges allowed for easy release from the mold during fabrication.

A finite element model of this test blade was constructed using the finite element program SAP 4a. A total of 180 three dimensional, isoparametric elements (eight node bricks) were used to simulate the polyurethane foam core. The skin of the sandwich was modelled using 420 orthotropic plate and shell elements whose properties were determined using the program lay-up. The root insert was modelled using the properties of the aluminized epoxy for the first four rows of brick elements in the root section. Boundary conditions of restricted rotations and displacements were placed on the nodes at the root to parallel the attachment of the blade to the hub as a cantilevered beam.

To determine the static stiffness of the blade using this model a 4.5 pound point load was placed hanging from the tip of the blade. A static deflection of 0.134 inches was predicted.

A modal analysis was performed to predict the fundamental frequency, and associated model shape. This frequency was predicted to be 32.37 Hz for first mode bending.

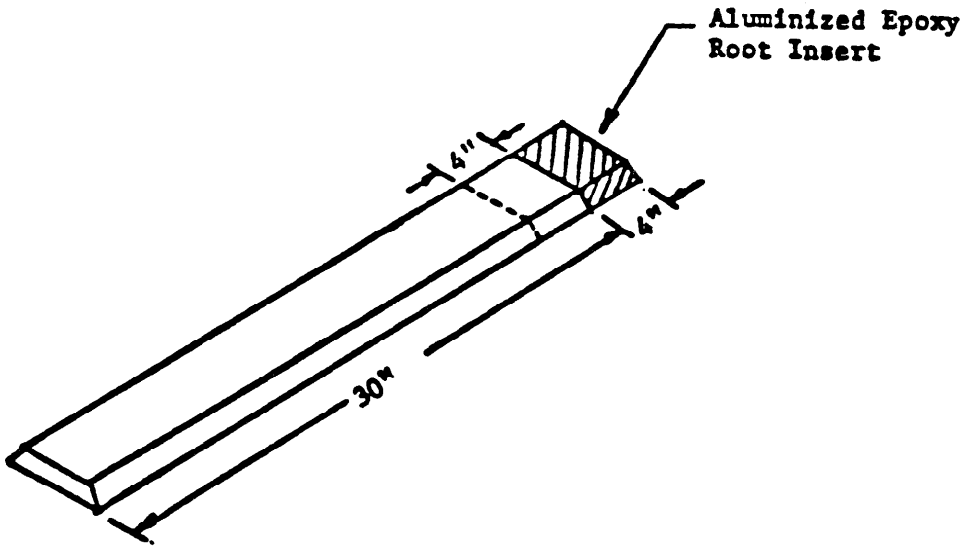

Figure 8. Fabrication test blade.

A new technique was proposed for construction of the blade. The approach was to mold the foam core, release it from the mold, apply the fabric skin around the foam and finally place the blade back in the same mold to cure. Since the blade is the thickness of the skin larger than the mold, when the mold is closed the foam core is compressed. This allows for ease of fabrication and also applies pressure to the skin which is desirable during cure.

Mold release for the foam (Carnuba wax) was first applied to the mold. Polyurethane foam (General Latex 16-F-2702) was mixed thoroughly in a 1:1 proportion and poured into the mold which was then closed. Foam density could best be controlled by the volume of liquid foam poured into the mold. After the foam was cured (about 3 hours) it was released from the mold. The section of the foam to be replaced by the epoxy root was removed by cutting it off. The foam core was dewaxed, epoxy mold release (PVA) applied to the mold, the core placed back into the mold, and the cover was closed. Aluminized epoxy was poured into the open end of the mold and allowed to cure overnight. After curing, the foam core and insert were removed in one piece. The skin also covers the root insert and since the epoxy was not compressible like the foam 0.1 inch was required to be milled out around the section.

A quasiisotropic lay-up ($0^0/90^0$ and $\pm 45^0$) was chosen for the skin because it lends itself to the orthotropic plate element and the use of woven material. Cloth was used to facilitate ease of fabrication of the initial design. In the fabric the fiber orientation is $0^0/90^0$ making it possible to obtain a quasiisotropic lay-up with two layers. The pattern for the skin was laid out on the cloth and cut with the fiber directions $0^0/90^0$ and $\pm 45^0$ both of woven roving. One layer of $0^0/90^0$ satin weave Kevlar was used for the outer surface as a surfacing mat. The cloth was laid out on a table and the epoxy (EPON 828, 100 parts and Jeffamine T-403, 49 parts) was applied with a brush. The wet cloth was then laid up on to the core material, placed into the mold, and the mold was closed. The mold and blade were then placed in an oven at 200^0F for 1 1/2 hours. It was then removed from the oven and allowed to cool for several hours. The mold was then opened and the blade removed from the mold.

EXPERIMENTAL TESTING AND ANALYSIS

Testing of the blade was carried out in the same manner to be performed on the full scale compressor blade. Retention of the test blade was accomplished by holding the root section in a mechanical testing machine under a compressive load of 5000 pounds. These conditions were maintained throughout all phases of testing.

While retaining the blade under a load of 5000 pounds as mentioned above, a point load of 4.5 pounds was hung from the tip of the blade on the centerline and the resulting deflection was measured by a dial indicator placed 1 inch behind the load.

A static deflection of 0.126 inches was measured when the load was applied. This represents a 6% difference from the predicted deflection of 0.134 inches.

TABLE III
MODAL ANALYSIS OF TEST BEAM

METHOD	FREQUENCY(Hz)
Finite Element Model	32
Experimentally Measured	30

An experimental modal analysis was performed on the test blade to verify the frequency prediction of the finite element model.

Using the same experimental techniques as used for the aluminum blade, the first mode frequency and associated mode shapes were determined for the test blade. Figure 9 shows the predicted (32 Hz) and experimental (30 Hz) frequencies and their associated mode shapes for the first mode. These frequencies differ by 6.6%.

Deviations of only 6% for the deflection and 6.6% for the natural frequencies indicate that the analytical methods used are a viable approach to the design of the composite blade.

COMPOSITE BLADE DESIGN

The design and fabrication of the composite compressor blade was undertaken in the same manner as the composite test blade. A finite element model

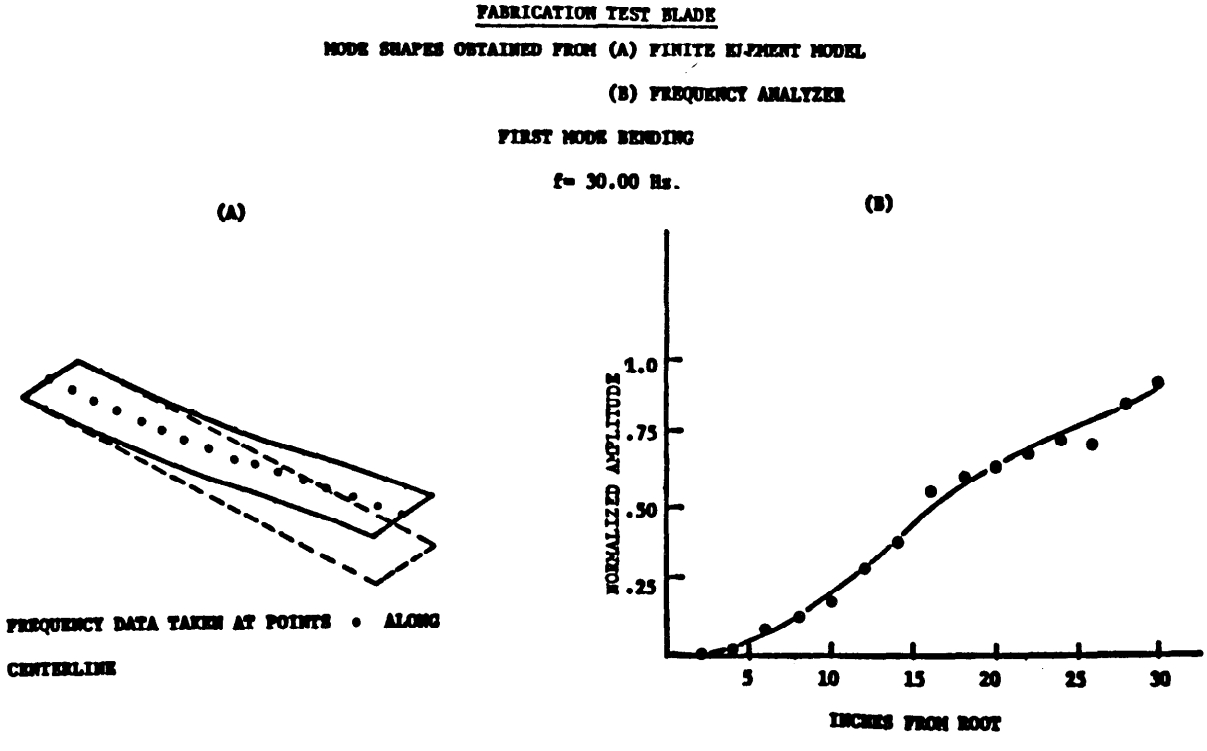

Figure 9. Modal analysis of test blade.

was constructed to evaluate the designs. Skin thickness, fiber orientation and material type were all adjusted to approach the natural frequency and static stiffness of the compressor blades presently in use.

A finite element model of the composite blade was constructed using SAP 4a. The foam core was modelled using eight node solid brick elements. Four node isoparametric plate elements (orthotropic) were used to simulate the composite skin. The root insert was modeled using eight node brick elements with aluminum properties. As in the metal blade, the same boundary conditions of restricting all displacements and rotations at the root were applied to the composite blade. The blades presently in use in the tunnel presented no problems within the present operating range so it was desirable to approximate their frequency response.

Results from the modal analysis of the computer model of the composite blade indicated that approaching the frequency response of the aluminum blades would present no problem. The results are displayed in Table II.

It was also necessary to approach the static stiffness of the aluminum blade because distortion of the aerodynamic shape of the blade would decrease its efficiency and also high bending stiffness would eliminate blade contact with the stators while the tunnel was in operation. Since matching the frequency response of the aluminum blade posed little problem, the limiting design criteria became static stiffness. For this reason different lay-ups, skin thicknesses, and material combinations were experimented with and their effect on overall stiffness of the resulting blade was observed.

Cloth was chosen in the preliminary design for its ease of lay-up. A quasiisotropic lay-up $(0/90, \pm 45)_{2\ n}$ was chosen as the lay-up orientation to produce uniform skin poperties. A final skin thickness of 0.15 inches of quasiisotropic Kevlar was chosen with 20% unidirectional graphite placed at the midplane of the lay-up in the radial direction. The iteration process to determine skin thickness vs. deflection is shown in Figures 10a and 10b, for lateral and torsional deformations respectively. The aluminum blade was approximately 30% stiffer in static deflection than the composite design for the prototype blade.

DETERMINATION OF CENTRIFUGAL LOADING

A preliminary calculation of centrifugal loading was performed using a lumped mass method. Using this method the centrifugal load at the root of the composite blade spinning at a speed of 700 RPM was predicted to be 16,447.97 pounds as opposed to 93,420.22 pounds for the aluminum blade. The weight of the airfoil section of the composite blade was calculated to be 9.97 pounds and for the aluminum design, 57.262 pounds, an 82.6% reduction. Although the composite design reduced the weight of the airfoil section 82.6%, because of the solid aluminim root insert the overall weight of the blade was reduced only 29%. A root section for the aluminum blade was obtained and the weight was added to the airfoil section to predict the total weight of the individual blade. These weights were 64.88 pounds for the composite blade and 90.97 pounds for the aluminum blade. The predicted weight of the aluminum blade represented a 3%

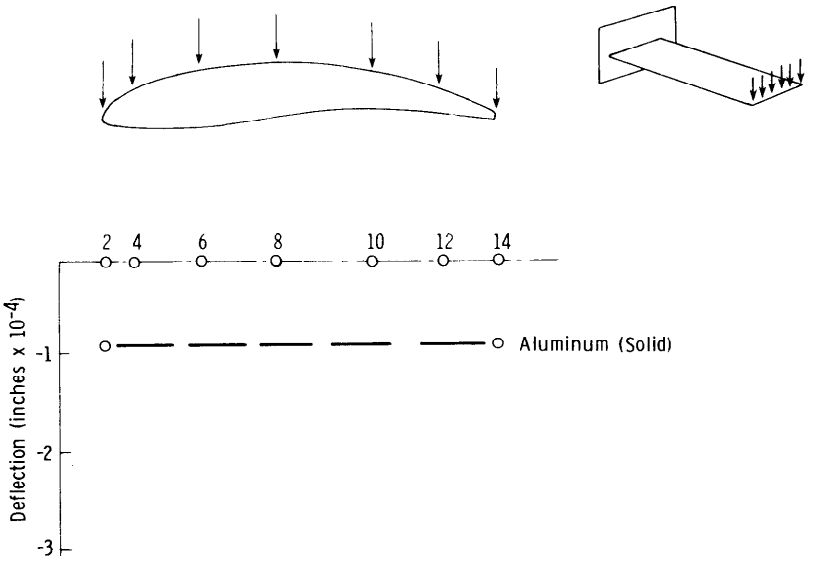

a. Relative tip deflection versus material for distributed unit load at tip.

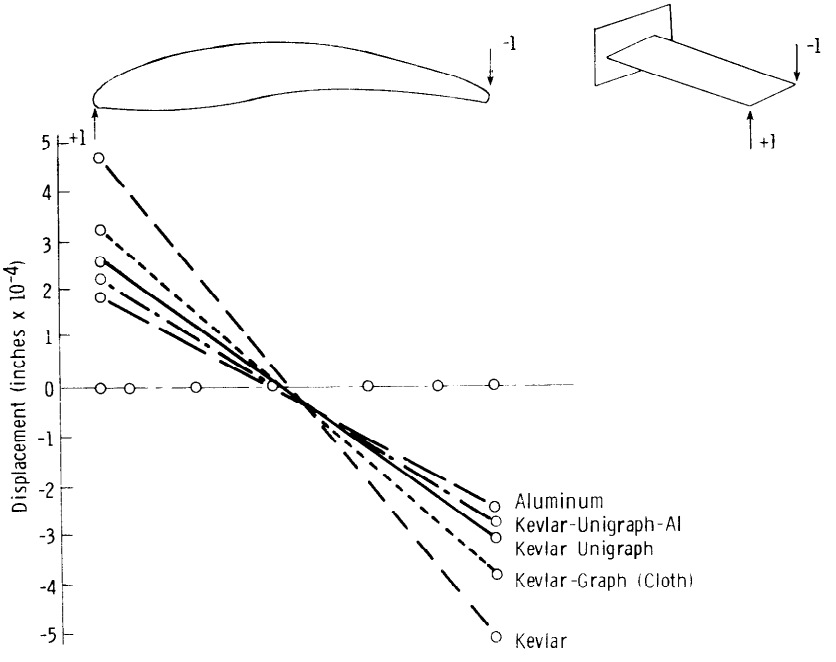

b. Relative twist at tip versus material for twisting load applied at tip.

Figure 10.

error from the actual weight of the aluminum blade which was measured to be 88.1 pounds. This reinforces the lumped mass method for calculating the centrifugal loading.

SUMMARY

The design and fabrication of a low cost composite replacement for the solid aluminum compressor blades of the transonic wind tunnel at NASA-Ames Research Center has been demonstrated.

The techniques used were verified using a simplified composite design as a test vehicle. The approach to be used to design and fabricate the full scale compressor blade was duplicated using this test blade. A finite element model was constructed and used to predict blade characteristics. Test blades were fabricated using an innovative two step squeeze molding technique. These test blades were utilized to initially test and perfect this fabrication concept. The experimental blade was tested and predicted blade properties were compared with those found experimentally. The tip deflection under a static point load of 4.5 pounds applied on the end of the blade was predicted to be 0.134 inches and was measured to be 0.126 inches. The natural frequency of the blade was predicted to be 32.68 Hz and was measured to be 30.00 Hz.

The close correlation between predicted and experimental results support the approach to the design and fabrication techniques applied here and indicate no problems during the eventual fabrication and testing of the full scale compressor blade.

The design of a composite replacement to the solid aluminum wind tunnel compressor blade was undertaken next. Finite element methods were utilized to analyze the existing aluminum design and to predict the properties of the composite replacement. The frequency response and static stiffness were to be the criteria for the design of a replacement.

Since the existing blades posed no vibrational problems within the present operating range of the tunnel it was desirable to match their frequency response of the aluminum blade with the composite design; however, a problem existed in developing the equivalent static stiffness. In the final design, unidirectional graphite was incorporated into the Kevlar skin to increase the static stiffness, resulting in a hybrid composite skin of 20% unidirectional graphite and 80% Kevlar cloth.

Theoretical centrifugal stress calculations were performed on the aluminum and composite blades using a lumped mass method. These loads were reduced 82.4% due to the decrease in weight of the composite design. Using this method, the total weight of the aluminum blade was predicted to be 90.9 pounds as opposed to the actual weight of 88.1 pounds, a 3% error. Since loading is a function of the square of the rotating speed, which dominates the calculation, the error in the centrifugal loading prediction should be even less.

The preliminary composite design using sandwich construction and an aluminum root section resulted in a composite blade design which decreased the major loading by 82%, reduced the weight of the blade by 29%, and was easy to

fabricate using the squeeze molding technique described. This reduction in blade weight should decrease the power requirements of the wind tunnel during operation.

The use of a composite design would greatly improve tolerance to impact damage and fatigue loading conditions found within the wind tunnel. The resulting increase in safe operation, and decrease in cost of fabrication support the effort to replace the metal compressor blades with those of a composite design.

REFERENCES

1. SAP 4a - "Structural Analysis Program For Static and Dynamic Response of Linear Systems," University of Lowell, Department of Mechanical Engineering, version 4a, September, 1980.

2. Structural Sandwich Composites Military Handbook MIL-HDBK-23A, Department of Defense, Washington, D.C.

3. Design and Use of KEVLAR Aramid in Aircraft Technical Symposium III, October, 1981.

4. B. Agarwal, L. Broutman, Analysis and Performance of Fiber Composites, John Wiley & Sons, New York, NY

EFFECTS OF SIMULATED LIGHTNING ON COMPOSITE AND METALLIC JOINTS*

WILLIAM E. HOWELL
NASA-Langley Research Center
Hampton, Virginia

J. ANDERSON PLUMER
Lightning Technologies, Inc.
Pittsfield, Massachusetts

ABSTRACT

Recent designs of both fixed and rotary wing aircraft show increased use of advanced composite materials and adhesively bonded joints in load carrying structures and in the area of fuel cells. Lightning strike is a potential hazard that aircraft may encounter. Therefore, the response of these advanced composite structures to lightning strikes becomes an important design criterion. Electrical arcing across bonded joints or mechanical fasteners inside fuel cells could cause severe structural damage to the aircraft.

The purpose of this paper is to report experimental data that characterizes the arcing damage to bonded and the breakdown voltages/currents of joints and access/inspection panels. The research was conducted jointly by Langley Research Center and Lightning Technologis, Inc. Tests were conducted to determine the behavior of existing metallic and composites designs when exposed to high current and voltage values associated with simulated lightning strikes. Figure 1 shows a tensile test specimen mounted in the electrical circuit. The specimen has a single-lap bonded joint with aluminum adherends. Four different levels of current were passed through specimens of this configuration to determine the structural damage threshold. The threshold was determined by strength loss indicated from tensile tests of specimens after exposure to a test current. Similar specimens with graphite/epoxy adherends also were tested. Both non-conducting and conducting adhesives were included in the tests.

In addition, specimens representing several bonded and/or bolted configurations used in fuel cell areas were evaluated. The specimen is representative of a wing access/inspection panel. Arcing at a dome nut, inside the fuel cell, was caused by a simulated lightning strike to the access panel. The configuration and several others were evaluated to determine the damage and arcing threshold.

The results of these tests indicate that current levels must be kept below 5-10kA, depending upon the design, in order to insure an arc free attachment and structural integrity. Additional data may be required to assure aircraft are designed to meet safety requirements.

---

* The full manuscript of this paper was not available in time to be included in these proceedings. A copy of the full paper can be obtained on request from the authors.

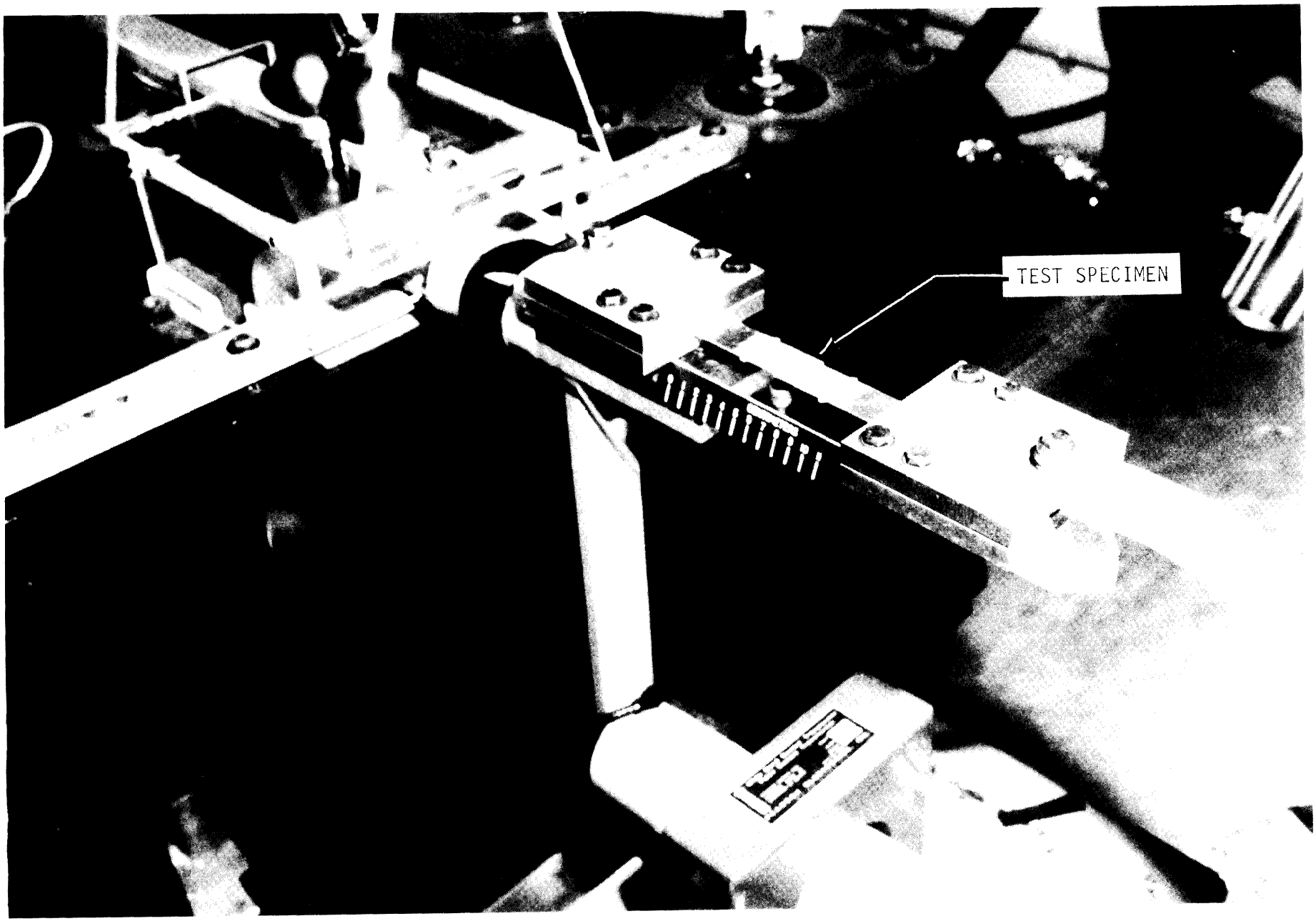

Figure 1.- Single-lap bonded joint test specimen mounted in test circuit.

SESSION IV: STRUCTURAL DESIGN

Chairman: R. Beeuwkes
Scientist Emeritus
Army Materials and Mechanics Research Center

CYCLIC TORSION OF A CIRCULAR CYLINDER 405

P. C. T. Chen, Army Armament R&D Command, and M. R. Aboutorabi and H. C. Wu, The University of Iowa

DETERMINATION OF PROOF LOAD CRITERIA FOR THE F-14 ARRESTING GEAR HOOK SHANK 416

K. D. Jordan, C. E. Dumesnil, and T. D. Gray, Vought Corporation

EVALUATION OF THE RELATIVE HYDROGEN EMBRITTLEMENT SUSCEPTABILITY OF ESR 4340 STEEL 439

L. Raymond, METTEK Laboratories, and C. Beneker, Parker Hannifin Corporation

A PHOTOELASTIC INVESTIGATION OF STRESSES AND LOAD DISTRIBUTIONS IN LUG-GROOVE JOINTS 454

Y. F. Cheng, Army Armament R&D Command

IMPROVED M-11 COPPER CRUSHER GAGE 471

J. M. Bender, Army Ballistic Research Laboratory

NONLINEAR ANALYSIS OF IN-BORE PROJECTILES 481

S. C. Chu, Army Armament R&D Command

CYCLIC TORSION OF A CIRCULAR CYLINDER

PETER C.T. CHEN
Research Mathematician
U.S. Army Armament R & D Command
LCWSL, Benet Weapons Laboratory
Watervliet, New York 12189

M.R. ABOUTORABI
Graduate Assistant

HAN C. WU
Professor of Materials Engineering
The University of Iowa
Iowa City, Iowa 52242

ABSTRACT

The improved endochronic theory of plasticity is applied to the case of a solid bar with circular cross section subjected to cyclic fully-reversed torsional loading. Numerical techniques are employed to obtain the solution. The parameters of the constitutive equations are determined from the test data of thin-walled specimens. These parameters are then used without alteration to compute stress distributions within the solid specimen. The relation of torque vs. strain at the outermost fiber of the solid specimen provides an ultimate check of this theory. This paper demonstrates an expanded use of the improved theory.

INTRODUCTION

Experimental observations indicate that when metallic materials are subjected to cyclic torsional loading, a hardening behavior similar to the case of uniaxial loading occurs. In a previous paper, Wu and Yip [1] successfully applied the endochronic theory of plasticity to describe the cyclic hardening phenomenon under uniaxial loading, and it is the objective of this paper to apply this theory to the case of cyclic torsional loading, of a thin-walled cylinder and a solid cylinder of circular cross-section and investigate the residual stress distribution.

BRIEF SUMMARY OF IMPROVED ENDOCHRONIC THEORY

The endochronic theory of plasticity developed by Valanis [2] is based on the notion of intrinsic time and the internal variable theory of thermodynamics. The original definition of intrinsic time has led to difficulties in cases where the history of deformation involves unloading. Valanis [3] has since introduced a new concept on intrinsic time to overcome these difficulties.

The intrinsic time ζ is a measure of irreversibility. A definition of new intrinsic time which is more closely representative of unloading behavior is given as follows:

$$d\zeta 2 = d\Omega_{ij}\, d\Omega ij \tag{1}$$

$$d\Omega_{ij} = de_{ij} - k_1 \frac{ds_{ij}}{2\mu_o} \tag{2}$$

where Ω_{ij} is a strain like tensor, e_{ij} and s_{ij} are deviatoric strain and stress tensors respectively, k_1 is a positive constant such that $0 \leqslant k_1 \leqslant 1$ and μ_o is shear modulus.

The general constitutive equation for shear response of a material with an elastic hydrostatic response and no coupling between deviatoric and hydrostatic behavior is:

$$s_{ij} = 2 \int_o^z \mu(z-z') \frac{de_{ij}}{dz'} dz' \tag{3}$$

where z is an intrinsic time which is related to ζ by the following time scale

$$\frac{d\zeta}{dz} = f(\zeta) \tag{4}$$

It has been shown in [3] that $f(\zeta)$ describes isotropic hardening and is therefore termed the hardening function.

Define

$$\mu(z) = \mu_o\, G(z) \tag{5}$$

where $G(0) = 1$ indicates initially elastic response. Using Laplace transform technique, (for details see Ref. [3]), eq. (3) becomes

$$s_{ij} = 2\mu_o \int_o^z \rho(z-z') \frac{d\Omega_{ij}}{dz'} dz' \tag{6}$$

in which, for the case of $k_1 = 1$,

$$\rho(z) = \rho_o\, \delta(z) + \rho_1(z) \tag{7}$$

where $\rho_1(z)$ is composed of a finite sum of exponential terms. A general constitutive equation in terms of initial yield stress s_y and plastic strain Ω_{ij} ($k_1 = 1$) can be obtained as

$$s_{ij} = s_y \frac{d\Omega_{ij}}{dz} + 2\mu_o \int_o^z \rho_1(z-z') \frac{d\Omega_{ij}}{dz'} dz' \tag{8}$$

by substituting eq. (7) into eq. (6) and defining $s_y = 2\mu_o \rho_o$. Note that at $z = 0$:

$$s_{ij} = s_y \left.\frac{d\Omega_{ij}}{dz}\right|_{z=0} \tag{9}$$

Also from eq. (2), the condition $\Omega_{ij} = 0$ gives the relation,

$$s_{ij} = 2\mu_o e_{ij} \tag{10}$$

Equation (10) merely attests to the fact that while z = 0 the deformation process is reversible and therefore the deviatoric stress response is elastic.

DESCRIPTION OF CYCLIC SHEAR RESPONSE

For pure shear deformation with $\rho_1(z)$ represented by one exponential term, one has

$$d\Omega = d\eta - \frac{d\tau}{2\mu_o} \tag{11.a}$$

and

$$2\mu_o \rho_1(z) = 2\mu_1 e^{-\alpha z} \tag{11.b}$$

where η is total shear strain and Ω is plastic shear strain. Eq. (8) yields

$$\tau = \tau_y \frac{d\Omega}{dz} + 2\mu_1 \int_o^z e^{-\alpha(z-z')} \frac{d\Omega}{dz'} dz' \tag{12}$$

with

$$\frac{d\zeta}{dz} = f(z) \text{ and } d\zeta = |d\ \Omega| \tag{13}$$

and τ_y is the shear yield stress. Using equations (12) and (13) and a suitable function f, the governing equations of torsional test of a thin-walled tube during loading, unloading and reloading can be derived. The initially elastic unloading (reloading) response and followed Bauschinger effect will be governed by the material property itself, provided that the intrinsic time measure is correct.

If the first unloading of stress-strain curve begins when intrinsic time measure ζ reaches ζ^*, the positive property of ζ requires equation (13) to be

$$d\zeta = -d\Omega \tag{14}$$

Define ζ^*_- and ζ^*_+ as loading and unloading measures around the neighborhood of ζ^* in ζ space. Then equation (12) leads to

$$\tau^- = \tau_y \left.\frac{d\zeta}{dz}\right|_{\zeta^*_-} + 2\ \mu_1 \int_o^{z^*_-} e^{-\alpha(z-z')} \frac{d\Omega}{dz'} dz' \tag{15}$$

$$\tau^+ = \tau_y \left.\frac{d\zeta}{dz}\right|_{\zeta^*_+} + 2\ \mu_1 \int_o^{z^*_+} e^{-\alpha(z-z')} \frac{d\Omega}{dz'} dz' \tag{16}$$

where τ^- amd τ^+ are stress states nearby ζ^* at loading and unloading processes respectively. In the limit, when $\zeta^*_- \to \zeta^*$ and $\zeta^*_+ \to \zeta^*$,

$$\tau^{-} - \tau^{+} = 2\,\tau_y \left.\frac{d\zeta}{dz}\right|_{\zeta^*} \tag{17}$$

Therefore the shear stress is discontinuous with a discontinuity of magnitude

$$\Delta\tau = 2\,\tau_y \left.\frac{d\zeta}{dz}\right|_{\zeta^*} \tag{18}$$

in the initially elastic unloading region. If the consequent loading reversals take place at ζ^{**}, ζ^{***}, ... then there is an elastic change of magnitude

$$\Delta\tau = 2\,\tau_y \left.\frac{d\zeta}{dz}\right|_{\zeta^{**},\ \zeta^{***},\ \ldots..} \tag{19}$$

in the shear stress. During these elastic responses the values of ζ and z remain unchanged.

During the elastic response, $d\zeta$ is zero and the constitutive equation is simply

$$d\tau = 2\,\mu_o\, d\eta \tag{20}$$

Once the change in stress is larger than $\tau^{-} - \tau^{+}$, then the material behavior is governed by equation (12).

TORSION OF A CIRCULAR CYLINDER

In laboratory experiments on torsion of solid bars, the recorded data are usually the strain at the outer fiber and the amount of externally applied torque. In order to describe these experimental results, the shear constitutive equation established in the previous section and based on a thin-walled tubular specimen should be applied together with the equations discussed in this section.

The external torque for a solid bar with a circular cross section is given as:

$$T_s = 2\,\pi \int_0^{r_a} \tau\, r^2\, dr \tag{21}$$

where τ is current shear stress state corresponding to location r, and r_a is the radius of cross section. The torque can be approximated by discretizing the circular cross section into a finite number of concentric circular rings and assuming τ to be constant over each ring. Thus

$$T_s = 2\,\pi \sum_{i=1}^{n} \tau_i\, r_i^2\, \Delta r_i \tag{22}$$

Now equations (12) and (13) along with equation (11.a) can be solved to yield τ_i at each fiber, if the value of η_i (shear strain) at that fiber is known. Geometrical considerations show that radial lines have to remain straight after deformation. Thus, one concludes that

$$\eta_i = \frac{r_i}{r_a}\,\eta_a \tag{23}$$

where η_a is the strain at the outer-most fiber.

Recall that there is a yield stress introduced in equation (8) when $k_1 = 1$ and $\zeta = 0$. Hence, an elastic core always exists during deformation whose radius r_e is easily computed as

$$r_e = \frac{\tau_y}{2\mu_o}\,\frac{r_a}{\eta_a} \tag{24}$$

If the experiment is strain controlled with strain at r_a varying between $-\eta_a$ and $+\eta_a$, and with η_a in the plastic range, then the elastic core radius remains fixed during all stages of loading after the first load reversal.

Now that η_i is known, the value of shear stress at each fiber can be evaluated and used in eq. (22). Note that at the points of load reversal, for the fibers in the plastically deformed region, there exists an elastic range governed by equation (19). This discrete type formulation of torque has the advantage of being capable of describing the transient and residual stresses in the bar as well.

COMPUTATION

The governing equations are equations (11.a), (12), (13), (22) and (23) which are summarized in below:

$$d\Omega = d\eta - \frac{d\tau}{2\mu_o} \tag{11.a}$$

$$\tau = \tau_y \frac{d\Omega}{dz} + 2\,\mu_1 \int_0^z e^{-\alpha(z-z')}\,\frac{d\Omega}{dz'}\,dz' \tag{12}$$

$$\frac{d\zeta}{dz} = f(z) \qquad \text{and} \qquad d\zeta = |d\Omega| \tag{13}$$

$$T_s = 2\,\pi \sum_{i=1}^{n} \tau_i\, r_i^2\, \Delta r_i \tag{22}$$

$$\eta_i = \frac{r_i}{r_a}\,\eta \tag{23}$$

Since the analytical solution of these equations is quite involved, and in particular requires different treatment and derivation for different hardening function f(z), a numerical scheme has been developed to solve the above equations. Since the relationship between ζ, the independent variable, and η, the controlled variable is indirect, iterative techniques are an integral part of this program.

In order to ascertain the degree of accuracy of numerical methods, a hypothetical case was assumed. Namely, the field equations were solved analytically using $f(z) = \exp(\beta z)$, and the results were compared with those obtained numerically. The difference between the two is so small that using numerical techniques does not introduce any significant amount of error.

RESULTS AND DISCUSSION

Once the accuracy of the computer program was established, it was used to predict the results of experiments performed on annealed AISI 4142 steel. The experimental results of cyclic torsion test obtained by the Plasticity Research Laboratory at The University of Iowa are presented along with the theoretical predictions in Figures 1 and 2. This material does not show any appreciable amount of cyclic hardening.

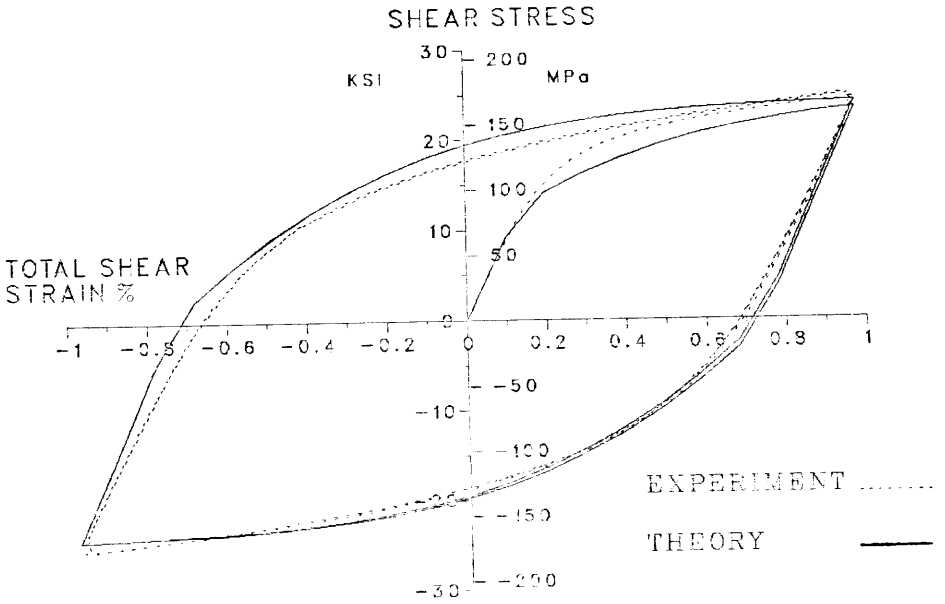

Figure 1. Shear Stress-Strain Curves for Thin-Walled Specimens

The most important factor in theoretical predictions is the choice of the hardening function $f(z)$. In this computation, the form

$$\frac{d\zeta}{dz} = C - (C-1)\, e^{-\beta z} \tag{24}$$

has been used because of its simplicity and its proven usefulness in case of cyclic loading, Ref. [1].

Following accepted procedures, the shear stress-strain curve for the material was obtained from a thin-walled tubular specimen, and the value of the material constant were determined from this data. The values of the

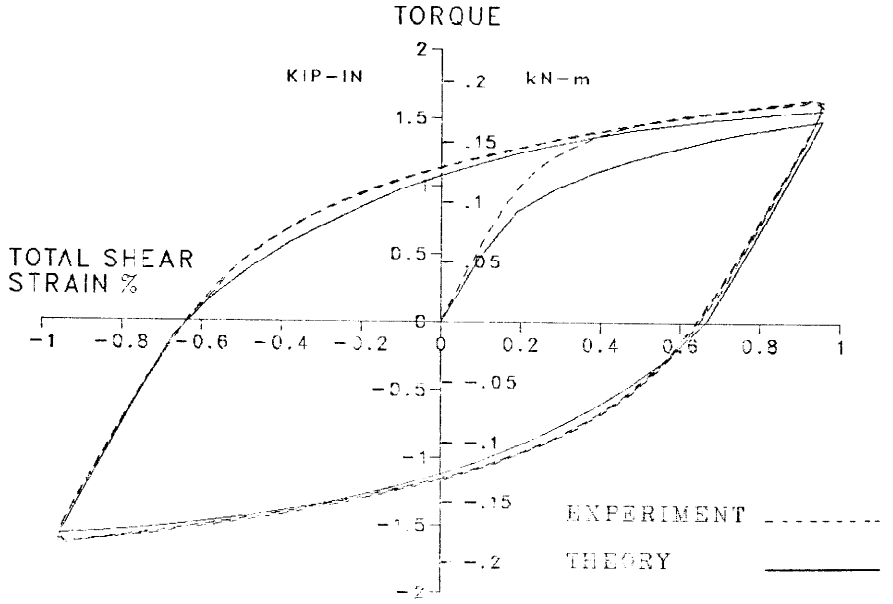

Figure 2. Torque-Shear Strain Curves for Solid Circular Cylinder

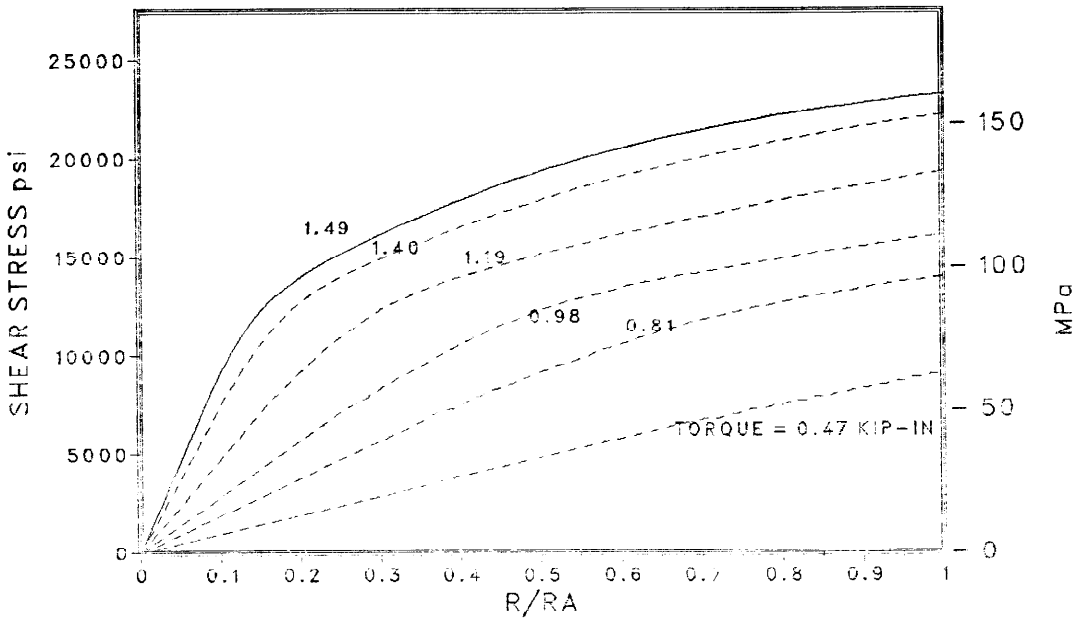

Figure 3. Stress Distribution at Different Stages of First Loading of Solid Cylinder

constants are: α = 550, β = 15,000, C = 1.9, μ_o = 1 x 10^7 psi (6.89 x 10^4 MPa), μ_1 = 3.6 x 10^6 psi (24.804 x 10^3 MPa), τ_y = 6,500 psi (44.79 MPa). As can be seen from Fig. 1 this set of constants prodict the experimental results reasonably well. The same set of constants were then used to predict the results for a solid bar test. As evidenced in Figure 2, theoretical and experimental results are in reasonable agreement.

As a consequence of the computational process the distribution of stress in the cross section is evaluated. Such distribution at different magnitudes of torque during the first loading half-cycle is presented in Figure 3. Notice that the outer fiber is the first one to yield; subsequently as more torque is applied, the radius of the elastic inner core gets smaller.

Figure 4 presents the distribution of the shear stress in the bar at different stages of the first unloading. The flat portion in the lower curves corresponds to the fibers which have surpassed this initial elastic unloading and started plastic unloading. An interesting observation can be made here, when the amount of reversed torque gets larger, the size of the plastically deformed region, i.e., the flat portion, gets bigger as well, but for each individual fiber the developed plastic stress does not increase accordingly. Rather, the applied torque is compensated for by elastic relief of shear stress in the internal fibers. The radius of the elastic core has been found to be r_e/r_a = 0.0913 for this computation.

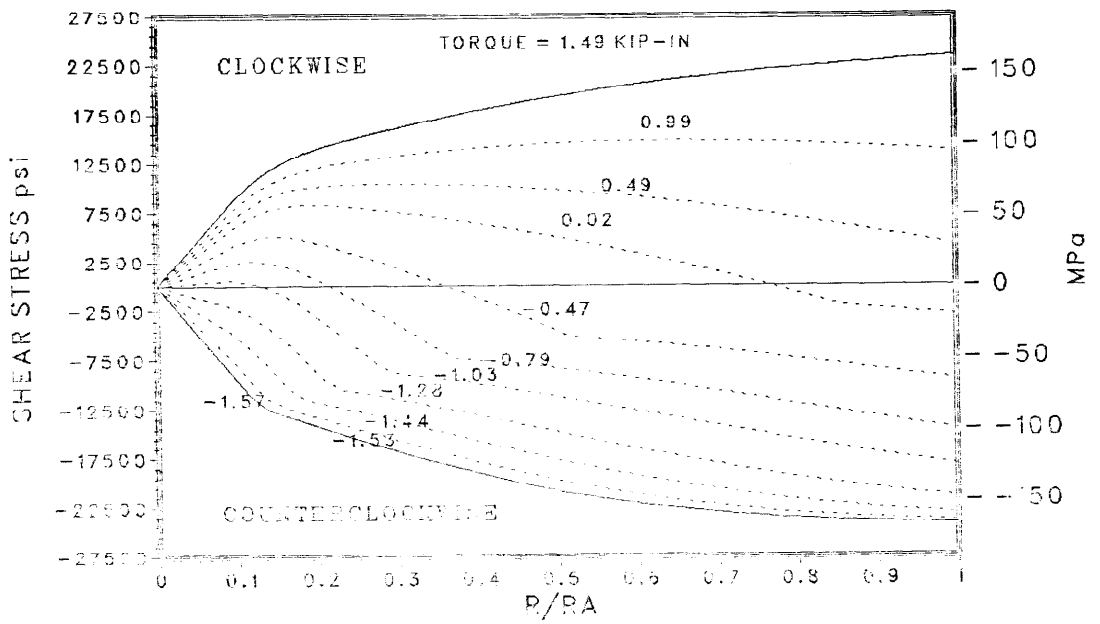

Figure 4. Stress Distribution at Different Stages of First Unloading of Solid Cylinder

The distribution of residual stresses at the end of first cycle where the applied torque is equal to zero, is presented in Figure 5.

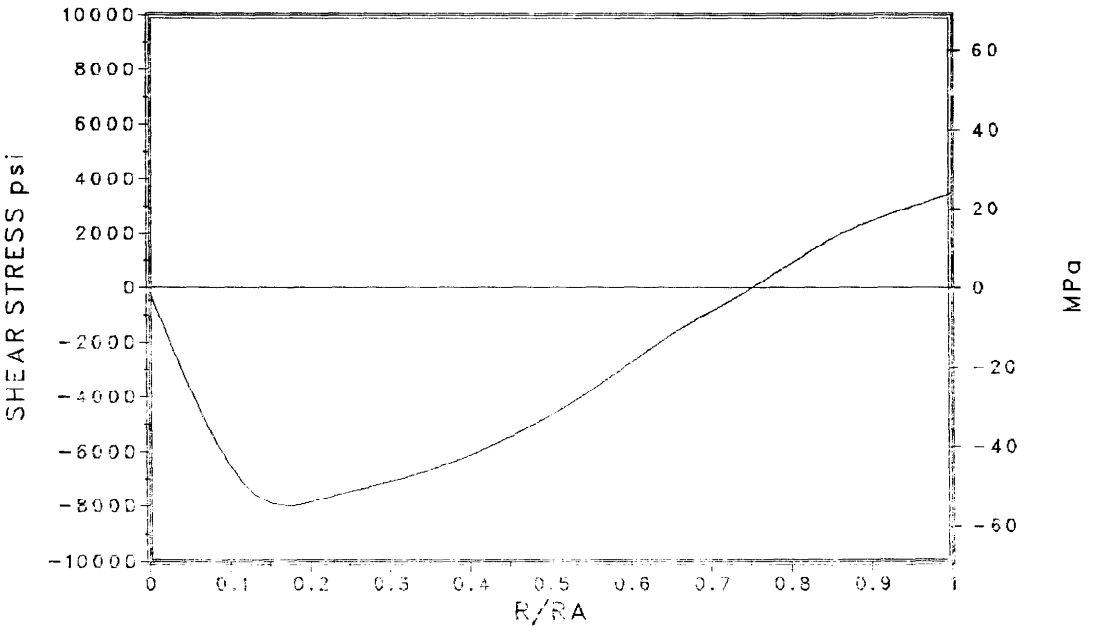

Figure 5. Residual Stress Distribution at Zero Torque

For purposes of investigating the implications of the model developed here, a hypothetical material with appreciable cyclic hardening behavior was studied. The shear stress-strain behavior of such material under fully-reversed torsional loading is presented in Figure 6. The material constants for this material were determined as: α = 500, β = 25, C = 1.5, μ_o = 1 x 107 psi (6.89 x 10^4 MPa), μ_1 = 4 x 10^6 psi (27.56 x 10^3 MPa) and τ_y = 10,000 psi (68.9 MPa). A steady loop is established after a few cycles.

Figure 7 presents the residual stress distribution at the end of reversal cycles up to and including the steady loop.

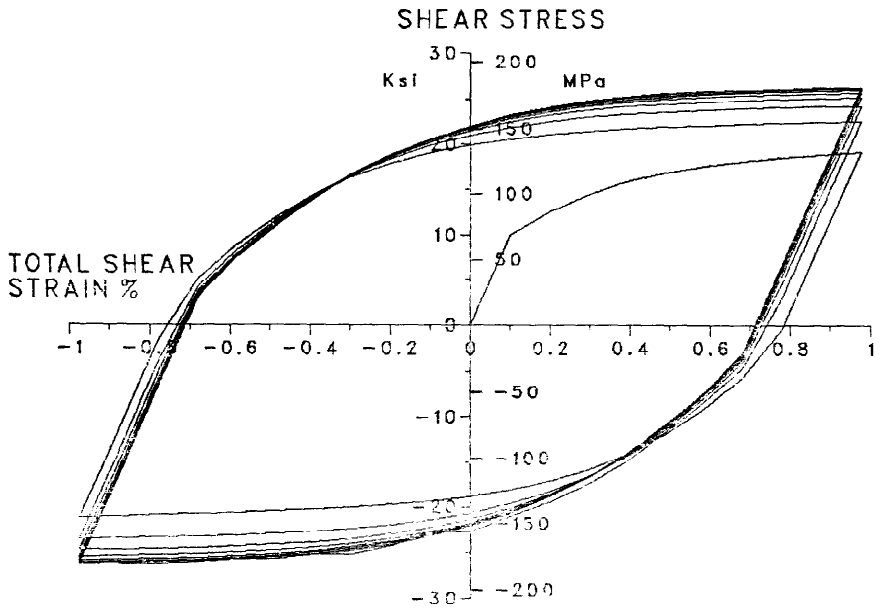

Figure 6. Theoretical Shear Stress-Strain Behavior of a Hypothetical Material

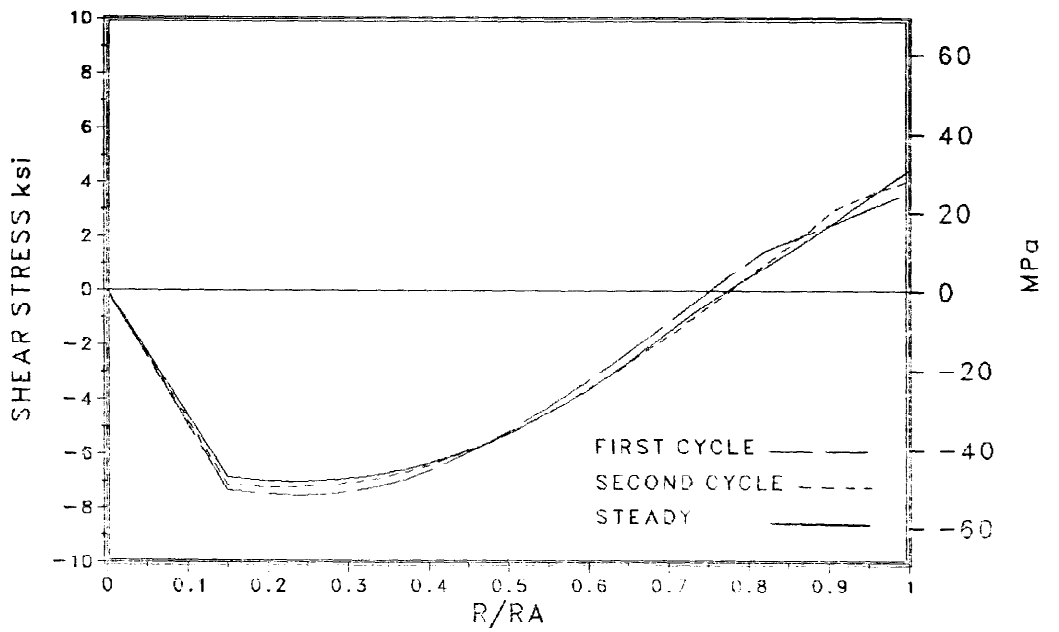

Figure 7. Residual Stress Distribution in a Solid Cylinder (Hypothetical Material)

ACKNOWLEDGEMENT

The authors acknowledge the support of U.S. Army Armament R & D Command for the work reported herein, conducted under Project Numbers 1L161102H570 and 1L161102AH60.

REFERENCES

1. Wu, H.C. and Yip, M.C., "Endochronic Description of Cyclic Hardening Behavior for Metallic Materials", ASME J. of Eng. Materials and Technology, v. 103, July 1981, 212-217.

2. Valanis, K.C., "A Theory of Viscoplasticity without a Yield Surface, Part I and II", Archives of Mechanics, v. 23, 1971, 517-551.

3. Valanis, K.C., "Fundamental Consequences of a New Intrinsic Time Measure - Plasticity as a Limit of the Endochronic Theory", Archives of Mechanics, v. 32, 1980, 171-191.

DETERMINATION OF PROOF LOAD CRITERIA FOR THE F-14 ARRESTING GEAR HOOK SHANK

KERRY D. JORDAN
Engineering Specialist

CARL E. DUMESNIL
Technical Project Manager

TERRY D. GRAY
Manager, Structures Development
Vought Corporation
Dallas, Texas 75265

ABSTRACT

This paper describes a test and evaluation program on the F-14 arresting gear hook shank. The objective was to develop criteria based on analysis and test results, whereby the proof load/inspection interval and overall service life of the hook shank could be safely extended. Fracture mechanics techniques provided a method of assessing the significance of proof tests and correlating proof loads with remaining life under operating loads. The results of this program showed that a two-phase proof load (axial followed by bending) could extend the proof-test interval from 100 to 125 arrested landing cycles. In addition, the total service life could be extended from 1000 to an indeterminate number of arrestments.

INTRODUCTION

This paper describes the results of a test and evaluation program conducted for the Naval Air Systems Command [1]. The original Navy overhaul/retirement criteria for the F-14 arresting gear required the hook shank be removed from the aircraft after every 100 carrier arrestments for inspection and axial proof test. The hook shank was retired from service after 1000 arrestments. The objective of this investigation was to develop criteria based on analysis and test results, whereby the proof load/inspection interval and overall service life of the F-14 arresting gear hook shank could be safely extended. The test program consisted of fatigue and damage tolerance testing of sixteen rejected F-14 hook shanks. The test data evaluation included considerations of scatter and salt water environment. Fracture mechanics techniques provided a method for assessing the significance of proof tests and correlating proof loads with remaining operating life.

The results of this program showed that a two-phase proof load consisting of a 226 kip (1.005 MN) axial load followed by a 134 percent limit bending load would ensure structural integrity for a minimum remaining life of 125 arrestments at the maximum operating load of 165 kips

(0.734 MN). In addition, the total service life could be extended to an indeterminate number of arrestments as long as the shank continued to successfully pass the proof test.

TECHNICAL APPROACH

The conventional proof test technique for qualifying a structural component takes on added significance when fracture mechanics theory is applied. To assess the condition of a component in terms of existing flaws, nondestructive inspection (NDI) procedures are generally relied upon. The proof test, however, can be considered one of the most positive inspection procedures available. A successful proof test actually defines the maximum functional relationship between applied stress and flaw size as defined by the crack tip stress intensity factor, K,

$$K = f(\sigma\sqrt{a}) \qquad (1)$$

where "σ" is the stress level and "a" represents the crack size. Fracture occurs when the stress and crack size are such that $K = K_c$, which is the critical stress intensity factor or the material fracture toughness. Therefore, fracture data generated from test can relate stress or load at failure to flaw size. This is presented schematically in Figure 1. It is seen that if a proof load, which is "α" times greater than the operating load, is successfully applied, then the maximum flaw which can exist in the part is a_i. If the critical flaw size under operating loads is determined as a_{cr}, then the minimum flaw growth potential is ($a_{cr} - a_i$).

In order to associate remaining life with the flaw growth potential, it is necessary to determine how long it takes a crack to grow from a_i to a_{cr} under operating conditions. One of the most predominate types of subcritical flaw growth is fatigue crack growth resulting from cyclic stresses. The methods used for predicting fatigue crack growth make use of flaw growth testing and the stress intensity concept.

It has been shown by Tiffany and Masters [2] that the number of cycles to failure at a given stress level depends on the initial stress intensity, K_i, compared to the critical stress intensity, K_c. Therefore,

$$N = f\left(\frac{K_i}{K_c}\right) \qquad (2)$$

where N is the number of cycles to failure. It is also seen that the stress intensity ratio is related to the ratio of initial flaw size to critical flaw size as follows

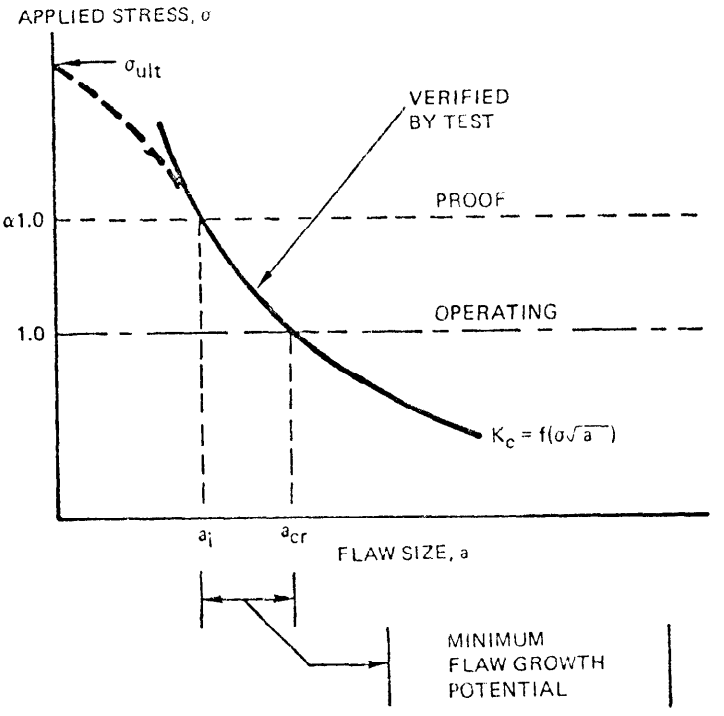

Figure 1 Stress vs Flaw Size Relationship

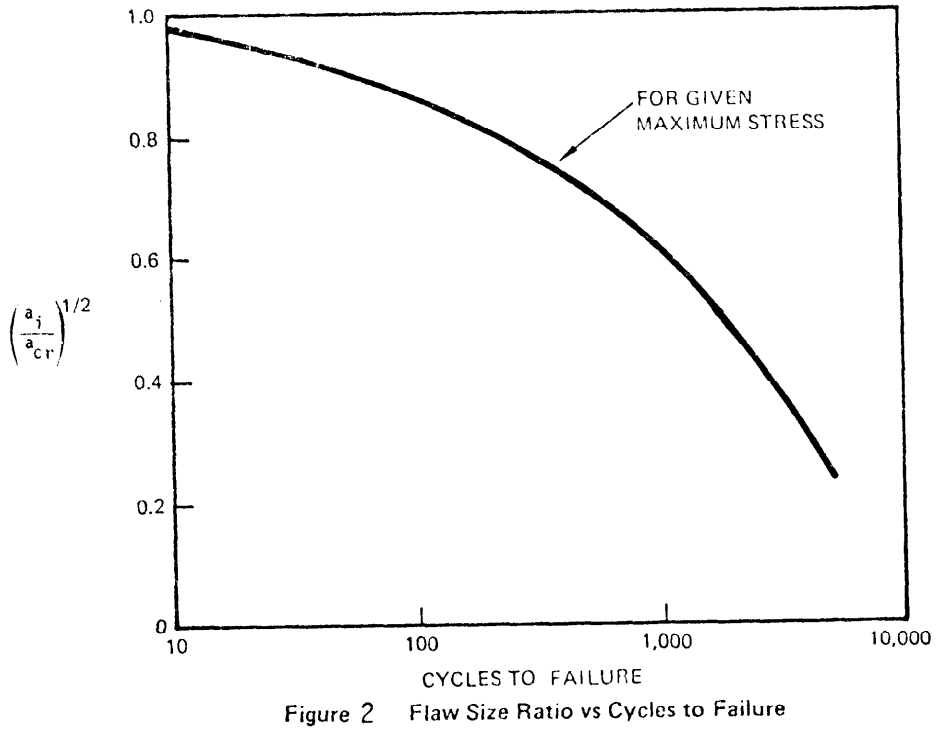

Figure 2 Flaw Size Ratio vs Cycles to Failure

$$\frac{K_i}{K_c} = \left(\frac{a_i}{a_{cr}}\right)^{1/2} \qquad (3)$$

Thus, test data can be used to develop the relationship between the flaw size ratio and the number of cycles to failure. This data may be presented in a form shown graphically in Figure 2. With this type of data, the cycles required for any given flaw to grow to critical size can be predicted.

Conversely, for a given life requirement, the maximum allowable initial flaw size can be determined. Knowing the maximum allowable initial flaw size for a required remaining life, data represented in Figure 1 can be used to establish the necessary proof load.

COMPONENT DESCRIPTION

The F-14 arresting gear hook shank is shown in Figure 3. The hook shank is a 300M machined steel forging heat treated to an ultimate tensile strength of 280 ksi (1930 MPa). The shank is a three-piece tubular section joined by flash welds. The forward end of the shank is pinned to a trunnion through a set of lugs. The aft end of the shank is a heavy section with the hook point fitting. The hook point is secured on the shank by a 3/4 inch (1.905 cm) diameter steel bolt.

On carrier arrestment, prior to cable engagement, bending (caused by hook bounce) is induced into the shank as a result of impact of the hook toe on the carrier's stern ramp and deck protrusions such as light covers. After hook bounce, the carrier deck cable is engaged by the hook point. During run out of the cable, arresting loads are transmitted through the shank and trunnion to the fuselage arresting gear keel structure. Bending is induced into the shank since the hook load is eccentrically applied at the point of attachment approximately 2.67 inches (6.782 cm) below the neutral axis of the shank section.

EXPERIMENTAL PROCEDURE

The test assembly included only the hook shank. All attachment hardware was locally manufactured to production specifications. The hook point was not utilized during testing, but was replaced by a machined steel shoe so that both vertical and axial loads could be applied to the shank. The shoe contained a cutout into which the hook shank was nested and secured by a 3/4 inch (1.905 cm) bolt. A schematic of the test fixture, with a test specimen installed, is shown in Figure 4.

All cyclic fatigue loading was performed using a load ratio, R = min. load/max. load, R = 0.02. One arrestment consisted of hook bounce followed by a 165 kip (0.734 MN) axial load. The bending moment representative of

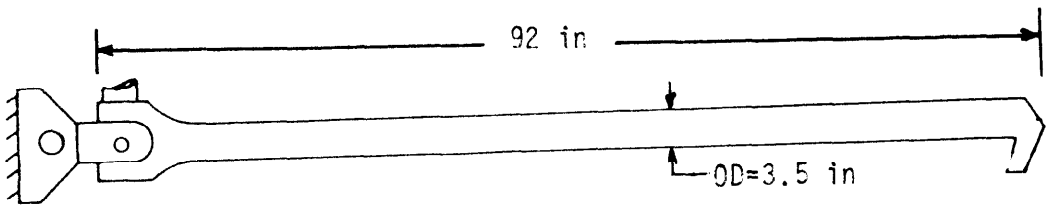

Figure 3 F-14 Arresting Gear Hook Shank

inch=2.54 cm

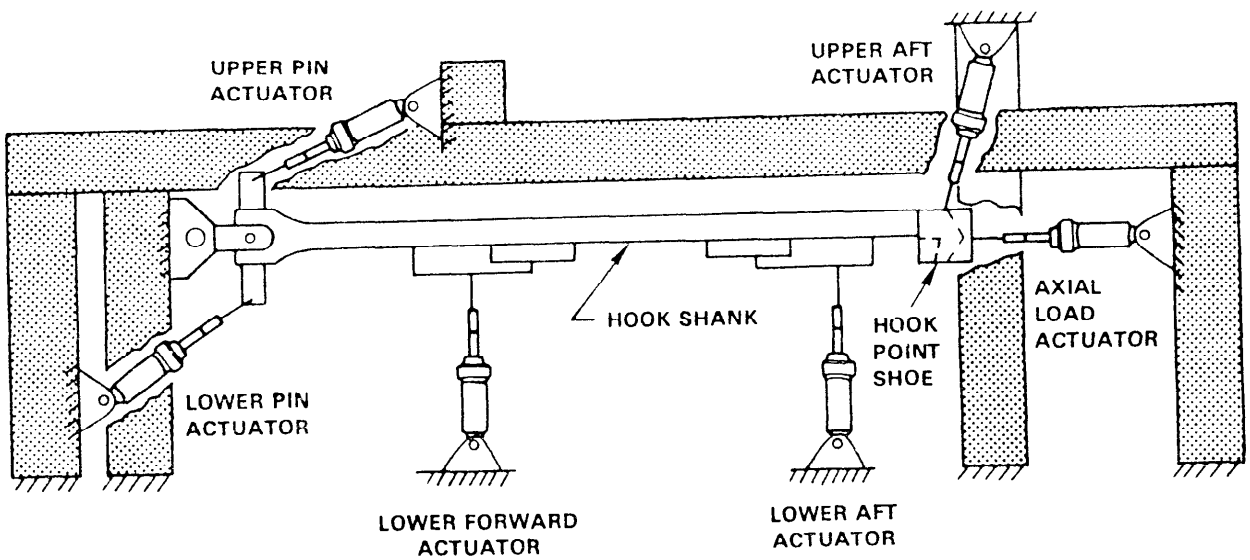

Figure 4 **Test Fixture Schematic**

the limit hook bounce condition (determined from a dynamic analysis) is shown in Figure 5.

In order to achieve the hook shank limit bending moment, loads were applied in the manner shown in Figure 6. Axial loading is shown in Figure 7. Testing was conducted using a two-step, ten-cycle block spectrum (Figure 8), consisting of nine cycles of 75 percent hook bounce followed by one cycle of limit hook bounce.

One specimen was tested in a lab air environment and the remaining specimens were tested in a salt solution environment. This environment was obtained by wrapping the flash weld portion of the hook shank in gauze saturated by a 3.5 percent salt water solution. The solution was applied frequently to maintain saturation.

Previous fatigue testing had located the area where fatigue cracking and failures were expected. This was on the shank lower surface in the immediate vicinity of the flash weld closest to the lugs. In order to initiate cracks in this location with a minimum amount of cyclic test time, provisions were made for preflawing some of the specimens.

Preflaws were induced using electrical discharge machining (EDM) techniques to produce an ELOX slot. This slot, being a small sharp notch, acts as a crack starter and controls the location of initiating cracks. A schematic showing the shape and location of the ELOX is presented in Figure 9.

ANALYSIS OF TEST DATA

Critical Locations

Failures occurred at three primary locations in the shank (see Figure 10): (1) the shank lower surface (LS) in the immediate vicinity of the flash weld closest to the lugs, which was the expected failure location; (2) the shank upper surface (US) of the weld closest to the lugs; and (3) from cracks originating under the bushing in the shank upper lug (UL). All three locations are critical. Hook shanks which fail in these locations may cause partial arrestment resulting in damage to or possible loss of an aircraft.

Critical Crack Depths and Flaw Shapes

Critical crack depths and flaw shapes for all tests were determined from post examination fractographic analysis. The results are shown in Table I.

Flaws which resulted in failures in the LS weld area can be grouped according to shape or aspect ratio. Aspect ratio (a/2c) is the ratio of

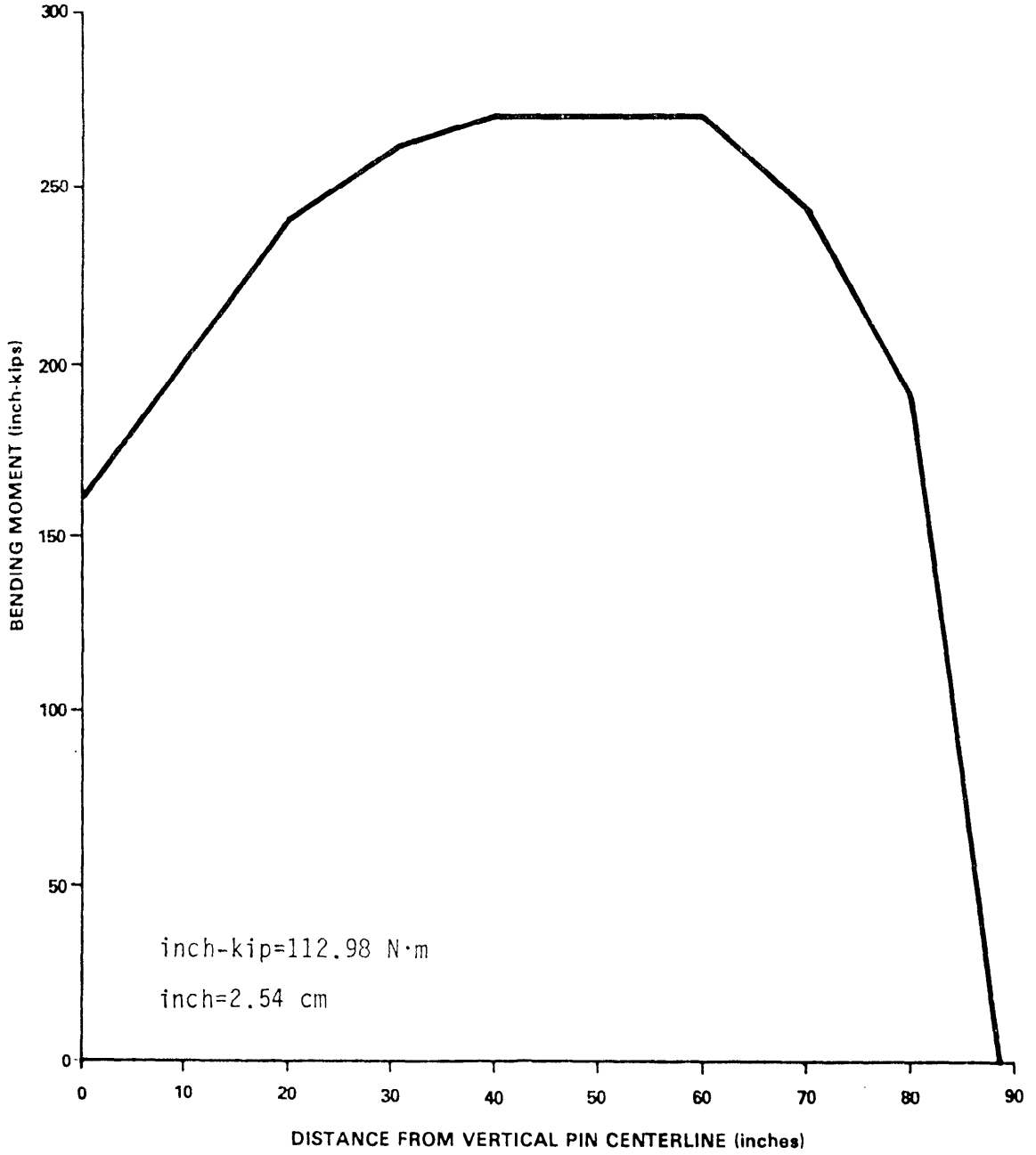

Figure 5 **Limit Hook Bounce Bending Moment Curve**

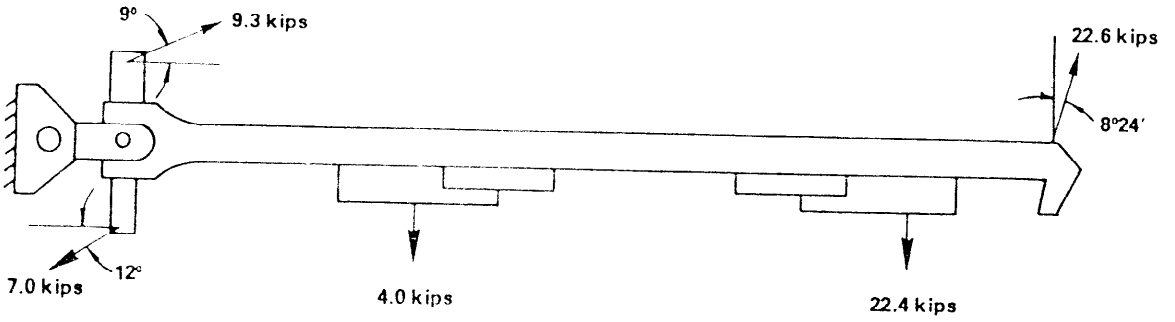

Figure 6 **Limit Hook Bounce Loading**

kip=4.4482 x10^3 N

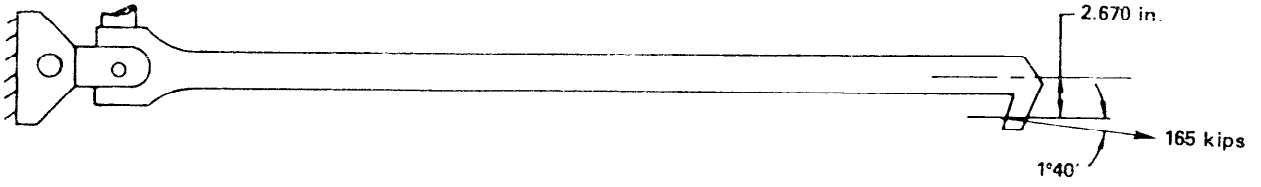

Figure 7 **Arrestment Loading for Cable Run Out**

inch=2.54 cm

kip=4.4482 x10^3 N

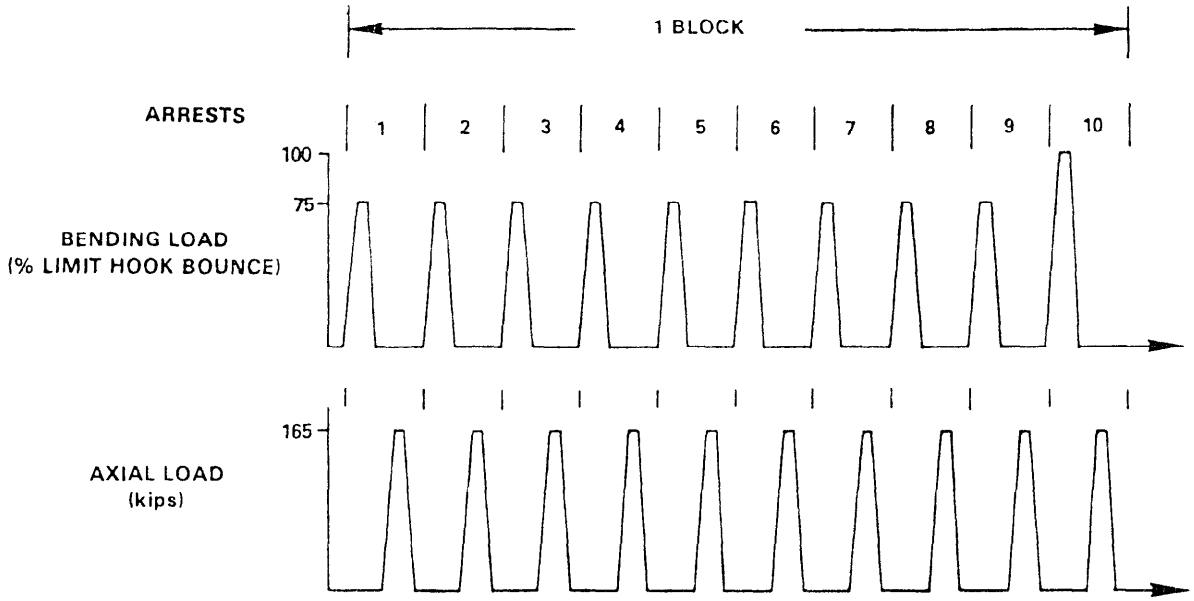

Figure 8 **F-14 Hook Shank Repetitive Spectrum**

kip=4.4482 x10^3 N

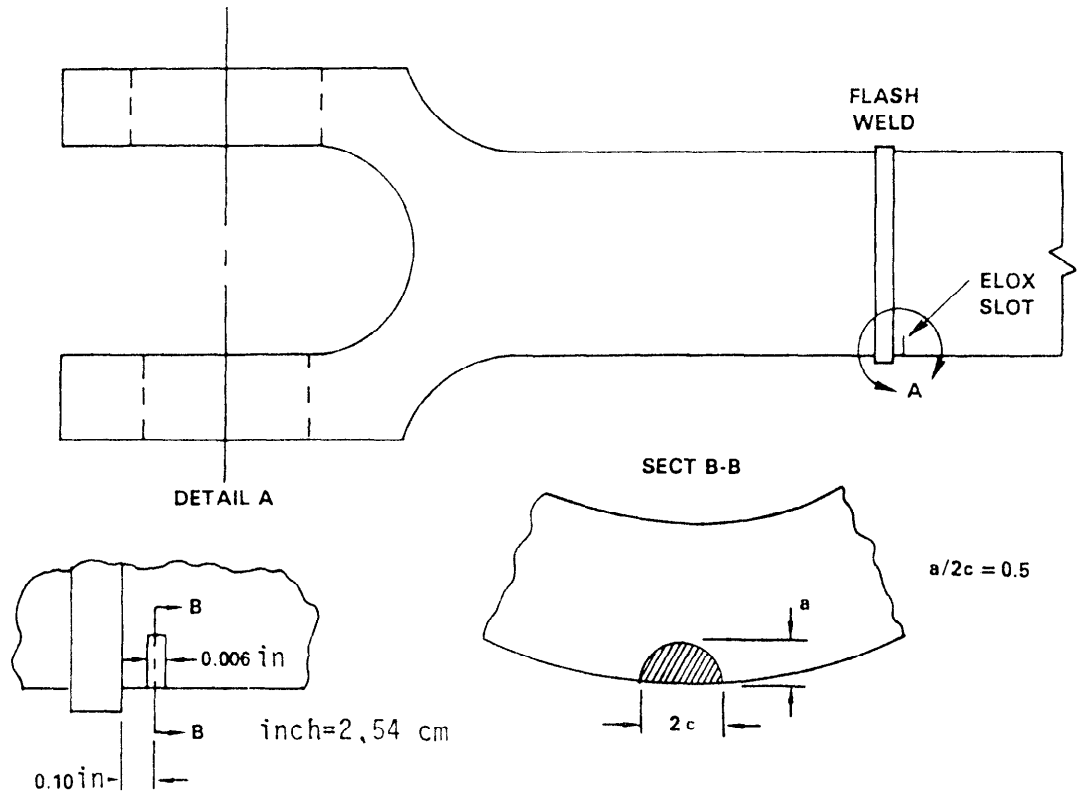

Figure 9 **Shape and Location of ELOX Preflaw**

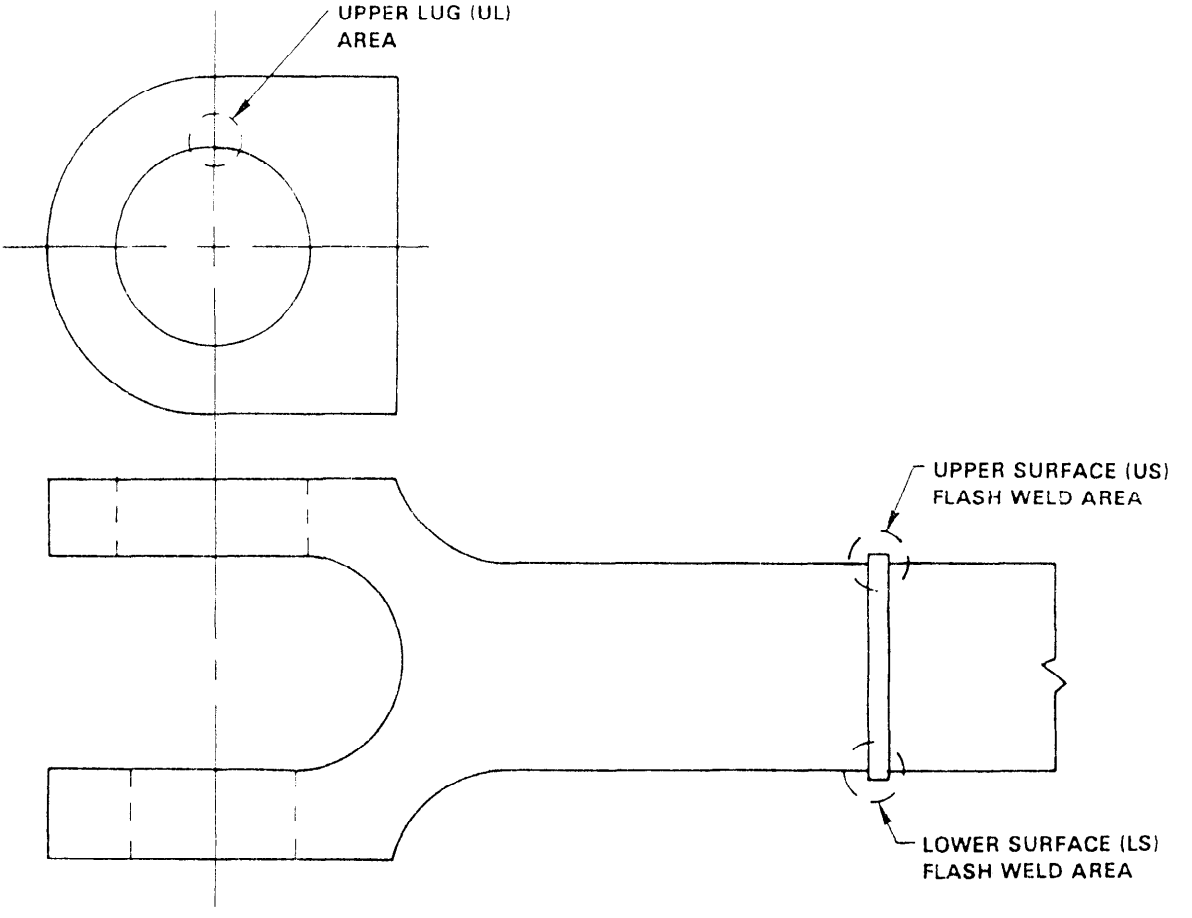

Figure 10 **Failure Locations**

TABLE I. F-14 HOOK SHANK TEST
FLAW ASPECTS RATIOS

TEST NUMBER	CRITICAL CRACK DEPTH, a_{cr}	SURFACE CRACK LENGTH, 2c	ASPECT RATIO, a/2c	LOCATION
1	0.095 in.	0.165 in.	0.6	LS
2	0.080	0.200	0.4	LS
3	0.060	0.510	0.1	LS
4	0.110 (1)	1.070 (2)	0.1	US
5	0.095	0.160	0.6	LS
6	0.090	0.125	0.7	LS
7	0.085	0.210	0.4	LS
8	0.080	0.180	0.4	LS
9	0.110	0.210	0.5	UL
10	0.040 (1)	0.270 (2)	0.1	LS
11	0.075	0.160	0.5	LS
12	0.190 (3)	0.240	0.4	LS
13	0.080	0.300	0.3	LS
14	0.060	0.670	0.1	US
15	0.070	0.580	0.1	US
16	0.110	0.170	0.6	US

NOTES: (1) AVERAGE OF TWO ADJACENT FLAW DEPTHS.

(2) COMBINATION OF TWO ADJACENT FLAWS.

(3) EMBEDDED ELLIPTICAL FLAW

(4) LS - LOWER SURFACE, US - UPPER SURFACE, UL - UPPER LUG

crack depth to surface crack length. Two failures (Tests 3 and 10) resulted from long, shallow flaws with a/2c = 0.1. The remaining failures were caused by near semi-circular flaws ($0.3 < a/2c < 0.7$).

Three failures which occurred in the US weld area (Tests 4, 14, 15) also had long, shallow flaws. The aspect ratio was 0.1 and the crack depths were 0.110, 0.060 and 0.070 inches (0.279, 0.152 and 0.178 cm) respectively.

Only one failure (Test 9) occurred in the UL section. The flaw was semi-circular in shape (a/2c = 0.5) and had a depth of 0.110 inch (0.279 cm).

Crack Growth Behavior

Crack growth was monitored during fatigue testing by visually inspecting the critical area using a mounted microscope (20X) and portable light source, as well as a fluorescent penetrant. Both techniques proved to be ineffective in detecting the existence and length of surface cracks. Due to the inability to obtain surface crack growth data during testing, the crack growth behavior was obtained utilizing the exhibited lives of the preflawed test specimens.

Crack growth behavior can be determined using the Paris crack growth equation

$$\frac{da}{dN} = C(\Delta K)^n \qquad (4)$$

where $\frac{da}{dN}$ = crack growth rate, inch/cycle (cm/cycle)

ΔK = stress intensity factor range, ksi $\sqrt{\text{in.}}$ (MPa $\sqrt{\text{m}}$)

C, n = material constants

Assuming that the preflaw began growing immediately upon cycling, a crack growth rate relationship in terms of material constants C and n can be determined. Using average values of da/dN and ΔK computed from the preflawed specimen tests, a least-squares linear regression was performed to determine material constants of $C = 8.561 \times 10^{-9}$ and $n = 2.032$. In order to be conservative, since crack growth does not occur immediately and in actuality is not constant, C was fixed and n was adjusted upward to a value of 2.2. Using these values ($C = 8.561 \times 10^{-9}$, $n = 2.2$), good correlation was achieved between initial flaw depth (a_i) versus cycles to failure (ΔN) predicted from the derived da/dN and the actual test data

(Figure 11). In addition, a best-fit linear regression analysis of the test points shows good agreement with the predictions.

Therefore, using this crack growth rate, initial flaw size versus remaining cycles was analytically determined for all critical locations. These curves, Figures 12-15, form the basis for proof load selection and include a 3.5 percent salt solution environment and a scatter factor of 2 on life (arrestments).

Residual Strength

In order to establish the significance of the proof test, data was generated which described residual static strength as a function of crack size. The residual strength versus flaw depth relationship is shown in Figure 16. It can be seen that the test data fits the analytically determined curves for flaw aspect ratios (a/2c) of 0.1 and 0.5 very well.

SELECTION OF PROOF LOAD AND INTERVAL

The long, shallow flaws (a/2c = 0.1) occurring in the LS weld area give the shortest shank life and therefore become the focal point for proof load selection. The largest acceptable axial proof load of 244 kips (1.085 MN), based upon local yielding of the attachment lugs, produces only enough stress in the LS weld to qualify the hook shank for one arrestment cycle. A higher stress is required; therefore, a bending proof load was selected.

A bending load of 134 percent limit hook bounce produces the published minimum yield strength of 300M steel of 230 ksi (1585 MPa) in the LS weld area. Using Figure 16, the maximum size of an undetected crack at this stress level is
a = 0.022 inch (0.056 cm). From Figure 12, a 0.022 inch (0.056 cm) initial crack size (a/2C = 0.1) will not grow to failure in less than 125 arrestment cycles for a maximum operating load of 165 kips (0.734 MN). This life is based on the curve which includes a scatter factor of 2.

For the near semi-circular flaws ($0.3 < a/2c < 0.7$) which also occur in the LS weld area, a 230 ksi (1585 MPa) stress will "proof out" a crack of a = 0.048 inch (0.122 cm). A 0.048 inch (0.122 cm) initial crack, see Figure 13, will not grow to failure in less than 380 arrestment cycles. Therefore, a bending proof load of 134 percent limit hook bounce with a proof-load interval of 125 arrestment load cycles was selected for the LS weld area.

A bending load produces compressive stresses in the other two critical locations. Therefore, an axial proof load must be applied in order to proof the US weld area and the shank UL. The axial proof load was selected based upon the same 125 arrestment interval used previously. The US weld area was the focal point for the determination of the axial proof load.

Figure 14 indicates that a 0.066 inch (0.168 cm) initial crack will

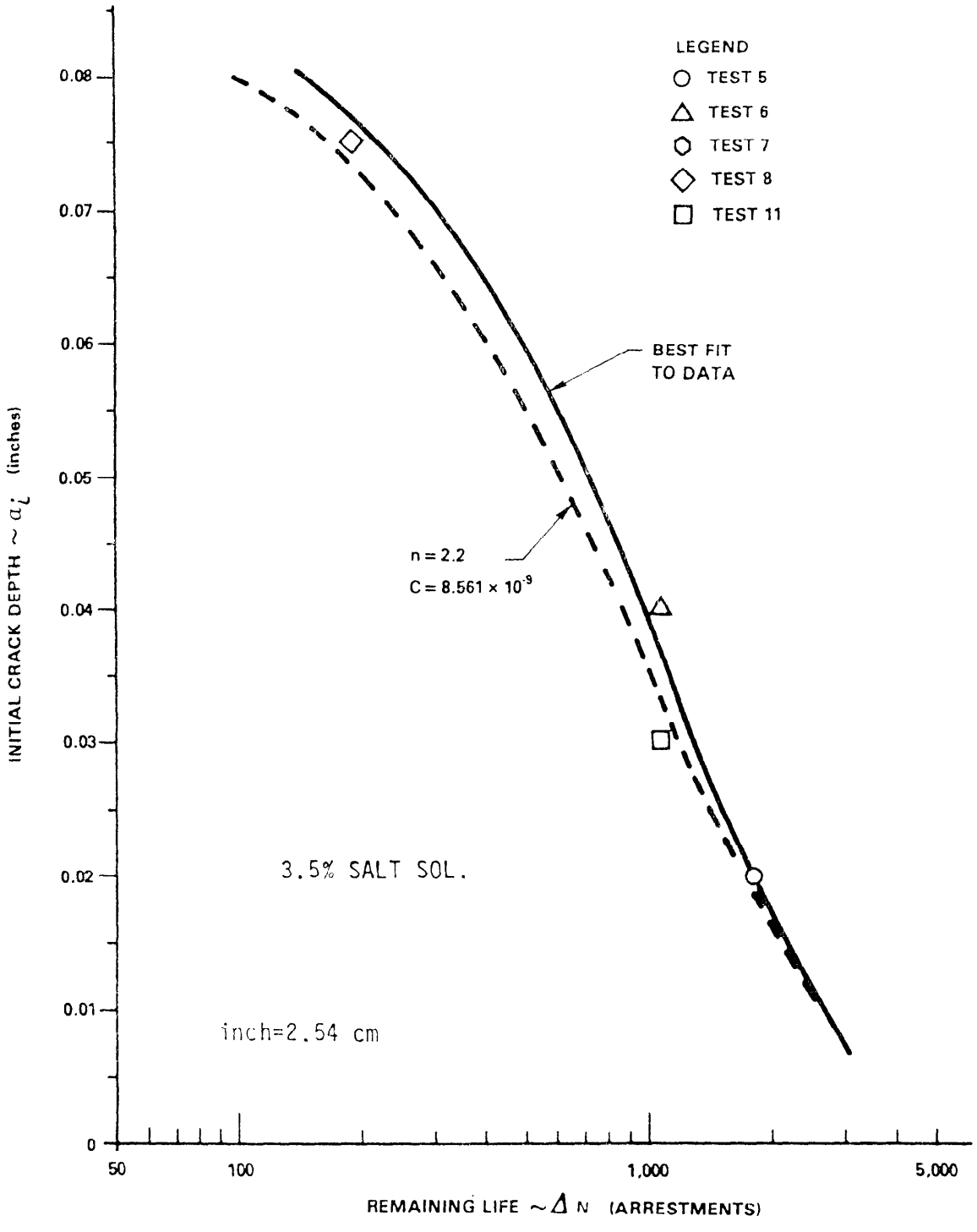

Figure 11 **Test Results of Preflawed Specimens**

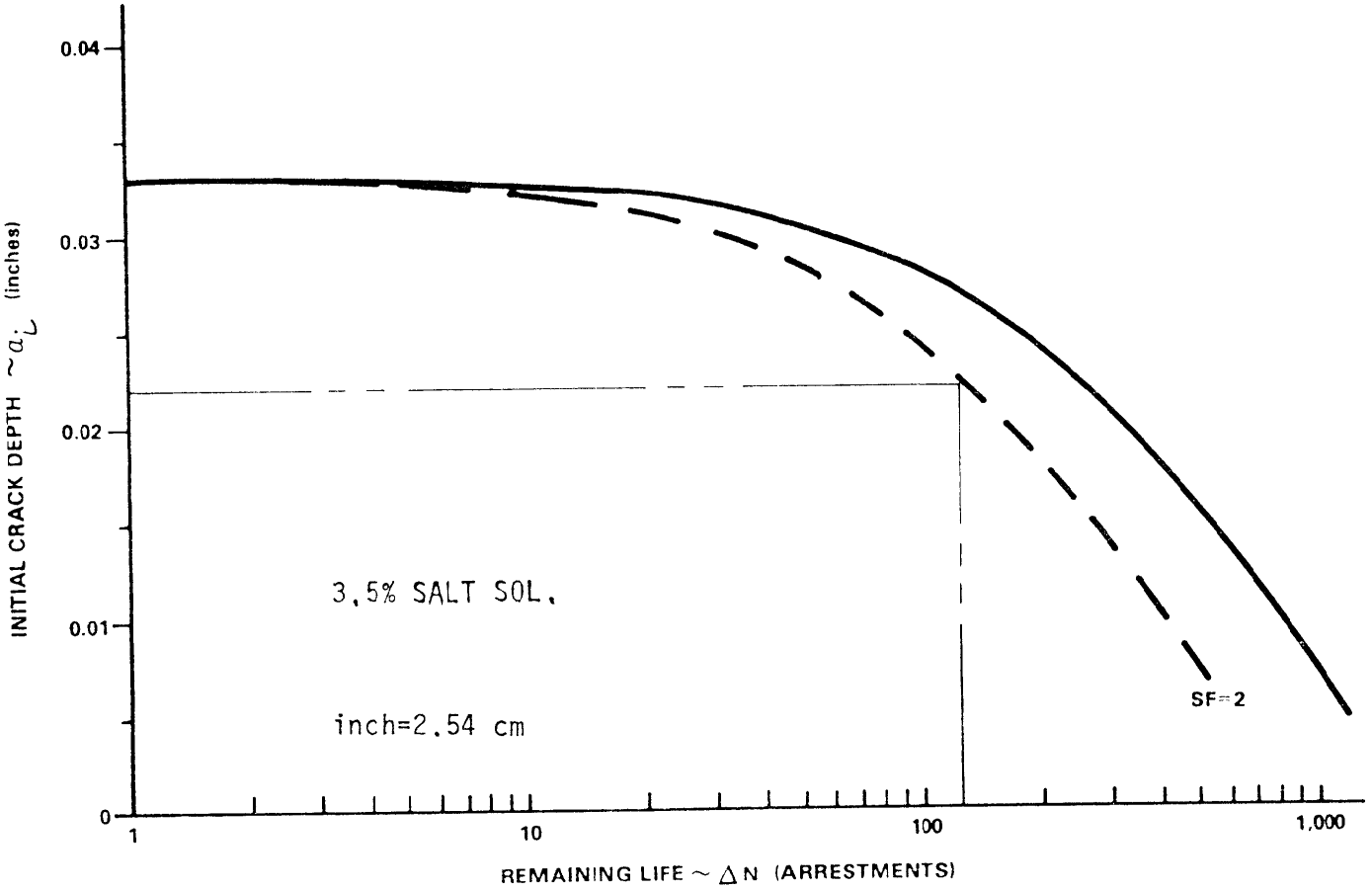

Figure 12 **Remaining Life for Lower Weld (LS) Area (a/2C=0.1)**

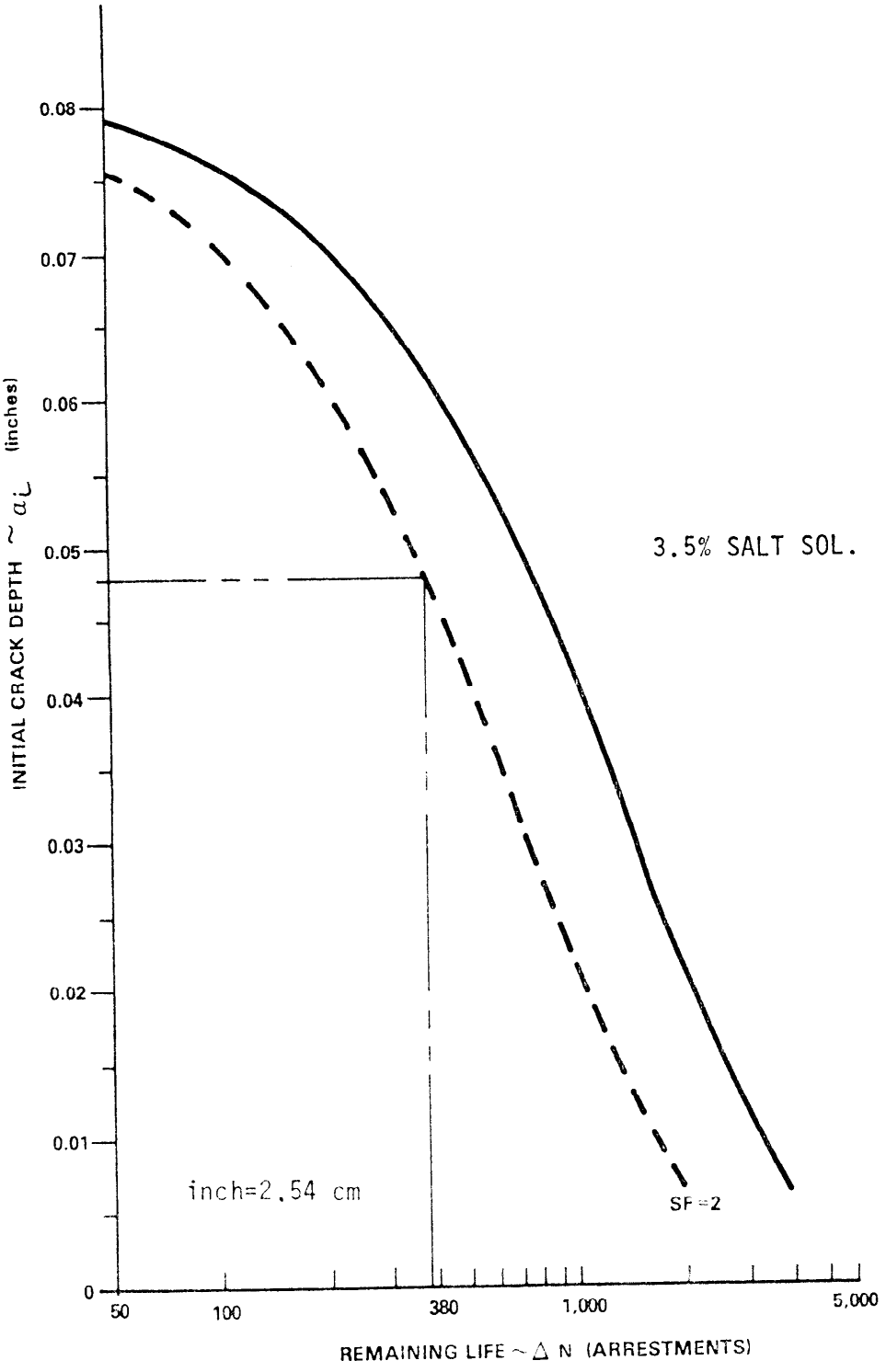

Figure 13 **Remaining Life for Lower Weld (LS) Area (a/2c=0.5)**

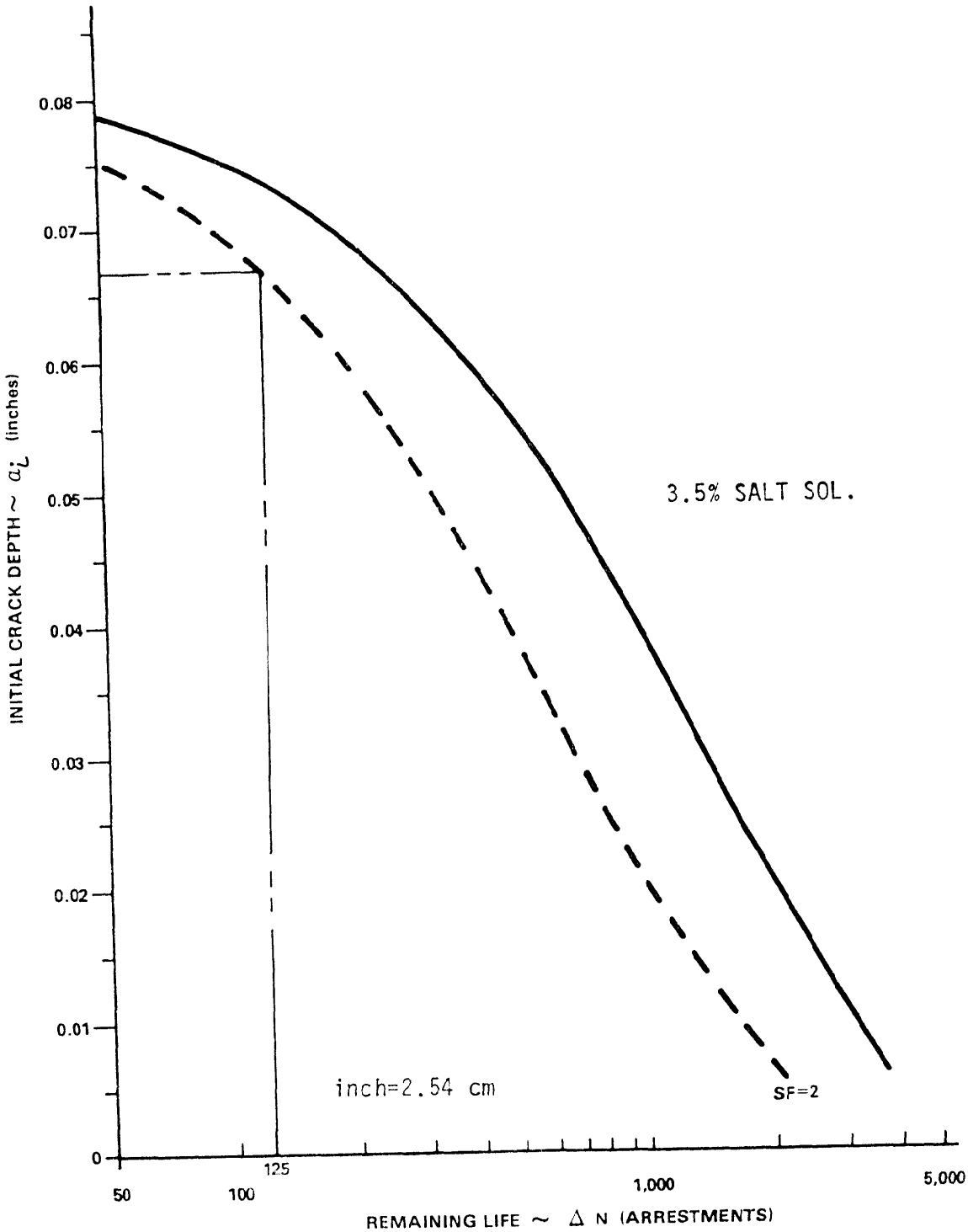

Figure 14 **Remaining Life for Upper Weld (US) Area (a/2c=0.1)**

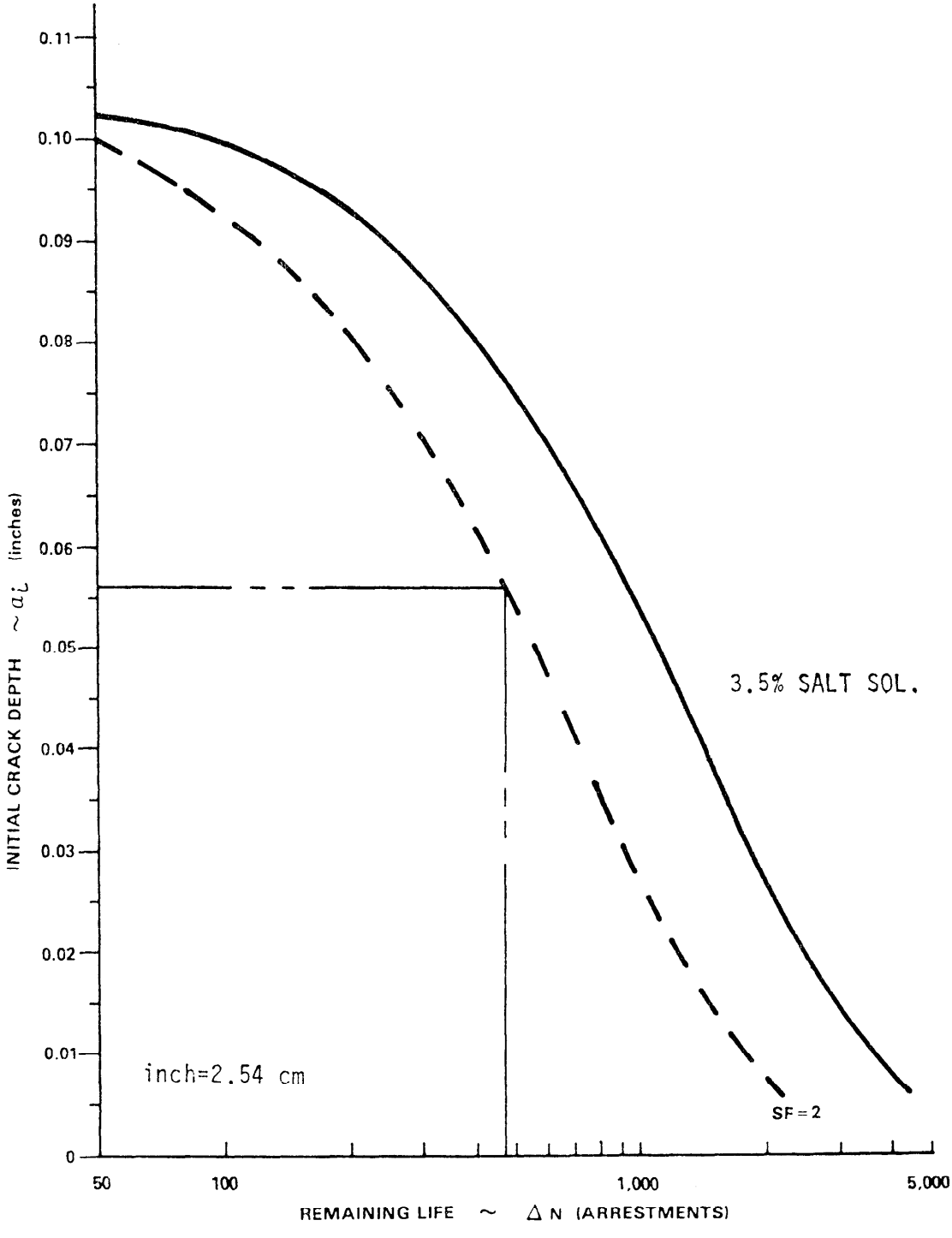

Figure 15 **Remaining Life for Upper Lug (UL) Area (a/2c=0.5)**

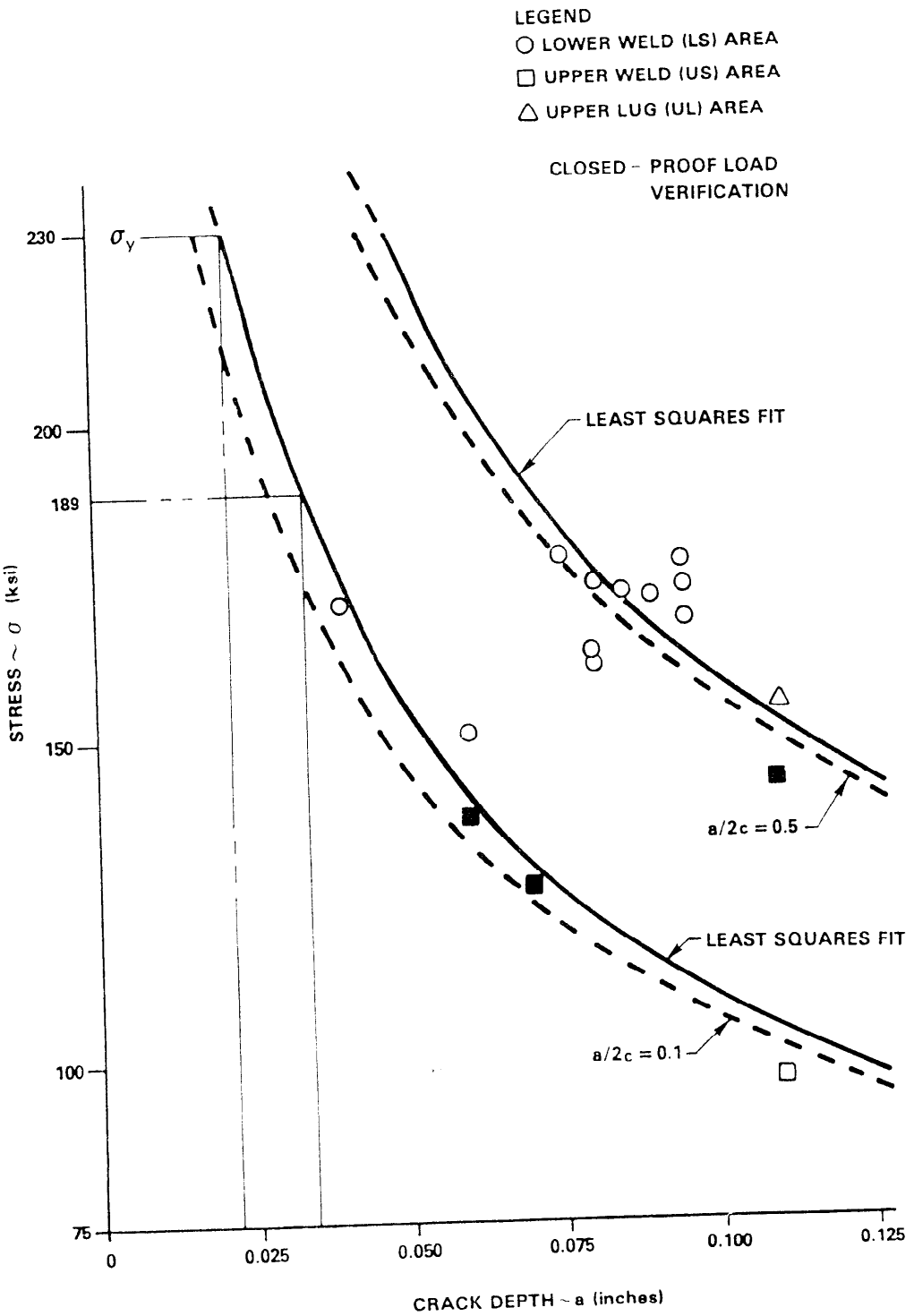

Figure 16 **Residual Strength as a Function of Flaw Size**

inch=2.54 cm

ksi=6.8948 MPa

not grow to failure in less than 125 arrestments. In order to proof a crack of this size a stress level of 134 ksi (924 MPa) must be achieved (see Figure 16). A 226-kip (1.005 MN) axial load produces the required 134 ksi (924 MPa) stress in the US weld area. The same 226 kip (1.005 MN) axial load will 'proof out' a crack of a = 0.056 inch (0.142 cm) in the UL section. An initial crack of this size will not grow to failure in less than 475 arrestments (Figure 15), well past the desired 125 arrestment interval.

Therefore, the verification tests were conducted using a two-phase proof load, axial followed by bending, applied with a proof-load interval of 125 arrestment load cycles. A summary of the proof loads and the corresponding arrestment intervals is presented in Table II.

VERIFICATION TESTING

The last three hook shank tests were designed to verify the proof-load/inspection interval concept as applied to this component. For a given proof load and proof-load interval, acceptable results are based on two conditions: (1) fatigue failures do not occur between proof loads (in other words, failures occur only at proof load application), and (2) the magnitude of the proof load is not detrimental to the subsequent service life interval for surviving components.

It should be pointed out that the use of this proof test criteria in service should not imply that hook shanks with detectable cracks would be allowed to continue on the aircraft. The proof test is designed as a safety measure to accompany standard inspection techniques which may in some cases overlook existing cracks. Any shank found to be cracked would, of course, be removed and replaced in service.

The verification tests were conducted to determine the end result assuming that the cracks went undetected. A summary of results for the three verification tests is presented in Table III.

Each specimen was tested to block spectrum loading where each block contained 113 cycles of 75 percent limit hook bounce, 12 cycles of limit hook bounce, and 125 cycles of 165 kips (0.734 MN) axial load. Each 125 arrestment block of loads was followed by a static two-phase proof test. The proof test consisted of an axial load of 226 kips (1.005 MN) followed by 134 percent limit hook bounce bending, each held for one minute.

The results show that all failures occurred during the proof load. This indicates that the 125 arrestment interval is indeed compatible with the two-phase proof load. Therefore, a hook shank that passes the proof test can be expected to last for a minimum of 125 more arrestment cycles.

CONCLUSIONS

The primary location for crack initiation is on the lower surface of

TABLE II. PROOF LOAD SUMMARY

Critical Location	AXIAL P. L. 226 KIPS a_i	Arrest. Interval	BENDING P. L. 134% LIMIT HOOK BOUNCE a_i	Arrest. Interval
LS (a/2c = 0.1)	0.034	1 (1)	0.022	125
(a/2c = 0.5)	0.071	96 (1)	0.048	380
US	0.066	125	-	-
UL	0.056	475	-	-

NOTES: (1) BASED ON LARGEST ACCEPTABLE AXIAL PROOF LOAD OF 244 KIPS (1.085 MN).

TABLE III. VERIFICATION TESTS FOR PROOF LOADS

AT 125-ARRESTMENT INTERVALS (1)

TEST NUMBER	NO. OF PROOF LOAD INTERVALS (3)	TOTAL LIFE (ARRESTMENTS)	FAILURE LOCATION
14	14	2400 (2)	US DURING AXIAL P.L.
15	40	5000	US DURING AXIAL P.L.
16	15	1875	US DURING AXIAL P.L.

NOTES: (1) EACH 125-ARRESTMENT BLOCK CONTAINS 113 CYCLES OF 75% LIMIT HOOK BOUNCE AND 12 CYCLES OF LIMIT HOOK BOUNCE.

(2) 650 ARRESTMENTS WERE APPLIED BEFORE THE START OF THE 125-ARRESTMENT PROOF LOAD SEQUENCE.

(3) PROOF LOAD HELD FOR 1 MINUTE IN EACH PHASE (AXIAL AND BENDING) AFTER EACH BLOCK.

the shank in the immediate vicinity of the flash weld closest to the lugs. The upper surface around this flash weld, as well as the upper attachment lug, become likely spots for crack initiation under extended service life.

The original service criteria called for a 160 kip (0.712 MN) axial proof load after every 100 arrestments. This program demonstrated that this criteria did not assure any remaining life for the hook shank.

The two-phase proof load (226 kips (1.005 MN) axial, 134 percent limit hook bounce) used in the verification testing qualifies the hook shank for 125 subsequent arrestments under a maximum operating load of 165 kips (0.734 MN). Based on verification tests, the proof load effectively tests for flash weld area cracks as well as cracks in the upper attachment lugs. All failures occurred during the proof load.

ACKNOWLEDGMENT

This investigation was conducted at Vought Corporation, Dallas, Texas, by the Structural Life Assurance Group of the Structures Development Section for the Naval Air Systems Command, Washington, D. C., under contract number N00019-80-C-0640.

REFERENCES

1. Jordan, K. D. and Dumesnil, C. E., "Structural Evaluation of the F-14 Arresting Gear Shank," Vought Report No. 2-51220/2R-53062, March 1982.

2. Tiffany, C. F. and Masters, J. N., "Applied Fracture Mechanics," Fracture Toughness Testing and Its Applications, ASTM STP 381, American Society for Testing and Materials, 1965, 249.

EVALUATION OF THE RELATIVE HYDROGEN EMBRITTLEMENT SUSCEPTIBILITY OF ESR/VAR 4340 STEEL

L. RAYMOND, Ph.D.
Mettek Laboratories
Santa Ana, California 92705

C. BENEKER
Bertea Controls Systems Division
Parker Hannifin Corporation

ABSTRACT

A test program was conducted to compare the relative hydrogen embrittlement susceptibility of 4340 steel with ESR and VAR remelt methods. The issue of ESR's susceptibility to hydrogen embrittlement arose when unexpected difficulties arose with critical parts on Army helicopter programs. High strength 4340 ESR steel is used in the control system actuators of these helicopters because of 4340 ESR's demonstrated superior ballistic tolerance. The conclusion was reached that 4340 ESR is more susceptible to hydrogen embrittlement than VAR. Of the various test methods evaluated, the step-load, Charpy-modified, cathodically polarized test method produced the most meaningful results within the framework of fracture mechanics.

INTRODUCTION

On July 2, 1979, Aviation Week announced that an Army helicopter was grounded because of a hydrogen embrittlement problem encountered in the main rotor control pistons. The problem encountered was attributed to an attempt to strengthen steel (HRC 50 and above) for increased resistance to small arms fire. While the grounding was in effect for six weeks the manufacturer of the main rotor flight controls had to supply new hardware which did not have the embrittlement problem and which still met the specified ballistic tolerance. Paralleling this effort, the manufacturer was utilizing the same high strength steel on another Army helicopter control system. Corrective actions also needed to be implemented on this program prior to a potential interruption of its flight test schedule.

The corrective actions consisted primarily of utilizing heavier, lower strength (180-200 Ksi) 4340 ESR parts for certain applications, and elimination of electrolytic plating wherever possible.

After the urgent problem of restoring the helicopters to flight status was resolved, unanswered questions remained as to why the manufacturer was unable to contain the hydrogen problem, in spite of what the experts agreed to be proper and prudent processing and heat treatment controls. The possibility suggested itself that 4340 ESR was more susceptible to hydrogen embrittlement than vacuum melted 4340, since the latter had been successfully used by the manufacturer without undue hydrogen problems. To investigate this possibility, the Army awarded a research contract. The primary findings of this investigation will be presented here.

However, before delving into the test results and work in progress, background information will be given regarding the reason for using ESR steel and some of the events culminating with the aforementioned grounding.

BALLISTIC TOLERANCE REQUIREMENTS

The threats which the flight controls must tolerate without a critical failure mode are as shown:

.30 Caliber	7.62mm	2550 ft/sec
.50 Caliber	12.70mm	1600 ft/sec

The control systems of recent Army helicopter designs have been qualified to the above requirements.

APPROACHES FOR ACHIEVING BALLISTIC TOLERANCE

To achieve ballistic tolerance, two basic approaches were used. First, piston heads and glands have patented break-away features, so that a certain amount of petalling or protrusions can be cleared with the force available from one intact hydraulic system. This approach provides only partial ballistic tolerance.

To achieve the total specified tolerance, some threats have to be defeated outright. For this purpose ESR steel, 4340 in particular, has been found to be superior, that is, most weight efficient. Extensive testing by the Army has led to this conclusion, and the manufacturer's limited testing has confirmed this.

PARTS MADE FROM 4340 ESR

A total of 31 control actuator parts were made from 4340 ESR steel. But the problem of hydrogen embrittlement was only encountered on parts, or their embrittlement coupons, which were electrolytically plated, that is, primarily chrome plated piston rods. Two typical piston configurations are shown on Figure 1.

The ensuing discussion will deal primarily with a main rotor piston. This piston was the trailblazer as regards problem identification and corrective action pertaining to experience with 4340 ESR steel.

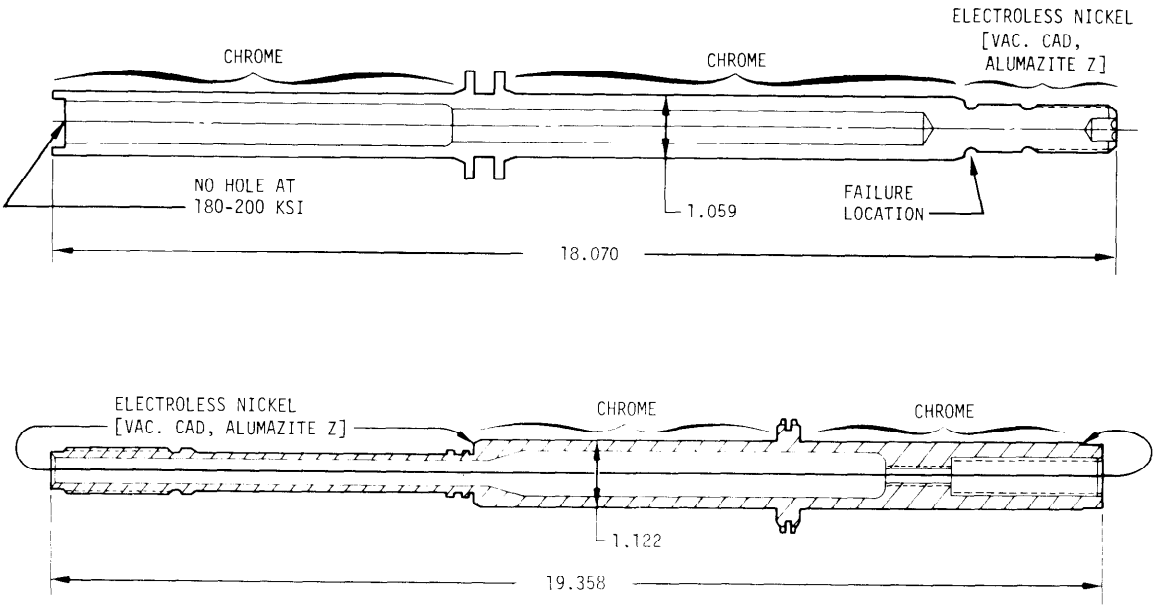

FIGURE 1. Typical Piston Configurations

THE FIRST PISTON FAILURE

Initially the problem of hydrogen embrittlement was not identified as cause for reduction of strength level. In retrospect this can be attributed to the fact that a secondary problem had contributed to the failure.

The first failure was found by the manufacturer in May, 1978, on a unit which had been returned from the field for a reason unrelated to the piston failure. Upon metallurgical examination a very small pre-existing thumbnail crack (approximate depth .050 with aspect ratio 0.1) was found at the failure origin. From this small pre-crack the failure had progressed in a manner suggesting hydrogen embrittlement (intergranular cracking).

It was not at all clear if a failure could have occurred without the pre-crack, or quench crack as it was later determined. Hence, aside from initiating hydrogen embrittlement controls, which later turned out to be ineffective, considerable emphasis was placed on the cause and elimination of the quench crack.

Upon careful inspection of all pistons, it was found that several others exhibited small quench cracks in the failure location. Although many suggestions were pursued in trying to eliminate these cracks on new heat treat lots, only one method proved effective. That was a change to using a salt furnace in place of a vacuum furnace for austenitizing the parts during the heat treat cycle. It is interesting to note that in making this change, not only did the quench cracking problem cease, but the distortion of parts in heat treatment was significantly reduced to

approximately 1/3 of what had been experienced on these parts. The explanation for this is that a vacuum furnace must use a colder quenching medium and hence, produces a greater thermal shock.

While the quench crack problem was being investigated and resolved, the hydrogen embrittlement problem was also addressed. In order to minimize exposure to hydrogen evolving processes, nickel plating in the failure area was replaced by vacuum cadmium covered by Alumazite Z. (The latter being necessary as a barrier between cadmium and titanium rod end.) Processing steps were carefully reviewed by various experts, and certain changes were made. But most significantly, two allegedly tried and proven hydrogen embrittlement detecting measures were initiated.

1. Every lot of electrolytically plated parts was accompanied by 5 embrittlement coupons made from the same material ingot as the parts. The notched embrittlement coupons were then loaded to 75% of their breaking strength for 200 hours.

2. Each individual piston was subjected to a load for 200 hours, producing a nominal tension stress at the critical cross section equivalent to 56% of the material yield strength. Considering stress concentration effects, local peak stresses exceeded the material yield strength. Failure of a single piston was cause for rejection of the entire lot.

These controls were in effect at the time of the second piston failure.

THE SECOND PISTON FAILURE

When the second failure occurred, there was considerable consternation when hydrogen embrittlement was identified as the cause. This time there was no quench crack associated with the failure to mitigate the hydrogen contribution to the failure. Yet, how could hydrogen be the cause with extra careful controls and monitoring as effected on these parts?

The seriousness of this failure was discussed and one consideration was that of redundancy. Since the main rotor control is a two parallel actuator arrangement, and since single system (i.e. one piston failed) operation was a design criterion, it was conceivable that an isolated piston failure could be tolerated.

While this was being discussed, a field returned actuator package arrived at the manufacturer's facility. Upon opening the shipping crate both actuator pistons were found to be severed. The responsible shipping personnel assured us that they had seen nothing amiss at time of shipment. Apparently both pistons had failed during transit.

SOLUTION TO HYDROGEN EMBRITTLEMENT

Since the established methods for hydrogen embrittlement control or detection had failed, the solution became one of avoidance. That is, the main rotor piston strength level was reduced to 180,000 psi. At this strength level hydrogen embrittlement can be successfully controlled by conventional processing. This same approach, lowering of strength level, was applied to certain other piston rods.

Lowering the strength level did compromise ballistic tolerance of the pistons, but they were still qualifiable to the requirements.

CONCLUSIONS BASED ON INDUSTRIAL EXPERIENCE

In view of the industrial experience, three conclusions can be drawn. These conclusions definitely apply to 4340 ESR and may apply to other high strength steels:

1. Successful testing of embrittlement coupons does not assure good parts.

2. Individual part testing, at 56% FTY for 200 hours, does not assure good parts. In fact, there is strong evidence to suggest that a sustained load test may initiate undetectable damage in the part.

3. The 200 hour time limit typically applied to sustained load hydrogen embrittlement tests is unrealistic. In some cases testing was continued past 200 hours, with failures occurring thereafter.

TEST PROGRAM, PHASE I - PERTINENT RESULTS

A test program was initiated to accurately evaluate the relative susceptibility of 4340 ESR/VAR steel.

For Phase I, five different versions of 4340 steel were evaluated, representing one air, two ESR and two VAR heats and two hardness levels.

Notched Round Bend (NRB)

Only the high hardness (about 53 HRC) notched round bend specimens could be successfully tested per ASTM F519. The lower hardness level (about 43 HRC) was too ductile to be broken in the bend fixture (Figure 2).

The purpose of this part of the program was to rank 4340 ESR from two different suppliers (labeled 4340B and 4340H), 4340 VAR plus a Si-modification (labeled 4340V and 4340M), and 4340 air melt (4340A) relative to their susceptibility to hydrogen embrittlement. All specimens were charged with hydrogen by cadmium plating per QQ-P-416C and omitting the final hydrogen

bake out treatment.

Two hydrogen charged specimens were loaded to fracture in order to determine the number-of-turns-to-fracture (NOTF). Figure 3 is a bar chart representing the different fracture load requirements and applied load levels. A 4340B specimen that was not plated is also included for comparison to illustrate the degradation due to hydrogen charging.

Four specimens were maintained at a load level of 0.75 NOTF. The time-to-fracture (TTF) in minutes is shown in Figure 4. The results suggest that (1) VAR is more resistant to hydrogen embrittlement than ESR or AIR melted 4340 steel; and (2) VAR-silicon modified 4340M was more resistant to hydrogen embrittlement than conventional 4340 VAR.

Figure 5 illustrates the significant degradation due to the introduction of hydrogen into the steel during cadmium plating per QQ-P-416C. Without plating, slightly more than 12 turns are required to fracture the specimen. Only 6-turns will fracture the specimen that has been plated. At a sustained load of 5-turns, the plated specimen breaks in less than 10 minutes; whereas the unplated specimen continues to run for greater than 10,000 minutes. When the load is increased to 9-turns, the specimen that was not plated, does not fracture even after 57,000 minutes. In fact, the specimen could not be fractured below the utlimate load determined in the initial fracture test. The purpose of this series of tests was to clearly illustrate the extent of strength degradation caused by residual mobile hydrogen introduced into the steel during the plating operation.

Another question answered by these tests is: "Does sufficient residual hydrogen exist in 4340 ESR to cause failure by hydrogen embrittlement?" These results strongly support the conclusion that sufficient residual hydrogen does not exist in as-processed 4340 ESR parts to cause hydrogen assisted cracking. Some external source of mobile hydrogen introduced during plating or other fabrication processes and possibly by in-service exposure must be the cause of many of the observed service failures. Although the other test results of this program do indicate that less of the mobile hydrogen is required to cause hydrogen assisted cracking in 4340 ESR steel than in 4340 VAR steel.

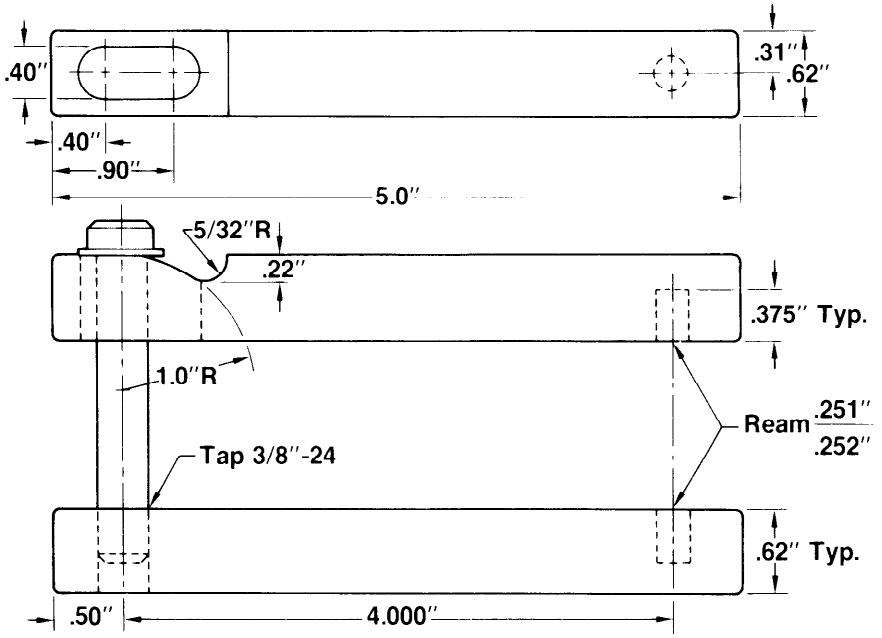

Figure 2. NRB Loading Bars

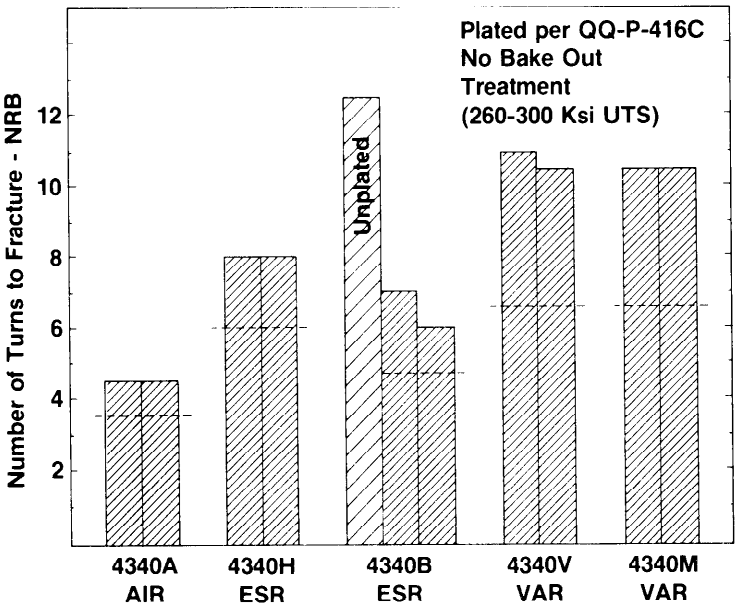

Figure 3. Notched Round Bend Strength (NBS) of Five High-Strength Conditions Tested in ASTM F519 Test Fixture

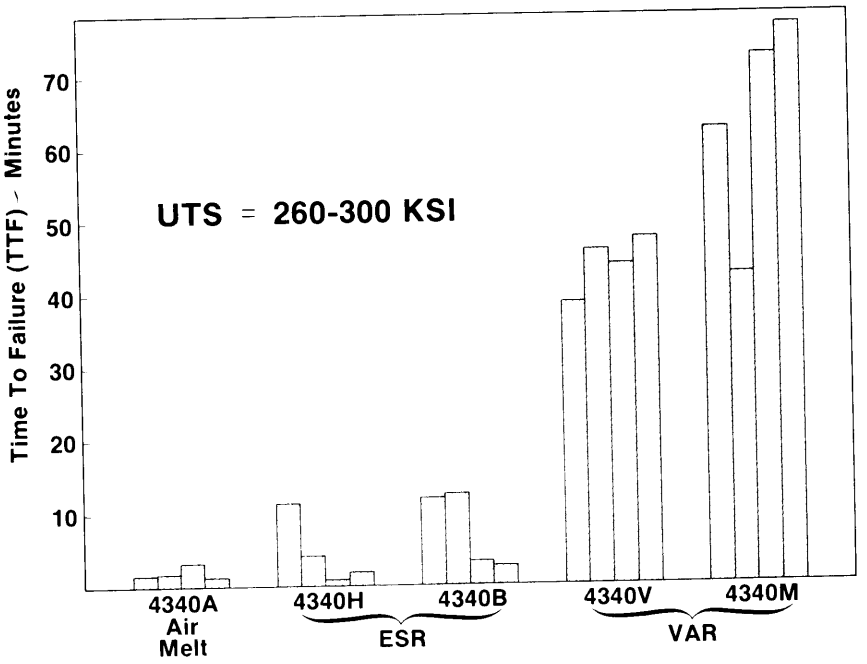

Figure 4. Time to Failure for High Strength Notched Round Bend Specimens Loaded in Air to 0.75 NOTF

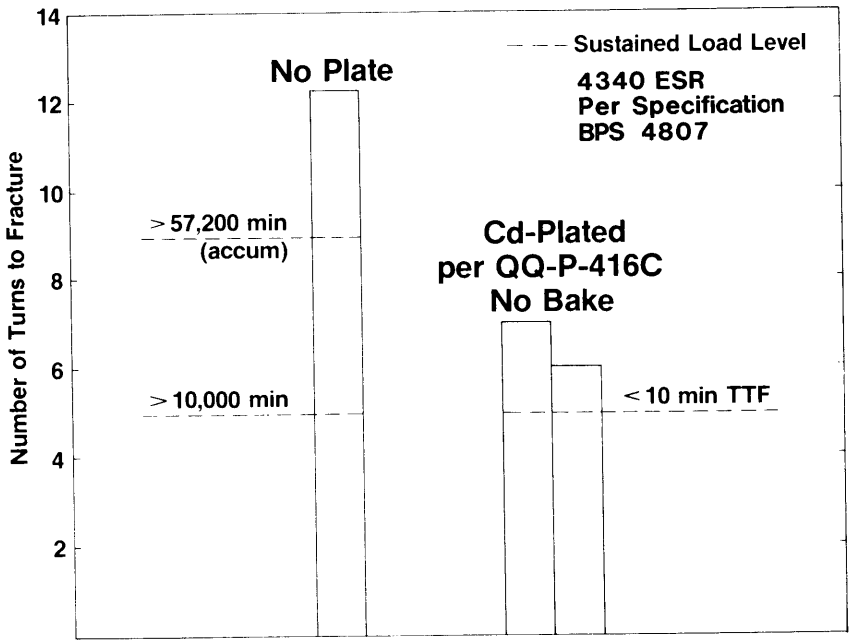

Figure 5. Degradation in Strength of 4340B Steel Due to Cd-Plating

TEST PROGRAM, PHASE II - PERTINENT RESULTS

While Task I compared five unrelated types of 4340, produced to different specifications, Task II is aimed at evaluating 4340 steel which is treated identically in every way except for the remelting process, ESR versus VAR. That is, the ESR steel and the VAR steel were derived from the same starting Argon Oxygen Degassed (AOD) ingot. Machining of test coupons, heat treating, processing and testing were conducted so as to assure equal treatment of ESR and VAR such that test result variations between the two types of specimens could be legitimately attributed to the remelting process. With regard to susceptibility to Hydrogen Embrittlement, several factors were considered: (1) three strength ranges, (2) two grain orientations, and (3) three test methods.

Notched Round Bend (NRB)
(Cd-Plated Test Specimens)

The contractor furnished machined NRB-specimens that represented two different grain orientations from the split 4340 ESR/VAR ingot. The test orientations were longitudinal and short transverse. The notched round bend strength was measured by installing the bend specimen in a test fixture as shown in Figure 2. The number of turns required to fracture one specimen, as-machined, with no surface treatments, was initially measured. Then a Cd-plated specimen that did not receive a hydrogen bake-out treatment, but instead a one hour, 300F homogenization treatment after plating per specification QQ-P-416C was also fractured. A fraction of the fracture load; i.e., six turns was used as sustained load during the TTF measurements.

The notched round bend strength as measured in number of turns for both the unplated and plated specimens is shown in Figure 6. As noted, the introduction of hydrogen from the plating process does cause a degradation in the strength, which is more significant in the ESR ingot than in the VAR ingot. The observation applies to all conditions tested, which includes two strength levels and two test directions. The lower hardness heat treatment was not used in this phase of the program because of the Task I experience which showed the method best suited for the high hardness steels.

The susceptibility to hydrogen embrittlement in the NRB test fixture is illustrated in Figure 7 where the TTF in minutes is plotted on a bar graph for the four conditions tested. As noted, the longitudinal orientation appears to have more resistance to hydrogen embrittlement than the short transverse orientation. In all cases, the VAR ingot performs as well or better than the ESR ingot. No clear advantage exists between the HP1-1 (290-320 Ksi) or BPS 4808 (260-290 Ksi) heat treatments.

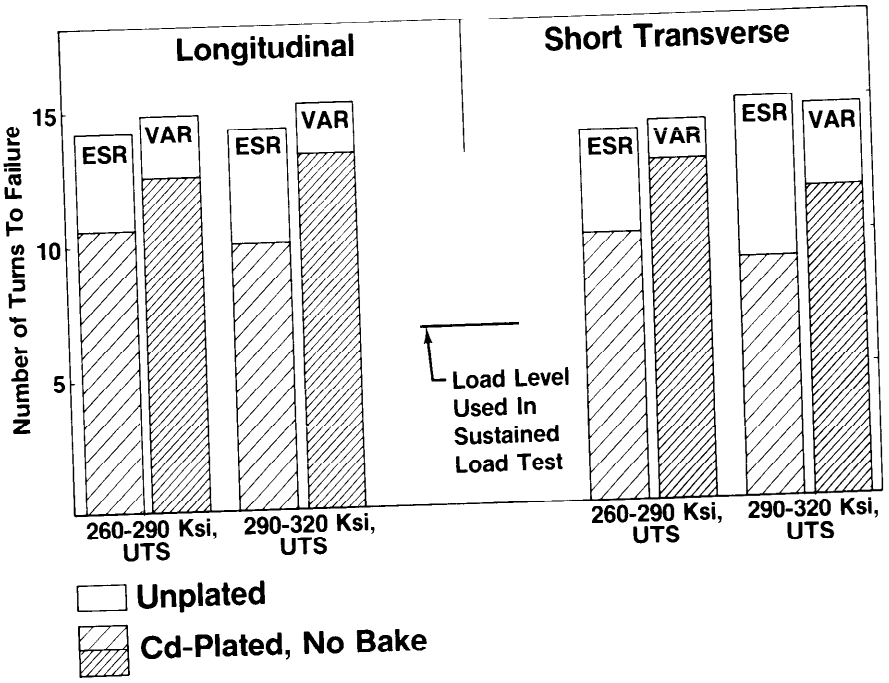

Figure 6. Notched Round Bend Strength for Cd-Plated and Unplated Specimens

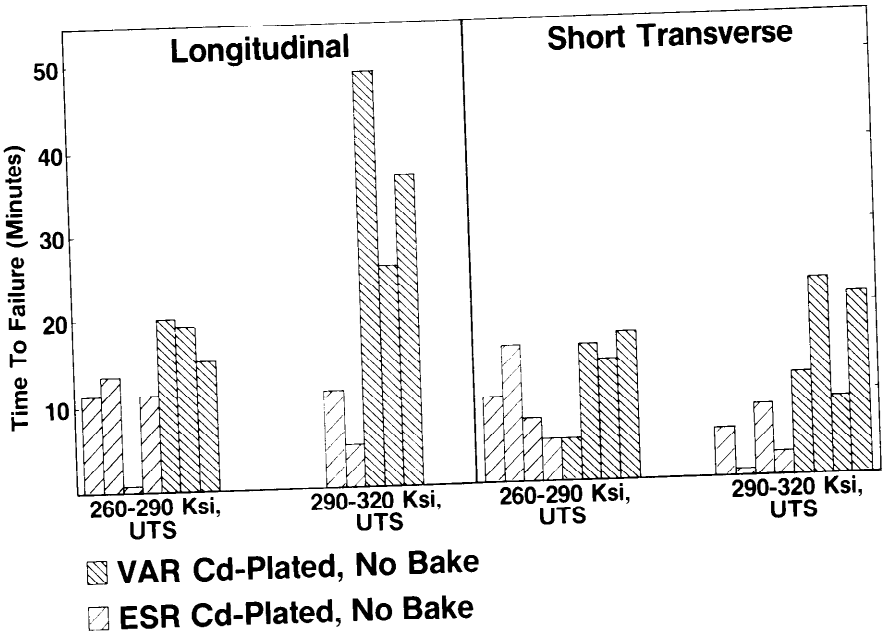

Figure 7. NRB-Sustained Load Test Results Loaded to 6-Turns in Air

Notched Round Tension (NRT)
(Potentiostatically Charged Test Specimens)

Notched round tensile bars with a threaded end were used to evaluate the susceptibility to hydrogen embrittlement of a split heat of 4340 steel at three hardness levels. The applied dead-weight or sustained load was at 75% of the notched tensile strength. In addition, a hydrogen environment was generated by using a test potential range from -0.9 to -1.1 volts vs SCE (Standard Calomel Electrode). A 3.5% salt water solution was used as the environment.

The loading sequence consisted of installing the NRT test coupon into a Satec 12-Kip sustained load creep frame with a very light load. The salt water solution was inserted into the Lucite container surrounding the test coupon. A level of the solution was maintained just below the notch area. At this point, the Standard Calomel, reference, and working electrodes were connected and the potential adjusted to the desired value. Once the potential was maintained, more solution was added until the level was above the notch; i.e., covered the notch. The 0.75 NTS load was then applied. At no time did the salt water solution come in contact with the upper threaded portion of the test sample. The lower thread was isolated from the environment.

The test program consisted of running three notched tensile coupons for each of six conditions in order to establish the NTS. The susceptibility to hydrogen embrittlement was then measured by recording the time-to-failure (TTF) in the salt water environment with the cathodic potential applied. Longer times imply greater resistance to hydrogen embrittlement cracking.

The test results were measured in minutes and are plotted on Figure 8 where the cathodic potential is on the vertical axis with a linear scale and TTF is on the horizontal axis with a logarithmic scale.

VAR is more resistant to hydrogen embrittlement at the highest cathodic potential (-1.1V) than ESR for the higher hardness (53 HRC). As the potential is decreased to -0.9V, the results appear to converge. For the lower hardness (43 HRC), the opposite appears to be true; i.e., VAR is more resistant than ESR at -0.9V and converges (or crosses) at -1.1V. No clear advantage exists with regard to the HP1-1 or BPS 4808 heat treatments.

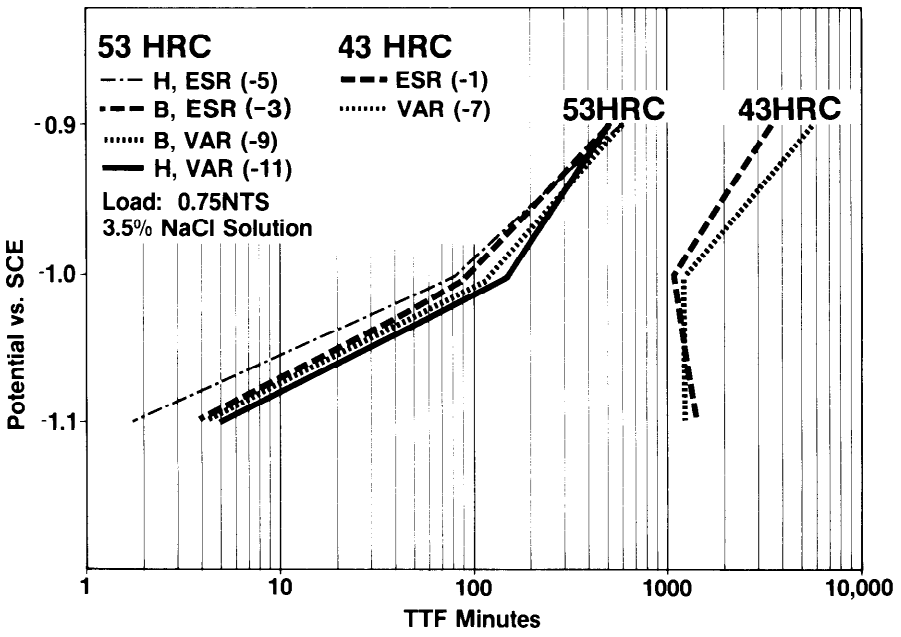

FIGURE 8. NRT Potentiostatic Test Results

EXPLORATORY WORK - In Progress

Step-Loaded CVN

Since neither the NRB or NRT test methods provide a design parameter such as KIscc, a test method developed by Raymond [1,2] for high-toughness ship steels was adapted for use with the 4340 ESR/VAR high-hardness steels. The method allows for determination of the threshold stress intensity (KIscc) and KIc with one side grooved Charpy V-notched (CVN) specimen. The hydrogen embrittlement test is completed in 8 hours, as compared to conventional test methods that use about one dozen test coupons, using one test machine for as long as 3,000 hours for each specimen.

The results of the test program are shown on Figure 9, where (1) VAR is seen having a higher threshold than ESR at both hardness levels, and (2) the threshold is higher for the lower hardness level, as expected.

Theory

The test fixture is a four point bend loading frame for a side-grooved, machine-notched, Charpy-sized specimen, where B = W = 0.394-in (10mm), a/W = 0.2, and B_N/B = 0.4. The bend equation where the maximum net local stress is given by:

$$\sigma_N = (36P/BW^2)/[(B_N/B)(1 - a/W^2)] \quad (1)$$

or,

$$\sigma_N(\text{Ksi}) = 2.3P \text{ (Kips)} \quad (2)$$

The test consists of step-loading in a cathodically polarized, 3.5% salt water environment until crack initiation begins. The stress corrosion or hydrogen embrittlement cracking index is given by

$$\text{NSR-SCC} = \sigma_N/\text{UTS} = 2.3\ [\text{P(Kips)}]/[\text{UTS(Ksi)}] \tag{3}$$

where P is the crack initiation load and UTS is the ultimate tensile strength that can be obtained from a hardness correlation.

Once the crack is initiated, the driving force can be expressed in terms of stress intensity, as per Tada [3], which in terms of the net stress is given by

$$K/\sigma_N = (1 - a/W)^2\ F(a/W)\ [\pi W(a/W)]^{\frac{1}{2}} \tag{4}$$

or approximated by

$$K/\sigma_N = 0.3\text{-in}^{\frac{1}{2}} \tag{5}$$

similar to the relationship derived by NMAB 328 [4] or,

$$K_{Ic}/\text{UTS} = 0.3\ \sigma_N/\text{UTS} = 0.3\ \text{Rsb} \tag{6}$$

or

$$K_{Ic} = (0.3\ \text{Rsb}).(\text{UTS}) \tag{7}$$

where Rsb is the specimen strength ratio per E399-81 and UTS is employed as per Succop and Brown [5].

Therefore, once slow crack growth has initiated and the sample pulled to fracture, the fracture toughness is then related to the fracture load $P_{a/W}$ by

$$K_{Ic} = 0.44\ \ P_{a/W}/(1 - a/W)^2 \tag{8}$$

or for a/W = 0.2

$$K_{Ic}(\text{Ksi-in}^{\frac{1}{2}}) = 0.69P_C\ (\text{Kips}) \tag{9}$$

Correspondingly,

$$K_{Iscc}(\text{Ksi-in}^{\frac{1}{2}}) = 0.69P_i\ (\text{Kips}) \tag{10}$$

Therefore, by step loading one Charpy-sized test specimen until crack initiation (P_i) occurs, the threshold stress intensity may be determined (Equation 10). Removing the sample from the hydrogen environment, baking for 24 hours at 300F and loading to fracture to measure P_C, provides the fracture toughness (Equation 9). To date, correlation with E399-81 test methods has been excellent.

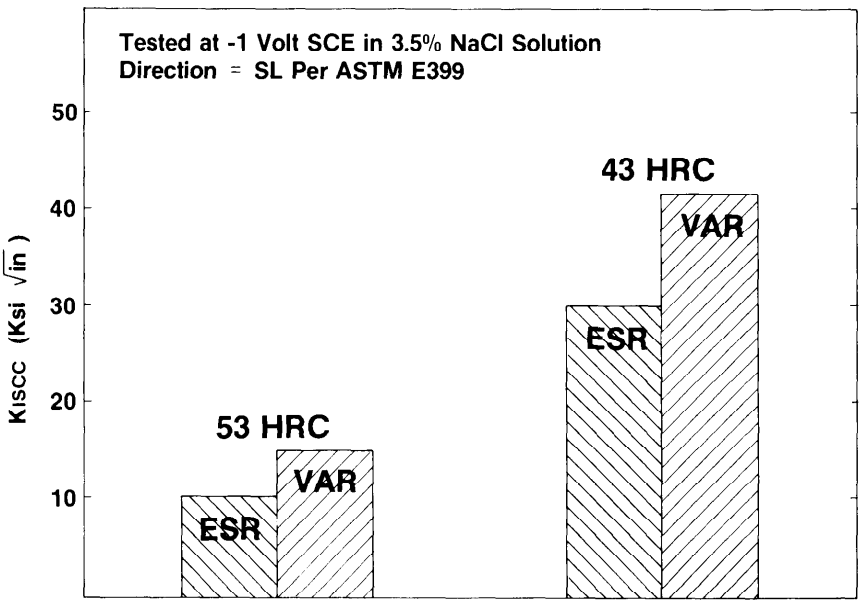

FIGURE 9. Effect of hardness and melting practice in the threshold stress intensity @ -1.0V, SCE in 3.5% NaCl solution.

CONCLUSIONS

At the same hardness level, VAR is shown to be more resistant to hydrogen embrittlement than ESR.

Residual hydrogen in the as-processed 4340 ESR parts is insufficient to cause hydrogen embrittlement but less external or mobile hydrogen (introduced during plating or other fabrication processes and possibly by in-service exposure) is required to cause hydrogen embrittlement cracking in 4340 ESR rather than VAR steel.

The use of a step-loaded, modified Charpy specimen in a cathodically polarized salt water environment appears to be the most reproducible and meaningful accelerated, low-cost hydrogen enbrittlement test method within the framework of fracture mechanics.

RECOMMENDATIONS

Work must be initiated to make 4340 ESR steel more resistant to hydrogen embrittlement.

Three areas that require further study are: (1) Alloy modification, (2) variations in heat treatment and (3) surface treatments.

The step-loaded CVN test method should be refined in order to take full advantage of its use as an accelerated, low-cost hydrogen susceptibility test method within the framework of fracture mechanics.

ACKNOWLEDGEMENT

The authors acknowledge the support of the Watertown Arsenal for the work reported herein, conducted under Contract Number DAAG46-81-C-0045. In particular Mr. Al Anctil's efforts in providing extra test coupons made possible testing beyond that originally planned. The cooperation of Hixson Metal Finishing and NETCO Laboratories also contributed significantly to the success of the test program.

REFERENCES

1. Raymond, L., "Screening Test for Hydrogen Embrittlement", International Symposium for Testing and failure analysis, Los Angeles, Ca. October 1981.

2. Raymond, L., and Crumly, W.R., "Accelerated, Low-Cost Test Method for Measuring the Susceptibility of HY-STEELS to Hydrogen Embrittlement," First International ASM Conference on Current Solutions to Hydrogen Problems in Steel, Washington, D.C., Nov. 1982.

3. Tada, E., Paris, P.C., and Irwin, G.R., "The Stress Analysis of Cracks Handbook," Del Research p.2.13

4. NMAB-328, "Rapid Inexpensive Tests for Determining Fracture Toughness," 1976.

5. Succop, G., Brown, Jr., W. F., "Estimation of KIc from Slow Bend Precracked Charpy Specimen Strength Ratios" ASTM STP 632, 1977 pp. 179-192

A PHOTOELASTIC INVESTIGATION OF STRESSES AND LOAD DISTRIBUTIONS IN LUG-GROOVE JOINTS

Y. F. Cheng, Mechanical Engineer
U.S. Army Armament Research and Development Command
Large Caliber Weapon Systems Laboratory
Benet Weapons Laboratory
Watervliet, NY 12189

ABSTRACT

A photoelastic investigation has been made on lug-groove joints* frequently found in weapon systems. Two profiles were studied: the British standard buttress (BSB) and the proposed profile with a longer fillet radius. The objectives were to determine the critical stress and load distribution, and to compare the results from both profiles. It was found that for joints made of the same material under axial tension, the first groove is the critical region, and the maximum fillet stress at the first groove is the critical stress. In a seven-groove joint, the first two lugs take 50 percent and 60 percent of the load in the BSB and the proposed profile, respectively. The proposed profile is weaker than the BSB profile under tension. Moreover, due to allowable machining tolerances, ideal simultaneous contacts in all lug-groove pairs do not occur. The worst possible case would happen when only one pair is in contact and the joint is reduced to a single-groove type. Further work is in progress.

INTRODUCTION

The practical motivation for this investigation arose out of a study of critical stresses at the core of kinetic energy penetrators. In a kinetic energy penetrator, the core and the sabot are connected through a series of ring-shaped lugs and grooves with British standard buttress (BSB) profile, Figure 1. The core of a penetrator failed transversely near the fillet of the rearmost groove during a test. The failure was brittle indicating the presence of a high tensile stress. In order to reduce the high tensile stress, a new profile with a longer fillet radius, Figure 2, was suggested by O'Hara [1].

In the BSB profile, each lug-groove pair has a truncated seven-degree conical contact surface. Allowable machining tolerances introduce difference in the angles, prevent simultaneous contacts in all lug-groove pairs, and affect load distribution among grooves. The worst possible case would occur when only one pair is in contact and the joint is reduced to a single-groove type. In the proposed profile, the initial contact has the form of a circumferential line instead of a conical surface.

*The lug-groove joint is different from the screw-thread joint in that the former has a series of ring-shaped lugs and grooves while the latter has a continuous advancing spiral with a helix angle.

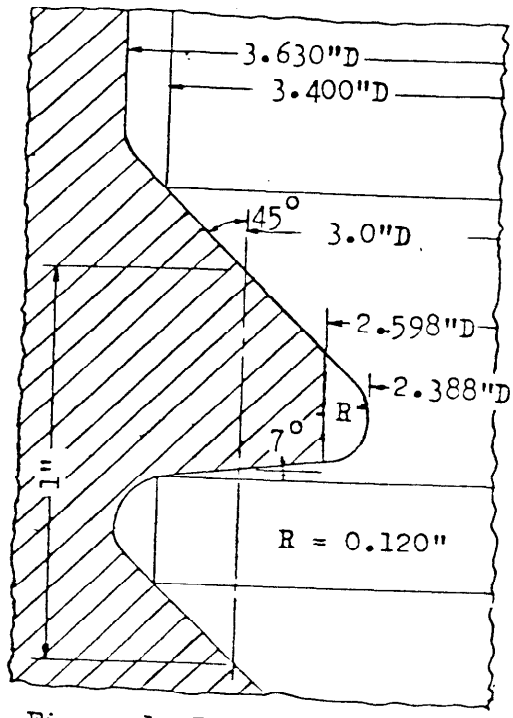

Figure 1. British Standard Buttress Profile

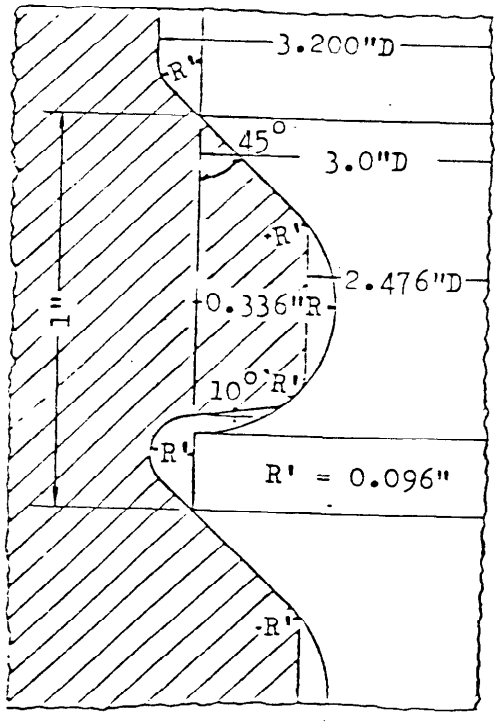

Figure 2. Proposed Profile

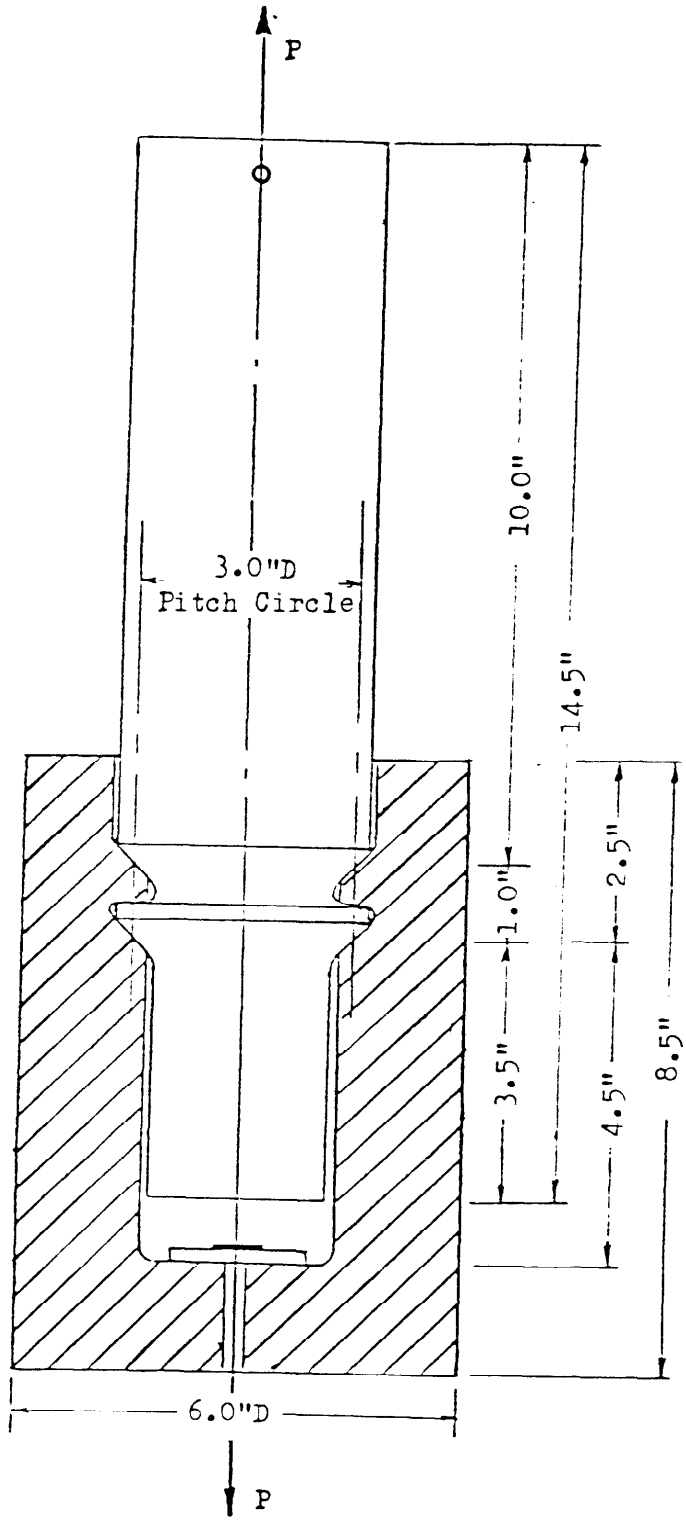

Figure 3. Sketch of Model 1

The objectives of this investigation were to determine fillet stresses, contact stresses, interior stresses at narrowest sections of the core and load distribution among grooves, and to compare critical stresses from both profiles. All data were obtained photoelastically by means of the three-dimensional shear-difference method [2,3].

In a kinetic energy penetrator, the core and the sabot are usually made of different materials and are subjected to additional external pressure. However, results presented here are limited to joints made of the same material and under tension. Further work on different materials and pressure load is in progress.

EXPERIMENTAL PROCEDURE

CONSTRUCTION AND LOADING OF MODEL

Four models were constructed of photoelastic material PLM4B, supplied by Measurement Group, Raleigh, NC. They represented a combination of single-groove joint, multi-groove joint, BSB profile, and the proposed profile, as listed in Table I.

Table I Model and Load

Model	Number of Lug-Groove Pairs	Profile	Load (lb)	Load (N)
1	1	BSB	59.1	263
2	1	Proposed	58.8	262
3	7	BSB	59.9	266
4	7	Proposed	59.9	266

Figure 3 shows a sketch of the first model. For the convenience of taking data and conservation of material, the groove in the model was scaled up eight times from the prototype while the pitch diameter only 2.72 times. The scaling difference has only negligible effect on stress distributions in the vicinity of the groove. The outer piece (sabot) consisted of two semicylinders. They were cemented together after assembly. Dowel pins made of the same photoelastic material were used to assure perfect alignment.

The model was loaded in axial tension by means of dead weights in a temperature-controlled furnace. The loaded model was slowly heated to the critical temperature of 250°F, which was held constant for eight hours, and then gradually cooled to room temperature at which time the loads were removed. The rate of heating was 10°F/hour, and the rate of cooling 1°F/hour.

The duration of the thermal cycle was about eight to nine days. The loads are listed in Table I.

SLICING PLAN

One meridian slice of 0.1 inch thick was removed from the core of each model for photoelastic observations. The plane of the slice was 90 degrees from the cement joint.

SCOPE OF INVESTIGATION

The tangential free boundary stresses along the groove fillet in the meridian slices were measured. Interior stress distributions along sixteen transverse narrowest sections through the groove root were determined (one section in single-groove model, seven sections in multi-groove model). Contact stresses in single-groove models were found. In addition, shearing stresses were determined along a vertical line joining groove roots in multi-groove models. These will be described later.

APPARATUS AND PRECISION OF MEASUREMENT

The photoelastic data, i.e., fringe orders and isoclinic angles, were measured by means of a photometer (Photovolt, Model 520M) and a small field polariscope specially designed for three-dimensional analysis. The photometer detected minimum light intensity. The polariscope had a super-pressure compact mercury arc (OSRAM) as its light source. The combination of a condensing lens, a pin hole, a collimating lens, and a monochromatic filter provided a field of collimated monochromatic light of 5461Å where the slice was placed. A pair of Glan-Thompson prisms were used as the polarizer and analyzer. They were coupled with a matching quarter-wave plate. Fractional fringe orders were measured by means of Senarmont's principle of compensation [4] with errors not exceeding ± 0.005 fringes. The error in isoclinics did not exceed ± 1 degree. A lens projected a 5X image of the slice onto a screen in front of the photomultiplier tube. The screen had an 0.03 inch pin hole which gave a resolution of 0.006 inch.

EXPERIMENTAL RESULTS

FILLET BOUNDARY STRESS σ_f

On the free boundary one of the principal stresses is identically zero and the remaining principal stress tangent to the boundary is given by the fringe order. Figures 4 and 5 show the distributions of the free fillet boundary stress, σ_f, in single-groove models. In the first model (BSB profile), the fillet stress has a maximum $(\sigma_f)_{max}$ of 61 psi (420 KPa) and is located approximately 21 degrees from the groove root toward the loaded surface. In the second model (proposed profile), $(\sigma_f)_{max}$ has a value of 98 psi (676 KPa) and is located approximately 43 degrees from the groove root toward the loaded surface. This value is almost 60 percent greater than that of the first model while their loads are practically the same. Similar distributions were obtained for the first three grooves in multi-groove

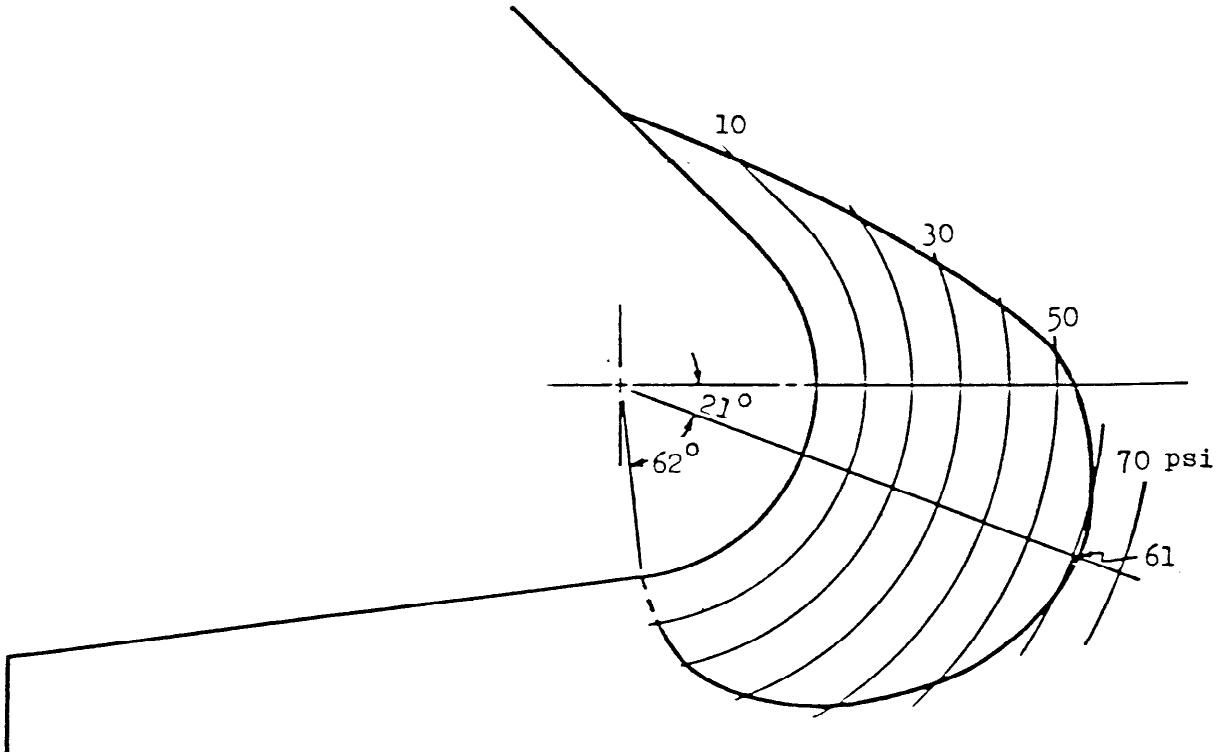

Figure 4. Fillet Boundary Stress, Model 1

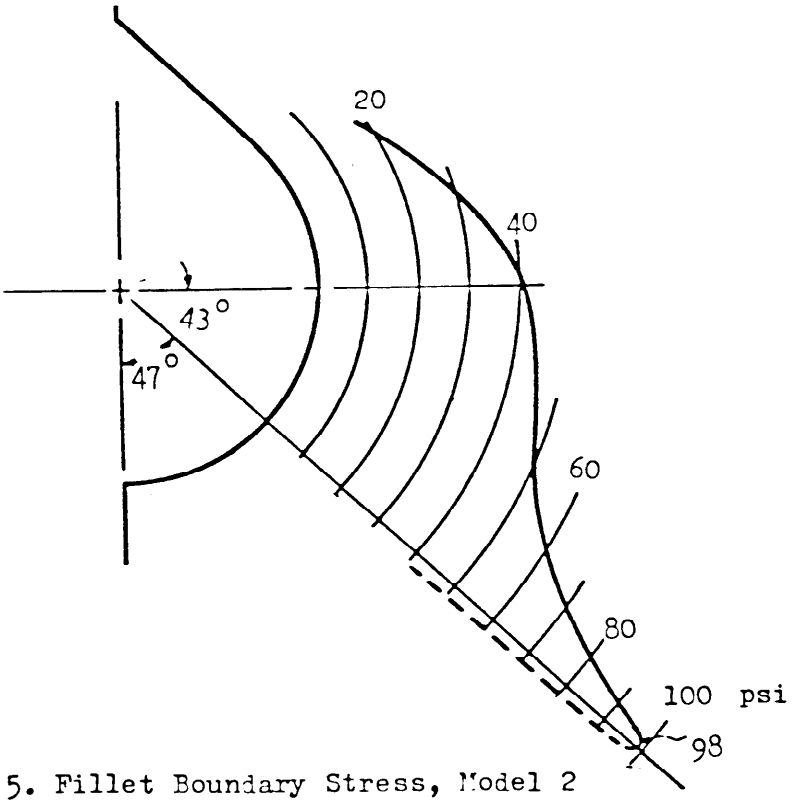

Figure 5. Fillet Boundary Stress, Model 2

models. The maximum was always found at some angular distance away from the groove root. Their magnitudes are listed in Table II.

Table II Values of $(\sigma_f)_{max}$ and $(\sigma_z)_{max}$

Model	Groove	$(\sigma_f)_{max}$ (psi)	(KPa)	$(\sigma_z)_{max}$ (psi)	(KPa)
1	1	61	420	54	372
2	1	98	676	42	290
3	1	50	345	48	331
3	2	48	331	33	228
3	3	28	193	17	117
4	1	76	524	37	255
4	2	57	393	20	138
4	3	50	345	11	76

RADIAL DISTRIBUTIONS OF STRESSES σ_r, σ_z, AND τ_{rz}

By means of the shear difference method [2,3] the distributions of stresses σ_r, σ_z, and τ_{rz} were determined along the radius of transverse narrowest section passing through groove root in single-groove models as shown in Figures 6 and 7. In the BSB profile, σ_z has a maximum, $(\sigma_z)_{max}$, of 54 psi (372 KPa); in the proposed profile, 42 psi (290 KPa). In both models, they are located at the root and are less than the corresponding $(\sigma_f)_{max}$. Similar distributions were found for all seven sections in multi-groove models. The values of $(\sigma_z)_{max}$ for the first three sections are included in Table II. It should be mentioned that due to the interest of preserving the slices, subslices were not prepared and the stress σ_θ was not determined. Also, the remaining shearing stresses $\tau_{r\theta}$ and $\tau_{z\theta}$ are identically zero.

LOAD DISTRIBUTIONS

Axial load P_i for each section was found by integrating $(\sigma_z)_i$ over the section. Thus

$$P_i = 2\pi\int(\sigma_z)_i r dr \qquad (1)$$

where subscript i denotes quantities relating to the ith section. Neglecting body force, the lug load is equal to the difference between neighboring section loads. They are shown in Table III and Figures 8 and 9.

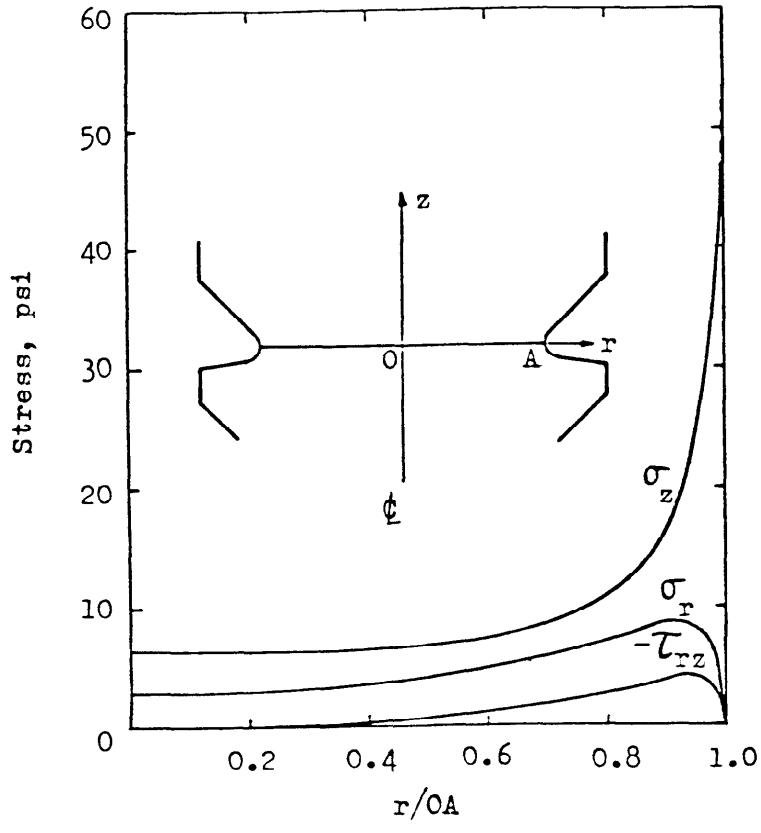

Figure 6. Distributions of Stresses σ_r, σ_z, and τ_{rz}, Model 1

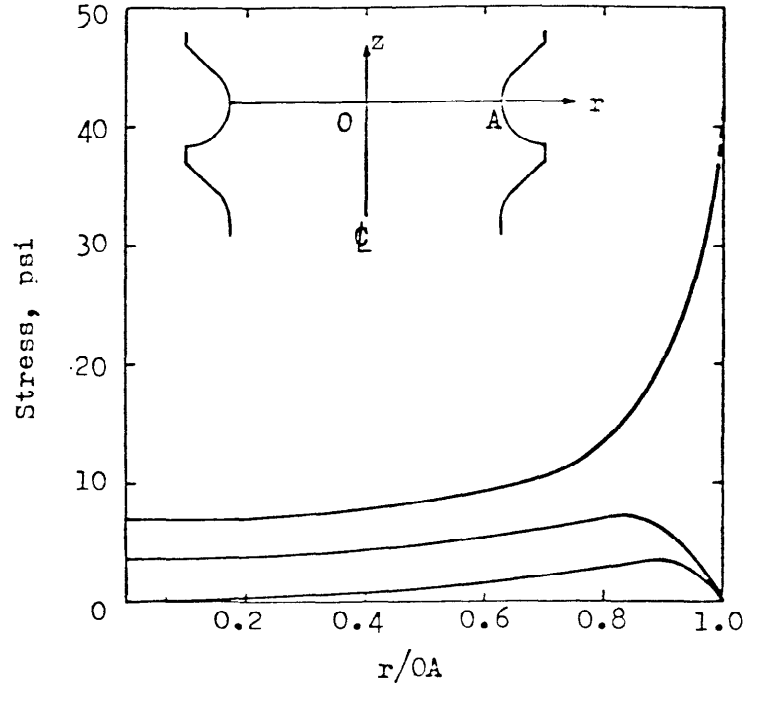

Figure 7. Distributions of Stresses σ_r, σ_z, and τ_{rz}, Model 2

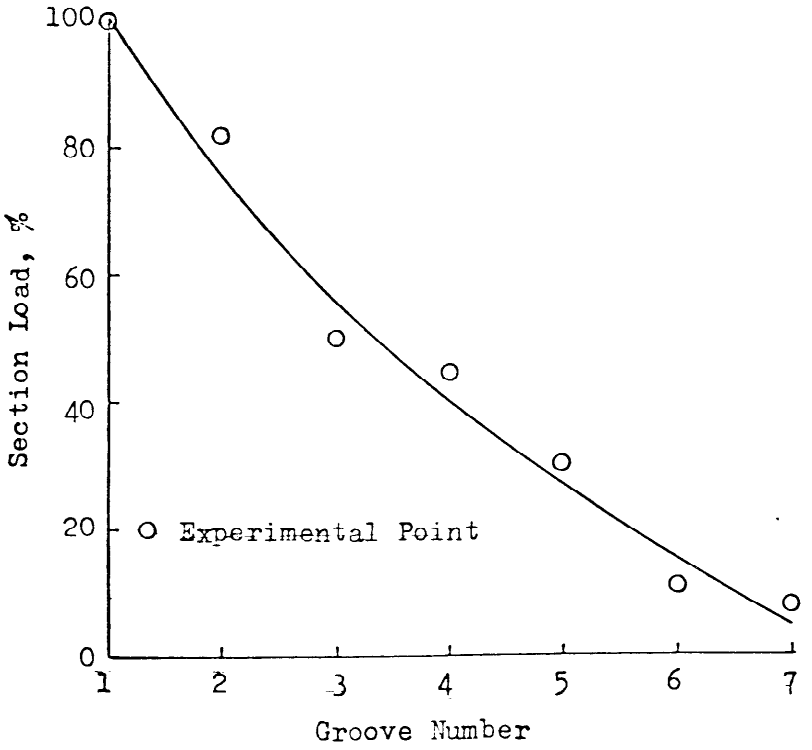

Figure 8. Distribution of Section Loads, Model 3

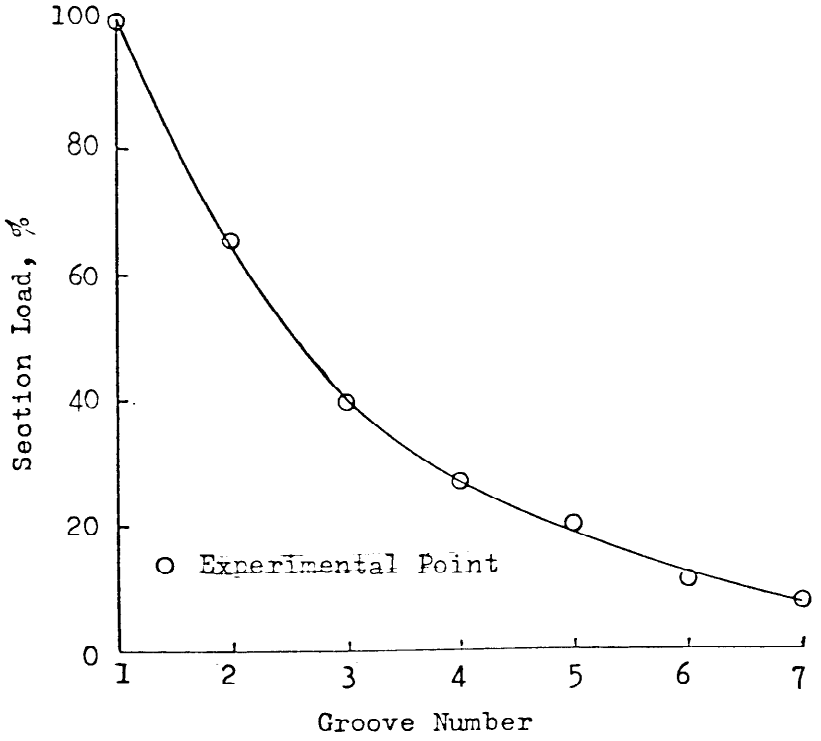

Figure 9. Distribution of Section Loads, Model 4

Table III Load Distributions

Model	Groove	Section Load (lb)	Section Load (N)	Lug Load (lb)	Lug Load (N)
3	1	59.9	266	10.5	46
3	2	49.4	220	19.4	87
3	3	30.0	133	3.3	14
3	4	26.7	119	8.7	39
3	5	18.0	80	11.2	51
3	6	6.6	29	1.8	8
3	7	4.8	21	4.8	21
4	1	61.2	272	21.1	94
4	2	40.1	178	15.6	69
4	3	24.5	109	7.8	35
4	4	16.7	74	4.4	19
4	5	12.3	55	5.8	26
4	6	6.5	29	1.5	7
4	7	5.0	22	5.0	22

CONTACT STRESSES

Contact stresses were determined for single-groove models. In the BSB profile, contact existed from point A to point E, Figure 10. Stresses were found along lines BB', CC', DD', and EE'. They were perpendicular to AE and separated from each other by a distance of AE/4. For lines BB', CC', and DD', the summation process of the shear-difference method was started at points B', C', and D', respectively, on the free boundary. Line EE' did not reach the free boundary. An auxiliary line D'E', intersected perpendicularly with EE' at E', was employed. The summation process along D'E' provided necessary data at point E', the starting point for line EE'. Figure 10 shows the distributions of stresses σ_n, σ_t, and τ_{nt} along contact surface AE. Both σ_n and τ_{nt} reached their maximum values of -60 psi (-414 KPa) and -28 psi (-193 KPa), respectively, at point E. In the proposed profile, the maximum compressive stress is given by σ_n of -180 psi (-1.24 MPa) at point E', Figure 11, and is

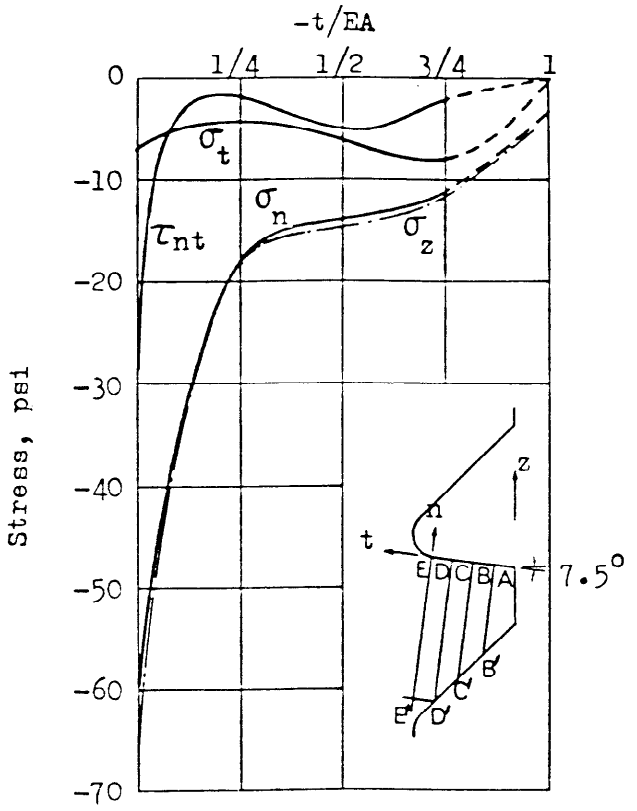

Figure 10. Distributions of Contact Stresses, Model 1

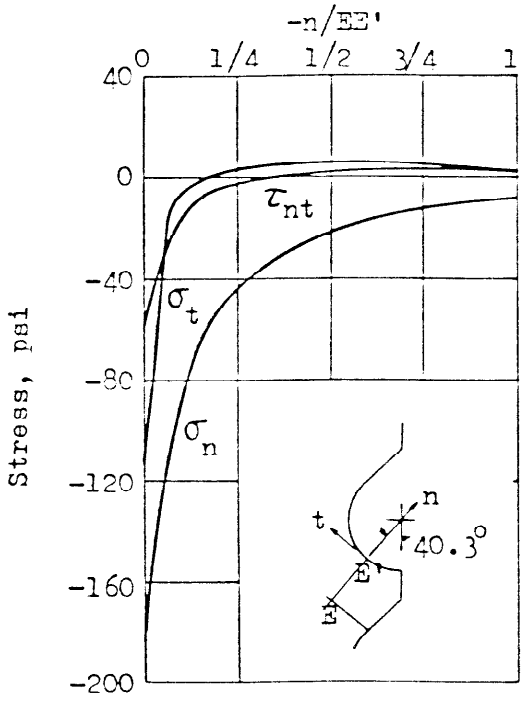

Figure 11. Distributions of Contact Stresses, Model 2

about three times of that in the BSB profile.

In the BSB profile, the angle between the loaded surface and the horizontal was found to be 7.5 degrees instead of 7 degrees. In the proposed profile, contact point E' made an angle of 40.3 degrees with the vertical instead of 45 degrees. These differences are probably caused by the combined effect of deformation and machining tolerances.

DISTRIBUTIONS OF SHEARING STRESSES τ_{rz} ON A VERTICAL LINE

Shearing stresses τ_{rz} were determined on vertical lines joining groove roots in multi-groove models. Figures 12 and 13 show respectively typical distributions in the BSB and proposed profile. The maximum value of τ_{rz} in the proposed profile is less than that in the BSB profile and is located further away from the groove root. This is probably caused by the longer fillet radius and the lower position of load.

DISCUSSIONS

CHECKS

Three independent checks were made.

1. The condition of equilibrium requires that the first section load to be equal to the applied load. A comparison between them is shown in Table IV.

Table IV Equilibrium Check

Model	Applied Load (lb)	(N)	First Section Load (lb)	(N)	Difference %
1	59.1	263	55.2	246	6.6
2	58.8	262	57.8	257	1.7
3	59.9	266	59.9	266	0.0
4	59.9	266	61.2	272	2.2

2. Contact stresses were checked by finding the stresses σ_z on the contact surface, and comparing the resultant with the applied load. The stresses σ_z were calculated by means of the usual stress transformation equation. The distribution of σ_z on the contact surface in the first model is included in Figure 10. The resultant was found to be 62.4 lb (278 N) compared to an applied load of 59.1 lb (263 N) with a difference of 5.3 percent. In the second model, the contact region extended over an arc of 12.5 degrees. Assuming a parabolic distribution of stresses over the contact region, the stresses σ_z

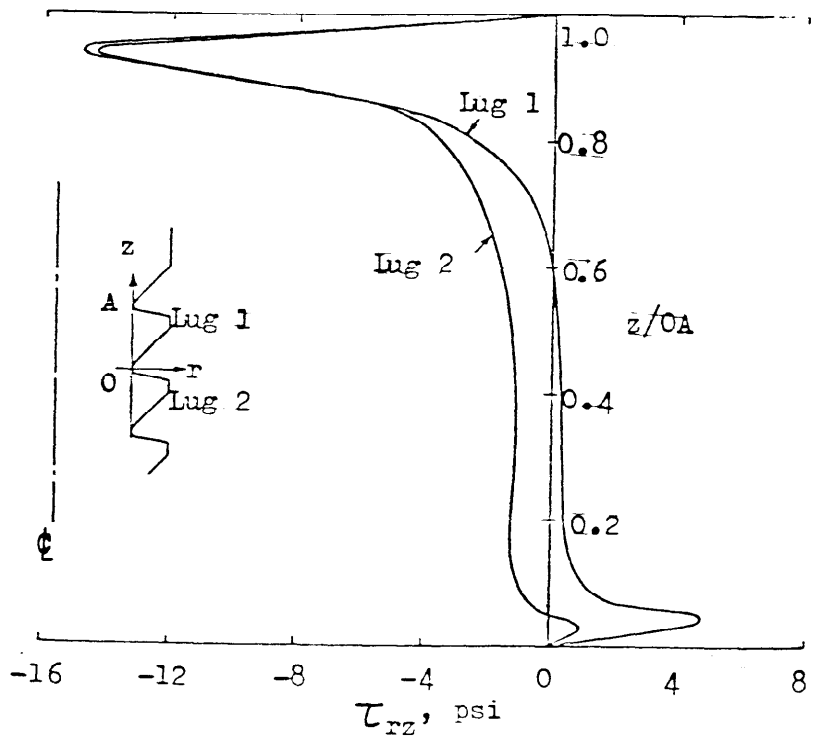

Figure 12. Typical Shearing Stress Distribution, Model 3

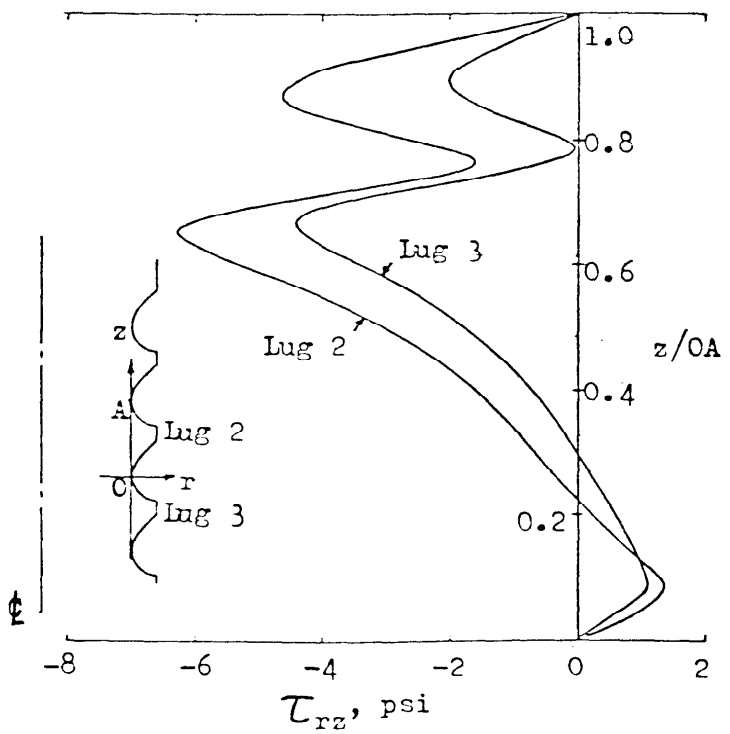

Figure 13. Typical Shearing Stress Distribution, Model 4

were calculated. The resultant was found to be 61.7 lb (274 N) compared to an applied load of 58.8 lb (262 N) with a difference of 4.9 percent.

3. The lug load can be found alternately by integrating shearing stresses τ_{rz} over the vertical surface of cylindrical section between lugs; thus, $2\pi r\int\tau_{rz}dz$. Table V shows the results for the first three lugs in multi-groove models as well as a comparison to those obtained by taking the difference between neighboring section loads.

Table V Lug Load by Two Methods

Model	Lug	Method 1* (lb)	(N)	Method 2† (lb)	(N)
3	1	10.5	46	10.0	45
3	2	19.4	87	20.1	89
3	3	3.3	14	3.4	15
4	1	21.1	94	20.6	92
4	2	15.6	69	14.8	66
4	3	7.8	35	7.3	33

*Method 1: Taking difference between neighboring sections.
†Method 2: Integrating τ_{rz}.

CRITICAL STRESS $(\sigma_f)_{max}$ AND ITS CONTROLLING FACTORS

Table II shows that the stress $(\sigma_f)_{max}$ is higher than the stress $(\sigma_z)_{max}$ in every groove. Hence, $(\sigma_f)_{max}$ is the critical stress. It can also be seen by comparing model 1 to model 2, or comparing model 3 to model 4, the stresses $(\sigma_f)_{max}$ in the proposed profile are higher than those in the BSB profile although the stresses $(\sigma_z)_{max}$ in the proposed profile are lower. Thus, the proposed profile is weaker than the BSB profile under axial tension.

An examination of Table VI reveals that the critical stress $(\sigma_f)_{max}$ depends on the section load and the lug load in addition to other factors. The dependency of lug load can be seen by comparing model 1 to model 3 groove 1. The difference of $(\sigma_f)_{max}$ between them indicates the influence of the lug load, since their section loads are practically the same. In model 3, groove 2 has a lug load 90 percent higher and a section load 18 percent lower than those of groove 1. The stress $(\sigma_f)_{max}$ in groove 2 is less than that in groove 1 shows the effect of the section load.

Table VI Section Load, Lug Load, and $(\sigma_f)_{max}$

Model	Groove	Section Load (lb)	(N)	Lug Load (lb)	(N)	$(\sigma_f)_{max}$ (psi)	(KPa)
1	1	59.1*	263*	59.1*	263*	61	420
3	1	59.9	266	10.5	45	50	345
3	2	49.4	220	19.4	87	48	331

*Applied load.

CRITICAL REGION

The condition of equilibrium requires that the load in the first section to be equal to the applied load. The load decreases monotonically in subsequent sections. Under ideal conditions, all lug-groove pairs contact simultaneously. The load in the first lug is a maximum and decreases monotonically in subsequent lugs. The first groove is the critical region. However, due to allowable machining tolerances simultaneous contacts are often not attained. The results in Table III suggests that in model 3, the second lug made initial contact and followed by lugs 5, 4, 1, 7, 3, and 6. Judging by the stresses $(\sigma_f)_{max}$ from Table II, the first groove is still the critical region.

LOAD DISTRIBUTIONS

Experimental results show that in seven-groove joints, the first two lugs take respectively 50 percent and 60 percent of the load in the BSB profile and the proposed profile, as shown in Table III and Figures 8 and 9. It is conservative in applying these findings to joints of more than seven lug-groove pairs.

STRESS CONCENTRATION FACTOR K

Stress concentration factor K was defined as

$$K = (\sigma_f)_{max}/(P/A) \qquad (2)$$

where P is the applied load and A the area of the cross section passing through the groove root. The values of K are listed in Table VII. Since the stress $(\sigma_f)_{max}$ depends on the section load and the lug load, unknown quantities in multi-groove joints, the values of K for multi-groove models are not practical.

Table VII Stress Concentration Factor K

Model	1	2	3	3	3	4	4	4
Groove	1	1	1	2	3	1	2	3
K	4.6	7.1	3.7	3.6	2.1	5.3	4.0	3.5

EFFECTS OF DIFFERENT SCALING RATIO

It is expected that the difference in scaling ratio has no effect on contact stress distributions, vertical shearing stress distributions, load distributions, and comparisons between the two profiles. It has no effect on the conclusion that the first groove is the critical region and the stress $(\sigma_f)_{max}$ is the critical stress. However, it may affect stresses on transverse sections and the stress concentration factor K.

HEYWOOD'S EMPIRICAL EQUATION

In 1948, Heywood [5] suggested an empirical equation of the following form

$$(\sigma_f)_{max} = [1 + 0.26(e/R)^{0.7}][1.5a/e^2) + (0.36/be)^{1/2}(1 + 0.25 \sin \gamma)](W/t) \quad (3)$$

for calculating the stress $(\sigma_f)_{max}$ in loaded projections, Figure 14, where W denotes the load, t the thickness, and the dimensions a, b, e, and R, and the angle γ are as shown in the figure. In this equation assumption was made that the maximum falls at point A, 30 degrees from the point of tangency on the fillet.

In the first model, e = 0.326 inch (8.3 mm) and R = 0.120 inch (3 mm). The length EA, Figure 10, was divided into eight equal segments. The dimensions a and b, and the angle γ were determined at midpoint of each segment by considering σ_n and τ_{nt} at the point and their geometries. Equation (3) was used to calculated $(\sigma_f)_{max}/(W/t)$ at each point, and $(\sigma_f)_{max}$ due to individual segment load was found. Their sum gave a value $(\sigma_f)_{max}$ of 57 psi (393 KPa) at a point 30 degrees from the point of tangency in comparison with the experimental result of 61 psi (420 KPa) at a point 62 degrees from the point of tangency, Figure 4.

In the second model, Eq. (3) cannot be evaluated due to the 40.3 degrees loading angle. However, experimental results show that the stress $(\sigma_f)_{max}$ falls at a point 47 degrees from the point of tangency, Figure 5. In multi-groove models, Eq. (3) is invalid since it does not include the section load.

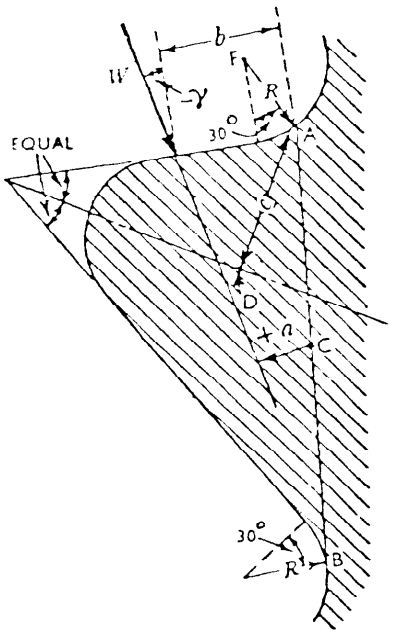

Figure 14. Dimensions Used for Calculating Maximum Fillet Stress by Heywood [5]

Recently, Allison and Hearn [6] reported the movement of maximum stress position around the fillet in a range of angle from 30 degrees to 70 degrees as load position varies. The experimental results are well within this range. Based on Allison's findings, the summation process is not valid since the maximum do not fall at the same position. This has an effect of reducing the stress $(\sigma_f)_{max}$ from its calculated value of 57 psi (393 KPa). Moreover, a, b, e, and γ in Eq. (3) are unknown quantities. Therefore, Eq. (3) is not applicable to the present problem.

CONCLUSIONS

The following conclusions are made for lug-groove joints of the same material under axial tension:

1. In each groove the stress $(\sigma_f)_{max}$ is always higher than the stress $(\sigma_z)_{max}$ and is located at a point some angular distance away from the groove root toward the loaded surface.

2. The stress $(\sigma_f)_{max}$ depends on the section load and the lug load in addition to other factors.

3. The first groove is the critical region and the stress $(\sigma_f)_{max}$ at the first groove is the critical stress.

4. The proposed profile is weaker than the BSB profile since it has a higher value of $(\sigma_f)_{max}$.

5. In a seven-groove joint, the first two lugs take 50 percent and 60 percent of the load in the BSB and the proposed profile, respectively. It is conservative in applying these findings to joints of more than seven lug-groove pairs.

6. Due to machining tolerances, ideal simultaneous contacts in all lug-groove pairs do not occur. The worst possible case would happen when only one pair is in contact and the joint is reduced to a single-groove type.

7. Heywood's empirical equation for calculating the maximum fillet stress in a loaded projection is not applicable to the present problem.

ACKNOWLEDGEMENT

Charles Cobb's participation in the experimental phase of this investigation is hereby acknowledged.

REFERENCES

1. Patent disclosure submitted to DRDAR-LC, Patent Law Division, by G. P. O'Hara, October 27, 1980.

2. Frocht, M. M. and Guernsey, R. Jr., "Studies in Three-Dimensional Photoelasticity: The Application of the Shear-Difference Method to the General Space Problem," Proceedings of the First U.S. National Congress of Applied Mechanics, December 1952, 301-307.

3. Frocht, M. M. and Guernsey, R. Jr., "Further Work on the General Three-Dimensional Photoelastic Problem," J. Applied Mechanics, Trans. ASME, v. 77, no. 2, June 1955, 183-189.

4. Jessop, H. T. and Harris, F. C., Photoelasticity: Principle and Methods, Dover Publications, New York, 1949, 176.

5. Heywood, R. B., "Tensile Stresses in Loaded Projections," Proceedings of the Institute of Mechanical Engineers, v. 155, 1948, 384-391.

6. Allison, I. M. and Hearn, E. J., "A New Look at the Bending Strength of Gear Teeth," Experimental Mechanics, v. 20, no. 7, July 1980, 217-225.

IMPROVED M-11 COPPER CRUSHER GAGE

JAMES M. BENDER
Mechanical Engineer
Ballistic Research Laboratory
Aberdeen Proving Ground, MD 21005

ABSTRACT

Recent testing of the M-11 Copper Crusher gage indicates that it does not meet the NATO standards for precision at the high end of its operating range. The Ballistic Research Laboratory (BRL), of the Armament Research and Development Command (ARRADCOM), at the request of the Materiel Testing Directorate (MTD), of the Test and Evaluation Command (TECOM), performed structural integrity analyses using the finite element method for mechanical behavior of solids. A design modification to the gage resulted from the analyses.

INTRODUCTION

The M-11 Copper Crusher gage is a self-contained, re-usable pressure gage used to measure peak pressure developed in the chamber of large caliber guns. Recently, the M-11 gage was tested against crusher gages from other NATO nations for precision. The M-11 gage (high pressure) failed to meet the precision requirements of less than 1% (2% for cold temperature extremes) deviation between gages. Table I was extracted from the report on the comparison trials [1] and tabulates the deviations of the gages for each nation at varying pressures and temperatures. The M-11 gage was tested at pressures from 1050 bars (27 Ksi, 186 MPa) to 5500 bars (81 Ksi, 559 MPa). MTD is the primary investigator of the M-11 gage's performance. They performed a similar test of the M-11 gage over the pressure range of 60 to 120 Ksi (414 to 828 MPa) at $72^{o}F$ ($22^{o}C$). Figure 1 displays the results of the test of the M-11 gage against the piezo-electric standard gage. The deviation is well beyond the limitations imposed by the NATO standardization agreement.

The BRL was consulted as part of the investigation to perform structural integrity analyses of the gage. The BRL's approach made extensive use of the finite element method for the mechanical behavior of solids. The goal was a modification to the design of the M-11 gage which would correct its operating flaws and extend the operating range to 120 Ksi (828 MPa).

---

1. "Third NATO Crusher Gage Comparison Trials 1977, by Order of NATO AC 225 Panel IV," Meppen, FRG, October, 1977.

Table I. Results of the Precision Test Indicating Percent Deviation Between Gauges

	FH 155-1 Low Pressure Gages						105 mm High Pressure Gages				
Pres. Level* / Temp. Level	500 (7.4)	1250 (18.4)	1850 (27.2)	1850 (27.2)	3000 (44.1)	4000 (58.8)	4000 mean (58.8)	4000 (58.8)	4750 (69.8)	5500 (80.9)	Nation
+ 21°C	1.3	0.5	0.4	0.5	0.4	0.4	0.4	0.4	0.6	0.9	FRG
- 40°C	1.6	0.6	0.5	0.8	0.6	0.8	0.85	0.9	1.0	0.5	FRG
- 10°C	1.2	0.6	0.4	0.5	0.4	0.5	0.5	0.5	1.0	0.7	FRG
+ 60°C	1.2	0.4	0.3	0.4	0.4	0.5	0.55	0.6	0.5	1.0	FRG
+ 21°C	1.0	0.4	0.1	0.8	0.2	0.4	0.3	0.2	0.1	0.3	F
- 40°C	0.5	0.3	0.3	1.3	0.8	1.9	2.05	2.2	1.2	1.1	F
- 10°C	0.7	0.4	0.4	0.3	0.3	0.9	0.8	0.7	0.7	0.7	F
+ 60°C	0.6	0.2	0.2	0.4	0.3	0.4	0.35	0.3	0.3	0.4	F
+ 21°C	0.8	0.2	0.8	1.0	0.8	1.0	1.05	1.1	0.6	1.3	NL
- 40°C	1.0	0.8	0.6	0.8	1.1	5.1	4.8	4.5	6.3	6.3	NL
- 10°C	0.7	0.9	1.6	0.7	0.4	0.5	1.0	1.5	1.7	1.7	NL
+ 60	0.8	0.9	0.8	0.7	0.6	0.3	0.55	0.8	0.4	0.3	NL
+ 21°C	0.7	0.4	0.5	0.6	0.8	0.6	0.5	0.4	0.5	0.5	UK
- 40°C	1.4	3.9	4.6	1.0	0.9	2.3	1.6	0.9	1.3	2.9	UK
- 10°C	0.4	1.1	2.5	0.5	1.3	0.9	0.65	0.4	0.9	0.8	UK
+ 60°C	0.6	1.1	0.8	0.4	0.7	1.0	0.6	0.2	0.6	0.4	UK
- 21°C	0.7	0.4	5.8	0.7	0.5	0.6	0.4	0.2	0.4	0.5	USA
- 40°C	0.2	0.4	3.3	0.3	1.0	1.5	2.4	4.3	1.7	2.1	USA
- 10°C	0.6	0.3	4.5	0.6	0.2	0.6	0.6	0.6	1.1	1.5	USA
+ 60°C	0.4	0.7	5.4	0.6	0.4	0.4	1.45	2.5	1.1	1.4	USA

*Units: bar (Ksi)

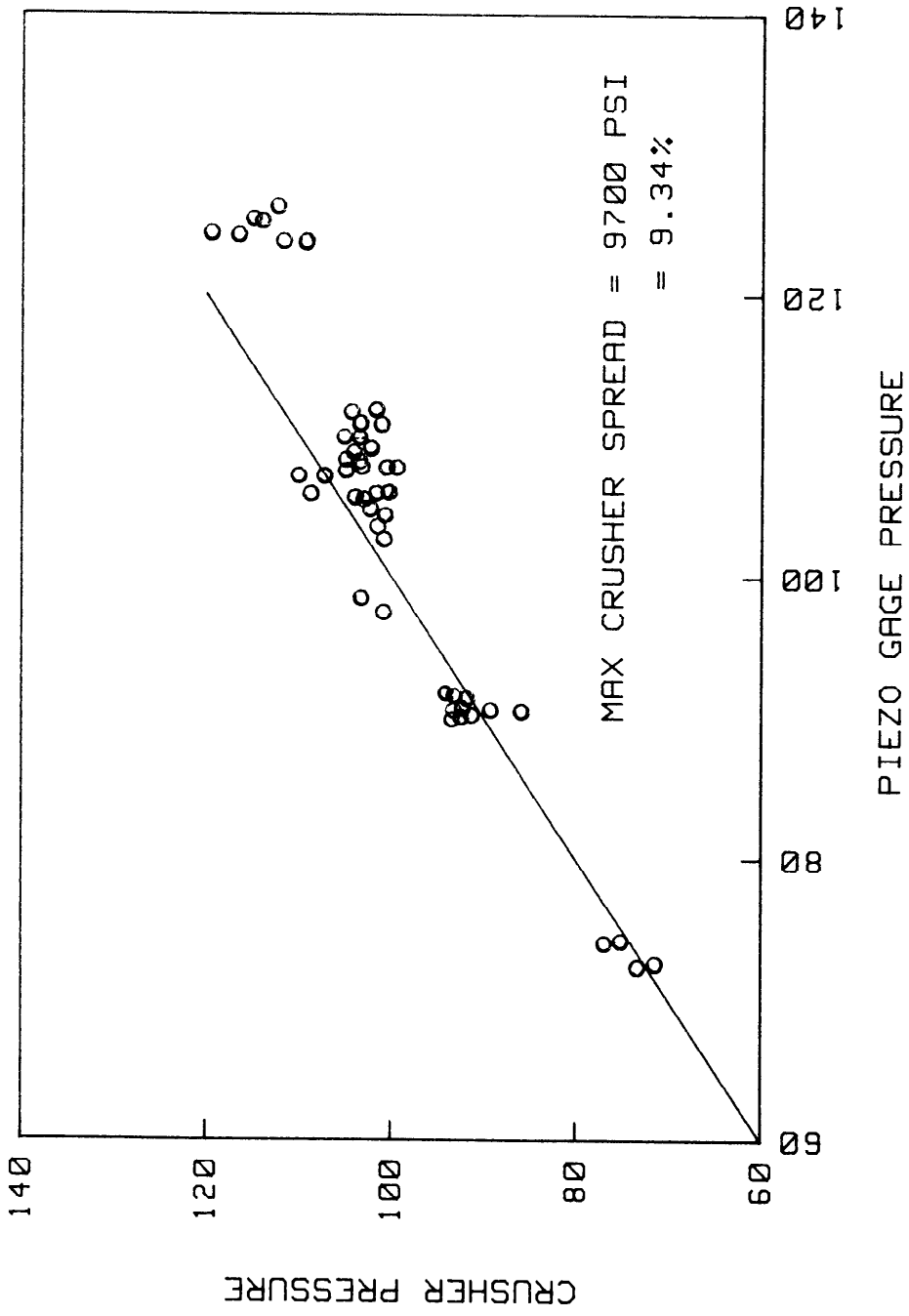

Figure 1. Crusher Pressure vs. Piezo Pressure of M-11 Gage

FINITE ELEMENT METHOD

The BRL relies heavily on its version of the SAAS II code [2, 3] and the accompanying grid generator written by the Rohm and Haas Company. The program also has the added feature of graphical output [4] which displays a deformed figure superimposed on the underformed figure.

A sketch of the M-11 gage is shown in Figure 2, from which the finite element grid in Figure 3 is derived. The loading scheme consists of pressurizing the entire exterior of the gage to 120 Ksi (828 MPa) including the sensing end of the piston. The crushing end of the piston is loaded with an opposing force to simulate the resistance of the copper sphere, the primary sensing element.

RESULTS

The result of the applied load is shown in Figure 4. The deformed grid's displacements are exaggerated 1000% for clarity. The most obvious deformation in the figure is the overlap of nodal points at the piston/bore interface. This is how the program indicates interference. The applied pressure has a direct path of action to the piston, thus clamping it before it has a chance to fully crush the sphere, as illustrated in Figure 4. However, due to the design tolerances, the bore and piston could have diameters such that the interference would not be as severe and the piston would be permitted its full travel, i.e., large bore/small piston. Also, the reverse could occur and result in a greater interference. The large spread of the data is attributed to this phenomenon. It is interesting to note that the gages used by the Federal Republic of Germany have similar piston/bore tolerances. However, at the assembly stage the pistons and bores are matched so that the diametral difference between them is nearly constant from gage to gage. Although this may be a solution to the M-11's problem, it could be very time consuming and costly to implement.

MODIFICATIONS

A more practical solution than piston/bore matching was to isolate the region of interference from the effects of the pressure. This was accomplished by shifting the path of pressure action to a region beyond the piston. It was determined that by shortening the piston and deepening the

---

2. Sawyer, S. G., "BRLESC Finite Element Program for Axisymmetric Plane Strain, and Plane Stress, Orthotropic Solids with Temperature-Dependent Material Properties," BRL Report 2539, Ballistic Research Laboratories, Aberdeen Proving Ground, MD, March 1971 (AD #727702).

3. Jones, R. M. and Crose, J. G., "SAAS II Finite Element Stress Analysis of Axisymmetric Solids with Orthotropic, Temperature Dependent Material Properties," Aerospace Corporation, San Bernadino, CA, September 1968.

4. Zimmerman, K. L., "PLOTS - The plotting Subroutine Incorporated in the BRLESC Finite Element Computer Program," BRL Report 2209, August 1972.

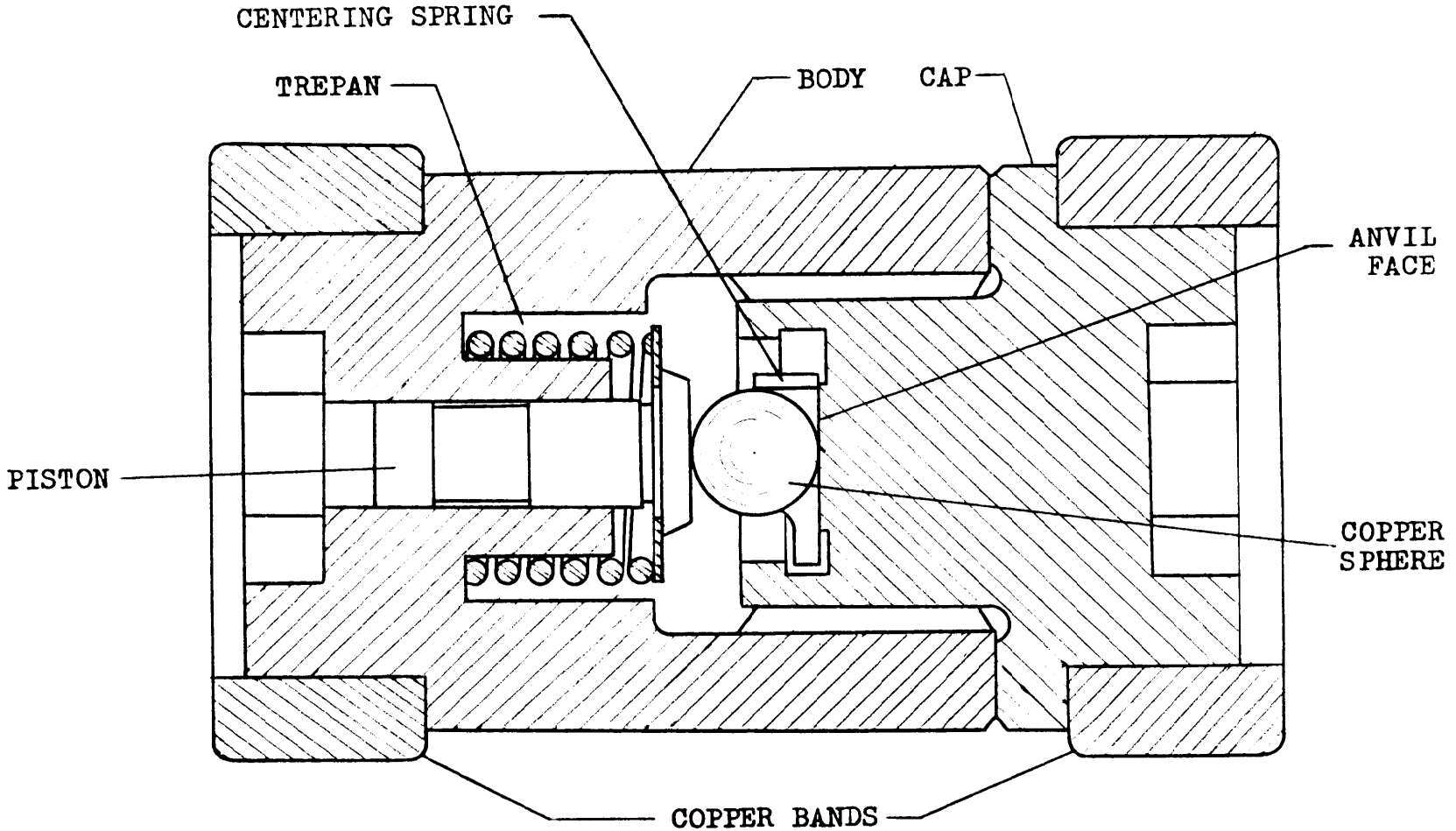

Figure 2. Assembly Sketch of M-11 Copper Crusher

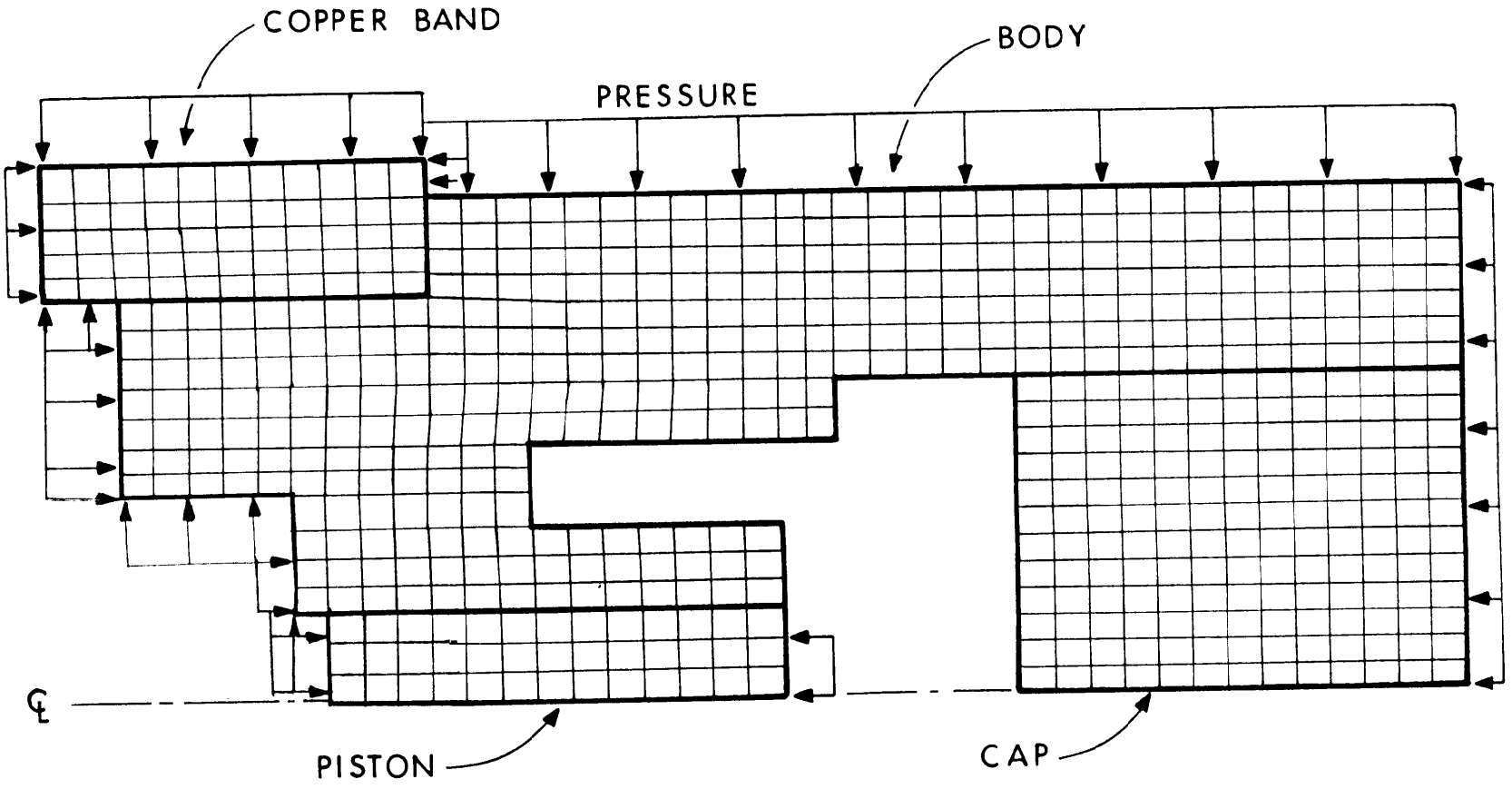

Figure 3. Finite Element Grid of Copper Crusher with Loading Scheme

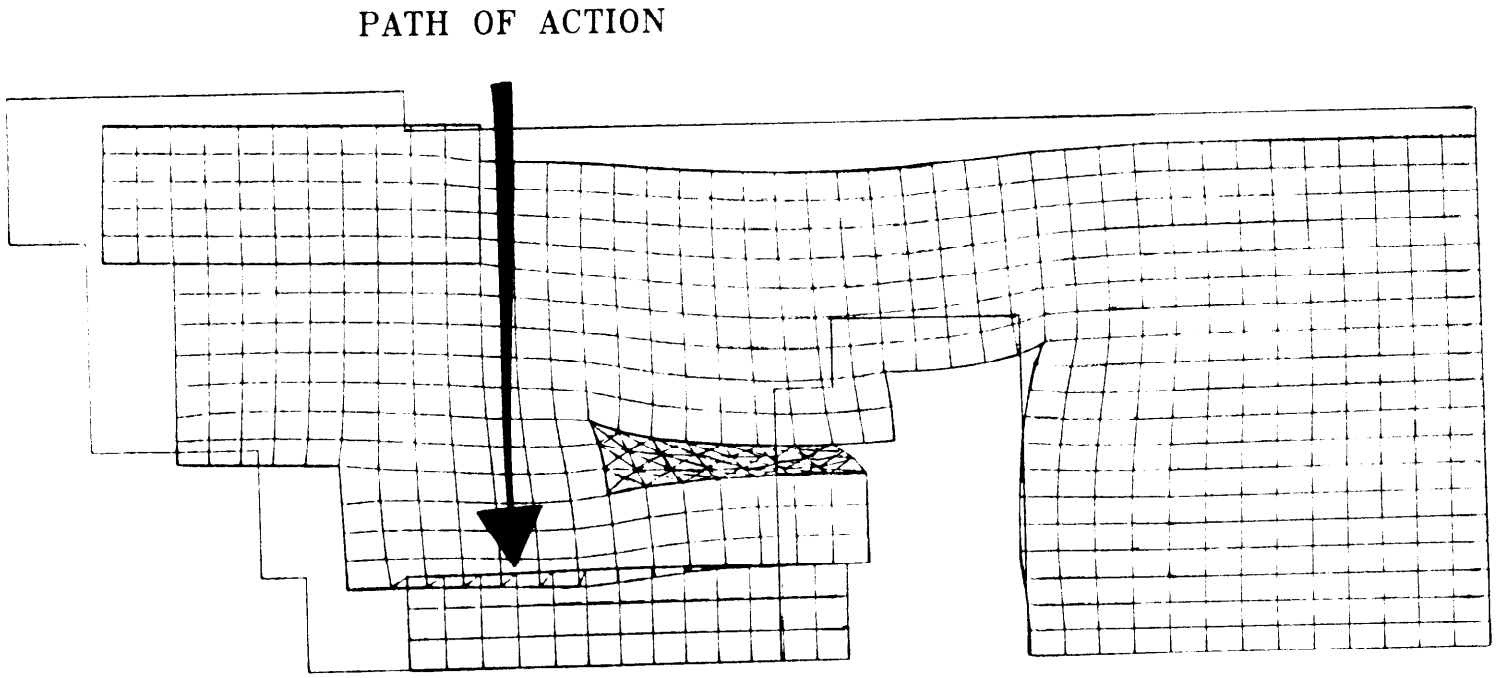

Figure 4. Deformed Finite Element Grid; Result of 80 Ksi (550 MPa)

trepan, the path of action is sufficiently shifted so as not to cause any interference at the bore (see Figure 5).

Several gages were fabricated with this modification and dynamically tested. Although the gages showed good agreement at high pressures, gas intrusion sufficiently damaged the inside of the gage so that repeated use was not possible. It was determined that the shortened piston left too much of the bore wall exposed to gas pressure. This pressure may have widened the bore at this point since there is no opposing pressure on the opposite side of the wall here. The additional clearance permitted the blowby of propellant gases into the gage. The dynamic tests were rerun with slightly longer pistons in the gages. The longer pistons would leave less bore wall exposed to pressure and, acting with the smaller bore wall further back, would create a better seal. This test produced the results shown in Figure 6 and demonstrates a marked improvement over the data shown in Figure 1.

DISCUSSION

It has been shown that the modified gage outperforms the present gage at $72^{o}F$ ($22^{o}C$) over the entire pressure range up to 120 Ksi (828 MPa). Although the gage's response was not simulated at high and low temperature extremes with the pressure, there is a high level of confidence that the gage will perform well in future hot and cold testing. A finite element analysis of the M-11 gage using a temperature boundary condition of $-40^{o}F$ ($-40^{o}C$) alone did not significantly alter the piston/bore clearances. It is evident from the data in Table I that the combination of temperature and pressure extremes are harmful to the operation of the gage. By isolating much of the pressure effects from the piston/bore region the apparent sensitivity of the gage to temperature extremes is minimized.

REFERENCES

1. "Third NATO Crusher Gage Comparison Trials 1977, by Order of NATO AC 225 Panel IV," Meppen, FRG, October 1977.

2. Sawyer, S. G., "BRLESC Finite Element Program for Axisymmetric Plane Strain, and Plane Stress,Orthotropic Solids with Temperature-Dependent Material Properties," BRL Report 1539, Ballistic Research Laboratories, Aberdeen Proving Ground, MD, March 1971 (AD #727702).

3. Jones, R. M., Crose, J. G., "SAAS II Finite Element Stress Analysis of Axisymmetric Solids with Orthotropic, Temperature Dependent Material Properties," Aerospace Corporation, San Bernadina, CA, September 1968.

4. Zimmerman, K. L., "PLOTS - The Plotting Subroutine Incorporated in the BRLESC Finite Element Computer Program," BRL Report 2209, August 1972.

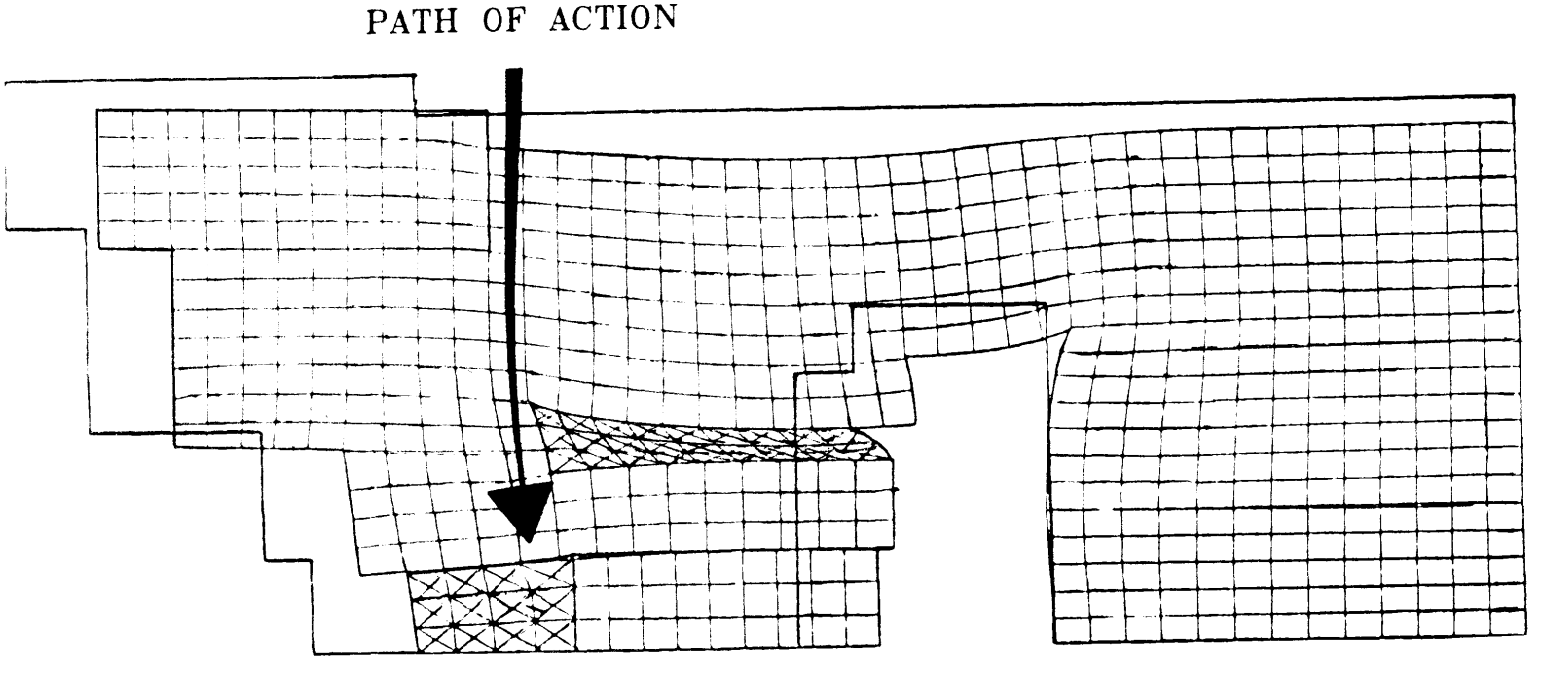

Figure 5. Result of 120 Ksi (838 MPa) Applied to M-11 Crusher Gage

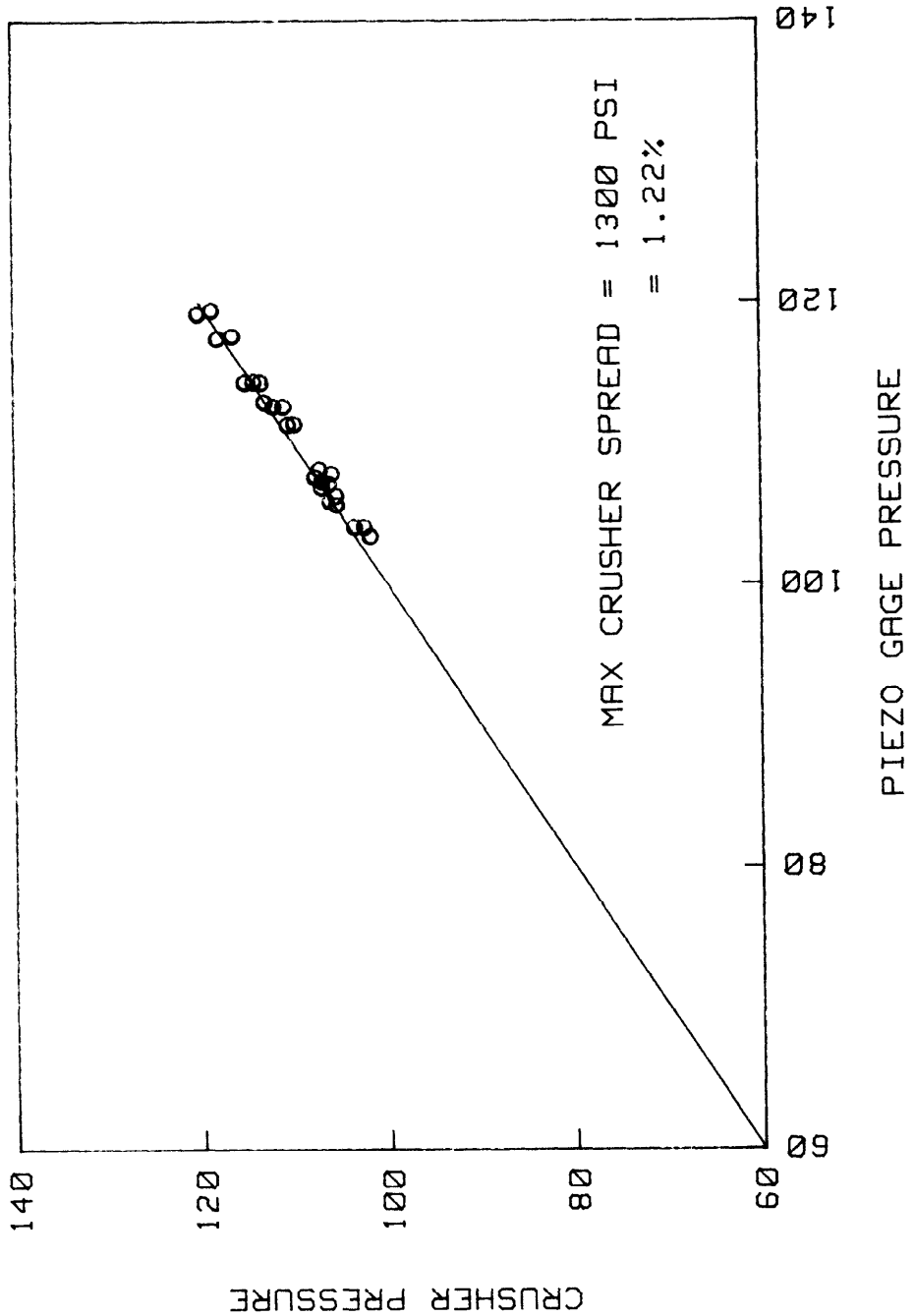

Figure 6. Crusher Pressure vs. Piezo Pressure of Improved M-11 Gage

NONLINEAR ANALYSIS OF IN-BORE PROJECTILES

SHIH C. CHU
Supv Mechanical Engineer
Technology Branch, Armament Division, FC&SCWSL
US Army Armament Research & Development Command
Dover, New Jersey 07801

ABSTRACT

In contrast to the traditional designing and analyzing techniques (theories of elasticity), the plastic flow in the projectile has been taken into account. On the basis of Drucker's flow rule of plasticity, the Von Mises flow criterion, and the strain-hardening and compressibility properties of a material, a nonlinear elastoplastic method has been developed for analyzing a projectile subjected to actual complicated firing conditions. Geometric nonlinearity has been considered by using the finite element technique. An incremental loading procedure has been used to consider the actual firing environment of a gun. The complete loading history which includes propellant gas pressure, rotating band pressure, setback force, and spin rate of a projectile was defined as a function of time.

INTRODUCTION

Projectiles are traditionally analyzed and designed by using theory of elasticity (1,2,3). In this approach, the entire projectile body is considered to be loaded within the elastic region. However, under actual firing conditions, the equivalent stress in some region of the projectile is much greater than the yield strength of the projectile material. Hence, plastic flow will be encountered in the projectile body. The present trend in stress analysis of weapon and ammunition components is to take into account, in a more rigorous fashion, the complex phenomena of plastic flow. This is due to the necessity of designing for maximum stress to achieve an optimal design. In this investigation, a more rigorous nonlinear technique is developed in order to predict the inelastic deformation and stress distributions of a projectile subjected to actual firing conditions. Both nonlinear material response and geometric nonlinearity have been taken into consideration. Nonlinearity of material properties has been taken into account by use of theories of plasticity. Geometric nonlinearity has been considered by use of the finite element approach. A complete inelastic stress analysis of a 175mm, M437, HE projectile subjected to Zone 3 charge has been conducted. A load history was defined which subjected the projectile to the loads at various time on the travel curve.

CONSTITUTIVE EQUATIONS

The primary objective of this investigation is to develop a more rational, nonlinear elastoplastic method for analyzing and designing a projectile to achieve in-bore structural integrity. The incremental stress-strain relations associated with the Von Mises yield criterion obeying the kinematic-hardening law for work-hardening materials will be used. The kinematic hardening law in the incremental theory of plasticity was originally proposed by Prager [4], for the deformation of isothermal solids. Later, Prager [5] extended these formulations to the nonisothermal condition for rigid work-hardening solids. Recently, Chu [6,7], expanded Prager's work for solids of more general deformation state. A brief outline of the constitutive equations used in the analysis is now given.

The total increment strain tensor, $d\varepsilon_{ij}$ is assumed to be the sum of elastic part, $d\varepsilon^e_{ij}$, plastic part, $d\varepsilon^p_{ij}$, and the part of thermal strain, $d\varepsilon^T_{ij}$, i.e.

$$d\varepsilon_{ij} = d\varepsilon^e_{ij} + d\varepsilon^P_{ij} + d\varepsilon^T_{ij} \tag{1}$$

The elastic strain components $d\varepsilon^e_{ij}$ are related to the incremental stress components, $d\sigma_{ij}$, by

$$d\sigma_{ij} = D_{ijkl}d\varepsilon^e_{kl} = D_{ijkl}(d\varepsilon_{ij}-d\varepsilon^P_{kl}-\beta dT\delta_{kl}) \tag{2}$$

in which β is the thermal expansion coefficient, dT, is the change in temperature, and δ_{kl} is Kronecker delta. For isotropic material, the 4th rank material tensor, D_{ijkl} is defined by

$$D_{ijkl} = \frac{E}{1+\nu}\ \delta_{ik}\delta_{jk} + \frac{\nu E}{(1+\nu)(1-2\nu)}\ \delta_{ij}\delta_{kl} \tag{3}$$

where E is Young's modulus and ν is Poission's ratio of material.

On the basis of the Von Mises yield criterion with temperature-dependent yield strength of a material, the yield surface can be represented as:

$$f = \frac{1}{2}\ S_{ij}S_{ij} - \kappa^2(T) = 0 \tag{4}$$

where

$$S_{ij} = (\sigma_{ij}-\alpha_{ij}) - \frac{1}{3}\ (\sigma_{kk}-\alpha_{kk})\delta_{ij}; \qquad S_{mm} = 0 \tag{5}$$

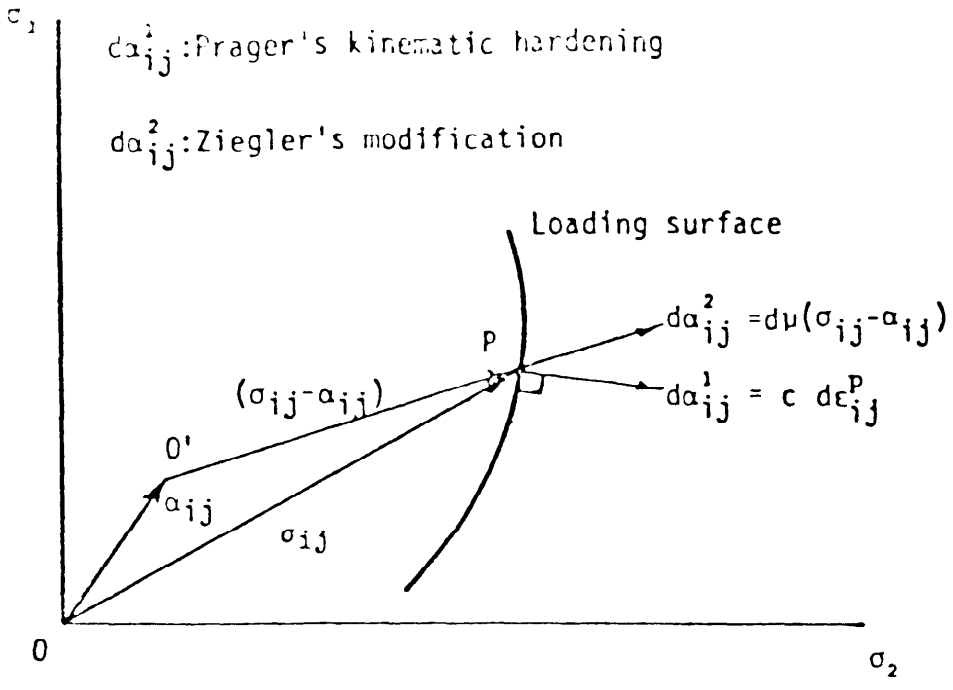

(a) Comparison of Prager's kinematic hardening rule with Ziegler's Modification

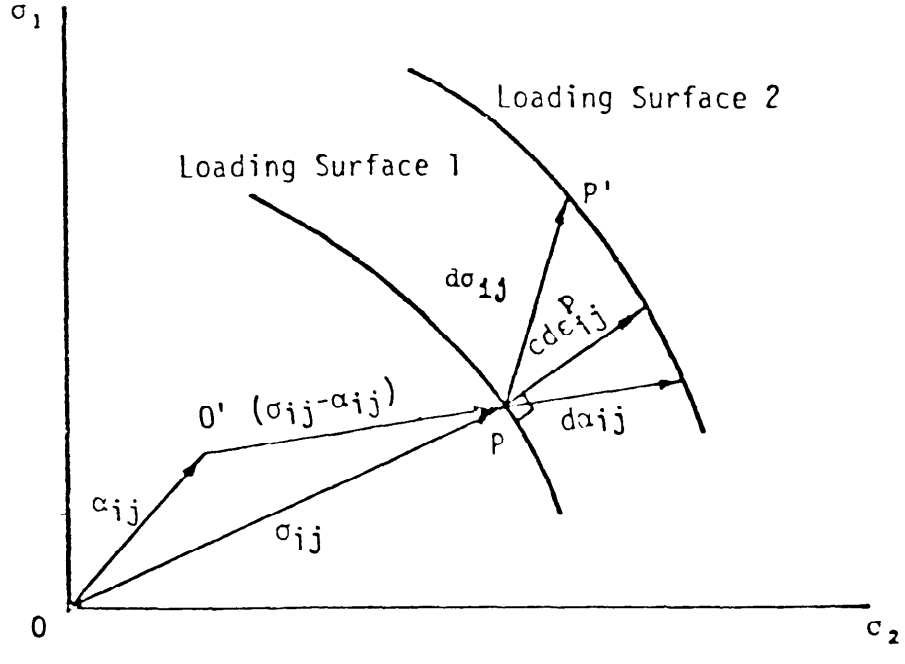

(b) Hardening rule and Definition of Plastic Strain Increment for strain-hardening material

Figure 1. Kinematic Hardening Rules

α_{ij} is a tensor representing the total translation of the center of the initial yield surface, and κ is related to the uniaxial yield stress $\kappa = \sigma_y(T)/\sqrt{3}$.

In addition to the yield condition, a constitutive relation between plastic strain increments, stress, and stress increments is required to describe the inelastic behavior of a material. The constitutive relation (flow rule) used in this investigation is based on Drucker's postulate for work-hardening material [8]. The flow rule is given as:

$$d\varepsilon^P_{ij} = d\lambda \frac{\partial f}{\partial \sigma_{ij}} \tag{6}$$

where $d\lambda$ is a positive scalar quantity. On the basis of Drucker's statement, this plastic strain increment tensor must lie on the outward normal to the yield surface at the instantaneous stress state.

Based upon Prager's kinematic-hardening rule [4,9] with Ziegler's modification [10], the increment of translation of the center of the yield surface is assumed to be directed along the radius vector connecting the center of the yielding surface to the instantaneous stress state, i.e.,

$$d\alpha_{ij} = (\sigma_{ij} - \alpha_{ij}) d\mu; \quad d\mu > 0 \tag{7}$$

where $d\mu$ can be determined provided the stress point remains on the translated yield surface during plastic flow, i.e.,

$$d\mu = \frac{\dfrac{\partial f}{\partial \sigma_{kl}} d\sigma_{kl} + \dfrac{\partial f}{\partial T} dT}{(\sigma_{mn} - \alpha_{mn}) \dfrac{\partial f}{\partial \sigma_{mn}}} \tag{8}$$

A comparison of Prager's hardening rule and Ziegler's modification was shown in Figure 1 (a).

During plastic loading, the consistency condition requires that

$$df = \frac{\partial f}{\partial \sigma_{ij}} (d\sigma_{ij} - C d\varepsilon^P_{ij}) + \frac{\partial f}{\partial T} dT = 0 \tag{9}$$

The plastic strain vector $Cd\varepsilon^P_{ij}$ is considered as the projection of $d\sigma_{ij}$ (and thus of $d\alpha_{ij}$) on the exterior normal to the yield surface, where C is a material constant. Hence, for small incremental of stress and strain, one can readily find that

$$d\lambda = \frac{1}{C}\frac{\frac{\partial f}{\partial \sigma_{ij}}\, d\sigma_{ij} + \frac{\partial f}{\partial T}dT}{\left(\frac{\partial f}{\partial \sigma_{mn}}\right)\left(\frac{\partial f}{\partial \sigma_{mn}}\right)} \tag{10}$$

Therefore, the flow rule becomes

$$d\varepsilon_{ij}^{P} = \frac{\frac{\partial f}{\partial \sigma_{ij}}}{C\left(\frac{\partial f}{\partial \sigma_{mn}}\right)\left(\frac{\partial f}{\partial \sigma_{mn}}\right)}\left(\frac{\partial f}{\partial \sigma_{kl}}\, d\sigma_{kl} + \frac{\partial f}{\partial T}dT\right) \tag{11}$$

If axisymmetric deformation is considered, with reference to the cylindrical coordinates (r, θ, z) the state is defined by the nonvanishing stress components $\{d\sigma\}^T = \langle\, d\sigma_r,\ d\sigma_\theta,\ d\sigma_z,\ d\tau_{rz}\,\rangle$ and strain components $\{d\varepsilon\}^T = \langle\, d\varepsilon_r,\ d\varepsilon_\theta,\ d\varepsilon_z,\ d\gamma_{rz}\,\rangle$. Then, the incremental stress-strain relations are found in the following matrix form:

$$\{d\sigma\} = [\bar{D}]\,\{d\varepsilon\} - \beta dT\,\{B\} \tag{12}$$

in which,

$$[\bar{D}] = \frac{\lambda}{\nu}\begin{bmatrix} 1-\nu & \nu & \nu & 0 \\ \nu & 1-\nu & \nu & 0 \\ \nu & \nu & 1-\nu & 0 \\ 0 & 0 & 0 & \frac{1-2\nu}{2} \end{bmatrix} - \eta_1 \cdot \begin{bmatrix} S_r^2 & S_rS_\theta & S_rS_z & S_r\tau_{rz} \\ S_\theta S_r & S^2{}_\theta & S_\theta S_z & S_\theta\tau_{rz} \\ S_zS_r & S_z\,S_\theta & S_z^2 & S_z\tau_{rz} \\ \tau_{rz}S_r & \tau_{rz}S_\theta & \tau_{rz}S_z & \tau_{rz}^2 \end{bmatrix} \tag{13}$$

$$\{B\} = \frac{E}{1-2\nu}\begin{Bmatrix} 1 \\ 1 \\ 1 \\ 0 \end{Bmatrix} - \frac{\eta_2}{\beta} \cdot \frac{\partial \kappa}{\partial T}\begin{Bmatrix} S_r \\ S_\theta \\ S_z \\ \tau_{rz} \end{Bmatrix} \tag{14}$$

$$\lambda = \frac{E\nu}{(1+\nu)(1-2\nu)} \tag{15}$$

$$\eta_1 = \frac{1}{g} \left(\frac{E}{1+\nu}\right)^2 \tag{16}$$

$$\eta_2 = \frac{2\kappa}{g} \cdot \frac{E}{1+\nu} \quad \text{and,} \tag{17}$$

$$g = 2\kappa^2 \cdot \left(\frac{E}{1+\nu} + C\right) \tag{18}$$

PROJECTILE CONFIGURATION AND MATERIAL PROPERTIES

The outline of a 175mm, HE, M437 projectile is shown in Figure 2. The projectile is made of steel. The material properties and stress-strain relation considered are shown in Figure 3.

LOADING CONDITIONS

The loads considered in this investigation simulate the environment in the gun barrel during firing. The four types of loading considered are shown in Figure 4:

1) Propellant gas pressure
2) Rotating band pressure
3) Setback force due to acceleration of projectile
4) Rotational velocity due to the spin of projectile

The frictional shear forces between the band and the barrel were neglected in this investigation. The loads were applied in incremental fashion; each load point simulated the physical interdependence of the loads at different times during the interior ballistic cycle. The detailed loading history for a 175mm HE, M437 projectile subjected to Zone 3 charge is shown in Figure 5.

METHOD OF SOLUTION

The projectile and all loading acting on the projectile are considered as axisymmetric. A cylindrical coordinate system (r, θ, z) is used in this analysis. By the assumption of axial symmetry, all variables are independent of angle θ; consequently, all derivatives, with respect to θ vanish. The displacement u_θ, and the shear stresses $\tau_{r\theta}$ and $\tau_{\theta z}$ vanish.

Due to the complexity of the geometry of a projectile and nonlinear material behavior, the finite element method (11, 12) was used to conduct the stress analysis. The analytical approach used in this investigation is the incremental loading technique, wherein at each step of loading a new stiffness matrix is formulated, in terms of the finite element model, and solved for incremental deformations, stresses, and strains.

To perform a finite element stress analysis, the cross section of a projectile is divided into a large number of small triangular and

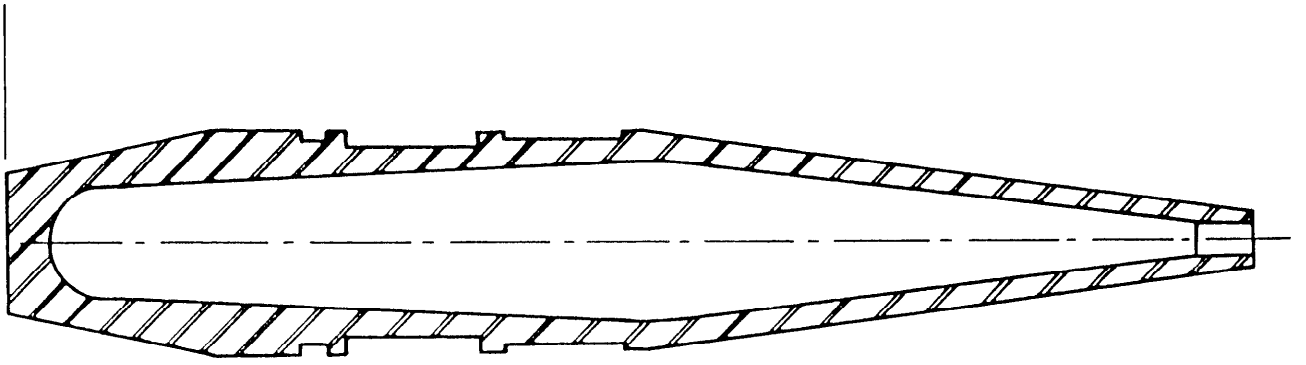

Figure 2. Projectile Configuration

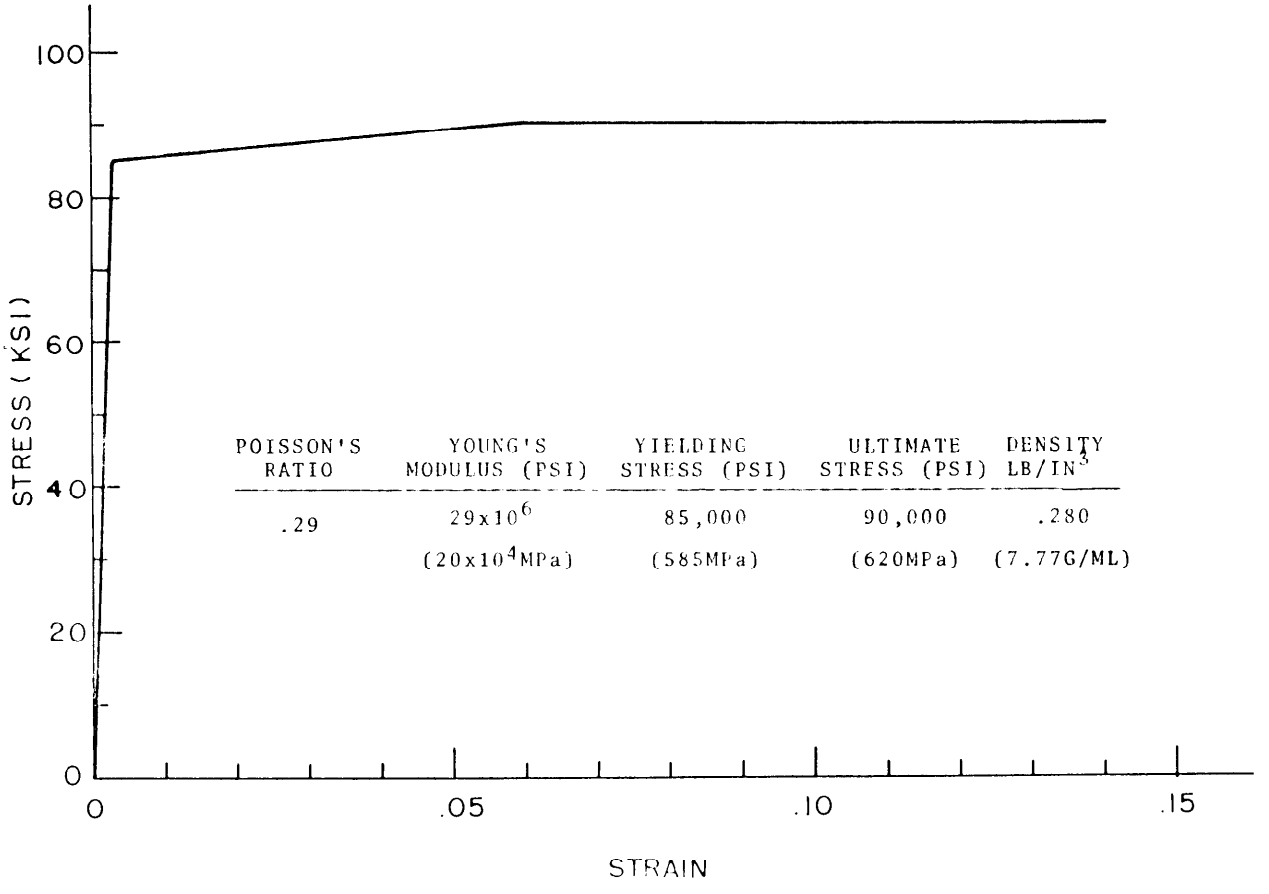

Figure 3. Stress-Strain Relation and Material Properties for Projectile Material

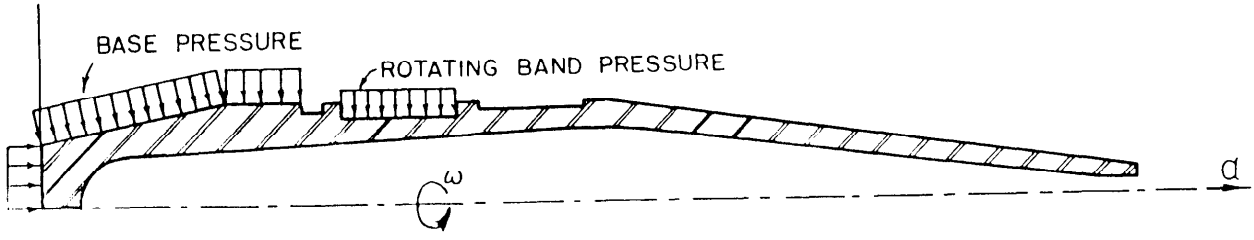

Figure 4. Loading Conditions

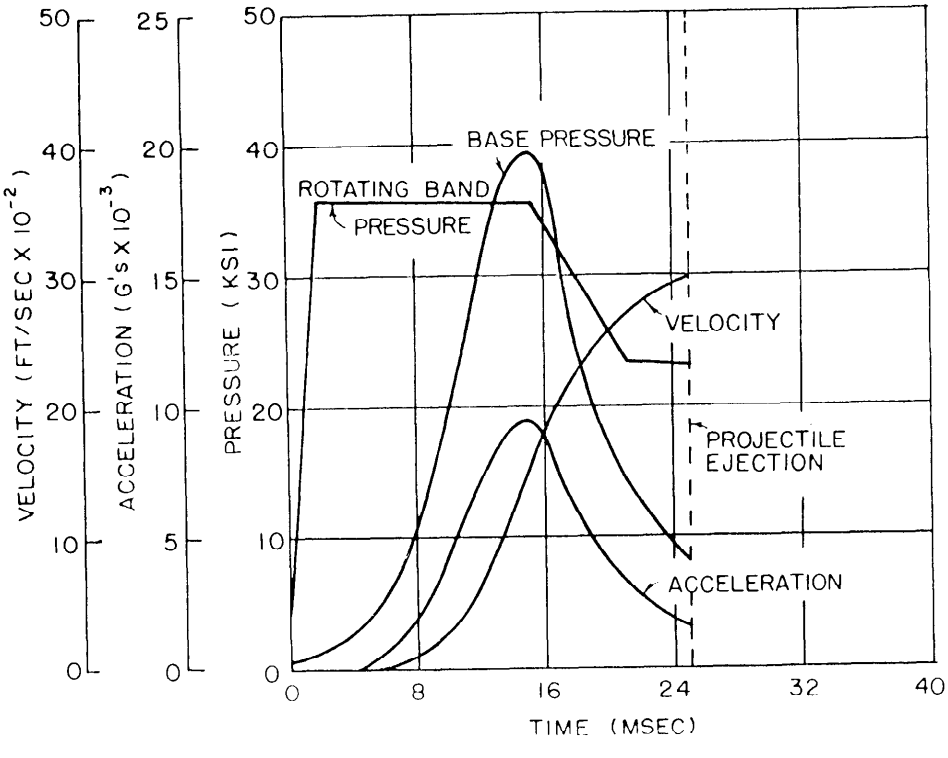

Figure 5. Loading History - A 175 mm, HE M437 Projectile Subjected to Zone 3 Charge

quadrilateral elements as shown in Figure 6. Only a few nodal points on the boundary need be specified; the remaining nodal points are obtained from an automatic mesh generating computer program. The grid was partitioned to place a finer grid at those areas of the body that are expected to undergo large stress.

COMPUTATIONAL RESULTS

The computational results presented in this investigation are based upon the following three major loading conditions as shown in Figure 5:

1) When rotating band pressure reaches the maximum value of 36,000 psi (245 MPa).

2) When both propellant gas pressure and setback force reach the peak.

3) At the time the projectile is ejected when the spin rate reaches the maximum at the muzzle end of the tube.

For each incremental of loading, the stresses and strains of each element and the displacement of each nodal point were calculated. The plastic flow has initiated within elements directly under the rotating band in the inner surface of the projectile at rotating band pressure reaching 25,000 psi (172 MPa). Based upon the Von Mises yield criteria, the equivalent stress for each element was calculated.

At maximum rotating band pressure, the material in the entire range below the rotating band is yielded. The plastic range in the projectile is indicated in Figure 7. The deformed configuration under maximum rotating band pressure is shown in Figure 8 by solid lines. The equivalent stress distribution along the projectile length at inner and outer surfaces is shown in Figure 9. The maximum equivalent stress has reached 85,300 psi (578 MPa) which is a little higher than the yield strength (σy = 85,000 psi = 584 MPa) and lower than the ultimate strength (σu = 90,000 psi = 620 MPa) of projectile material. The maximum plastic strain encountered is 0.004 in/in, which is relatively small.

At maximum propellant gas pressure and maximum setback force, the plastic flow has taken place in several places in the projectile as shown by the shaded areas in Figure 10. The deformed configuration is shown in Figure 11 by solid lines. The dashed line configuration is the undeformed configuration. The equivalent stress distribution along the projectile length at inner and outer surfaces is shown in Figure 12. The plastic range has been expanded several places between z = 1.6 inches (4.06 cm) and z = 17.3 inches (44 cm). The maximum equivalent stress in the projectile is 85,300 psi (587 MPa). The maximum plastic strain is 0.004 in/in.

At the time the projectile reaches the muzzle end while the spin rate has attained the peak, the maximum equivalent stress has only reached

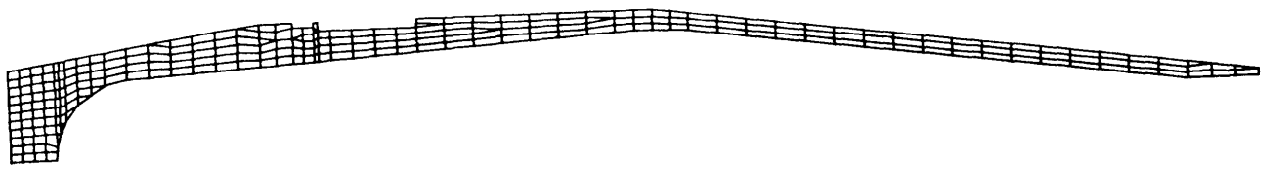

Figure 6. Finite Element Presentation of a Projectile

Figure 7. Plastic Zone in the Projectile at Maximum Rotating Band Pressure

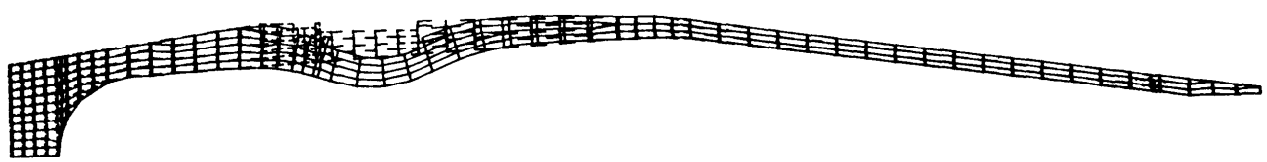

Figure 8. Deformed Grid Mesh at Maximum Rotating Band Pressure

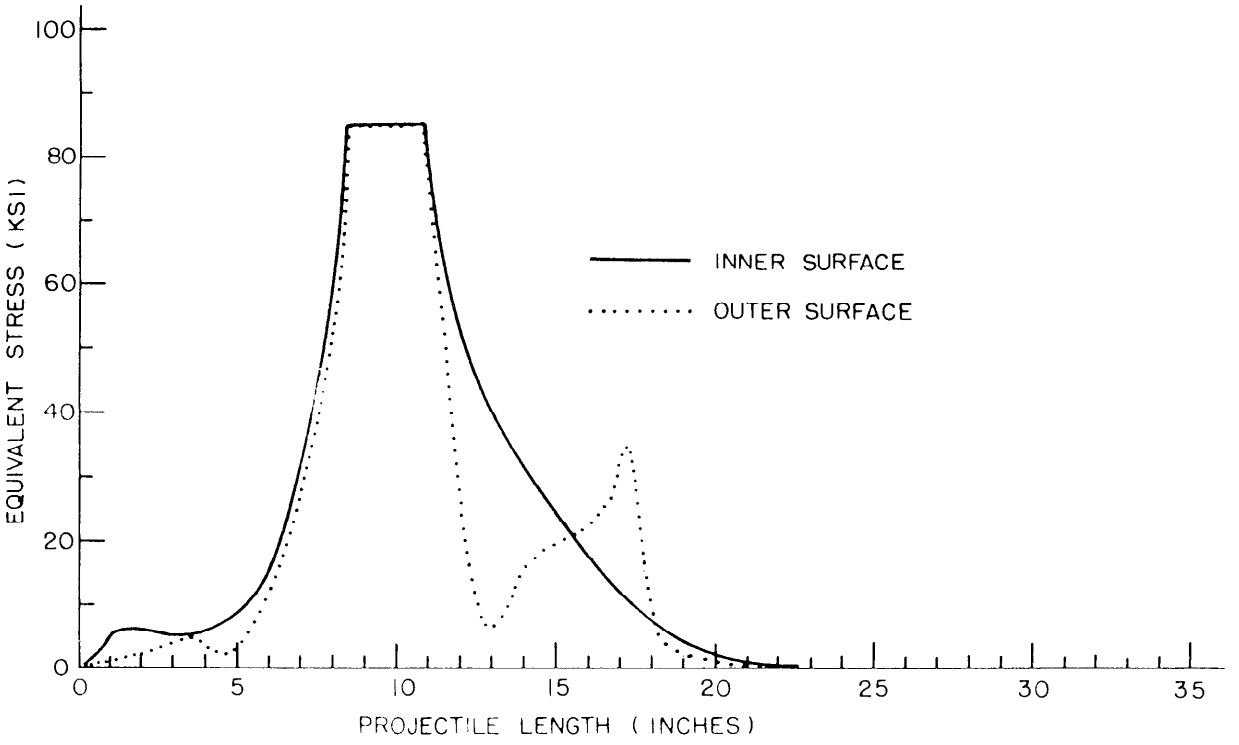

Figure 9. Equivalent Stress Distribution Along the Projectile While the Rotating Band Pressure Reaches the Maximum

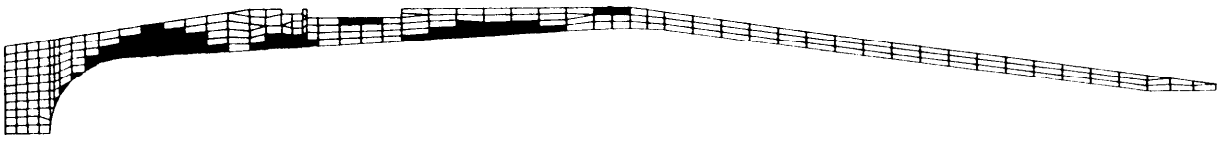

Figure 10. Plastic Zone in the Projectile at Maximum Propellant Gas Pressure and Maximum Setback Force

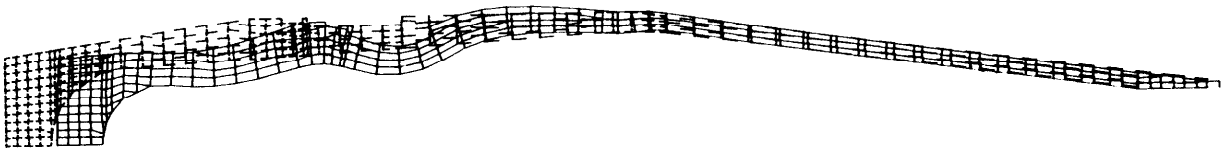

Figure 11. Deformed Grid Mesh at Maximum Propellant Gas Pressure and Maximum Setback Force

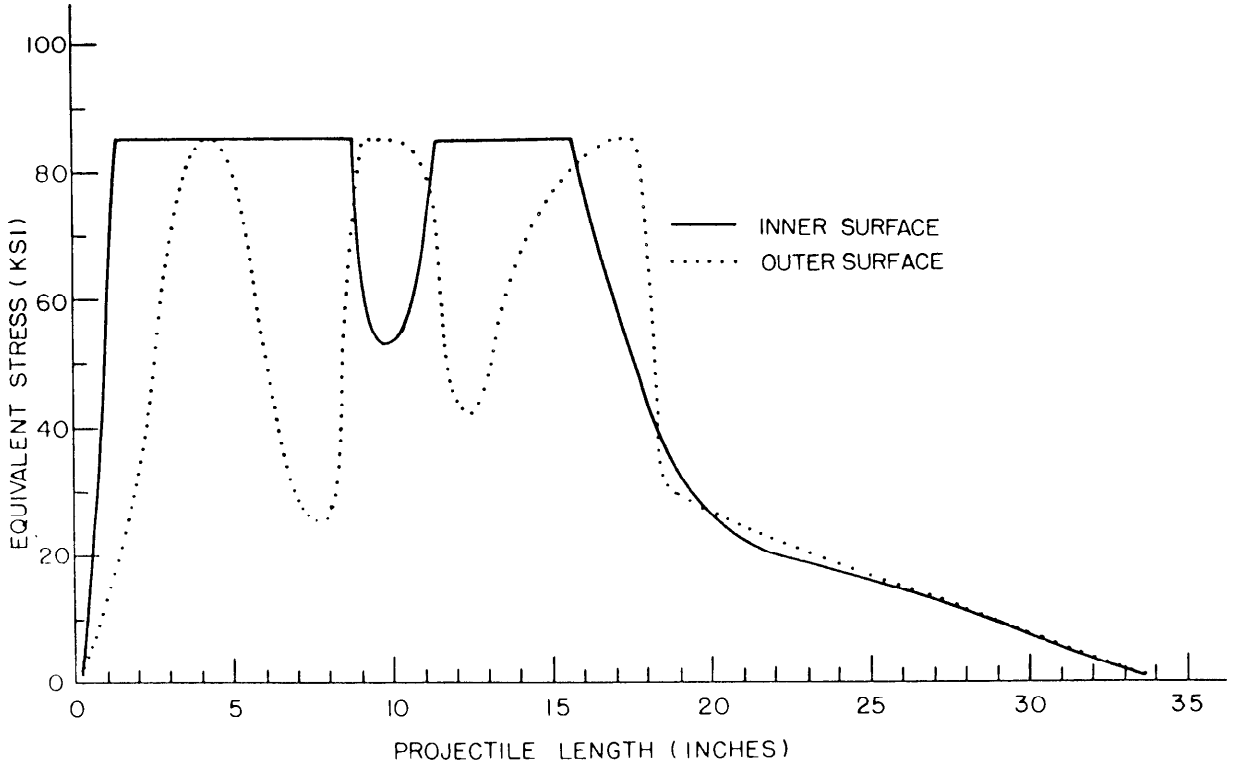

Figure 12. Equivalent Stress Distribution Along the Projectile at Maximum Propellant Gas Pressure and Maximum Setback Force

46,000 psi; hence the entire projectile body is in elastic range. The deformed configuration is shown in Figure 13.

The maximum equivalent stress of 85,300 psi (587 MPa) was reached during the entire loading process. This value is greater than the yielding strength (σy = 85,000 psi = 584 MPa) and smaller than the ultimate strength (σu = 90,000 psi = 620 MPa) of the projectile material. If the investigation was based on elastic analysis, the maximum equivalent stress could reach a value which would be much higher than the ultimate strength of the projectile material. This is the reason that a nonlinear analysis has been adopted, since a more rigorous stress analysis can only be obtained by using nonlinear theories of plasticity.

CONCLUSIONS

On the basis of Drucker's flow rule of plasticity, the Von Mises flow criterion, and the strain-hardening and compressibility properties of a material, a more rational rigorous nonlinear elastoplastic analytic method has been developed for analyzing and designing a projectile subjected to actual complicated firing conditions. In contrast to the traditional designing and analyzing techniques (theories of elasticity), the complex phenomenal plastic flow in the projectile has been taken into account.

Both nonlinear material response and geometric nonlinearity have been taken into consideration. Nonlinearity of material properties has been taken into account by use of theories of plasticity. Geometric nonlinearity has been considered by use of the finite element technique. An incremental loading procedure has been used to simulate the actual firing environment of a gun. The complete loading history which includes propellant gas pressure, rotating band pressure, setback force, and spin rate of a projectile was defined as function of time.

At each incremental of loading, the critical region is determined. In this region, the equivalent stress in general is above the yield strength of material; however, it is below ultimate strength of the material. The plastic strain has taken place in the region; however, maximum equivalent plastic-strain at inner surface is below 0.004 in/in, which is relatively small.

Based upon this investigation, the plastic zone in the projectile has been identified and accurately located for each incremental of loading which simulates the actual fire environment in a gun. The developed technique will provide a more rigorous stress analysis tool for projectile design. The potential design flaws and critical regions of a projectile can be identified before the projectile is made and tested.

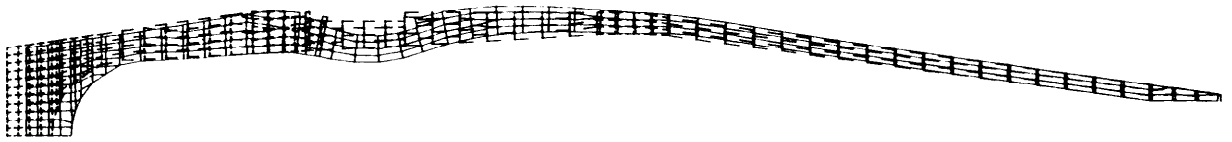

Figure 13. Deformed Grid Mesh as the Spin Rate Reaches the Maximum

REFERENCES

1. DePhillipo, T.E., and Booth, A.W., "Mathematical Model for Determining Stresses in Projectile Bodies", Report R-1939, Frankford Arsenal, Oct. 1969.

2. Mechanical Engineering Department, New York University, "Principal and Combined Stresses of the Shell, HE 155mm M197", Picatinny Arsenal Report, U38115.

3. Elder, A.S., Burns, B.P., and Hurban, J.M., "Stress Analysis of 175mm Projectile, HE M437", BRL Memorandum Report 2113.

4. Prager, W., "The Theory of Plasticity: A Survey of Recent Achievements (Hames Clayton Lecture)", Proc. Inst. Mech. Eng. 69 (1955).

5. Prager, W., "Nonisothermal Plastic Deformation", Proc. Koni, Ned. Akad., Van Weton, Series B, 61, NO (3), 1958.

6. Chu, S.C., "Nonisothermal Elastoplastic Deformation of Work-Hardening Solids", Paper presented at Joint ASME/ASCE Mechanics Conference, University of Colorado, 22-24 June 1981.

7. Chu, S.C., "An Incremental Approach to Nonisothermal Elastic-Plastic Deformation", Proc. 27th Conference of Army Mathematicians, 1981.

8. Drucker, D.S., "A More Fundamental Approach to Plastic Stress-Strain Relations", Proc. 1st U.S. National Congress Applied Mechanics, New York 1952.

9. Prager, W., "A New Method of Analyzing Stresses and Strains in Work-Hardening Plastic Solids", Journal App. Mech. Vol. 23, 1956.

10. Ziegler, H., "A Modification of Prager's Hardening Rule", Quarterly of Appl. Math. Vol. 17, 1959.

11. Zienkiewicz, O.C., "The Finite Element Method in Engineering Science", McGraw-Hill, 1971.

12. Marcal, P.V., and King, I.P., "Elastic-Plastic Analysis of Two-Dimensional Stress Systems by the Finite Element Method", Inter. J. Mech., Vol. 9, No. 3, 1967.

AUTHOR INDEX

Aboutorabi, M. R.	The University of Iowa	Iowa City, IA	405
Ahmad, J.	Battelle Columbus Labs	Columbus, OH	143, 177
Baker, D. J.	Army Aviation R&D Command	Moffett Field, CA	318
Barnes, C. R.	Battelle Columbus Labs	Columbus, OH	143
Bender, J. M.	Army Armament R&D Command	Aberdeen, MD	471
Beneker, C.	Parker Hannifin Corp.	Irvine, CA	439
Bostaph, G. M.	Army Aviation R&D Command	Hampton, VA	288
Chang, C. I.	Naval Research Labs	Washington, DC	129
Chen, P. C. T.	Army Armament R&D Command	Watervliet, NY	405
Cheng, Y. F.	Army Armament R&D Command	Watervliet, NY	454
Chu, S. C.	Army Armament R&D Command	Dover, NJ	481
Crenshaw, W. L.	Army Natick Labs	Natick, MA	43
deLorenzi, H. G.	General Electric Company	Schenectady, NY	203
Dumesnil, C. E.	Vought Corp.	Dallas, TX	159, 416
Elber, W.	NASA-Langley Research Ctr.	Hampton, VA	288
Elliott, G.	University of Toronto	Toronto, Canada	271
Ernst, H. A.	Westinghouse R&D Center	Pittsburgh, PA	215
Fanucci, J. P.	Kaman AviDyne	Burlington, MA	257
Finnegan, S.	Naval Weapons Center	China Lake, CA	28
Foye, R. L.	Army Aviation R&D Command	Moffett Field, CA	318
Gray, T. D.	Vought Corp.	Dallas, TX	159, 416
Hansen, J. S.	University of Toronto	Toronto, Canada	271
Heimdahl, O. E. R.	Naval Weapons Center	China Lake, CA	28
Hopper, A. T.	Battelle Columbus Labs	Columbus, OH	177
Houghton, C. D.	Army Materials & Mechanics Research Center	Watertown, MA	380
Houghton, W. W.	Army Materials & Mechanics Research Center	Watertown, MA	380
Howell, W. E.	NASA-Langley Research Ctr.	Hampton, VA	400
Huffington, Jr., N. J.	Army Armament R&D Command	Aberdeen, MD	13
Jordan, K. D.	Vought Corp.	Dallas, TX	416
Kanninen, M. F.	Battelle Columbus Labs	Columbus, OH	143, 177
King, A. O.	Army Materials & Mechanics Research Center	Watertown, MA	318
Kiwan, A. R.	Army Armament R&D Command	Aberdeen, MD	80
Landes, J. D.	Westinghouse R&D Center	Pittsburgh, PA	215
Leis, B. N.	Battelle Columbus Labs	Columbus, OH	177
Lempriere, B. M.	The Boeing Aerospace Co.	Seattle, WA	66
Lenoe, E. M.	Army Materials & Mechanics Research Center	Watertown, MA	7
Lush, A.	Kaman AviDyne	Burlington, MA	43

Matthews, Jr., C. M., BG	Army Tank-Automotive Command	Warren, MI	9
McElman, J. A.	University of Lowell	Lowell, MA	380
Merkord, D. L.	Vought Corp.	Dallas, TX	159
Milligan, R. W.	Kaman AviDyne	Burlington, MA	43
Neal, D. M.	Army Materials & Mechanics Research Center	Watertown, MA	343
Papaspyropoulos, V.	Battelle Columbus Labs	Columbus, OH	177
Petrie, S. P.	Army Materials & Mechanics Research Center	Watertown, MA	318
Plumer, J. A.	Lightning Technologies, Inc.	Pittsfield, MA	400
Rathke, R. A.	Martin Marietta Corp.	Denver, CO	238
Raymond, L.	METTEK Labs	Santa Ana, CA	439
Ringers, B. E.	Army Armament R&D Command	Aberdeen, MD	96
Roylance, M. E.	Army Materials & Mechanics Research Center	Watertown, MA	380
Rummel, W. D.	Martin Marietta Corp.	Denver, CO	238
Scavullo, M. A.	Army Armament R&D Command	Watervliet, NY	110
Schulz, J. C.	Naval Weapons Center	China Lake, CA	28
Sibert, G. W., COL	Army Materials & Mechanics Research Center	Watertown, MA	3
Sih, G. C.	Lehigh University	Bethlehem, PA	129
Spiridigliozzi, L.	Army Materials & Mechanics Research Center	Watertown, MA	343
Tennyson, R. C.	University of Toronto	Toronto, Canada	271
Trantina, G. G.	General Electric Company	Schenectady, NY	203
Underwood, J. H.	Army Armament R&D Command	Watervliet, NY	110
Wu, H. C.	The University of Iowa	Iowa City, IA	405